Exploitation of Super(de)wettability *via* Scalable Hierarchical Surface Texturing

William S. Y. Wong

A thesis submitted for the degree of

Doctor of Philosophy at

The Australian National University

December 2017

Contents

Abstract

The field of wettability is an age-old topic that has been revitalized in the last two decades. Historically, the diverse physical phenomena of wetting has influenced the development of inventions that dates back to the paleolithic era (2,600,000 to 10,000 BC) in the form of charcoal and ochre -based cave paintings, or the mesolithic (10,000 to 5,000 BC) and neolithic (5,000 to 2,000 BC) periods as pottery and soaps. Since the end of the Stone Age, human civilizations and scientific discoveries have progressed by leaps and bounds. Despite the advances in metallurgy, optics, chemistry, mechanics, mathematics and electricity, our understanding of fluid-surface interactions remained stagnant until 1804. Between 1804 and 1805, Thomas Young[1] described the concept of a wetting contact angle, which controls the equilibrium shape of a fluid droplet on a surface, thus making wettability a quantified branch of physics. The late entry of this scientific field is astounding, considering the ubiquitousness of water on Earth. Despite Young's discoveries, the area remained largely unexplored. Work on wettability was intermittent, with Edward Washburn[2] on capillary effects in 1921 and later on, Robert Wenzel[3] and Cassie-Baxter[4] in 1936 and 1944 on the wetting of rough interfaces.

In 1997, almost exactly 20 years ago, the field was rejuvenated by the corresponding discoveries of superhydrophilicity (water droplets spread into a sheet) and superhydrophobicity (water droplets ball up), by Wang et al.[5] and Neinhuis et al.[6,7] respectively. Since their work into these distinct super(de)wetting states, the field has grown exponentially (Figure 1). Today, its revival can be attributed to biomimetics (engineering mimicry / imitation of life) and a revolutionized understanding behind super(de)wetting mechanisms that are found in nature. The precise combination of hierarchical (multi-scale) texturing with select surface chemical composition is vital towards fabricating interfaces with specialized wetting properties. Knowledge behind the careful control of surface texturing holds immense potential for enabling a plethora of user-defined functional interfaces. As of the time of writing, the field of wettability encompasses multiple domains, such as superhydrophilicity (water-loving),[8] slippery superhydrophobicity (water-fearing),[9] adhesive superhydrophobicity (an unintuitive love-fear relationship with water),[10]

superoleophobicity (oil-fearing), superamphiphobicity (water- and oil-fearing),[11] superomniphobicity (all-fearing)[12] as well as a range of other important intermediary, cross-environment wetting states.

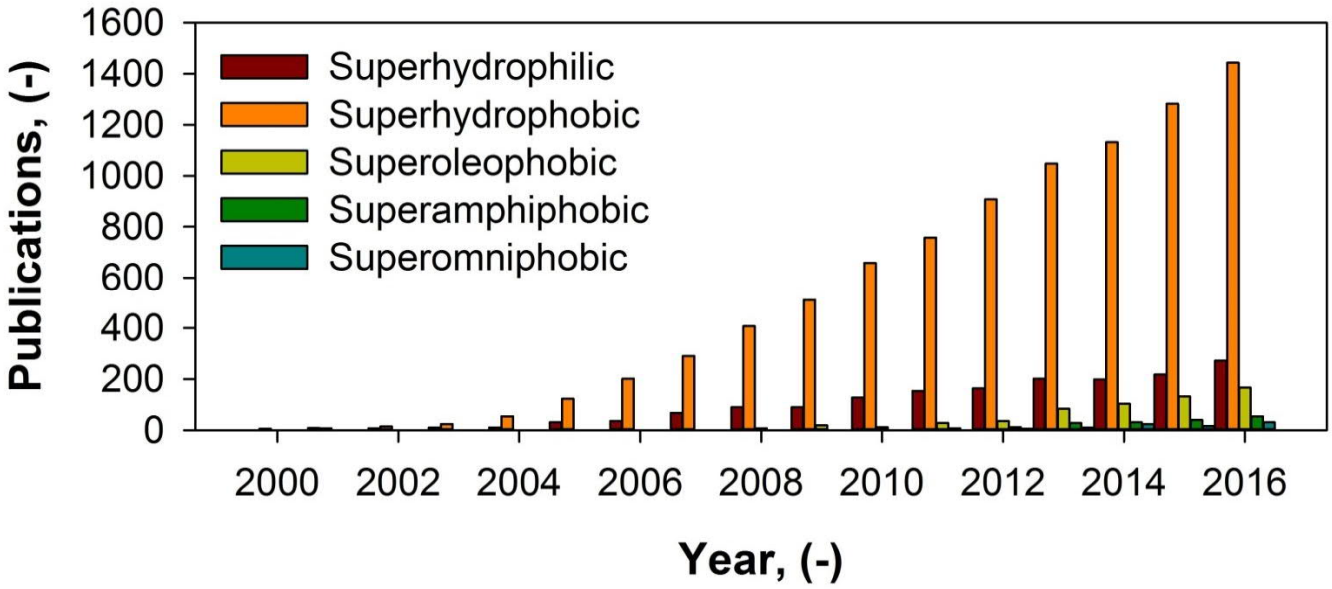

Figure 1. Burgeoning momentum in the field of super(de)wettability. Number of publications vs. year: superhydrophilicity, superhydrophobicity, superoleo(amphi)phobicity and superomniphobicity.

Methods employed for achieving super(de)wettability can be broadly classified under 2 sub-classes. The first relies on intricate top-down photolithography (-drawing with light) or templating-based designs[12,13] while the other uses the realms of chaotic, but deterministic and scalable bottom-up self-assembly[11,14]. Both routes are promising for the development of unique super(de)wetting states, albeit with considerable drawbacks on both fronts. For instance, while lithography and templating have demonstrated exemplary surface texturing precision and super(de)wetting performance, these methods remain limited by poor scalability, complexity and costs in instrumentation and operation. Alternatively, scalable and cheap bottom-up self-assembly methods can exist within complex electro-, hydro-, aero-, thermal- or thermo-dynamically varied regimes. Consequently, each system requires intense cross-optimization research efforts in determining niche operating parameters.

In this work, we explore a series of highly promising hierarchically structured material interfaces that were enabled by understanding, taming and controlling scalable but chaotic bottom-up methods. To this end, we demonstrate their potential within the entire super(de)wetting spectrum, showcased through a series of coatings and further exemplified by functional micro(fluid)mechanical systems (M-F-MS).

Declaration of Authorship

I, William S. Y. Wong, hereby declare that this thesis titled: “Exploitation of Super(de)wettability via Scalable Hierarchical Surface Texturing” and the work presented in it are my own. I confirm that:

- This work was done wholly while in candidature for a research degree at the Australian National University.
- Where I have consulted the published work of others, this is always clearly attributed. References are provided collectively as a whole at the end of this manuscript. This encompasses both unpublished and published works.
- Where I have quoted from the work of others, the source is always given. With the exception of these quotations, this thesis is my own original work.
- I have acknowledged all main sources of help.

_____

William S. Y. Wong

December 2017

August 2018 (Revised)

List of Publications

This thesis is presented as a combination of published papers; manuscripts prepared for submission and traditional thesis chapters. All published and unpublished papers were written during the course of supervised candidature and were based upon research undertaken during the course of candidature. Published papers are subject to copyright by the appropriate publishing house. These articles were reproduced with permission and copyright notices are cited at the corresponding declaration pages.

Publications and manuscripts included as chapters of this thesis (unless otherwise stated):

1. **Wong, W. S. Y.*** and Tricoli, A.*****, Multi-Scale Engineering and Scalable Fabrication of Super(de)wetting Coatings, *Advanced Coating Materials* **2018**, Wiley-Scrivener.
   (Invited Contribution, Accepted, In Press).

2. **Wong, W. S. Y.*** and Tricoli, A.*, Cassie-Levitated Droplets for Distortion-Free, Low Energy Solid-Liquid Interactions.
   ACS Applied Materials and Interfaces 2018, 10, 13999-14007. (Not included)

3. **Wong, W. S. Y.**, Gengenbach, T., Nguyen, H. T., Gao, X., Craig, V. S. J. and Tricoli, A., Dynamically Gas-Phase Switchable Super(de)Wetting States by Reversible Amphiphilic Functionalization: A Powerful Approach for Smart Fluid Gating Membranes.
   Advanced Functional Materials 2017, 28, 1704423. https://doi.org/10.1002/adfm.201704423.

4. **Wong, W. S. Y.**, Liu, G., and Tricoli, A., Superamphiphobic Bionic Proboscis for Contamination-Free Manipulation of Nano- and Core-Shell Droplets.
   Small **2017**, *1603688.*

5. **Wong, W. S. Y.**, Liu, G., Nasiri, N., Hao, C., Wang, Z. and Tricoli, A., Omnidirectional Self-Assembly of Transparent Superoleophobic Nanotextures.
   ACS Nano **2016**, 11 (1), 587-596.

6. **Wong, W. S. Y.**, Li, M., Nisbet, D. R., Craig, V. S. J., Wang, Z. and Tricoli, A., Mimosa Origami: a Nanostructure-enabled Directional Self-Organization Regime of Materials.
   Science Advances **2016**, 2, e1600417.

7. **Wong, W. S. Y.**, Stachurski Z. H., Nisbet D. R. and Tricoli, A., Ultra-Durable and Transparent Self-Cleaning Surfaces by Large-Scale Self-Assembly of Hierarchical Interpenetrated Polymer Networks.
   ACS Applied Materials and Interfaces **2016**, 8 (21), 13615-13623.

8. **Wong, W. S. Y.**, Gutruf, P., Sriram, S., Bhaskaran, M., Wang Z., and Tricoli, A., Strain Engineering of Wave-like Nanofibers for Dynamically Switchable Adhesive/Repulsive Surfaces.
   Advanced Functional Materials **2016**, 26, 399-407.

9. **Wong, W. S. Y.**, Nasiri, N., Liu, G., Rumsey-Hill, N., Craig, V. S. J., Nisbet, D. R. and Tricoli, A., Flexible Transparent Hierarchical Nanomesh for Rose Petal-Like Droplet Manipulation and Lossless Transfer.
   Advanced Materials Interfaces **2015**, 2, 1500071.

10. **Wong, W. S. Y.**; Nasiri, N.; Rodriguez, A. L.; Nisbet, D. R.; Tricoli, A., Hierarchical amorphous nanofibers for transparent inherently super-hydrophilic coatings.
    Journal of Materials Chemistry A **2014**, 2, 15575-15581.

#1st authorship denotes a *ca.* 75% overall contribution to the 1) idea, 2) experiments, 3) data analysis and interpretation, 4) analytical computation and 5) drafting of the manuscript. Includes *ca.* 40% contribution during the technical review and response process.
*Corresponding authorship denotes at least 50% contribution during the technical review and response process.

“Das Volumen des Festkörpers wurde von Gott geschaffen, seine Oberfläche aber wurde vom Teufel gemacht.”

“God created solids, but the devil made their surfaces.”

Wolfgang Pauli (1900-1958),

Nobel Laureate in Physics (1945)

Acknowledgements

I would like to firstly acknowledge my colleagues and friends in Canberra, whose unwavering support along this remarkable journey of self-realization, is much appreciated. The shared pain and joy of each project's success and failure will forever be fondly remembered. In particular, I would also like to thank the many fellow (Ph.D) students at the RSE and RSPE for their help and advice along the way. In alphabetical order: A. L. Rodriguez, C. Asselineau, C. Hu, G. Liu, H.T. Nguyen, M. Hamidi, M. Taheri, M. Quinn, N. Rumsey-Hill, R. Bo, S. Kumar and X. Gao.

I would acknowledge the support of my supervisors, A/Prof. Antonio Tricoli, Dr. Zbigniew Starchurski and Prof. Vincent Craig, who constantly encouraged me to explore the infinite possibilities available behind each of my projects. The technical expertise and experimental aid provided by Zbigniew and Vincent were vital towards realizing numerous goals and project outcomes. The countless theoretical discussions with them have helped to vastly improve my understanding of this field of research. I would like to thank the help, instrumentational support and advice rendered by my colleagues at the Research School of Engineering (RSE) and Research School of Physics and Engineering (RSPE), in particular, Dr. Adrian Lowe and Dr. Takuya Tsuzuki. I would like to thank the ANU and the Australian Federal Government for the Ph.D research fellowship, without which none of this would have ever been possible. Having since departed the ANU to the Max Planck Institute for Polymer Research in Mainz, Germany for my postdoctoral position, I would also like to thank my current supervisors for their help, understanding and assistance during the final leg of my Ph.D: Prof. Dr. Doris Vollmer and Prof. Dr. Hans Jürgen Butt. I gratefully thank and acknowledge many at the Physics at Interfaces group for their welcoming hospitality. I would also like to acknowledge the European Commisson for funding my Marie Skłodowska-Curie ESR fellowship, under the Horizon 2020 program.

Gratitude extends to our collaborators, nationally and internationally. I thank Dr. Zuankai Wang and his group at the City University of Hong Kong for their experimental, theoretical and miscellaneous support to our work. I would like to thank RMIT's A/Prof. Madhu Bhaskaran and Dr. Philipp Gutruf, CSIRO's Dr. Thomas Gengenbach and countless other collaborators, all of whom I am privileged and honoured to work with. The assistance provided by our support staff, in particular, Colin Carvolth, is also gratefully acknowledged.

Last but not least, I would like to thank God, and my family for tolerating my absence during these years of pursing my dream in this stunningly beautiful part of Australia. I will be eternally grateful for the emotional support rendered during some of my darkest and toughest times.

Abbreviations

CA	Contact Angle (WCA- Water Contact Angle)
SA	Sliding Angle
TA	Tilt Angle
CAH	Contact Angle Hysteresis
ACA	Advancing Contact Angle
RCA	Receding Contact Angle
SSA	Specific Surface Area
DIDO	Drop-In, Drop-Out
UV	Ultra-Violet
SEM	Scanning Electron Microscope
TEM	Tranmission Electron Microscope
3D	Three-Dimensional (1D, One, 2D, Two)
RPM	Revolutions per Minute
VDW	Van der Waals
PVD	Physical Vapor Deposition
CVD	Chemical Vapor Deposition
APCVD	Atmospheric Pressure Chemical Vapor Deposition
PECVD	Plasma-Enhanced Chemical Vapor Deposition
HFCVD	Hot-Filament Chemical Vapor Deposition
MOCVD	Metal-Organic Chemical Vapor Deposition
ALD	Atomic Layer Deposition
PDMS	Polydimethylsiloxane
PS	Polystyrene
PVC	Poly(vinyl chloride)
PMMA	Poly(methyl methacrylate)
PCL	Polycaprolactone

PVP	Polyvinyl pyrrolidone
PTFE	Polytetrafluoroethylene
PET	Poly(ethylene terephthalate)
PI	Polyimide
PP	Polypropylene
PC	Polycarbonate
PVA	Poly(vinyl alcohol)
PE	Polyethylene
PAA	Poly(acrylic acid)
PAH	Poly(allylamine hydrochloride)
PDDA	Poly(diallyldimethylammonium chloride)
PEDOT	Poly(ethylenedioxythiophene)
PHEMA	Poly(2-hydroxyethyl methacrylate)
PLA	Poly(lactic acid)
PLLA	Poly(lactic acid) with L-Lactide
PDLA	Poly(lactic acid) with D-Lactide
PGA	Poly(γ-glutamic acid)
PVDF	Polyvinylidenefluoride
PPy	Polypyrrole
PMC	Perfluoromethacrylates
PNIPAAm	Polyisopropylacrylamide
MMA	Methyl methacrylate
St	Styrene
nBA	N-butyl acrylate
SiMA	3-[tris[(trimethylsilyl)oxy]-silyl]propyl methacrylate
EDOP	3,4-ethylenedioxypyrrole
ProDOP	3,4-propylenedioxypyrrole
NMP	N-methyl pyrrolidone

HF	Hydrogen fluoride
HFIP	Hexafluoroisopropanol
HFP	Hexafluoropropylene
HI	Hydrogen iodide
AFPB	Alkyl-fluorobenzene
PFOTS	1H,1H,2H,2H-perfluorooctyltrichlorosilane
PFTS	1H,1H,2H,2H-perfluorodecyltriethoxysilane
PFDTCS	Perfluorodecyltrichlorosilane
PFOA	Perfluorooctanoic acid
FAS	Fluoroalkylsilane
POSS	Polyhedral oligomeric silsesquioxane
Fluoro-POSS	(1H,1H,2H,2H-heptadecafluorodecyl)$_8$SiO$_{12}$-POSS
F-POSS	Fluoro-POSS
TMMOS	Trimethylmethoxysilane
TEOS	Tetraethyl orthosilicate
TMPSi	Trimethoxypropyl silane
APS	3-aminopropyl-triethyoxysiloxane
AAO	Anodic aluminum oxide
GO	Graphene oxide
CNT	Carbon nanotube
SWNT	Single-wall nanotube
MWCNT	Multi-wall carbon nanotube
SNT	Silica nanotube
NW	Nanowires
LbL	Layer-by-Layer
LB	Langmuir-Blodgett
SAMs	Self-Assembled Monolayers
SiO_2	Silica

TiO_2	Titania
Al_2O_3	Alumina
Mn_3O_4	Manganese Oxide
ZnO	Zinc Oxide
SnO	Tin Oxide
F-SiO_2	FAS-fluorinated Silica
F-TiO_2	FAS-fluorinated Titania
NP(s)	Nanoparticle(s)
SLIPS	Slippery Fluid Infused Porous Surfaces
MFMS	Microfluidmechanical Systems

1. Introduction

The customization, design and fabrication of surfaces with specialized wetting properties is a field of science and engineering that has had immense influence on both research and industrial sectors over the last two decades.[5,12,15-18] From a historical perspective, the field of superwettability can be traced to its roots in biomimetics.[19] Today, a multitude of methods and materials are readily available for facilitating the achievement of many unique wetting states. Transcending beyond simple hydrophobicity and hydrophilicity, a variety of super(de)wetting phenomena is now known to exist. Many of such discoveries correspond to their biological inspirations, such as the superwetting-driven nutrition of superhydrophilic Spanish moss (*Tillandsia usneoides*);[20] the self-cleaning superhydrophobic lotus (*Nelumbo nucifera*);[7] the highly adhesive superhydrophobic roses (Rosaceae);[21] or the oil-impermeable springtail (*Folsomia candida*) exoskeleton.[22] In late-2000s to mid-2010s, the geometrical optimization of a re-entrant profile[11] provided additional insight beyond biomimicry, and has since enabled the realization of the now largely artificial superomniphobic state[12]. Since the first foray into the field of wettability by Young,[1] Wenzel[3] and Cassie-Baxter[4], leaps and bounds in our understanding of interfacial wettability has been achieved.[23] Today, we can engineer surfaces that exhibit or even dynamically transit from superamphiphilic to superamphiphobic states. Wettability has also been investigated not just in-air, but also extends to more complex surface-in-water or surface-in-oil models.[19] Despite the very different interfacial profiles, extreme wetting states (super-"X"-philic / phobic) rely on exploiting hierarchical, multi-modal, micro- and nano- textures for function. The infancy of the field was initially cradled by precise, top-down nanotechnological methods. However, the development and advancement of methods beyond top-down lithography or templating techniques are essential towards furthering the industrial maturation of the field. Scalable design of functional super(de)wetting interfaces possesses potential for interdisciplinary domains ranging from microfluidics,[24] nano-, micro-droplet manipulation,[25,26] self-assembly,[27] oil-water separation,[28] and advanced coatings technologies[29].

1.1. Industrial Significance and Applications

The demand for specialized wetting interfaces stems from both the research and industrial sectors. Current discoveries have already revolutionized how we interact with various fluid systems (Figure 1.1). Inherently superhydrophilic materials, sustained by radical-induced self-cleaning properties,[5] have led to the invention of anti-fogging glass.[5,30] Superhydrophilicity has also been used for remediating bio-fouling,[31,32] lab-on-a-chip styled micropatterning,[15] and even in advanced cooling systems for enhanced heat transfer[33]. Superhydrophobicity has proven to be equally beneficial, with immense promise for corrosion protection,[29] anti-icing,[34] drag reduction,[35] stain-proof coatings,[36] high-temperature catalysis,[37] microfluidics,[38-40] and nano-droplet manipulation[10,25,26,41-43]. In recent years, the novel combination of these extreme properties garnered new perspectives, with demonstrated potential for fog-harvesting,[44] fluid patterning,[15,45,46] oil-water separation,[47] self-assembly[27] and even smart fluid-gating membranes[48,49]. The later discovery of the superior superoleo(amphi)phobic state unveiled even greater potential, demonstrating anti-oil fouling properties,[12,50-59] manipulation of complex fluids,[50,60] fluid separation membranes,[52,53,61,62] self-powered fluid-transportation,[63,64] stimuli-responsive membranes,[50] and even immersion-stable plastron layers.[22] The final frontier of superdewetting was discovered in the form of superomniphobicity, which showcases perfectly contamination-proof capabilities even against ultra-low surface tension[1] fluids (10-20 mN/m).[12,65,66]

Despite the very different super(de)wetting properties and associated applications behind these functional interfaces, the trifecta achievement of 1) facile scalability, 2) robust and stable states of super(de)wetting and 3) highly transmissive transparency[29,67,68] has still remained a far prospect. Even today, researchers in the field have rarely demonstrated success on all three fronts. Maturation

[1] Water has a surface tension of 72.8 mN/m while organic oils and solvents typically have surface tensions of 30-35 mN/m and 25-30 mN/m respectively. A lower surface tension tends to result in poorer intermolecular cohesion within a fluid droplet, and thus fluid spread / wetting over a surface.

of the field has, however, led to the reliable achievement of at least two of these three fundamental requirements, culminating in intensified interest by commercial and industrial sectors.

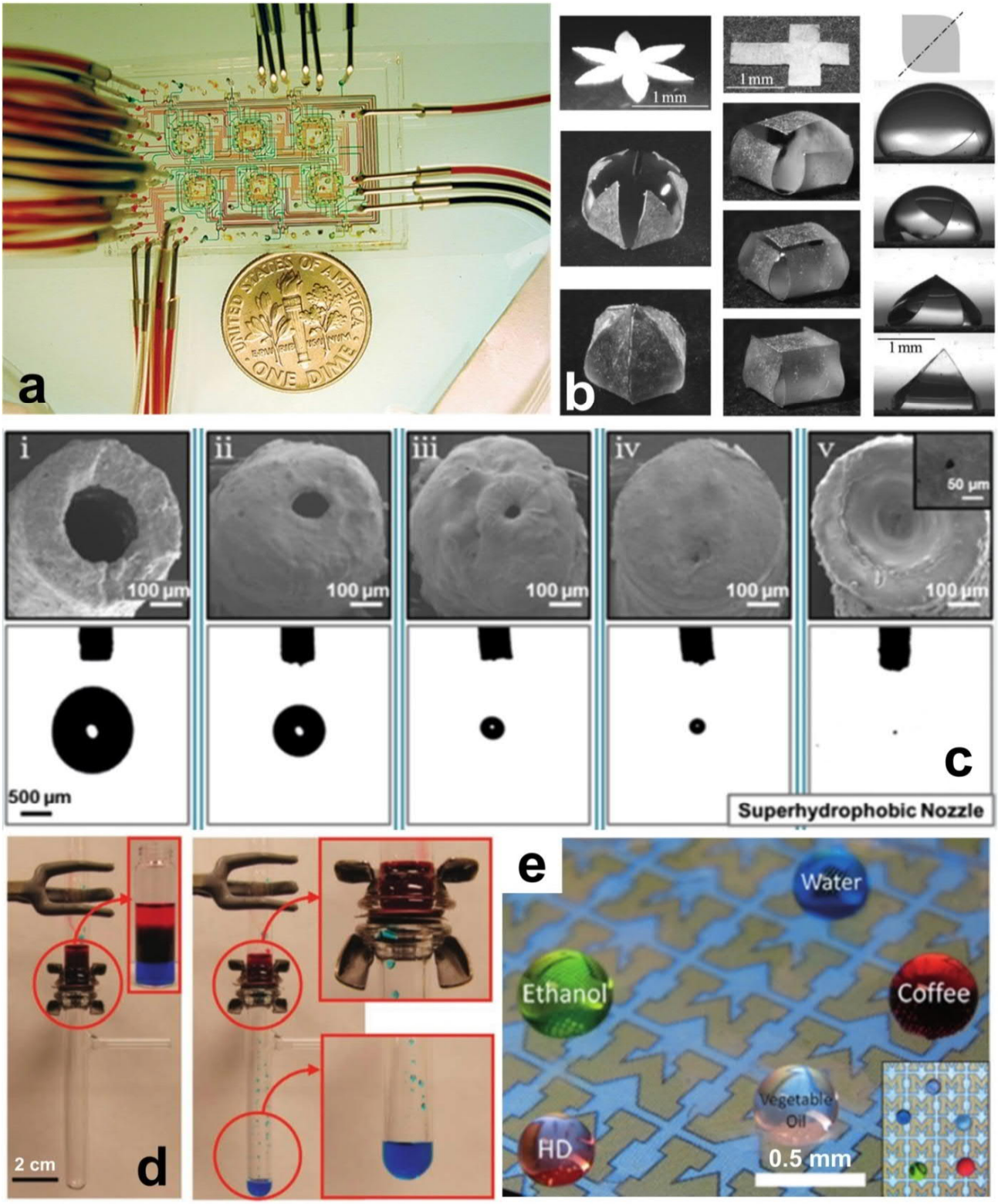

Figure 1.1. Science of wettability in action. a) Microfluidic chips with micro- and nano- sized channels.[69] b) Fluidic origami and the self-assembly of materials through exploiting surface tension-driven bending of thin films.[27] c) Ultrafine micro- and nano- water droplet production through superhydrophobic nozzles.[25] d) On-demand oil-water separation.[70] e) Advanced super-phobic coatings technologies.[66]

1.2. Overview of Synthetic Processes

The synthetic routes for micro- and nano-structured materials are often split into two distinctive philosophical groups. The first variant comprises of a series of top-down methods, such as the traditional method of templating.[10] Today, top-down techniques have greatly expanded into more sophisticated means such as optical and nano- lithography. These methods are capable of fabricating a variety of intricate interfacial architectures, such as pillars,[39,71] textured pillars,[72] cones,[73] inverse trapezoids,[74] T-shaped hoodoos[75] and even doubly re-entrant mushroom-like structures[12]. However, these methods are largely plagued by poor scalability, draconian requirements and costs in instrumentation and operation.

The second variant utilizes bottom-up self-assembly. It is facile, rapid and typically much cheaper. In contrast to the ordered designs and steps attributed to lithography, bottom-up techniques use highly chaotic but deterministic regimes of electro-, hydro-, aero-, thermal- and / or thermo-dynamics in achieving structural design and function.[76] Despite the increased research effort needed in determining niche operating domains, this route is generally not limited by scale. Today, the family of techniques in bottom-up self-assembly ranges from intra-, inter-, macro- and supramolecular-methods.[76] In this work, we explore 3 promising techniques for the scalable design of hierarchical features for super(de)wetting (Figure 1.2).

1) Liquid Flame Spray Pyrolysis

Flame pyrolysis is a well-known technique in nanoparticle (NP) research.[77-79] The method is capable of rapidly synthesizing three-dimensional (3D) fractal nanomaterials with ultra-high specific surface areas (SSA).[80,81] This unique nanoparticle (NP) processing technique enables the synthesis of both coatings and bulk powders with tunable thicknesses, particle and agglomerate sizes. Materials synthesized exhibit ultra-high porosity and unique roughness profiles. This is a promising method that has yet to be extensively investigated for super(de)wettability.

2) Electrospinning

Electrospinning is a technique bearing roots from research in biomaterials engineering.[82] This method enables the synthesis of one-dimensional (1D) cylindrical fibers with tunable potential for 3D micro- and nano- bead-like structures. Coating roughness can be varied by virtue of introducing these multi-scale structures.[83] Such cross-dimensional combinatory profiles supplements the field of hierarchical coatings while bearing promise for the synthesis of micro-porous, flexible and free-standing films with tunable tensile and wetting properties.[84]

3) Aerosolized Wet-Spray

Aerosolized coating precursors (wet-spraying) is one of the most industrially-friendly, hassle-free techniques that can be easily ported from the laboratory to manufacturing or even end-users. Coatings developed from this technique are typically denser than the two methods described before, but morphological geometries remain highly tunable. This depends largely on the precursors and substrates used, and can result in spray-on fibers,[85] papillae,[86] fractal agglomerates,[87] nano-ribbons and nano-rods.[88]

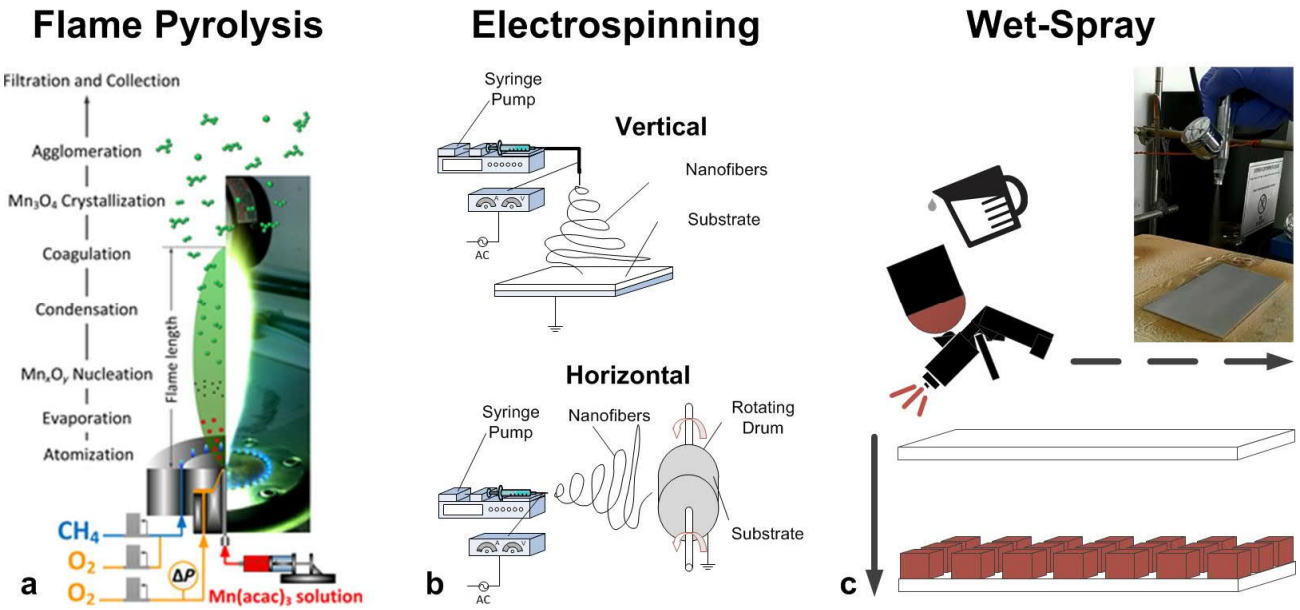

Figure 1.2. Proposed bottom-up self-assembly methods. Scalable aerosol-based techniques for developing hierarchically structured coatings in this work: a) liquid flame spray pyrolysis,[81] b) electrospinning, c) wet-spray-coatings with bottom-up self-structuring polymeric materials.

1.3. Aim and Purpose of Research

The work here highlights the use of bottom-up techniques for creating highly scalable super(de)wetting interfaces which rival the performance demonstrated by complex top-down methods. The successful use of such industrially-scalable systems in enabling high performing (de)wetting functional interfaces will be of interest to many cross-disciplinary fields. To achieve these goals, we probed the chaotic but deterministic bottom-up processes[89-92] to understand, control and exploit the mechanics behind micro- / nano-structural and intramolecular assembly. Taming such chaotic behaviors allowed us to exploit their inherently deterministic nature for the precise control and development of specific surface geometries.[89,92] The culmination of our research achievements is epitomized in the facile development of a range of specialized super(de)wetting states (Figure 1.3), with engineering proof-of-concepts that showcase their massive potential for sophisticated microfluidmechanical systems (MFMS).[89,90,93,94]

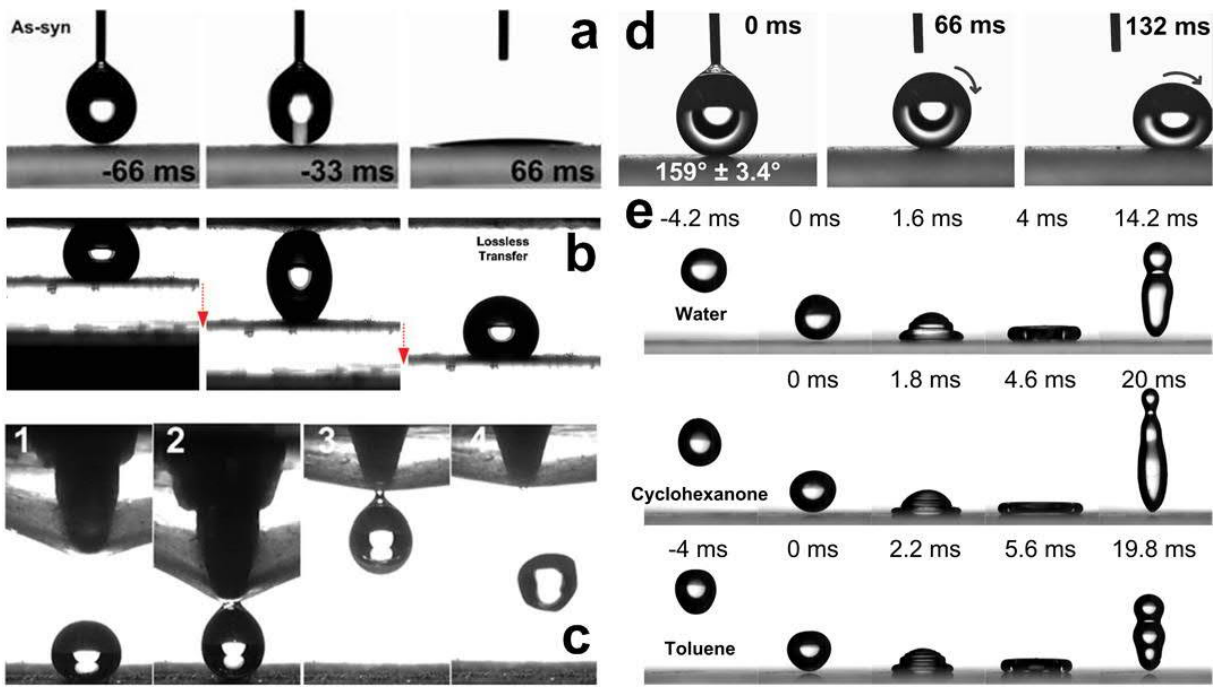

Figure 1.3. Super(de)wetting spectrum. Scalable development of a) superhydrophilic,[95] b) petal-like adhesive superhydrophobic,[89] c) petal-to-lotus adhesive-to-repulsive superhydrophobic,[90] d) low-hysteresis lotus-like superhydrophobic[91] and e) superoleo(amphi)phobic surfaces.[92]

This work supplements the toolboxes of nanotechnologists and surface scientists with novel scalable methods that may soon realize real-world micro- and nano- fluidic control applications.

1.4. Structure of Thesis

Chapter 1 illustrates a broad overview of the field of research. It explains the motivation behind the research undertaken, potential industrial implications as well as the methods employed.

Chapter 2 highlights key literature that relates directly to this work's objective: its inspiration, state-of-the-art methods, their associated performance and drawbacks as well as short sections on rationalizing conceptual designs for resolving drawbacks sustained by prior art. Each unique super(de)wetting state will be covered comprehensively. While the core of this manuscript is targeted at bottom-up self-assembly techniques, top-down methods will also be briefly acknowledged, owing to their key foundational roles in the field. We also propose re-defined sub-classifications, in order to better demarcate key performing limits and associated exemplifications.

Chapters 3-10 will highlight the key research findings of our work, with a primary focus on the scalable synthesis of super(de)wetting surfaces. We will traverse through the entire currently known spectrum of wettability, going from superhydrophilicity up to superoleo(amphi)phobicity. Within each chapter, we describe the synthetic technique of choice, the hierarchical (multi-scale)[2] structural and chemical composition of the resulting interface, detailed characterization of its properties as well as its associated super(de)wetting performance. We have also chosen, on occasions, to explore potential applications behind these different wetting behaviors for functional engineering purposes. These findings are segmented into separate chapters, which possess their own introductions, results and discussions, conclusions and experimental sections, which were extracted in part or whole from published work.

Chapter 11 represents the summary of our findings and their contributions to the field. We briefly discuss the future prospects of the field and the most promising areas in the coming years.

[2] [2] Hierarchical refers to the presence of multi-scale features (at least 2 levels), *e.g.* micro- and nano- scale structures. Fractal morphologies are naturally hierarchical; whose multi-scale dimensions can sometimes extend to ≥ 3 levels. These references will be used repeatedly and interchangeably throughout the thesis.

2. Literature Review[3]

2.1. Fundamentals of Wettability

In 1804, Thomas Young investigated the cohesive forces behind interactions at fluid-interfaces, surface tensions, and capillary effects. His work culminated in the description of contact angle (CA), thus founding the field of wettability.[1] Young's equation is a simple but elegant formula that constitutes the basis of the field today.[19] A perfectly flat solid (S) is interfaced with 2 fluids, the air / gas / vapor (A/G/V) and the liquid (L) phases: A liquid droplet resting on a flat horizontal surface will form a naturally occurring bead-like profile (Figure 2.1).

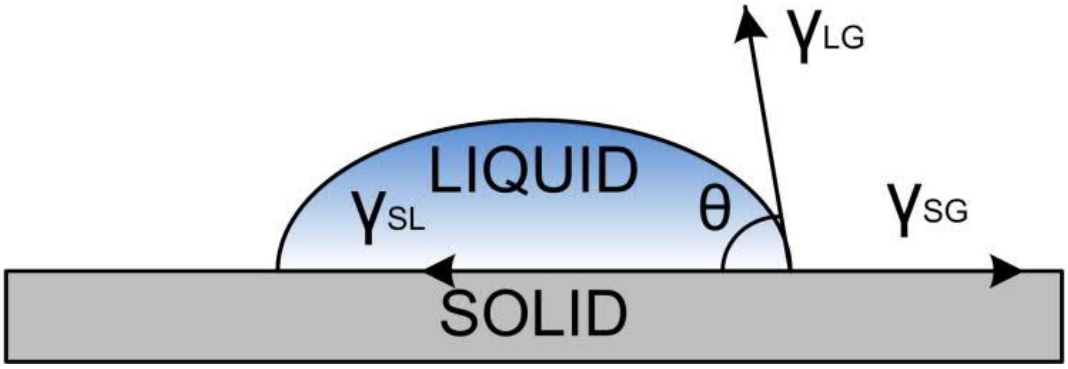

Figure 2.1. Young's Equation. Contact angle interpreted as an equilibrium force balance between interfacial surface tension forces (γ) for Young's equation.

$$\gamma_{SG} - \gamma_{SL} - \gamma_{LG} cos\theta \tag{2.1}$$

where γ_{SG} is the solid-gas interfacial energy, γ_{SL} is the solid-liquid interfacial energy and γ_{LG} is the liquid-gas interfacial energy. θ is the characteristic or Young's contact angle.

In reality, solid surfaces are seldom perfectly flat, and Young's equation was further adapted in the 1930-40s, through the work of Wenzel and Cassie-Baxter investigating rough surfaces.[3,4] In the 1950-60s, other essential and fundamental wetting mechanisms such as the concept of contact angle

[3] A book chapter authored by Wong, W. S. Y. and Tricoli, A., entitled: *"Multi-Scale Engineering and Scalable Fabrication of Super(de)wetting Coatings"*, in the book titled: *"Advanced Coating Materials"* has been accepted after peer-review in 2018, which is scheduled for publication in Fall 2018 by Wiley-Scrivener. This thesis' review chapter is associated with this publication in whole or part thereof.

hysteresis (CAH) and contact line pinning-depinning were explored.[96-98] Despite advances in our understanding of the physical system, the field was devoid of practical engineering applications.

In the early 1990s, the birth of biomimetics and bioinspiration rejuvenated the field. Bioinspired concepts are typically derived from a naturally and visually occurring phenomenon that demonstrates potential for desirable real-world applications. From an engineering perspective, much remains to be discovered. The bioinspired mastery and control over interfacial properties of materials could unveil unique engineering applications beyond our wildest imaginations.

2.1.1. Defining Hydrophilicity and Hydrophobicity

The wetting dynamics on solid interfaces is governed by both surface chemistry and physical morphology. Wetting can be observed statically by using static / equilibrium contact angles (CAs), or dynamically by using contact angle hysteresis (CAH), tilt / sliding angles (T/SA). While the fundamentals developed by Young,[1] Wenzel,[3] Cassie and Baxter[4] remain valid, recent developments in the field have generated alternative paradigms of understanding that challenge these traditional theories.

Young's Model

Traditionally, surfaces that possess a Young's contact angle, $\theta < 90°$ are considered hydrophilic, while those that have a $\theta > 90°$ are considered hydrophobic. This limit stems from the Young's equation,[1] where interactions between the 3 phases occur on a perfectly smooth surface. This ideal physical model balances upon the solid-gas (SG), solid-liquid (SL) and liquid-gas (LG) interfaces.

$$cos\theta = \frac{\gamma_{SG} - \gamma_{SL}}{\gamma_{LG}} \qquad (2.2)$$

In reality, one antithetical proposal re-considers the actual chemical and structural state of moleculer cohesion within a liquid, suggesting a revised limit of 65° between hydrophilicity-phobicity. Berg et al. demonstrated this by measuring the long-range attractive and repulsive forces exhibited by surfaces, analyzed using the plate adhesion method between 2 surfaces ($\theta > 65°$ or $\theta < 65°$).[99] Here,

a delicate state of repulsion-attraction was found in the chemical potential of the water, measured at the scale of nanometers. This limit was found to occur at the plate water adhesion tension of ca. 30 dyn/cm. With surfaces with inherent $\theta > 65°$, long-range attractive forces in water continue to persist, indicative of the hydrophobicity demonstrated by the surfaces. With surfaces of $\theta < 65°$, repulsion was detected, indicative of the hydrophilicity induced by the surfaces.

The consequence of such findings, supported by a multitude of experimental work,[19,100-102] may result in the revision of many fundamental wetting theories. However, the limit of 65° brings about much more meaningful interpretations to the chemical-physical behavior of real-world scenarios when compared to the traditional mathematically-defined 90°.[19,100,101] For the readers' reference, the minimum and maximum Young's characteristic contact angle on flat surfaces, θ on inorganic materials or highly fluorinated compounds ranges from 0° to 118° respectively.[8,103]

2.1.2. Defining Superhydrophilicity and Superhydrophobicity

More than a century after Young's findings, the use of surface roughness in enhancing wettability was described by Wenzel and Cassie-Baxter.[3,4] Despite the contention stemming from the debatable validity of the hydrophobic-hydrophilic limits,[99,102] the Wenzel and Cassie-Baxter equations continue to represent the closest respective theoretical approximations to both the superhydrophilic and superhydrophobic states today.[3,4]

Wenzel's Model

Surface roughness, r, is defined as the ratio of the actual area of a rough surface to the geometrically projected area, and can be used in evaluating the changes in surface free energy (dG) during contact line displacement (or drop motion), dx, where θ_a is the apparent contact angle observed.

$$dG = r(\gamma_{SL} - \gamma_{SG})dx + \gamma_{LG}cos\theta_a \quad (2.3)$$

where γ_{SL}, γ_{SG} and γ_{LG} are the interfacial free energies at the solid-liquid, solid-gas and liquid-gas interfaces respectively.

The thermodynamic equilibrium is achieved when dG = 0, and by incorporating Young's equation, $cos\theta = \frac{\gamma_{SG}-\gamma_{SL}}{\gamma_{LG}}$, the Wenzel equation is derived,[3]

$$cos\theta_W = rcos\theta \quad (2.4)$$

where r is the roughness ratio, θ is the characteristic contact angle (Young's contact angle), θ_W is the apparent or Wenzel contact angle. Given that r is always larger than 1 in real-world surfaces, surface roughness is known to enhance wettability with hydrophilic materials ($\theta < 90°$) while enhancing dewettability with hydrophobic materials ($\theta > 90°$).

Cassie-Baxter's Model

While the Wenzel equation assumes complete wetting throughout the surface asperities, the Cassie-Baxter equation takes into consideration of partial wetting, fundamental to the air-gap trapping superhydrophobic state.[9] This is quantified under the dimensionless variable of wetting fraction, f, the fraction of the solid area wetted by the liquid. The heterogeneous state of wetting is considered over infinitesimal fractions, f_i, of the composite surface.[4]

$$cos\theta_{CB} = \sum f_i cos\theta_i \quad (2.5)$$

Considering a composite surface of two compounds, the total free energy difference, dG, can be described as,

$$dG = f_1(\gamma_{SL} - \gamma_{SG})_1 dx + f_2(\gamma_{SL} - \gamma_{SG})_2 dx + \gamma_{LV} dx cos\theta_a \quad (2.6)$$

Minimization of free energy results in the Cassie-Baxter equation,[4]

$$cos\theta_a = f_1 cos\theta_1 + f_2 cos\theta_2 \quad (2.7)$$

In a (1) water-solid and (2) water-air system, $f_1 + f_2 = 1$. In addition, the contact angle of the water-air interface is 180°. These conditions are also valid for other fluids, thus giving the general equation,

$$cos\theta_{CB} = r_f f cos\theta + f - 1 \quad (2.8)$$

The superhydrophobic state is thus represented as the composite solid-air interface.

where θ_{CB} is the Cassie-Baxter contact angle and r_f is the roughness ratio of the wet area. During complete wetting, also known as the Wenzel state, f = 1 and r_f = r, and the Cassie-Baxter equation becomes the Wenzel equation.

Today, it is widely known that both the Cassie and Wenzel states exist at their local energy minima (Figure 2.2), and the inducement of Cassie-Wenzel transitions (and vice versa) is only achieved by energy input. It should, however, be noted that the Cassie-Wenzel theories are only applicable for static wetting behaviors on completely homogenous surfaces.

Real-world dynamically interacting heterogeneous surfaces, on the other hand, experience vastly different fluid-surface contact lines, and must be analyzed using dynamic methods such as contact angle hysteresis.[104]

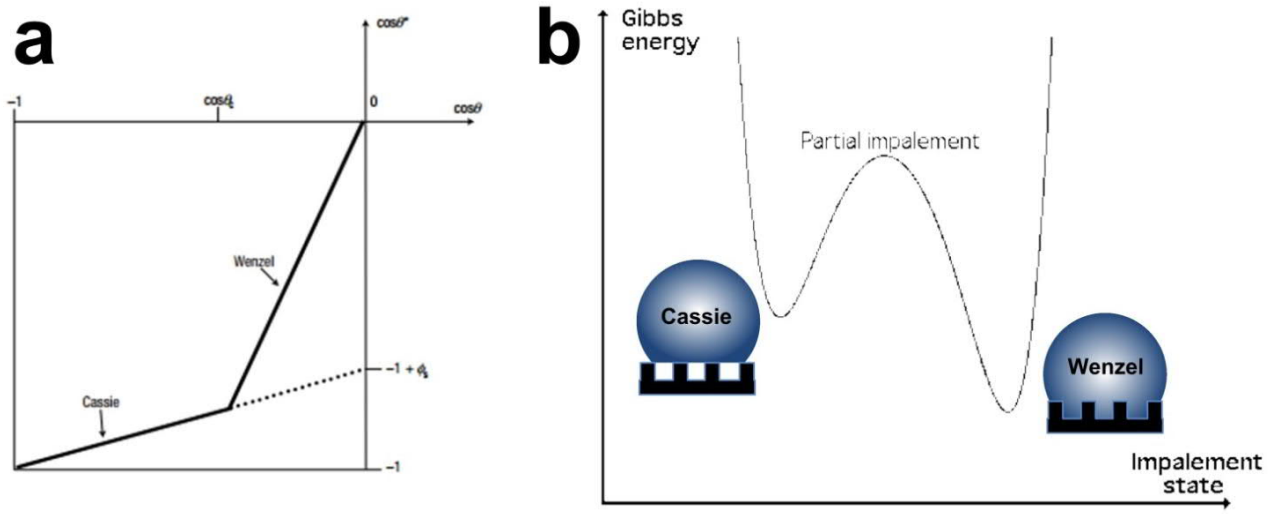

Figure 2.2. Wetting on rough interfaces. a) Moderate states of hydrophobicity are described by the Wenzel regime, where 90° < θ < θ_c, where θ is the observed CA and θ_c is CA enhanced by surface texturing. When θ > θ_c, air gaps are trapped between the interface, forming the triple-phase state of wetting, also known as the Cassie regime, with Φ_s representing the fraction of wetted solid. The Cassie regime can also occur at times with θ < θ_c, and these metastable states are indicated by the broken line.[9] b) Schematic description of the Gibbs free energy when transiting along the Cassie-Baxter and Wenzel states through partial "impalement" *via* energy input.[105]

Contact Angle Hysteresis

In the 1960s, the concept of contact angle hysteresis[104] was ascribed to the ratio of liquid-molecule to surface-pore dimension, providing a quantification for surface inhomogeneities. In the subsequent years leading up to the 1990s, most of the research in wettability focused on improving the theoretical and analytical understanding of these dynamic interfacial behaviors. Today, it can be simply expressed experimentally as the hysteresis of a sessile droplet's contact angle when its contact line is made to advance (advancing contact angle, ACA) and recede (receding contact angle, RCA) along a target surface. However, despite an improved understanding of the dynamic behaviors of wetting surfaces, some contention remains deeply entrenched within fundamental wetting theories. In 2007, much debate[106-108] surrounded a paper published by Gao and McCarthy,[109] where they questioned the validity of Wenzel and Cassie-Baxter equations in interpreting advancing, receding contact angles, and the associated contact angle hysteresis. They challenged the Wenzel and Cassie-Baxter equations' emphasis on contact area, instead of contact line, for the prediction of dynamic contact angles. This is a valid argument, owing to the fact that contact line advancement,[110,111] and thus dynamic contact angle is characterized by overcoming a series of activation energy peaks. This is sometimes observed as the "stick-slip"[112] behavior in highly heterogeneous surfaces. The debate eventually led to the derivation of a generalized form of the Wenzel and Cassie-Baxter equations, where they are integrated with x-y dimensional considerations and thus valid within and between each transitional zone governing the infinitesimal contact lines.[108] This was also supplemented by the notion that the Wenzel and Cassie-Baxter equations exist in both local and global perspectives, with pre-specified parameters being used solely in their respective scenarios.[113] Later, further theoretical studies suggest that both Wenzel and Cassie-Baxter equations remain good estimations of contact angles on rough surfaces under one primary condition. They are valid when the size of the droplet is much larger than the dimensional or chemical heterogeneity.[114] However, evaluation of experimental work by Erbil and Cansoy[115] into the accuracy and validity of theoretical Wenzel and Cassie-Baxter equations proved otherwise. The work revealed substantial experimental-theoretical invalidation of

computed Wenzel and Cassie-Baxter contact angles, particularly on superhydrophobic surfaces.[115] Today, the community largely acknowledges the difficulty of appropriate assessment and interpretation of contact angles on rough surfaces. This is further exacerbated by the occasional and differential pinning of contact lines on random defects[43,44] owing to different topological wetting behaviors.[116-118] A series of dynamically transiting wetting behaviors exist between the Wenzel and Cassie-Baxter wetting models. Considering the lack of concrete conclusions behind work into validating (or invalidating) the Wenzel and Cassie-Baxter equations for contact angle hysteresis, further use or approximations in particularly contentious situations should be preceded with care.

Today, contact angle hysteresis can be used to estimate the apparent surface free energy of roughened surfaces (γ_s^{app}). This was developed by Chibowski[119-121] by observing apparent dynamic contact angles derived during the contact angle hysteresis test.

$$\gamma_S^{app} = \frac{\gamma_l(1+cos\theta_{adv})^2}{(2+cos\theta_{rec}+cos\theta_{adv})} \quad (2.9)$$

where γ_l is the surface tension of probe fluid (mN/m), θ_{adv} and θ_{rec} are the advancing and receding contact angles respectively.

This equation highlights the dominant effect of the advancing contact angle, showcasing differences between a simple phobic and a super-phobic surface. Surface heterogeneity manifesting as surface adhesion can then be aptly represented by the secondary effect of the receding contact angle. The dimensionless retentive adhesion force ($F_{R\text{-}SA}$) can, in fact, be computed based on the contact angle hysteresis of an interface.[122]

$$F_{R-SA} = -2k \sin\left[\frac{2\theta_{adv}-CAH}{2}\right] \sin[\frac{-CAH}{2}] \quad (2.10)$$

where k represents a contact line correction, which is $4/\pi$ when the contact area is circular in nature and CAH is the contact angle hysteresis (θ_{adv} - θ_{rec}).[122]

Variants of Superhydrophilicity

Superhydrophilicity represents a superwetting state where the apparent water CA (WCA) is lower than 5-10°, typically occurring when a surface and its roughened asperities are completely wetted. However, multiple examples of inorganic surfaces that are morphologically flat, such as freshly cleaned glass, quartz, cleaved mica also appear "superhydrophilic-like", owing to their naturally achieved ultra-low CAs.[8]

Today, the research community[8,16] has unanimously agreed upon the condition that only heterogeneous, roughened surfaces ($r > 1$) can be considered superhydrophilic. Surface roughness has thus become a prerequisite for defining superhydrophilic materials / surfaces.[8,16] Without this, exceedingly vast variants of mundane materials risk erroneous classification. However, the true definition of superhydrophilicity remains vague owing to its highly dynamical nature. It can be further sub-categorized into 2 dominant modes as highlighted below.

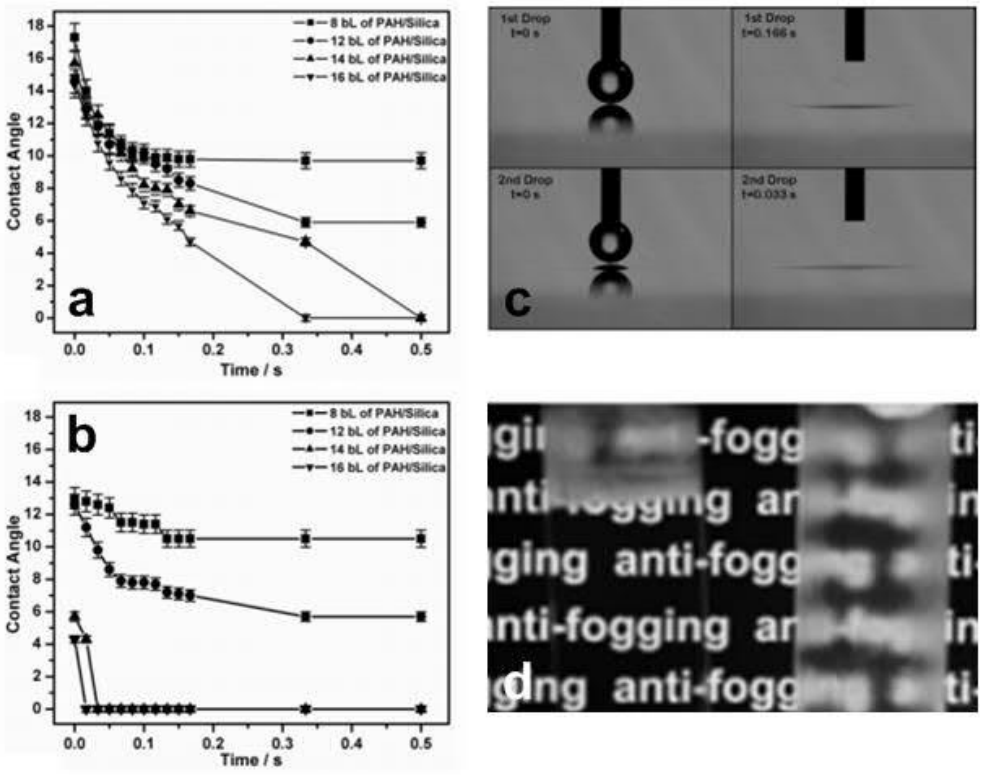

Figure 2.3. Ideal superhydrophilicity. Dynamic CAs (time-dependent) with respect to the spread of the a) first and b) second deposited droplet with respect to deposited bilayers. c) Droplet spread on a superhydrophilic surface (1st and 2nd droplet). d) Demonstration of superhydrophilic anti-fogging performance.[123]

Ideal Superhydrophilicity

The original definition of superhydrophilicity was simple, and argues simply for a droplet-interface to reach a CA of ca. 0-10° without considering time-upon-contact.[5] In later years, the research community gave superhydrophilicity a much stricter requirement, necessitating the rapid spread of a liquid droplet within just 0.5 s to achieve a CA of ca. 0-10°.[19,30,123]

These time-dependent considerations are very relevant, owing to the presence of other "superhydrophilic" surfaces with marginally slower spread dynamics. We propose the sub-classification of this superwetting state with ultra-rapid dynamics as ideal superhydrophilicity (Figure 2.3).

Hemi-wicking Superhydrophilicity

The second mode of superwetting descended from the original definition of superhydrophilicity, where CAs of ca. 0-10° are achieved without strict time-dependence.[5] This alternative mode of superwetting is known most commonly today as (super)wicking or hemi-wicking superhydrophilicity.[124-126] This state describes a wetting phenomenon that exists between ultra-rapid superhydrophilic spreading and hydrophilic imbibition.[124,127]

The wetting mechanism occurs through actively moving contact lines that sequentially achieve the Wenzel state of penetrated wetting. Unlike ideal superhydrophilicity, materials that realize this property can have significantly lower surface energy, aided by surface morphology enabled capillary effects.[93,124-126,128,129] Owing to these marginally different mechanisms, hemi-wicking superhydrophilicity requires more time to achieve ultra-low CAs, which could take place in seconds or even minutes.[93,124-126,128,129] However, equilibrium CAs often reach 0°,[93,124,126] contrasting certain ideal superhydrophilic surfaces.[8,30,95] The resulting physical phenomenon is comparable to but more ubiquitous than those with ideal superhydrophilicity. For instance, this effect occurs in everyday materials such as paper, thin porous films, membranes and other micro- and nano-porous

surfaces. We propose the sub-classification of this capillarity-enabled superwetting state as hemi-wicking superhydrophilicity (Figure 2.4).

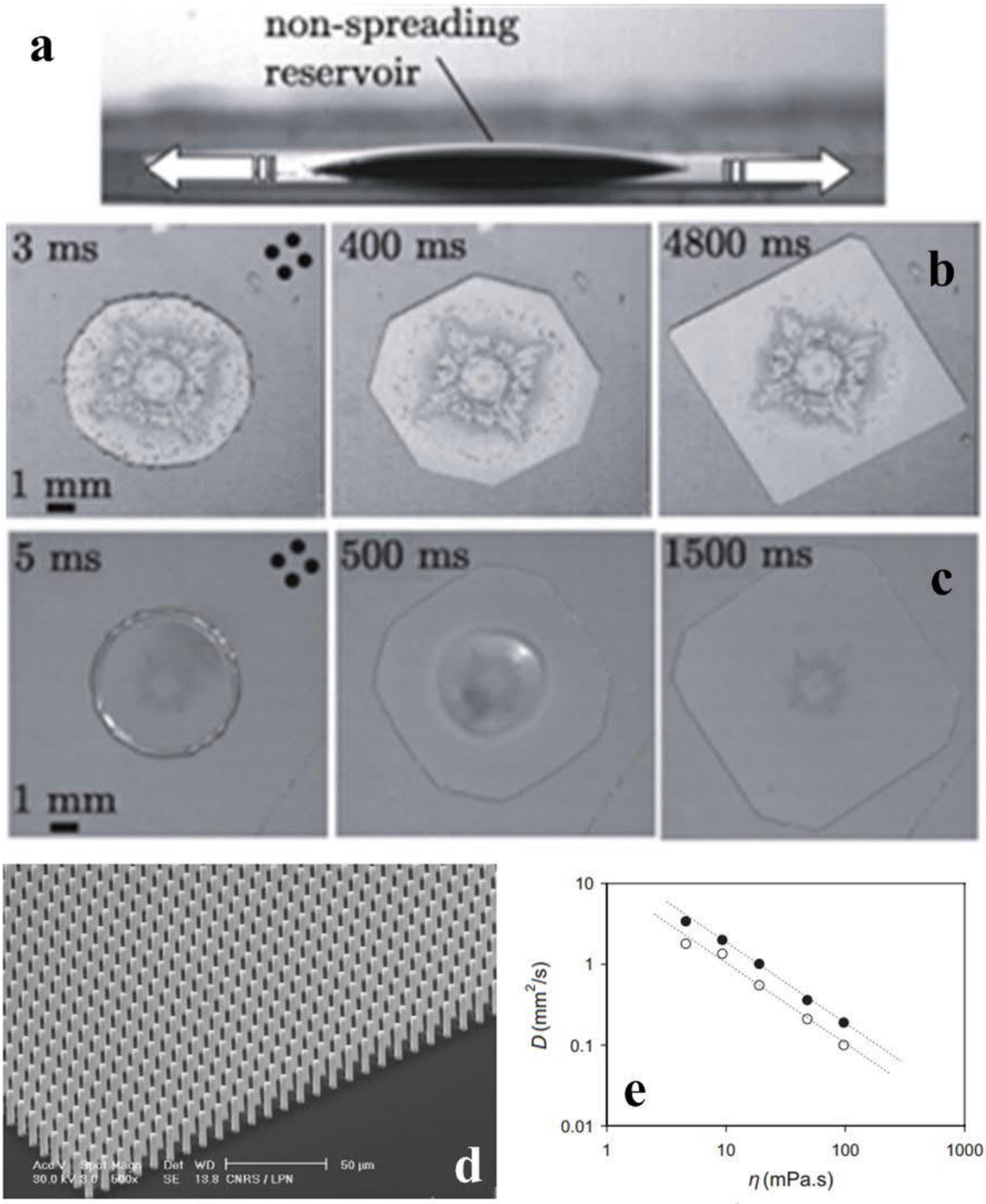

Figure 2.4. Hemi-wicking superhydrophilicity. a) Side profile of a spreading droplet on a micro-textured surface. Spreading occurs by the imbibition of the texture from a macroscopic reservoir (arrows). Droplet assembly b) into a square or c) a circle, can be controlled by specific texturing parameters.[130] d) Silicon surface decorated with a forest of micropillars for analysing hemi-wicking dynamics. e) Dynamic wetting coefficient as a function of fluid viscosity.[124]

Variants of Superhydrophobicity

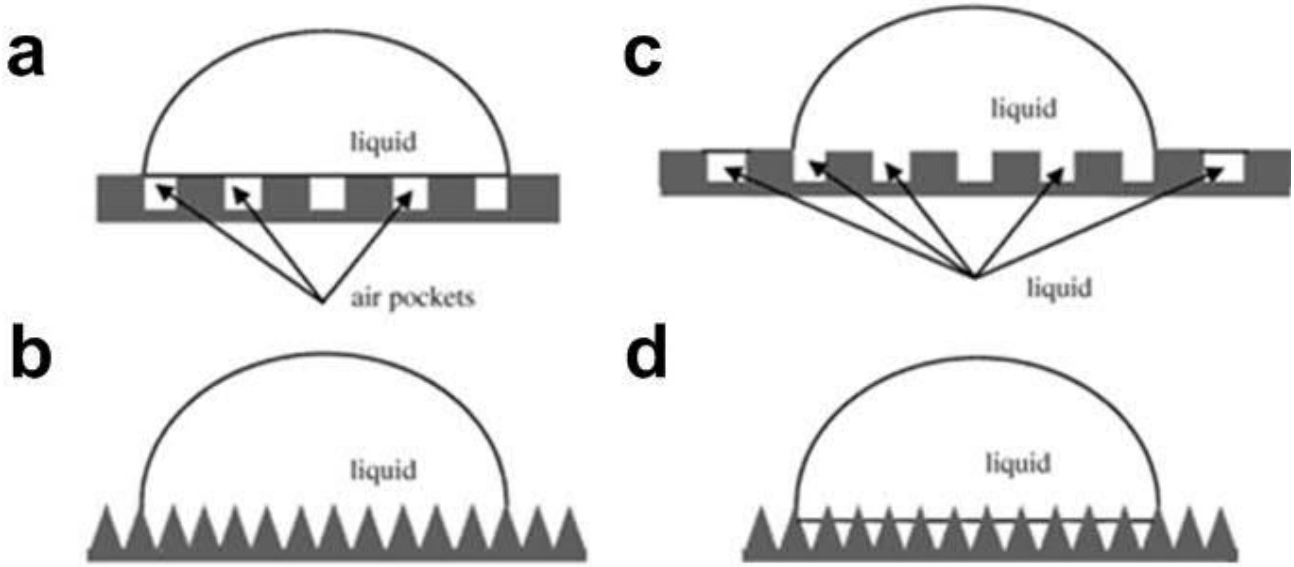

Figure 2.5. Various wetting states occurring on rough surfaces. a) Cassie air-trapping state, b) Wenzel fully wetting state, c) Cassie impregnating wetting state (micro-structures are penetrated but nano-structures remain dry) and the d) mixed wetting state (wetting in reality, with partial surface penetration, giving rise to hysteresis).[131]

The term superhydrophobicity was originally attributed to extremely hydrophobic surfaces, where water no longer simply beads up, but instead forms a near-perfect sphere. In accordance to the heterogeneous triple-phase wetting of the Cassie-Baxter state, superhydrophobicity relies on both surface chemistry and morphology (or roughness), while warranting a pre-requisite CA limit of > 150°. However, in recent years, increasing amounts of research revealed that different variants exist within the traditional superhydrophobic state (CA > 150°).[19,101,132] These new findings split the field of superhydrophobicity into separate sub-sections of lotus-slippery and rose-adhesive superhydrophobic states, corresponding to the sub-categorizations of Cassie-Baxter, Wenzel and Cassie-Impregnating profiles (Figure 2.5).

Ideal Lotus Superhydrophobicity

The traditionally defined state of superhydrophobicity is known to exist as the Cassie-Baxter wetting state, first observed and quantitatively analyzed as the lotus effect.[4,6,7,9,133] At the micro- and nano-level, this is visually depicted as a state with triple-phase contact lines having distinctive water-solid-

air interfaces. This is also sometimes known as the fractional-wetting state. The solid-water contact areas are defined as a fraction *f* while the air-water contact areas are defined as the complementary (*f*-1).[4,133] Air pockets between the surface and water droplet are indefinitely preserved, thus enabling a superhydrophobic state with low adhesion (Figure 2.6). Today, lotus-like superhydrophobicity is defined around static CAs, dynamic wetting properties and contact line depinning characteristics.[96,134-136] This is typically represented by a CA > 150°, a SA < 10° and a CAH < 25°.[132,135]

Petal-like Adhesive Superhydrophobicity[4]

Despite the early discovery of hydrophobicity[4] and superhydrophobicity,[6,7] an intermediate mode of wetting that exists between the two remained hidden until only very recently. This is a sub-variant of superhydrophobicity that is highly adhesive, known most commonly today as the petal-effect; and was only discovered and understood as recently as 2008.[10] In the following years, work on the petal-effect revolutionized the community's understanding towards the various sub-domains of superhydrophobicity.[132,137] At first glance, the petal-effect appears to be superficially identical to the lotus-effect, with properties such as a very high static CA (> 150°). However, analysis of its dynamic wetting properties reveals starkly contrasting differences, with the petal-effect possessing much higher adhesive properties when compared to the lotus-effect (more than an order in adhesion forces).[26,132] At the point of discovery, the extremely non-intuitive droplet pinning nature of adhesive superhydrophobic surfaces was unprecedented. During its early inception, the effect was so confusing that it bore two names. The first was the "gecko-effect",[138] which we now typically attribute to dry adhesives and tape technologies.[139] Over time, the research community re-aligned itself with the

[4] The petal-effect, or the adhesive mode of (superhydrophobicity) as detailed here, is sometimes debatable (in terms of official terminology) owing to complications involving its predecessor, the lotus-effect based superhydrophobicity. The original definitions into superhydrophobic states were indicated by David Quéré in 2003 as a state with high WCA of > 150°, measured at 160-175° and low CAH, measured at just 5° (A. Lafuma et al., *Nat. Mater*. **2003**, 2, 457). The presence of surface penetration, Wenzel or Cassie-Impregnating is considered enough by some to discount these surfaces from bearing the classification of "superhydrophobic". Despite these definitions, the terms "superhydrophobicity" and "with adhesive states/modes" have been and are still used interchangeably within the community (L. Feng et al., *Langmuir*, **2008**, 24, 4114, 136 and B. Bhushan et al., *Phil. Trans. R. Soc. A* **2010**, 368, 4713). For the sake of clarity and simplicity, the petal-effect will be consistently labelled as "adhesive petal-like superhydrophobicity".

more popular and appropriate nomenclature of “petal-effect”, owing to the very physically similar wetting phenomenon found on rose (*Rosaceae)* petals.[10] This will be the classification of choice in this work. Although the petal-effect was first presented in 2008,[10,138] the mechanism of adhesive superhydrophobicity was only extensively investigated and understood in later years.[132,137] Today, it is technically identified as the Cassie impregnating wetting state.[127,131,132] This is a hybridized wetting profile where water penetrates partially into microstructural features (Wenzel), while air-gaps from nano-structures prevent complete penetration (Cassie). This uniquely achieved state of partial impregnation facilitates droplet anchoring while inhibiting the Wenzel state of wetting (Figure 2.7).[21,132] In the years that followed, the petal-effect generated an impetus that led to an explosion of interest in the field, with much research work being directed towards understanding its unique behavior and functionality.[21,38,132,137,140,141]

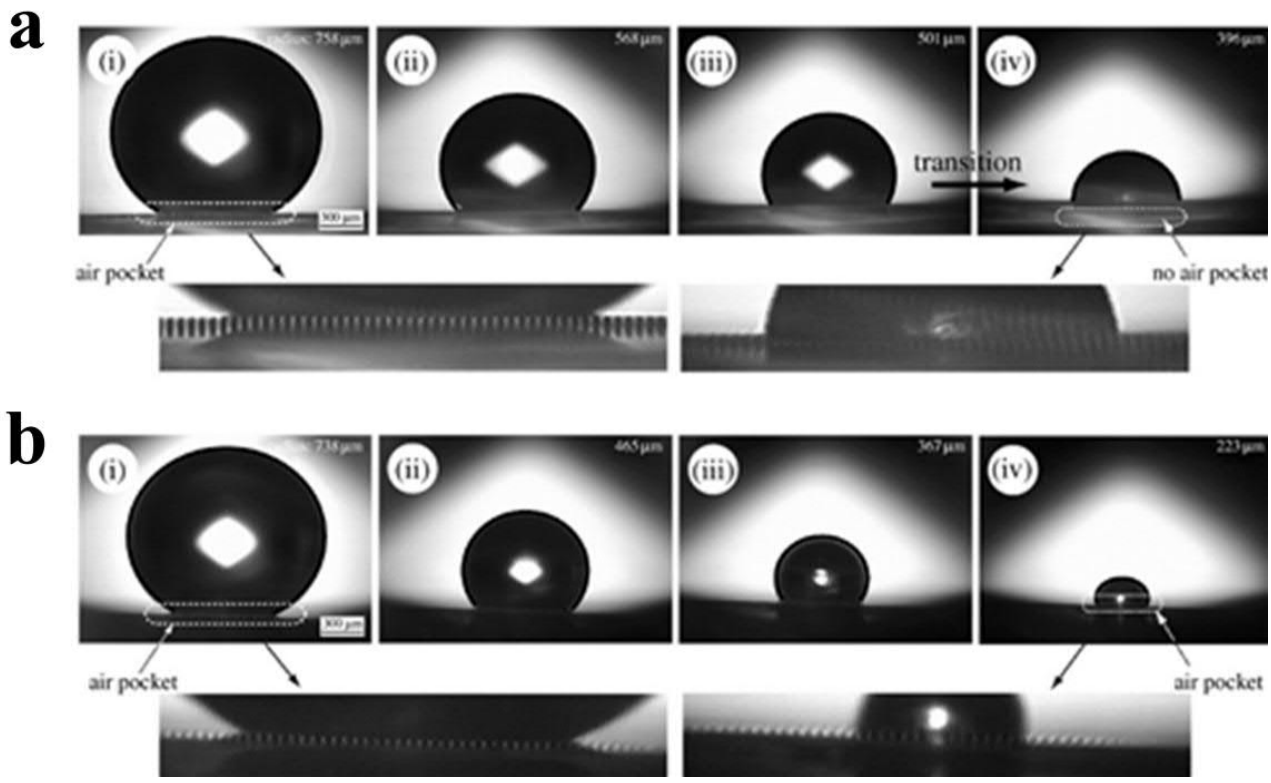

Figure 2.6. Cassie-Baxter to Wenzel wetting. Observations of an evaporating droplet’s fluid-solid interface on a) a micro-structured and b) a hierarchically structured surface. Time interval between successive photos was 60 s. a) On the micro-structured surface, as the droplet reached a diameter of 396µm (original diameter of 750µm), the Cassie-Baxter regime was lost through its transit into a state of Wenzel wetting. b) On the hierarchically structured surface, air pockets which were visible at the feet of the droplet existed until the droplet is completely evaporated.[136]

Today, adhesive petal-like superhydrophobicity is termed for surfaces having a static water CA (WCA) of more than 150°, high CAH that ranges between 40-80° and no SA (droplet pinning). It can also be defined around its adhesive properties, with an adhesive strength of up to 120 μN[26,43,89,142,143] and a droplet carrying capacity of up to ca. 10 mg[43,138,143-146]. However, the efficiency of droplet detachment remains unclear. As of the time of writing, much of the research on petal-like interfaces do not place emphasis on residual droplets and clean interfacial detachment.[21,38,135,138,142,143]

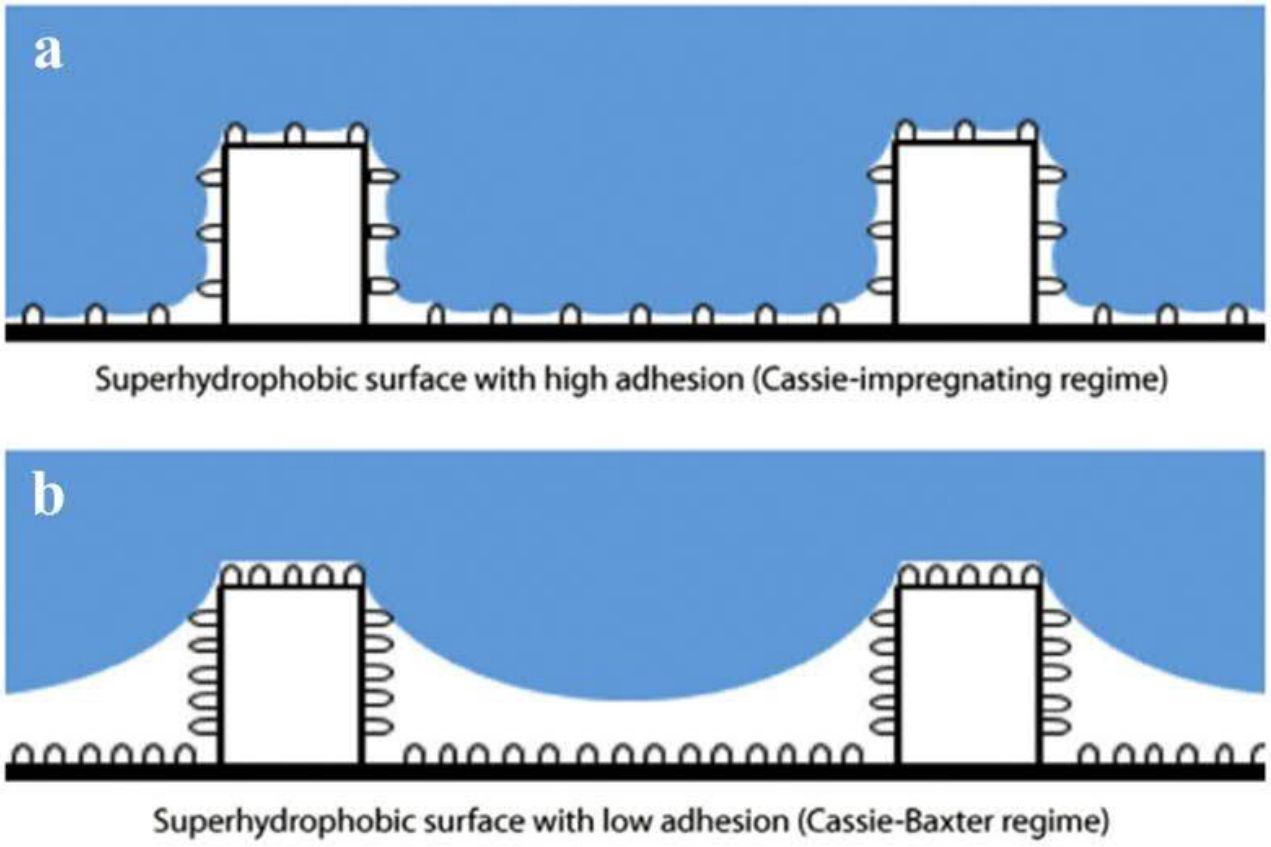

Figure 2.7. Cassie-Baxter to Cassie-Impregnating. The rose petal-effect functions through the a) Cassie-impregnating regime, where it operates in stark contrast to the b) lotus-effect under the Cassie-Baxter regime. This differential wetting behaviour allow the penetration of micro-structures while preventing infiltration of nano-structures.[21]

2.1.3. Defining Superoleophobicity, Superamphiphobicity and Superomniphobicity

Superoleophobicity and Superamphiphobicity

A recent extension to superdewetting interfaces comes in the form of superoleophobicity. Superoleophobicity is generally defined for surfaces that demonstrates high CAs > 150° when interacting with low-surface tension (γ) non-polar oils and organic solvents (γ < 30 mN/m). Akin to

the progress made towards understanding lotus-like superhydrophobicity, the sole analysis of static CAs does not ascribe the standard state of superoleophobicity. As of the time of writing, these surfaces must also have low SAs, < 5-10° and low CAH, generally < 5-25° towards a variety of oils.[14,19,50,56,147] When superhydrophobicity co-exists with superoleophobicity, it constitutes superamphiphobicity (amphi- meaning both)[5].[14]

Today, reports describing superoleophobic / superamphiphobic surfaces are much fewer compared to those demonstrating superhydrophobicity. This is largely attributed to the somewhat different requirements in surface morphology and chemistry. Firstly, surface chemistry of superoleo(amphi)phobic surfaces must be modified with fluoro-organics (-CF_3),[103] and cannot utilize the fluoro-free chemistry that is sometimes exploited by superhydrophobicity.[68,148-150]

Secondly, surfaces can no longer be simply roughened in accordance to the Cassie-Baxter equations, but instead require carefully designed re-entrant morphologies.[11,151] The consideration of pitch-density and penetration robustness is also paramount towards achieving the superoleo(amphi)phobic effect. Tuteja et al. derived these dimensionless parameters that semi-quantitatively highlight the functionality of both stochastically and lithographically developed surfaces. The first is known as the dimensionless robustness parameter, H*, which represents the functional capability of a superoleo(amphi)phobic surface in resisting fluid sagging and penetration. The second is known as the dimensionless spacing ratio, D*, which defines the pitch distances of the surface features.[151]

$$H^* = \frac{2[(1-cos\theta)R+H]l_{cap}}{D^2} \quad (2.11)$$

$$D^* = \frac{R+D}{R} \quad (2.12)$$

where R is the average feature size, D is the spacing between features, H is the feature height, θ is the Young's CA and l_{cap} is the capillary length of the probe fluid.

[5] Surfaces that exhibit the non-intuitive combination of superhydrophilic-superoleophobic properties do exist (J. Yang et al., *J. Mater. Chem.* **2012**, 22, 2834.), but they are exceedingly rare and not fully understood.

Increasing inter-feature spacing, D, results in a high D* which corresponds to higher apparent CAs (thus superoleo(amphi)phobic CA) due to fractional contact. However, the increase in D leads to a decrease in H*, which in turn enables droplet penetration due to fluid sagging heights, thus resulting in increased adhesion, SAs, CAHs and even the Wenzel effect. The combined optimization of both parameters is essential towards achieving robust, penetration-free superoleo(amphi)phobic surfaces. Some of the highest H* and D* configurations come from the nano-nail[152] and microhoodoo[11] features.[151] However, the fractal and stochastically assembled interfaces typically experience comparatively lower H* and D* values.[151]

Notwithstanding tremendous progress, superoleo(amphi)phobicity suffers from the same limitations of scalability, transparency and robustness that plagues superhydrophobicity, albeit at a greater magnitude.[22,59,65,153-155] Despite these massive challenges, superoleo(amphi)phobicity represents the next most practical frontier in the field of superdewettability. The many stringent industrial requirements in surface dewetting have led to the insufficiency of plainly superhydrophobic coatings. Low surface tension fluids such as surfactant-laced water, soaps, detergents or organic oils and solvents are able to wet superhydrophobic coatings, inducing functionality losses or even complete coating destruction.[29]

Superomniphobicity

Expansion of superdewetting beyond superoleo(amphi)phobicity is found within the strictest definitions of superomniphobicity. Superomniphobicity represents the very last frontier in the field of superdewetttability. These surfaces are capable of preserving the Cassie-Baxter wetting state even with ultra-low surface tension fluids ($\leq$ 20 mN/m, down to 10 mN/m[12]), with CA > 150° and SA < 10°.[12,65] At the point of writing, owing to the rarity of superomniphobicity, CAH is rarely analyzed,[66] but akin to the definitions outlining lotus superhydrophobicity and superoleo(amphi)phobicity, it is likely to be < 25°.

Superomniphobicity, by definition (omni- meaning all),[11,12] should only encompass interfaces that are impossible to wet by any known liquid. This includes fluids that have a much lower surface tension than those typically repelled by superoleo(amphi)phobic surfaces. As of the time of writing, the lowest surface tension of a fluid tested for superomniphobicity is fluorohexane (FC-72), which possesses a surface tension of just 10 mN/m.[12] The superomniphobic texture capable of such extraordinary performance is a lithographically designed double re-entrant profile which demonstrates the delicate preservation of the Cassie-Baxter state (CA > 150°, SA < 10°) during contact with fluorohexane. This texture currently represents the state-of-the-art in terms of absolute dewetting performance.[12]

However, owing to gradients of functionality even within the sub-field of superomniphobicity, the established limit is commonly identified at ca. 20 mN/m.[12,65,66] Variations in performance depend on actual structural-surface chemistry configurations.[12,65,66] At the lower performance limit of superomniphobicity, the probe fluid of choice tends to be octane or n-heptane (21.7 and 20.14 mN/m respectively).[12,65,66,156,157] An interface's inherent ability in preserving a Cassie-Baxter super-phobic state with these fluids is indicative of its superomniphobicity.[65,66]

Re-entrant Profiles

As described in sections above, superoleo(amphi)phobicity and superomniphobicity are both reliant on the use of re-entrant profiles. These re-entrant profiles (Figure 2.8) can come in the form of inverse trapezoids at its minimum,[74] or serif T-shaped[75] hoodoo structures at their maximum[11,12]. The re-entrant texturing plays an essential role by prohibiting contact line advancement, thus making the wetting of such structures thermodynamically unfavorable.[11,12,155,158,159] Despite the functional superiority of these micro- nano- architectures, they currently require extremely complex, unscalable means of fabrication (*e.g.* nanolithography).[11,72] No scalable technique (*e.g.* bottom-up self-assembly)[160] to date, has been reported as being capable of assembling such well-defined, precise and tunable topologies.

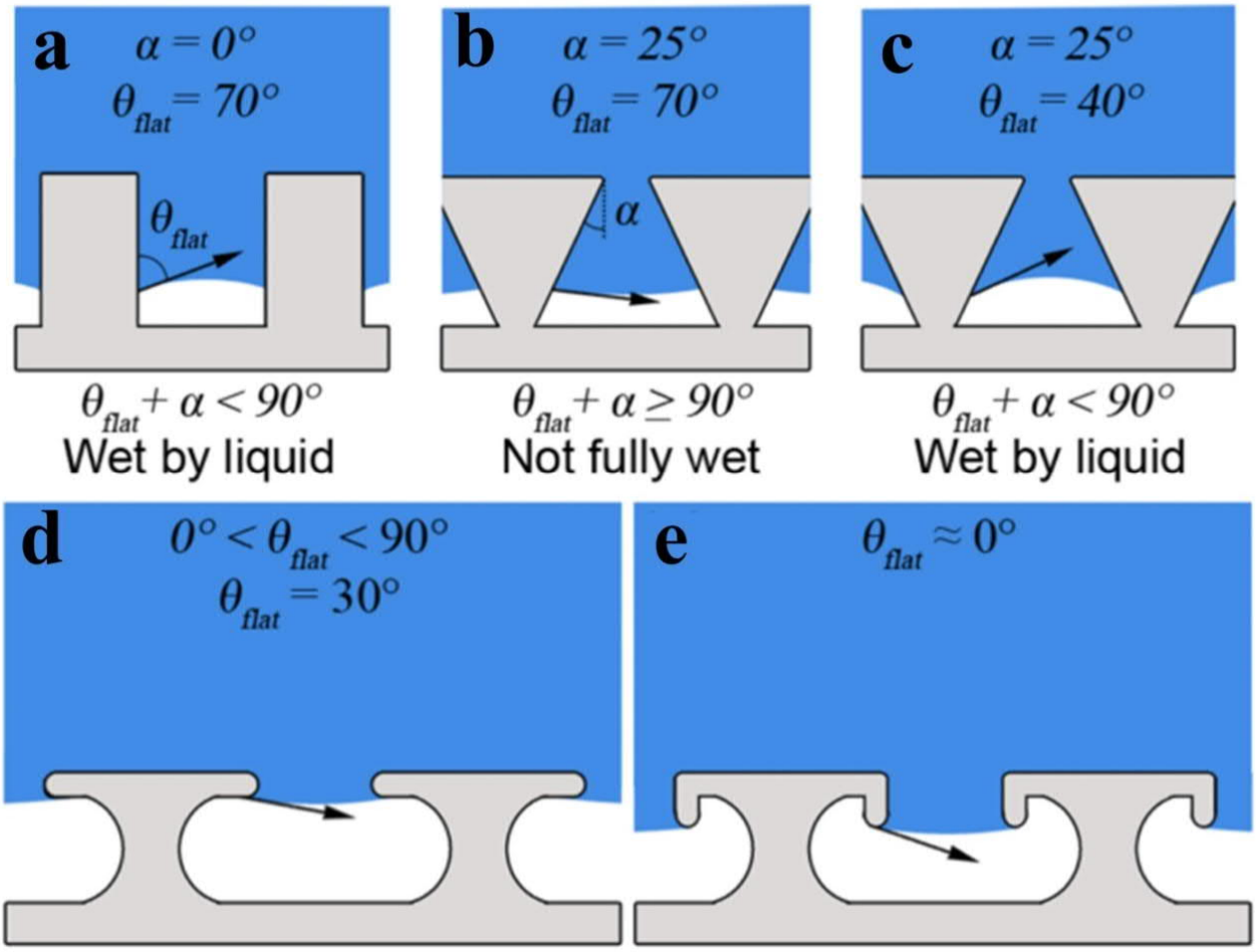

Figure 2.8. Impact of re-entrant profiles on superdewettability. a) Non re-entrant profile, wettable by common liquids that have a Young's CA (θ) more than 90°. Schematic of re-entrant profiles (inverse trapezoids) b) inhibiting or c) permitting fluid penetration by virtue of the ratio between re-entrancy (α) and Young's CA (θ).[158] d) Superoleo(amphi)phobic microhoodoos, which function with fluids possessing a characteristic CA or a Young's CA (θ) down to just 30°. e) If a secondary re-entrant profile is created orthogonal to the first, double re-entrancy is induced. Contact line advancement thus becomes thermodynamically unfavourable even for fluids that are completely wetting, with characteristic CA or Young's CA (θ) of 0°.[158]

Shades of grey: Superoleo(amphi)phobicity to Superomniphobicity

The definitions of and differences between superoleo(amphi)phobicity and superomniphobicity were once blurred given the flurry of research output during their early inception.[14,22,65,161-163] In order to distinctively segregate highly performing interfaces (superomniphobicity) from the others (superoleo(amphi)phobicity and below), re-definition of operational boundaries may be required.

Here, we aim to present a thorough literature review which outlines key definitions associated with the graduated levels of performance (Figure 2.9). For instance, potentially erroneous

definitions[57,74,87,164] may be attributed to superdewettability that functions only against common edible or commercial oils, with surface tensions of > 30 mN/m. This intermediary state of wetting exists between superhydrophobicity (> 72 mN/m) and high-functioning superoleo(amphi)phobicity (< 30 mN/m), and should be differentiated from the latter and more importantly: superomniphobicity. Morover, this intermediate is also fairly prevalent, but no official classification exists owing to historical reasons.[74,87,164] This limit originated from the first super-oil-repellant surfaces, hinted in 1997 *via* the use of rapeseed oil, thus coining the term (-oleo meaning oil).[55] The work demonstrated CAs of > 150°, with fluids of surface tensions higher than 40 mN/m,[55] which was once widely accepted, but is scarcely the acknowledged definition today.[19,50,65,153,165]

However, it was not until 2007 that a thorough understanding of superoleo(amphi)phobic profiles and their associated performance was established.[11] Today, the probe liquid of choice for assessing true superoleo(amphi)phobicity is hexadecane, which has a surface tension of 27.5 mN/m.[14,72] Typically, more than one organic fluid must also be used for justifying claims to superoleo(amphi)phobicity.[11,14,155]

Interfaces that are capable of repelling fluids lower than or equals to 20 mN/m, such as n-heptane[56,157] or fluorocarbon (FC-72) fluids[12], should be categorized separately under superomniphobicity. This definition is most suited for classifying such omnipotent repellent capabilities.[12,65,66] Despite most of today's literature touting the superior contamination proof properties of both superoleo(amphi)phobicity and superomniphobicity, a distinctive gradient of performance still exists between the two. Notwithstanding claims of "superomniphobicity" which are actually closer to "superoleo(amphi)phobicity [6] ",[57,59,166,167] very few pieces of research[12,65,66] have actually demonstrated true superomniphobicity. Variations in performance from superoleo(amphi)phobicity to superomniphobicity are largely attributed to nature rather than design. Many of these sub-classes

[6] For the sake of clarity, superoleophobicity and superhydrophobicity will be classified under superoleo(amphi)phobicity in Chapter 2, in efforts to distinguish this sub-class from solely superoleophobic-superhydrophilic variants (Footnote 5). Readers should note that the term, superoleo(amphi)phobicity, is equivalent to superamphiphobicity.

in the domains of high-performing superdewettability are admittedly very difficult to define. For instance, how would highly performing superoleo(amphi)phobic properties (down to 25 mN/m) be classified against lower performing counterparts (down to just 30 mN/m to 70 mN/m)?

Hereinafter, we propose the following sub-classifications. Superomniphobicity, highly and mildly superoleo(amphi)phobicity are defined for a Cassie-Baxter state (CA > 150°, SA < 10°, CAH < 25°) for fluids with surface tensions of < 20 mN/m, 20-30 mN/m and 30-72 mN/m respectively.

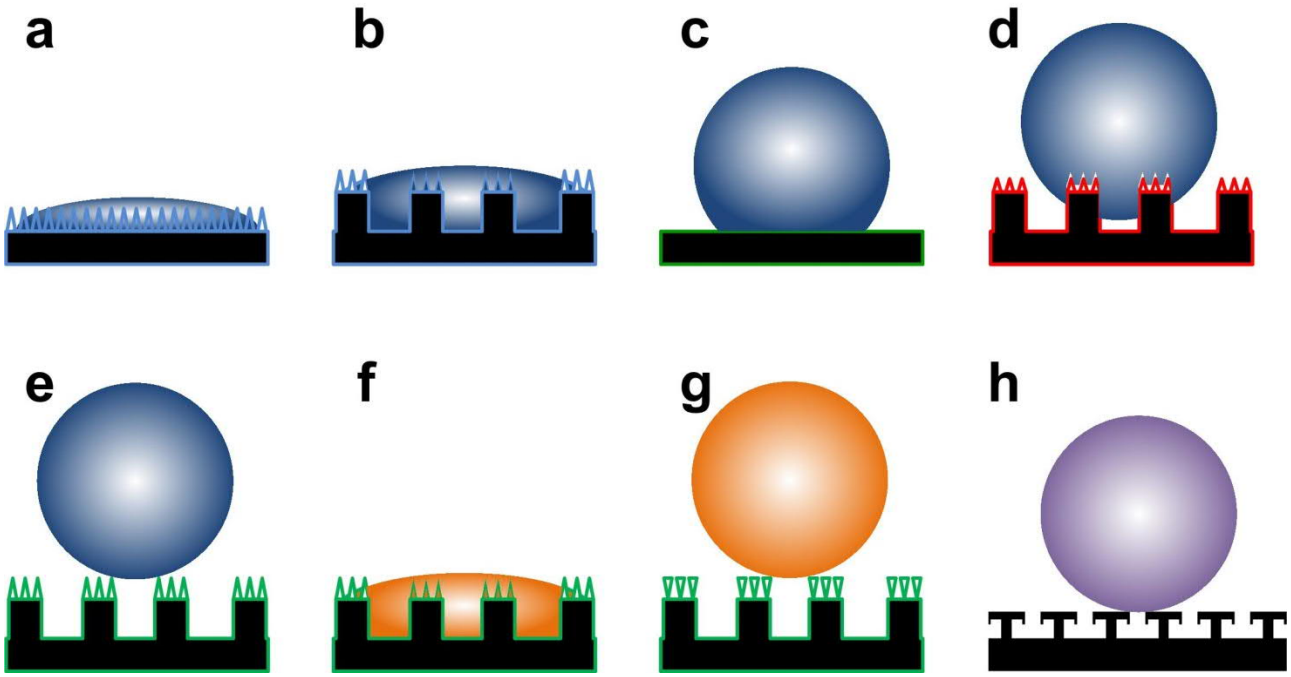

Figure 2.9. States of wettability, a) superhydrophilicity b) hemiwicking superhydrophilicity to hydrophilicity, c) hydrophobicity, d) adhesive superhydrophobicity, e) slippery superhydrophobicity, f) superhydrophobicity-superoleophilicity, g) superoleophobicity-superamphiphobicity, h) superomniphobicity.

2.1.4. Cross-Environmental Wetting States

The current descriptions above apply primarily to the solid-air-liquid triple phase. The other dominant and equally interesting state of wettability exchanges the air phase for oil, giving rise to the triple interface of solid-oil-liquid (typically water). When the solid's air gaps are replaced with water, wetting states such as underwater superoleophobicity and underwater superoleophilicity can exist. Alternatively, when the infiltrated medium is oil, states such as underoil superhydrophobicity and underoil superhydrophilicity can be achieved. Such specialized wetting states are actually not very different from the traditional "in-air" phase, as the same triple phase interactions are still present (Figure 2.10).

Underwater Superoleophobicity

When water completely replaces the air phase (in-air superhydrophilicity),[168-170] oil must now interact with the solid-water interface instead of the solid-air interface. As oil and water are immiscible, the small amounts of water trapped in the solid gaps are able to suspend oil droplets, enabling underwater superoleophobicity. Analogous to in-air systems, underwater superoleophobicity can also only occur with the aid of roughness. This effect was quantified by the use of patterned silicon pillars,[171] where micro-structuring and micro-nano-structuring induced extremely low adhesion states, down by up to 25 times. Today, this effect is widely understood as a fluid-suspended Cassie-Baxter state.

Underwater Superoleophilicity

Considering the three-phase interactions induced in underwater superoleophobicity, underwater superoleophilicity may seem at best unintuitive, and at worst impossible. However, if this triple-phase contact line is disrupted by re-introducing air near the solid (*e.g.* through the use of a superhydrophobic substrate), the in-water oil wetting dynamics are now changed.[172] With the use of denser-than-water oils, contact lines spread through the entire triple-phase system thus resulting in underwater superoleophilicity.

Underoil Superhydrophobicity

The replacement of air in the air-solid-water interface with oil leads to the triple phase of oil-solid-water. An in-air superoleophilic surface can be used to achieve this state, where small amounts of entrapped oil between the solid surface are now available to suspend water droplets, thus resulting in underoil superhydrophobicity.[173,174]

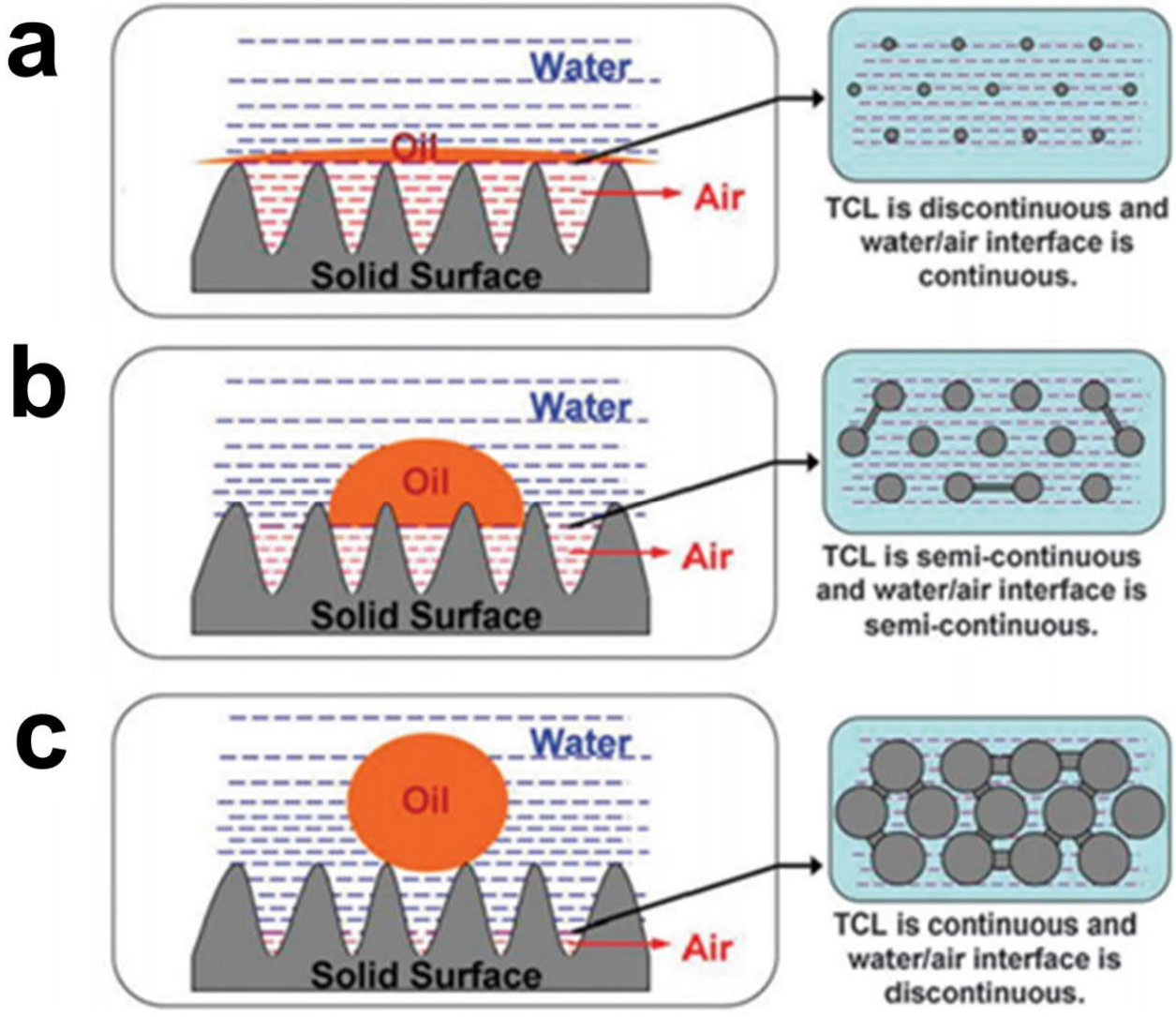

Figure 2.10. Cross-environment wetting states. Wetting states of an oil droplet exposed to an immersed underwater substrate with roughness. The left represents the wetting states while the right indicates the triple-phase contact line at the air-water interface. a) Oil droplet spreads out at the water-air-solid interface. b) Oil droplet does not spread completely due to the semi-continuous contact lines posed by the water-air-solid interfaces. c) Oil droplet suspended by thin layers of water on the solid profile (continuous TCL, total contact line), and is thus no longer influenced by the presence of air.[172]

Underoil Superhydrophilicity

Considering the relative surface energies of water (72 mN/m) and oils (20-40 mN/m), wetting will always take precedence with oils, thus making superhydrophilicity unintuitive. An underoil superoleophilic-superhydrophilic substrate will be wetted and thus no longer capable of water wetting. Alternatively, an underoil superoleophobic-superhydrophobic substrate will not work because of its dewetting properties. The solution makes use of an in-air superhydrophilic substrate that is pre-wetted with water in order to induce a water-solid interface before oil-immersion. As such, the water-solid interface is preserved, and can be used for inducing wetting by subsequently interacting water droplets.[175]

2.1.5. Characterization Techniques

Wettability was traditionally only characterized with static contact angles (CAs).[5-7,176] With the advent of the multiple modes of (super)wettability today, the use of dynamic methods such as contact angle hysteresis (CAH),[96,104] sliding angles (SAs), fluid immersion[22,177] and droplet bouncing[18,178,179] has become essential (Figure 2.11).

Static Contact Angle Analysis

Fluid droplets that range from 2 to 10 μL are commonly used, depending on the actual intended application or measurements.[12,13,38,57,153,155] This is commonly performed *via* the sessile drop method. A droplet is first dispensed out of the needle, forming a pendant droplet. The pendant drop is then made to meet the target surface. At this point, the needle is withdrawn, thus resulting in droplet detachment. While the increase in droplet sizes is known to marginally increase contact angles ($\Delta CA < 5°$) with super-phobicity, the angle of view, mode of measurement, profile fitting and inherent human errors pose much greater influence.[180] For instance, fitting of droplets rely on mathematical models, such as the circling, ellipse, tangent, Laplace-Young or Bashforth-Adams methods.[181,182] The variations between models could result in measurement inaccuracies of up to 20°, and can lead to different interpretations behind the true wettability of a surface.[180] Alternatively, human errors

often stem from the camera's angle of view. Depending on the relative angle of elevation between the camera and the droplet-interface, variations of up to 5-10° can occur.[183]

While super-phobicity can be analysed using a single image frame, super-philicity can only be assessed *via* a series of video frames. A droplet of fluid (*e.g.* 5 µL) is deposited onto a surface *via* the sessile drop method. A high-speed camera is simultaneously used to measure the rate of droplet spread, analyzed frame-by-frame.[30,123] Notwithstanding the active nature of this method, it should not be confused with dynamic contact angle analysis, as we will highlight in the next sections. Despite the prevalent usage of static contact angles in providing preliminary characterizations, they remain fairly unreliable in assessing a surface's true wetting characteristics; and the use of dynamic contact angle analysis is often employed to supplement static contact angle data.

Dynamic Contact Angle Analysis - Contact Angle Hysteresis

Work on the dynamic analysis of wettability started from the 1950s,[96-98,181,184,185] but is still continually revised and improved even today.[181,182,186] Dynamic wettability analysis enables the meticulous probing of intricate three-phase contact line behaviors, thus providing much more characteristic information about heterogenous, real-world surfaces. More importantly, the contact angle hysteresis analysis of a surface enables the precise classification and sub-categorization of highly similar, but inherently different super-phobic states (*e.g.* rose vs. lotus effects). Today, a myriad of techniques is available for achieving in-depth understanding of the many sub-variants of super(de)wettability. This includes methods such as the drop-in, drop-out (DIDO), evaporative CAH, tilted plate CAH, dynamic Wilhelmy or Washburn's capillary rise amongst others. Regardless of the methods and their associated variations, CAH is typically assessed by the difference between the measured ACAs and RCAs.[38,135]

$$\theta_{CAH} = \theta_{adv} - \theta_{rec} \tag{2.13}$$

The DIDO technique is one of the most popular and universal methods for dynamic contact angle analysis, sometimes also referred to as the droplet expansion-contraction method. Fluid is first

pumped in as a droplet (*e.g.* from 0 μL to 10 μL) onto the target surface and thereafter pumped out (*e.g.* from 10 μL to 0 μL), enabling the dynamic analysis of the ACAs and RCAs respectively. A low flow rate, *e.g.* 0.1 μL/s, enables gentle movement of the contact line across the test domain, thus assisting smooth contact line probing. The ACA typically approaches a maximum value while the RCA approaches a minimum value. Perfectly flat and homogenous surfaces, as defined by Young, will not exhibit any hysteresis. However, real-world surfaces are almost always rough and heterogeneous. Super-phobic surfaces that possess high static CAs can have either high or low CAH values, interpreted as variations in heterogeneity and retentive adhesion.[95,122,135] For surfaces that are heterogeneous in either (or both) physical structuring or surface chemistry, smooth contact line motion is impeded by uneven domains, causing drops in dynamic contact angles due to line pinning.

However, the point at which ACAs and RCAs are selected remains highly debatable, particularly so for the latter. ACAs are typically measured at their maximum, after the rising contact angle plateaus. This is well-supported by multiple pieces of work in the literature.[13,134,135,181,182] However, RCAs experience much greater variation. This is in part, caused by needle-influenced fluid distortion during the final phases of fluid withdrawal.[182] Today, a balance between the analysis of 1) final droplet volume,[135] 2) plateauing RCAs (do not always exist[7])[135,182] while avoiding 3) droplet-distortion[13] is used to justify the point where RCAs are measured.[181] Despite the numerous advances in CAH measurements since its original inception, further improvements[182] must be made to promote adaptation to new superoleo(amphi)phobic and superomniphobic states.[12,13,187]

Dynamic Contact Angle Analysis - Sliding Angle

The alternate mode of dynamic contact angle analysis is represented by the sliding angle (SA). This is sometimes also referred as the tilt angle (TA). Sliding or tilt angle refers to the critical substrate tilt that would result in sliding of a resting sessile droplet. A super-phobic surface tends to have a sliding

[7] Surfaces with high CAs and high CAHs, or "adhesive super-phobic" interfaces, tend to have an ever-decreasing receding contact angle (RCA). This is a phenomenon that is attached to strongly-pinned contact lines, leading to a continuously moving tangent along the droplet profile's arc (H. Teisala et al., *Langmuir* **2012**, 28, 3138.).

/ tilt angle < 10°, indicative of extremely low adhesion. The SA/TA can be and is commonly reported in tandem with CAH. While SA/TA is superior to CAH in representing actual super-phobic performance in a real-life scenario, its inherently uncontrollable variations in droplet size and tilt speed (°/s) prohibit its effective comparison across studies.[188]

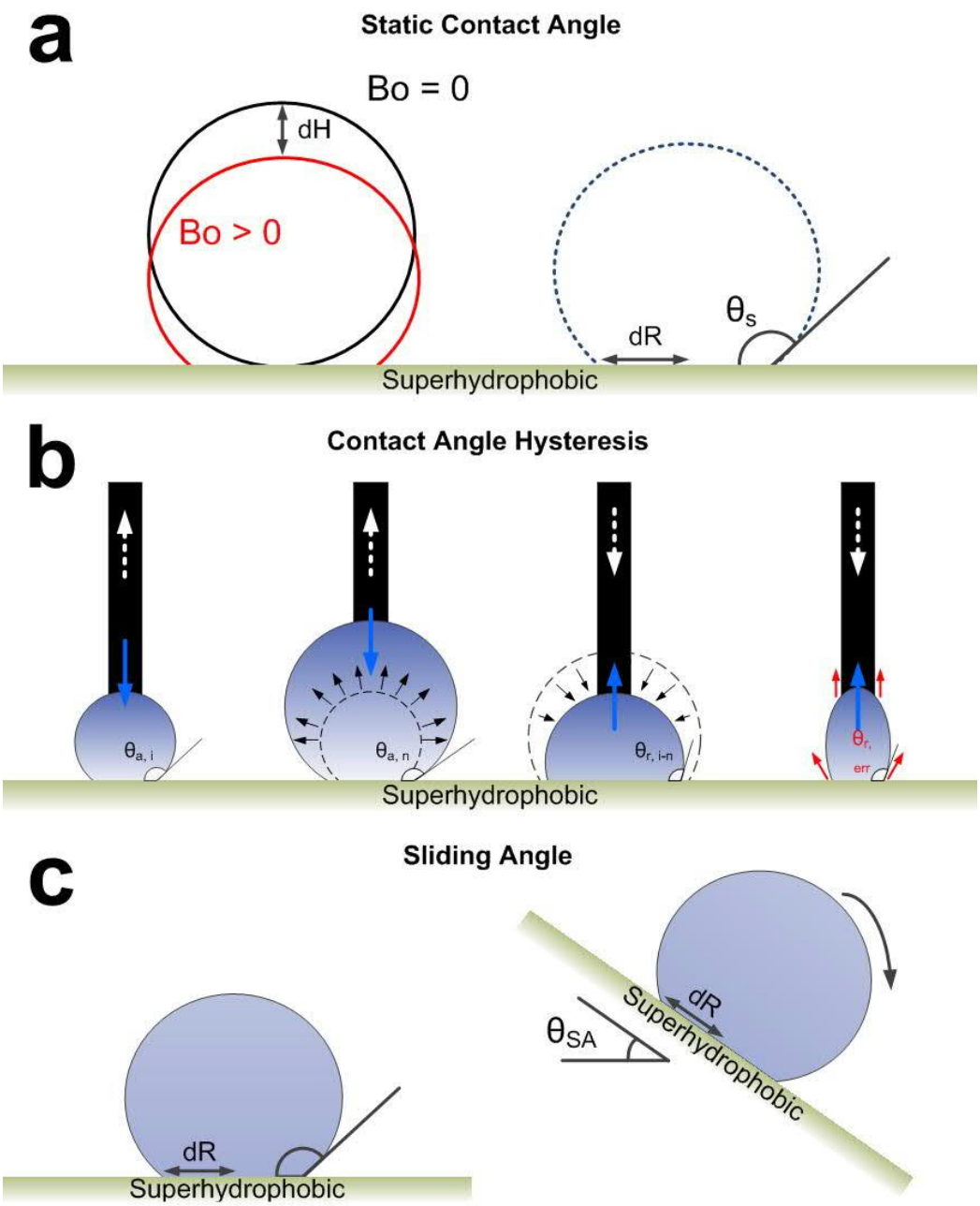

Figure 2.11. Static vs. dynamic contact angle analysis. Static contact angle analysis: a) Gravity induced sagging of droplet profiles can amplify measurement variations in goniometric systems. Super-phobic CAs (> 150°) are particularly affected, as demonstrated by potentially erroneous analytical profiles. b) Schematics describing the measurement of CAH through the drop-in, drop-out (DIDO) method. c) Sliding angle schematics of a super-phobic droplet that slides off upon a certain tilt angle.

Other Modes of Dynamic Analysis - Droplet Bouncing and Fluid Immersion

New modes of analysis exist today, such as the droplet compression method,[189] droplet bouncing[178] and fluid immersion[22]. These methods are designed to impose increased pressure on the liquid-solid interface, thus achieving a better understanding towards the critical breakthrough pressure in different surface geometries (Figure 2.12).

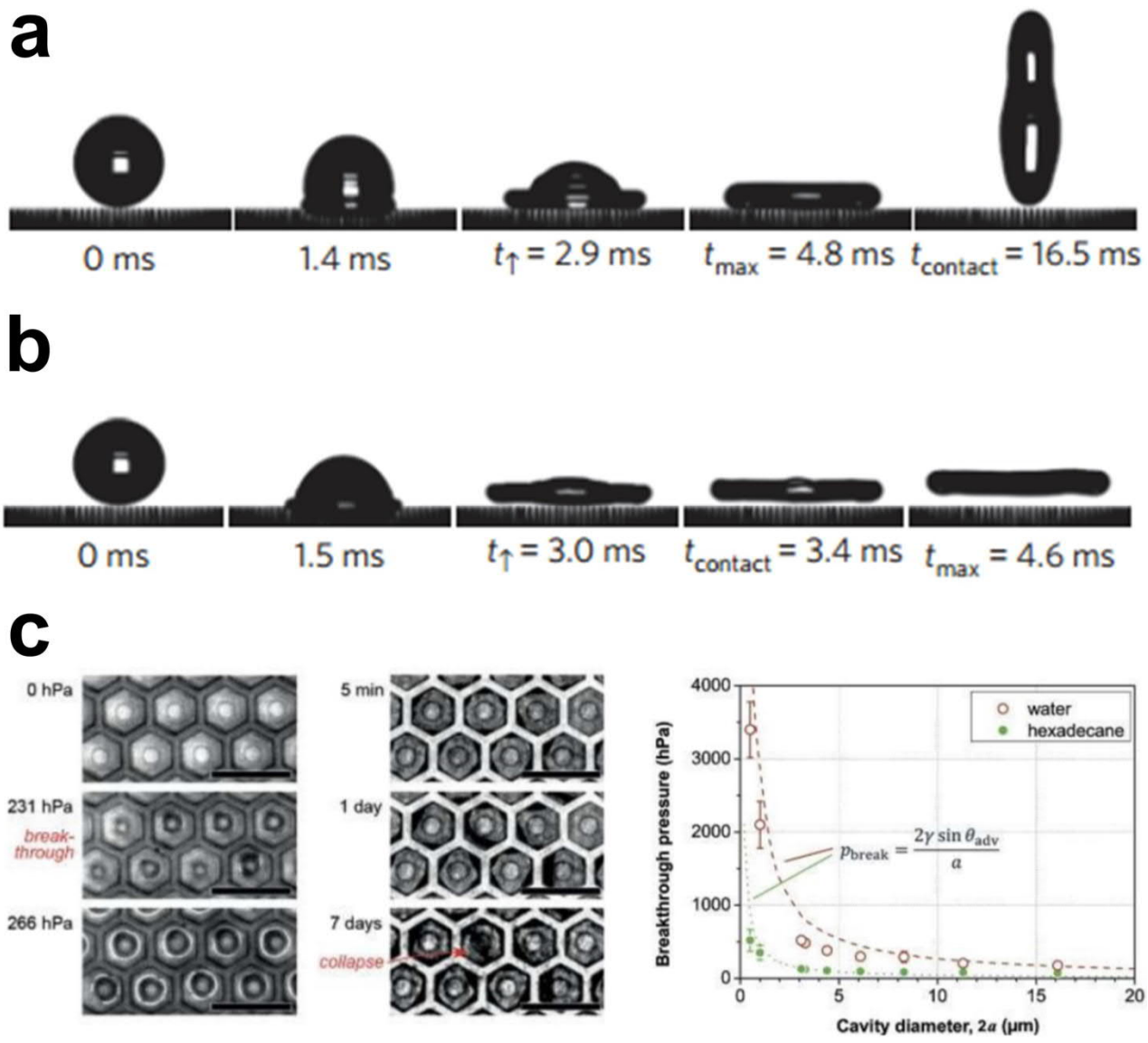

Figure 2.12. Alternate modes of dynamic analysis. Droplet impact on a patterned superhydrophobic surface by varying droplet impact parameters, such as the Weber number (We): a) Droplet impact showcasing normal impact, with contact detachment at 16.5 ms after penetration and capillary recoiling, We = 7.1. b) Droplet impact with departure of the drop in a pancake-like shape at We = 14.1.[179] c) Immersion experiments showcasing the pressure- or time- dependent collapse of plastron layers on super-phobic membrane cavities.[22]

In the droplet bouncing technique, absorption or poor-bouncing (satellite droplets) of the treated droplet on the surface indicates higher adhesive properties and poorer robustness (high CAH or SA) while clean desorption or elastic-bouncing of droplets suggests extremely low adhesive properties and improved robustness.[105] More importantly, the latter also indicates an elevated critical breakthrough pressure that can be correlated against the inertial capillary timescale.[18,178] These measurements, however, have yet to be directly linked or compared with the CAH and SA data measured on the same surfaces owing to their inherently different dynamics.[18,178,179,190]

In the fluid immersion technique, dynamically increasing fluid pressure is exerted on the super-phobic surface. The most common mode involves the use of hydrostatic pressure, with increasing immersion depth scaling linearly to increasing pressure. The pressure is increased gradually until the fluid meniscus breaks through the interfacial features, typically resulting in an optical difference in reflectance.[22] This analytical method is, however, framed around a pragmatic objective. For instance, superhydrophobicity does not persist for extended periods underwater due to the eventual dissolution and thus loss of the air-gap.[177] Considering the importance of the Cassie-Baxter air-gap preservation in designs for drag reduction or extended immersion, these tests are key towards the future development of immersion-stable super-phobic engineering interfaces. Lately, it has also become vital towards testing advanced super-phobic membranes with touted -omniphobic and -oleo(amphi)phobic properties.[22]

2.2. Nature to Artificial: Bioinspired Engineering

Nature, through millions of years of environmentally-driven adaptation and evolution, gave rise to a myriad of biological organisms with unique characteristics that bear immediate engineering applications.[7,10,22,49,138,191-193] Today, biomimetics and bioinspired materials have demonstrated universal and far-reaching societal impact. Products range from membrane filtration systems inspired by the baleen whale,[194] biomimetic catalytic systems inspired by immobilized bacteria[195] or even soft robots[196] inspired by soft but highly functional organic tissues. In the fields of surface science and wettability, bioinspiration has been even more prevalent, owing to the unique ways organisms have evolved their epidermal layers for optimal interactions with their natural environments.[10,22,132,197] Bioinspired interfacial engineering aims to adapt such high functioning systems found in nature as practical solutions to problems faced by both research and industrial sectors. Here, we will introduce prominent examples of bioinspiration, ranging from superhydrophilicity[5] (superwetting) to super(hydro-, oleo-, amphi-)phobicity[7,188] (superdewetting).

2.2.1. Superhydrophilicity

Superhydrophilicity in plants (Figure 2.13) can occur in those that are either permanently wet or others that are capable of rapidly absorbing water over their surfaces. The former does not require a specific surface morphology, and are most commonly found in submerged plants.[6] The latter variant, however, possesses pores, hairs and geometrically roughened interfaces. One particularly interesting mode of absorption comes in the form of absorptive hairs (*hydathodes*). Spanish Moss, *Tillandsia usneoides*,[198] for instance, makes use of multicellular absorptive trichomes, a fine outgrowth of hairs that realizes rapid water-absorbing capabilities. In mosses, superhydrophilicity comes as an advantageous evolutionary property during nutrient uptake, where they replace the need for well-defined roots or vascular systems. In terms of absolute superwetting performance, the fastest known superhydrophilicity occurs on the leaves of the *Ruellia devosiana*, a Brazilian wild petunia, which achieves a superhydrophilic CA of 0° within 0.2 s.[199] A combination of hydrophilic secretions with

surface hierarchy such as hairs and channel-like structures, contributes to its superior performance. In fact, its leaves are so superhydrophilic that water moves against gravity, induced by the capillary-based suction stemming from these synergized physicochemical properties.[199] Superhydrophilicity is also exploited for creating slippery surfaces,[200] which are then used by carnivorous plants for capturing prey; or for the rapid evaporation of moisture on leaves, thus preventing undesirable biofilm growth while promoting transpiration[8].

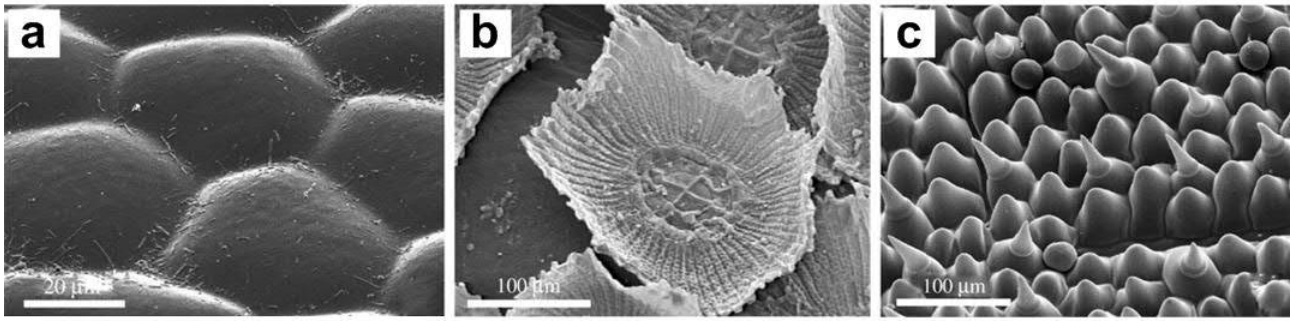

Figure 2.13. Superhydrophilic plants. a) Comparatively untextured water plant (*Anubias barteri*), submerged. b) The epiphytic Spanish moss (*Tillandsia usneoides*) with its characteristic multicellular water-absorbing hairs. c) The multi-cellular epidermal layers of the Brazilian petunia (*Ruellia devosiana*).[198]

As of the time of writing, synthetic superhydrophilicity has rarely been directly influenced by bioinspiration, owing to the dominant use of artificial photoactive inorganic materials.[5,201] However, with recent advances in hemi-wicking superhydrophilicity, concepts stemming from the use of bioinspired surface hierarchies such as fibers,[95,202] hairs[30,128] and micro-channels[93,124,126,203] are slowly gaining momentum.

2.2.2. "Lotus-like" Low-Adhesion Superhydrophobicity

Today, the lotus-effect is world-famous for its superior water-shedding properties. Despite the early contributions by Wenzel,[3] Cassie-Baxter[4] and numerous pieces of fundamental research into the wetting properties of rough surfaces[96-98,181,184,185] the lotus-effect was only scientifically quantified in 1997 by Barthlott and Neinhuis.[6,7] They found that the unique combination of micropapillae structures (microstructural) and hydrophobic wax secretions (low surface energy) is capable of inducing very high WCAs coupled to low SAs (Figure 2.14). This understanding was later expanded,

which emphasized the need for hierarchical / multi-scale textures (micro- and nano- roughened).[188] The phenomenon, albeit named the "lotus-effect" (*Nelumbo nucifera)*, also occurs within a large variety of other water-repellent; self-cleaning plants.[6] This series of work established the importance of micro- and nano-structural texturing, typically found in plants as epicuticular wax crystals. These wax crystals can be configured as tubules, platelets, rodlets, ribbons, dendrites and threads.[6] With an improved understanding of the phenomenon, such enabling knowledge led to the creation of the first artificial superhydrophobic surfaces in the years that followed.[9,133,149,188] Since their first inception, much work has been directed towards achieving a scalable and practical state of superhydrophobicity, which continues even today.[54,204-208]

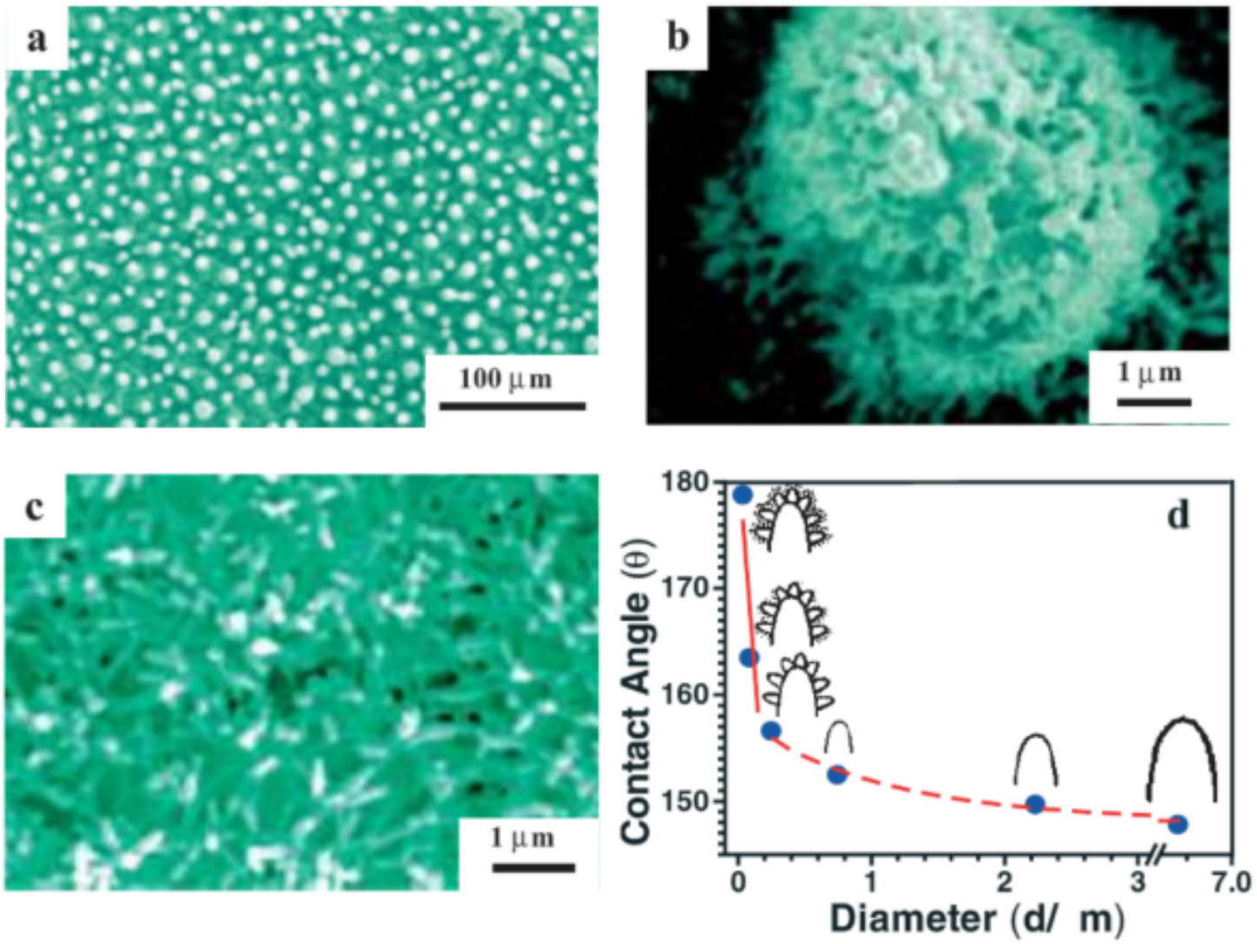

Figure 2.14. Superhydrophobic lotus leaf. a-c) SEM micrographs of a lotus leaf (*Nelumbo nucifera*), where epidermal cells form a papilla-like structure made up of dense layers of epticuticular waxes with hierarchical (micro- and nano- roughness) textures. d) Fitted curve based on calculated CAs versus diameters of protruded micro- and nano-structures.[188]

2.2.3. "Petal-like" High-Adhesion Superhydrophobicity

In recent years,[10] an alternate mode of superhydrophobicity was discovered, naturally present on the petals of the red rose, *Rosaceae* (Figure 2.15).

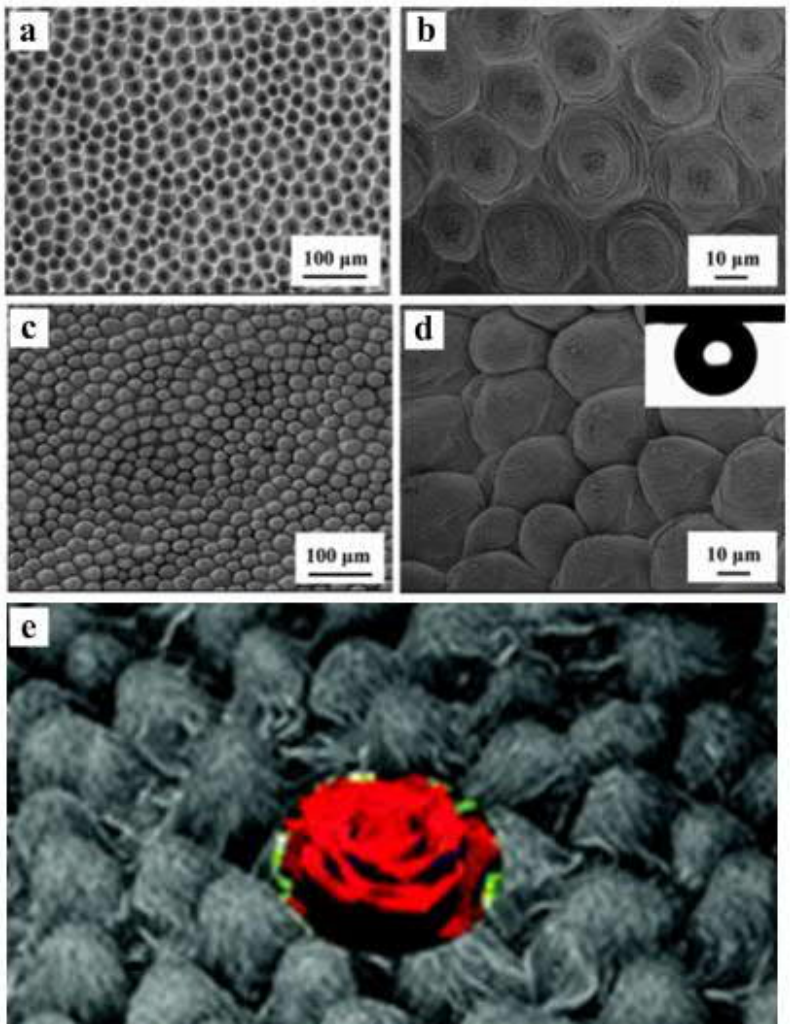

Figure 2.15. SEM micrographs of template duplicated petal-like superhydrophobic surfaces. a,b) PVA negatives and c,d) PS positives using e) actual rose petals as templating molds.[10]

Unlike the low-adhesion based superhydrophobicity that is observed in the lotus, the rose petal possesses a state of superhydrophobicity with high droplet adhesion. This phenomenon, aptly coined the petal-effect, is capable of pinning droplets up to 10 µL in size while maintaining the renowned superhydrophobic state (CA > 150°).[10,21,38,137] Today, this unique adhesive superhydrophobic state is understood as the Cassie impregnating wetting state, where water partially penetrates into the microstructural papillae of the petal surface. However, air gaps present along nano-structured folds prevent complete penetration, thus inhibiting the Wenzel state of complete wetting.[21,132] Such highly

adhesive but superhydrophobic surfaces holds great potential for the field of droplet microfluidics, where near-spherical and configurable volumes of fluid are mechanically manipulated on “sticky” chips for “drop-on drop-off” micro-reactors.[26,43,89,138,143,145,146]

2.2.4. Anisotropic Low-Adhesion / High-Adhesion Superhydrophobicity

Isotropic superhydrophobicity that results in randomly orientated sliding water droplets is well-known and clearly illustrated by the lotus-effect. However, nature has evolved other functional interfaces capable of enabling directional droplet sliding, also known as anisotropic superhydrophobicity. This is attributed to the presence of directionally patterned surface structures.

Anisotropic superhydrophobicity was first discovered in the rice leaf, *Oryza sativa*.[188] While the same hierarchically structured (micro- and nano- roughnened) papillae are present on rice leaves as on the lotus, they are aligned in one-dimensional, linear, parallel row-like patterns (Figure 2.16).[188] When water droplets are allowed to roll along the grain, parallel to the longitudinal axis of the leaf, SAs are extremely low, reaching just 3-5°. However, when water droplets are made to roll against the grain, perpendicular to the longitudinal axis of the leaf, SAs reach up to 9-15°. From a fundamental perspective, the minute differences in pitch distances between the directional axes (x- and y- axes) across the leaf are capable of generating differential dewetting gradients.

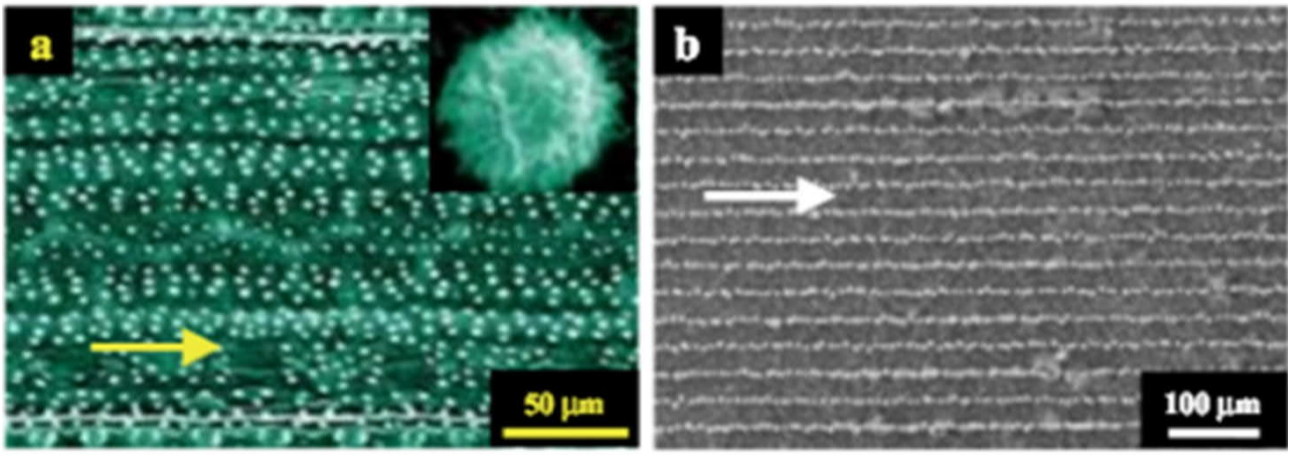

Figure 2.16. Rice-leaf anisotropic superhydrophobicity. a) SEM micrograph of a rice leaf (*Oryza sativa*), where well-aligned, mono-dimensional epidermal cells form parallel rows of hierarchical textures. b) Artificially synthesized carbon nanotube (CNT) structures with parallel alignments.[188]

While the anisotropic dewetting gradients found in the rice leaf are evident, further "improvements" to anisotropic differential dewetting effect were later found in the butterfly's wings *(Morpho eaga)*.[209] The wetting properties of a butterfly's wings are no longer simply controlled by mono-dimensional micro-papillae that are spaced across marginally different pitch distances, but by columns of precisely directed scales (Figure 2.17).

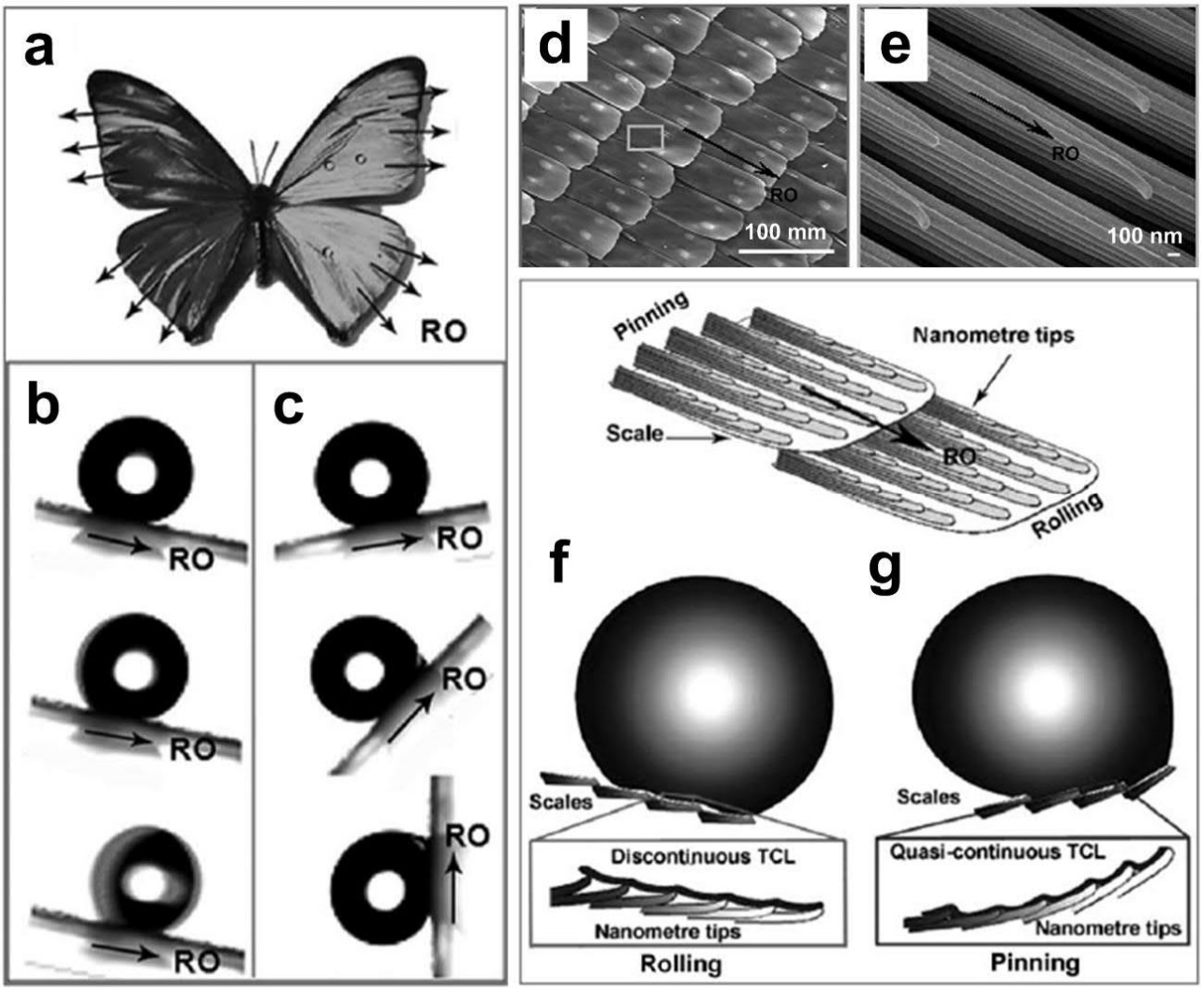

Figure 2.17. Butterfly scales' anisotropic superhydrophobicity. The a) Morpho butterfly's wings exhibiting b) low-adhesion superhydrophobicity when approaching the scales from inside to out (with respect to the body), and c) pinning superhydrophobicity when approaching the scales from outside to in (with respect to the body). The wings are comprised of aligned columns of hierarchically structured d) micro- and e) nano-structured scales.[209] Models for the mechanism suggest that the motion of the droplet f) down the scale "terrace" takes place through a discontinuous three-phase contact line (TCL), with air-gaps that enable the smooth sliding motion. When droplets are made to g) slide up against the scale "terrace", a continuous TCL exists with minimal air-gaps, results in droplet pinning.

These scales demonstrate superior duality in superhydrophobic wettability, operating based on the droplets' directional approach towards or away from the body of the butterfly. When water droplets on the butterfly's wings are directed towards the body (outside to inside), a highly adhesive state of petal-like superhydrophobicity occurs, halting the droplet in its tracks. However, when the droplet is directed away from the body (inside to outside), a highly slippery state of lotus-like superhydrophobicity takes precedence, enabling rapid droplet shedding.[209] These distinctive properties grant the butterfly advantageous self-cleaning properties while preventing it from being drenched, even under rainy flight conditions. Such unique, naturally-evolved properties offer important insights towards their artificial design and exploitation, which could lead to the invention of smart material interfaces with useful directional dewetting properties.

2.2.5. Superhydrophobic-Hydrophilic Patterning

Considering the very different wetting physicality and purpose behind each naturally occurring super(de)wetting state, it may seem unintuitive, impractical or even impossible for super-hydrophobicity and -hydrophilicity to exist in close proximity on a single organism.

However, a unique combination of superhydrophobic-hydrophilic array patterns was found on the backs of beetles native to the Namib Desert, *Stenocara gracilipes*.[210] The integration of superhydrophobicity with hydrophilicity allows the beetle to extract water from its ultra-dry environment *via* a concept known as "fog-harvesting".[210]

In the highly arid Namibian desert, early morning fogs represent a short-lived but immensely valuable source of water. The Namib beetle's back is made up of bumps (0.5 mm diameters, 0.5-1.5 mm pitch) that are covered by hydrophilic material, separated by waxy epidermal troughs that are superhydrophobic. Saturated water vapor interacts with the beetle's shell, forming condensates on the hydrophilic bumps, eventually forming larger droplets. These droplets ultimately reach a critical size and detach from the bumps, moving into the channels where they encounter the superhydrophobic

tracks. These droplets move through the channels / troughs *via* gravity, leading into the beetle's mouth, providing effective hydration under such environmental scarcity.[211]

The synergy of such differential super(de)wetting and non-intuitive wetting designs demonstrates immense promise for many unrealized engineering applications.

2.2.6. Superoleo(amphi)phobicity

While superhydrophobicity is now known to be ubiquitous in nature, superoleo(amphi)phobicity is much rarer, particularly in-air superoleo(amphi)phobicity. In-water superoleophobicity is less impressive when considering absolute superdewetting properties. Fish scales / skins, for instance, are known to possess underwater superoleophobic properties.[171] This effect stems from an in-air superhydrophilic hydrogel-like slime coating, which is capable of trapping a thin layer of water, a phenomenon related to in-air superhydrophilicity.[171] The repulsion of oil is enabled by this thin layer of entrapped water that results in underwater superoleophobicity.

In contrast, in-air superoleo(amphi)phobicity requires a meticulously designed re-entrant surface structure coupled to ultra-low surface energy density. This challenging combination must be sufficiently optimized to prevent the adhesion of oils, which typically possess fairly low surface energy density / surface tension. In nature, the springtail hexapod, *Folsomia candida*, is the only reported organism whose skins demonstrate some degree of superoleophobicity (Figure 2.18).[22,75]

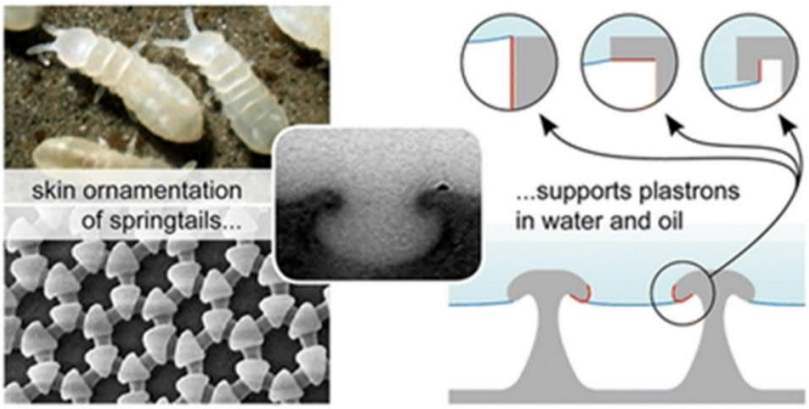

Figure 2.18. Superoleophobicity in nature. The springtail (*Folsomia candida*) skin's surface textures resemble mushroom-like re-entrant profiles. This enables the preservation of a plastron layer in both water and oil, thus achieving superoleophobicity.[75]

Springtails evolved this ability because of their rain-flooded habitats and cutaneous respiratory system. The evolutionary development of these epidermal re-entrant features improves the breakthrough pressure of the interface, thus preventing fluid penetration that plagues many superhydrophobic surfaces. More importantly, these unique structures also demonstrate in-air superoleo(amphi)phobic properties, owing to the energetically unfavorable progress of contact lines. For instance, olive oil cannot easily wet the springtail's skin but instead forms a plastron layer. On the other hand, olive oil would readily wet a superhydrophobic lotus leaf owing to its much lower surface tension.[22,75]

2.2.7. Notable mentions

The complete list of nature-inspired engineering designs for super(de)wettability are too diverse and numerous to cover.[19] Sub-categorization of these features into specific nanostructural designs or applications would make classification even more challenging. In the interest of brevity, a few other famous examples are listed in this section for reference.

Mosquito-inspired Superhydrophobic Anti-Fogging Lenses

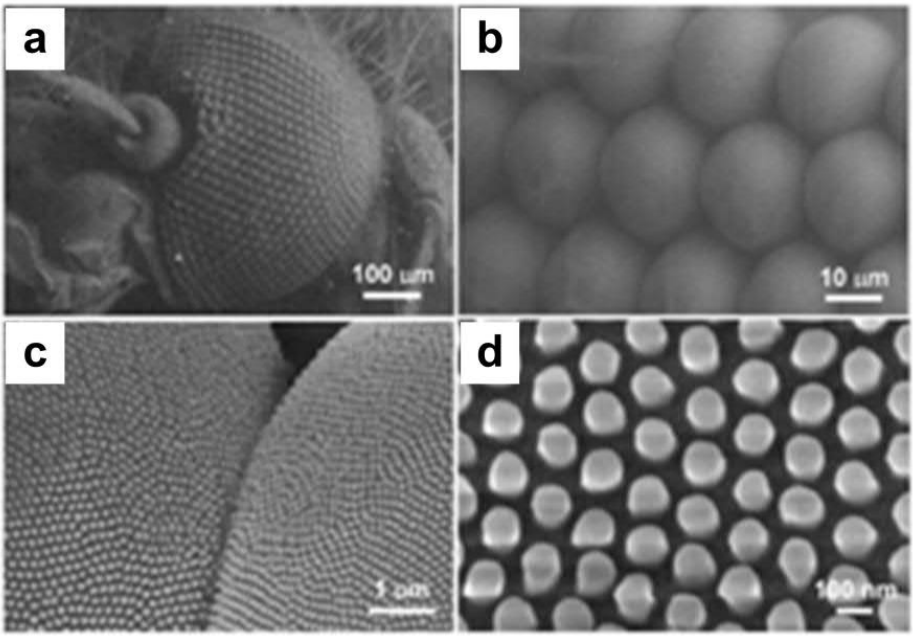

Figure 2.19. Superhydrophobicity for anti-fogging. a) SEM micrograph of a single mosquito eye. b) A hcp micro-hemisphere (*ommatidia*). c) Two neighboring *ommatidia*. d) Hexagonal ncp nano-nipples covering an *ommatidial* surface.[212]

In contrast to the use of superhydrophilicity for anti-fogging glass,[30,123] mosquitos' superhydrophobic compound eyes have also been shown to possess anti-fogging properties, by virtue of its micro- nano-texturing.[212] Unlike the contamination risks that continually threaten the functionality of superhydrophilicity,[16,20,30] superhydrophobicity is a much more long-lasting option, owing to its ultra-low surface energy and inherently anti-contamination properties. Successful implementation and design of optical systems inspired by mosquitos' compound eyes (Figure 2.19) could potentially revolutionize maintenance-free anti-fogging coatings under harsh, chemically-contaminated humid environments.[212]

Water Strider -inspired Superhydrophobic Appendages for Micro-robots

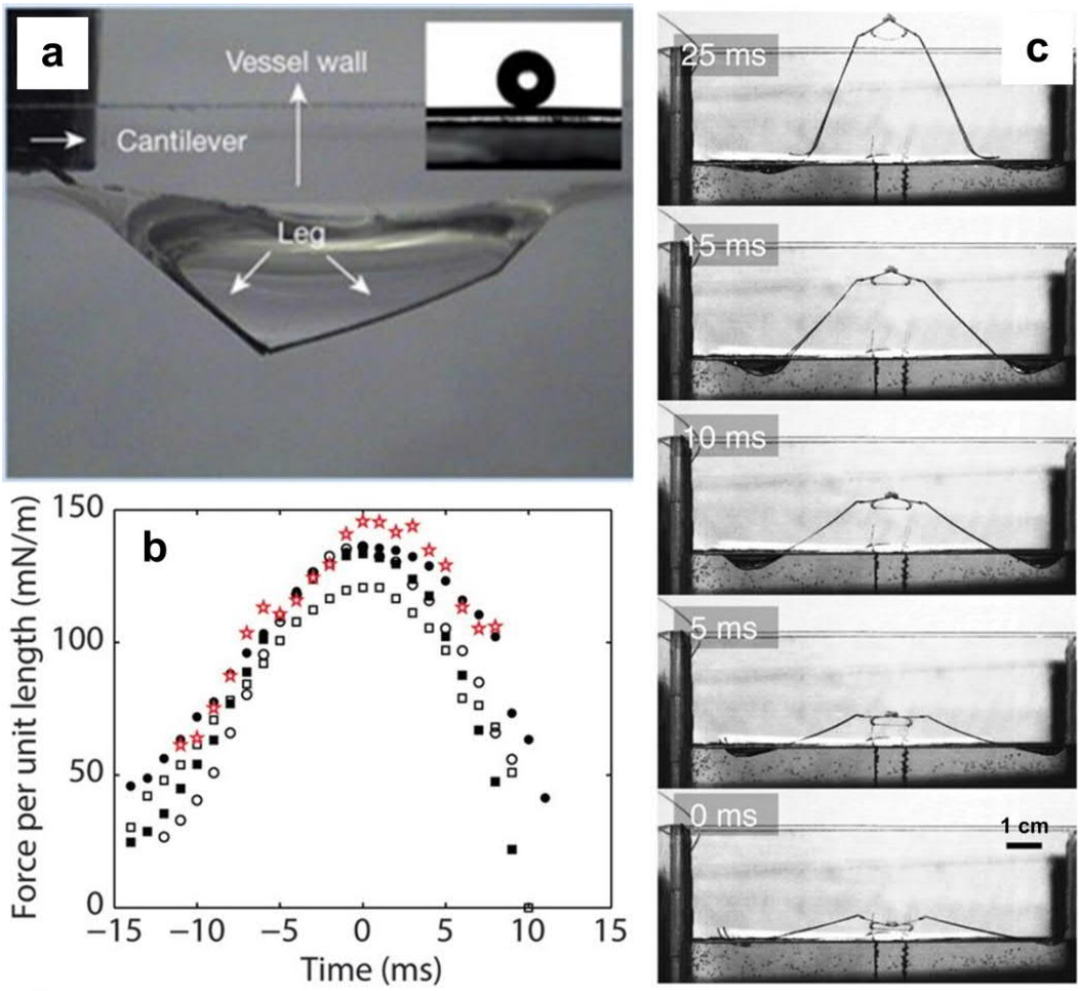

Figure 2.20. Superhydrophobicity for bioimimetic robots. a) The non-wetting leg of a water strider. Typical side view of a maximal-depth dimple (4.38 ± 0.02 mm) just before the leg pierces the water surface. Inset, water droplet on a leg; making a CA of 167.6 ± 4.4°.[213] b) Force comparisons on a water strider's leg (b/w symbols) vs. bioinspired robotic legs (red stars) during the jump. c) High speed optical imaging of the bioinspired on-water jumping robot.[214]

The water strider's superhydrophobic legs allow the insect to walk and move effortlessly on water.[214] The Cassie-Baxter state of interfacial contact with water is remarkable and cannot be easily penetrated until excessive immersion. Jiang et al. calculated in 2004,[213] that the buoyant force on one leg is enough for supporting the body weight of the insect by 15 times. This supplements the insects' ability to navigate even rough and turbulent waters, due to its high breakthrough pressure properties (Figure 2.20).

In 2015, this effect was exploited for the design and construction of micro-robots that mimic the superior on-water stability of the water strider.[214] Micro-robots constructed were not just able to slide or walk on water, but were even capable of jumping and lifting themselves off the surface, just like the insect.

Salvinia -inspired Stability of Underwater Superhydrophobicity

The *Salvinia* is a submerged water plant that offers an interesting paradigm to the design of near- or under- water superhydrophobic structures. Typical superhydrophobic interfaces tend to lose their superhydrophobic properties within hours or a few days upon immersion, due to the gradual loss / dissolution of trapped air.[177]

The *Salvinia*, however, is covered by complex hairs that are shaped like "egg-beaters". This complements the rest of the leaf's surface, which are coated in nano- wax crystals. These combined features give rise to naturally occurring in-air superhydrophobicity. However, upon immersion, the tips of the "egg-beater" structures demonstrate a paradoxical hydrophilic property.[215]

The tips of the "egg-beaters" are hydrophilic, paradoxically forming pinpoint locations on the interface that stabilizes the fluid meniscus, resulting in local energy minimums (Figure 2.21). Fluctuating disturbances to the fluid meniscus that cause fluid penetration or detachment will require further activation energy. As such, the triple-phase contact line is extremely stable, and the plastron's underwater stability is preserved for extended periods of time.[215] The in-water stability of the superhydrophobic salvinia leaf offers interesting insights into creating surfaces with immersion-stable

superhydrophobicity, showcasing potential maritime applications in drag-reduction and anti-fouling.[177,215]

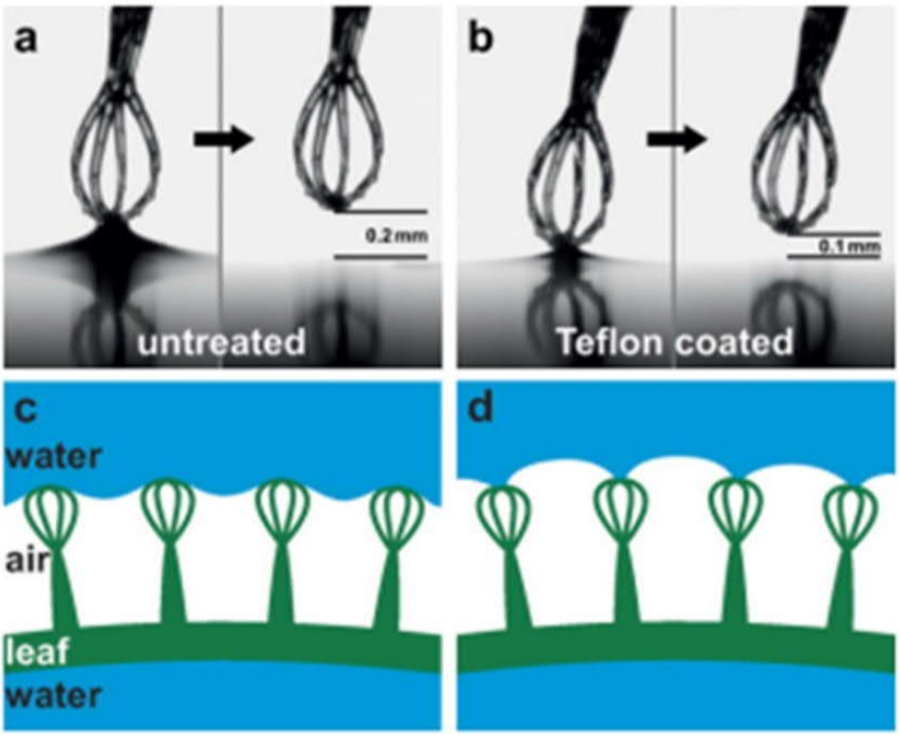

Figure 2.21. Underwater superhydrophobicity. Meniscus-pulling experiment with an a) untreated and b) Teflon-coated hair. The tip of the untreated hair a) is hydrophilic, leading to stronger pinning to the water surface compared to the Teflon coated hair. Distance during meniscus detachment is included. c,d) Schematic of the air retention by a submerged Salvinia leaf (green). Both c) hydrophobic repulsion and d) pinning by the attractive hydrophilic tips of the hairs effectively stabilize the air-water interface.[215]

Proboscis-inspired Micro-Mechanical Bionic Probes

Another example of non-intuitive combinatory wetting in organisms is found in the butterfly's proboscis (Figure 2.22). The exterior and top-sections of the proboscis are hydrophobic-superhydrophobic while its interior and bottom-sections are hydrophilic-superhydrophilic. The hydrophilic-superhydrophilic interiors enable efficient capillary action of fluids into the butterfly's proboscis during food uptake, while the hydrophobic-superhydrophobic exteriors enable self-cleaning.[216] Such a unique combination of wetting properties can inspire the design of ultra-efficient, contamination-free micro-mechanical bionic tools that could contribute to advanced microfluidic technologies.[94,193,217]

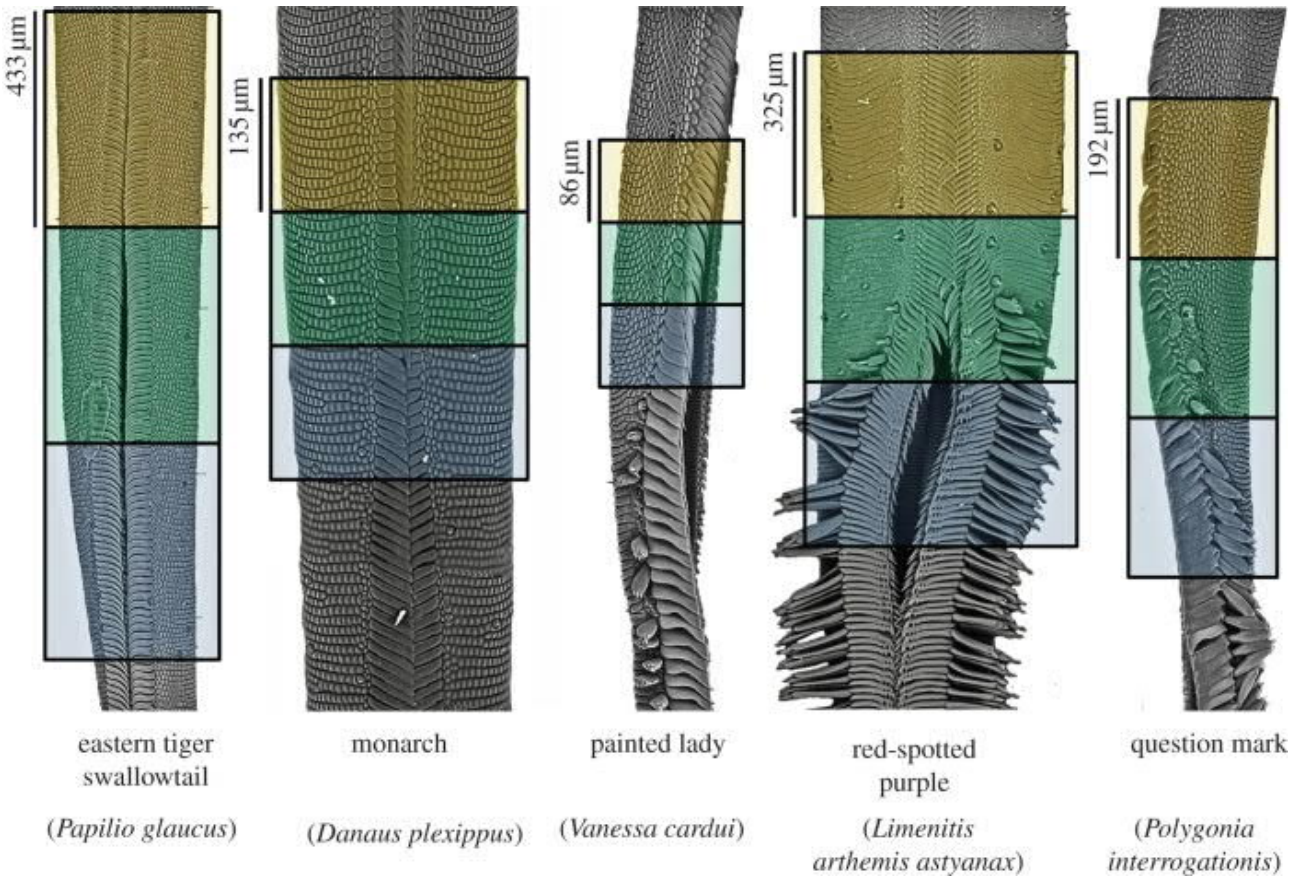

Figure 2.22. Scanning electron micrographs of butterfly proboscises. The associated wettability of each region is denoted as blue:hydrophilic, green:transitional and yellow:hydrophobic.[216]

Pitcher-inspired Slippery Liquid Impregnated Porous Surfaces (SLIPS)

In recent years, the study of superdewetting self-cleaning coatings has led to the development of slippery surfaces.[200] This family of surfaces was inspired by the pitcher plant, of the genus *Nepenthes* (Figure 2.23). The carnivorous pitcher plant survives in habitats with poor soil nutrition and relies heavily on trapping and consuming insects. The pitchers have thus evolved several key fundamental characteristics, including anistropicity (to direct prey into the trap) and slippery amphiphilicity (a thin layer of trapped slippery fluids within the surface).[218] Contact between the feet of the insects and the plant's epidermis is thus drastically reduced, and insects that venture too far would involuntarily slide into the pitcher. Implementation of such a system to engineering coatings will not enable a superphobic state (CA > 150°), but could maintain a fluid separation layer. This isolated layer prevents fluid contamination simply by virtue of a contactless interface. Operational functionality is also user-defined and tunable, simply by using a different porous interface or a substitute fluid.[219-223]

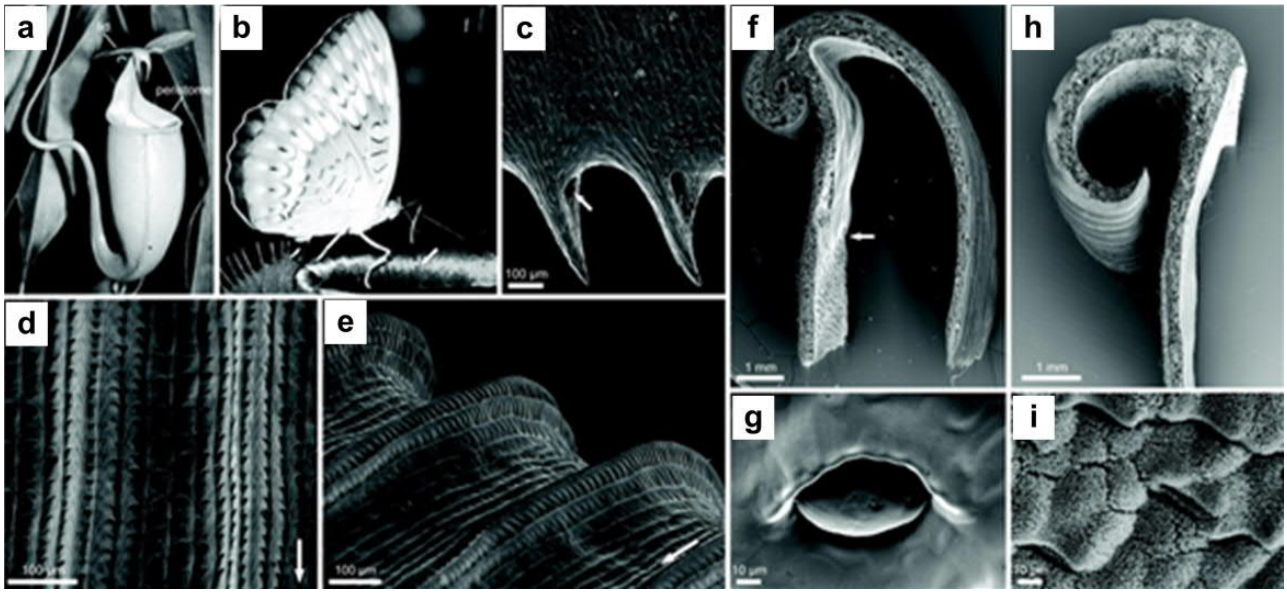

Figure 2.23. ***Nepenthes*** **pitcher and the morphology of its peristome.** a) Pitcher. b) Butterfly harvesting nectar from the peristome's surface. Peristome channels are filled with nectar secreted from pores that are found along the inner walls of the peristome (arrow). c) Underside of the peristomes' inner walls possess cone-shaped projections with nectar pores near their bases (arrow). d-e) Peristome surface with first- and second-order parallel ridges, giving rise to anisotropic properties. Arrows indicate slipping direction toward the inside of the pitcher. f) Transverse cross-section of the peristome. Surface roughness transitions from the rough digestive zone to smooth surfaces under the peristome (arrow). g) Digestive glands on the inner pitcher walls. h) Transverse cross-section of the peristome. i) Waxy inner pitcher wall.[218]

2.3. Templating, Lithography and Beyond

A thorough review on super(de)wettability will not be complete without acknowledging the contributions of top-down micro- and nano-texturing techniques, such as templating and lithography. Precisely nanotextured interfaces have provided strong fundamental basis for both theoretical and experimental validation of numerous wetting phenomena. This includes studies on highly dynamic surface properties such as droplet contact time,[179] directed mobility[190,224,225] and contact line depinning[13,226].

Templating

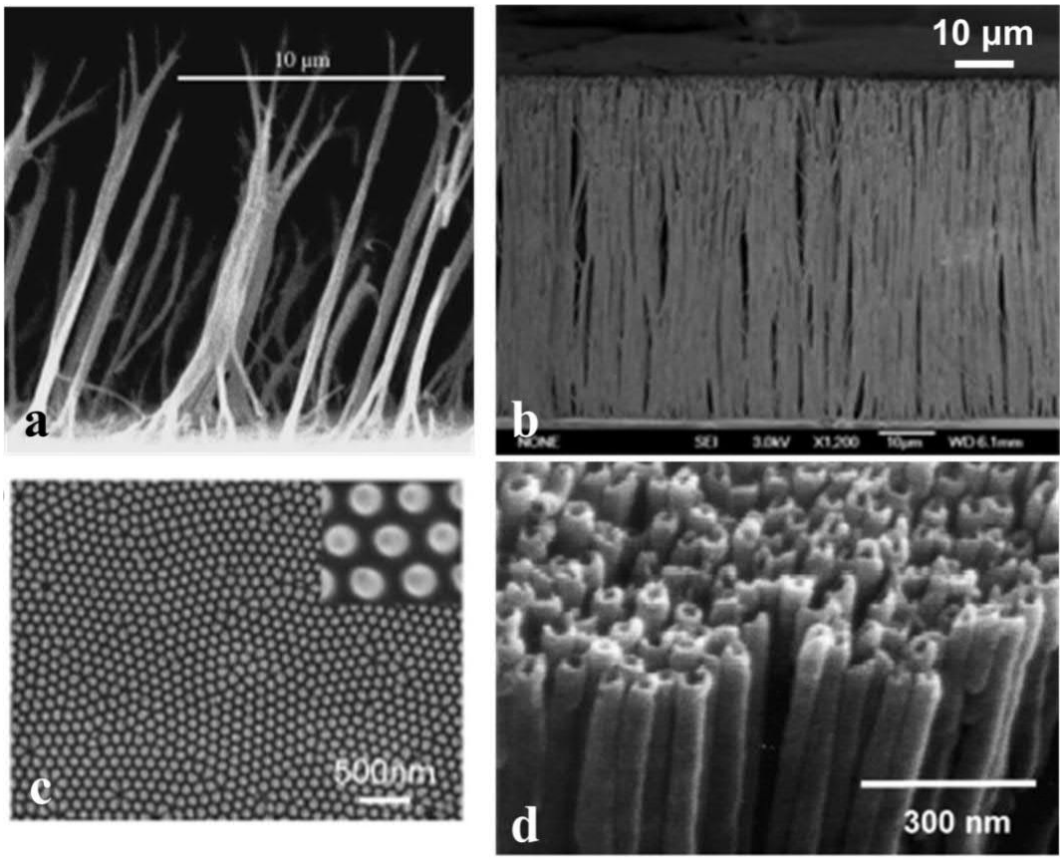

Figure 2.24. Templating as a means for nano-texturing. Template-developed nanotubular structures from a) PVA,[227] b) PS,[143] c) PC[228] and d) carbon[229].

Templating has been used as a fundamental means for achieving precise micro- and nano-structural molding.[96,98] It can be used on both natural geometries,[10] as well as a variety of man-made textures such as etched metals,[98] anodic aluminum oxide (AAO),[230] and lithographically designed templates[71] amongst others.[96,208,231]

Through this, complex structures such as spikes, stripes and nanofibers can be fabricated from a variety of materials: poly(vinyl alcohol) (PVA),[227] polystyrene (PS),[143] polycarbonate (PC)[228] and even carbon[229] (Figure 2.24). In conjunction with the use of high surface roughness and pre-designated surface chemistry, correspondingly desired states of super(de)wettability can be achieved. Today, templating has been extensively used in most domains of super(de)wettability, such as petal-like superhydrophobicity,[10,26,42,138,143] lotus-like superhydrophobicity[232-235] and even super(oleo)amphiphobicity[22,74,75].

(Photo)-lithography

Lithography is vastly superior to templating when considering precision and control over surface texture designs. However, it is also largely plagued by poor scalability, draconian requirements and significant costs in instrumentation and operation. Nevertheless, lithography is capable of fabricating a variety of intricate interfacial architectures, such as straight-wall pillars,[39,71] textured pillars,[72] cones,[73] inverse trapezoids[74], T-shaped hoodoos[75] and even doubly re-entrant structures[12] (Figure 2.25).

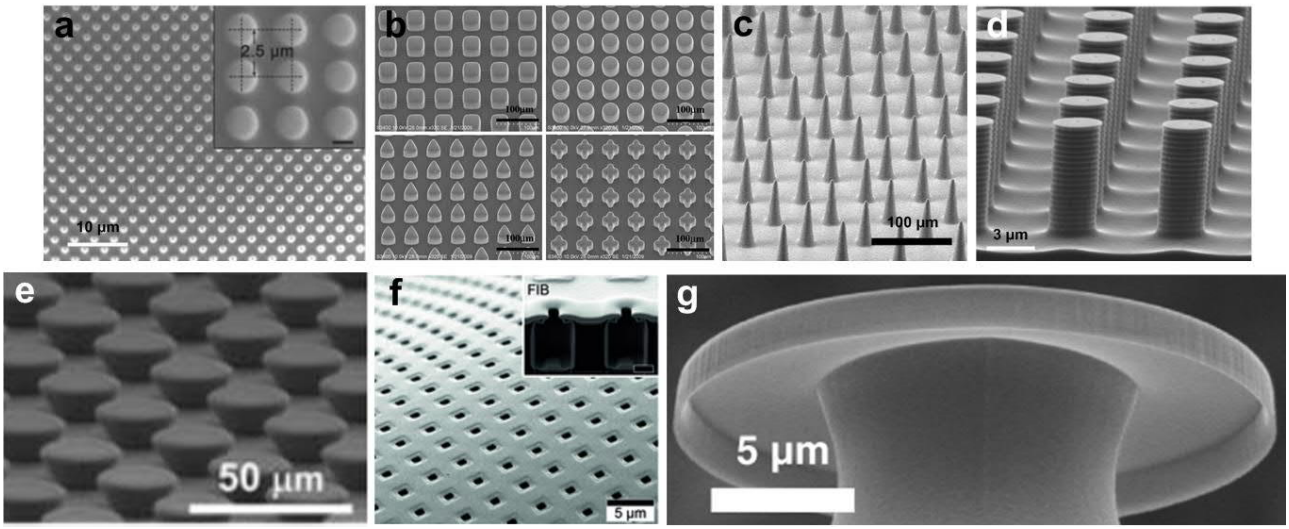

Figure 2.25. Soft-, Nano-, Optical- Lithography. Accuracy and precision of lithography-developed micro-features: a) Soft PDMS pillars on flexible films,[39,71] b) square, triangular, round and cross-shaped PDMS pillars,[49] c) cone-shaped PDMS pillars for fog-havesting,[73] d) silicon pillars with multiple re-entrant texturing,[72] e) inverse trapezoidal PDMS pillars with re-entrant profiles,[74] f) reverse imprint lithography based T-shaped hoodoo-like re-entrant profiles (PFPEdma),[75] g) doubly re-entrant profiles (mushroom-like) from silicon texturing.

Owing to its capability for regular and potentially limitless surface design, this method has been instrumental in advancing the forefront of super(de)wettability. Today, it continues to spearhead new discoveries for super(de)wetting states that range from superhydro(phil)phobicity to superomniphobicity.[12,187,236] It was most notably described as a means for achieving super(-oleo, -amphi, -omni)phobicity through the design of T-shaped re-entrant microhoodoos.[158,237] This was later expanded into a "serif T"-like profile, resulting in the concept of double re-entrancy.[12] This specific surface architectural design achieved the most ideal state of superomniphobicity,[12] whose absolute dewetting performance is yet to be surpassed by any other means at the time of writing.

Scalable Bottom-up Texturing Approaches

Despite numerous advances in top-down techniques, bottom-up self-assembly methods are comparatively more facile, rapid and usually cheaper. In stark contrast to the ordered designs and steps attributed to templating / lithography, they utilize highly chaotic but deterministic regimes of electro-, hydro-, aero- and thermo-dynamics for achieving structural design and function.[76] Despite the increased research effort needed in determining niche operational zones, these routes are usually quite scalable. Today, the number of bottom-up self-assembly techniques is continuously increasing, ranging from intra-, inter-, macro- and supra-molecular methods.[76] We will review in the following sections, comprehensively, bottom-up means that have been used to achieve the different domains of super(de)wettability.

2.4. Superhydrophilicity

Here, we will review methods that have achieved both definitions of superhydrophilicity, ideal and hemi-wicking aided.[16] As described in sections above, although the equilibrium contact angle (CA) behaviors are very similar, they can be dynamically and fundamentally different.

2.4.1. Fabrication and Materials

Historically, materials that are hygroscopic and readily soluble in water are known to be hydrophilic. This resulted in the early classification of hydrophilicity for many inorganic salts, such as NaCl, KCl, or $NaHCO_3$.[8] Later, this definition expanded into the analogous sub-classification of organic compounds, such as water-soluble polymers.[8] However, the use of solubility in determining hydrophilicity is misleading. The balance of intermolecular forces between a liquid and a solid is heavily muddled by the entropic changes that come with material solvation. Other researchers also considered the polar-polar interactions between materials[238] and particle partitioning at oil-water interfaces[239] as a means for classifying hydrophilicity. However, no definitive conclusion could be agreed upon.

Today, hydrophilic materials are officially defined with the use of static CAs, albeit with a heavily debated demarcation of < 90°.[99] This definition was originally aimed at providing a facile means of material selection, with choices that can be used to manifest hydrophilic and; with roughness, superhydrophilic states. The category includes biological membranes, inorganic hydroxylated metallic oxides and minerals (silica, SiO_2, titania, TiO_2, zinc oxide, ZnO, alumina, Al_2O_3, silicates, SiO_4^{4-} etc.), ionic crystals, metals and even many polymers. In fact, many more hydrophilic (CA < 90°) materials exist in contrast to their hydrophobic (CA > 90°) counterparts. For instance, the latter variant is only known to exist with the presence of completely saturated hydrocarbons and fluorinated materials. Unsaturated bonding or heteroatoms such as oxygen introduces polarity which would theoretically result in the loss of hydrophobicity.

However, this long-standing classification may require serious re-consideration, in view of new findings behind the limits of long-range attractive / repulsive forces between hydrophilic and hydrophobic surfaces by Berg et al (Figure 2.26).[99] In concurrence with the independent work on the free energy of hydration by van Oss,[240] a new proposed hydrophilic limit of CA < 65° has gathered immense interest and attention. From an experimental perspective, very hydrophilic materials seem to be exceedingly commonplace. This is substantiated by the many pristine hydrophilic surfaces that we see around us, including glass, quartz, cleaved mica, metals (gold, silver, chromium, copper) and many other types of hydroxylated metallic oxides. In fact, according to the Young's equation, a CA of 0° relies on the sole criterion of a solid surface energy, γ_s that exceeds 72 mN/m. This aligns to many experimental observations, where materials with surface free energies lesser than that of water (72 mN/m) are typically hydrocarbon-based polymers.[241] Paradoxically, highly wettable materials are not easily and commonly observed in reality. Due to the very high surface free energy of such materials, their functionality is short-lived as they are rapidly contaminated by adventitious organics. The surface adsorption of organic moieties onto such highly active surfaces affects their ability for long-term retention of superwetting functionality.

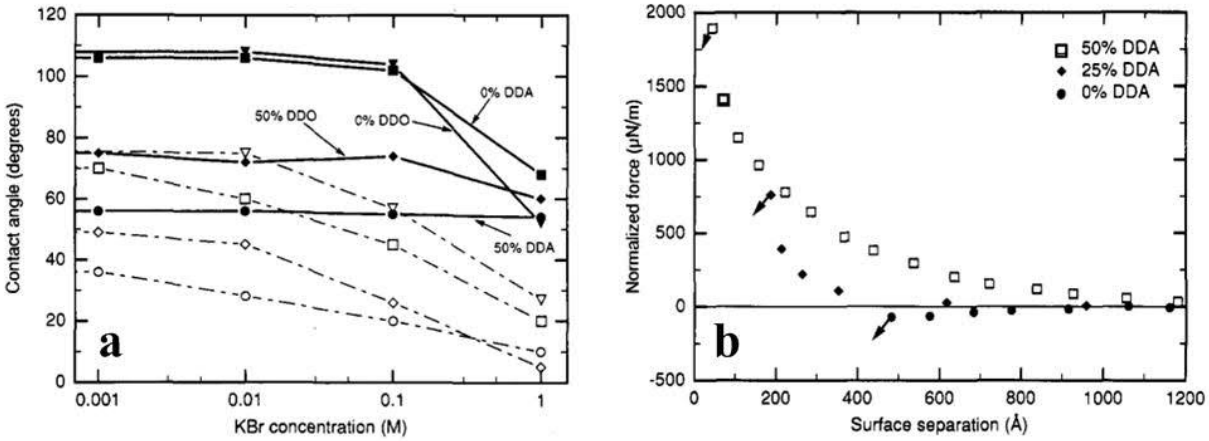

Figure 2.26. Long-range attractive / repulsive forces. a) Advancing (filled symbols; solid lines) and receding (open symbols; broken lines) CAs for aqueous KBr solutions on carboxylic (DDA containing) and hydroxy (DDO-containing) monolayers at two different compositions (0% and 50% of bipolar substance), as a function of KBr concentration. b) Normalized forces as a function of distance D, measured between two mica cylinders coated with a carboxylic DDA layer. Force curve for 0% DDA (filled circles) was measured in pure water, while KBr solutions were used for 25% DDA (filled diamonds) and 50% DDA (open squares). Arrows indicate transitions into adhesive contact.[99]

While the longevity of superwetting interfaces can be slightly enhanced by using highly porous morphologies, their operational functionality can hardly be described as permanent. Today, functional superhydrophilicity needs to be achieved within limits of acceptable stability even when exposed to an environmental cocktail of volatile organics. In recent years, new techniques have been used to achieve the state of superwetting, through exploiting coupled physical phenomena. Today, methods for achieving superhydrophilicity include the exploitation of hydroxylation, photoactivation, roughness-induced wicking, molecular self-assembly or a combination of the above.

2.4.2. Ideal Superhydrophilicity

Ideal superhydrophilicity is defined by its ability to rapidly spread a water droplet over its surface, culminating in a CA of just 0-10° within 0.5s.[30,123] To date, superwetting performance capable of matching this condition represents the strictest known definition of superhydrophilicity.

2.4.2.1. Surface Oxidation and Hydroxylation

Engineering advances made in recent decades have enabled the development of facile surface treatment by plasma,[242,243] corona,[244,245] ozone,[246,247] flame,[245,248] and ions[249] (Figure 2.27).

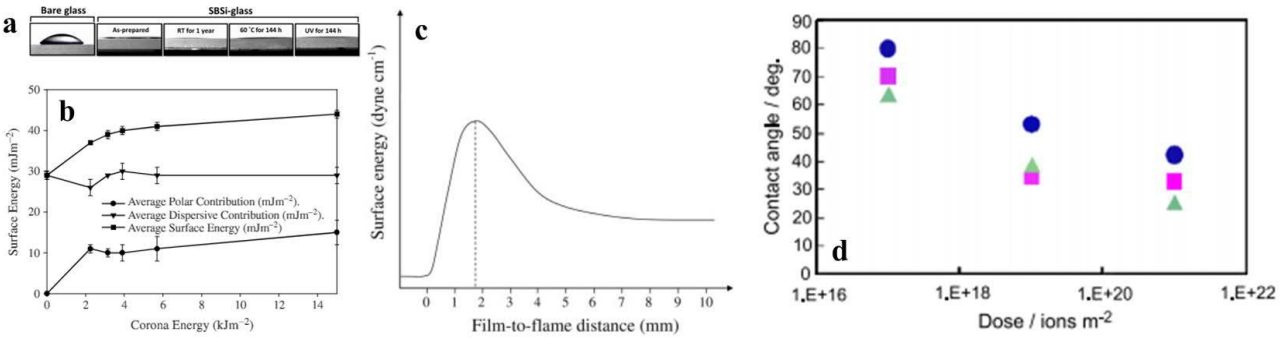

Figure 2.27. Surface hydroxylation by plasma-, corona- and flame- treatment for superhydrophilicity. a) CA measurements for bare and plasma- treated SBSi-glass substrates.[250] b) Surface energy and its polar and dispersive components of corona-discharge-treated PP film as a function of corona energy.[244] c) General trend of the surface energy values of flame-treated polyolefin films as a function of the film-to-flame gap.[248] d) CA as a function of dose for ion implanted hydroxyapatite.[249]

These methods enable the rapid oxidative modification of surfaces without affecting bulk material properties. Plasma[242,243] and corona[244,245] treatment, for instance, uses highly energetic electrons

for the cleavage of surface molecular bonds. This results in the formation of surface free radicals that react with surrounding oxygen or water vapor to give oxygen or hydroxyl terminated functionalities.[251] Flame treatment enables the thermal combustion of a surface's functional groups, thus forming hydroxyl radicals that results in the oxidation of a material surface.[248] These methods typically result in extensive oxidation or hydroxylation and therefore can be applied to inorganic,[242,243,249] organic[244,245] and even metals[247] for achieving superwettability.

Hydroxylation of materials can alternatively be performed by using concentrated bases. Alkali etching of titanium,[252] glass[253] and polymers[254] have all been shown to produce the superwetting phenomenon. Alkali treatment induces direct surface hydrolysis, creating a series of carboxyl or hydroxyl terminated surface groups, thus promoting their hydrophilicity.[255] The combination of these surface oxidation-hydroxylation processes with hierarchically textured materials, such as nanoporous glass,[253] nanofibers,[254] porous metals[247,252] and metallic oxides[249], could enable the fabrication of ideally superhydrophilic surfaces.

Fujima et al. showcased the use of hot $NaHCO_3$ for etching sponge-like nanoporous silica glass, giving rise to a long-lasting (> 140 days) superhydrophilic state in an ambient laboratory environment. However, neither the optical properties, nor time taken for CA to be < 10° are typically analyzed here.[253] In a separate study, Wang et al. demonstrated the use of NaOH-Methanol hydrolysis of poly(butylene terephthalate) to create a series of hierarchical fibrous surfaces, which achieved a CA spread to < 10° within just ca. 0.2 s.[254]

Despite the superior superhydrophilic performance that is demonstrated by plasma-, corona-, and flame- enhanced surface modifications, they are debilitated by ambient durability. Hydrophilic surface groups are highly energetic, and can suffer from functional failure if adventitious organics are adsorbed.[238] In the case of organic polymer substrates, we must not ignore the effects behind the surface reorganization of polymeric chains. This is a common phenomenon that is found in superhydrophilic polymers, culminating in the eventual burrowing of functional hydroxyl groups.[256]

Today, polar groups that are produced from surface oxidation can be rapidly lost when placed in contact with ambient air for extended periods of time (hours to days).[242,256-259] These drawbacks result in the largely draconian protocol of storing freshly prepared superhydrophilic materials in highly polar mediums, such as water, in order to preserve their functionality.[8] However, even the short timeframe between preparation and storage is sometimes insufficient for preventing surface contamination.[260] This consideration gave rise to the use of photoactivity in many superhydrophilic coatings, where ultraviolet (UV)-irradiation-activation is used as an *in-situ* method of self-oxidation, thus enabling the regeneration of functionality.[5,261-263]

2.4.2.2. Photoactivation

In 1997, the first practical demonstration of self-regenerating superhydrophilicity was performed by Wang et al.[5] Wang et al. described the use of UV irradiation of TiO_2 to induce Ti^{3+} sites, ideal for dissociative water adsorption and thus superhydrophilicity. The Ti^{3+} sites that are formed during UV-activation generate hydroxyl radicals are capable of leading to superhydrophilic and self-cleaning properties simultaneously (Figure 2.28). The prevalence of UV in sunlight has also made the method very commercially viable. Engineering concepts that exploit *in-situ* self-regeneration of superhydrophilicity in TiO_2 have been demonstrated for many intervention-free applications. This includes work in anti-fogging,[30,257] microfluidics,[257] self-cleaning,[262] and even switchable wettability[264].

Today, photoactive inorganic materials include TiO_2[5] and ZnO,[265] which are both actively studied for the synthesis of superhydrophilic surfaces under different applications.[201,259,265-268] Notably, hydrophilic SiO_2[269] is also sometimes used as a synergistic, performance enhancing filler-material with these two photoactive compounds.[30,201,260] However, these purely photoactive or blended photo(in)active hydrophilic materials still rely heavily on micro- and nano-structural morphology for realizing superhydrophilic states. This concept has been demonstrated through the use of scalable techniques such as metal-organic chemical vapor deposition (MOCVD),[270] physical or chemical

vapor deposition (PVD/CVD),[270,271] aerosol-deposited nanoparticle (NP) layers,[30,80] spincoating,[272] electrospinning[261,273,274] amongst others.

Despite the prevalent use of titania, titania-silica or titania-indium oxide and other configurations,[259,266,267,269] one of the longest lasting state of superhydrophilic coatings synthesized belongs to the use of zinc oxide. Zhou et al. demonstrated the sol-gel synthesis of micro-spherical clusters of ZnO nanorods. The coatings demonstrated > 6 months (or ca. 183 days) of superhydrophilicity at a CA of 1.2°. Unfortunately, neither the optical properties, nor time taken for CA to be < 10° was analyzed. Nonetheless, the potential for these sol-gel synthesized coatings are vast, as parallel studies have been shown to be capable of rapid-droplet spread coupled to highly transparent properties (< 6% losses).[30,95]

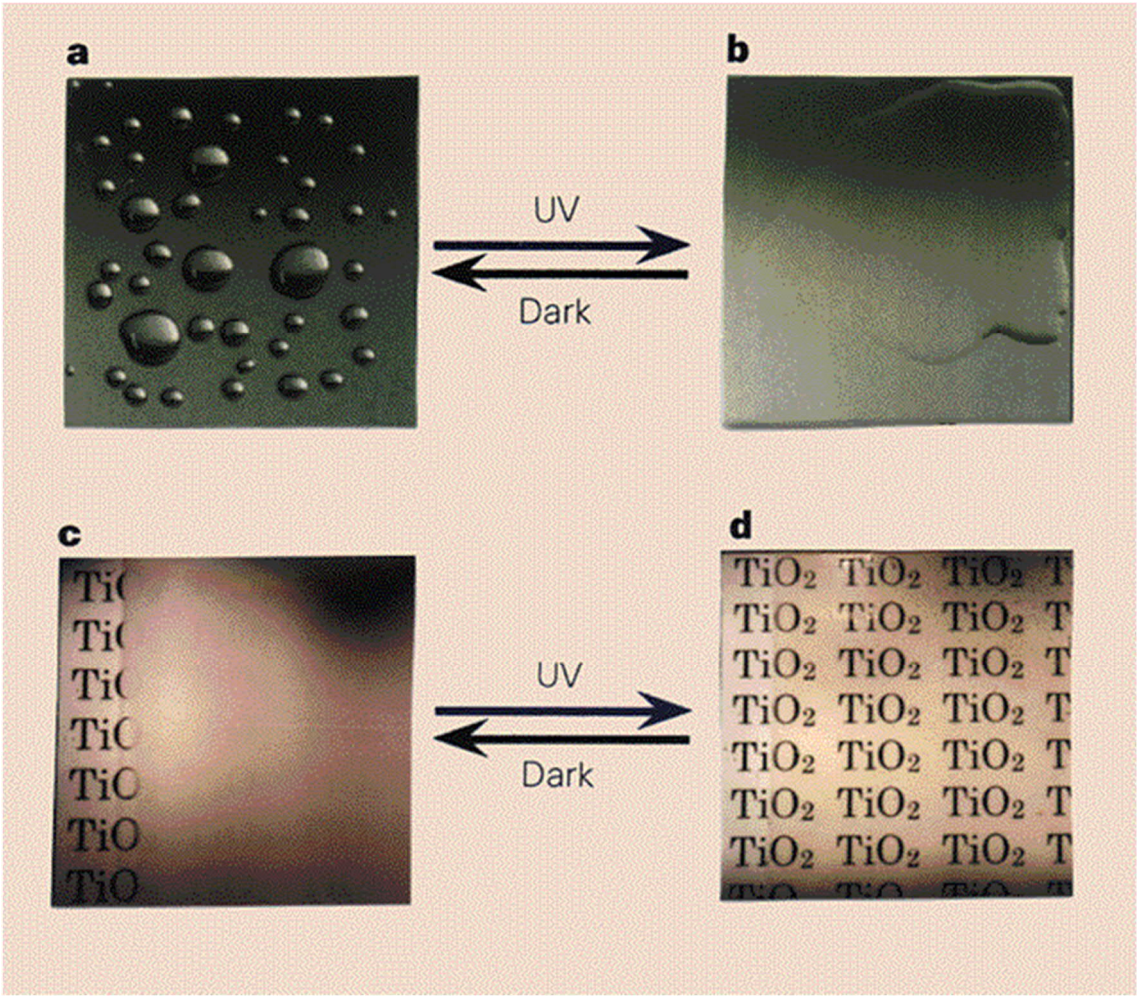

Figure 2.28. UV-induced superhydrophilicity. (a-b) Hydrophobic-hydrophilic properties of TiO_2 coatings upon sequential exposure to UV irradiation-and-darkness. (c-d) Antifogging properties of the coating demonstrated by subjecting the UV-treated coatings to steam.[5]

2.4.2.3. Wet Deposition

One of the fastest droplet spread performance by a morphologically-enhanced surface was achieved by Cebeci et al. in 2006, where a series of PAH/SiO_2 bilayers were deposited by dip-coating. The resulting morphologies were composed of nanoparticle agglomerates. The surfaces were capable of enabling droplet spread to < 10° CA within 0.16 s, and were stable in dark ambient environments for more than a year. They were also highly transmissive, at 96-99.5% between wavelengths of 400 to 800 nm.[123] Dong et al. also synthesized superhydrophilic silica composites from a series of sonication, spin-coating and annealing steps. The resulting bi-layers formed micro- and nano-structured islands, which enabled a droplet spread to < 10° CA within 0.17 s. Surfaces were highly transmissive, at 80-88% between wavelengths of 400 to 800 nm, with between 2-10% losses from bare glass substrates.[272]

2.4.2.4. Electrospinning

Although electrospinning has been previously investigated as a means towards achieving superhydrophilicity, the time-of-spread was largely ignored.[261] In 2014, Wong et al. synthesized a series of amorphous titania nanofibers that retained partial organic content. However, they were able to exhibit rapid superhydrophilic spreading of droplets to < 10° CA within 0.4 s, and were stable in storage for a tested limit of > 72 hours. Moreover, they also exhibited highly transmissivity, at 90-94% between wavelengths of 400 to 600 nm, with between 2-6% losses from bare glass substrates.[95]

2.4.2.5. Aerosol Deposition

An alternate exemplary means for achieving scalable, geometry-independent superhydrophilic coatings stems from the use of aerosol deposition. This was demonstrated by Tricoli et al. in 2009, through the synthesis of silica nanowires and titania nanolaces. The silica-titania composites were able to achieve superhydrophilic spreading of droplets to < 10° CA within 0.5 s, and were stable in storage for a tested limit of > 50 hours. Optical properties of such superhydrophilic surfaces were

excellent, approaching 100% transmittance from 300 to 500 nm with slight anti-reflectance characteristics above 365 nm.[30]

2.4.3. Hemi-Wicking Superhydrophilicity

Despite the immense progress that is achieved by the research community in successfully transitioning from plasma-corona-flame dependent to UV-photoactivated superhydrophilicity, truly intervention-free superhydrophilicity remains a distant goal. One primary limitation that continues to persist in the above methods lies in the need to preserve ultra-high surface energies.[238] Without self-regeneration[5,261-263] characteristics, longevity is scarcely possible. In very recent years, the appearance of a slower but equally effective state of superwetting, which is known as hemi-wicking superhydrophilicity,[124] appears to resolve these standing issues (Figure 2.29).

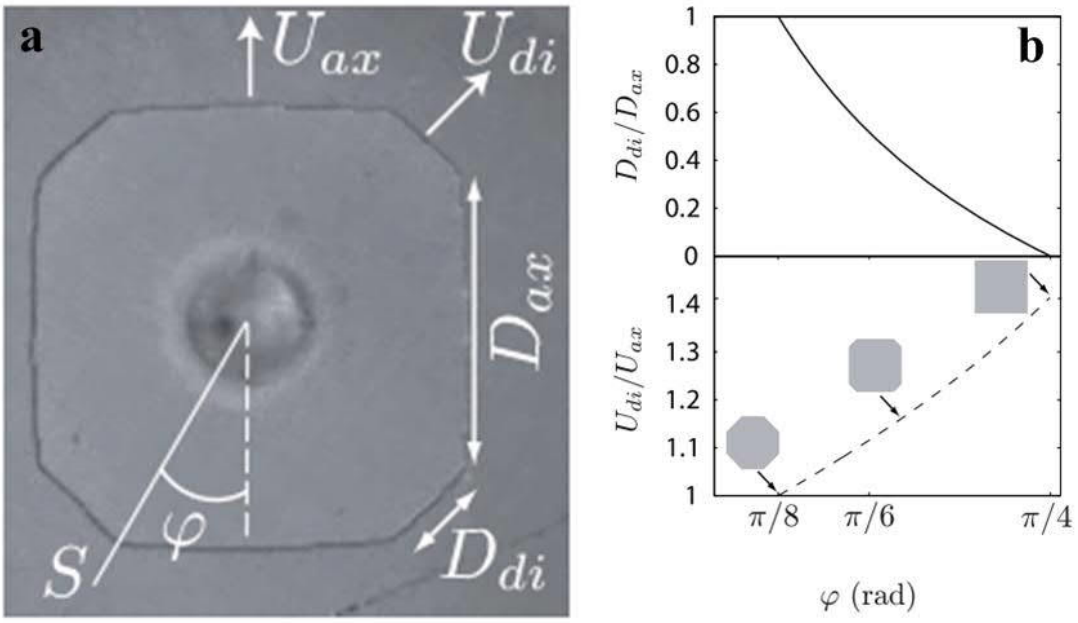

Figure 2.29. Hemi-wicking dynamics. a) Evolution of the facet size-ratios D_{di}/D_{ax} and velocity-ratio U_{di}/U_{ax} as a function of the angle φ. The dashed line corresponds to $U_{ax}/\cos\varphi = U_{di}/\cos(\pi/4-\varphi)$. Inset: top view of an isopropanol droplet spreading on a surface roughness defining the variables U_{di}, U_{ax}, D_{di}, D_{ax}, and φ.

These hemi-wicking superhydrophilic surfaces are a) permanently superhydrophilic in ambient-air without the need for re-activation and are b) capable of sustaining much larger degrees of contamination while preserving function.[30,124] On hindsight, this reflects the surface characteristics of the superhydrophilic leaves belonging to *Ruellia devosiana*, a wild Brazilian petunia. The petunia's

leaves are composed of a complex surface hierarchy of hairs and channel-like structures, which enables superior capillarity effects, akin to hemi-wicking superhydrophilicity.[199]

2.4.3.1. Capillarity-(Structure) Enhanced Fluid Imbibition

Wicking is a ubiquitous phenomenon which is seen in every-day mundane materials such as paper, fabrics, rocks and even kitchen sponges. However, wicking[124] presents fresh perspectives towards the development of alternative superhydrophilic interfaces with contamination-proof capabilities. While the basis of wetting in both hemi-wicking and ideal superhydrophilicity is similar in terms of contact line advancements, they remain fundamentally different. Wicking departs from the traditional understanding of superhydrophilicity, primarily due to its dominant use of structure-dependent capillary-based driving forces.[2] Contrasting the ideal state of superhydrophilicity, hemi-wicking does not require very high interfacial surface energies. Deviation from this draconian requirement comes as an advantage as it suggests that surfaces can sustain much larger degrees of atmospheric contamination before an eventual loss of functionality. The use of lower, but more robust surface energy states, coupled to capillary-wicking features, realizes the steady and gradual fluid imbibition that is observed within hemi-wicking.

However, in contrast to ideal superhydrophilicity, hemi-wicking superhydrophilicity tends to result in complete wetting (CA = 0°) owing to the constant interfacial driving forces.[130] The dynamic wetting behaviors have been classically studied using a forest of micropillars.[124] Wicking dynamics within a regularly patterned rough surface is explained through similar Washburn equations that were originally defined for the capillary effect.[2,124] Per these definitions, taller micro-structured films will result in much more rapid wicking behaviors as compared to a shorter, similarly structured surface. The increasing conduit / channel sizes culminate in improved wicking speeds. However, this effect can plateau, and wicking speeds eventually become independent of increasing channel dimensions. This occurs because the driving forces through the conduits / channels eventually balances against the viscous friction posed by movement of the fluid.[124] Despite the many advantages posed by this

system, hemi-wicking's demonstrated rate of droplet spread is not comparable to speeds observed in ideal superhydrophilicity.[30,124] This drawback could be severe depending on its intended application. Anti-fogging for instance, requires droplet spread to occur in less than 0.5 s for function,[123] contrasting the much larger timeframe (seconds to minutes) taken by hemi-wicking superhydrophilicity. Unfortunately, owing to such slower dynamic spreading behavior, the full potential of hemi-wicking superhydrophilic coatings is still largely unexplored.

Today, research in this area continues to be directed towards the synthesis of superhydrophilic coatings that are 1) highly functional (rapid spread), 2) UV-independent, 3) long-lived and contamination-proof.[123,269]

2.4.3.2. Organically-enhanced Wettability

Thiol-Gold Functionalization

Surface assembly of organic layers on materials is a known and adequately studied phenomenon. In the early 1990s, Whitesides et al. pioneered the use of self-assembled monolayers (SAMs) for tuning the wettability of surfaces.[275-277] A combination of organothiols[275] and carboxylic acids[276,277] were used in conjunction with gold for self-assembling wetting-tunable surfaces *via* permanent sulphur-gold bonding[278]. In later years, Notsu et al. demonstrated the achievement of superhydrophilic states by imparting multi-scale roughness to the gold substrates.[236] The use of organothiols can also be applied to other (precious) metals, such as silver, copper, platinum and palladium.[8]

Silane Functionalization

Chloro- and alkoxy- silanes have been used extensively for the functionalization of metallic oxides, ranging from SiO_2,[279-282] Al_2O_3,[283,284] TiO_2[285] amongst others. Functionalization occurs through the nucleophilic substitution of the surface hydroxyl, resulting in the formation of a silanized graft and the side-products of HCl or alkyl-ol.

Huang et al. demonstrated the use of zwitterionic sulfobetaine silane (SBSi) for the functionalization of oxidized surfaces (wire meshes). Coatings demonstrate excellent wettability, with CAs of < 5°, coupled to excellent transmissivity, ca. 100% at 480 nm. Surfaces were also resilient to pencil scratch test and ambient environment exposure for more than a year.

Thiol-yne Click Functionalization

The thiol-yne reaction occurs between a thiol (R-S-H) and an alkyne (R≡R), first reported in 1949,[286,287] and later re-discovered in 2009[288]. Today, it is also known as click chemistry, which demonstrates immense potential for designer-polymers. Click-chemistry enables facile functionalization of polymers with alkyne functional groups, thus departing from traditional metal- and oxide- dependent substrates for surface functionalization (Figure 2.30).[15,45,289]

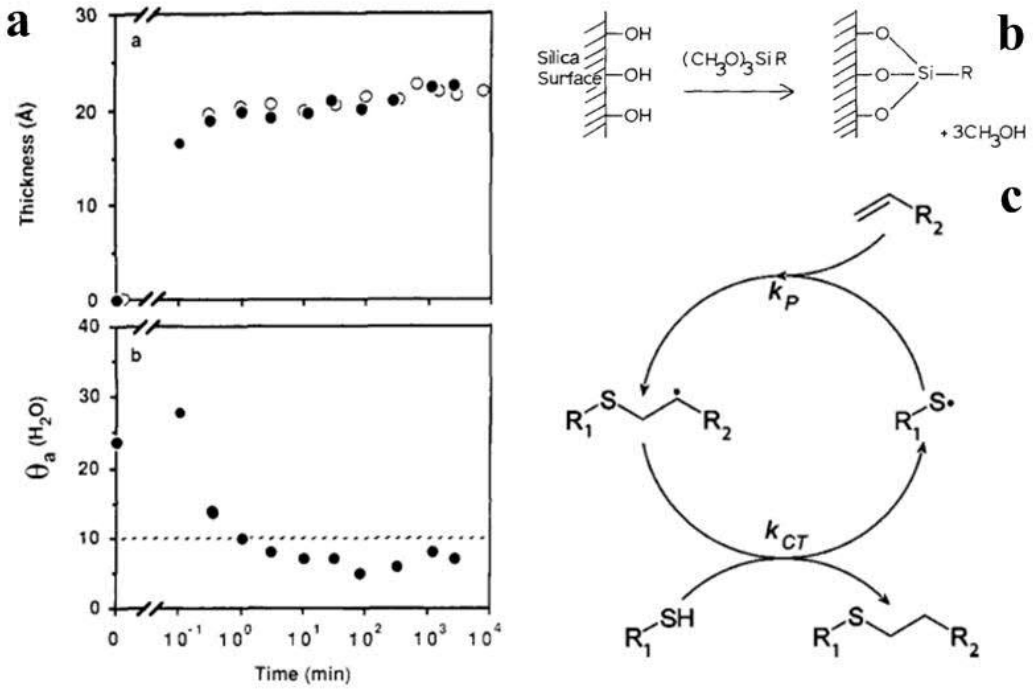

Figure 2.30. Organothiol functionalization. a) Kinetics of organothiol adsorption for wettability-modifications.[275] b) Tri-alkoxy silanization of SiO_2 surfaces.[279] c) Sequential addition and hydrogen abstraction during thiol-ene polymerization.[288]

Amphiphiles

Amphiphilic assembly of mono- or multi-layer organics can occur *via* surface adsorption from either a solution or vapor phase.[290] This has been traditionally demonstrated through a Langmuir-Blodgett

(LB) film. Thin organic layers self-assemble spontaneously on surfaces, depending on the relative surface free energies, thus altering the wettability of materials. The choice of organic layers for achieving hydrophilicity can be made by selecting polar end groups. More specifically, hydrophilicity is best attained with functional groups that possess enhanced affinity with water molecules, such as hydroxyls (-OH) or carboxyls (-COOH).[276,277,291] However, as of the time of writing, despite evidently improved hydrophilicity, this method has not been able to independently achieve perfect superhydrophilicity that demonstrates WCAs of 0°.[8] Physically adsorbed monolayers are also known to possess poorer stability as compared to chemically bonded layers during fluid interaction.[290] These temporarily induced states of wettability can, however, be potentially exploited for facile, reversibly-switchable states of wetting.

2.4.4. Drawbacks

Despite the superior superhydrophilic performance demonstrated by plasma-, corona-, flame-enhanced surface modifications, they are debilitated by ambient durability. Hydrophilic moieties are highly energetic, and can suffer from functional failure if adventitious organics are adsorbed.[238] In the case of organic polymer substrates, we must not ignore the effects behind the surface reorganization of polymeric chains. This is a common phenomenon that is found in superhydrophilic polymers which culminates in the burrowing of functional hydroxyl groups.[256] Today, polar groups that are produced from surface oxidation can be rapidly lost when placed in contact with ambient air for extended periods of time (hours to days).[242,256-259] These drawbacks result in a largely labor-intensive protocol of storing freshly prepared superhydrophilic materials in highly polar mediums, such as water, in order to preserve their functionality.[8] However, even the short timeframe between preparation and storage is sometimes insufficient for preventing surface contamination.[260] This consideration gave rise to the use of photoactivity in many superhydrophilic coatings, where UV-irradiation-activation is used as an *in-situ* method of self-oxidation, thus enabling the continued regeneration of functionality.[5,261-263] However, even UV-regenerated materials continue to suffer from organic contamination, rapidly losing functionality.

2.4.5. Concept

In view of the drawbacks and immense potential behind the field of superhydrophilicity, we aim to showcase the scalable synthesis of superwetting surfaces through facile one-step methods. Attempts will be made specifically to overcome well-known drawbacks (UV-dependence, longevity and facile-functionalization) while retaining functional performance. We then incorporate the culmination of these interfacial designs for real-world engineering applications.

a) We first explore if superhydrophilicity is a state that can be achieved only through the use of anatase or rutile TiO_2, which are photoactive materials that rely heavily on UV-activation. To this end, we investigate the use of amorphous mesoporous TiO_2, enhanced with ultra-high specific surface areas for enabling long-lived states of UV-independent superhydrophilicity.
b) We then investigate the concept of hemiwicking while revisiting the idea of surface modification by using volatile and non-volatile amphiphiles. Hemiwicking remains a new topic in the field of superhydrophilicity, thus conferring it much unknown potential. Alternatively, amphiphile-aided surface modifications were last explored almost 30 years ago.[276,277,291] Uniquely combining these old and new domains of knowledge could potentially open new research areas pertaining to the future development of functional, long-lasting superwetting interfaces.

2.5. Superhydrophobicity

Here, we will review methods capable of achieving lotus-like and petal-like superhydrophobicity.[132] As described in sections above, although static CA behaviors are similar in both modes of superdewettability, they are fundamentally very different when assessed dynamically. Super(de)wetting, in contrast to superwetting, is typified by the use of hydro- and fluorocarbons, combined with roughened hierarchical surfaces. Thus, the methods below may not always stand alone, but could sometimes be integrated for achieving the desired super(de)wetting effect.

2.5.1. Fabrication and Materials

Materials used for attaining a superhydrophobic state (lotus or rose) are in stark contrast with those that are used for superhydrophilicity. For instance, hydro- and fluorocarbons ($-CH_3$, $-CF_3$) are typically used instead of hydroxyls and carboxyls (-OH, -COOH).

Lotus-Effect

Extremely low surface energies are much more desirable, as they enable the achievement of high CAs. The use of organic-based materials is thus much more ubiquitous, with candidates that include plastics and polymers (< 35 mN/m). Today, hydro- and fluorocarbons represent dominant means for achieving a robust superhydrophobic Cassie-Baxter state. The former variants are known for being much greener, considering the negative environmental impact behind synthesizing fluorinated compounds.[292,293] In contrast to the relative rarity of hydrophilic materials, hydrophobicity appears to be much more pervasive. Their presence in both natural and synthetic materials enhances the design flexibility of superhydrophobic materials (Figure 2.31).[132,133] Alternatively, fluoro- and alkyl-functionalization of inorganic materials can also enable superdewetting. This is possible because functional wettability is typically attributed to less than 5 nm of the top-most surface chemistry. As a result, bulk material hydrophobicity is not always mandatory.

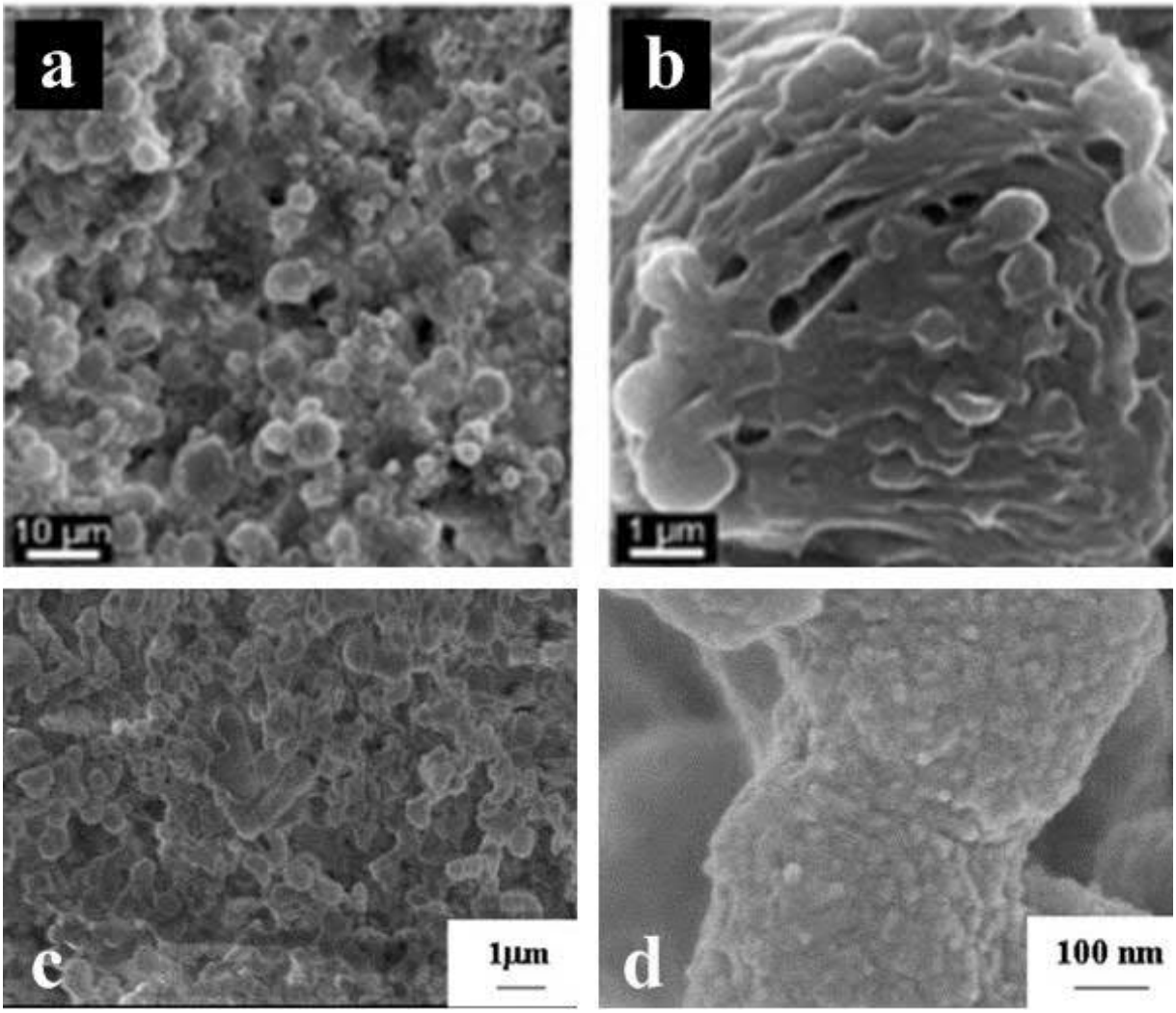

Figure 2.31. Fluoro-free superhydrophobic hierarchical micro- and nano-structures. Natural to artificial superhydrophobicity in self-similar structures. a) Beeswax and b) carnauba wax (3:7 w/w) prepared by annealing treatment.[293] c) Superhydrophobic PVC films formed by ethanol-water induced non-solvent phase separation. d) Magnified nano-profiles.[294]

Petal-Effect

Differentiation of the petal- from the lotus- effect comes in designing a penetration-susceptible morphology. As a result, similar hydrocarbon based materials that are used for the lotus-effect, such as polystyrene (PS)[42,143,295] and polydimethylsiloxane (PDMS)[138] are also commonly used. Unlike the lotus-effect, excessively low surface energies[296] that are imbued by fluorinated compounds (-CF_3 with 6.7 mN/m)[103] should be avoided. Fluorinated materials can result in departure from the petal-effect, causing the full Cassie-Baxter lotus-effect. Very low surface energy states can lead to inadequate contact line pinning, thus resulting in droplet slide and detachment.[296] Here, an optimal material design typically involves moderately low levels of surface energy (20-40 mN/m). This must

then be coupled to morphologies with infiltration-prone micro-structures that are integrated with nano-structures still capable of preserving air gaps.

2.5.2. Ideal Lotus Slippery Superhydrophobicity

Lotus-like superhydrophobicity is characterized by a CA > 150°, a SA < 10° and a CAH < 25°.[132,135] The ideal lotus-like superhydrophobic coating would require mechanically durable, optically transparent and highly functional dewetting properties. Due to the inherent and required surface roughness that is involved with superhydrophobic materials, good transparency (or transmittance) can be difficult to achieve.[29,67,68] Moreover, with efforts to increase robustness of superhydrophobic surfaces, interfacial designs tend to lean towards self-repeating rough structures.[29,297,298] This leads to intensified scattering / hazing and thus even lower transparency (or transmittance). This obviously goes in contradiction towards achieving all three primary dominant aims of the field.[297,299,300] Notwithstanding such limitations, we will review the current suite of techniques for attaining lotus-like superhydrophobicity.

2.5.2.1. Plasma

Plasma demonstrates a facile method for achieving rough hierarchical textures. Oxygen plasma etching of low surface energy materials such as polytetrafluoroethylene (PTFE) induces the surface roughness required for superhydrophobicity (Figure 2.32).[301] Plasma can also be used as a fluoro-functionalization technique, where CF_4 plasma is used to create layers of -CF_2 and -CF_3 functionalities.[302,303] This was eventually expanded to incorporate $H_2C{=}CHCO_2CH_2CH_2(CF_2)_7CF_3$ plasma, which gave rise to improved superhydrophobicity, owing to the longer perfluorocarbon chains.[304] While the previous examples demonstrate ultra-thin poly(perfluorocarbon) coatings (ca. 10 nm),[304] the technique can be used to facilitate complete plasma polymerization of fluoro-monomers, forming a superhydrophobic fractal-based polyfluoropolymer film.[298] Growth of such films is not limited by substrate type, and can be performed on poly(ethylene terephthalate) (PET),[148] polyimide (PI)[305] or polypropylene (PP),[303] or even silicon[306]. More importantly, owing to the

nature of oxygen plasma etching or C_xF_y plasma polymerization of monomers, coatings that are prepared using this method are inherently porous, hierarchical and highly tunable.

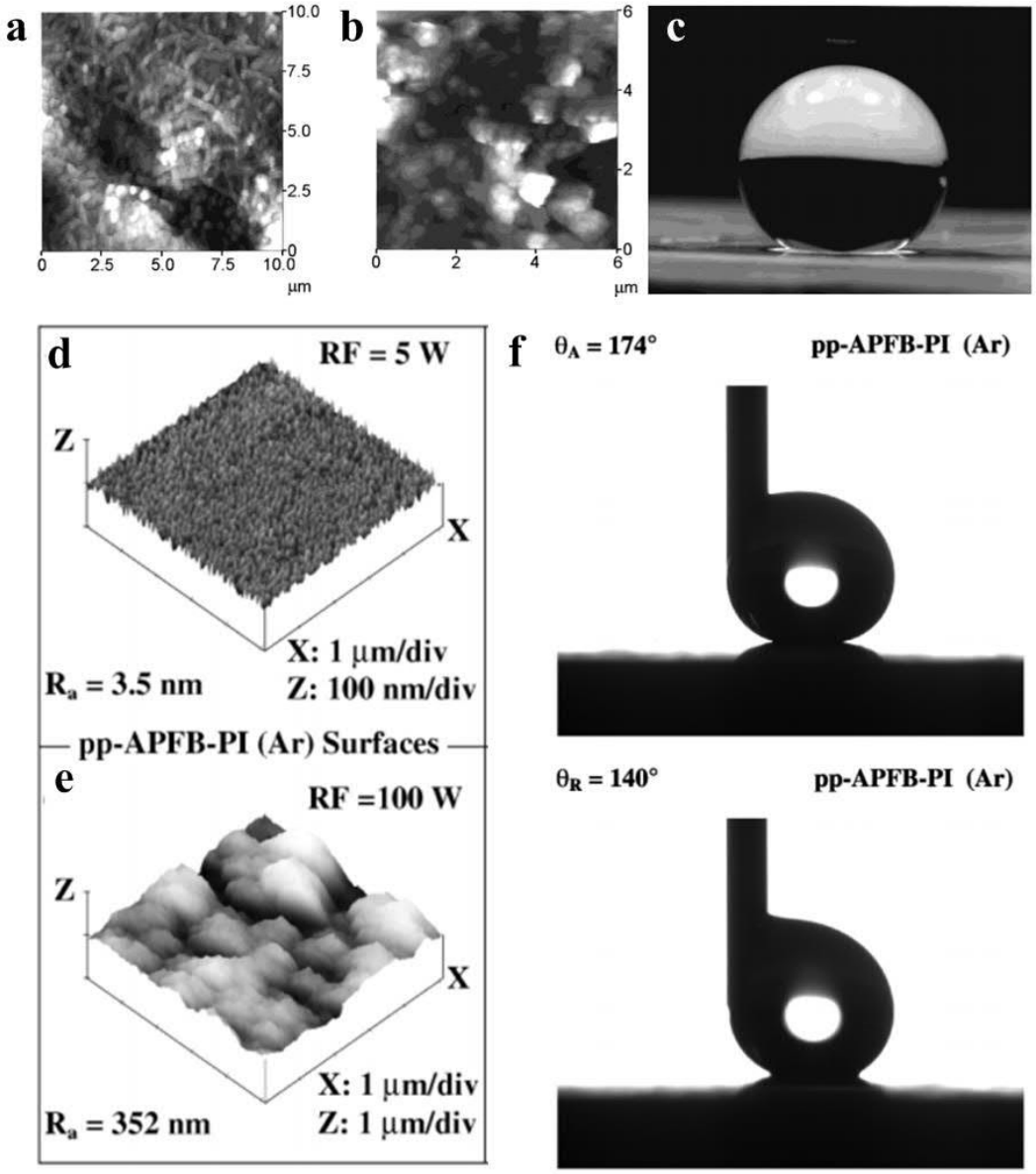

Figure 2.32. Plasma-induced superhydrophobicity. a) Oxygen plasma treated flat-PTFE, b) Oxygen plasma treated porous-PTFE, c) Superhydrophobic properties of oxygen plasma treated porous-PTFE with a 6 µL droplet.[304] d-e) Plasma-polymerized alkyl-fluorobenzene (AFPB) on PI in Argon (pp-AFPM-PI(Ar)). f) ACA and RCA analysis on superhydrophobic pp-AFPB-PI(Ar) surface.[305]

2.5.2.2. Phase Separation

Amongst bottom-up techniques, phase separation is one of the simplest methods that can be employed for developing superhydrophobic surfaces and materials. It exploits demixing instabilities of multi-component mixtures for the self-assembly of very rough hierarchical textures (Figure 2.33). The

phase separation of a polymer solution during treatment with non-solvents gives rise to spontaneous microstructural evolution through nucleation, Ostwald ripening, and then spinodal decomposition.[149,294]

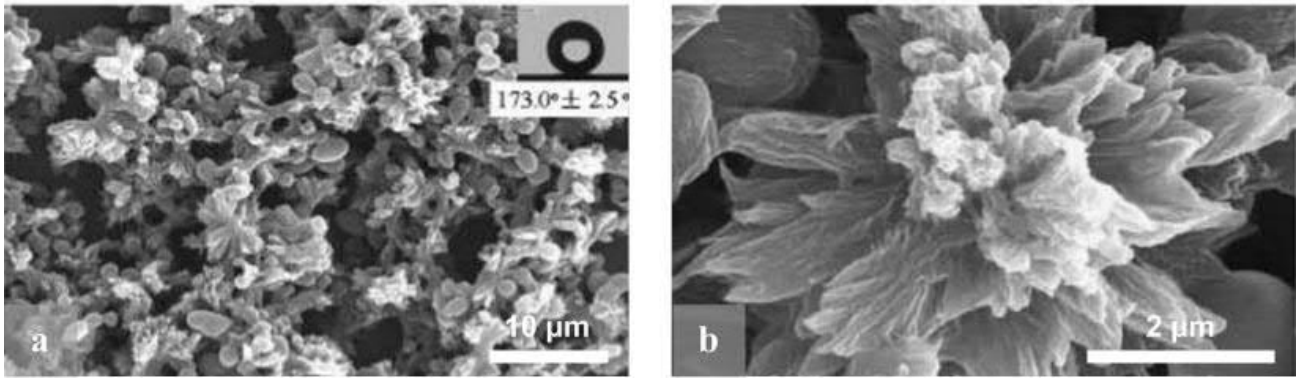

Figure 2.33. Phase separation induced superhydrophobicity. a) Low-density PE through a xylene (solvent) - cyclohexanone (non-solvent) demixing process. b) Enlarged view of the floral structures formed.[307]

Crystallization behavior, time and nucleation rates are initial demixing parameters that are user-tunable, leading to highly fractal textures that can potentially be user-defined. Some key parameters include polymer solution concentration, temperature and the choice of non-solvent. The choice of polymer and eventual superhydrophobicity can simply be adjusted in accordance to surface energies. Despite minor geometrical variations, the rough fractal texturing gives rise to CA enhancements.

In contrast to other methods, this is usually a fluorine-free technique, and is thus considerably more environmentally friendly. Polymers such as polycarbonate (PC),[308] polypropylene (PP),[149] polyethylene (PE)[307] and poly(vinyl chloride) (PVC)[294] have all been extensively used for achieving facilely synthesized superhydrophobic surfaces through phase separation.

2.5.2.3. Sol-Gel

Sol-gel can be spontaneous or temperature-aided and either contained in a solvent or water as respective solvothermal or hydrothermal processes. Spontaneous sol-gel techniques are typified by their use of reactive precursors, with terminations such as -chloro or -alkoxide groups that reacts readily with environmental traces of water. The process takes places through a hydrolysis step,

followed by condensation of the intermediates, eventually resulting in the formation of metallic oxides. A catalyst (anionic) is also sometimes used to enhance the deprotonation of precursor compounds, thus speeding up the reaction. The sol-gel process tends to result in micro- and nano-structured materials which, when combined with user-selected precursors, could give rise to a wide variety of functional materials (Figure 2.34).[309-314]

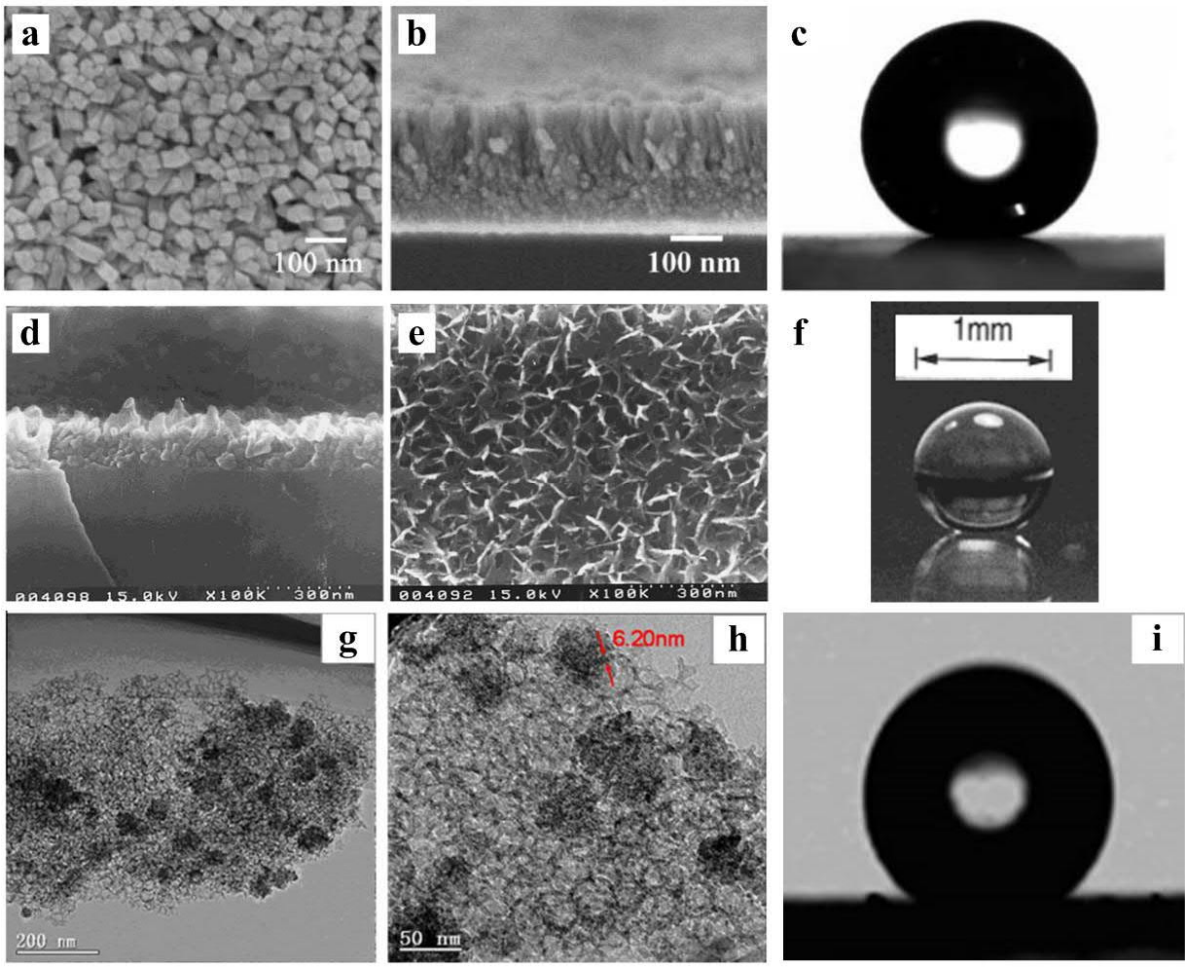

Figure 2.34. Sol-gel developed superhydrophobicity. a-c) FESEM micrographs and wetting properties of superhydrophobic SnO_2 nanorod films.[315] d-f) FESEM micrographs and wetting properties of superhydrophobic Al_2O_3 flower-like structured thin-films.[309] g-i) TEM micrographs and wetting properties for superhydrophobic mesocellular foams loaded with TiO_2 nanocatalysts.[316]

Al_2O_3, for instance, could be developed into ultra-transparent films with rough, fractal and flower-like textures.[309,310,317] Organosilicates can also be used for the fabrication of silica-gel foams[311,312] that possess highly porous morphologies. Other metallic oxides with even more unique surface architectures can also be achieved, such as TiO_2,[313] ZnO,[318] or SnO_2[315] nanorods. The sol-gel synthesized textured coatings, if not already superhydrophobic, can then undergo fluoro-

functionalization *via* a variety of means to achieve superdewetting. Sol-gel products can sometimes be integrated with hydrophobic organics within a single-step, by completing the process in the presence of metal-organic precusors, such as TiO_2-NH_4F.[316]

2.5.2.4. Micro- and Nano-Structural Self-Assembly

Within the series of scalable bottom-up methods, self-assembly is a means that has demonstrated immense potential for the organization and formation of structures at the micro-, nano- and even molecular- scales. Some sub-variants of self-assembly exploit the presence and affinity of molecular-level moieties or naturally occurring capillary effects.[76] The macro-behavior of such interactions can define large-scale structural conformations, leading to an almost autonomous formation of regularized structures.[319-322] Cascaded effects behind such functional group-to-group interactions culminate in molecular-, micro- and even macro-scaled interfacial interactions.[76] Owing to their finely orchestrated coordination, their propensity for creating highly regular macro-scaled hierarchies is immense.

Colloidal lithography, for instance, is a bottom-up technique that exploits this concept for fabricating highly ordered nanopatterning arrays. It is a simple, low-cost technique that is versatile down to feature sizes of below 100 nm. This was a process that was first demonstrated by Fischer in 1981,[323] where microsphere patterns were used as colloidal masks for the subsequent deposition of platinum with array-like designs (Figure 2.35). In later years, this was exploited for super(de)wetting applications.[324-327] To this end, Love et al. integrated colloidal lithography with thiol-gold functionalization for superhydrophobic nanopatterns. Interfacially assembled SiO_2 nanospheres were first formed as highly regular lattice-like structures before gold deposition. This resulted in the formation of gold half-shells after SiO_2 removal.[324] Self-assembled monolayers (SAMs) of hexadecanethiolate were then used to functionalize these gold nanopatterns, resulting in functional superhydrophobicity with a WCA of 155° and a SA of 1°. Similar concepts were used in the following years to develop superhydrophobicity through the the colloidal assembly of SiO_2, TiO_2 and PS

microspheres.[325,326,328] Wang et al. developed colloidal crystal films of amphiphilic latex spheres, from poly(styrene(St)-n-butyl acrylate(nBA)-acrylic acid), which demonstrate statically tunable superhydrophilic-to-superhydrophobic properties. Tuning ratios of St/nBA resulted in configurable wettability. More interestingly, the technique demonstrated the ability for temperature-induced controlled assembly of polymeric microspheres, which opened new insight to the limits of colloidal lithography.[329]

Self-assembly of superhydrophobic materials can also take advantage of interfacial interactions between low and high surface energy states, thus giving rise to uniquely configured particles.[300] This has been shown through emulsification-aided radiation polymerization, which enabled the self-assembly of raspberry-like SiO_2-PS[295] and SiO_2-PDMS[150] supraparticles with superhydrophobic properties.

2.5.2.5. Dip- and Spin-Coating

Methods employed within this broad technique includes dipcoating and spincoating,[300,330] methods that are typically aided by capillarity-based depletion forces. Xu et al. demonstrated the spincoating of fluoro-functionalized SiO_2 particles that were suspended in a fluorocarbon solvent. Precisely tuned particulate-solvent interactions were exploited here for creating highly regularized planar coatings from nanoparticle (NP) solutions. The homogenized surface energy profiles from both components enabled well-defined mono-particle layered coatings. These profiles stand in contrast to typical surface tension derived “nanoparticle islands” that are found in most wet deposition regimes. As a result, the very regularly deposited particle-layers gave rise to an extremely transparent superhydrophobic surface.[300] Spincoating of SiO_2, ZnO and ITO on glass and polymer substrates have also been used to demonstrate transparent, superhydrophobic coatings with improved robustness.[68] Combination of spincoating with sol-gel processes has been shown to develop anti-reflective superhydrophobic coatings with ultra-high transmissive properties, which could bear promise for solar cell applications.[331]

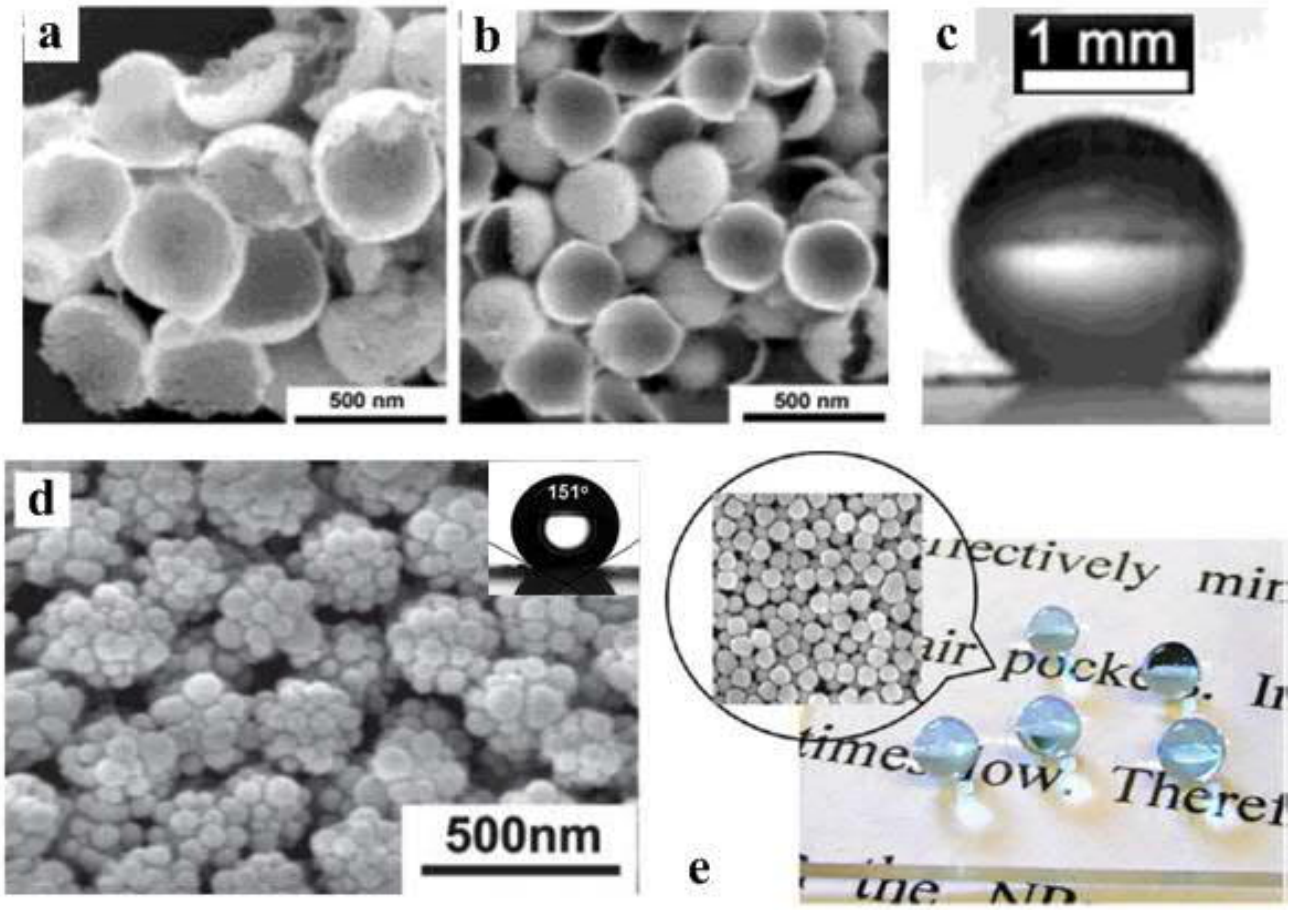

Figure 2.35. Self-assembled films of superhydrophobic micro- and nano-particles. Scanning electron micrographs of a-c) 10 nm thick gold half shells formed by colloidal lithography, made c) superhydrophobic by a $C_{16}S$ coating.[324] d) PS-SiO_2 raspberry hybrid particles[295] and e) near-planar superhydrophobic fluoro-functionalized SiO_2 nanoparticles assembled through the spincoating of a homogenized solution of fluorosolvent-suspended fluoro-functionalized SiO_2.[300]

Spincoating of nanoparticles could be integrated with polymers such as PMMA,[330] or PDMS and PTFE,[332] thus forming functional superhydrophobic composites. This expands into the use of calcium carbonate suspensions and stearic acid for fluoro-free superhydrophobic coatings.[333] However, spincoating is often difficult to perform on curved substrates, while its sister technique, dipcoating, is able to provide a similar but more versatile protocol.

Although functionally similar to spincoating, dipcoating is less dependent on substrate geometries. It has been used for the facile creation of superhydrophobic coatings on a variety of substrates, such as fabrics,[334] copper templates,[335] glass[336] and cellulose sheets[337]. This method is being continuously developed, and has been shown to form nanodots,[338] nanotriangles,[338,339] polygonal,[339] nanorings,[340] shuttlecocks,[341] zigzagged nanowires (NWs),[342] and even nanocones[327]. However,

despite being cheaper and more scalable than standard top-down methods, colloidal self-assembly (and its more chaotic sub-variants) are still limited by patterning precision, homogeneity, defects and suitability for macro-scale deposition (> 100 cm^2).

2.5.2.6. Layer-by-Layer (LbL)

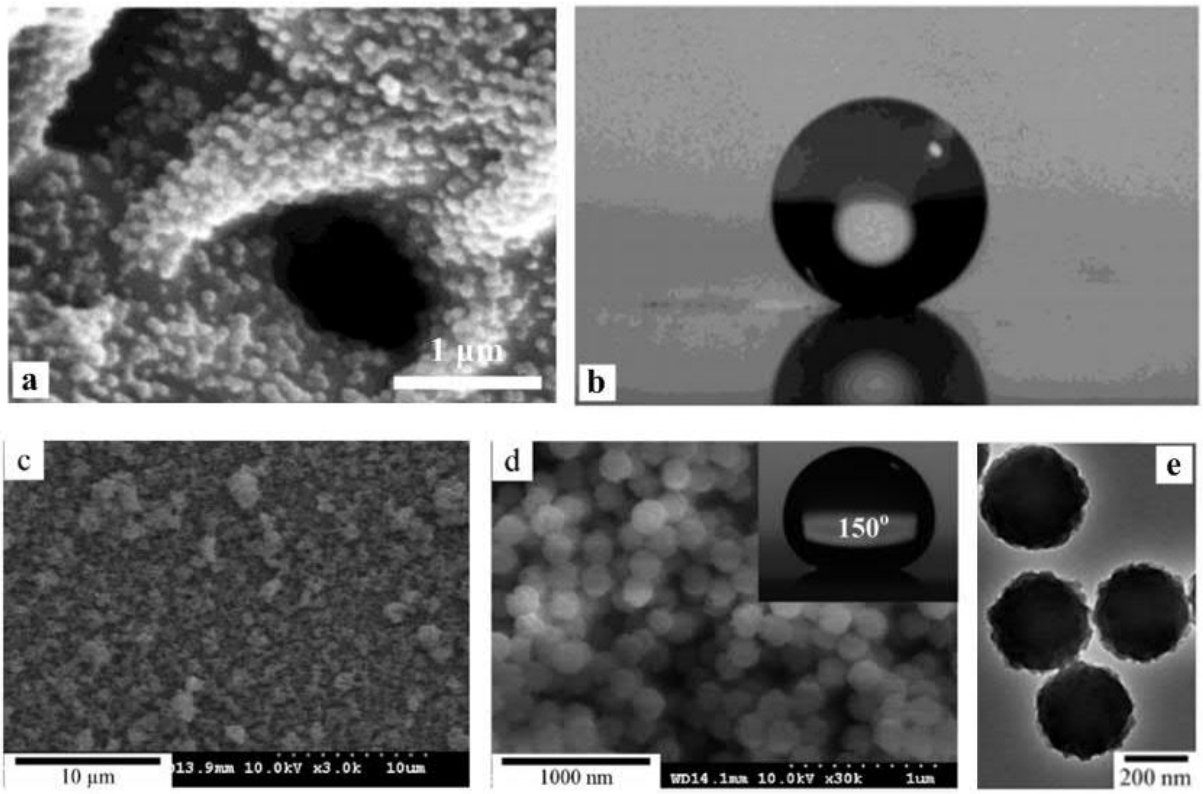

Figure 2.36. Layer-by-Layer developed superhydrophobic films. Scanning electron micrographs of a-b) LbL PAH/PAA-SiO_2, with b) superhydrophobic properties.[343] c-d) Scanning electron micrographs of LbL PDDA/surface-roughened- SiO_2 followed by hydrophobic modification. e) SiO_2-nanospheres textured by a self-templated etching route.[344]

The layer-by-layer (LbL) technique is a method that evolved from the Langmuir-Blodgett (LB) system, now integrated into sequential dip / spray-coating processes (Figure 2.36). In contrary to thin monolayers that were developed in standard LB films, LbL films are formed by the alternating deposition of layers of oppositely charged materials, washed in between each cycle.[345] Such polyelectrolyte layers can come in the form of poly(acrylic acid) (PAA) and poly(allylamine hydrochloride) (PAH), sometimes integrated with SiO_2 nanoparticle suspensions.[343,346]

Other polyelectrolytes such as poly(diallyldimethylammonium chloride) (PDDA) can also be used, sometimes with pre-modified surface roughened SiO_2 nanoparticles.[344] Owing to the multiple-

dipping cycles required, the speed of coating is naturally slower than other bottom-up methods. However, Ji et al. accelerated the LbL growth phase by inducing enhanced ion exchange *via* bi-conjugated silver ions. This results in the exponentially accelerated growth of multilayered hierarchical films.[347] The process can even be integrated with other materials, such as gold, in order to develop a multi-functional LbL film within a single process.[348] These polyelectrolyte-formed composite layers typically require fluorination before achieving superhydrophobicity.[86,299,349]

2.5.2.7. Aerosolized Wet-Spray

In recent years, maturation of the field has resulted in tremendous efforts towards developing industrially-scalable superhydrophobic coatings. Much of the work focuses on the use of highly scalable techniques such as spray-, spin- or dip- coating.[29,86-88,300,332,350-352] Even when compared to the highly pragmatic spin- and dip-coating methods, spray-coating still represents the most scalable and industrially viable technique. Today, the wet-aerosol deposition of nanomaterials (Figure 2.37) for superhydrophobic coatings and films is widely acknowledged for their immense potential behind future commercialization and industralization.[86,353]

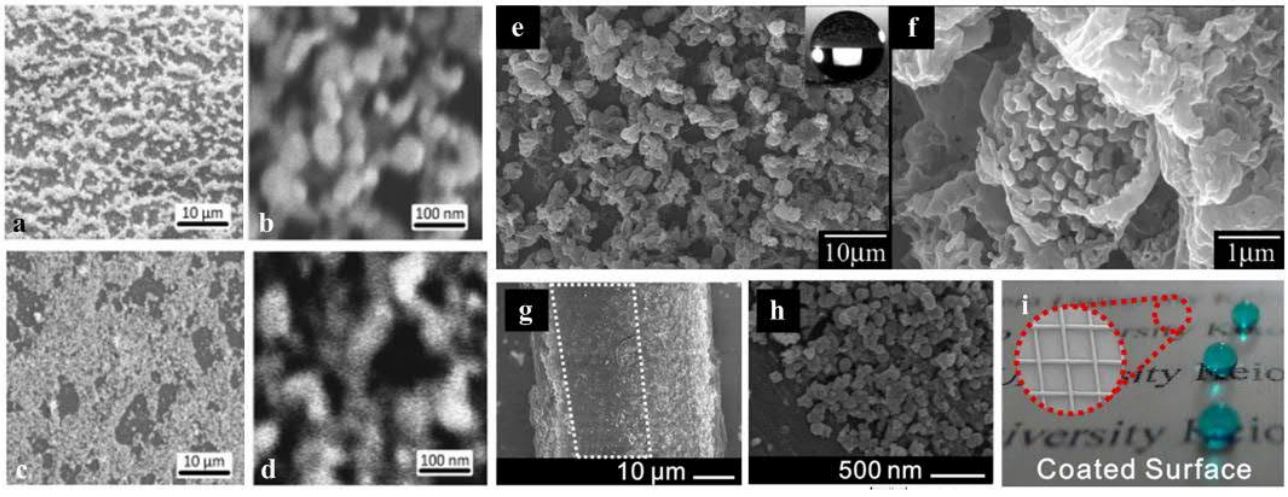

Figure 2.37. Spray-deposited superhydrophobic micro- and nano-particles. Scanning electron micrographs of spray-deposited superhydrophobic a) SiO_2 at low and b) high magnification and c) ZnO at low and d) high magnification on glass.[68] e-f) Superhydrophobic spray-deposited poly(SiMA-co-MMA) at low and high magnifications.[350] g-i) Superhydrophobic polyester meshes formed by spray-deposited SiO_2-PFOTS (1H,1H,2H,2H-perfluorooctyltrichlorosilane).[354]

Although wet-spray aerosolization appears to be superficially simplistic, it can be highly customizable. Operating parameters such as deposition-height, dispersion pressure, nozzle diameters and precursor compositions are highly tunable. More importantly, when the technique is used correctly, it has been shown to be capable of producing extremely homogenous and transparent thin films.[262,297] Owing to its facile nature, the variety of precursors and materials involved are extremely diverse. Despite these extensive variations, the synthesis of superhydrophobic coatings by wet-aerosols can still be broadly classified under 2 primary categories: a) pre-functionalized and b) *in-situ* functionalized material.

The former is obvious and more ubiquitous, where fluoro- or hydro-carbon functionalized materials are first re-suspended using suitable solvent-surfactant combinations, coupled to appropriate agitation.[68,299,300,353] Environmentally-friendly fluoro-free formulations are also preferred if only superhydrophobicity (not superoleo(amphi)phobicity) is desired.[88] While pre-functionalized materials are sometimes deposited on their own, they can also be integrated with sprayable polymers such as polystyrene (PS)[355] or perfluoroalkyl methacrylic copolymers (PMCs)[87] to give an additional degree of roughness.[355] Regardless of the precursor's formulation, the spray-deposition process itself is typically capable of rapidly creating superhydrophobic interfaces, by virtue of aerosolization-induced roughness.[262,354]

In fact, it is not mandatory to use completely-functionalized materials, since wettability is a surface effect that occurs only within the top few nanometers of an interface. Steele et al. demonstrated this by integrating unfunctionalized ZnO nanoparticles with highly fluorinated perfluoroalkyl methacrylic copolymers. Spray-deposition of this composite mixture gave rise to nanoparticle-roughened functional superhydrophobic coatings.[87] Aerosolization-induced roughening has also been showcased for pure polymer systems, as demonstrated by Hwang et al. with a co-polymer comprising of 3-[tris[(trimethylsilyl)oxy]-silyl]propyl methacrylate (SiMA) and methyl methacrylate (MMA). Spray-deposition resulted in naturally roughened polymeric morphologies, which when optimized,

gave rise to highly transparent (60-85% transmittance) superhydrophobic films with CA, SA and CAH of 178°, 0° and 0° respectively.[350]

A bi-layer system was also designed by Wong et al. in 2016, which highlighted the first-reported use of a sprayable interpenetrated polymeric network (IPN) system in combination with fluoro-functionalized silica. The self-assembled IPN coating was hierarchically textured with a series of micropapillae-like bumps and nano-dimples. Superhydrophobicity was achieved with CA, SA and CAH of 161°, 0° and 3° respectively. This binder-silica system was able to sustain up to 300 Taber abrasion cycles, extended exposure to UV-C, oil- and acid- immersion. A 70-80% transmittance was reported between 400 to 800 nm, with a 10-20% loss from bare substrates.[91]

Alternatively, the concept of *in-situ*, in-flight functionalization presents a much more interesting paradigm towards the rapid application of one-step superhydrophobic coatings. This is typically realized by the use of precisely chosen precursor compositions. The use of precursors formulated from metallic salts-alkanethiols;[351] organofluoroacids on metallic substrates[153] or even direct treatment with fluorinated chlorosilanes,[354] have all demonstrated immense potential for achieving functionalization and surface texturing within the same step.

Spray-deposition for superhydrophobicity is, however almost limitless in its applicability towards a wide range of substrate geometries and materials. Till date, it has been demonstrated on metal meshes,[351] paper,[352] glass,[356] polymers,[354] and even wood and stone.[91] Notwithstanding stringent optical characteristics, extremely tough superhydrophobic coatings have been demonstrated.[29] However, a challenging balance between robustness and optical transparency / transmissivity remains to be achieved.[91,350]

For instance, Lu et al. presented an ultra-robust F-TiO_2-in-paint based nanocomposite coating that can be applied *via* dip- or spray-coating. The resulting coating was able to sustain up to 40 cycles of sandpaper abrasion (Grit 240, 100 g, 10 cm travel) while maintaining a CA of around 164°. However,

key characteristics such as SA/CAH and damage-to-failure were not reported. The coating that was deposited on glass was also highly opaque, and does not appear to allow any light transmission.[29]

Despite numerous advantages, wet-spray-deposition of superhydrophobic coatings is also limited by the physical dimensions imposed by its spray plume. As a result, they remain unsuitable for ultra-demanding 3D substrate geometries, such as high-aspect ratio hollow objects.

2.5.2.8. Liquid Flame Spray Pyrolysis

One solution to developing superhydrophobic coatings on highly convoluted 3D geometries comes in the form of an ultra-fine mist of nanoparticles. The much larger plume size achieved by this technique enables better depth penetration and coverage consistency (Figure 2.38).

For instance, while the smallest conventionally achieved droplet size in a wet-aerosol spray reaches a minimum diameter of a few microns,[357] flame spray aerosols are known to achieve distinct nanoparticle distributions of just a few nanometers.[78,358] This makes it highly suitable for processes that include micro-patterning,[80] CVD-like aerosol-growth,[30] or the permeation and coating of complex geometries[79].

This method is also highly scalable, and can be easily integrated into industrial roll-to-roll processing, thus enabling ultra-high throughput of functional nano-structured coatings.[359] To date, liquid flame spray pyrolysis has been demonstrated for a range of superhydrophobic coatings.[135,360-363] With an optimization of deposition parameters, this technique can even be applied for heat-sensitive materials such as paper[297,364,365] and polymers[92].

Interestingly, despite the high temperatures involved, the superhydrophobic coatings generated by flame spray pyrolysis appear to be one-step processes that are currently attributed to either *in-situ* carbonaceous[365] or short-chain organic functionalization[360]. Thus, these are also largely fluoro-free environmentally-friendly processes.

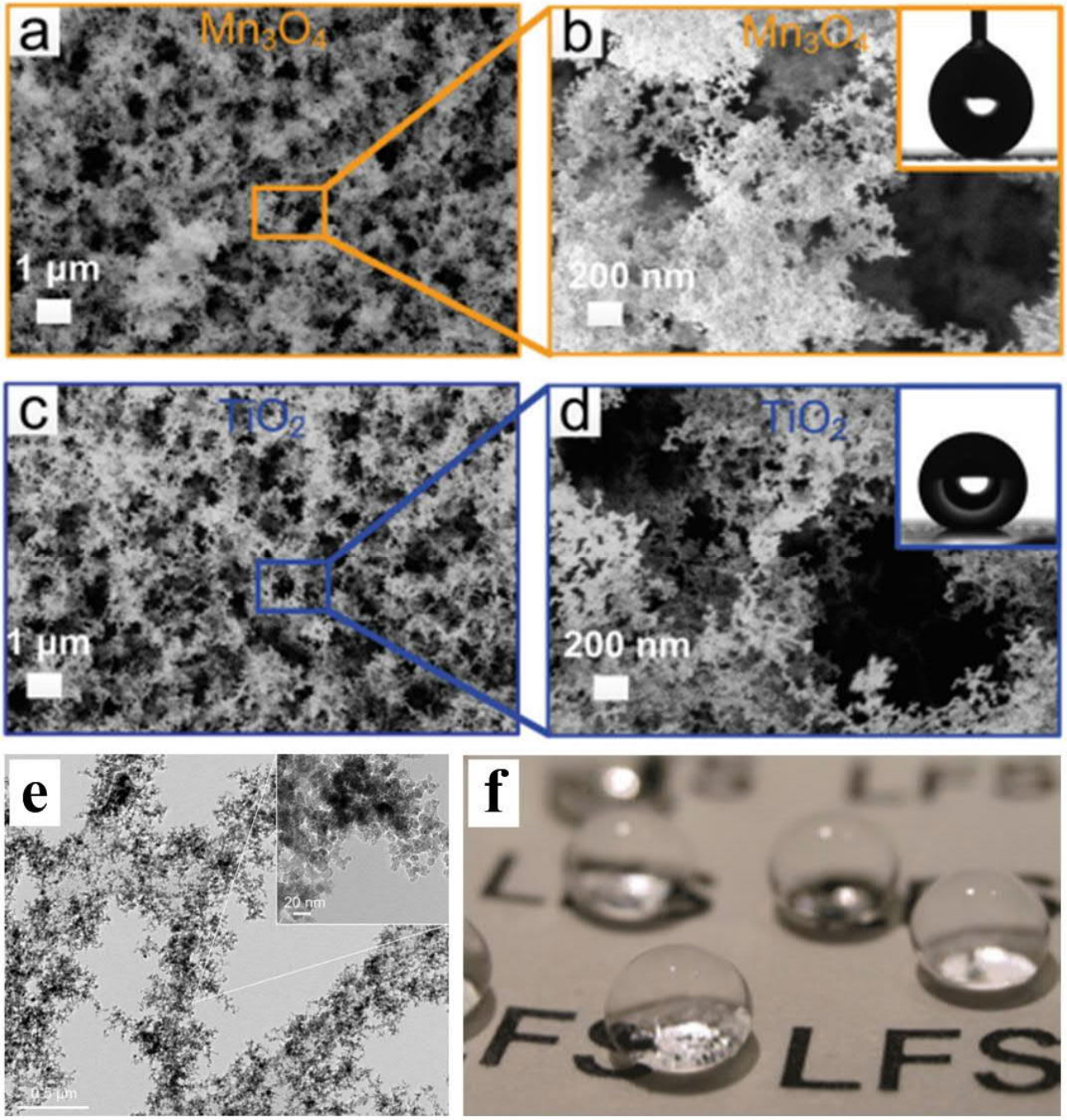

Figure 2.38. Liquid flame spray derived superhydrophobicity. Scanning electron micrographs of liquid flame spray-deposited *in-situ* superhydrophobic a-b) M_3O_4, c-d) TiO_2.[360] e) Transmission electron micrographs of liquid flame spray-deposited TiO_2 (on paperboards) with f) superhydrophobic properties.[365]

2.5.2.9. Electrospinning

Electrospinning and electrospraying exploits the electrohydrodynamic instability of polymer solutions for low-cost and rapid development of micro- and nano-structured films (Figure 2.39).[366] It is also commonly used with molten precursors in a variant known as melt-electrospinning, which

avoids the presence of solvents in the developed product.[367] These techniques are capable of creating both 1D structures such as solid-, porous-, or core-shell- fibers or 3D structures such as beads or spheres.[133,368-370] Hierarchical multi-scale features are stochastically deposited on a grounded substrate, thus establishing a micro- and nano- textured morphology. Deposition parameters range from applied voltages, working distances, flow rates, needle profiles and precursor compositions (polymer type and concentration, metal-organics, solvents, surfactants).[84]

As superhydrophobicity is inherently dependent on hierarchical texturing, electrospinning / spraying offers a facile[371] and scalable method for the fabrication of coatings and stand-alone membrane-like films.[83,133] Lotus-like superhydrophobicity with high CAs (CA > 150°) and low SAs (< 10°)[83,191] has been obtained by electrospinning beaded morphologies[371,372]. However, lotus-like superhydrophobic structures that utilize such porous micro-spheres (ca. 5 µm) are fairly unstable, and must be supported by a network of nanofibers (< 100 nm).[133]

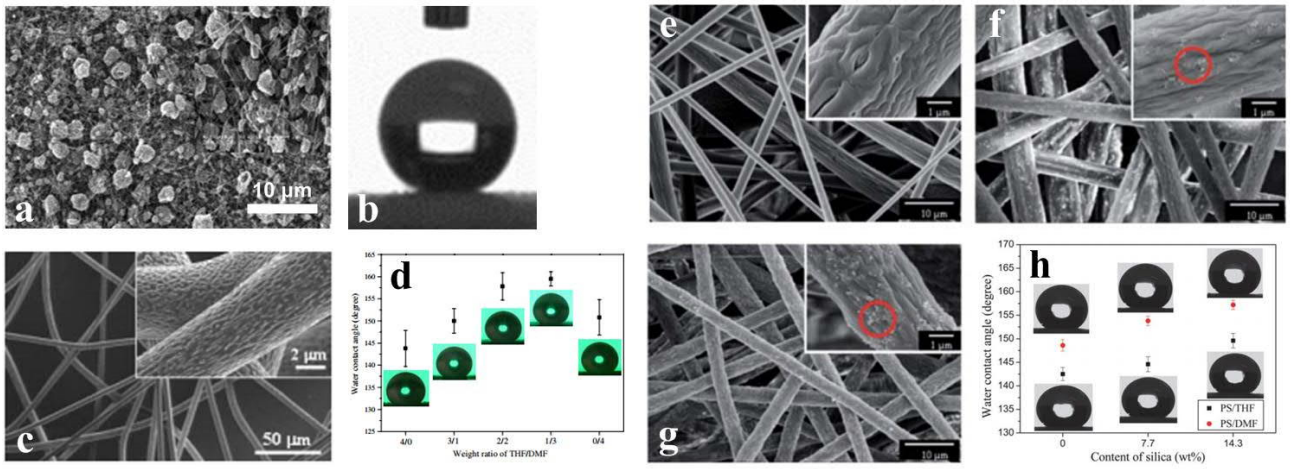

Figure 2.39. Electrospinning-derived superhydrophobicity. Electrospun a) bead-on-string PS film showcasing b) superhydrophobic properties;[371] c) Rag-wort leaf-like textured PS fibers showing d) superhydrophobic properties;[83] e-g) Textured PS fibers by nano- SiO_2 blending (0 wt%, 7.7 wt%, 14.3 wt% respectively), showing improvements in h) superhydrophobicity.[191]

Alternatively, fibrous morphologies tend to result in WCAs below 150°, potentially due to water penetration into large pores that are present between fibers.[372,373] However, superhydrophobic coatings can be achieved by electrospinning surface-contorted nanofibers, which are reminiscent of

nature's superhydrophobic ragwort leaves.[83] Other variants of nanoparticle-roughened nanofibers were also found to exhibit lotus-like superhydrophobicity.[191]

While hydrophobic polymers such as PS and PVC[374] are most commonly used in electrospinning for achieving a state of superhydrophobicity, it has also been demonstrated with composite-based graphene-roughnened TiO_2 nanofibrous membranes.[374]

2.5.2.10. Electrodeposition

Electrodeposition can also be used to fabricate micro- and nano-structured materials (Figure 2.40). It is particularly useful for synthesizing metallic oxides, metals or even conductive polymer coatings. The nature of electrodeposition makes it the coating technique of choice for superhydrophobic metallic or metallic oxide coatings, which are not easily processed *via* other means. Notwithstanding the size of the electrochemical bath, this deposition technique is highly advantageous as it does not discriminate against substrate geometries and dimensions.

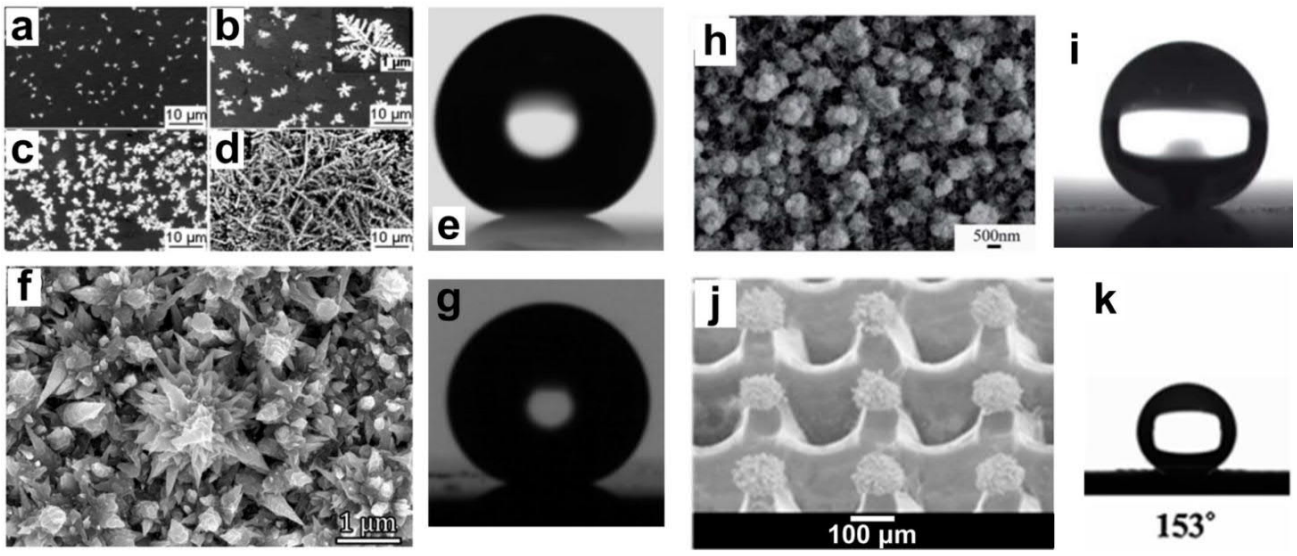

Figure 2.40. Electrodeposition derived superhydrophobicity. a-e) Scanning electron micrographs of branch-like Ag aggregates formed by electrodeposition after a) 2 s, b) 40 s, c) 200 s and d) 1600 s respectively, with e) superhydrophobic properties.[375] f) Flower-like micro- and nano-structured Ni-Co films with g) superhydrophobic properties.[376] h) Electrodepositied Al_2O_3 micropapillae with i) superhydrophobic properties.[377] j) Electrodeposited copper on laser ablated morphologies with k) superhydrophobic properties.[378]

To date, superhydrophobic metallic coatings have demonstrated the use of morphologies such as gold clusters,[348] dendritic silver,[375] nickel-cobalt clusters,[376] aluminum papillae,[377] copper aggregates[379-381] and micropillars[378]. Surface texturing by electrodeposition is highly tunable. For instance, Xu et al. tuned the formation of grape-like micro-structures to petal-like sheets,[382] simply by varying parameters within the copper electrodeposition process. Superhydrophobic and conductive polymer films are typically made up of organo-thiols, such as poly(ethylenedioxythiophene) (PEDOT) and its associated derivatives.[383-385] Electrodeposited polymers have also been showcased for a series of superhydrophobic nano-rod,[383] nano-fibrillar[384] and nano-fibrous[385] morphologies.

2.5.2.11. Vapor Deposition

In recent years, the ability to design specific surface morphology has gained immense attention for the field of super(de)wettability.[12,14,75,155] Achievement of scalable, regular and highly predictable nano-textures through a non-invasive vapor phase treatment could revolutionize how we design and fabricate highly functional interfaces. Today, vapor deposition methods include both chemical vapor deposition (CVD) and physical vapor deposition (PVD). These methods have been shown to create very regular nano-structures with tunable heights and cross-sectional profiles (Figure 2.41).

CVD relies on the use of a volatile precursor that is typically delivered in a carrier gas. The mixture enters a chamber where it encounters the substrate, thereafter interacting with and adhering to it. Surface adsorption leads to nucleophilic attack and the eventual formation of stable covalent bonding which culminates as an integrated coating layer.

Geometries such as nanotubes, honeycombs and nano-islands can be fabricated using various CVD techniques (atmospheric pressure, AP, plasma-enhanced, PE, hot-filament, HF).[386-388] Their inherent micro- and nano-structural hierarchy, in combination with surface chemistry (intrinsic or otherwise), is used to induce a superhydrophobic state. The technique is very versatile, and ranges from the pyrolysis of organic precursors,[387] deposition of alkoxysilanes,[389] integration of fluoro-alkyl silanes

for one-step fluorination[386] or the two-step PECVD-HFCVD coating of carbon nanotubes (CNTs) followed by a thin coating of PTFE for functionalization.[388] It has also been demonstrated for the growth of superhydrophobic silicone (PDMS) nanofilaments.[54,390]

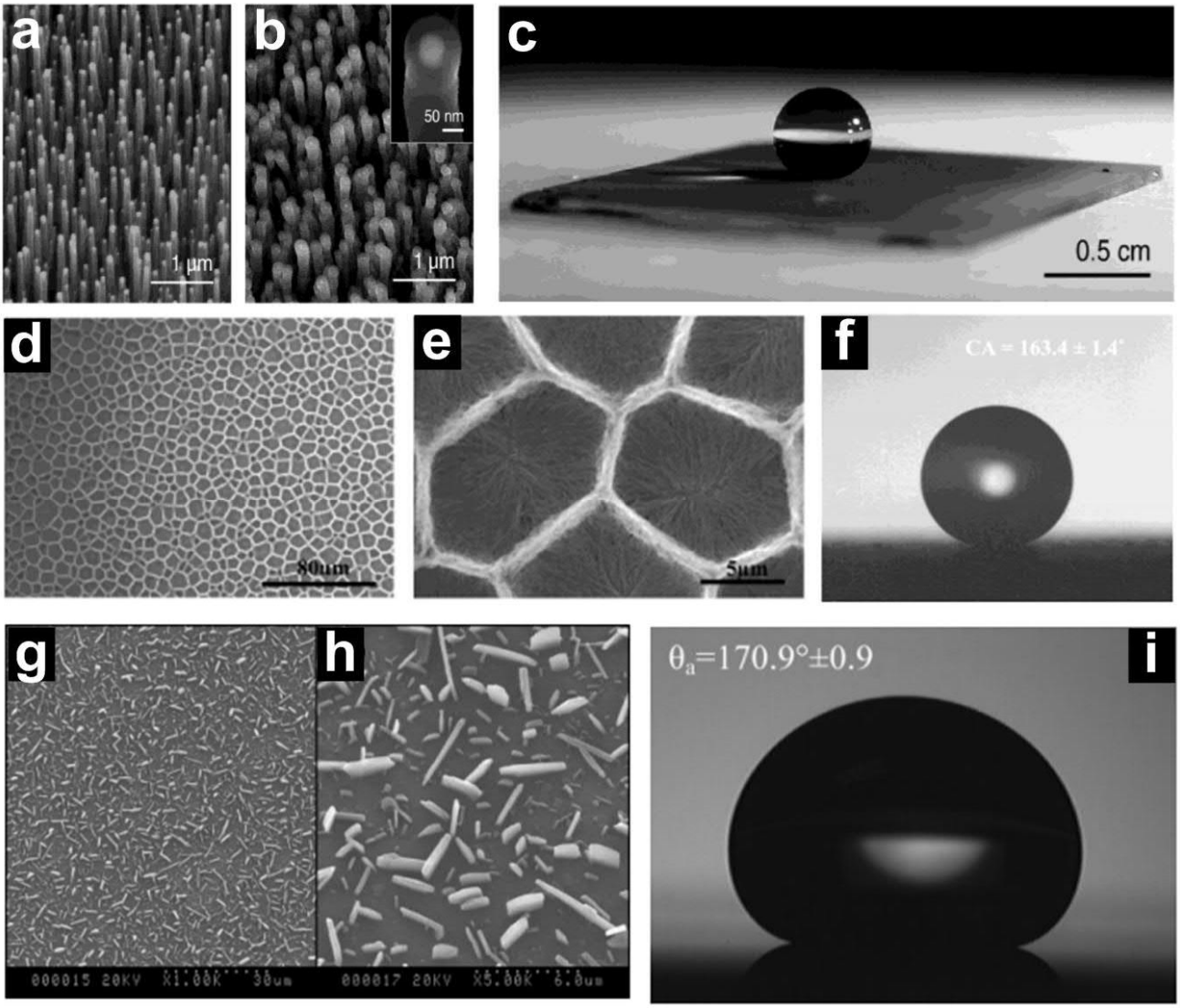

Figure 2.41. Vapor deposition (Chemical and Physical) for superhydrophobicity. a-c) Scanning electron micrographs of carbon nanotube (CNT) forests with c) superhydrophobic properties.[388] d-f) Large-area honeycomb pattern aligned carbon nanotubes (ACNTs) with f) superhydrophobic properties.[387] g-h) n-hexatriacontane platelet-like surface with i) superhydrophobic properties.[391]

Optimization of optical[392,393] and wear properties[393,394] in PECVD was also separately investigated by Wu et al., who revealed tunable mechanical improvements to the system by varying partial pressures of precursors (trimethylmethoxysilane, TMMOS). However, improved mechanical properties tend to come at the cost of lower water repellency and hence superhydrophobicity.[393]

Besides their tremendous potential for surface texturing, the use of CVD for modifying surface chemistry is also intensely valued. This is a function that has been briefly described in prior sections, where it has been used for supplementing surface texturing processes such as sol-gel, LbL, nano- and micro-strutural self-assembly, or even flame spray pyrolysis. Such a facile means of surface energy tuning helps to enable rapid functionalization, leading to the achievement of superhydrophobic states on pre-roughened / textured surfaces.[13,14,159,187]

The first variant of PVD (evaporative) operates by the vaporization of a source material through high powered lasers or heat, thus inducing material vaporization. The material then encounters and coats substrates *via* direct condensation. There are typically no chemical reactions occurring during this physical process. This method has been used for the deposition of PTFE nano-islands,[395] n-hexatriacontane platelets[391] and silver nanoparticles[396].

Sputtering is the second variant of PVD, which possesses similar line-of-sight requirements, but does not involve direct material vaporization. Instead, a flood of plasma-charged particles (ions) is generated. Ions are then driven towards the substrate from the target by electrostatic acceleration. It is almost always performed in vacuum. Sputtering may also sometimes make use of reactive precursors, thus named reactive sputtering. In contrast to evaporative PVD or CVD, coatings formed by sputtering are typically much denser, owing to the much higher energy of deposition experienced by the ions during the coating process. The most common mode of sputtering is radio-frequency magnetron sputtering, which has been used to deposit superhydrophobic coatings such as micro-islands of rare-earth oxides,[37] fluoropolymers on poly(ethylene terephthalate) (PET),[397] polytetrafluoroethylene (PTFE)[398] or gold[399] and zinc[400]. However, owing to the lack of proficiency by sputtering in developing hierarchical topology, they tend to be coupled to methods such as lithography,[37] laser ablation,[397] thermal treatment[400] and even pre-[398] or post-[399] surface texturing. In some instances, optimization of the sputtering process (working distance[401] and power[402]) appears to be capable of generating *in-situ* roughened and superhydrophobic coatings.[401,402]

2.5.2.12. Mechanical and Wet-Chemical Methods

Besides the above techniques, a variety of other methods also exist for facilely enabling states of superhydrophobicity. Today, the known literature is too voluminous to list, but the most notable mechanical and wet-chemical methods are highlighted below (Figure 2.42).

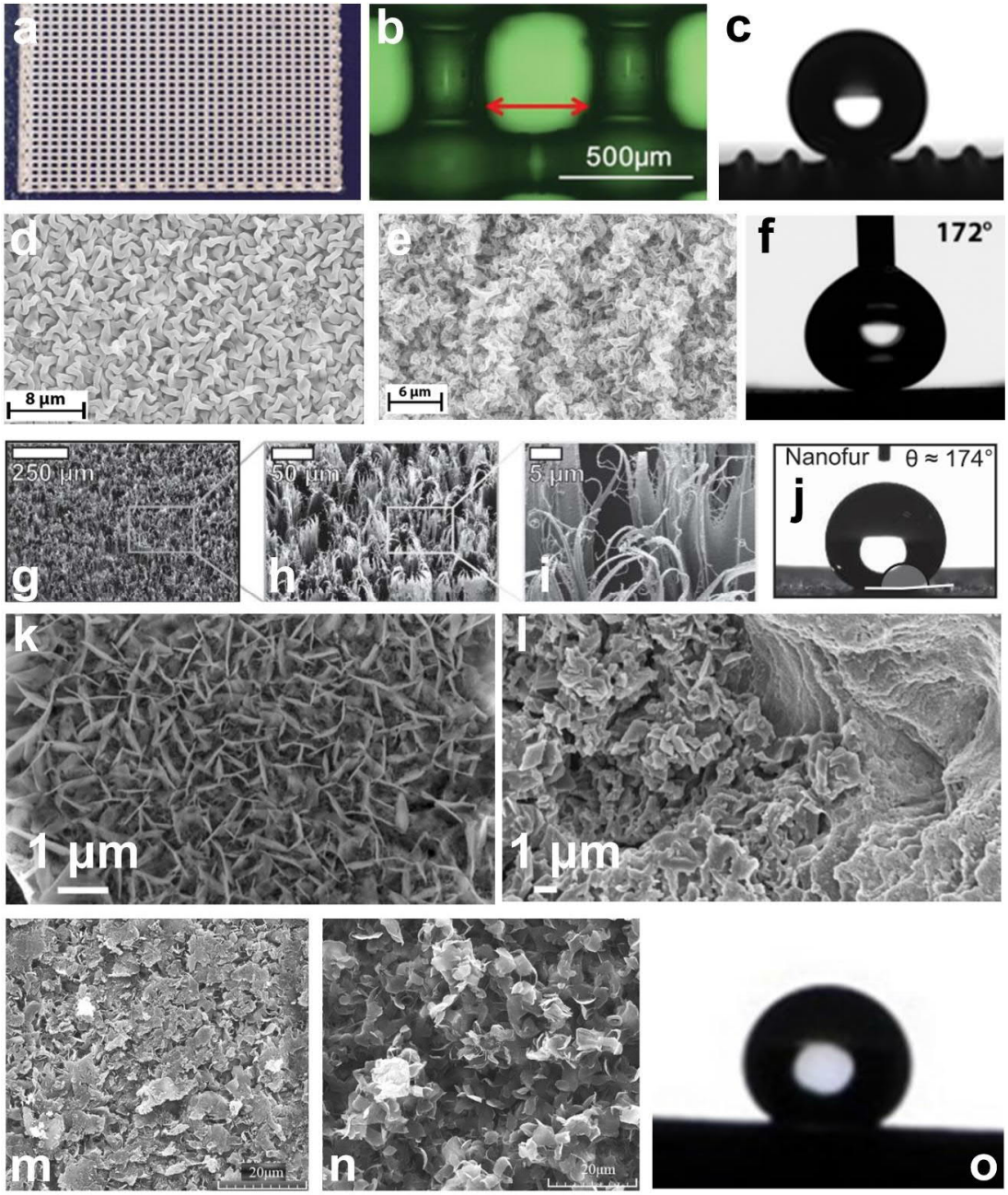

Figure 2.42. Other mechanical methods for achieving superhydrophobic films. a-b) 3D-printed porous membrane (0.37 mm pore size) with c) superhydrophobic properties.[403] d-e) 168 nm and 19 nm thick wrinkled Teflon films with f) superhydrophobic properties.[404] g-i) Fractal surface topology of hot-pulled nano-fur surfaces with j) superhydrophobic properties.[405] k) Petal-like etched structures (Fe_2O_3).[406] l) Granular structures of FeF_3 and CrF_3.[406] m-n) Flat platelet-like sheets from etching with o) superhydrophobic properties.[407]

Inkjet and 3D Printing

With the advent of inkjet and 3D printing technologies, their use in micro-patterning superhydrophobic surfaces is slowly gaining momentum. They have been tradiationally used for creating printable microfluidic channels on phase-separation derived superhydrophobic paper,[408] lipid hydrophilicization of superhydrophobic glass,[409] and dopamine hydrophilicization of superhydrophobic textured SiO_2.[410] Water-soluble ink-jet printed patterns are sometimes also used as sacrificial scaffolds.[411,412] While hydrophilicization of superhydrophobic surfaces tend to take precedence owing to its simplicity, superhydrophobic patterning has also been achieved by Ngo et al. through the laser-printing of superhydrophobic fluoro-functionalized SiO_2 blended toners.[413]

3D printing is a technology that is in its early stages of infancy and the as-printed millimeter-sized printed features still possess pitch distances that are too large for inducing a functional Cassie-Baxter state. However, the resolution of 3D printing has been gradually improving over the years. Lv et al. recently demonstrated the synthesis of membrane mesh lattices with superhydrophobic properties. The ink comprised of PDMS precursors that were impregnated with hydrophobic SiO_2 powders for enhanced roughness. The 3D-printed mesh lattices achieved achieving functional states of lotus-like superhydrophobicity, with a CA of ca. 160°.[403]

Thin Film Wrinkling

The dependence of superhydrophobicity on rough hierarchical structures can be exploited by employing the natural surface wrinkling of thin films. Examples in nature range from the wrinkling of bio-cellular epidermal layers of skin[414] to geological wrinkles[415]. In the field of thin film coatings, spontaneous wrinkling[416] is traditionally treated as an unwanted defect, and significant research efforts were once directed towards developing perfectly flat surfaces.[417] Wrinkling-induced superhydrophobicity can be achieved by the use of wrinkled PDMS, formed by sequential pre-stretch and UV-oxidation. The oxidation results in a thin inflexible layer of silica, which forms wrinkled patterns after relaxing the PDMS sub-layer. Functionalization of the wrinkled silica layer results in

lotus-like superhydrophobicity.[418] PDMS has also been used as a template for growing thin, rigid polymeric top layers, such as polyaniline.[419] Other methods also include electrodeposition-induced wrinkling in poly(ethylenedioxythiophene) (PEDOT) polymer films,[420] shrink-wrap wrinkled Teflon[404] and hierarchical wrinkling that is induced by nano-imprint lithography of poly(2-hydroxyethyl methacrylate) (PHEMA)[421], coupled to standard compression methods.

Film wrinkling can be exploited as a dynamic behaviour. Li et al. exploited the concept of wrinkling for an on-line tunable system which responds to different levels of humidity. These stimuli-responsive films were developed based on the sequential cross-linking and wrinkling of LbL-assembled poly(acrylic acid)-poly(allylamine hydrochloride) (PAA/PAH) films that were impregnated with fluoroalkylsilane (FAS) functionalized SiO_2 nanoparticles. Resulting wettability ranged from hydrophobicity to superhydrophobicity, achieving a maximum CA and minimum SA of 157° and 2° respectively.[349] Wong et al. demonstrated a mechanically-dynamic wetting system by wrinkling 1D nano-structures, thus culminating in superhydrophobic wave-like nanofibers. This was achieved by combining aligned electrospinning and substrate pre-stretching.[90] Superhydrophobic CA, SA and CAH of 167°, 5° and 7° were respectively attained.

Nanofur and Embossed-Hot Pulling

Nanofibers have always been a foundational cornerstone in superhydrophobicity.[133,230] Since its original inception, minimal changes have been made to the most popular and primary mode of synthesizing nanofibers: electrospinning.[90,133,223,230,273,422] In recent years, a technique birthed from the industrial method of embossing and hot pulling gave rise to a uniquely functional nano-structured fur-like morphology.[405] The dense nanohair(fur)-like structures are highly scalable, and can be simply “hot-pulled” from a slab of PC by a sandblasted mold.[405,423] The fur has a non-uniform diameter that ranges from microns to just 200 nm, naturally enabling the hierarchical profile needed for superhydrophobicity. It has demonstrated its universal functionality across different platforms, and has been shown for applications that extends to SLIPS,[405] long-lived underwater

superhydrophobicity,[405] oil-water separation,[424,425] solar cells[426] and even drag reduction.[177] Superhydrophobicity was showcased at CA, SA and CAH of 170°, 10° and 30° respectively for these series of surface coatings.[405]

Acid-etched Metals

Etching of metals to produce rough corrugated profiles is a well-known procedure. This process is particularly suitable for rapidly developing superhydrophobic metal surfaces, owing to its ability for directly modifying the top-most layers of metallic materials. Metals such as 304 and 316 stainless steel,[406] copper[407] and aluminium[314,427-429] are all suitable candidates. A variety of etching solutions can be utilized, including hydrofluoric acid,[406] stearic acid,[407,428] potassium hydroxide and lauric acid[314,427,429]. Morphologies that are synthesized can be vastly different, ranging from petal / platelet-like,[406] granular-like,[406] nano-plates,[407] micro-structured pits,[427] micro-cuboids,[314,428] or nano-flakes[429]. The superhydrophobization of such textured surfaces can simply be conducted by fluoropolymer deposition,[406] or the condensation of other metal-organics such as $Zn(AC)_2$.[314] Moreover, they also show enormous potential for one-step etch-functionalization procedures. For instance, Bahrami et al. and Varshney et al. demonstrated the use of stearic acid and lauric acid for the respective modification of copper and aluminium, achieving inherent superhydrophobicity upon synthesis, with CAs and SAs of 155°, 153° and 7°, 5° respectively.[407,427]

2.5.3. Petal-like Adhesive Superhydrophobicity

Unlike the slippery repulsive state of lotus-like superhydrophobicity, petal-like superhydrophobicity is defined as a highly adhesive, sticky state of wetting that is characterized by a CA > 150°, no SA and a CAH >> 25°.[132,135]

Akin to the lotus-effect, petal-like superhydrophobicity is deeply rooted in biomimetics, as one of the first artificial demonstrations of the effect was in fact realized by templating natural rose petal surfaces.[10] This eventually led to the synthetic development of nanotubular based structures that

were synthesized from artificial AAO templates.[43,138,143,430] The use of these verticalized nanotubes was particularly important because of the new understanding that was achieved behind this artificially attained petal-effect. When attempts were made to pull apart the water-solid interface, negative pressure is generated, thus inhibiting detachment. Each hollow tube profile behaves like a suction-cap, which results in a pressure-induced adhesion mechanism.

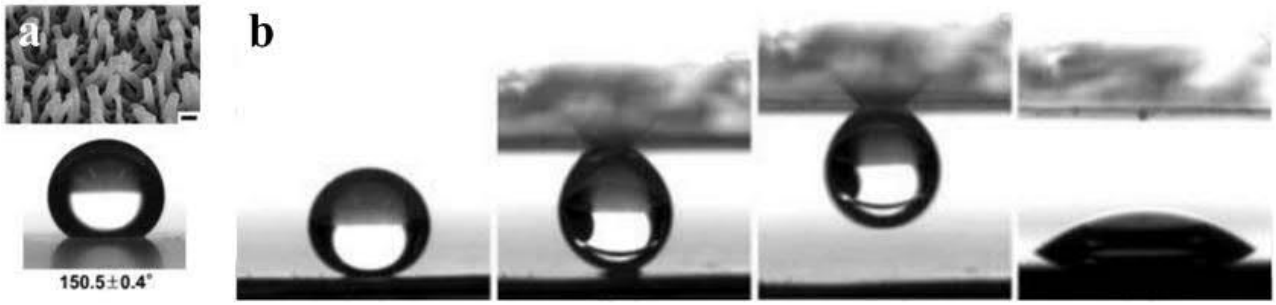

Figure 2.43. Superhydrophobic petal-effect properties. a) Nanotubular morphology b) Nanotubular surface demonstrating mechanical hand-like properties.[138]

These state-of-the-art top-down techniques possess excellent droplet carrying performance that is coupled to contamination-free droplet transfer.[26,138] For instance, Cho et al. demonstrated the use of such exemplarily functioning interfaces for carrying droplets up to 12 mg in mass while exhibiting lossless transfer (Figure 2.43).[138] However, the templating of Anodic Aluminum Oxide (AAO) substrates remains highly unscalable. The template synthesis of such micro- and nano-hierarchies cannot be easily duplicated on large substrate surfaces, thus impeding the development of such highly functional technologies.

While templating remains popular even today,[431] many other scalable bottom-up techniques have demonstrated success in duplicating the petal-effect. However, the performance of petal-like superhydrophobicity from scalable bottom-up self-assembly remains somewhat limited when compared to those developed by templating / lithography. This generally extends to poor CA and CAH performance, susceptibility to contamination, and inferior specific adhesion.[38,135,138,142,432-434] From the perspectives of design and scale, the use of non-scalable techniques can drastically impact industrial development.

2.5.3.1. Sol-Gel and Hydrothermal Synthesis

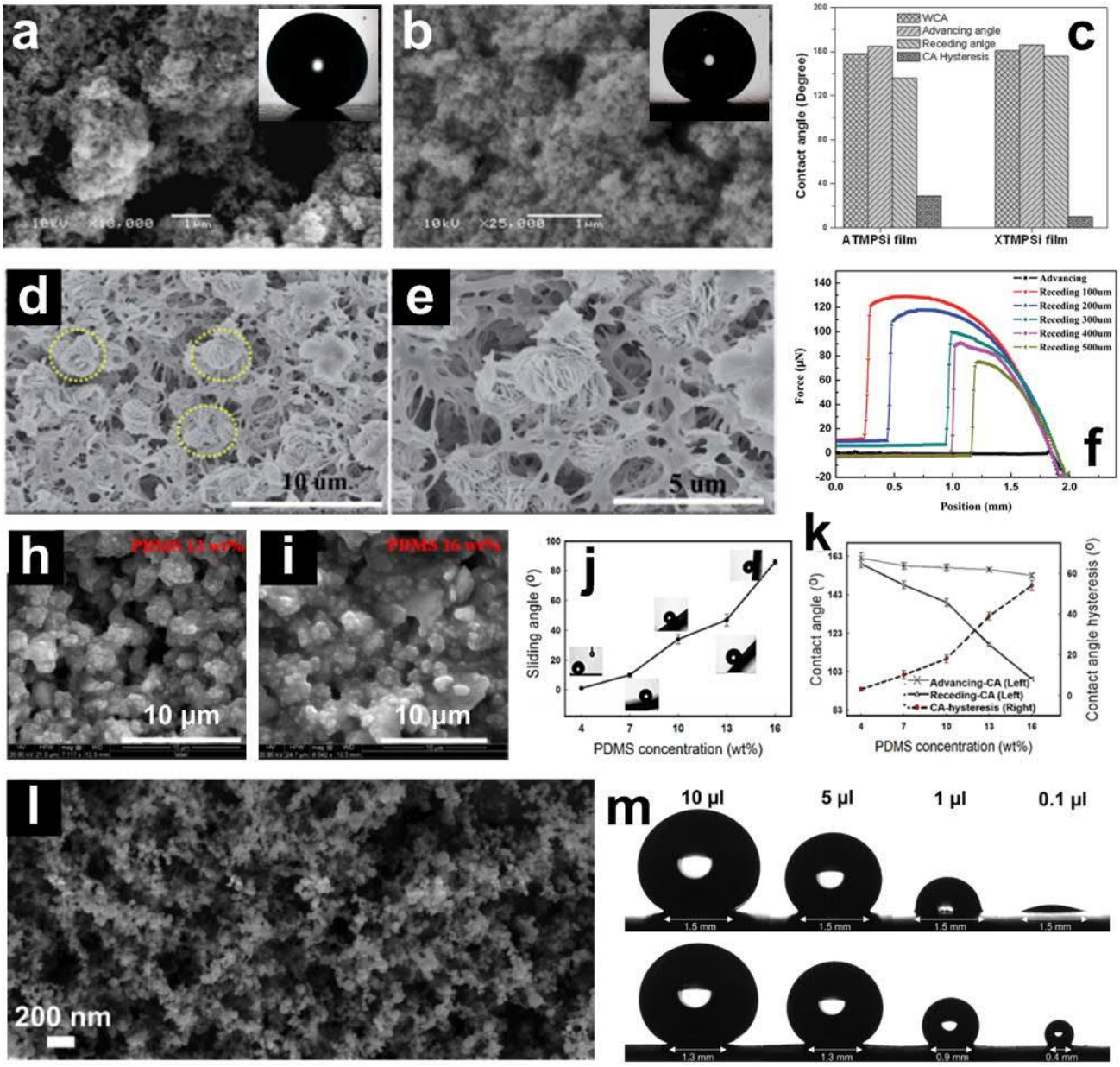

Figure 2.44. Controlled synthesis (sol-gel, blending, flame pyrolysis) of petal-like superhydrophobicity. a) Aqueous TMPSi-synthesized films and b) xylene TMPSi-synthesized films with c) variable adhesion properties.[435] d-e) Stereo-complex bottom surfaces of phase separated PLLA/PDLA films with different f) adhesion properties with microstructural thicknesses.[436] h-i) Composite blended, PDMS concentration-tuned (low to high) surface morphologies with j) increasing SAs and k) CAHs.[437] l) Fractal-based liquid flame spray pyrolysis derived TiO_2 nanoparticle networks with m) variable adhesion properties, as measured by the evaporative RCA method.[135]

One scalable method of synthesizing nanotubes was demonstrated by hydrothermally treating TiO_2 anatase powders with tetrabutylammonium hydroxide, followed by electrophoretic deposition. While the as-synthesized TiO_2 nanotubes were superhydrophilic in nature, subsequent functionalization by

fluoroalkylsilanes (FAS) resulted in adhesive superhydrophobicity. A CA of 152° was reported, alongside inverted droplets. However, no other static or dynamic wetting properties were reported.[438] Interestingly, these nanotubes were not packed in a vertical fashion that was described before,[26,138] but were instead scattered and lying on their sides.

Okada et al. demonstrated the sol-gel synthesis of hierarchically textured TiO_2 nanoparticles for developing amorphous TiO_2 films. The morphologies derived range from nano-sheets, platelet-like to funnel-like brush textures. This was achieved by pH-tuning the sol-gel process, eventually giving rise to nano-structures with adhesive superhydrophobicity. The most optimal petal-like superhydrophobicity was achieved with a CA of 152°, coupled to a droplet carrying capacity of 8 mg. However, lossless droplet transfer was not demonstrated, a key property belonging to state-of-the-art petal-surfaces.[439]

2.5.3.2. Controlled Silane Functionalization

The functionalization of nanomaterials with hydrocarbon- or fluoroalkylsilanes (FAS), coupled to suitable morphologies, is well-known for conferring a state of lotus-like superhydrophobicity.[205,299] In 2012, Ramanathan and Weibel demonstrated the use of different solvents (water-ethanol vs. xylene) in controlling the surface chemistry of TiO_2 during the sol-gel treatment of TMPSi (Figure 2.44). Although the post-deposition surface roughnesses were comparable, CAH of the aqueous-borne TiO_2 was almost triple that of the xylene-borne variant (30° vs. 10°). This is attributed to the absorption of water into the TiO_2 matrix during aqueous functionalization, thus preventing complete coverage of the oligomeric siloxanol during functionalization.[435]

The most optimally performing features demonstrated petal-like superhydrophobicity with a CA and CAH of 159° and 29° respectively, with droplet carrying capacity of 4-6 mg. However, they did not demonstrate lossless droplet transfer. Nonetheless, such a scalable, controllable and tunable surface functionalization technique showcases a facile non-mechanical method for tuning lotus-to-rose superhydrophobicity.[435]

2.5.3.3. Phase Separation

Phase separation is typically a chaotic process that is guided by spontaneous events such as nucleation, Ostwald ripening, and spinodal decomposition (Figure 2.44).[149,294] However, the process remains to be tunable, owing to key controllable dependent variables.

Gao et al. demonstrated the synthesis of phase-separated poly(lactic acid) (PLA), treated using N-methyl pyrrolidone (NMP) and water, as respective solvent to non-solvent induced phase separation. Membranes with hierarchical micro- and nano-textures, possessing highly controllable and predictable length-scales were produced. Optimization was demonstrated by increasing membrane thicknesses, which in turn controls the speed and time of solvent-non-solvent penetration, therefore resulting in the associated increase in the presence of multi-dimensional structures.

As a result, thinner films are restricted to much smaller single-scale nanostructures, thus resulting in higher surface adhesion properties (up to 132 μN). The facile tunability of this technique was even demonstrated with different areas of the membrane, resulting in domains that possess low adhesion, bordered by zones with high adhesion.[436]

2.5.3.4. Micro- and Nano-Structural Self-Assembly

Amongst methods involved in synthesizing functional coating interfaces, bottom-up self-assembly holds immense promise due to their facile, rapid and commercialization-friendly nature (Figure 2.45).

Ding et al. demonstrated the use of composite structural self-assembly for the fabrication of hollow closed-cell graphene oxide (GO) spheres. A freezing process was then used to induce shrinkage, resulting in the formation of nanowrinkles on the GO nanosheet based shell. Degree of wrinkling can be controlled by stirring speed during synthesis. The wrinkled skin is then exposed to HI vapor, thus fixing the formed structures. CAs were modified from hydrophobic states, from 125° up to 153°, which demonstrated petal-like adhesive superhydrophobicity. Surfaces functioned exemplarily as

petal-like interfaces, with CA and CAH of 153° and 120° respectively. Droplet carrying capacity was measured at up to 77.8 μN or 10 mg, coupled to lossless droplet transfer.[144]

Multi-scale surface texturing can also be performed by self-assembling supraparticles. Xu et al. used a series of dip-coating steps to create raspberry-like corona-on-core particles. Coated surfaces were superhydrophobic, with CA and CAH of 158° and 43° respectively. Droplet carrying capacity was achieved at a limit of 10 mg but no clean droplet transference was demonstrated.[295]

2.5.3.5. Composite Blending

Petal-like superhydrophobicity is not limited to the use of inorganic metallic oxides, metal-organic sol-gel and organic polymer casting. A combination of these materials can also be used in enabling the effect. Nine et al. integrated nano- and micro- particles of TiO_2 and Al_2O_3 into a PDMS pre-polymer (Figure 2.44). The presence of these inorganic particles induces controllable surface roughnesses, leading to micro- or micro- and nano- scale asperities. Increasing PDMS to particle ratio leads to predominantly single-scale micro-textures, giving rise to a CA and CAH of 153° and 55° respectively. Droplet carrying capacity was demonstrated by an inverted droplet at a maximum tested load of 5 mg.[437]

2.5.3.6. Liquid Flame Spray Pyrolysis

Besides schemes that involve the use of organic materials, traditional methods involving inorganic material synthesis can also be exploited. Teisala et al. demonstrated this by using the flame spray pyrolysis technique (Figure 2.44), with the synthesis of functional nano-structures on micro-textures that realized variable and controllable pitch distances.[135] Through this technique, CAH was tuned from 31° up to > 100°.[135] Here, the petal-effect was targeted by approaching it from the lotus-effect *via* tuning of structural-adhesion[135] properties. While the explicit petal-effect was not demonstrated, these textures most certainly possess the range and potential for achieving droplet pinning and carrying capabilities.

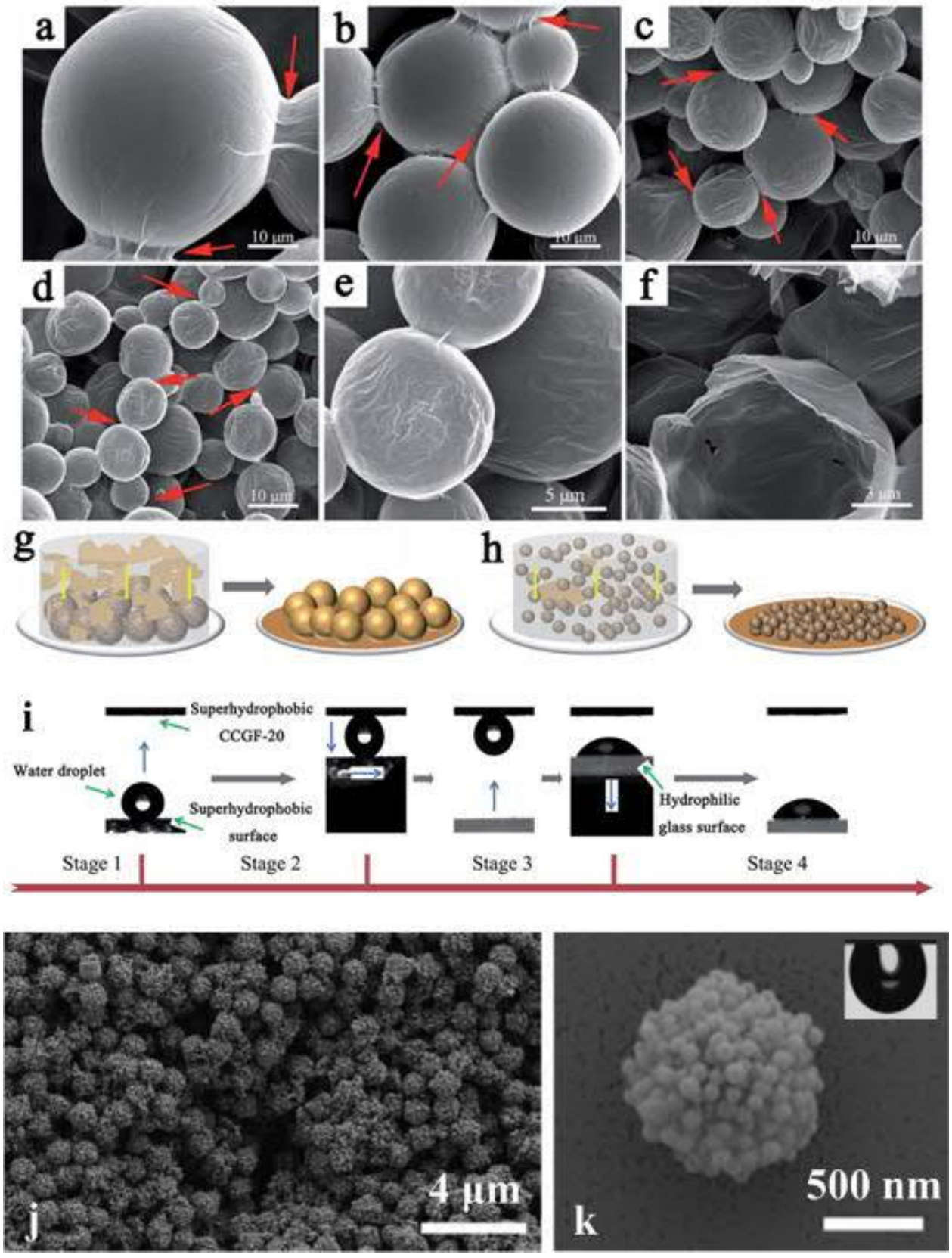

Figure 2.45. Self-assembling methods for petal-like superhydrophobicity. a-f) Wrinkled GO nano-shells with different rotational speeds during Pickering emulsions (RPM: 8k, 12k, 16k, 20k) and magnifications of (e-f) RPM: 20k respectively. g-h) Schematized filtration process for large and small microspheres respectively. i) Water droplet transportation using the most wrinkled, RPM: 20k synthesized GO nanoshells.[144] Self-assembled j) particle films with hierarchically structured k) raspberry particles demonstrating the petal effect.[38]

2.5.3.7. Aerosolized Wet-Spray

Aerosolization and spray-deposition of polymeric precursors can be used to synthesize hierarchical beaded and fibrous textures. Paul et al. demonstrated the production of bead-on-string features from the wet-spray casting of a composite blend of SiO_2 particles and PS nanofibers (Figure 2.46). Structures formed were very similar to those demonstrated in electrospinning (Section 2.5.3.8), comprising of hierarchically textured beads and an interconnected network of nanofibers. However, in this series of work, the petal-effect was far from being achieved, with static CAs being consistently << 150°.[440]

2.5.3.8. Electrospinning

Electrospinning for lotus-like superhydrophobicity has been demonstrated through a multitude of studies since the mid-2000s.[83,133,191,371-373] Owing to the vast amounts of research into electrospinning that resulted in lotus-like superhydrophobicity, the use of electrospinning for the petal-effect was much rarer. However, from 2014-2017, several pieces of research work investigating the use of electrospinning for attaining the petal-effect helped fill significant gaps in our understanding for scalably achieving the state-of-the-art petal-effect (Figure 2.46).

Gong et al. demonstrated the use of fluorinated polyimide (PI) for synthesizing micro- and nano-indented bowl-like particles that are linked by nanofibers. These indentations were attributed to the petal-effect, where withdrawal of water from the dents is believed to cause a negative suction pressure, thus preserving the adhesive state.[142] This hypothesis aligns with previous work on nanotubular structures. Droplet inversion, coupled to a carrying capacity of 120 μN was reported.[138] However, in an anti-thethical demonstration, Yoshida et al. synthesized nanofibers that were comprised of poly(γ-glutamic acid), grafted with phenyl groups (γ-PGA-Phe). While these nanofibers were perfectly fibrous, they too exhibited adhesive and stable superhydrophobic properties. Here, the authors attributed the increased superhydrophobicity to increasing grafting density, which achieved the petal-effect at maximum grafting, showcasing a CA of 154° with droplet inversion.[441] Despite

these controversial results, neither Gong nor Yoshida showcased dynamic wetting properties in the form of SA or CAH. In addition, these works also did not address the potential for lossless droplet transfer.[138,441]

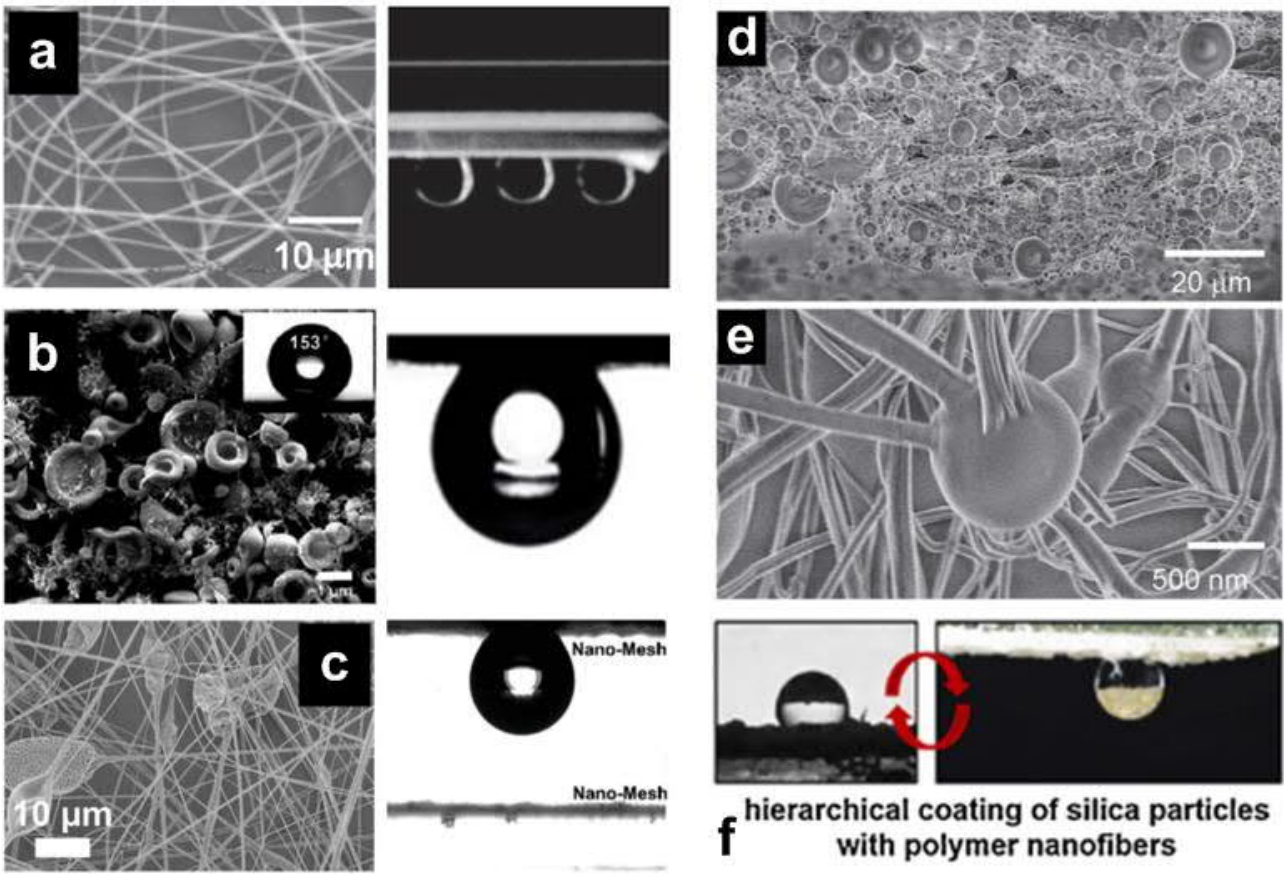

Figure 2.46. Electrospun and wet-sprayed petal-like superhydrophobicity. a) Scanning electron micrograph of electrospun fibers from 20% γ-PGA-Phe-80 solution in Hexafluoroisopropanol (HFIP), with petal-like wetting properties.[441] b) Electrospun bowl-shaped beads of fluorinated PI, with petal-like wetting properties.[142] c) Electrospun part-bead, part-fiber PS with petal-like wetting properties.[89] d-e) Scanning electron micrograph of structured coatings prepared by spray-coating for d) hierarchical structures of SiO_2 particles that are e) incorporated into PS nanofibers for f) adhesive superhydrophobicity.[440]

In 2015, Wong et al. reported on the use of a standard hydrophobic polymer, PS, in developing a range of electrospun micro- and nano-structures, ranging from pure beads to fibers. The beaded hemispherical structures achieved were very similar in profile to those reported before,[142] but were lotus-like superhydrophobic with relatively low adhesion. Alternatively, fibers synthesized at the micro- to nano- scales appear to aid in wettability and thus increased adhesion properties. This culminated in the synthesis of a part-bead, part-fiber based film, which demonstrated an ideal petal-

effect showcasing lossless transfer. A water CA and CAH of 152° and 57° was reported, coupled to a droplet carrying capacity of 12 mg and 113 μN. The increased adhesion is attributed to the hybrid combination of beads and fibers within a 3D stacked film that allows fluid penetration into its inter-fiber micropores while preventing complete Wenzel wetting *via* interstacked beads with lotus-like superhydrophobic properties.[89]

Despite the presence of research that has attributed the petal-effect to fibers,[441] beads[142] and beaded-fibers,[89] the petal-effect relies inherently upon delicately controlled surface chemistry and morphology. Both factors must be carefully tuned for each system and their associated requirements. Moreover, this transitional zone is highly sensitive and only metastable under minor disturbances. Increasing hierarchy or lowering solid surface energy will lead to the Cassie dewetting lotus-effect, while decreasing hierarchy or increasing solid surface energy will result in Wenzel wetting.

2.5.3.9. Electrodeposition

Electrophoretic deposition of solvothermal-treated TiO_2 nanotubes, followed by fluoro-functionalization, is a method that has previously demonstrated adhesive superhydrophobicity (Figure 2.47).[438]

However, this process can also be performed independently. Liang et al. showcased the use of electrodeposition for the synthesis of hexagonal Zn-Co microplates with nanopores. This was enabled by the electrodeposition on carbon steel substrates *via* zinc sulphate and potassium aluminum sulphate electrolytes. The relative superhydrophobicity can be tuned by changing the surface roughness of the electrodeposited material by secondary chemical replacement during the electrodeposition process. Surface roughnesses were highly tunable, ranging from micro- to multi-scale roughnesses with increasing replacement time. The optimally performing samples possessed a petal-like superhydrophobic surface with a CA of 155°. They were also capable of carrying droplets up to 11 mg, with clean droplet transfer (ca. 100%) properties.[146]

2.5.3.10. Mechanical Methods

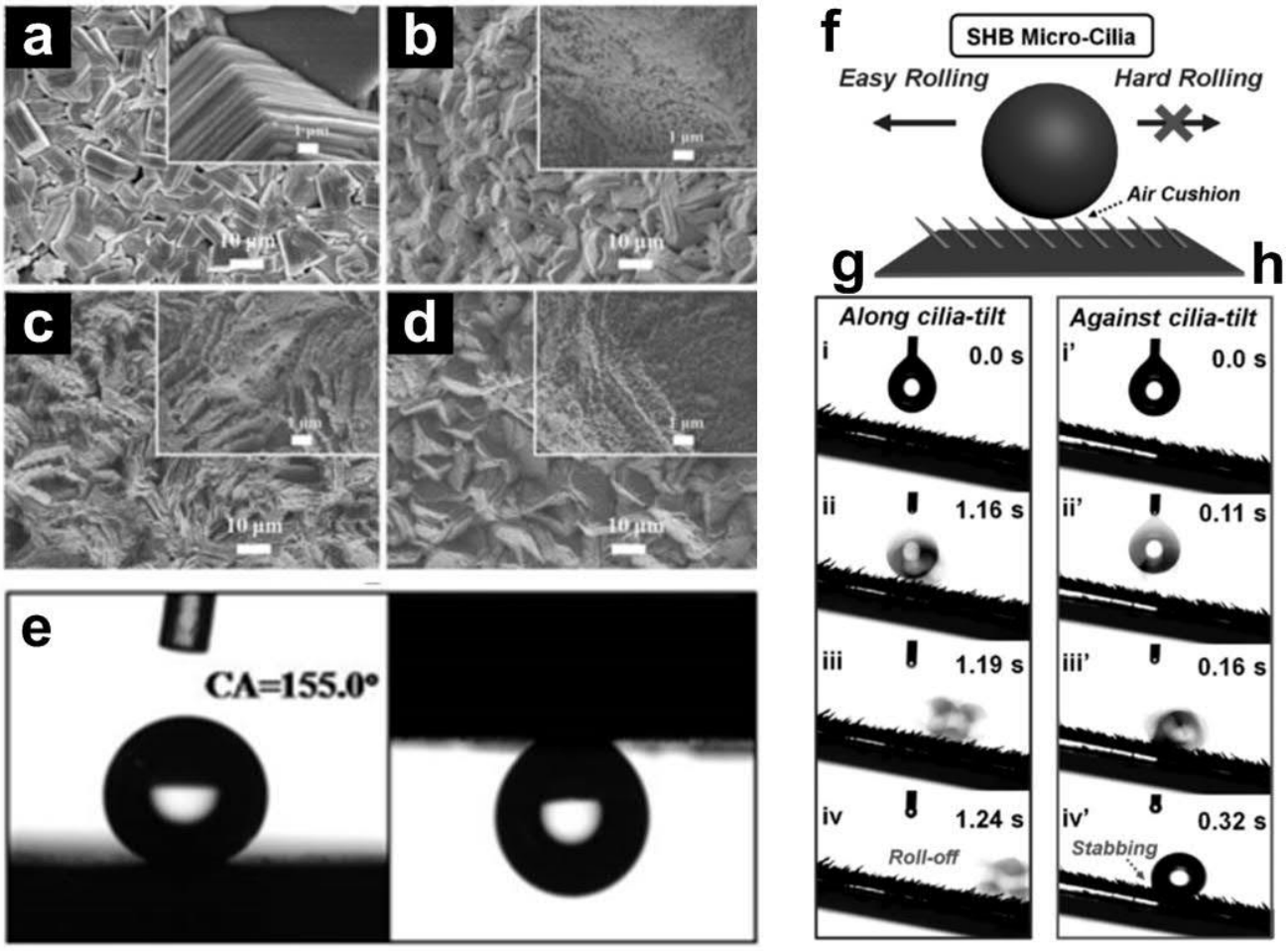

Figure 2.47. Electrodeposition-derived and mechano-actuated petal-like superhydrophobicity. a-d) Scanning electron micrographs of Zn substrates after electrodeposition with different electrodeposition parameters (time-dependent replenishment of chemicals), showing the e) adhesive superhydrophobic petal-effect.[146] f) Superhydrophobic micro-cillia that are magnetically controlled, enabling g) roll-off by anisotropic alignment and h) droplet halting by interfacial droplet stabbing.[442]

Notwithstanding the exemplary performance of the above coating methods, various mechanically-inspired means have also been demonstrated for achieving the petal-effect. By definition, mechanical methods are primarily dynamic in nature and usually require some form of actuation / activation. These methods are also typically designed to transcend the metastable domains that are occupied by the petal-effect, switching actively from Cassie-Baxter to Wenzel wetting states.

Cao et al. demonstrated the use of magnetically-responsive micro-cilia for switchable lotus-to-rose surfaces (Figure 2.47). These were fabricated *via* a magnetic-field induced polymerization process that resulted in small, magnetic rod-like protrusions.[442] The resulting interface functions according

to morphological profile changes between cilia-alignment and orientation, in mechanical modes very similar to that found on butterfly scales.[442] Droplet locomotion along the micro-cilia led to smooth droplet roll-off while reverse motion against the micro-cilia led to droplet stabbing; penetration and thus pinning. Surface pinning was so effective that droplets can be tilted 90° without roll-off. Surfaces exhibited CA and CAH of > 150° and 80-120° respectively. However, no droplet transfer was demonstrated.[442]

The use of mechano-regulation for the petal-effect was demonstrated by Tang et al., where hydrophilic fibers were integrated with a superhydrophobic mesh *via* a fiber-through-hole mechanical design. The hydrophilic fibers attach to the droplet by virtue of standard Wenzel wetting, but droplets can be mechanically detached when the fiber is drawn back up the holes of the mesh. This is unique as it demonstrates on-demand control and programmable attachment-detachment of fluid microdroplets. CA of the surface was measured at 151°, coupled to a carrying capacity of 11.8 mg. Notwithstanding the original state of Wenzel wetting during droplet attachment, lossless droplet transfer was also apparently demonstrated.[443]

2.5.4. Drawbacks

Lotus-like Superhydrophobicity

Despite the range of superhydrophobic coatings that have been presented in the literature today, much discrepancy remains with regards to true industrial performance. In part, this stems from the varaiable extent of analysis in wetting behavior (CA, SA and CAH), optical properties (transmittance), mechanical durability (mechanical abrasion, i.e. Taber, sandpaper, AFM, droplet impact, etc.), UV-, acid-, alkali-, heat- and immersion- resistant properties. Moreover, industrial standards and requirements are generally too specific when contrasted with research objectives. Considering these differences, it is admittedly difficult to cross-compare absolute performance.

A thourough and uniform set of tests would need to be established for future research endeavors, in order to facilitate standardization of cross-displinary optimizations.

Petal-like Superhydrophobicity

Despite the successful development of petal-like superhydrophobic interfaces, one primary parameter remains largely ignored. This relates to the contamination-proof or detachment-residue free nature of such petal-like interfaces. In contrast to the well-sustained air-gaps present in the lotus-effect, the petal-effect is designed to be partially penetrated. This leads to questions on whether successful separation of droplet-interfacial profiles is achievable when required. As of the time of writing, there exists only a couple of manuscripts that clearly elaborates on this factor.[26,89] Much of the research remains vague on the topic of potentially contaminating[422] the petal-surface.[21,38,135,138,142,143] This contamination threat presents a crucial drawback that could limit the implementation and use of such surfaces as single- or array- based droplet control devices.

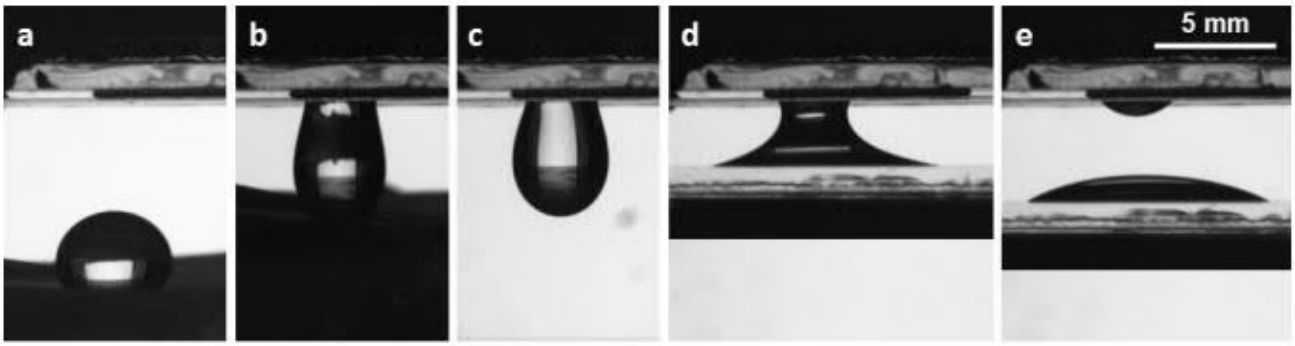

Figure 2.48. Non-ideal petal effect. Demonstrated (a-e) by showcasing a-d) concave water-to-surface capillary bridge with residual droplets e) upon transfer.[422]

2.5.5. Concept

Considering the limitations behind current scalable techniques used in achieving superhydrophobicity, we must acknowledge difficulties that stem from multiple research directions. We will also review and differentiate the roles of lotus-like and petal-like superhydrophobicity alongside their current definitions. Attempts are made specifically to resolve drawbacks in both systems while retaining functional performance. Priorities are directed as follows: 1) transmittance / transparency and 2) mechanical robustness and reliability. Finally, we demonstrate the superiority of our methods in advanced functional coatings that could bear immediate industrial applications.

Lotus-Effect

a) We first investigate the potential of synthesizing superhydrophobic coatings based on a single-step functionalization procedure, centered on flame-aerosol assisted aerosolized deposition.
b) We then develop a series of wet-synthesis and wet-aerosol deposition processes for enhancing the robustness of inherently weak superhydrophobic coatings. To this end, we will incorporate the use of polymeric binder materials in order to enhance the robustness of superhydrophobic surfaces.

Petal-Effect

a) We first investigate scalable methods for synthesizing perfectly lossless rose petal-like interfaces, focusing on contamination-free detachment, enabled through convex capillary bridges. This will be coupled with demonstrating state-of-the-art performance that matches or surpasses current petal-like surfaces' droplet carrying capacity ($\geq$ ca. 10 mg).
b) We then demonstrate cross-domain (Cassie-Baxter to Wenzel) tunability of adhesion within the petal-effect, by reversibly and dynamically tuning its corresponding wettability and adhesion from a petal- to a lotus- like superhydrophobic state.

2.6. Superoleophobicity and Superamphiphobicity[8]

Superoleo(amphi)phobicity is characterized by a CA > 150°, a SA < 10° and a CAH < 25°, with probe fluids of surface tensions between 20 to 72 mN/m. We have, in the prior sections, proposed the further sub-classification of superoleo(amphi)phobicity into highly superoleo(amphi)phobic (20-30 mN/m) and mildly superoleo(amphi)phobic (30-72 mN/m) variant. For the sake of thoroughness, we will not discriminate between the two variants. However, for the sake of clarity, we will also strive to report the performance (surface tension, CA, CAH and SA) accorded to each morphological profile utilized for achieving superoleo(amphi)phobicity. In addition, owing to the infancy of this research area, we will also review the literature within this sub-field with much greater emphasis on selected performance parameters than prior chapters.

2.6.1. Fabrication and Materials

Superoleo(amphi)phobicity can only be achieved by using heavily fluorinated fluorocarbon groups (-CF_3 with 6.7 mN/m).[103] This contrasts the synthetic processes involved for superhydrophobicity, where simple hydrocarbons or polymers (ca. < 35 mN/m) are sufficient for attaining acceptable limits of superhydrophobic performance with water.[83,390,444,445] Naturally, interfaces that are capable of repelling hydrocarbon fluids (20-40 mN/m) cannot be practically synthesized out of the same organic configurations, owing to their similarities in surface energies.[103]

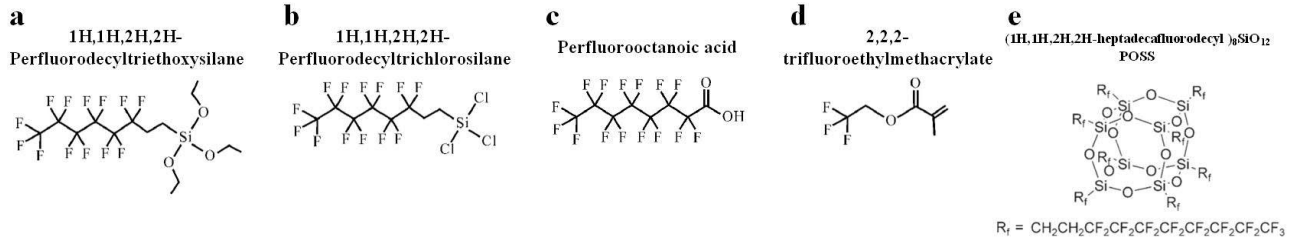

Figure 2.49. Fluorinated compounds for synthesizing superoleo(amphi)phobic coatings. Broad categories include a) alkoxysilanes, b) chlorosilanes, c) fluorinated carboxylic acids, d) fluoro-methacrylate precursors or e) fluorinated octameric POSS.

[8] The lower limit of superoleo(amphi)phobicity exists with the fluid heptane (γ = 20.1 mN/m), while its upper limit has been tested with the fluid diiodomethane (γ = 50.8 mN/m). The most common test fluid, however, is hexadecane (γ = 27.5 mN/m).

This is also the primary reason why most superhydrophobic surfaces are not superoleophobic, revealing the large chasm between these functional dewetting interfaces. Today, almost all superoleo(amphi)phobic surfaces utilize fluorinated materials, which range from fluorinated silanes,[14,72] fluorinated carboxylates,[161,446] fluorinated polymers[447,448] or highly fluorinated nanoparticles such as the series of fluorinated polyhedral oligomeric silsesquioxanes (F-POSS)[449] (Figure 2.49). However, superoleo(amphi)phobicity is difficult to achieve even with such optimized surface energy states.[300,450] This is attributed to the secondary requirement of having specifically textured re-entrant profiles (Figure 2.50). These re-entrant profiles are necessary for preventing the naturally occurring contact-line advancements by low surface tension fluids into the hierarchical architectures.[72]

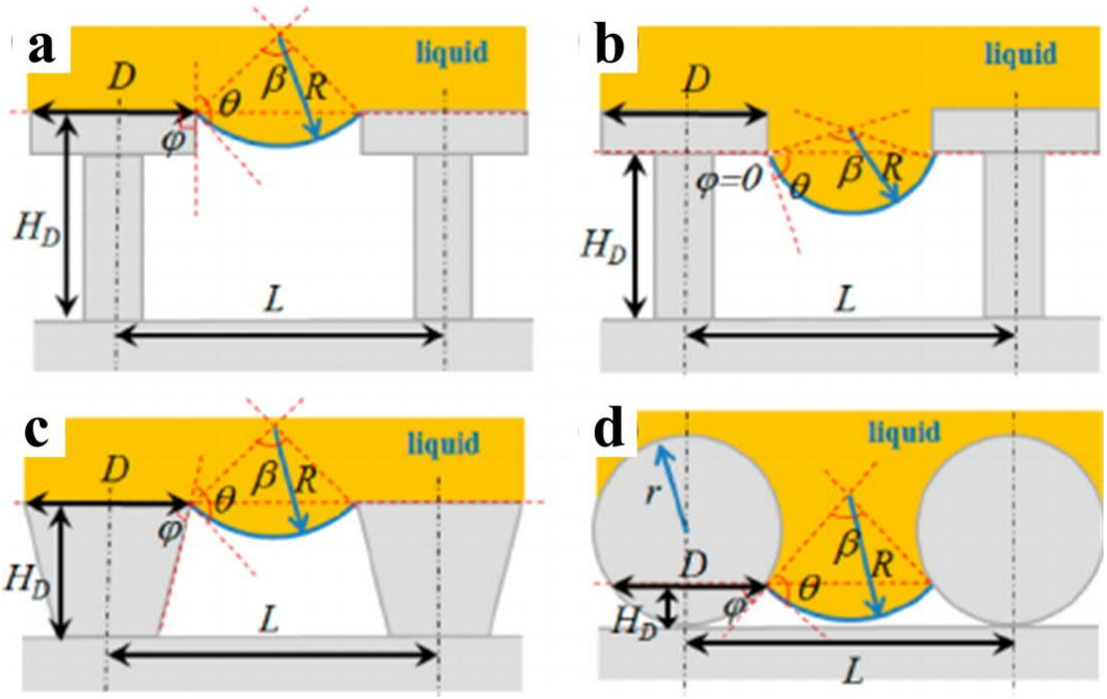

Figure 2.50. Pinning of contact line on various re-entrant or overhanging structures. a) T-shaped microhoodoo structures, pinned on top edge. b) T-shaped microhoodoo structures, pinned on bottom edge. c) Inverse trapezoid structures. d) Sphere-like or fibrous (cylindrical cross section) structures.[451]

This can be understood by understanding Young's CAs of most low surface tension fluids on surfaces, which tend to be < 90° even after fluoro-functionalization. Contact line advancement into hierarchical features is thus possible on vertical profiles bearing 0° in re-entrancy (such as pillars, fractal agglomerates, vertical nanotubules). However, when a re-entrant profile is created at > 0°, the

advancement of contact lines can become artificially impeded at the very edges of these geometrical features. The contact line is thus pinned and surface penetration is inhibited. This effectively prevents the Cassie-Baxter state of wetting. Notably, re-entrant textures need not be vertically and identically repeating, as contact line advancement is halted only at the very first or maximum point of re-entrancy.[187]

2.6.1.1. Nanofilaments, Fabric Fibers, Meshes and Tubes

Cylindrical fibers or spheres are known to possess a particularly unique re-entrant profile.[160] While the upper hemisphere of the cylinder / sphere (side-profile) resembles a standard cone and is thus easily wetted, the bottom hemisphere experiences an alternate state of wetting. With the progress of the contact line past the equator (of the side profile), a gradually increasing state of re-entrancy ensues. This starts from 0° at the equatorial tangent, and gradually increases to 20°, 45° and 60°. At these undefined limits, the re-entrancy is sufficient in preventing contact line advancements of many highly wetting fluids (Figure 2.51). This unique mode of contact line pinning prevents further advancement of the wetting fluids, thus preserving the Cassie-Baxter state of dewetting. Such understanding has led to the facile achievement of superoleo(amphi)phobicity on a series of cylindrically-shaped substrate materials, such as fabrics,[51,52,61,452,453] paper[454,455] and meshes[56,65].

Self-Assembled Nanofilaments

Independent synthesis of superoleo(amphi)phobic cylindrical profiles were first demonstrated by Zimmermann et al., who exploited the use of silicone nanofilaments for achieving superoleo(amphi)phobicity, demonstrating -phobicity to hexadecane (CA = 140°, γ = 27.47 mN/m) and diiodomethane (CA = 165°, SA = 10°, γ = 50.8 mN/m).[453] This was further improved in later years, by further optimizing hierarchical geometry and surface chemistry. These revised silicone nanofilament coatings were capable of achieving highly superoleo(amphi)phobic properties to hexadecane (CA > 170°, SA < 3°, γ = 27.47 mN/m).[51] Today, the concept of a re-entrant cylinder / sphere is much more prevalent in the synthesis of superoleo(amphi)phobic fabrics.

Fabrics

In combination with the naturally re-entrant profiles of fabric fibers, dip- or spray- coating can also be utilized to enable states of superoleo(amphi)phobicity.

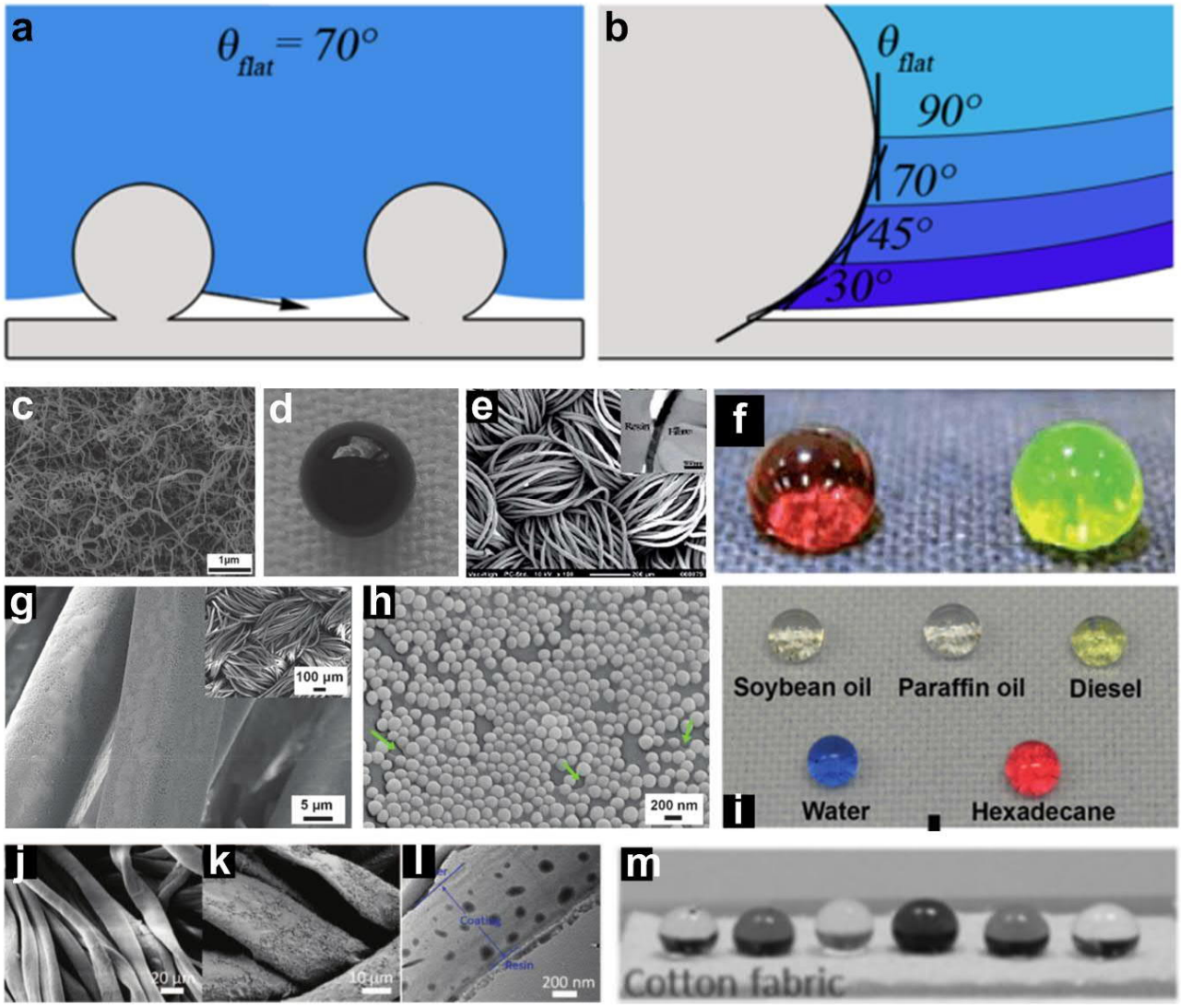

Figure 2.51. Fiber-based re-entrant profiles for superoleo(amphi)phobicity. a,b) Schematic of re-entrant profiles (fiber-based) inhibiting fluid penetration.[158] Scanning electron micrographs of c) silicone coated polyester textiles, with a droplet of d) crude oil.[52] e-f) Vapor polymerized conductive superoleo(amphi)phobic coatings on polyester, with droplets of f) water (left) and hexadecane (right).[452] g-h) Polyester fibers coated with h) SiO_2 NPs-HFA-TiO_2 with i) superoleo(amphi)phobicity.[50] j-l) Cotton fibers coated with PTFE NPs-FAS-Zonyl321 with superoleo(amphi)phobicity to m) glycerol, olive oil, water, mineral oil, hexadecane and paraffin oil.[456]

Xu et al. dipcoated polyester fabrics in TiO_2-SiO_2 sol-gels to create microfibers that are textured with micro- and nano- particle agglomerates. Upon fluoro-functionalization with a perfluorinated acid,

superoleo(amphi)phobicity was achieved, with a hexadecane (γ = 27.47 mN/m) CA of 151°. However, the CAH was extremely high at 141°, which is indicative of Wenzel wetting.[457]

Composite based materials can also be used to the same effect. Nishizhawa et al. spray-coated precursor solutions of SiO_2-perfluoromethacrylates (PMC) onto textiles for the synthesis of superoleo(amphi)phobic fabrics. Textured fabrics were microfibrous with distinctive micro- and nano- particle agglomerates, showcasing a hexadecane (γ = 27.47 mN/m) CA of 152°. Wang et al. dipcoated polyesters in $FeCl_3$-fluoroalkylsilane (FAS), followed by the vapour-phase polymerization of polypyrrole (PPy). Coated polyester fibers were superoleo(amphi)phobic to hexadecane (γ = 27.47 mN/m) with CA and SA of 154° and 15° respectively.[452]

Zhou et al. designed a one-step *in-situ* functionalized precursor that is comprised of PTFE nanoparticles and fluoroalkylsilanes (FAS) suspended in Zonyl321 (DuPont). The solution can be spray- or dip- coated on fabrics, resulting in micro- and nano- roughened hierarchies. Superoleo(amphi)phobicity was achieved with hexadecane (γ = 27.47 mN/m), at CA and SA of 151° and 13° respectively.

Enhanced one-step sol-gel condensation can also be used as a facile means for the rapid coating of fabric materials. Lovingood et al. demonstrated the use of microwave assisted SiO_2 condensation on cotton swatches with fluoroalkylsilane (FAS). Micro-textured cotton possessed distinctive nanoparticle-clustered coatings that showcased superoleo(amphi)phobicity with ethylene glycol (γ = 47.7 mN/m) at a CA of 153°.[458]

Improving on this concept, Leng et al. utilized a three-step process for the treatment of superoleo(amphi)phobic cotton, involving the Stöber growth of SiO_2 microparticles followed by surface adsorption of 3-aminopropyl-triethyoxysiloxane (APS). The samples were then treated with fluoroalkylsilanes (FAS), thus enabling superoleo(amphi)phobicity. Cotton fibers developed by this process possessed enhance surface hierarchy, composed of nanotextured micropapillae-like features.

Optimally developed variants demonstrated superoleo(amphi)phobicity with hexadecane (γ = 27.47 mN/m) CA and SA of ca. 150° and 15-30°.[459]

The most exemplarily performing superoleo(amphi)phobic fabrics were developed by Pan et al., who demonstrated the fluorosilanization of cotton fabrics, which resulted in high CAs (151°) even with solvents down to hexane (γ = 18.43 mN/m), which in fact, crosses over into domains of superomniphobicity. However, SAs were all comparatively high, showing 18° with hexadecane and reaching up to 31° with hexane.[61]

Despite tremendous advancements in superoleo(amphi)phobic fabrics, durability was not initially explored. This changed with the development of self-healing superoleo(amphi)phobic fabrics. The concept was first demonstrated by Wang et al. *via* the coating of F-POSS and fluoroalkylsilanes (FAS) on polyester fabrics. CAs with hexadecane (γ = 27.47 mN/m) reached up to 155°, while wetting CAs with tetradecane (γ = 26.56 mN/m) were ca. 152°. Plasma and heat-treatment (135 °C) were used in tandem to destroy and restore superoleo(amphi)phobicity. Cyclic damage-recovery tests were performed to and beyond 100 cycles, indicative of excellent self-healing capabilities. However, recovered surfaces were only operational to hexadecane, where CA remained above 150°. For tetradecane, CA decreased below 150° and superoleo(amphi)phobicity was lost.[460]

Robustness of such fabrics were later further improved by Zhou et al. *via* a two-step process. This was first performed by using a SiO_2 sol-gel dipcoating process for surface roughening. It was then followed by a second dipcoating process using a resin binder comprised of a polyvinylidenefluoride (PVDF)-hexafluoropropylene (HFP)/FAS solution. These sequential steps gave rise to superoleo(amphi)phobic fabrics with enhanced robustness. As-synthesized fabrics had hexadecane CA and SA of ca. 160° and 8° respectively. They were mechanically robust after laundry cycles and were resistant to both acids and bases. Notably, they are now more resistant to multiple cycles of plasma-heat treatment recovery.[461]

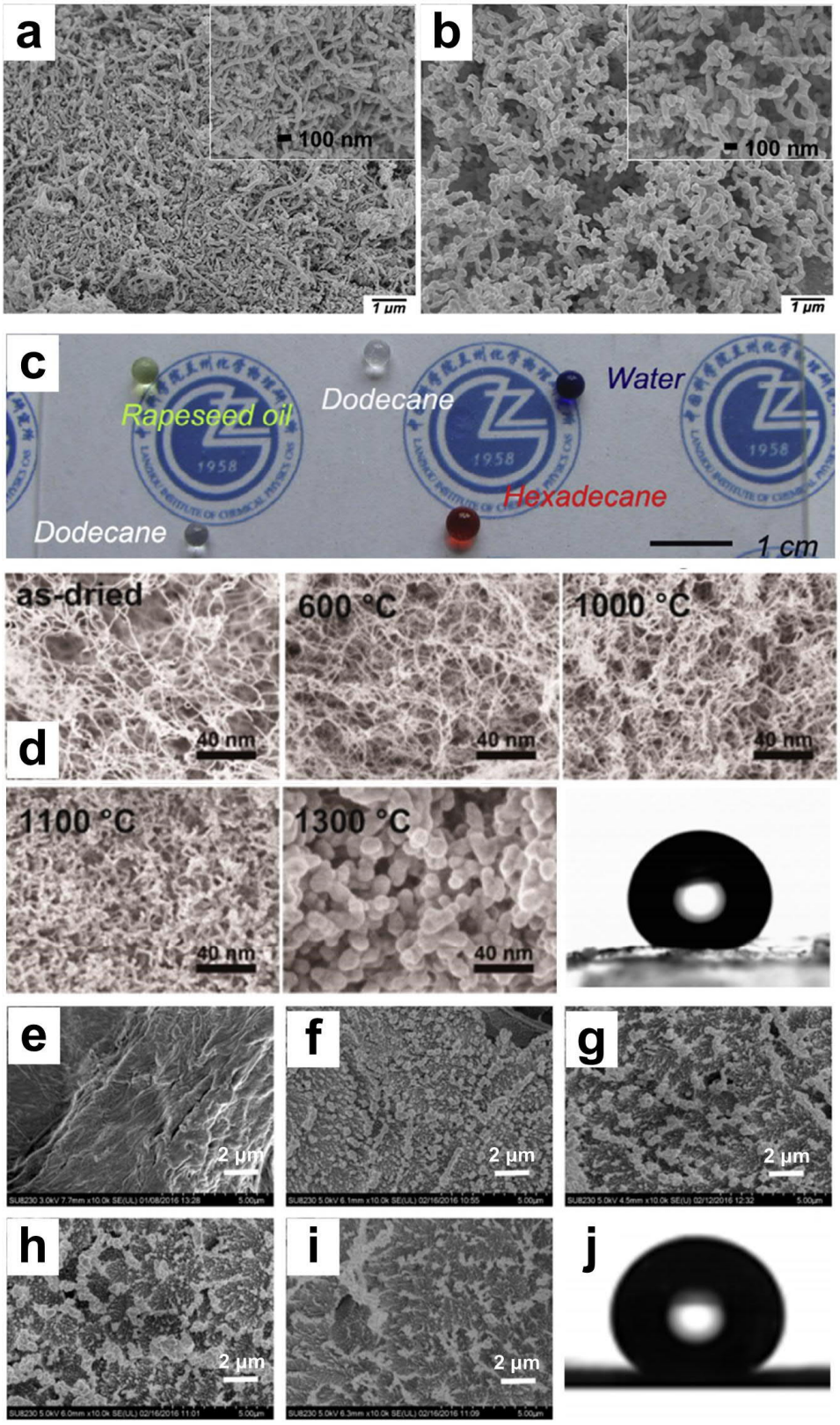

Figure 2.52. Fiber and paper-based superoleo(amphi)phobicity. a,b) SEM micrographs of sprayed CNTs-SiO_2 coating before and after thermal treatment. c) Superoleo(amphi)phobicity of CNTs-SiO_2 coating with water, dodecane and hexadecane.[462] d) SEM micrographs of as-dried boehmite nanofibers and calcined Al_2O_3 monoliths, with superoleo(amphi)phobicity towards hexadecane.[463] e-i) Paper fibers ranging from un-etched (e) to plasma-etched at f-i) 15, 30, 45, 60 minutes and subsequently vapor functionalized. j) Superoleo(amphi)phobicity demonstrated with hexadecane.[455]

Nanotubes and Nanofibers

Departing from the use of inherently fibrous fabric materials, nanotubes and nanofibers also represent immensely useful raw materials for the surface texturing of superoleo(amphi)phobic coatings. Zhu et al. demonstrated the use of carbon nanotubes (CNTs), coated with sol-gel SiO_2 which were then fluoro-functionalized with fluoroalkylsilanes (FAS). The textured nanotubular coatings showcased superoleo(amphi)phobicity, reaching dodecane (γ = 25.4 mN/m) CA, SA and CAH of 154°, 5° and 6° respectively.[462] Li et al. fabricated a superoleo(amphi)phobic coating by using spray-coated multi walled carbon nanotubes (MWCNTs). MWCNTs were first modified by sol-gel condensation reactions with methyltrimethoxysilane. They were then mixed into PDMS precursors and spray-coated onto glass. Calcination of the as-deposited composite coating led to the formation of SiO_2 nanotubes (SNTs). Upon wet-functionalization with fluoroalkylsilanes (FAS), superoleo(amphi)phobicity was achieved with decane (γ = 23.8 mN/m), showcasing CA and SA of 155° and 8° respectively.[464]

The use of nanotubes within composite materials has also been fairly successful. Wang et al. demonstrated the use of fluoro-functionalized multi wall carbon nanotubes (MWCNTs) in fluorinated polyurethanes for spray-coated microfibers with micro- and nano- textures. Superoleo(amphi)phobicity was achieved with multi-alkyl-cyclopentanes (γ = 31 mN/m) at CA and SA of 152° and 15°.[465] The spray-coating of carbon nanofibers and perfluoromethacrylates (PMC) by Das et al. demonstrated the formation of random micro-bumps and clustered bundles of carbon nanofibrous. This surface possessed superoleo(amphi)phobic performance against mineral oil (γ = 28.5 mN/m), with CA and SA of 164° and 9° respectively.[85]

Alternatively, inorganic fibers can also be used. Hayase et al. utilized a sol of boehmite nanofibers, which was then fluoro-functionalized with fluoroalkylsilanes (FAS). The resulting nanofibrous surfaces were superoleo(amphi)phobic, with hexadecane (γ = 27.47 mN/m) CA of 155°.[463] Alternatively, Li et al. spray-coated a solution of hydrated magnesium aluminum silicate with rod-

like micro-structures. These structures were then chemically modified by the hydrolytic condensation of an organic-silicate and a fluoroalkylsilane (FAS) within a single pot reaction. They were then added to more fluoroalkylsilanes (FAS) before being spray-coated onto various substrate surfaces. As-synthesized superoleo(amphi)phobic surfaces were predominantly rod-like, cross-linked within a web-like macro-system. Optimally developed coatings were tested at a superoleo(amphi)phobic limit of dodecane (γ = 25.4 mN/m) with CA and SA of 160° and 7° respectively.[466]

Paper Fibers

In recent years, the cheap, environmentally friendly, inherently fibrous and ubiquitous availability of paper has led to its utilization in superoleo(amphi)phobicity (Figure 2.52). It was first exploited by Jin et al. through the use of refined and grounded pulp, followed by freeze drying and fluoro-functionalization with fluoroalkylsilanes (FAS). The resulting aerogel-like cellulose network of nanofibers were superoleo(amphi)phobic with a mineral oil (γ = 35.3 mN/m) CA of 158°. However, wetting was noted to be in the Wenzel pinning state.[467]

The use of paper was later demonstrated by Li et al. by the use of home-made pulp, functionalized using sequential plasma etching and fluoropolymer deposition. Optimal conditions could produce superoleo(amphi)phobic surfaces with hexadecane (γ = 27.47 mN/m) CA of 154°. However, hexadecane droplets were also pinned onto the surfaces even after tilting, indicative of a Wenzel penetrated state.[454] Very recently, this was improved to a true state of superoleo(amphi)phobicity wihout pinning, even when contacting hexadecane (γ = 27.47 mN/m) droplets, demonstrating CA and SA of > 150° and 8° respectively.[455]

Despite their exemplary performance, the need for and use of such specialized substrate materials (such as fabrics, paper, meshes etc.) represents a major drawback. As a result, minus the exception of self-assembling silicone nanofilaments,[51] the vast majority of these techniques cannot be easily scaled on a range of other variable material surfaces. Nonetheless, there exists a plethora of other

techniques that do not rely on the explicit fiber-cylinder re-entrant profile for achieving superoleo(amphi)phobicity. These methods will be highlighted in the following sections.

2.6.1.2. Dip- and Spin- Coating

Dipcoating synthesis of superoleo(amphi)phobic coatings is an extremely versatile and scalable technique (Figure 2.53), as we have seen in previous sections. It does not discriminate against substrate geometries or dimensions, and represents one of the few truly industrially viable methods.

Wang et al. first dipcoated PET substrates in SiO_2-silicone, which were later treated with plasma before fluoro-functionalization with fluoroakylsilanes (FAS). A micro- and nano- agglomerated profile was developed, which revealed superoleo(amphi)phobic properties with hexadecane (γ = 27.47 mN/m), demonstrating CA, SA and CAH of 153°, 4° and 4° respectively.[468]

This can also be used with purely inorganic pre-structured materials. For instance, Zhang et al. dipcoated substrates with TiO_2-walled carbon nanotubes (CNTs), followed by fluoro-functionalization with fluoroalkylsilanes (FAS). This resulted in the formation of tubular structures with micro-globules that were coated in nano-flakes / platelets. These hierarchical coatings were super(oleo)amphiphobic with silicone oil (γ = 21.5 mN/m), at CA and SA of 160° and 5.9° respectively.[469]

The dipcoating process can be exploited with select polymer-solvent combinations for inducing desired surface modifications. Brown et al. described the process of dipcoating PC substrates with acetone-nanoparticle mixtures for nanoparticle-polymer swelling and impregnation. Interestingly, micron-spherulites of agglomerated nanoparticles were integrated into the surface of the polymer, with hierarchically textured re-entrant morphologies. Upon fluoro-functionalization, resulting films demonstrated superoleo(amphi)phobicity, with a hexadecane (γ = 27.47 mN/m) CA and SA of 154° and 5°.[155]

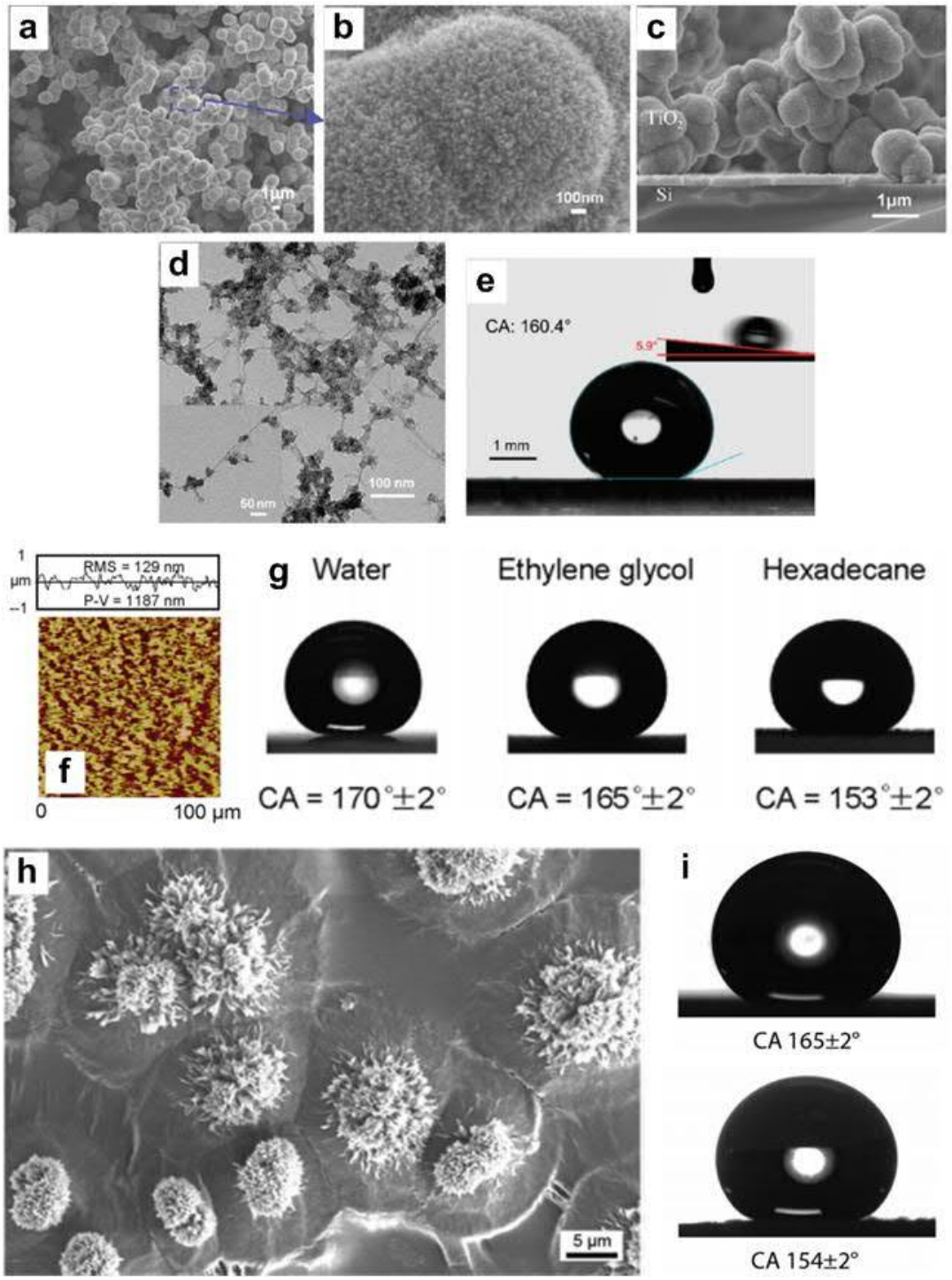

Figure 2.53. Dipcoated superoleo(amphi)phobic micro- and nano- textures. a) SEM micrographs of the TiO_2 / single-wall nanotube (SWNT) porous coating. b) Cross-sectional view of the coating shows overhanging structures formed by the TiO_2/SWNT clusters. c) High-magnification view of the coating surface shows that the surface of TiO_2 particles is covered by nanocrystals, forming hierarchical surface structures. d) TEM micrograph of the TiO_2/SWNT hybrid clusters. e) Droplet of silicone oil resting and rolling off the superoleo(amphi)phobic coating.[469] f) Surface height maps and sample surface profiles of dipcoated PET with methylphenyl silicone resin with g) superoleo(amphi)phobic properties.[468] h-i) Acetone-nanoparticulate aggregations of "re-entrant" stumps induced by PC crystallization, enabled through the immersion-induced phase separation of thin PC films. Films demonstrated i) superoleo(amphi)phobicity to water (top) and hexadecane (bottom) respectively.[155]

Spincoating is a technique that can be used for the controlled assembly of nano- and micro-structural coatings. Hsieh et al. demonstrated the use of the unique inherent re-entrancy by using spherical SiO_2 spheres for superoleo(amphi)phobicity. Separate colloidal systems of uniform SiO_2 spheres (20 nm and 300 nm) were used for two-step spincoating, thus resulting in hierarchical roughness. A fluoro-methacrylic polymer was then utilized as a surface coating. The hierarchical textures comprised of large SiO_2 microspheres that are covered in nanospheres, mimicking the dual scale roughness of a lotus leaf (Figure 2.54). This configuration was tested down to isopropanol (γ = 23.4 mN/m), and demonstrated a super-phobic CA and CAH of ca. 145° and 3.5° respectively.[470]

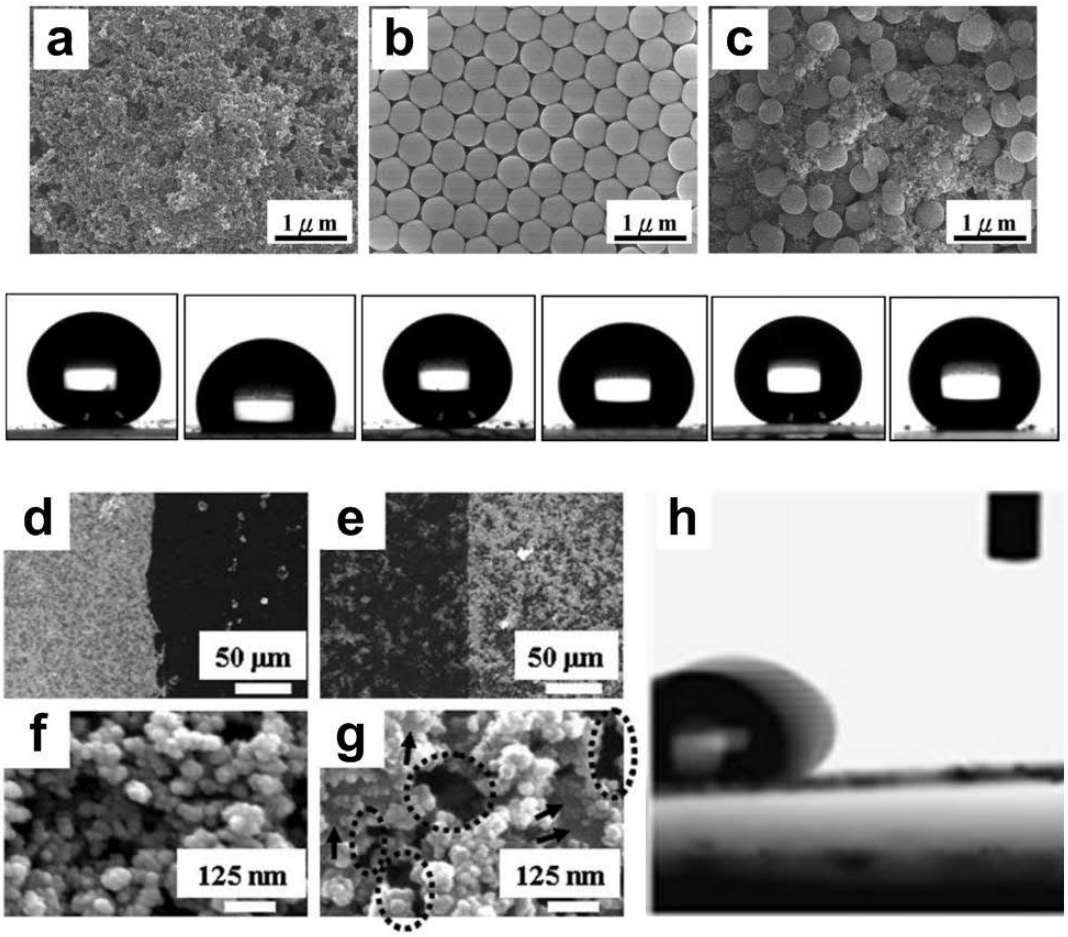

Figure 2.54. Spincoated superoleo(amphi)phobic micro- and nano- textures. a,b,c) SEM micrographs of different SiO_2 stacking layers. a) One-tier small scale roughness, b) one-tier large-scale roughness and c) two-tier hierarchical roughness, with corresponding wettability with (below, left) water and (below, right) sunflower oil.[470] Peel-off tests on d) as-spun PDMS-SiO_2 and e) after PFTS treatment. f-g) Before and after PFTS treatment under high magnification, the presence of polymer bridges and over-hanging structures are circled for reference, which are indicative of re-entrancy. h) Sliding behaviour of a diiodomethane droplet. 1H,1H,2H,2H-perfluorodecyltriethoxysilane, PFTS.[471]

Spincoating has also been used to develop superoleo(amphi)phobicity *via* templates from composite materials. He et al. demonstrated this concept through a SiO_2-PDMS broth, which was deposited on a substrate, cured and sintered before being etched and fluoro-functionalized with fluoroalkylsilanes (FAS). Nanoparticle agglomerates were formed with the presence of overhangs, demonstrating a superoleo(amphi)phobic performance limit against diiodomethane (γ = 50.8 mN/m) with CA, SA and CAH of 141°, 6° and 12° respectively.[471]

2.6.1.3. Layer-by-Layer (LbL)

The LbL technique is traditionally performed by using dipcoating. However, Brown et al. pioneered a series of studies into superoleo(amphi)phobic coatings that were derived from a facilely spray-coated LbL system. The LbL assembly of poly(diallyldimethylammonium chloride) (PDDA)-SiO_2 was followed by the CVD of fluoroalkylsilanes (FAS). This process created micro- and nano-roughened agglomerates, showcasing superoleo(amphi)phobicity with octane (γ = 21.5 mN/m), at CA, SA and CAH of 153-157°, 4° and 4° respectively.[472,473] This was also later integrated with the use of fluorosurfactants, which formed a similar morphological structure, showing superoleo(amphi)phobic properties with hexadecane (γ = 27.5 mN/m), at CA and SA of 157° and 4° respectively.[474]

2.6.1.4. Sol-Gel

Notwithstanding successful instances where sol-gel is combined with spray-coating (Section 2.6.1.6) for developing super(oleo)amphiphobic surfaces, sol-gel can sometimes be used as a stand-alone technique (Figure 2.55). Sheen et al. co-precipitated tetraethyl orthosilicate and 1H, 1H, 2H, 2H-perfluorodecyltriethoxysilane (TEOS-PFTS) under a sol-gel directed process which formed, within a single step, hierarchical nanoparticle agglomerates. They were superoleo(amphi)phobic against diiodomethane (γ = 50.4 mN/m) with a CA of 159°. Organic soya oils were however, capable of overcoming the Cassie-Baxter dewetting state.[475] Jin et al. created superoleo(amphi)phobic sol-gel based aerogel networks, which when fluoro-functionalized using fluoroalkylsilane (FAS) CVD, led

to superoleo(amphi)phobic properties against paraffin oil (γ = 33 mN/m) with CA, SA and CAH of 150°, 10° and 38° respectively.[476]

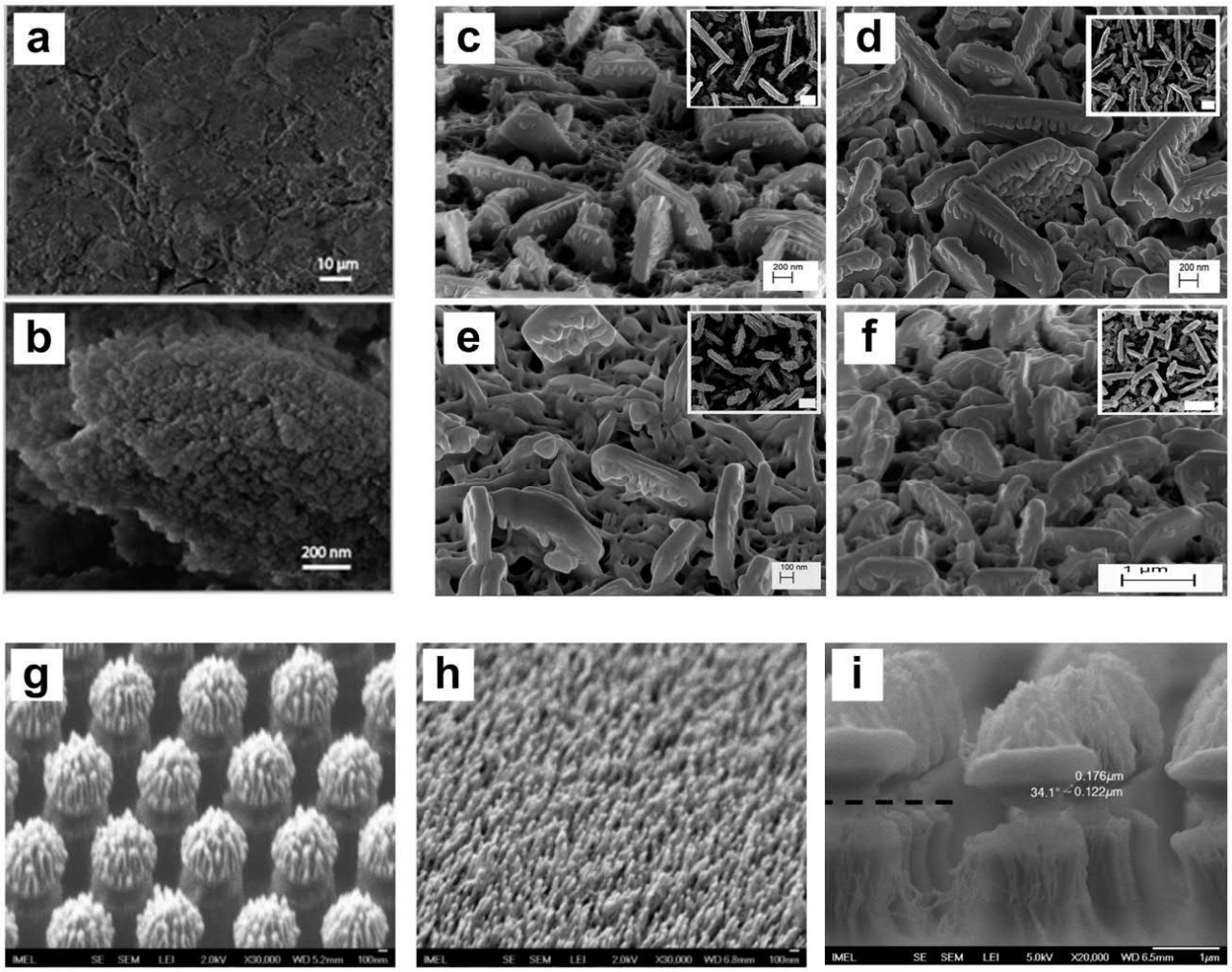

Figure 2.55. Sol-gel and self-assembly of superoleo(amphi)phobic multi-scale features. a-b) Sol-gel synthesized SiO_2 aerogel surface with repeated, self-similar fractal textures within a networked structure.[476] c-f) SEM micrographs of hierarchical textures that are formed by evaporating n-paraffin waxes of variable chain lengths on silicon: c) $C_{36}H_{74}$ + $C_{50}H_{102}$, d) $C_{36}H_{74}$ + $C_{44}H_{90}$, e) $C_{40}H_{82}$ + $C_{44}H_{90}$, and f) $C_{36}H_{74}$ + $C_{40}H_{82}$.[477] g) Micropillars with hierarchical, triple-scale roughness produced by the combination of colloidal lithography of 1 μm particles followed by plasma etching. Dual-scale nanoroughness on top of the pillars formed during plasma etching g) with and h) without colloidal particles. i) Undercut, reentrant topography of PMMA pillars with 3 μm PS colloidal microparticle lithography followed by a two-step etching process in oxygen plasma.[292]

2.6.1.5. Micro- and Nano-Structural Self-Assembly

Self-assembly is a method that is often integrated into other modes of synthesis (Figure 2.55). However, it can also be utilized by itself for enabling micro- and nano-structural texturing. Pechook et al. demonstrated the thermal evaporation-deposition of perfluorotetracosane, a fluorinated wax

material. Upon condensation, they formed hierarchically rough fractal-based platelet structures that were orientated inter-orthogonally. They were superoleo(amphi)phobic to hexadecane (γ = 27.47 mN/m) with CA and CAH of 152° and 8° respectively.[478] Zhu et al. used a sandblasting-assisted Ag deposition technique for self-assembling dendritic silver branches with micro- and nano- textures. Fluoro-functionalization of the surface with fluorinated-thiols resulted in superoleo(amphi)phobicity against hexadecane (γ = 27.47 mN/m), with CA and SA of 153° and 18° respectively.[479]

Colloidal lithography has been scarcely used for developing superoleo(amphi)phobicity. However, Ellinas et al. demonstrated the use of this technique on PMMA, followed by plasma texturing and perfluorocarbon deposition. Hierarchical micro pillars with distinctive re-entrant undercuts were formed. Despite the efforts, these surfaces were only superoleo(amphi)phobic to diiomethane (γ = 50.4 mN/m), with CA and CAH of 153° and 9° respectively. Unfortunately, organic oils and hexadecane were able to overcome its Cassie-Baxter dewetting states.[477]

Despite such advances, the bottom-up self-assembly of superoleo(amphi)phobic textures remained severely limited by the use of still-fairly unscalable and complex techniques. Improvements to these methods are needed for achieving greater tunability, scalability and future potential. The very first practical foray into creating scalable super(oleo)phobic coatings relied on the use of a candle's aerosol. Deng et al. synthesized candle soot deposits that are agglomerated but also surprisingly fractal, demonstrating superoleo(amphi)phobicity after steps involving facile chemical vapor templating and fluoro-functionalization (Figure 2.56).[14] Superoleo(amphi)phobicity was tested at a limit of tetradecane (γ = 26.5 mN/m), showcasing CA and SA of 154° and 5° respectively.[14] Further development of this concept led to the synthesis of superoleo(amphi)phobic coatings on stainless steel meshes. Superoleo(amphi)phobic meshes are capable of floating on liquids such as water, peanut oil or hexadecane, enabling biomimetic effects such as floating water lilies and water striders, albeit on oil.[480]

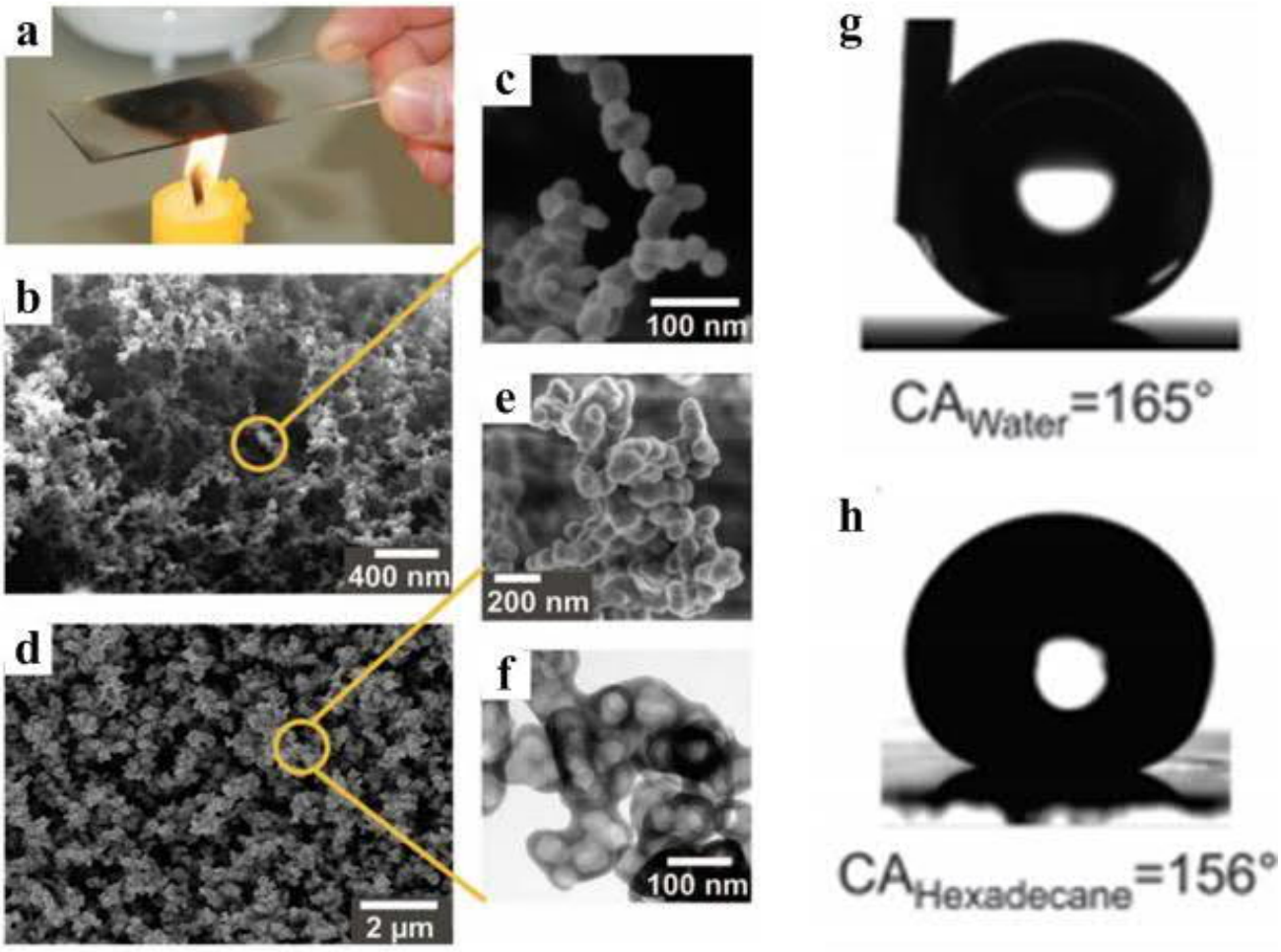

Figure 2.56. Candle soot superoleo(amphi)phobicity. Super(oleo)amphiphobicity from a) candle soot templating. b,c) Scanning electron micrographs of pristine soot deposits before and d,e) after CVD coating with a SiO_2 shell and calcination at 600 °C. f) Transmission electron micrograph revealing the thin templated SiO_2 shells. Highly fractal textures were noted, but no real re-entrant morphology can be clearly observed. The surfaces, were however, superoleo(amphi)phobic, with g) superhydrophobic and h) superoleophobic properties.[14]

2.6.1.6. Aerosolized Wet-Spray

Spray-deposition of superoleo(amphi)phobic coatings represents one of the strongest candidates for industrialization and commercialization. The standard process involves a two-stage design. Sol-gel or surface functionalization is first used for creating functional precursor solutions. The subsequent aerosolized deposition of as-synthesized precursors on substrates provides enough surface hierarchy

for achieving superoleo(amphi)phobicity (Figure 2.57). Owing to the versatile spray-deposition step, the use of a large range of substrate types and geometries are possible.

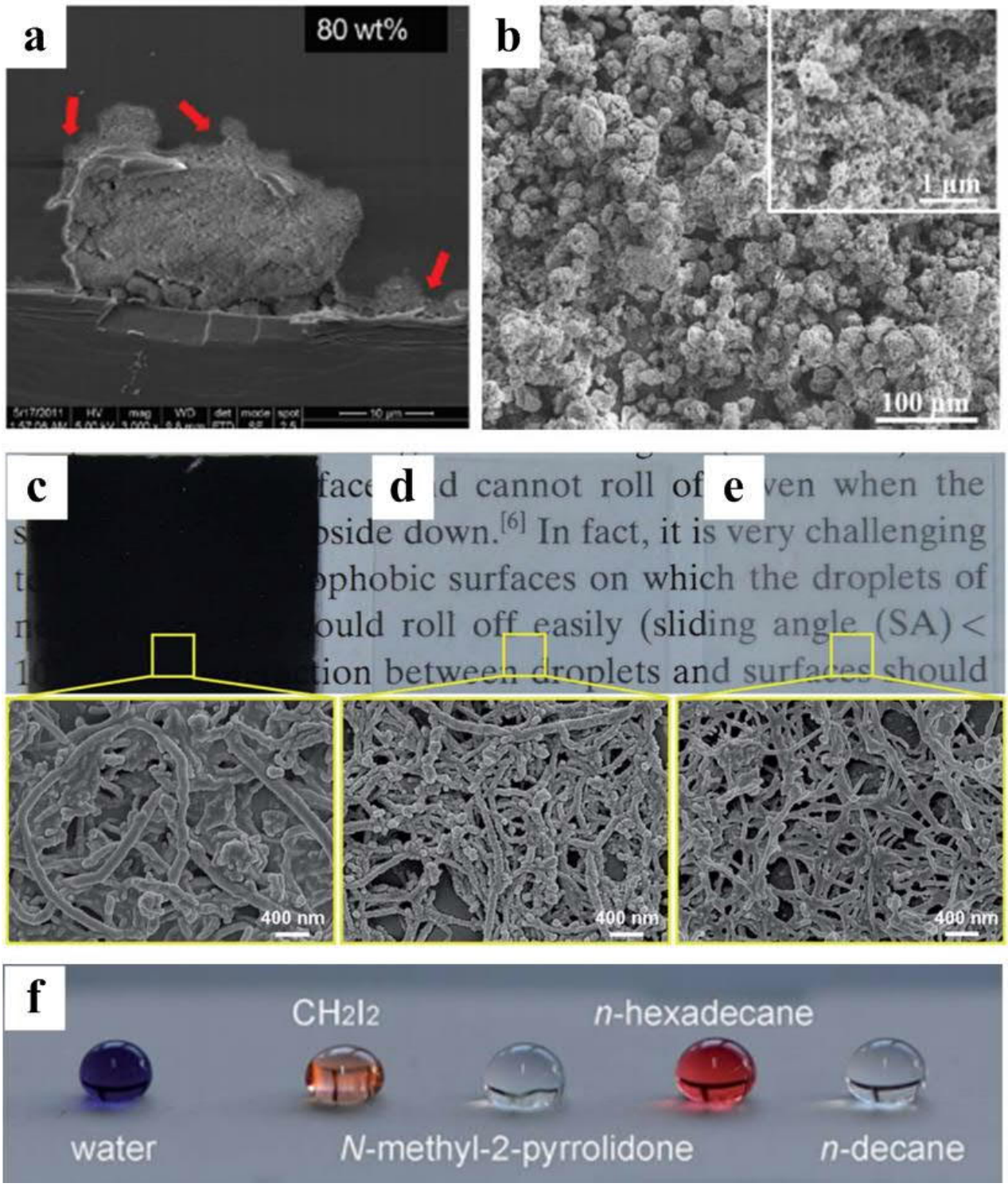

Figure 2.57. Stochastically spray-deposited superoleo(amphi)phobic micro- and nano- textures. a) Fluoro-functionalized SiO_2 / fluoropolymer coatings' side-profiles, with red arrows indicating "re-entrant" domains.[447] b) Wet-spray-deposited fluoro-functionalized SiO_2 with "re-entrant textures".[59] c) SEM micrographs of M-MWCNTs-PDMS, d) SNTs and e) SNTs-perfluorodecyltrichlorosilane (PFDTCS). f) Superoleo(amphi)phobicity demonstrated with water-to-decane.[464]

The spray-casting of composite materials that integrates unfunctionalized micro- and nano-particulate materials with fluoropolymers demonstrates much potential (Figure 2.58). Steele et al. presented a spray-on nanocomposite material using polymeric CF_2 clusters.[87] Unfunctionalized ZnO powders and perfluoroalkyl methacrylic copolymers were used in the precursor solution, resulting in a morphology that comprises of spherical micro- and nano- clusters. At its tested limit of operation, hexadecane (γ = 27.47 mN/m) revealed a CA and CAH of 154° and 6° respectively.[87] Hsieh et al. also demonstrated the use of unfunctionalized P25 TiO_2 with perfluoromethacrylates (PMC) for spray-on fractal-based hierarchically rough surfaces. However, they were only barely superoleo(amphi)phobic to ethylene glycol (γ = 47.7 mN/m) at a CA of 144°.[481]

This combination can be reversed, with the use of highly functionalized nanoparticles and non-fluorinated polymers. Srinivasan et al. presented a unique composite material that is composed of wet-sprayed PMMA and F-POSS, which formed corpuscular, bead-on-string and fibrous structures. Distinctive micro- and nano- hierarchical textures were observed in each. By increasing the weight percentage of F-POSS, they pushed functional super(oleo)amphiphobic performance to its limits. Decane (γ = 23.8 mN/m) exhibited a CA, CAH and SA of > 150°, 41° and 37° respectively. Heptane (γ = 20.14 mN/m) was able to fully wet the surface, resulting in the Wenzel state.[482] Alternatively, Yang et al. prepared slurries of poly(diallyldimethylammonium chloride) (PDDA)-SiO_2/sodium perfluorooctanoate, which when spray-deposited, formed hierarchical surface textures of micro- and nano- roughened agglomerates. Surfaces were superoleo(amphi)phobic against dodecane (γ = 25.4 mN/m) with CA and SA of 152° and 10° respectively.

The combination of fluorinated nanoparticles and polymers have also been conceptualized for fully perfluorinated composites. Campos et al. demonstrated the spray-coating of fluorinated SiO_2 nanoparticles within a fluoropolymer. This formed a composite coating which comprises of surface agglomerates resembling a series of cuboids, spheres, cliffs with overhangs etc. Fractal density of the fluorinated SiO_2 improved with its increasing mass fraction, as did superoleo(amphi)phobic performance. At its operational limit, a CAH of 7° was achieved for dodecane (γ = 25.4 mN/m). The

Cassie-Baxter state completely collapsed upon testing with decane (γ = 23.8 mN/m), with ACAs and RCAs of just 77° and 5° respectively.[447] Muthiah et al. spray-deposited a mix of hydrophobic SiO_2 and fluoro-acrylics, resulting in nanoparticulate agglomerates which were superoleo(amphi)phobic with hexadecane (γ = 27.47 mN/m) at CA, SA and CAH of 148°, 3° and 9° respectively.[483] Xiong et al. spray-coated hydrophobic SiO_2 integrated with thiol-functionalized perfluoroacrylates. The combination produced hierarchically textured composites with globular raspberry-like features. These superoleo(amphi)phobic surfaces were functional with hexadecane (γ = 27.47 mN/m), possessing CA, SA and CAH of 155°, 4° and 9.5° respectively. However, while it was able to "bead-up" a droplet of PDMS (γ = 19 mN/m), no CA, SA or CAH data were reported.[484]

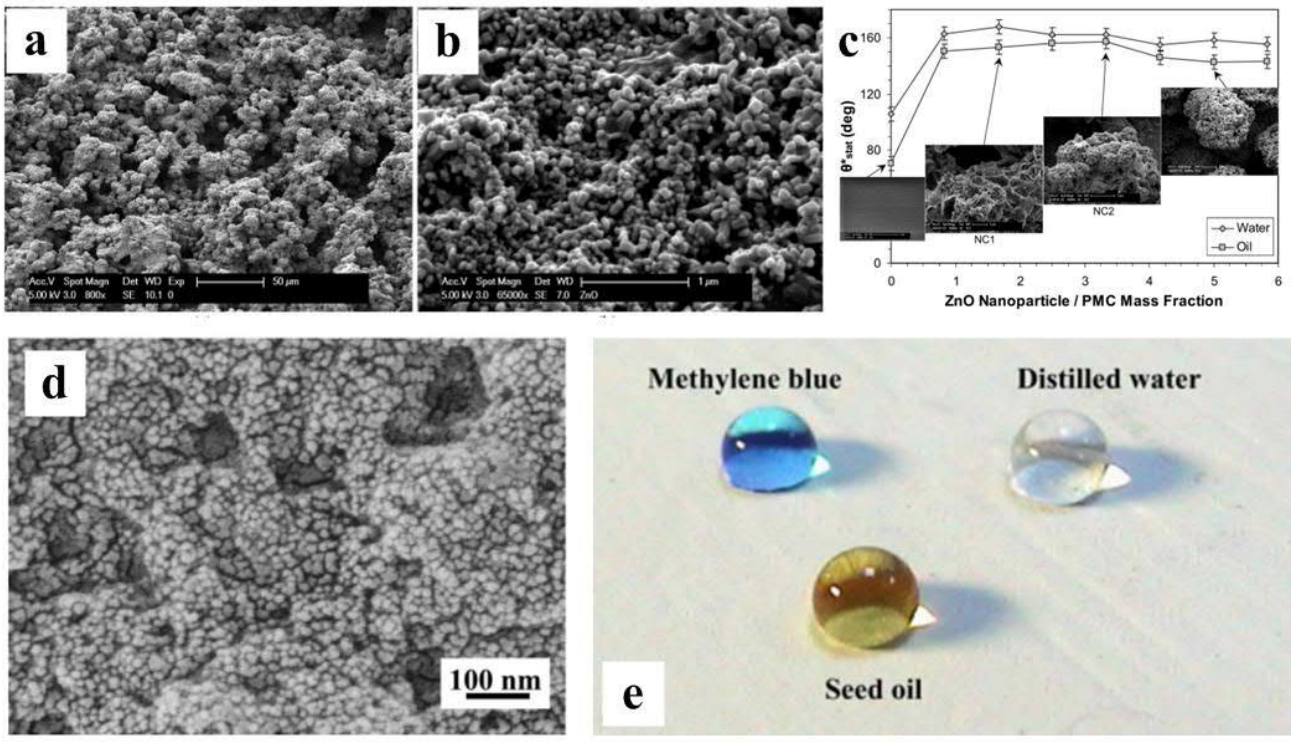

Figure 2.58. Spray-deposited superoleo(amphi)phobic nanocomposite morphologies. a) SEM micrographs of nanocomposite coatings showcasing a) microroughness and b) nano-rough self-similarity. c) Apparent static CA of water and oil as a function of ZnO to PMC mass fractions.[87] d) Spray-deposited TiO_2-PMC surfaces with fractal-based roughness. e) Superoleo(amphi)phobicity of coatings to water and oil.[481]

Composite superoleo(amphi)phobic materials could also be presented in the form of multi-layer films. Vahabi et al. described the spray-coating of fluorinated SiO_2 nanoparticles on a polyurethane layer. Subsequent immersion in water and detachment resulted in a free-standing superoleo(amphi)phobic

film. Silanization time and surface coverage were extensively investigated and were found to be key parameters for enabling the most desirable superoleo(amphi)phobic state. Optimally developed surface morphologies comprised of aggregated fluoro-functionalized SiO_2 particles that are hierarchically (micro- and nano-) roughened. These multi-layer films operated at a tested limit of dodecane (γ = 25.4 mN/m) with CAH and SA of 9° and 8°. They were also stable to light touch, but not extensive abrasion.[59]

Wet-spray deposition can also be performed *via* a one-step process with highly reactive precursor broths. Yang et al. used a copper-based perfluoro-dispersion that was concocted from copper acetate and active perfluorinated acids. Spray-deposition of this actively functionalizing broth onto various surfaces enabled rapidly realized states of superoleo(amphi)phobicity.[161] Optimally developed surfaces were composed of fractal hierarchical agglomerates, showcasing a functional limit of superoleo(amphi)phobicity with dodecane (γ = 25.3 mN/m), at CA and SA of 150° and 20° respectively.

2.6.1.7. Liquid Flame Spray Pyrolysis

The use of flame spray pyrolysis expands on the flame soot technique (Section 2.6.1.5) while incorporating various advantages (scalability, tunability, etc.) that are comparable to / surpasses standard wet-aerosol spray methods (Section 2.6.1.6). Flame spray pyrolysis is a method that generates a cloud of nanoparticle aerosol that experiences highly controllable self-assembly on target substrates, thus giving rise to tunable agglomerate profiles (Figure 2.59).[30,77,78,80]

Tuominen et al. demonstrated the use of this method for developing TiO_2 nanotextures, followed by the plasma deposition of perfluorohexane. These fractal structures were coated on Birch wood samples. The most optimally developed samples achieved functional CA and SA of 158° and < 10° respectively, against olive oil (γ = 32 mN/m). However, samples failed when exposed to hexadecane, with a demonstrated CA of 130°-135°, indicative of fluid pinning and the Wenzel state.[485]

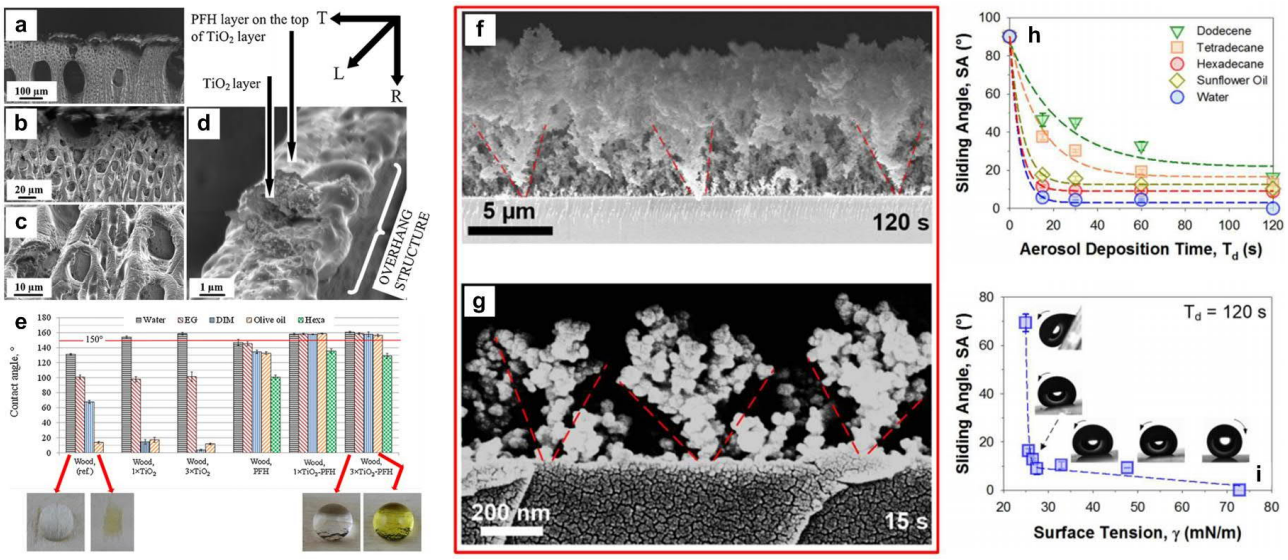

Figure 2.59. Liquid flame spray pyrolysis (LFSP) derived hierarchical agglomerates with re-entrant morphologies. a-c) Cross section of the coated wood samples at successive magnifications of 3× TiO_2-PFH coated wood, d) the overhang structure is seen to extend over the edges. e) Static CAs of water, ethylene glycol, diiodomethane, olive oil and hexadecane on (1× and 3×) TiO_2-PFH coated wood.[485] f-g) Cross-sectional SEM analyses of the inherent re-entrant nanotextures with a LFSP-SiO_2 deposition time of (f) 120 s and (g) 15 s. h) SA of water (72.8 mN/m), sunflower oil (32.9 mN/m), hexadecane (27.47 mN/m), tetradecane (26.56 mN/m), and dodecene (25.6 mN/ m) as a function of the aerosol deposition time. (i) SAs on the 120 s aerosol deposited nanotextures as a function of the liquid surface tension.[92]

Wong et al. optimized the use of flame spray pyrolysis under the diffusion regime for ultra-transparent, flexible and superoleo(amphi)phobic coatings. The omnidirectional deposition method did not discriminate against substrate type or geometry, with coatings that were successfully developed on glass, metals and plastics.[92,94] The self-assembly dynamics enabled by flame spray pyrolysis within the diffusion regime were also further investigated. Distinctive re-entrant profiles were, for the first time, experimentally and analytically determined, proving the tunable viability of scalably self-assembled superoleo(amphi)phobicity. The surface fractal agglomerates resembled crowns of broccoli plants, demonstrating increasingly re-entrant profiles alongside growth. The most optimal samples possess operational limits between dodecene (γ = 25.6 mN/m) and cyclohexane (γ = 24.95 mN/m), having CAs and SAs of 160° and 150°, 16° and 65° respectively. A sharp transitional wetting regime from the Cassie-Baxter to Wenzel state took place between these fluids, resulting in spontaneous surface penetration and pinning.[92]

Notably, the performance of this series of superoleo(amphi)phobic surfaces[92,94] surpasses that presented by Tuominen et al.,[485] which was only operational down to a liquid surface tension of 32 mN/m. The evidence of such deviations in performance within a single technique suggests potential tunability and improvements under further optimization of deposition parameters.

2.6.1.8. Electrospinning

Owing to the naturally occurring fibrous nature of electrospun materials, it plays a significant role in pioneering the scalable development of re-entrant profiles and thus superoleo(amphi)phobicity. In 2007, Tuteja et al. proposed and demonstrated the use of scalable electrospun materials for achieving superoleo(amphi)phobicity.[11,156] In the first instance, electrospun F-POSS-PMMA blends demonstrated increasing oleophobicity with increasing composite mass density of F-POSS.[11] However, the ACA and resulting CAH measured for hexadecane (γ = 27.47 mN/m) and decane (γ = 23.83 mN/m) were only ca. 150° and 30°, 142° and 40° respectively.[11]

Surface morphologies were later expanded to include beads, bead-on-string and fiber-based profiles. These demonstrated hexadecane CAHs of 6°, 12° and 19° respectively, optimized with the beaded structures. SA was also just 5° for the beaded profiles. However, these optimized beaded structures lose the composite state of wetting with fluids of surface tensions below 21 mN/m, and were unable to transcend into domains of superomniphobicity. In contrast, the fibrous configurations preserved a composite interface (albeit with an ACA of just 140°) down to heptane (γ = 20.14 mN/m), with a SA of 5° and a CAH of 30°.

This unexpected behavior was attributed to the feature spacing ratio vs. robustness parameter, which is defined by the complex combination of re-entrant angles, associated profile heights and fluid sagging depths. The electrospinning process couples these parameters closely, for instance, *e.g.* a smaller spacing leads to higher CAs but less dewetting robustness / stability.[156]

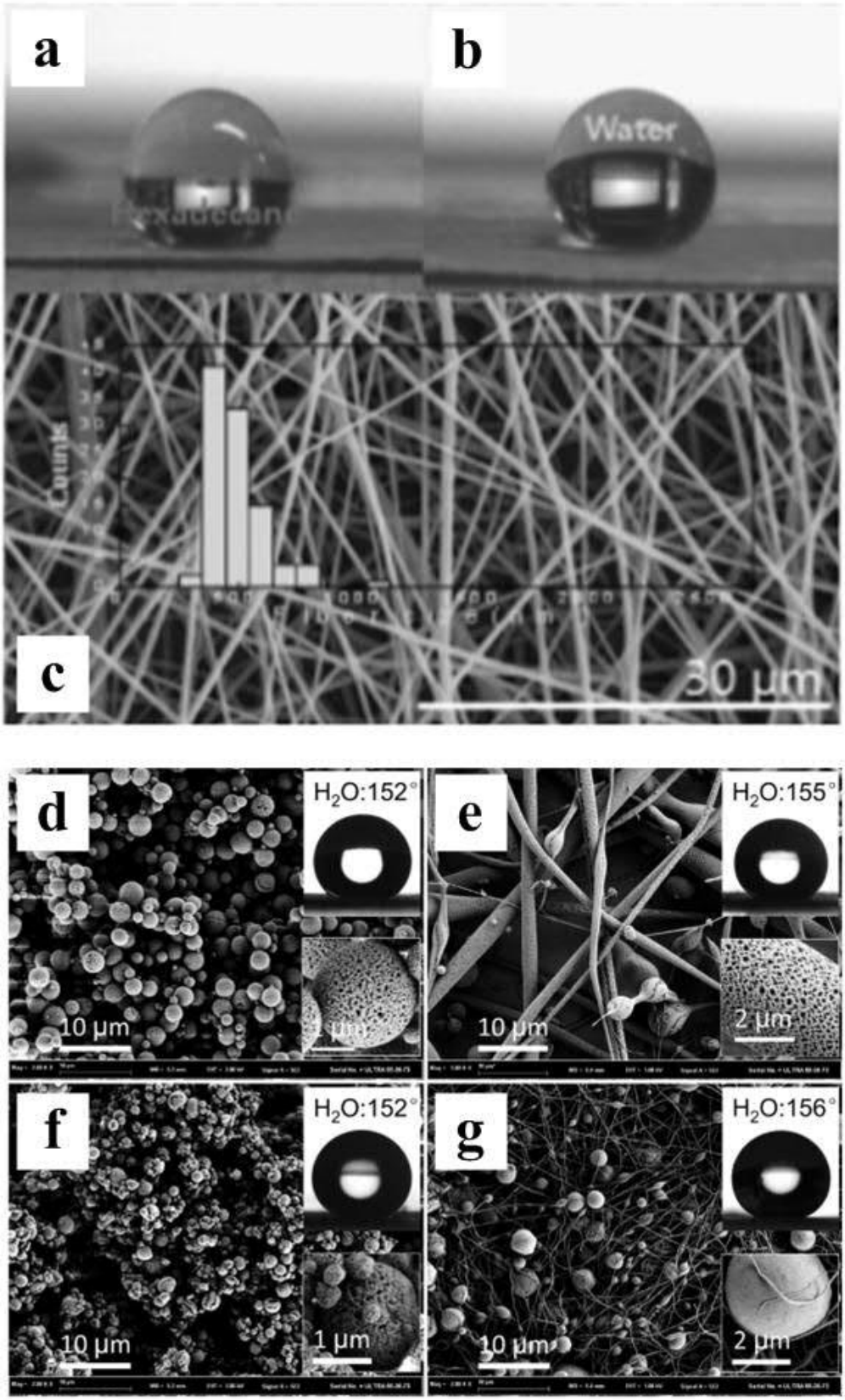

Figure 2.60. Electrospun superoleo(amphi)phobic polymers. Electrospun superoleo(amphi)phobic ptFEMA fibers with a) hexadecane and b) water. c) ptFEMA fiber diameters averaged at ca. 50 nm.[486] d) SEM micrographs of electrospun films of PS-b-PMTFPS-b-PS triblock copolymers at working distances of d) 10 cm, e-g) 15 cm. Superhydrophobicity demonstrated in insets. Superoleophobicity on optimal samples towards hexadecane (γ = 27.47 mN/m) only demonstrated a CA of 134° but was coupled to a SA of 9°.[487]

Departing from the use of specialized F-POSS nanomaterials, Ganesh et al. showcased the use of electrospun TiO_2 that was followed by fluoro-functionalization with fluoroalkylsilanes (FAS) for achieving superoleo(amphi)phobicity. The resulting nano-rice shaped TiO_2 structures had hexadecane (γ = 27.47 mN/m) and dodecane (γ = 25.3 mN/m) CA, SA and CAH of 139°, 15°, 12° and 128°, 15°, 14° respectively.[488] This discrepancy between the CA and effective SA/CAH is unknown.

Expanding beyond the work of F-POSS, inorganic and composite materials, Choi et al. demonstrated the fabrication of a pure polymer based fiber web (Figure 2.60). This comprised of a highly fluorinated poly(2,2,2-trifluoroethyl methacrylate) (ptFEMA) fiber mesh that was developed by optimized electrospinning. Optimized nanofiber diameters were found to be at 500 nm, which were capable of preserving very high CAs with hexadecane (γ = 27.47 mN/m), measured at 154°. However, neither SAs nor CAH properties were appropriately addressed.[486] Yi et al. also demonstrated the use of poly[methyl(3,3,3- trifluoropropyl)siloxane]-polystyrene (PMTFPS)-PS triblock polymers with electrospinning to form electrospun hierarchically textured bead-on-string features (Figure 2.60). The limits of performance ranged up to superoleo(amphi)phobicity with hexadecane (γ = 27.47 mN/m) CA and SA of 134° and 9° respectively.[487] The co-axial electrospinning of Teflon coated bead-on-string micro- and nano- textured fibers was also attempted by Han et al., but this configuration only achieved a dodecane (γ = 25.3 mN/m) CA of 130°.[489]

2.6.1.9. Electrodeposition and Electrochemical Etching

Metals represent one of the most important categories of engineering materials today. The facile and successful development of superoleo(amphi)phobic metals could present immense engineering potential. The corrosion and biofouling of metals caused by oil-water contamination in heavy industries such as the oil and gas or aviation sectors could potentially be permanently rectified by using multi-functional superoleo(amphi)phobic coatings. We acknowledge the operational

differences between electrodeposition (cathode) and electrochemical etching (anode), but both methods will be highlighted in this section.

Electrochemical Etching

The first reports on super(oleo)amphiphobic metal surfaces date back to work on aluminum.[55] Tsujii et al. described the perfluorododecyl phosphate functionalization of anodically oxidized aluminum (Figure 2.61). Anodically oxidized aluminum has a rough, agglomerated surface texture that is coupled to fractal geometry. When functionalized with fluoro-phosphates, the hierarchical interface exhibits superoleo(amphi)phobicity. However, while rapeseed oil (γ = 35 mN/m) appears to have a superoleo(amphi)phobic CA of > 150° while possessing a low SA, decane (γ = 23.83 mN/m) only formed a CA of ca. 120°.[55] Fukii et al. expanded on this concept by combining oblique angle magnetron sputtering deposition of Al-Nb alloys with anodic-oxidation. Surfaces were significantly more regular, and demonstrated great potential for the scalable development of micro-pillar arrays. More interestingly, the micropillars were sub-patterned by nanopillars which extend orthogonally from its primary features. Superoleo(amphi)phobicity was achieved simply by fluoro-phosphate functionalization. At the limits of performance, superoleo(amphi)phobicity was demonstrated with a hexadecane (γ = 27.47 mN/m) CA and CAH of 151° and 6° respectively.[490]

This technique has since expanded to other material types. Wu et al. demonstrated a facile means towards the rapid synthesis of Al_2O_3 nanowires (NWs) *via* high field anodization. This made use of an enhanced electrochemical etching technique with aluminum foil, comprising of high electrical fields and Na_2SO_4 activation. A fractal 3-D morphology with multi-faceted terrace-like nanowire (NW) forests was derived. Upon fluorosilanization, superoleo(amphi)phobicity was achieved, demonstrating a tested limit with silicone oil (γ = 22 mN/m) CA and SA of 150° and 12° respectively.[491]

Electrochemical etching was also demonstrated with titanium, where Wang et al. showcased a three-step surface texturing-functionalization process. This involved electrochemical etching in a NaCl

solution to create micro-structures, followed by surface anodization with NH_4F, HF and ethylene glycol for nano-texturing. This resulted in the scalable formation of TiO_2 nanotubes. Thereafter, surface modification was performed with fluoroalkylsilanes (FAS), thus giving rise to superoleo(amphi)phobicity. At its operational limit, it demonstrated a hexadecane (γ = 27.47 mN/m) CA and SA of 155° and 7° respectively.[492]

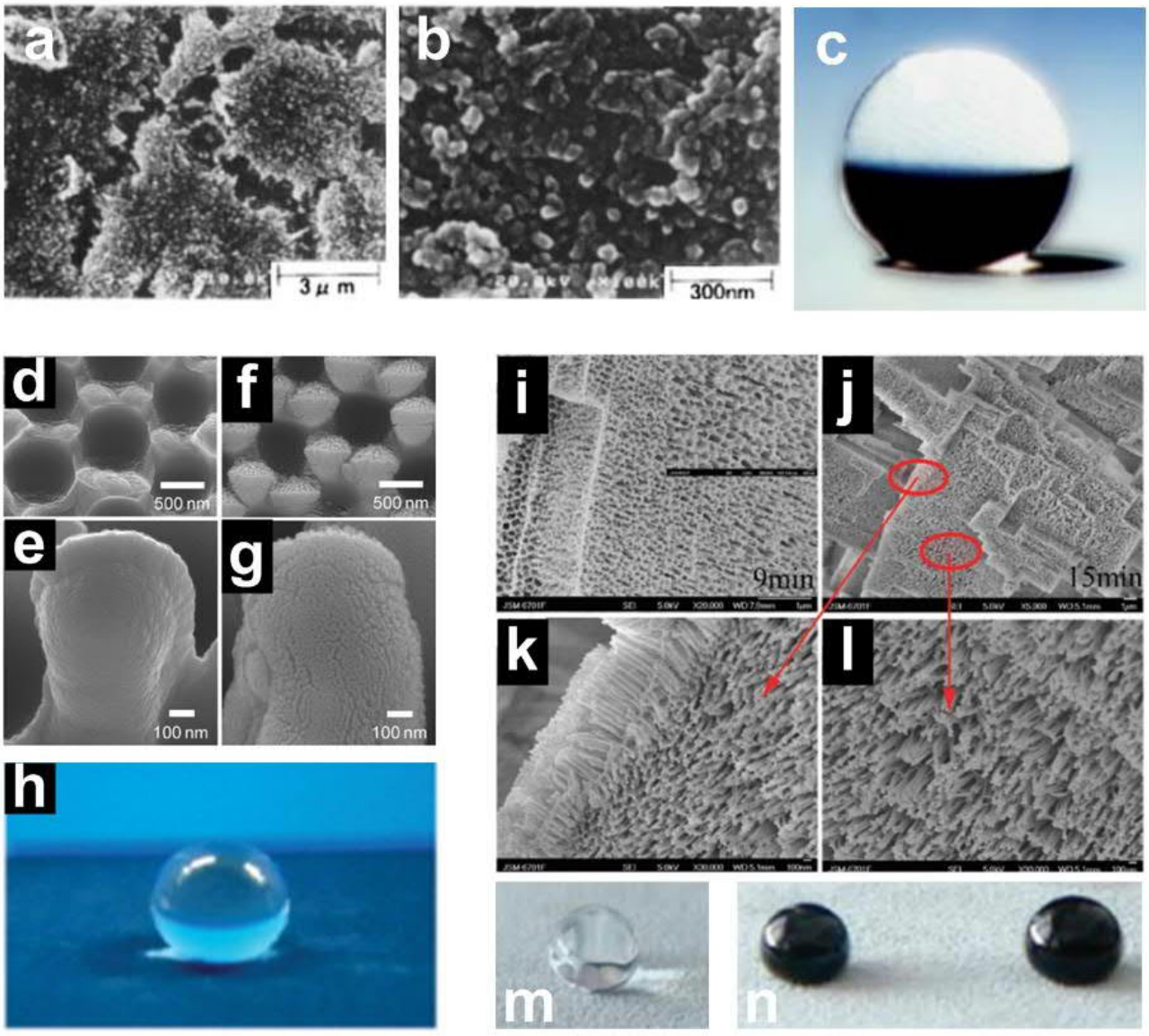

Figure 2.61. Anodic oxidation and etching-enhanced superoleo(amphi)phobicity. SEM micrographs of anodically oxidized aluminium plate with fractal morphologies at a) low-magnfication and b) high-magnification with c) superoleo(amphi)phobicity with rapeseed oil.[55] SEM micrographs of oblique angle magnetron sputtered Al-Nb specimens d) before and f) after anodic oxidation for nanoroughness on micropillars, at e-g) higher magnifications respectively. h) Superoleo(amphi)phobic properties of coatings developed.[490] i-l) High field oxidation for the formation of multi-faceted NW forests, with demonstrated superoleo(amphi)phobic properties to m) silicone oil and n) crude oil.[491]

The use of electrochemical etching on semiconductors was demonstrated by Gao et al. with the pore-texturing of silicon films by using gold-nanoclusters assisted procedures. These porous silicon films possessed deep and slanted pores, aided by the preferential etching of the Si ⟨100⟩ face. Upon fluorosilanization, films were superoleo(amphi)phobic, showing hexadecane (γ = 27.47 mN/m) CAs of ca. 151°.[493]

Electrodeposition

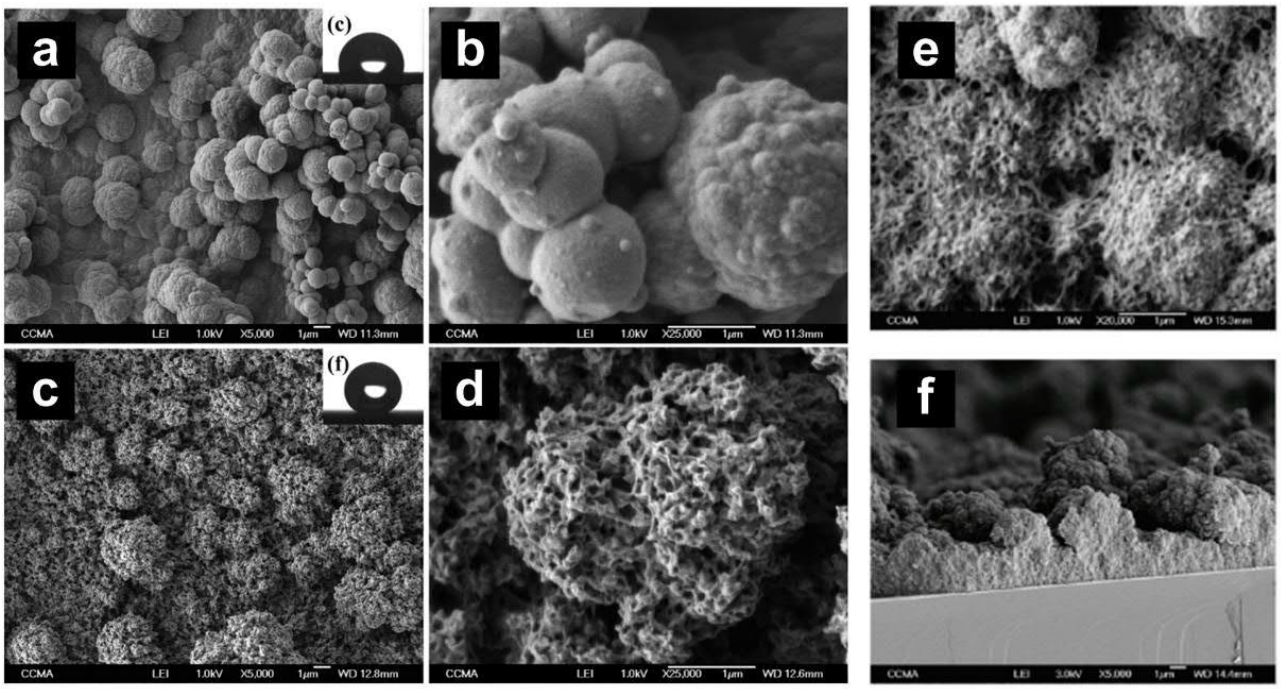

Figure 2.62. Electrodeposition formation of superoleo(amphi)phobic micro- and nano- textures. SEM micrographs of electrodeposited a-b) fluorinated PProDOP surfaces with spherical and cauliflower-like surfaces. c-d) Electrodeposition of fluorinated PEDOP, in contrast, possesses very porous features down to the nano-meter length-scale.[448] e-f) Electrodeposited fluorinated derivatives of EDOP monomers (polyEDOPC_3F_8), with enhanced nanoroughness.[494]

Electrodeposition is a process that is not limited to metallic materials, but can also be used towards the development of conductive polymer films. Darmanin et al. electrodeposited conductive films of 3,4-ethylenedioxypyrrole (EDOP) and 3,4-propylenedioxypyrrole (ProDOP) monomers (Figure 2.62). This was later expanded to include fluorinated monomers which, under optimization, showed diiodomethane and hexadecane (γ = 27.47 mN/m) CAs of 152° and 145° respectively. No explicit SAs were reported, but very low hysteresis and SAs for fluorinated PEDOP films were noted. This

can be attributed to the enhanced nanoporosity and roughness present on the porous sphere-like agglomerates that make up the PEDOP films.[448] Bellanger et al. later expanded on this work, and presented the electrodeposition of fluorinated derivatives of EDOP monomers. The micro- and nano-roughened polymeric granular networks demonstrated superoleo(amphi)phobicity, with hexadecane (γ = 27.47 mN/m) CA, SA and CAH of 152°, 11° and 2° respectively.[494]

2.6.1.10. Perfluoro-acid Etching / Chemical Etching and Metallic Perfluoronates

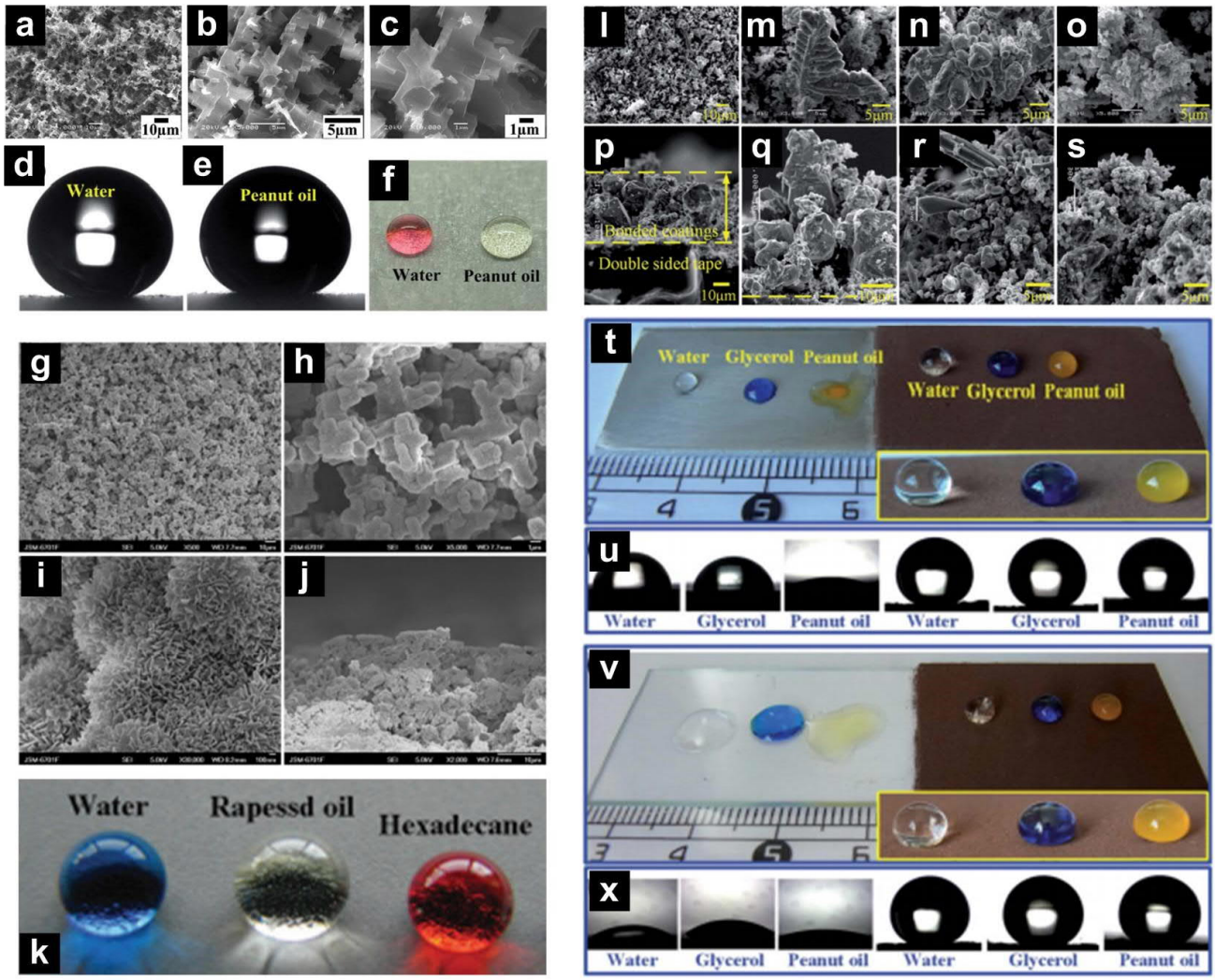

Figure 2.63. Electrochemical etching and PFOA modification of superoleo(amphi)phobic coatings. a-c) SEM of electrochemically etched Al surfaces with d-f) superoleo(amphi)phobicity to water and peanut oil.[153] g-j) Multi-scale texturing of aluminium plates by HCl etching and boiling water nanotexturing. j) Side-profile of nanotextured interfaces and k) superoleo(amphi)phobic properties of the treated Al.[446] l-s) SEM micrographs of superoleo(amphi)phobic coatings with multi-scale structures with superoleo(amphi)phobic properties on t-u) host substrate and v-x) glass slide.[495]

The use of electrochemical etching can sometimes be further integrated with perfluorinated acid functionalization, where already-fractal textures are *in-situ* functionalized for super(oleo)amphiphobicity (Figure 2.63). This is a surface functionalization step that can be used to supplement electrochemical etching, and is highly effective on metallic substrates. Song et al. used electrochemical etching for the texturing of aluminum substrates, followed by perfluorinated acid functionalization for developing superoleo(amphi)phobicity. Optimally developed samples possess micro- and nano- cuboidal corrugations, and were tested with peanut oil (γ = 35 mN/m), which revealed CA and SA of 160° and 8° respectively.[153]

The electrochemical etching step can also be substituted with chemical-based etching. Yang et al. demonstrated a simple two-step etch-functionalization procedure *via* sequential HCl and perfluorooctanoic acid (PFOA) etching. Microstructural agglomerates covered by nano-flakes were developed, thus achieving surface hierarchy. Performance of the surface was exemplary, demonstrating hexadecane (γ = 27.47 mN/m) CA, CAH and SA of 155.6°, 8° and 7.2° respectively. However, it became much more adhesive with decane (γ = 23.8 mN/m), with CA, CAH and SA of 151.5°, 45.1° and 40.1° respectively.[446]

Besides its use as a supplementary functionalization step for (electro)chemically etched materials, perfluorinated acids have also demonstrated the achievement of surface texturing and functionalization within a single step, thus bypassing constraints of these pre-steps. Chen et al. immersed electrodeposition-formed copper powder in perfluorooctanoic acid (PFOA) for simultaneous etch-functionalization. A superoleo(amphi)phobic powder was thereafter derived. Structures obtained were highly fractal and diversified, resembling corals with micro- and nano-agglomerates, integrated with pillar-like protrusions, pits and pores. At its tested operational limit, it demonstrated superoleo(amphi)phobicity towards benzyl alcohol (γ = 38 mN/m), with CA and SA of 151° and 11° respectively. Superoleo(amphi)phobic powders can thereafter be facilely applied by standard wet-spray-deposition on a variety of substrates.[495]

The complete integration of surface texturing and functionalization within a single step bears immense promise for a variety of metal-based substrates. Meng et al. used electrochemical reactions in perfluorocarboxylic acid ($CF_3(CF_2)_8COOH$) solutions for the one-step texturing-functionalization of various substrate materials, ranging from zinc, aluminum, nickel, iron and zinc-iron alloys. Zinc, for instance, oxidizes readily into Zn^{2+} ions which then react with perfluorocarboxylic acids to form zinc perfluorocarboxylates. Over extended periods, the etching process is capable of creating functional hierarchical profiles that are comprised of micro- and nano- petal-like sheets.[496] However, superoleo(amphi)phobic performance was only demonstrated against rapeseed oil (γ = 35 mN/m) with CA and SA of 155.6° and 10° respectively. Interestingly, from an alternate perspective, they also found tunable variations in surface wettability when using perfluorocarboxylic acids that have different chain lengths.[496]

The excess infusion of active perfluorinated acids into porous materials demonstrates the novelty of achieving self-healing superoleo(amphi)phobic metals. Wang et al. synthesized superoleo(amphi)phobic porous Al_2O_3 substrates with impregnated perfluorooctanoic acid (PFOA). The impregnated Al_2O_3 was nanoporous and fractal in nature, with cuboidal projections over multiple length and height scales. Superoleo(amphi)phobicity was achieved with the demonstrated limit of hexadecane (γ = 27.47 mN/m), having a CA of ca. 150°. These impregnated surfaces were capable of recovering from plasma damage between self-healing cycles. A healing time of ca. 6 hours at 70 °C is typically incurred, which can be attributed to the reflow of the active perfluorinated agents.[497]

2.6.1.11. Physical Etching

Physical etching can be performed by using plasma exposure or chemical etching (Figure 2.64). Instances of chemical etching described in this section do not utilize any perfluorinated acids for texturing / functionalization. These stochastic patterning techniques are rarely capable of one-step etch-functionalization, and typically require subsequent surface functionalization. Ellinas et al. demonstrated the use of plasma etching on PMMA, which resulted in the formation of nanofilaments.

When these nanofilaments were coalesced and fluoro-functionalized, they form nanotextured micro-hills that were superoleo(amphi)phobic, showcased with soya oil (γ = 34 mN/m) CA, SA and CAH of 157°, 8° and 4° respectively. When tested with hexadecane (γ = 27.47 mN/m), resulting CA and CAH of 142° and 10° were achieved.[498] Plasma-etching of PMMA was also demonstrated by Gnanappa et al., which resulted in capillary-collapsed nanofibers that formed tree-trunk like structures with nanoroughness. Following the plasma deposition of perfluorocarbons, states of superoleo(amphi)phobicity were achieved with diiodomethane (γ = 50.4 mN/m) at CA and CAH of 155° and < 5° respectively. However, when tested with soya oil (γ = 32 mN/m), a CA of only 138° was achieved.[499]

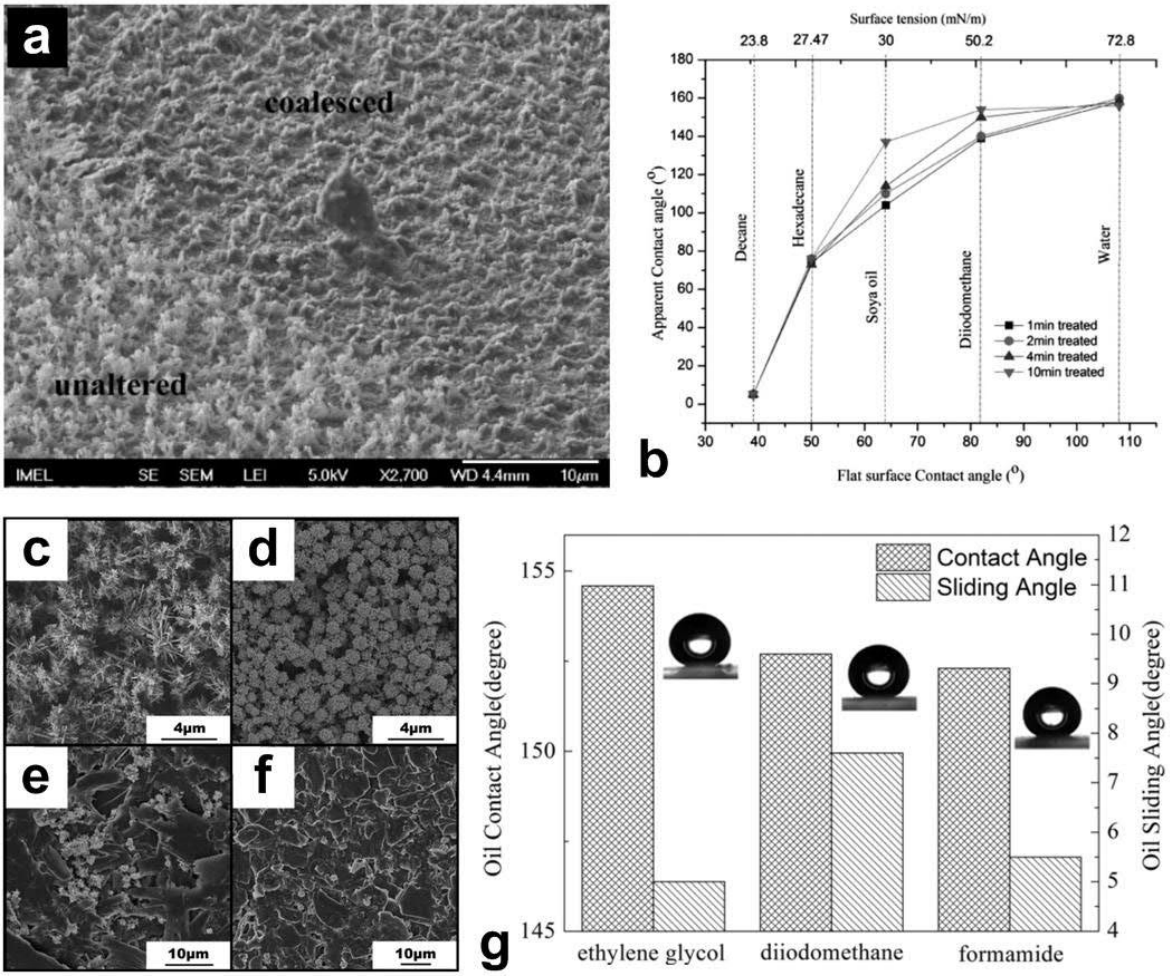

Figure 2.64. Plasma and chemically etched morphologies for superoleo(amphi)phobicity. a) Topography of a 10 min oxygen plasma etched PMMA surface in the region with a water-droplet coalesced nanotexture. Superoleo(amphi)phobic properties after depositing fluorocarbon polymer films with b) CA > 150° with diiodomethane.[499] c-f) Pompon-shaped $FeSe_2$ particles synthesized with $FeSO_4.7H_2O$ with d) different HF concentrations (c to f increasing). g) Water and oil wettability with sample d), pompon-shaped $FeSe_2$ particles.[500]

Chemical acid / base etching of metallic substrates are also reported to be capable of varying degrees of surface texturing. Lee et al. synthesized copper nanowires (NWs) from the NaOH-$(NH_4)_2S_2O_8$ etching of copper substrates. After the deposition of fluorinated wax *via* thermal evaporation, hierarchically roughened wax-coated nanowires (NWs) demonstrated superoleo(amphi)phobicity with hexadecane (γ = 27.47 mN/m) CA and CAH of > 150° and < 10°.[501] Ou et al. etched copper substrates with nitric acid and sodium hydroxide in the presence of surfactants to produce micro- and nano- pits having leaf-like flakes that were coated in micro-flower-like balls. Fluoro-functionalization with thiols resulted in superoleo(amphi)phobicity with hexadecane (γ = 27.47 mN/m) CA and SA of 158° and 20°.[502] Yao et al. hydrolyzed copper in ammonia, followed by thiol fluoro-functionalization, thus giving rise to micro-clusters of dandelion-like nanoneedles. Superoleo(amphi)phobicity was achieved with hexadecane (γ = 27.47 mN/m) CA and CAH of 162° and 10°.[503]

Yuan et al. etched iron substrates with acetic acid and hydrogen peroxide, which were then fluoro-functionalized with perfluorocarboxylic acid. The perfluorocarboxylic acid used here did not result in surface texturing, and was only responsible for the modification of surface chemistry. The resulting micro-clustered nanorods (in spherical dandelion-like clusters) demonstrated superoleo(amphi)phobicity with rapeseed oil (γ = 36 mN/m), having CA and SA of 151° and 16°.[504] Yu et al. demonstrated the etching of iron diselenium, a semi-conductor, with HF, revealing the formation of pompon-, chips-like morphologies. Upon fluoro-functionalization with fluoroalkylsilanes (FAS), superoleo(amphi)phobicity was achieved, with ethylene glycol (γ = 47.7 mN/m) CA and SA of 155° and 5° respectively.[500]

2.6.2. Drawbacks

Today, scalable techniques that do not require direct line-of-sight tend to be based on metal substrates and perfluorinated acids,[161,446] or inherent fabric and mesh-like morphologies.[61,156,459,461] Their applications are thus inherently limited by substrate type. From an optical perspective, close to none of these prior works have seriously considered transmittance / transparency properties.

In addition, almost all geometries that were developed by stochastically-assembled surfaces are impossible to quantify when compared to templated or lithography-based models.[11,13,66,74,151] As a result, they are harder to substantiate or support without elaborate mathematical models.[78,92] The lack of visual profile confirmation limits our understanding behind scalably derived re-entrancy for superoleo(amphi)phobicity. This could hinder optimizations and improvements to morphological geometries and thus performance, unlike the use of lithographical designs.

2.6.3. Concept

In this work, we first review the state-of-the-art processes for superoleo(amphi)phobicity. Inspired by methods that could enable scalable stochastic synthesis of superoleo(amphi)phobic coatings, we employed the use of an unexplored aerosol-based technique (liquid flame spray pyrolysis). The scalability of this technique is well-known and extensively investigated within other fields, showcasing enhanced scaling control and tunability. For our purposes, we attempted to predict and control degrees of re-entrant texturing by investigating the system under computational aerosol dynamics. This process was later exploited for its versatility and wide-applicability towards texturing complex surface morphologies.

a) Firstly, we aim to design scalable superoleo(amphi)phobic coatings under substrate- and geometry- independence. This is coupled to the proposed development of an aerosol-based geometrically-tunable system.
b) Secondly, we probed the limits of this technique and utilized it to coat the insides and outsides of commercially available needle tips. This was performed down to an internal diameter of just 260 µm. Through this, we fabricated superoleo(amphi)phobic microtools that wield immense potential for nano-droplet production, dry-fluid-probe and contactless droplet manipulation systems.

2.7. Superomniphobicity

The previous sections on superoleo(amphi)phobicity demonstrates super-phobic operation with low surface tension liquids down to 20-21 mN/m.[156] However, scalable techniques that are capable of achieving superomniphobicity to or below 20 mN/m remain highly scarce. Many of the listed examples of superomniphobicity in the literature are actually just superoleo(amphi)phobic, with a distinctively limited dewetting performance of γ_{min} = 25 mN/m.[57,59,472,483] Moreover, much of the work into scalable variants of superomniphobicity (γ_{min} = 15-18 mN/m) still pales in comparison to those that were achieved by photolithography (γ_{min} < 10 mN/m). As of the time of writing, top-down methods such as templating or lithography are still commonly used for facilitating successful superomniphobic surface texturing (Figure 2.65).[167,505]

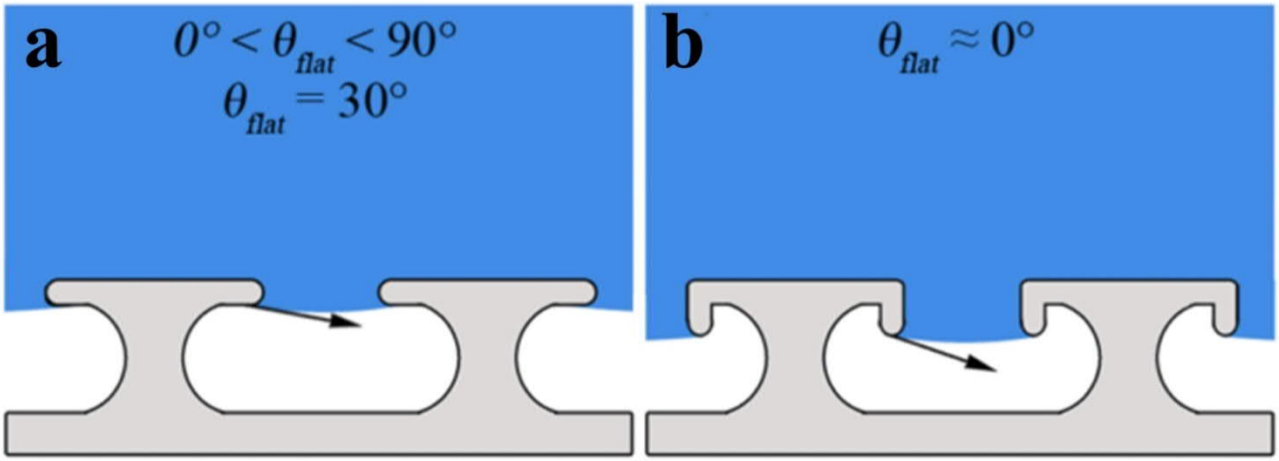

Figure 2.65. Superoleo(amphi)phobicity to superomniphobicity. a) Superoleo(amphi)phobic microhoodoos, which function with fluids that possess a characteristic CA or a Young's CA (θ_{flat}) down to just 30°. b) If re-entrant properties are further enhanced using a mushroom-like configuration, double re-entrancy is induced. Contact line advancement then becomes thermodynamically unfavourable even for fluids that are completely wetting, bearing a characteristic or Young's CA (θ_{flat}) of 0°. This results in superomniphobic capabilities.[158]

2.7.1. Fabrication and Materials

Basic modes of superomniphobicity were first demonstrated by the use of lithographically developed re-entrant structures such as microhoodoos,[156] followed by fluoro-functionalization.[11] Scalable methods such as electrospinning,[156] appear to confer acceptable levels of superomniphobic

functionality. However, states of superomniphobicity that are achieved with electrospinning appear to rely on heavily fluorinated materials, such as fluorinated polyhedral oligomeric silsesquioxanes (F-POSS).[156] The cylindrical profile is also typically exploited alongside such low surface-energy materials.[157] As such, functional substrates of choice continue to include materials such as fibrous paper, fabrics or even wire meshes.[65,66]

Despite immense progress, several limitations in functionality remain. These series of work (micro-hoodoos, electrospun F-POSS, fluorinated meshes / fabrics) showcased super-phobicity with fluids of surface tensions down to just 15-20 mN/m. Fluids with lower surface tensions such as fluorocarbons (10 mN/m) are known to preserve their superwettability even on highly textured and fluorinated surfaces.

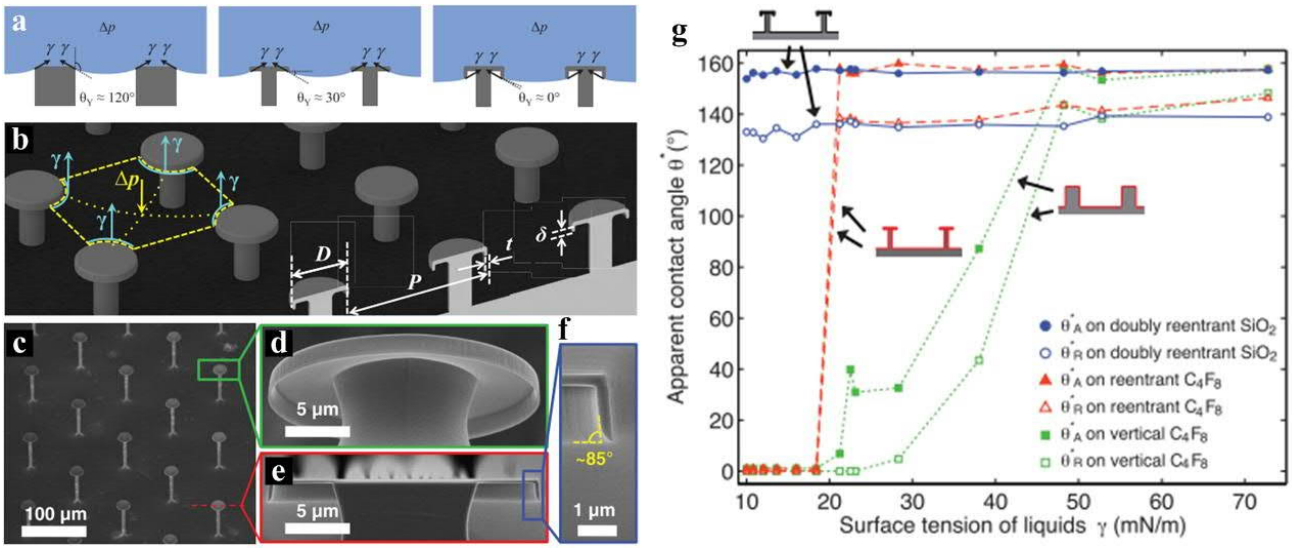

Figure 2.66. Lithography-development of a perfectly superomniphobic surface. a) Comprised of doubly re-entrant textures, as compared to the superoleo(amphi)phobicity's single re-entrant textures, or the superhydrophobic pillar-typed texture. b) Schematic of lithographical design. Scanning electron micrographs of c) the arrayed structure, d) the doubly re-entrant cap structure of the mushroom-like profile, e) side-profile of the cap structure, with a second re-entrant angle of 85°. g) Superomniphobicity of the surface, showing an apparent CA of > 150° even for fluids with a surface tension of just ca. 10 mN/m.[12]

In 2014, the limits of superomniphobicity were again revised, following a landmark discovery on a truly superomniphobic surface (Figure 2.66). This groundbreaking work approached the problem from a purely geometrical perspective. Liu et al. exploited the design of doubly re-entrant mushroom-

like textures, which did not require any fluoro-functionalization.[12] The superior dewetting properties were enabled simply through the double re-entrancy and preserved ultra-stable Cassie-Baxter wetting states, demonstrating super-phobicity even with fluorocarbon fluids having surface tensions of 10 mN/m.[12]

The unique doubly re-entrant mushroom-like textures prevented fluid penetration due to establishing profiles for immensely unfavorable contact-line advancement.[12] This enabled the superdewetting repulsion of even fluorohexanes, which were previously able to wet then state-of-the-art superomniphobic surfaces (Figure 2.67).[11,65]

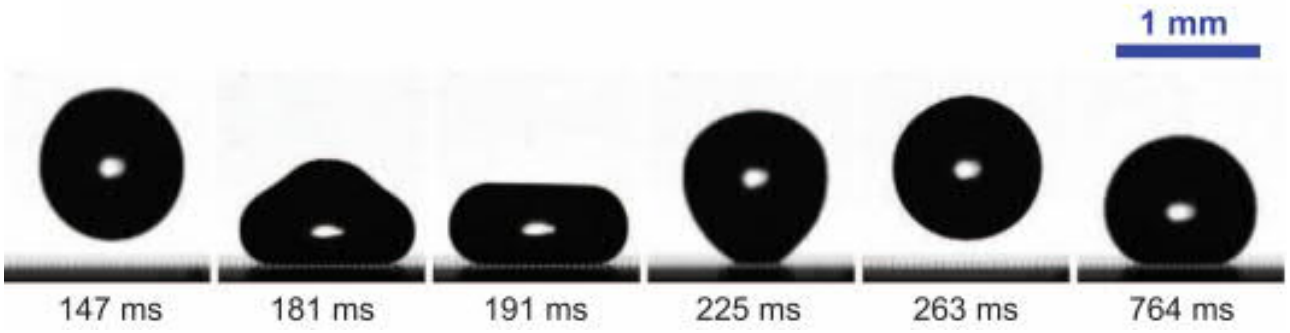

Figure 2.67. Super-repellent properties of doubly re-entrant superomniphobic features. This was demonstrated even with very low surface tension fluids such as fluorocarbon oils, FC-72 (γ = 10 mN/m), showcasing their unprecedented superomniphobic properties.[12]

2.7.1.1. Electrospun Bead-on-String-(on-Mesh)-like Profiles

To date, while the -CF_3 functional group[103,506] represents the lowest state of surface energy, and thus the most logical choice in the design for fluoro-derived superomniphobicity, certain perfluorinated materials appear to be particularly successful.[507] F-POSS represents some of the lowest surface energy compounds ever produced, estimated at a γ_{SV} of 10 mN/m.[508] By comparison, the pure -CF_3 group possesses a γ_{SV} of 6.7 mN/m.[103]

A F-POSS molecule consists of a polyhedral oligomeric silsesquioxane (POSS) cage that is surrounded by fluoroalkyl functional groups (optimum surface chemistry) bearing no hydrocarbon moieties besides those immediately next to the silicon atoms. It represents a class of composite

material with one of the lowest surface energy types, that have been successfully integrated into various functional coating systems.[11,66,156]

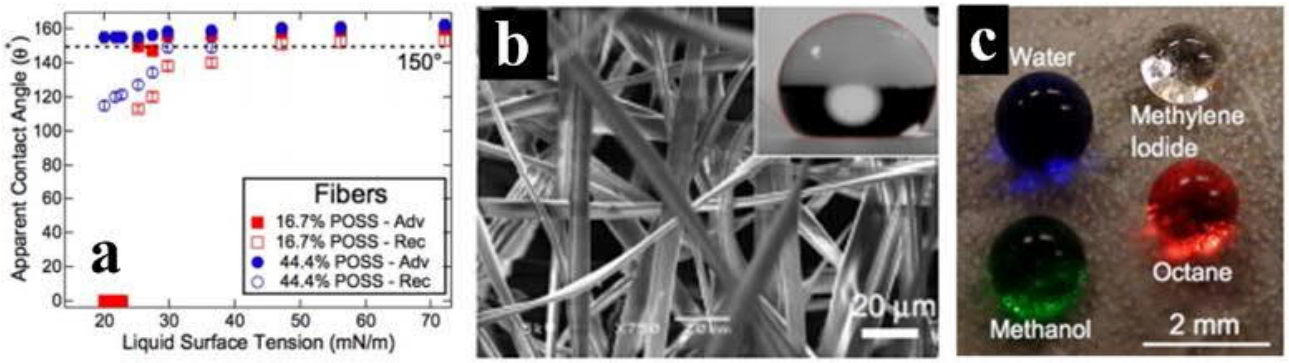

Figure 2.68. Electrospun superomniphobic micro- and nano-fibers. Electrospun PMMA/F-POSS composite with a) superomniphobic properties down to a fluid surface tension of 20 mN/m. b) Purely fibrous structures exhibited enhanced properties as compared to beads or bead-on-string morphologies. Inset: droplet of hexadecane on the surface. c) Beading of different fluid types on the fibrous coating, with octane representative of the superomniphobic state.[156]

F-POSS was first used by Tuteja et al. for approaching superomniphobicity. Performance here was pushed to the lower limits of superoleo(amphi)phobicity or the upper limits of functional superomniphobicity. Octane (γ = 21.7 mN/m) droplets beaded up on the electrospun surface upon contact (Figure 2.68).[11] The bead-on-string morphology demonstrated desirable extents of re-entrancy, and was later used towards the development of functional superomniphobicity. The high density of F-POSS was also later used in a composite bead-on-string coating by Tuteja et al. for achieving superomniphobic properties with heptane (γ = 20.14 mN/m), demonstrating an ACA of 140°, SA of 5° and CAH of 30°.[156]

Electrospinning of F-POSS composites were later integrated with the use of metallic meshes. Kota et al., demonstrated the coating of stainless steel meshes (macro-length scale re-entrancy) with electrospun microbeads of PMMA-F-POSS composites (micro-length scale re-entrancy). Such combined hierarchical texturing based on these multi-scale re-entrant profiles conferred superomniphobicity, showcasing a n-heptane (γ = 20.14 mN/m) CA and CAH of 155° and 4° respectively.[56]

This was also later further improved on, within the same research group, by Pan et al., who electrospun PDMS-F-POSS morphologies on stainless steel meshes for achieving super-phobic CA, CAH and SA of > 150°, 6° and 1.5° respectively with PDMS (γ = 19.8 mN/m).[65] Despite the immense multi-year efforts made by Tuteja et al. from octane (γ = 21.7 mN/m)[11] to Pan et al. on PDMS (γ = 19.8 mN/m),[65] their success demonstrates the immense potential behind the use of F-POSS composites for superomniphobicity (Figure 2.69).

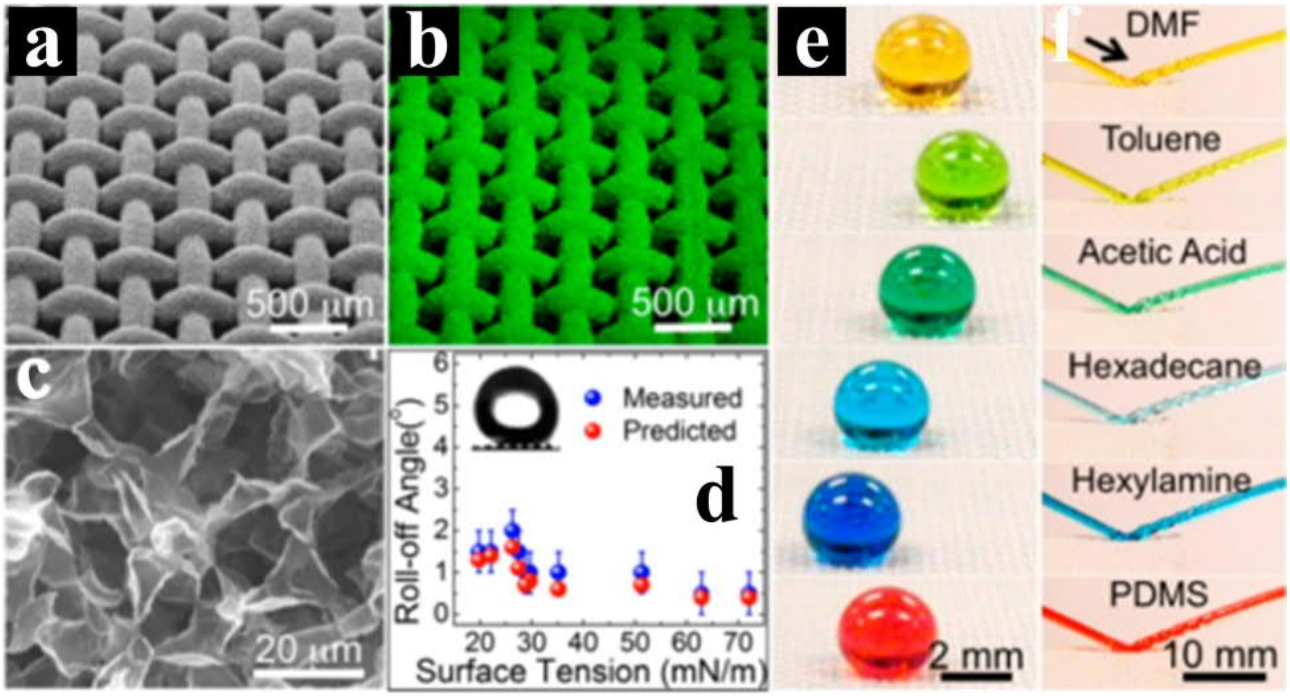

Figure 2.69. Electrospun superomniphobic multi-scale fractal features on wire meshes. Superomniphobic surface comprised of electrospinning a) cross-linked PDMS and 50 wt% F-POSS on a stainless steel wire mesh 70. b) Elemental mapping of fluorine on the hierarchically structured mesh. c) Scanning electron micrographs of the electrospun texture. d) Roll-off angles of various liquids down to ca. 20 mN/m. e) Droplets and f) jets of different fluids on a superomniphobic surface, showing super-repellency.[65]

2.7.1.2. Controlled Etching of Metallic Meshes

Nakayama et al. revisited the use of re-entrancy *via* the use of metallic meshes. Aluminum meshes with hierarchical nanopores and micrometer etch-pit morphologies were formed by a combination of chemical etching in a mixed solution of HCl and $CuCl_2$, followed by anodization in a H_2SO_4 electrolyte (Figure 2.70). Using optimized etching parameters (acid concentration etc.), these

hierarchical structures demonstrated superomniphobic properties, tested at a limit with hexane (γ = 18.4 mN/m) with CA and CAH of ca. 158° and < 5° at its optimum.[509]

2.7.1.3. Controlled Sol-Gel Growth

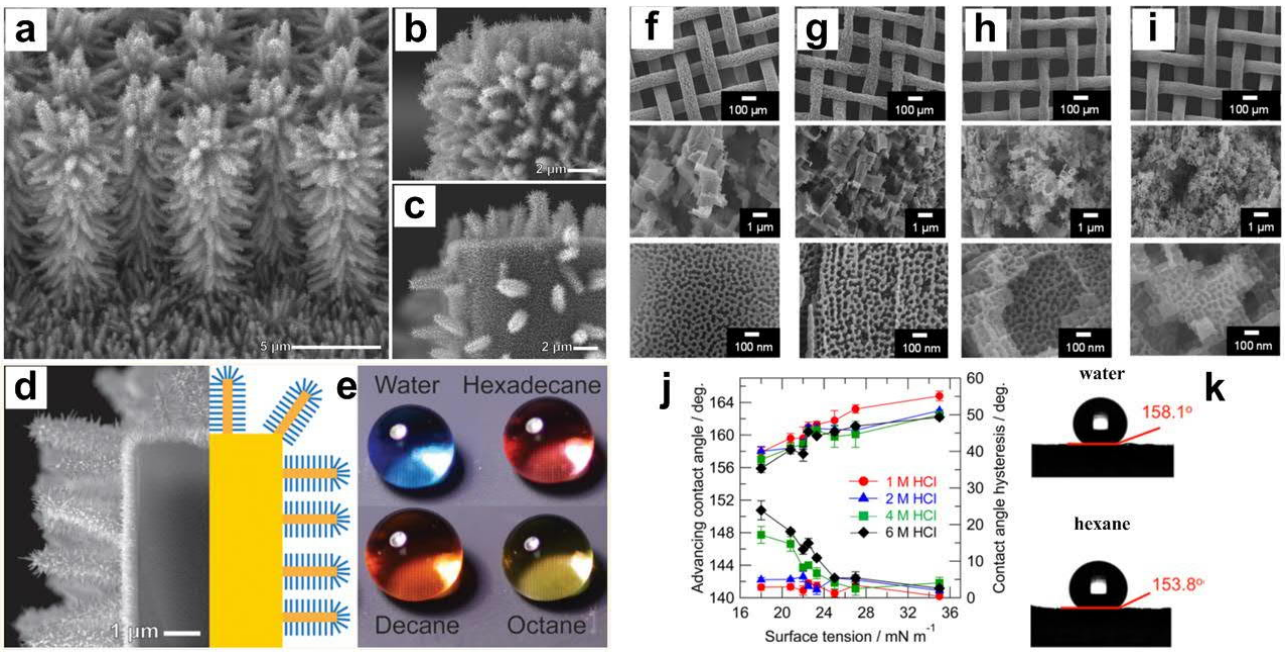

Figure 2.70. Re-entrant texturing by controlled hydrothermal growth and etching. SEM micrographs of hyperbranched structures with three levels of hierarchy. a) Branched ZnO NWs on Si microposts, b) branched NWs grown with higher density of "trunks" and c) branched NWs grown with lower density of "trunks". d) Final net structure with distinctive re-entrancy based on orthogornal-to-micropost features, and superomniphobic performance with water-to-octane.[157] Controlled etching of aluminum mesh surfaces with micrometer-etched pits and nanopores. f-i) The etched pits were formed with increasing molar concentrations of HCl solutions. j) Superoleo(amphi)phobicity with functionality even against low surface tension fluids such as k) hexane (γ = 18.4 mN/m).[509]

Bielinski et al. demonstrated scalable superomniphobic surfaces *via* the use of atomic layer deposition (ALD) based ZnO seeding on a substrate, followed by partial TiO_2 overlayers for partial micro-blocking. The ZnO seeds were then hydrothermally grown to form nanopillars. These nanopillars were then again covered with TiO_2 overlayers for partial nano-blocking, followed by further hydrothermal growth. The resulting hyperbranched structures had multiple levels of hierarchy, comprising of micro-, nano- and sub-nano- posts. After optimizing inter-micro-posts distances, these tri-level hierarchical structures demonstrated superomniphobic properties, tested at a limit with n-heptane (γ = 20.14 mN/m), with CA and CAH of ca. 160° and 29° at its optimum (Figure 2.70).[157]

2.7.1.4. Hybridized Lithography

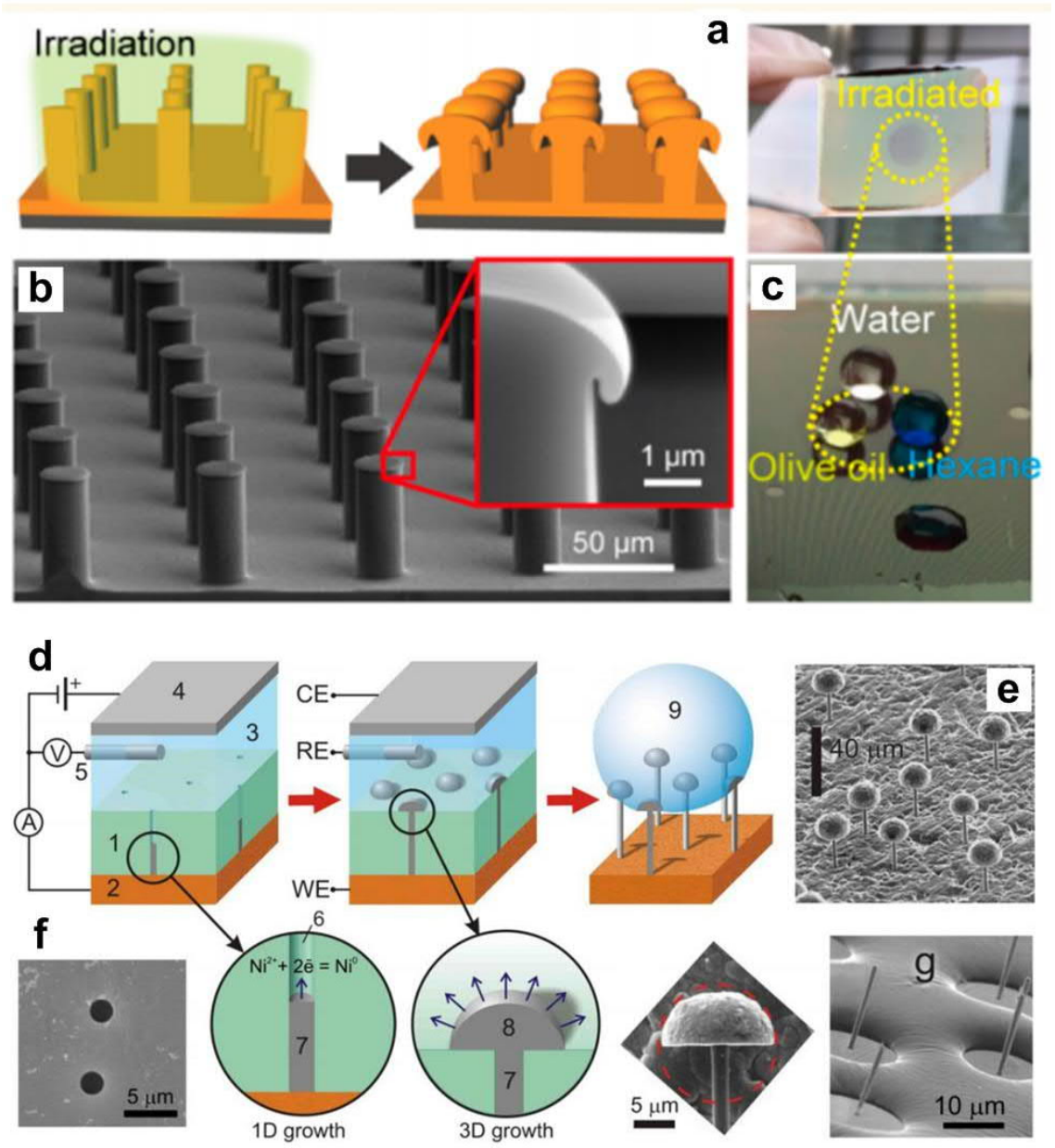

Figure 2.71. Hybridized lithography. a) Soft-molding of an azopolymer to form a micropillar array, followed by illumination with circularly polarized light to induce melting of the tips of micropillars to give mushroom-like features. b) SEM micrographs of mushroom tip. c) Superomniphobic properties against water, olive oil and hexane (γ = 18.4 mN/m).[505] d) Three-electrode electrodeposition setup consisting of a track-etched template, metal electrode and Ni deposition which is localized on one side of the template. e) SEM micrograph of a cluster of electrodeposited Ni micronails. f) SEM micrograph of a PC template. g) SEM micrograph of the Cassie-Baxter state for an epoxy resin droplet sitting on a bed of Ni micronails.[510]

While the doubly re-entrant features demonstrated by Liu et al. in 2014[12] are exemplary for superomniphobicity, it is difficult to envision their scale-up. Today, hybridized lithography methods can be used in medling top-down and bottom-up methods (Figure 2.71). Such techniques utilize a

simpler lithographical step, *e.g.* culminating in regular pillar-like surface features. This is then followed by a scalable processing step realizes the functional re-entrant surface morphologies.[66,505]

Choi et al. made use of a simple molding process that enabled the fabrication of templated azopolymer cylindrical posts. The localized photofluidization of the posts was then achieved by a laser, thus enabling reorganization of pillar tips to give mushroom-like re-entrant profiles. Reactive ion etching for fluoro-functionalization *via* C_4F_8 was then used in completing the superomniphobicization.[505] At the surface's operational limit, they remain super-phobic to hexane (γ = 18.4 mN/m), with CA, CAH and SA of ca. 150°, 20° and < 10° respectively.[505]

Grigoryev et al. made use of a template assisted electrodeposition set-up for synthesizing a surface that is made up of Ni micronails. Micronails had a distinctive hemispherical cap, formed against the flat profiles of the original track-etched templates. Removing the template enabled the release of these micro-nails. After a thiol-based fluoro-functionalization, micro-nails were capable of preserving a Cassie-Baxter superomniphobic state even with isopentane (γ = 15 mN/m), with tested CA and CAH of ca. 158° and 40° respectively.[510]

2.7.2. Drawbacks

Current limitations to the synthesis of superomniphobicity are severe. Notwithstanding the poor scalability and costs involved with lithography,[12] scalable methods employed are still largely considered to be inherently dependent on the use of specific substrate morphologies.[65,66] At the time of writing, most scalable techniques (spray- and dip- coating, etc.) have never been demonstrated on their own, and must be integrated into lithographically-aided systems for function.[88,429] The use of specialized nanoparticles, such as the F-POSS class of materials, also adds to the complexity / cost of the designs. Despite such drawbacks, the highest commendation lies with the fact that both top-down and bottom-up designs were developed simultaneously and were achieved almost together within the same timeframe.[11] Notwithstanding their infancy, these techniques already demonstrate promising possibilities for achieving superomniphobicity *via* potentially scalable means.

2.8. Switchable Wettability

In recent years, sub-fields of wettability started venturing into domains that extend beyond functional coatings. This resulted in the realization of many intriguing interfacial properties that exceed those that are found in our natural environments. One particularly interesting sub-field involves the concept of switchable wettability. Such "switchable" modes of wettability do not occur in nature as the climate and habitat of an organism tend to dictate the evolution of a specific extreme behavior (superwetting or superdewetting). From an engineering perspective, unprecedented advantages could accompany the design of a single material interface capable of switchable wetting properties. The ability to actively transition between wetting states through environmental- or human-directed inputs could pose immense influence on future designs in fluidic engineering. Today, examples range from (super)wettability switching[128,511,512] to surface-fluid adhesion tunability[39].

2.8.1. Definition

Interfaces capable of switchable wettability all depend on a similar fundamental concept. Their surface free energies and morphologies are designed to be highly sensitive to changes in their environments. Re-configuration of surface moeties can be induced by external stimuli, thus leading to changes in surface wettability. A flat surface tends to have a WCA range of between 0° (highest surface energy)[5] and 120° (lowest surface energy)[103,304]. This corresponds to the surface energy range of > 1200 mN/m[513] to just 6.7 mN/m[103].

The lower wetting limit (CA = 0°) is typically reached even without using materials with the highest possible surface energy.[238] To induce superdewettability (CA > 150°) and superwettability (CA = 0°) with materials bearing moderate surface energies, hierarchical morphologies will need to be implemented. Inherently roughened surfaces are required for transitioning between superhydrophilicity to superhydrophobicity and vice versa. The methods vary, but the most commonly employed techniques range from thermal-,[514,515] photo-,[5,516,517] ionic-, pH-,[518] electro-[519] and mechanical- inputs[518,520].

2.8.2. Fabrication and Materials

Owing to the surface energy demands in both wettability extremities, materials with smart switching capabilities are usually designed from inherently hydrophilic or hydrophobic materials. Wettability enhancements can then be simply achieved *via* the use of surface roughness. Such inherently superhydrophobic or superhydrophilic materials achieve "switchability" simply by modifying surface functional groups, thus enabling the opposite wetting extremity.[519,521]

Notably, these concepts didn't immediately achieve superwetting and corresponding superdewetting states.[514,515,522,523] From a historical perspective, these designs arose from fundamental research that probed transitional wetting behavior by virtue of self-assembling molecules on a range of flat surfaces. By incorporating these designs with hierarchical texturing, superwettability-dewettability switching was eventually achieved.

2.8.2.1. Thermal-responsive

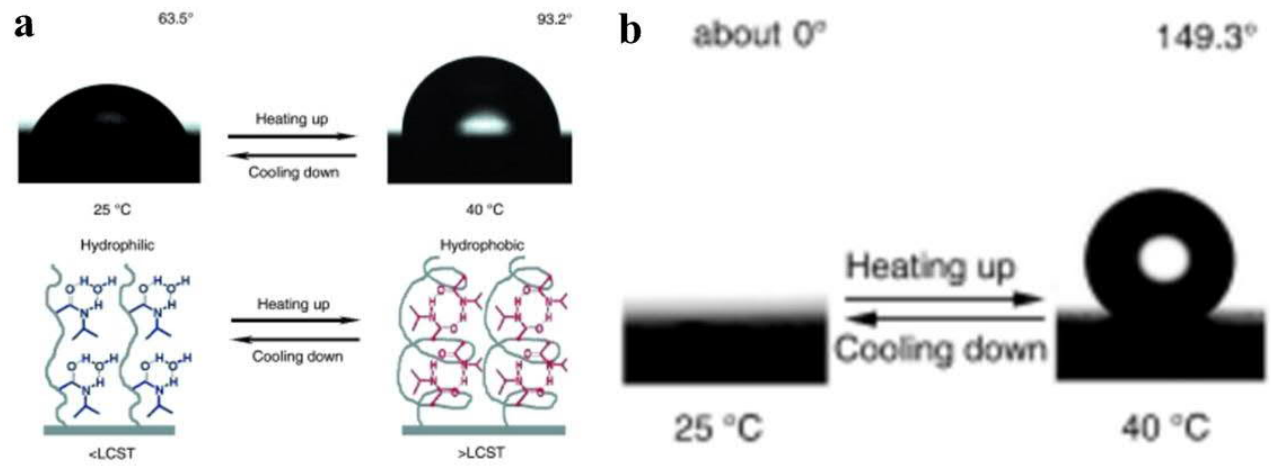

Figure 2.72. Switchable wettability by thermal-responsivity. a) Thermal-responsive polymers with a Young's WCA of +15° (flat surface) with an increased temperature of 30 °C. b) Hierarchically roughened thermal-responsive polymers showing superwettability and superdewettability upon temperature change (15 °C).[233]

Thermal-responsivity for hydrophilic-hydrophobic transitions represents some of the first investigations into the concept of switchable wettabilities. Owing to the flexible nature of polymer chains, they harness the potential of undergoing surface and bulk conformational changes upon

exposure to different environments (Figure 2.72). One particularly thermo-responsive polymer, polyisopropylacrylamide (PNIPAAm), has been demonstrated as a hydrophilic-hydrophobic switchable material.[514] Upon surface texturing enhancements, switchable superhydrophilic-superhydrophobic properties were attained.[514,515]

2.8.2.2. Photo-responsive

Photo-responsivity and UV-induced superhydrophilicity represents one of the first and most fundamental cornerstones in the field of superhydrophilicity (Figure 2.73). The susceptibility for UV-induced superhydrophilicity makes such materials highly suited for hydrophobic-to-hydrophilic transitions. This effect was first discovered and demonstrated in 1997 on particulate TiO_2 surfaces.[5] TiO_2 achieves superwetting functionality *via* surface reconfiguration of Ti^{4+} to Ti^{3+} sites, thus resulting in readily available H_2O adsorption localities. Today, TiO_2 remains the material of choice when considering UV-induced superhydrophilicity.[5,516,517,524]

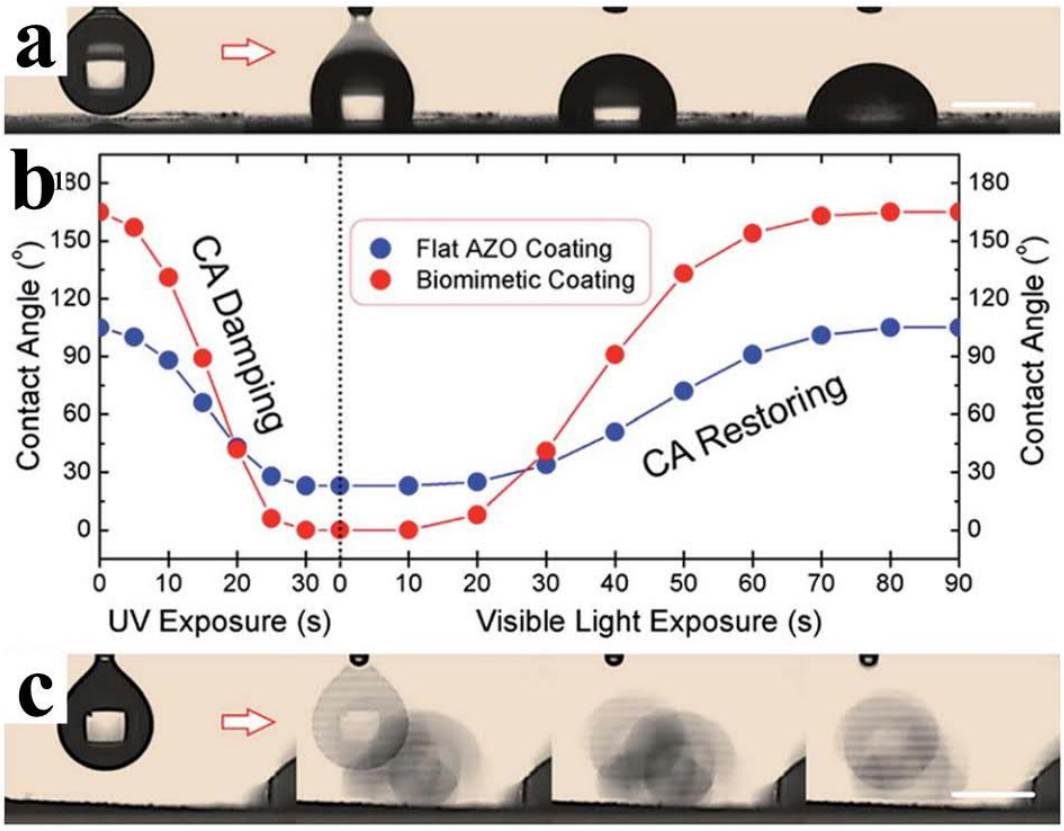

Figure 2.73. Switchable wettability by UV-responsivity. a) Wettability profile changes (increasing hydrophilicity) with increasing UV light exposure (20 s). b) WCA evolution upon UV- and visible light exposure. c) Restoration of superhydrophobicity upon visible light irradiation for 90s.[525]

Besides TiO_2, alternatives for photoactive superhydrophilic coatings have expanded to the use of zinc oxide (ZnO),[525] tin oxide (SnO) and vanadium oxide (V_2O_5)[526]. For instance, vanadium oxide is inherently slightly hydrophilic. However, upon its integration with an alkylamine, they turn superhydrophobic. This occurs through the re-organization of alkyl groups on the material surface, thus resulting in a low surface energy state. Further exposure of the vanadium oxide to UV irradiation induces the formation of electron-hole pairs, giving rise to surface oxygen vacancies (V^{5+} to V^{3+}) and reversible superhydrophilicity.[526]

Switchable super(de)wettability was also demonstrated *via* organic materials, through the photoisomerization of azobenzene chromophores. Azobenzene undergo *cis-trans* surface conformational changes upon UV or visible light irradiation. This switching behavior results in molecular re-configuration that gives rise to completely different surface wetting properties.[525]

2.8.2.3. pH-responsive

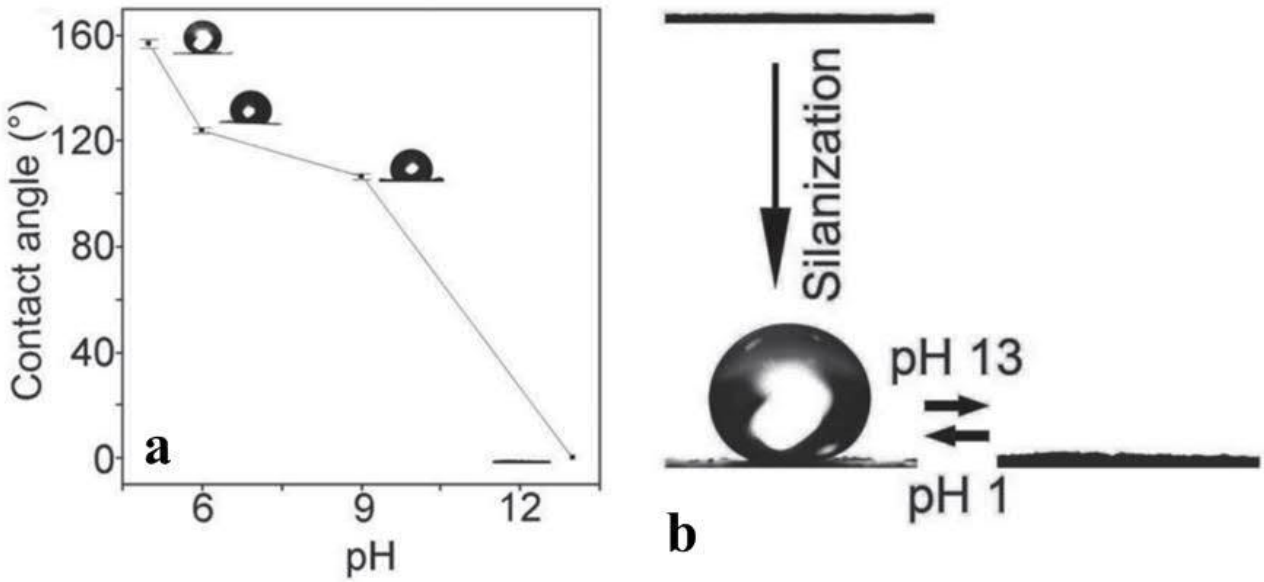

Figure 2.74. Switchable wettability by pH responsivity. a) pH-responsive polymers showing states of superdewettability (pH < 5) and superwettability (pH > 12), with b) reversible, switchable response.[518]

pH-induced switchable super(de)wetting has drawn considerable attention in recent years (Figure 2.74). Building upon the work by the group of Whitesides on organothiol-functionalized gold,[275-277] micro- and nano-structured gold surfaces were modified with monolayers of $HS(CH_2)_9CH_3$ and

$HS(CH_2)_{10}COOH$. The hydrocarbon and carboxylic groups control and enable the respective superdewetting and superwetting states.

A superhydrophobic response can be generated by exposing the surface to acidic droplets while a corresponding superhydrophilic response occurs when interacting with alkaline droplets. Superhydrophilic states are attributed to the deprotonation of the carboxylic group by alkalis. Alternatively, the superhydrophobic state is preserved due to a lack of surface reactions with the hydrocarbon groups, coupled to minimal molecular re-configurations.[523] For fluid separation applications, such properties can be integrated into hydrogel based membranes that have inherent pH-sensitivity, thus enabling their use as fluid gates.[518]

2.8.2.4. Mechanically-triggered

Mechanical designs for transiting wettability are one of the most obvious and easy to achieve given its direct physical intervention. This mode of stimulation has a direct impact on the effective pitch distances, and thus super(de)wettability (Figure 2.75).[136]

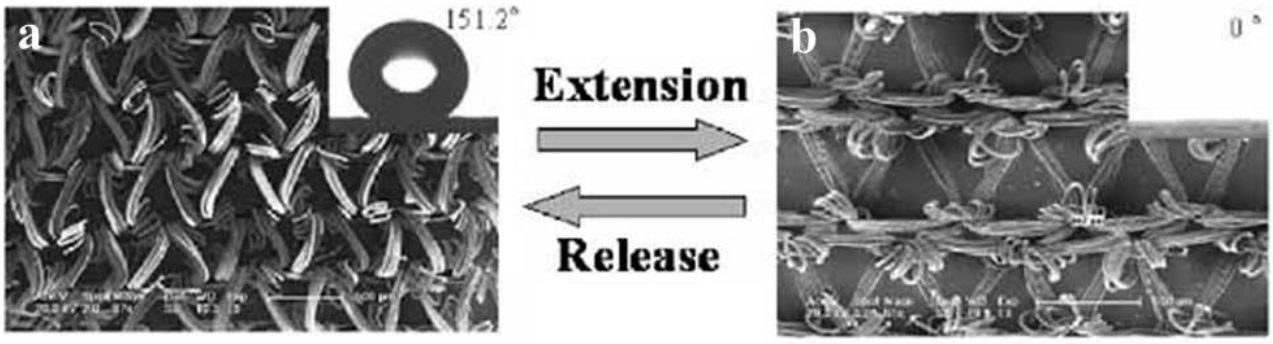

Figure 2.75. Switchable wettability by mechanical stimulation. a-b) Mechanical extension and release of a polyamide membrane, showcasing respective superdewetting and superwetting properties.[520]

Gold films, for instance, can be stretched and relaxed to give wetting-variable interfaces.[17] The stretching of PTFE hierarchical films revealed transitional wetting profile that ranges from a CA of 108-165°.[527] This concept was also demonstrated with the use of porous materials, by mechanically straining and relaxing a triangular netting of polyamide, thus resulting in respective superhydrophilic

and superhydrophobic wetting properties.[520] Mechanical strain can even be combined with other stimuli-responsive materials for the fabrication of complex fluid gating devices (Figure 2.76).[518]

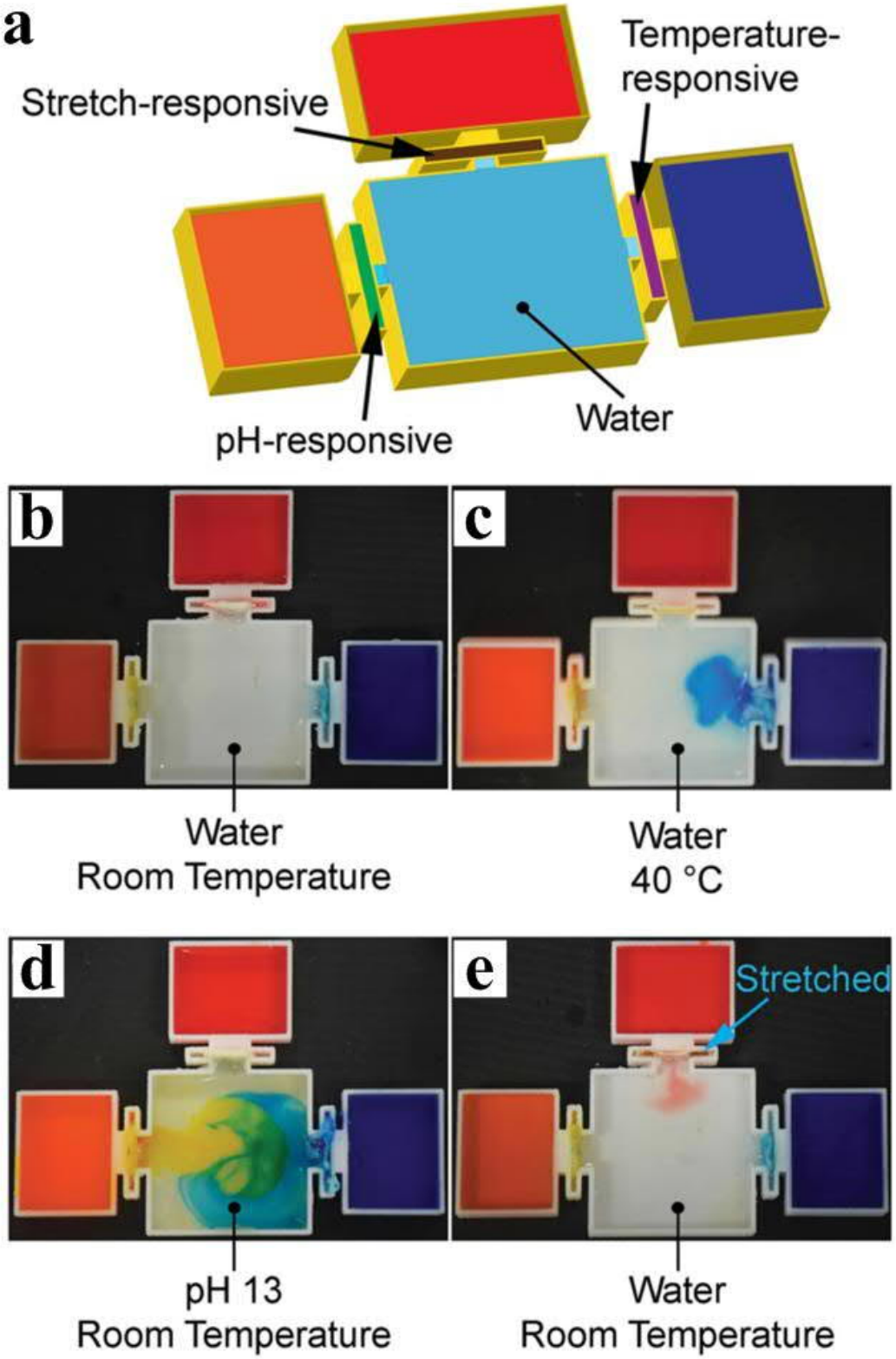

Figure 2.76. Switchable wettability by multi-stimuli triggering mechanisms. a) pH-, mechanical- and thermal- responsive hydrogel as a fluid gating system. b) control, unstimulated, c) temperature triggered, d) pH triggered, e) mechanically triggered system.[518]

2.8.2.5. Electro-responsive

Electrowetting is another means which has been extensively used in the field of switchable wettability. For instance, it was first demonstrated with self-assembled monolayers (SAMs) that possess charged organic groups, giving a 20-30° variation upon charge reversal.[528] This was later improved to a wetting range of Δ60° through the use of a nano-structured surface[522]. Such wettability variations are typically enough for inducing transitions from the Cassie-Baxter to Wenzel wetting states, thus enabling fluid imbibition (Figure 2.77). Successful implementation of electrowetted membranes can lead to on-demand water-oil separation applications, simply through the use of an applied voltage which induces instant wettability.[519]

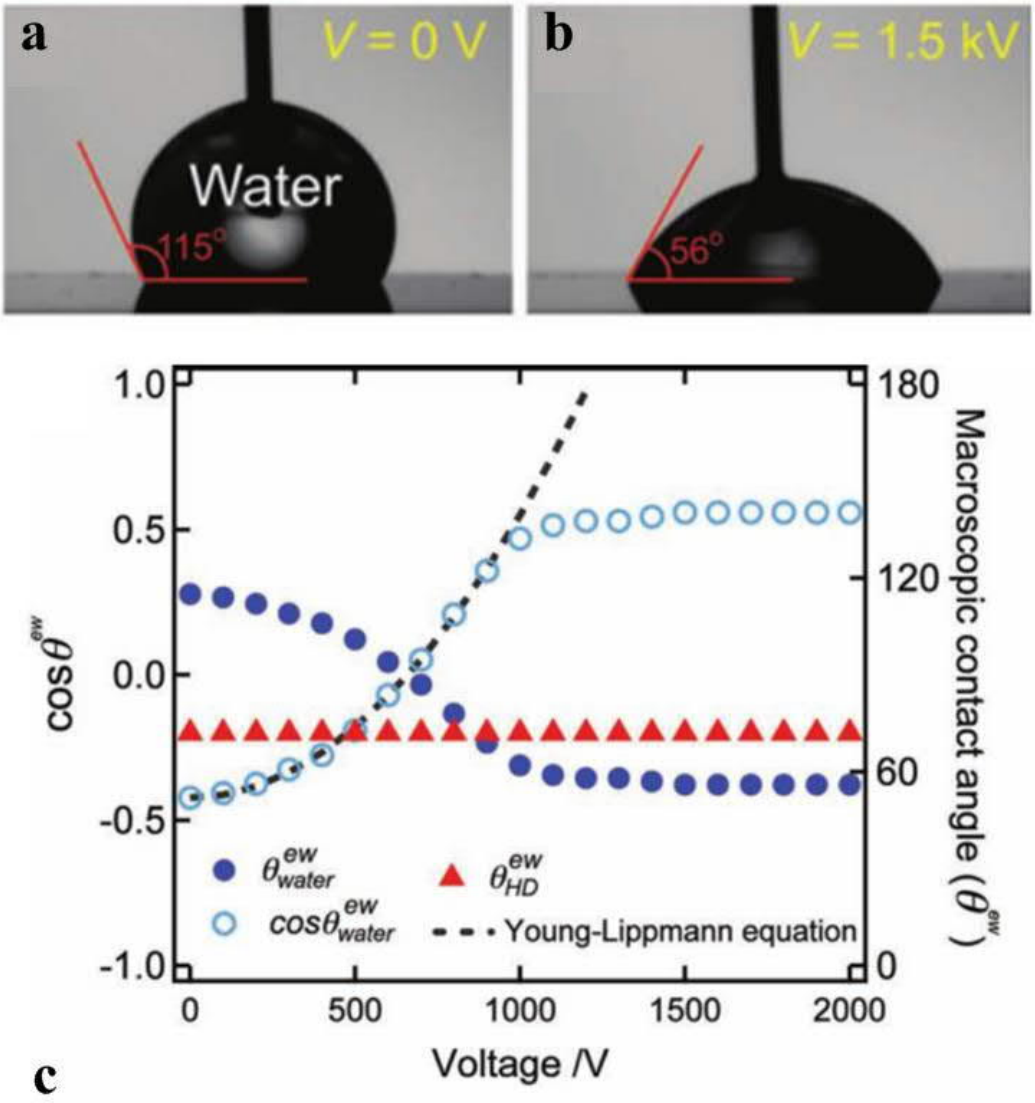

Figure 2.77. Switchable wettability by electrical-inducement. a-b) Electro-induced wettability, with a c) ΔCA of 60° upon applying voltages.[519]

2.8.2.6. Vapor-triggered

Vapor-triggered wettability is comparatively rare, considering operating difficulties for temporarily switching superhydrophobic low-energy states to superhydrophilic high-energy states and back. However, its successful implementation has immense potential for the fields of fluid gating and control. It does not require additional requirements such as heating, pH tuning, UV-irradiation, electrical-stimulation or mechanical stretching. The chemical signaling vapor trigger enables a non-invasive and naturally driven process that occurs by diffusion alone. The first demonstration of this concept came from ammonia-responsive indium oxide nano-structures, which showcased switchable surface wettability that ranged from superhydrophilicity to superhydrophobicity.[529]

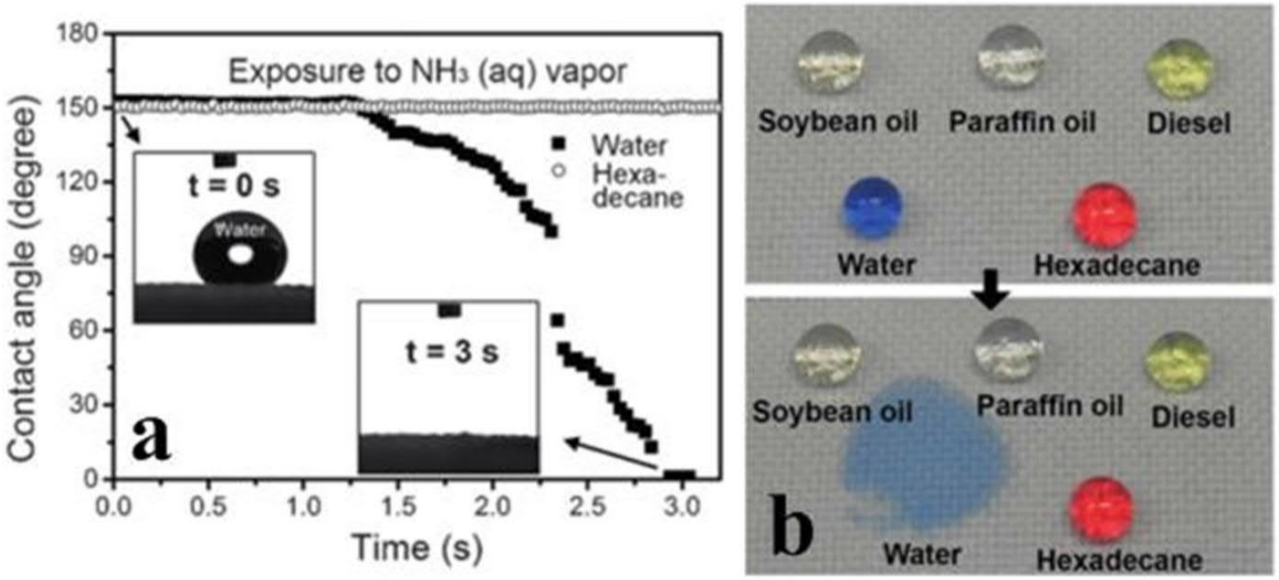

Figure 2.78. Switchable wettability by vapor-triggering. a) Ammonia vapor induced wettability changes functional fabrics from superhydrophobicity to superhydrophilicity. b) Switching hydro-wettability of a super(oleo)amphiphobic surface, with water being completely wettable/dewettable while other lower surface tension fluids such as oils and solvents remain in superoleophobic states.[50]

The use of ammonia was later expanded to its use in triggering superhydrophilicity from superoleo(amphi)phobic TiO_2-based membranes (Figure 2.78). This is attributed to the formation of hydrophilic ammonium carboxylate moieties upon cleavage of titanium carboxylate coordination bonding in fluorocarboxyl-functionalized TiO_2. The flexible membrane material derived was capable of extreme switchable wetting, resulting in the exemplary demonstration of vapor-triggered oil-water separation.[521] Today, notwithstanding the relatively facile use of ammonia gas for inducing a

reversible state of functionalization, no other surface re-configuration methods have been investigated.[521,529]

2.8.3. Drawbacks

The primary drawbacks impeding the area of switchable wettability come in the form of the "trigger". Triggers that include thermal-, electro-, photo- and mechanical- means typically require additional instrumentation for enabling switchable functionality of the surface. pH-responsive variants are more versatile, but require very restrictive fluid compositions which are ultimately undesirable for broad applications. Alternatively, vapor triggers appear to be the least invasive, and could potentially represent revolutionary valve-less fluid gating systems. However, some limitations persist, such as the introduction of potentially undesirable ammonia (which is reactive and corrosive) into a system.[50] Thermal reversal of wettability by cleaving ammonium carboxylates also occur at relatively high temperatures. This introduces further complications, such as the need for coordinated heating requirements. As of the time of writing, room-temperature, vapor phase enabled switchable super(de)wettability does not currently exist.

2.8.4. Applications

The use of switchable wettability has arguably, some of the most far-reaching applications in the field. Considering the burgeoning interest in this area by both research and industrial players, a multitude of new mechanisms are heavily researched on for achieving switchable wettability. The variety of stimuli that is capable of resulting in a responsive behaviors is testament to its broad applicability and function. In this work, we have attempted to cover the most popular means, but this list is not exhaustive.[530] For instance, other sources of stimulation, such as solvents with triblock-copolymer brushes,[531,532] or counterion-exchange[533,534] in ionic liquids, can also enable CA modifications. Although these methods are still in their infancy, with a maximum CA variation of between 15° to 45°, much potential remains considering the progress of their predecessors.[514,528]

The dynamic alteration of effective surface energy and wetting properties hold the most promise for a new generation of smart materials. Extreme and reversible super(de)wettability that functions in response to external stimuli reduces the need for direct human intervention between desired wetting states. In particular, they are well-positioned for applications that require remote operation (Figure 2.79). For instance, they are highly suited for use in tunable optics,[535] microfluidics,[536] fluid gates[511,537] and even systems for droplet manipulation[26,138].

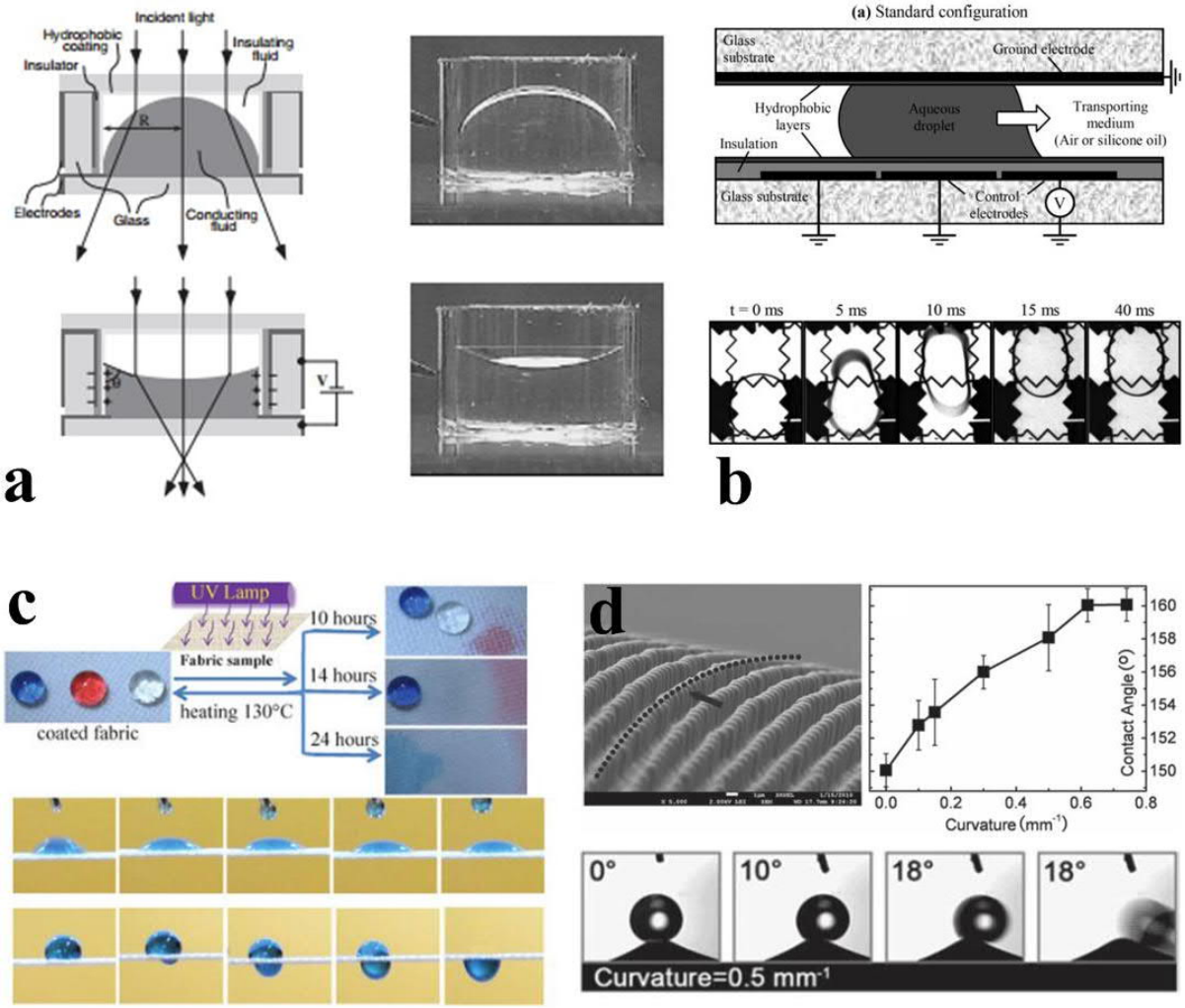

Figure 2.79. Applications of stimuli-triggered wettability. Schematics of the cross-sectional profile of a liquid-based variable lens with its associated optical image of a completed electrowetting lens with (convex from light source) and without voltage (concave from light source) application.[535] b) Side-profiles of a digital microfluidic device (schematized), where aqueous droplets are moved along hydrophobic surfaces *via* electrowetting. Timelapse optical photographs of droplet propulsion through a conduit.[536] c) A superoleo(amphi)phobic fabric with UV-induced wettability which results in superwettability for water (blue), soybean oil (clear) and hexadecane (red). Fluid gating system demonstrated through the selective permeability upon UV-exposure.[511] d) Curvature induced CA variation of a superhydrophobic PDMS pillar-based surface. CA ranged from ca. 150° to 160°. Roll-off detachment of a droplet occurs upon curving the flexible profile.[26]

2.9. Combinatory Wetting

Combinatory wetting represents one of the higher-order variants in wettability engineering. In contrast to the dynamic but monotonic nature of superhydrophilic-superhydrophobic switchable materials, this chapter introduces the physical combination of static states of superwetting and superdewetting. Such combinations can sometimes lead to uniquely unexpected material and coating behaviors, where they could be exploited for practical engineering applications, such as artificial fog-harvesters,[44,210] patterned microfluidic chips,[15,40,45,46,289] smart fabrics,[538] oil-water separation[28,539,540] and even directional[49] fluid gates[511]

2.9.1. Definition

Combinatory wetting is considerably difficult to fundamentally define. In general, it represents a material or coating with distinct, but static super-phobic and super-philic localities. The wetting properties of either should ideally not change over time or use. Definitions of superhydrophilicity / superamphiphilicity or superhydrophobicity / superamphiphobicity should also preferably align to standard definitions (CA = 0° or > 150° respectively). It should however, more importantly, be defined around the use of both super(de)wetting properties for functions that would not exist without which. This may come in the form of operational functionality or efficiency.

2.9.2. Fabrication and Materials

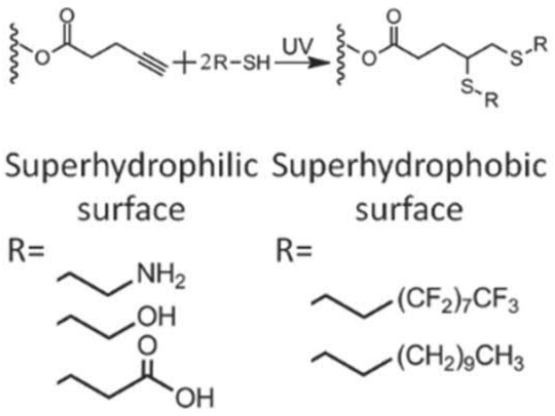

Figure 2.80. Thiol-yne based click chemistry. Rapid modification of alkynes with superhydrophilic or superhydrophobic groups.[45]

Materials and techniques used for achieving super-phobicity and super-philicity on a single material interface which exists in the form of heterogenous layers, patterns or segments are similar to those exploited homogenously. This involves the initial development of a base framework of super-phobicity or super-philicity prior to selective functionalization, which then enables the formation of desired functional heterogeneity or other unique additive effects (Figure 2.80).

The following sections highlight some of the most popular demonstrations of these concepts. However, this is not an exhaustive list of examples that is poised to outline all known combinatory wetting designs.

2.9.2.1. Surface Patterning

Achieving superhydrophobicity-superhydrophilicity in a heterogeneous patterned design is very similar to achieving each separate homogenous super(de)wetting state.

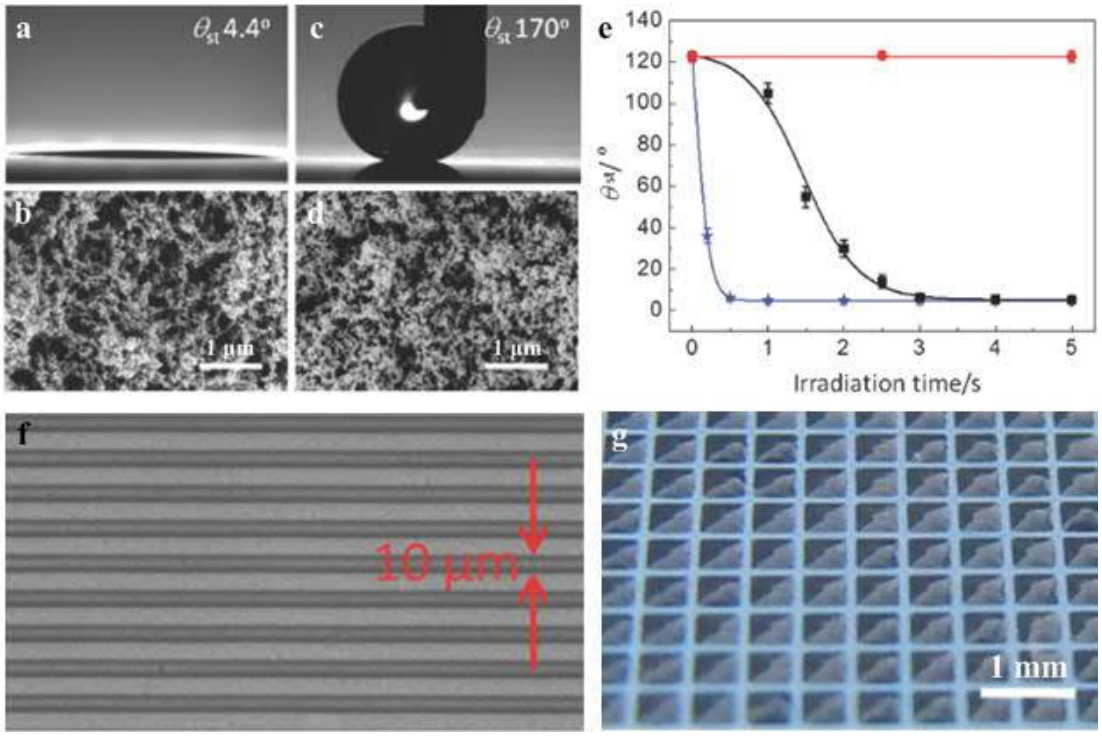

Figure 2.81. Thiol-yne based click-chemistry fluid patterning. UV- thiol-yne induced a,b) superhydrophilicity and c,d) superhydrophobicity on a porous structure. e) Seconds-initialized wettability modifications. f,g) Fluid patterning down to resolutions of just 10 μm.[45]

However, special techniques are often required for synthesizing materials with wetting duality. This is particularly important for patterning surfaces with micrometer and sub-micrometer resolution. For

instance, a superhydrophobic base substrate can be patterned by imprinting superhydrophilicity *via* photolithography.[541] The order of conferring superhydrophobicity and superhydrophilicity can also be reversed.[46]

Alternatively, a simple method for developing patterned interfaces involves the use of rapid thiol-yne based functionalization (Figure 2.81). The flexibility behind thiol-yne functionalization allows for the facile integration of user-defined superhydrophilicity or superhydrophobicity, but remains highly dependent on UV-irradiation.[45] Very recently, this technique has even expanded into patterned designs for low surface-tension fluids (Figure 2.82).[289]

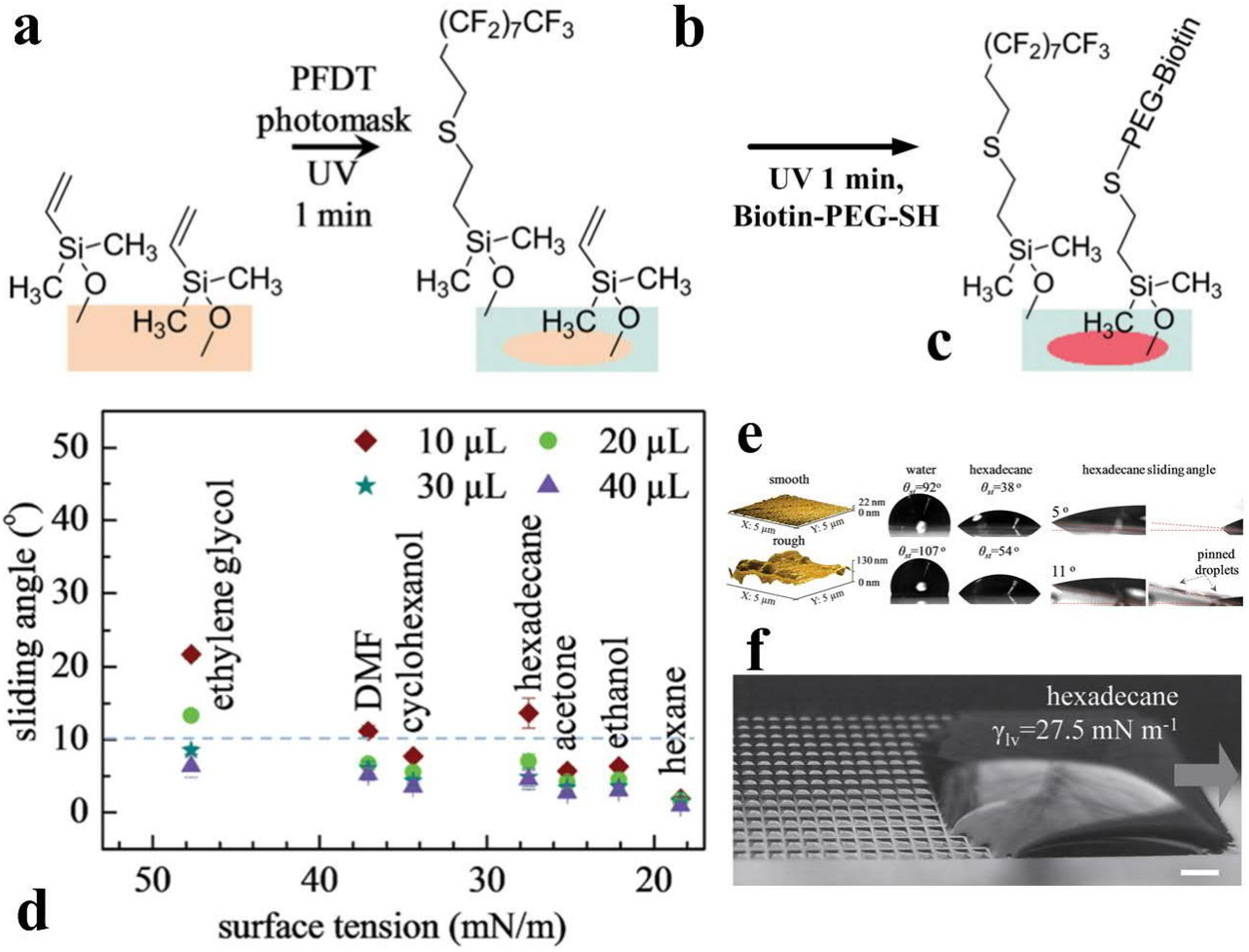

Figure 2.82. Thiol-yne based click chemistry fluid patterning for low surface tension fluids. UV-thiol-yne induced a,b) super-phobicity and c) super-philicity. d) SAs for various low-surface tension fluids and droplet sizes. e) CA images of water and hexadecane on smooth and roughened PFDT-functionalized interfaces with corresponding hexadecane SAs. f) Fluid patterning using a mass of hexadecane that slides across the patterned interface.[289]

Alternatively, fluid patterning can also be performed by the precise deposition of very fine droplets directly onto a non-patterned substrate. The combination of this deposition method aided by computerized iteration is shown to be capable of developing well-patterned pico-liter spots.[542] Applications stemming from patterned surfaces vary, but could potentially range from biomimetic fog-harvesting designs[210] to biomicrofluidics[45] or even advanced printing technologies[542].

2.9.2.2. Janus Materials as Superhydrophilic-Superhydrophobic Layers

The concept of Janus biphasic materials has been extensively investigated in the fields of designer nanoparticles, where incredible feats such as micro-robotics[543,544] and self-assembly[543,545,546] were demonstrated. However, exploitation of such unique biphasic properties for wettability remains in its infancy. Besides a handful of papers highlighting the unique use of their asymmetric wettability[545] in membrane technologies,[28,47,49,547] no other applications have been explored (Figure 2.83).

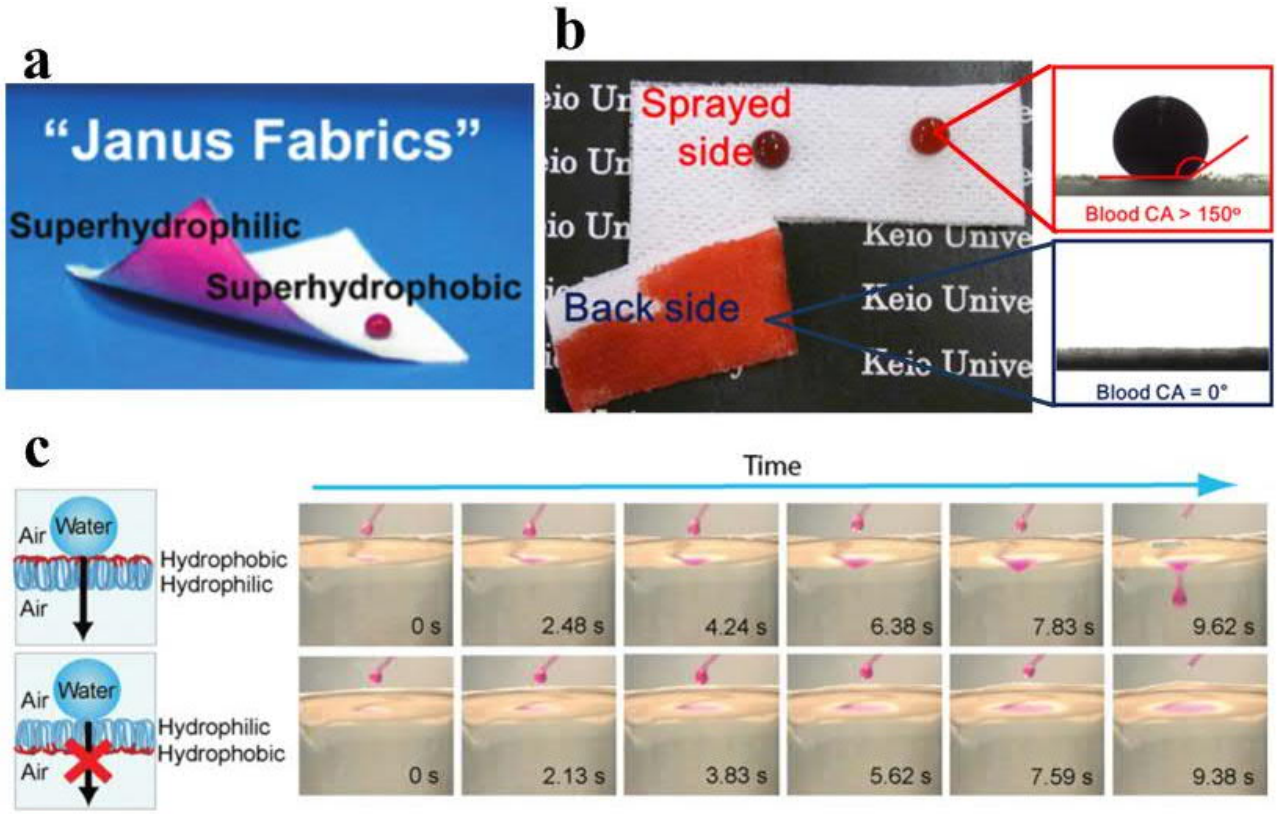

Figure 2.83. 2D Janus systems. a) Janus fabrics with superhydrophilic-superhydrophobic properties.[538] b) Janus-typed bandages for superior blood absorption capabilities, while preserving excellent decontamination properties.[47] c) Fluid-gating membranes using Janus fluid control.[49]

2.9.2.3. Super-phobicity along Gradients

Superhydrophobic, or even superoleophobic gradients are a very recently discussed phenomena.[64,548] While anisotropic wetting is today well-understood and studied,[209,218,442,549] graduated superhydrophobicity reveals a completely different paradigm. Gradients of wettability have been shown in nature to be capable of driving fluid flow within narrow conduits,[550] which has since been replicated for designs in self-propelling micro-droplets (Figure 2.84).[64,551]

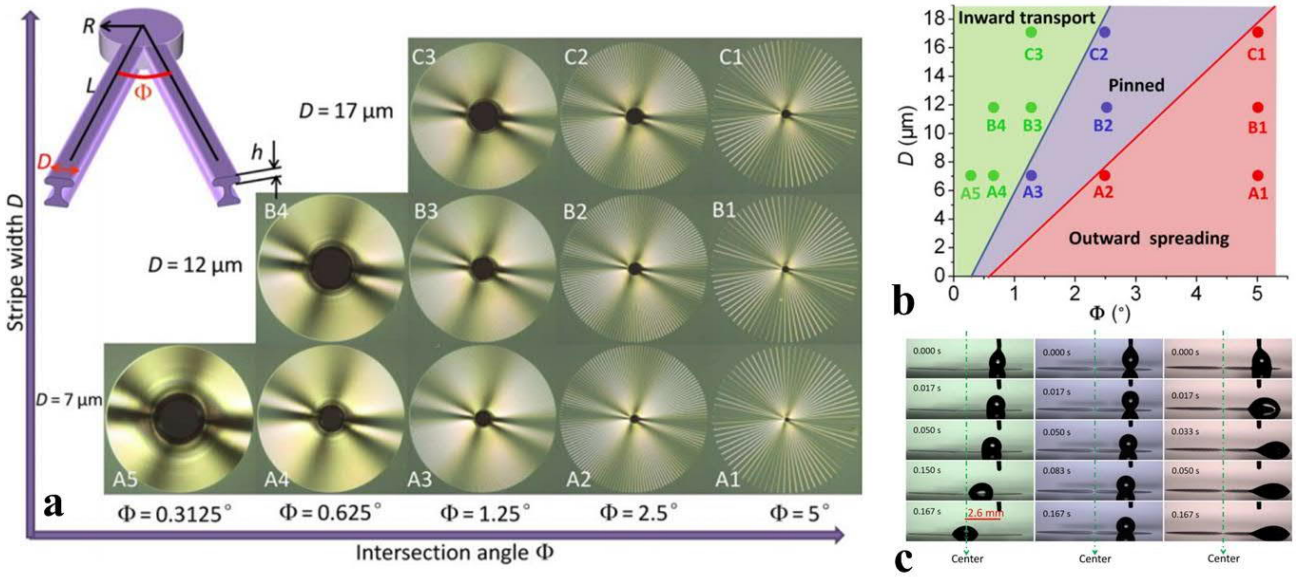

Figure 2.84. Superoleophobic gradients and spontaneously propelled fluids. a) Radially inscribed gradients with superoleophobic properties. b) Domains of fluid motion, ranging from inward transport (green), fluid pinning (blue) or outward spreading (red) depends on the design parameters of D (strip width) and Φ (intersection angle of radial strips). c) Optical images of fluid propulsion (green), pinning (blue) or spreading (red).[64]

2.9.2.4. Slippery Liquid Infused Porous Surfaces (SLIPS)

SLIPS represent a general movement away from superhydrophobicity, superoleophobicity and superomniphobicity. Considering the still-largely non-scalable, poorly transparent nature of the series of superdewetting families,[29] SLIPS has gathered immense momentum and popularity. While SLIPS will not be covered extensively in this manuscript, its impact on the field should be duly acknowledged. SLIPS function by virtue of combining a superhydrophobic surface (with very low surface energy) with a fluorocarbon oil that has even lower surface energy (ca. 10 mN/m). The fluorocarbon oil sits on the surface of the hierarchical superhydrophobic interface, by virtue of

impregnation and van der Waals (vdW)-aided retention (Figure 2.85).[219] Interfacial wetting properties become akin to that of the fluorocarbon oil, thus becoming a very slippery interface having low CAH for water, oils, solvents and even ice.[219,552] Considering the range of superhydrophobic materials that can be used as the base substrate layer, its potential is wide ranging, extensive and ubiquitous.[220,223,553,554]

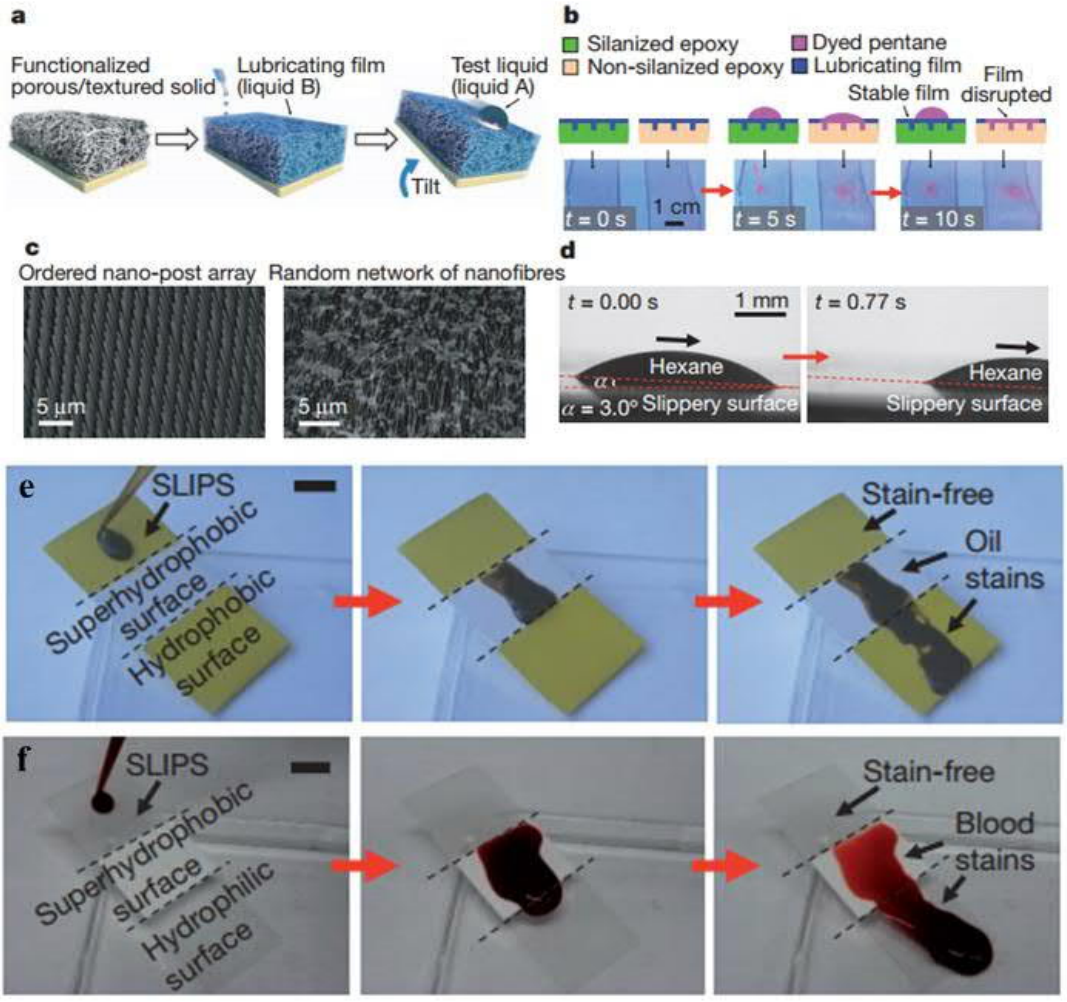

Figure 2.85. Design of Slippery Liquid Infused Porous Surfaces (SLIPs). a) Schematics of a SLIPS surface, where a functionalized textured solid is infiltrated with a lubricating film of low-surface energy, enabling a physically smooth and homogenous film. b) Displacement properties of lubricating films on silanized or non-silanized epoxy substrates. c) SLIPS' porous textures, comprising of a nano-post array or nanofibers. d) Hexane sliding off the surface. e) Comparison of a SLIPS' surface with superhydrophobic and hydrophobic variants using oils. f) Comparison of a SLIPS' surface with superhydrophobic and hydrophilic variants using blood.[200]

SLIPS surfaces are however not without their disadvantages, as they are inherently oily in texture, and might not be feasible for select applications. They also function on the basis of oil retention, which still slowly erodes away with continued use.[221,222]

3. Superhydrophilicity *via* Amorphous Titania Nanofibers

Abstract

Ultra-high specific surface area, hierarchical TiO_2 nanofibers were synthesized by electrospinning. 1D nano-structures were directly self-assembled into highly porous films for transparent superhydrophilic coatings. Evolution of key structural properties such as fiber morphologies and compositions, were mapped from the as-prepared sol-gel up to a calcination temperature of 500 °C. Main fiber restructuring processes, such as the Ti-O amorphous-crystalline transitions and polymer decomposition were correlated to the resulting optical and wetting performance. Conditions for low-temperature synthesis of hierarchical, amorphous, mesoporous TiO_2 nanofibers with very high specific surface area (SSA) were determined. The wetting properties of these nanofibrous films were investigated with respect to the achievement of inherently superhydrophilic surfaces not requiring UV-activation. The surface stability of these amorphous TiO_2 nanofibers was assessed against current state-of-the-art crystalline superhydrophilic TiO_2. They showcase excellent anti-fogging performance even upon extended storage (72 h) in darkness.

3.1. Introduction

Since their first synthetic fabrication over a decade ago, superhydrophilic surfaces have attracted substantial scientific interest.[5] This is largely attributed by their capability of achieving a water sheeting effect within a very short timeframe (ca. 0.5 s)[123,201,555]. The resulting implications with respect to the condensation, evaporation and transport of (non- and atmospheric) water have led to their consideration for numerous commercial applications. Today, this includes anti-fogging,[257,556] self-cleaning,[557] anti-fouling,[32] bio-implants,[31] micro-lenses,[535] lab-on-a-chip,[558] microfluidics,[257,559] fog-harvesting,[560] and heat transfer enhancement.[33]

Multiple lab-scale methods have been successfully established for the synthesis of superhydrophilic coatings. This includes plasma, electrochemical treatment,[257] reactive ion etching,[556] micropatterning[32,560] and flame spray pyrolysis.[30] However, the actual wetting mechanisms are still intensely debated. The complete spread of a water droplet on a surface (superwetting) is expected on materials having high water affinity. This is typically induced by generating high surface concentrations of hydroxyl (-OH) groups.[561,562] As a result, ideal superhydrophilicity leads to a CA (θ) nearing 0. An analysis of surface energy for highly wettable materials, according to Young's equation gives:

$$\gamma_s \geq \gamma_1 + \gamma_{sl} \tag{3.1}$$

where γ_s is the solid surface free energy, γ_l is the liquid surface free energy (surface tension), γ_{sl} is the solid/liquid interfacial free energy. Considering that this is the case for many materials (with the notable exception of organic polymers),[241] superhydrophilicity should be fairly common. However, spontaneously superhydrophilic surfaces are rarely observed. Today, this is attributed to the presence of adventitious contamination by airborne organics/gases. They are rapidly adsorbed on such highly surface active materials, causing compositional variation

to the surfaces.[260,563] To overcome these limitations, morphological modifications such as surface texturing have been utilized to enhance chemically-driven water spreading.[16]

Titanium dioxide (TiO_2) is a widely utilized photocatalytic and UV-augmented material with high H_2O affinity that has been investigated for its photoactive,[261,263] self-cleaning,[261,262] optical[564] and chemical sensing[565] properties. Traditionally, the superhydrophilicity of TiO_2 films has been found to correlate closely to UV exposure.[5,258,267] For instance, UV-induced superhydrophilicity has been investigated using thin sol-gel derived polycrystalline TiO_2 films annealed at 500 °C. These films required surface activation, becoming superhydrophilic when exposed to UV irradiation and hydrophobic when kept in the dark.[5] Similar behaviors have been observed for amorphous TiO_2 films.[258,267] This is a main limitation of TiO_2, where superhydrophilicity is lost within a few minutes[260] to one day[259,266,563] in the absence of UV irradiation.

Doping of sol-gel derived TiO_2[201,266] and mesoporous surface enhancement[566] have been used to promote UV-independent superhydrophilicity.[566] Highly rough TiO_2 films deposited by metal-organic vapor deposition were found to prevent the oxidation of Ti^{3+} during periods of darkness. They were thus able to maintain superhydrophilicity for extended periods (2-3 days) post UV-activation.[270] Amongst other TiO_2 synthesis methods, electrospinning is a scalable, atmospheric process that offers several structural advantages. Electrospun coatings are continuously self-assembled during synthesis, leading to a very porous multi-layer structure having considerably higher flexibility than PVD/CVD-made films.[270,271] Compared to aerosol-deposited nanoparticle layers, electrospun nanofibrous films also possess enhanced mechanical stability.[30,80] Electrospinning of polyvinyl pyrrolidone-titanium (IV) isopropoxide (PVP-TTIP) sol-gel mixtures has led to some of the thinnest TiO_2 fibers so far reported.[273,274] However, optimization of TiO_2 nanofiber compositions and sub-nano morphologies for UV-independent, superhydrophilic coatings remains to be explored.

Here, the synthesis of amorphous TiO_2 nanofibers for the fabrication of transparent and inherently superhydrophilic coatings was investigated. The evolution of key fiber structural properties was mapped as a function of calcination temperature, correlated to morphology, bulk and surface compositions. This leads to a well-characterized set of amorphous and crystalline TiO_2 nanofiber coatings. Structural-functional correlations of these materials were established with respect to their wetting and optical properties. A novel hierarchical amorphous TiO_2 nanofiber morphology with excellent anti-fogging performance was identified and compared to state-of-the-art anatase crystalline coatings.

3.2. Results and Discussion

Synthesis and Characterization of Hierarchical Nanofibers

The as-prepared nanofibers had a flexible structure with notable formation of hoop and spiral shapes (Figure 3.1a) upon evaporation of the solvent utilized for TEM preparation. Their appearance was flaky, revealing a porous morphology and a very rough surface. Upon low temperature (T_s = 250-350 °C) calcination, the fibers' diameters shrunk rapidly (Figures 3.1b and 3.1c), leading to increased rigidity and relatively smooth surface morphologies. Increasing the calcination temperature to 500 °C had minimal impact on the fiber size but increased surface roughness, resulting in a granular appearance with a grain size of ca. 20 nm (Figure 3.1d, inset). This is in line with previous reports on high-temperature calcined TiO_2 fibers,[564] with enlarged grains attributed to crystal nucleation.

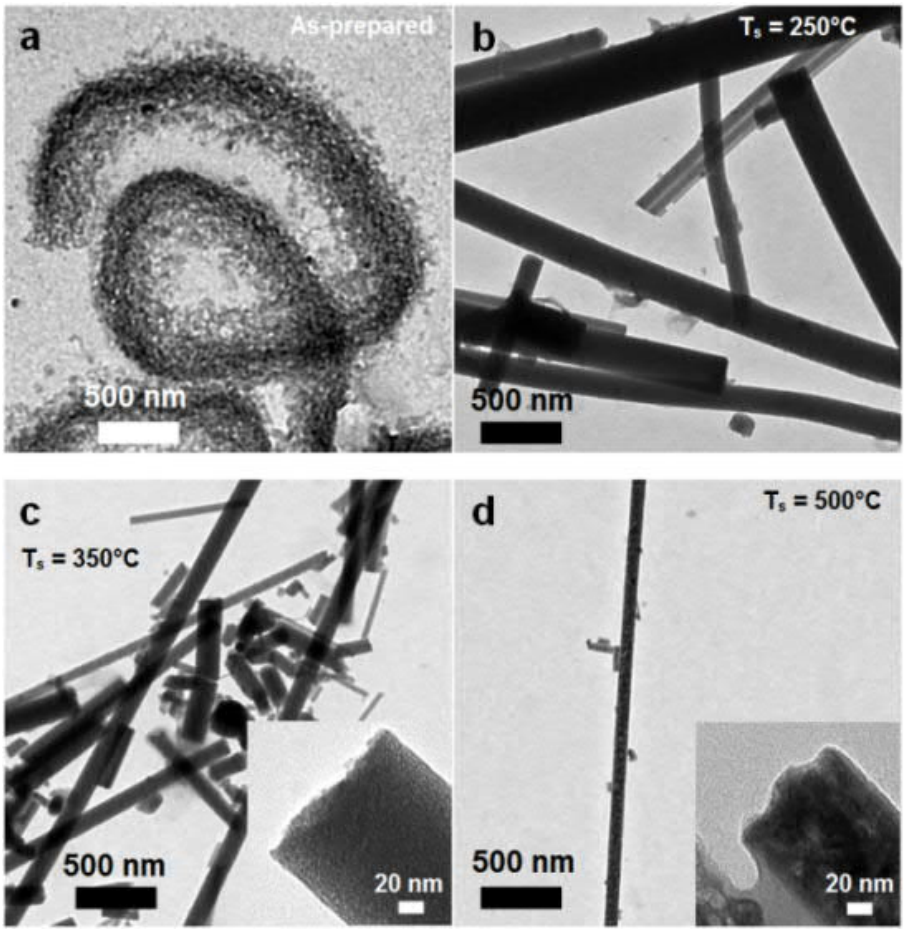

Figure 3.1. TEM micrographs of a) as-prepared and calcined at b) 250 °C, c) 350 °C and d) 500 °C TiO_2 nanofibers.

SEM analysis (Figure 3.2) supported these observations, with the average fiber diameter count decreasing from 412 nm ± 104 nm of the as-prepared (Figure 3.2a) to 80.8 nm ± 44.5nm of the 500 °C calcined samples (Figure 3.2f). The distribution of fiber diameters follow a Gaussian distribution, and the variable diameters are within limits as described in the literature .[567] Such a distribution is induced by the chaotic but tunable regime of electrospinning, during which phases of a) whipping instability and b) uneven fiber stretching coexist to form a nanofibrous coating. The largest reduction in fiber diameters from 210 to 128 nm was observed with the increase of calcination temperatures from 300 to 350 °C. Detailed analysis from 350 to 500 °C revealed that the roughening and restructuring of the fiber surface occurs for $T_s \geq 400$ °C. This was in-line with the granular morphology observed by TEM (Figure 3.1d, inset) and is attributed to the nucleation of TiO_2 crystals on the nanofiber surfaces (Figure 3.2d).

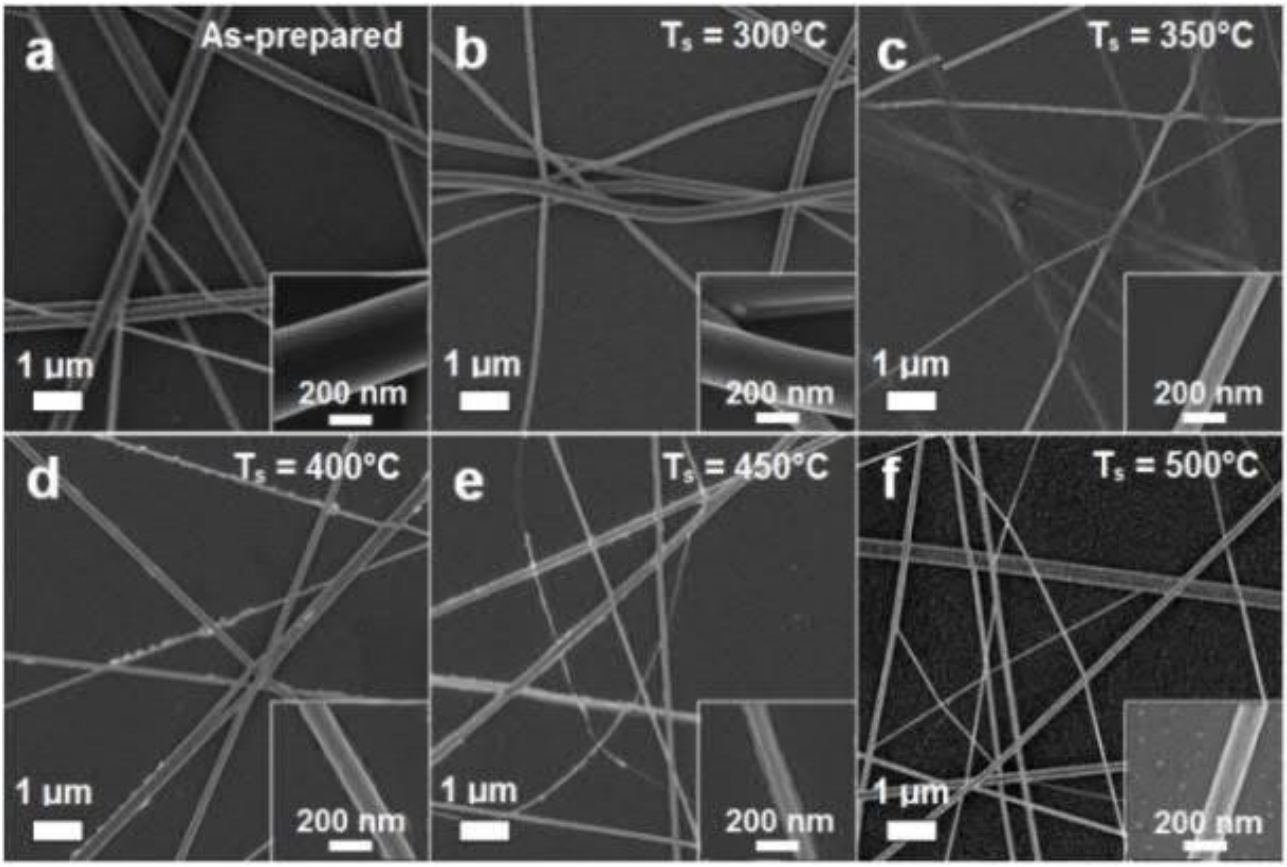

Figure 3.2. SEM micrographs of a) as-prepared and calcined fibers at b) 300 °C, c) 350 °C, d) 400 °C, e) 450 °C and f) 500 °C.

Although the visible TEM and SEM fiber diameter decreased monotonously with increasing calcination temperature, the available surface for water adsorption was optimal below 500 °C. Figure 3.4 shows the specific surface area (SSA) of the fibers (Figure 3.4, triangles) as a function of the calcination temperature. The SSA increased drastically from ca. 65 to 106 m^2/g with increasing T_s from 300 to 350 °C. This is only partially justified by the fiber diameter reduction observed by SEM and TEM (Figure 3.2b,c). Instead, it is mainly attributed to the formation of a mesoporous surface structure. The decrease in fiber diameters is attributed to the desorption of (PVP) polymer residuals.

The XRD spectra of the calcined samples (Figure 3.3) provided further understanding of the observed surface restructuring (Figures 3.1 and 3.2). Up to a calcination temperature of 350 °C, the TiO_2 nanofibers were amorphous with no visible diffraction peaks (Figure 3.3). At a T_s of 400 °C, anatase crystals with an average size of 8.8 nm nucleated. Further increasing T_s (450 °C) increased average crystal size to 12.0 nm while preserving the pure anatase structure. At 500 °C, the formation of a small amount (8.2 wt%) of rutile was observed and the anatase d_{XRD} reached 17.4 nm. This is in line with the roughened TEM morphology observed at 500 °C. The multi-granular texture of the fibers can be attributed to the formation of large anatase crystals.

Increasing the calcination temperature step-wise to 500 °C from 350 °C resulted in a 50% SSA reduction. This was characterized by an initial SSA drop to 42 ± 5 m^2/g at 450 °C and thereafter its leveling-off up to 500 °C. Considering that the fiber diameter of the 350 °C calcined samples was slightly larger than that of the 500 °C ones, the higher SSA of amorphous TiO_2 nanofibers indicates a mesoporous surface morphology. This is further supported by the large pore volume and small (4.7 nm) average pore size measured upon partial removal of the organic scaffold at 350 °C (Table 3.1).

At a higher magnification (Figure 3.1c, inset) the fibers calcined at 350 °C had a more discrete structure, suggesting the presence of nano-scale pores. The high SSA achieved here by these amorphous nano-structures (T_s = 350 °C) is comparable to the highest reported for TiO_2 nanofibers.[565,568,569] It is also, at the time of writing, the highest ever achieved with the PVP-TTIP system. These amorphous fiber coatings combine the macro-scale porosity of the fiber layers (Figure 3.2c) with the nano-scale roughness of their mesoporous surface (Figure 3.4a,b). The synergized surface hierarchy generates an optimum condition for the rapid penetration and spreading of water despite the absence of surface active crystallinity.

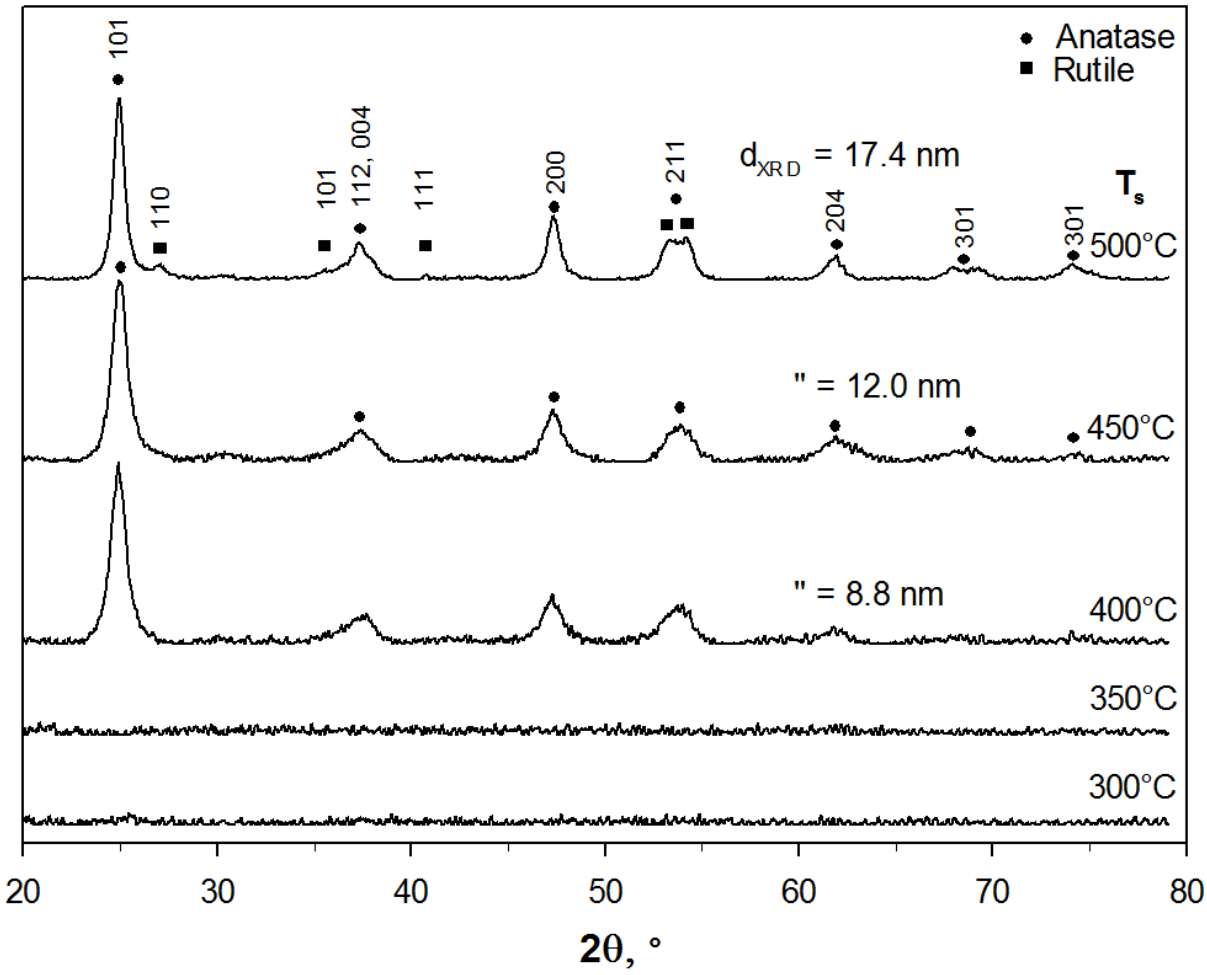

Figure 3.3. XRD spectra of the calcined fibers and corresponding anatase and rutile phase peaks. The average crystal size was 8.8, 12.0 and 17.4 nm for the 400, 450 and 500 °C samples.

Optical and Wetting Performance

The optical performance of the nanofiber coatings was investigated as a function of the calcination temperature. Figure 3.5 shows the transmittance at an incoming light wavelength

of 400 nm (circles) and 600 nm (triangles) from the as-prepared to the 500 °C calcined samples. The as-prepared coatings' transmittance was ca. 77.5% for both wavelengths. This was attributed to the presence of PVP and large fiber diameters (ca. 440 nm), leading to more intensive light scattering and absorption. Calcining the samples to 250 °C increased transmittance by ca. 10%, in line with the suggested partial decomposition and desorption of the PVP matrix.

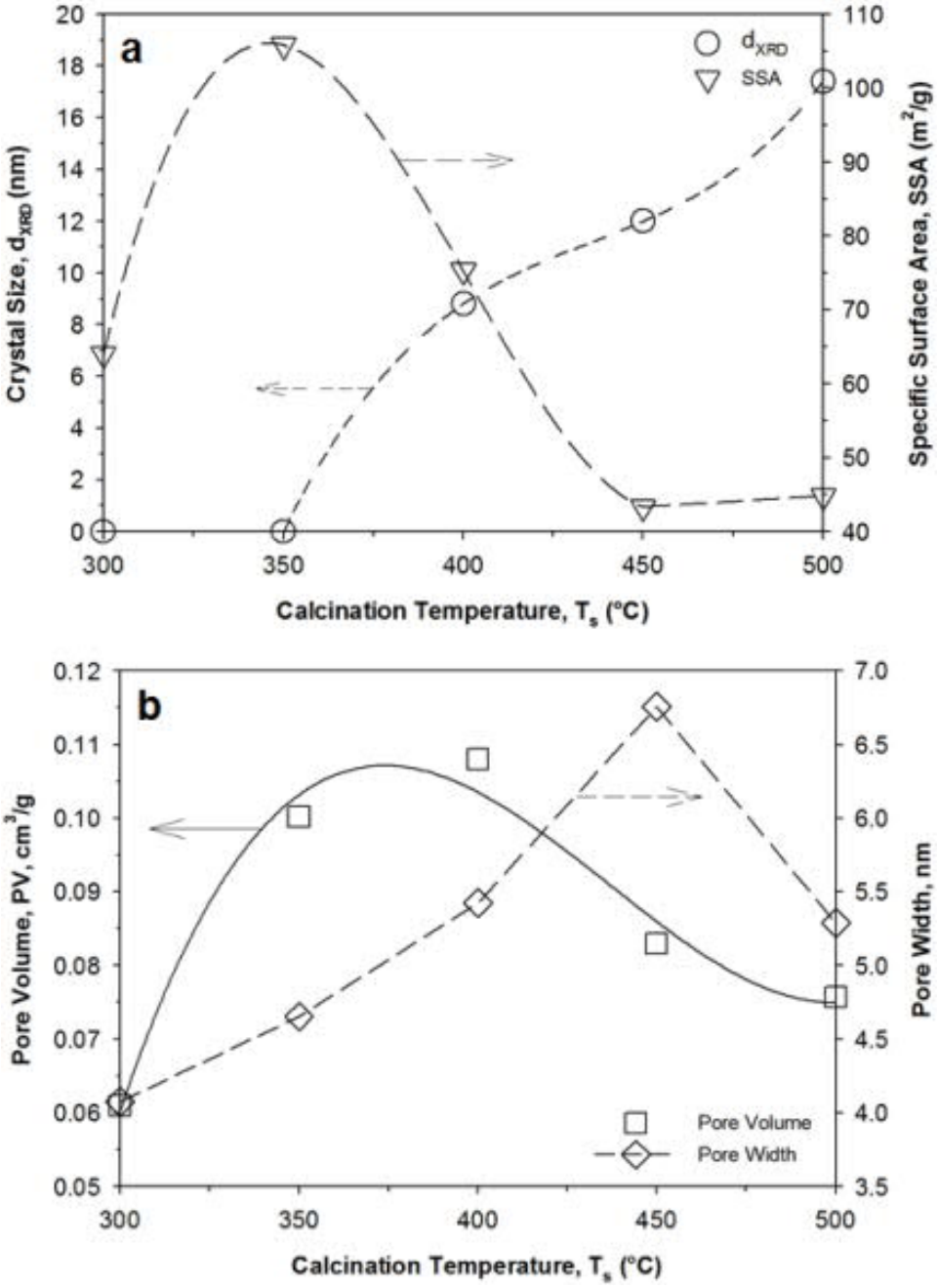

Figure 3.4. a) Average crystal size (d_{XRD}, circles) and specific surface area (SSA, triangles) as a function of the calcination temperature (T_s). b) Pore volume (PV, squares) and pore width (PW, diamonds) as a function of calcination temperature (T_s).

Increasing T_s to 350 °C gradually increased the transmittance up to ca. 92.5% and thus just ca. 2.5% below that of the bare glass slides. Further increments in T_s (up to 500 °C) did not enhance light transmittance. This is in line with the stabilization of the fiber diameter observed by SEM and TEM (Figures 3.1 and 3.2) and the relatively insignificant amounts of organic residuals detected by FTIR at 350 °C (Figure 3.8). Transmittance values between 85%[262] to 90%[261] are considered sufficient for most optical applications.

The coating performance obtained here is comparable to several state-of-the-art coatings,[261,262] showcasing the suitability of these amorphous nanofibers for applications in micro-lenses, solar cells and photo-detectors.

Table 3.1. Properties and performance of the TiO2 fibers, compared across the literature

Morphology	**d_{EM} nm**	**SSA m^2/g**	**PV cm^3/g**	**CA_i (°)**	**CA_d (°)**	**Ref.**
Amorphous TiO_2 fibers T_s = 350 °C	128 ± 32	105.8	0.100	8.5	9.2	This work
92wt% anatase fibers T_s = 500 °C	81 ± 45	44.8	0.076	0.0	7.0	This work
ES anatase fibers	100-200	60	-	2.0	-	[261]
ED Amorphous NPs	-	-	-	12	39	[258]
FSP NPs	-	-	-	5-8	10	[30]

d_{EM} - fiber diameter determined by EM. PV - pore volume of fibers. CA_i - initial CA upon synthesis. CA_d - CA after incubation in darkness for > 12 h. ED - Electrodeposited. FSP - Flame spray pyrolysis. ES - Electrospun. NPs - Nanoparticles.

The long-term coating wetting properties were quantified as a function of the calcination temperature by measuring dynamic WCAs after keeping the samples in the dark for 72 h (CA_d). Figure 3.6 compares the dynamic WCA for the 350 °C (triangles) and 500 °C (square) calcined coatings with bare glass (circles).

Upon a contact time of 0.5 s, the CA_d of the bare glass converged at ca. 25°. In contrast, glass with the 350 °C and 500 °C calcined coatings reached a CA_d of ca. 8.1 ± 1° (t_c = 0.5 s). Although the latter had a slightly lower CA_d (Table 3.1), these effects were minimal, and the actual performance was almost indistinguishable with both coatings satisfying superhydrophilic requirements. The wetting enhancements attributed to the amorphous nanofibers can be traced to its larger SSA and pore volume (Table 3.1), compensating for the higher H_2O affinity of the anatase-based surfaces.

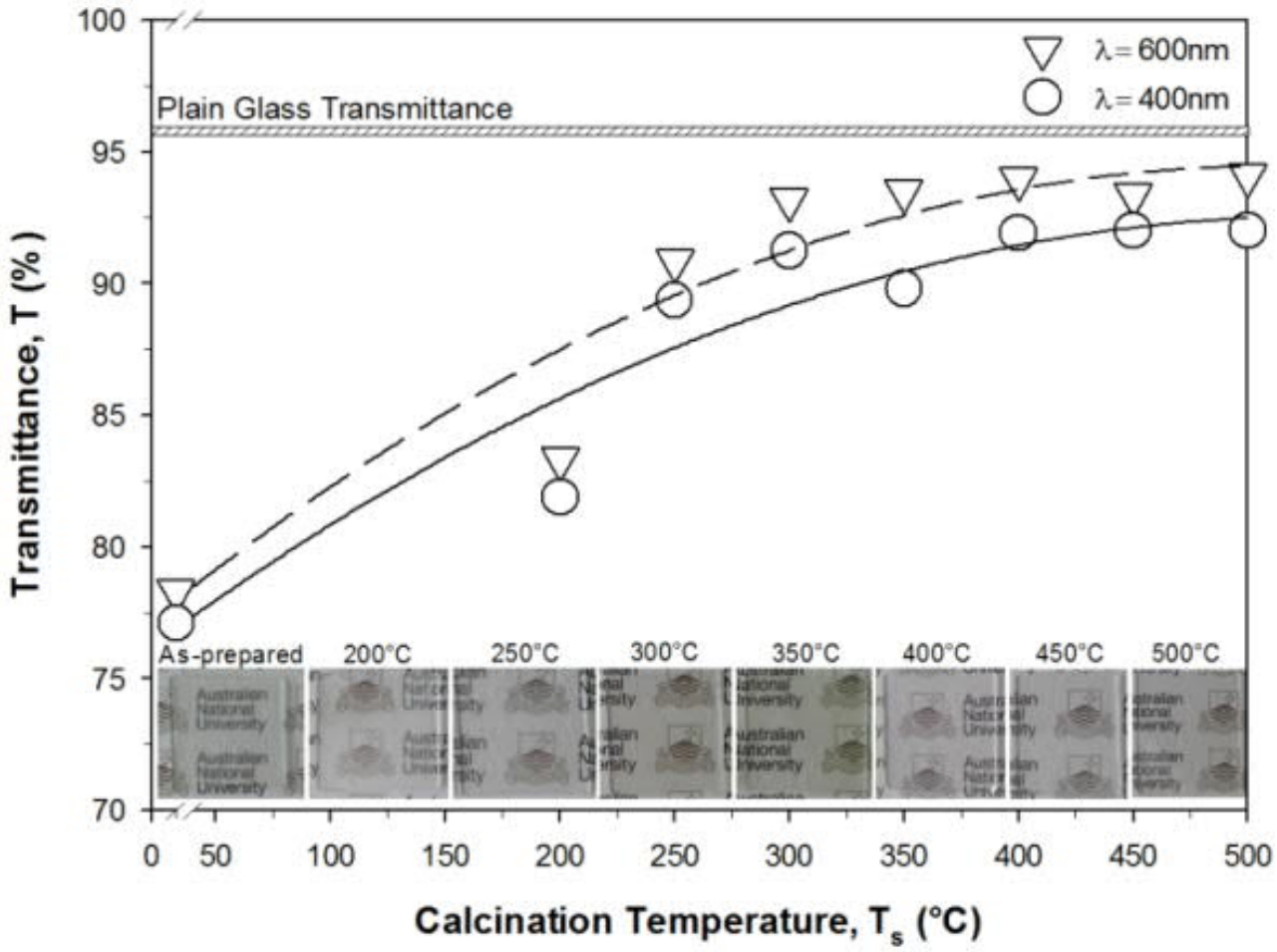

Figure 3.5. Light transmittance through the coatings at a wavelength of 400 nm (circles) and 600 nm (triangles) as a function of the calcination temperature. Higher resolution images of insets (as-prepared to 500 °C treatment are included in Figure S3.3 for reference.

It is worth noticing that the initial CA at 0.5s (CA_i) of the 500 °C samples (Table 3.1) was 0° indicating a partial deactivation of the anatase surface upon 72h in darkness. In contrast, for the amorphous fibers the initial (8.5°) and post-light deprivation (9.2°) CAs (Table 3.1) were nearly identical suggesting inherent superhydrophilicity.

Figure 3.7 shows the initial dynamic WCA at 0.5 s as a function of the calcination temperature. The as-prepared coatings (Figure 3.7) were hydrophobic with a CA of 115°. The CA_d decreased sharply with increasing calcination temperature with an asymptotic behavior. The largest CA drop occurred from 100 to 250 °C (CA_{d_250C} = 25°). Further increasing T_s to 350 °C led to a CA_d of below 10° and thus to the attainment of superhydrophilicity (CA_{d_350C} = 9.2°).

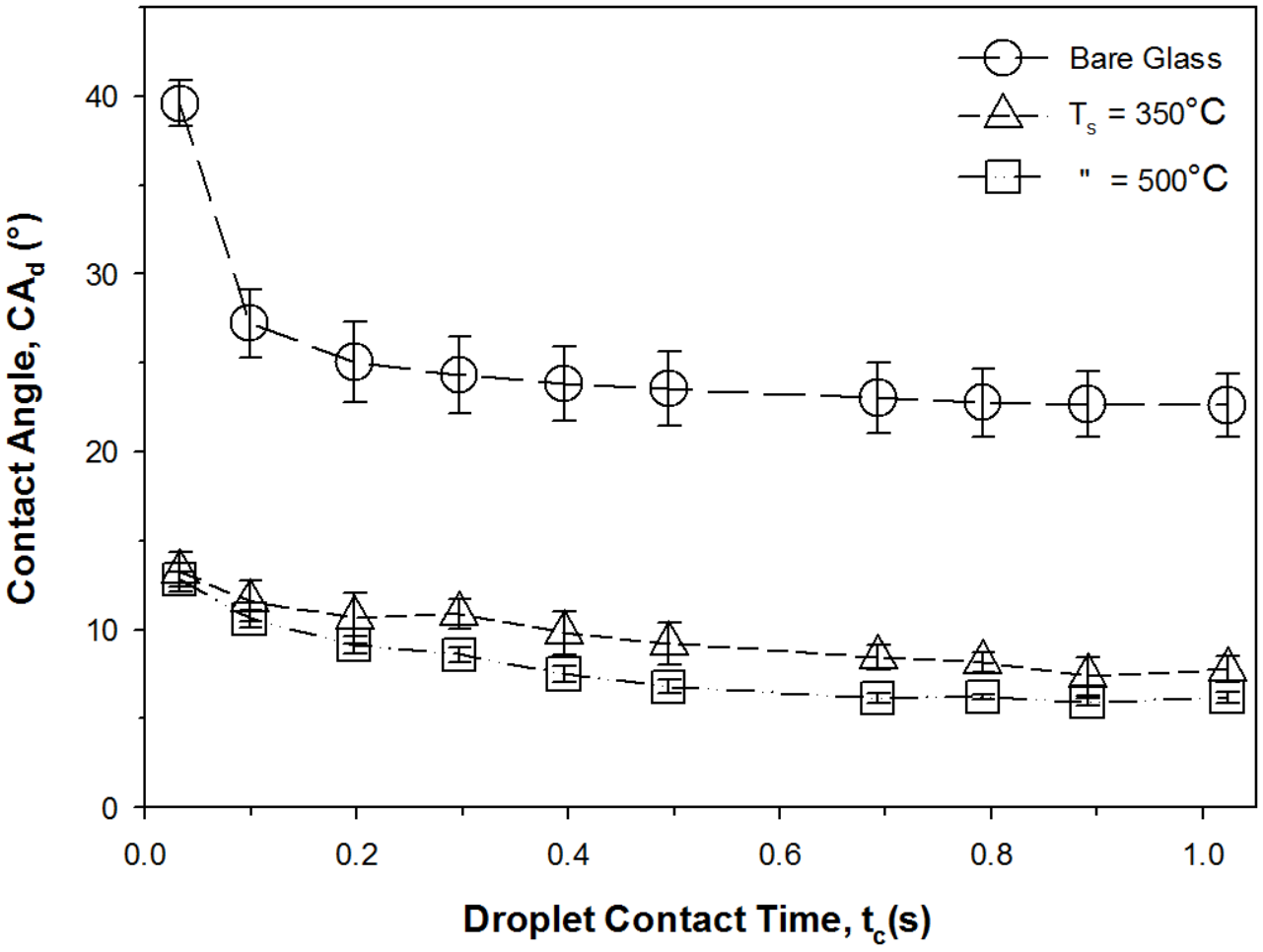

Figure 3.6. Dynamic WCA of bare (circles) and TiO_2 nanofibers coated glasses calcined at (triangles) 350 °C and (squares) 500 °C after 72 h in the darkness.

Small reductions (≈ 1°) in CA were obtained for $T_s \geq 400$ °C. To assess the durability of the films, subsequent multi-drop tests were conducted on the 350 °C and 500 °C calcined films. No variation of the WCA and macroscopic film structure was observed up to 6 h of wetting-drying cycles. The coatings' anti-fogging performance was assessed by placing the bare and coated glass slides in a water vapor stream. Uncoated glass fogged within a few seconds due

to the condensation of water droplets (Figure 3.7, insets). The coating calcined at 300 °C demonstrated reduced fogging and improved transmittance. However, the background visibility was still severely hindered by partial fogging. The coatings calcined at $T_s \geq 350$ °C demonstrated excellent anti-fogging performance with a clear and transparent appearance during the entire period of vapor exposure. This indicates that even with the partial evacuation of organics, the use of ultra-high SSA mesoporous structures can enable superhydrophilicity. These results show, for the first time, that low-temperature synthesized amorphous TiO_2, not requiring UV-activation, can achieve comparable wetting performance to traditional crystalline anatase assembled at much higher temperatures.

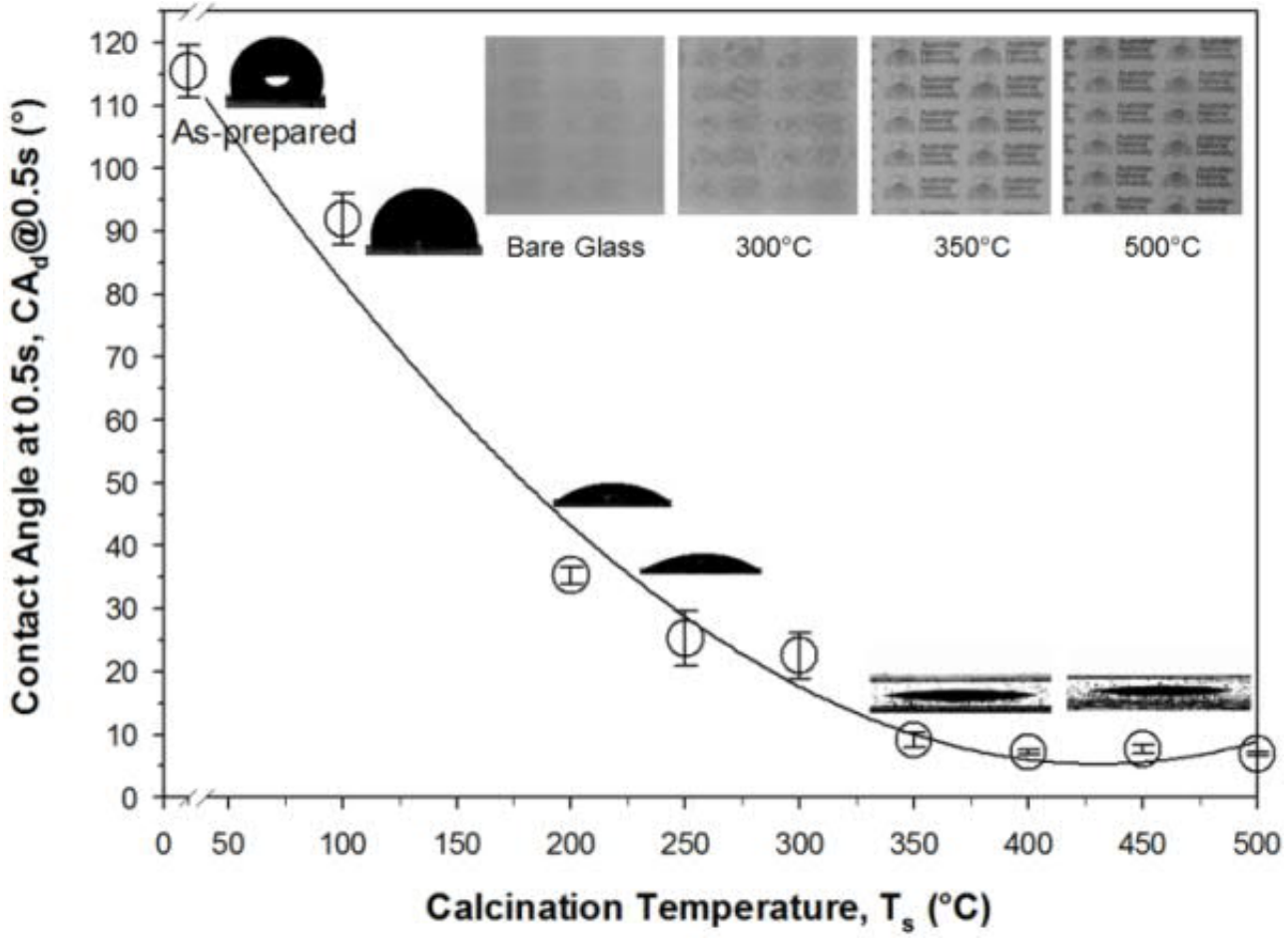

Figure 3.7. Dynamic WCA and (insets) optical images of water droplets as a function of the calcination temperature. Optical images (top right insets) of bare and coated glass in a water vapor stream.

Nanofiber Surface Analysis

To explain the strong variation in wetting and anti-fogging performance observed from 300 to 350 °C, the fiber surface composition was investigated by FTIR. The decomposition onset of the PVP matrix was found to take place between 250-350 °C, in line with previous reports[570,571] where diminishing organic peaks[572] such as C=O stretch at 1650 cm^{-1}, CH_2 scissor at 1419 cm^{-1}, CH_2 twist, wag and C-N stretch at 1200-1300 cm^{-1} occurred. The Ti-O bonds were found to become predominant at a calcination temperature of 250 °C as indicated by strong inorganic Ti-O peaks[573] between 450-550 cm^{-1}. This explains the strong drop in CA (ΔCA = 90°) observed for calcination temperatures above 200 °C (Figure 3.7).

Further increasing the calcination temperature led to a reduction of organic related peaks that completely disappeared only at 400 °C. These findings further indicate that the dynamics of fiber shrinkage is controlled by the decomposition and desorption of the polymeric precursors (Figures 3.1 and 3.2). The remaining organic peaks (~1650 cm^{-1}) at 350 °C were mostly attributed to distorted C=O, and appeared to have a minimal impact on the surface water affinity (Figure 3.7). A peak at 2340 cm^{-1} was also found for $T_s \geq 400$ °C, suggesting the presence of physisorbed carbon dioxide (CO_2).

This is in line with previous reports indicating considerable adsorption of atmospheric CO_2 on crystalline TiO_2. It is worth noting that, even after an extended incubation period of 8 days, the amorphous TiO_2 (T_s = 350 °C) did not develop this CO_2 peak. This is in line with the TGA analysis of the fiber mats (Figure S3.1), revealing that most of the organics are desorbed between 300 and 400 °C. Preservation of minute organic groups could have hindered the physisorption of atmospheric CO_2. Furthermore, analysis of the thermal decomposition at isothermal conditions (Figure S3.2) suggests that the critical transitional temperature for organics removal and achievement of superhydrophilicity is close to 350 °C.

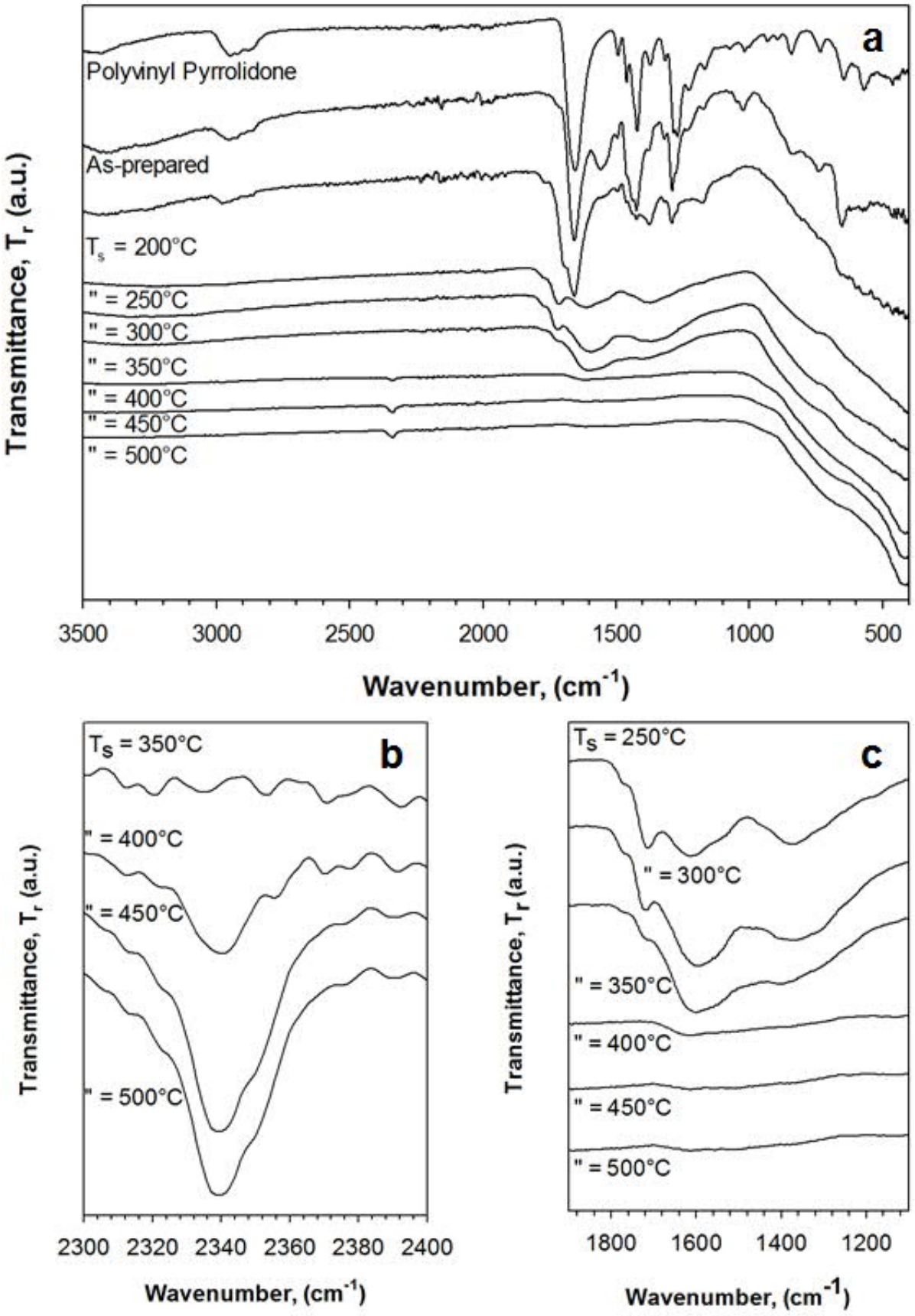

Figure 3.8. FTIR spectra a) of electrospun TiO_2 nanofibers as a function of the calcination temperature (T_s). Magnifications of the FTIR spectra from b) from 2300cm^{-1} to 2400cm^{-1} depicting atmospheric CO_2 adsorption, and c) from 1100cm^{-1} to 1900cm^{-1} depicting the loss of organics between 250-400 °C.

3.3. Conclusions

An optimal TiO_2 nanofiber morphology was determined for the fabrication of flexible, non-UV augmented superhydrophilic coatings having superior transparency and anti-fogging performance. For the first time, it is shown that very-high SSA (> 100 m^2/g), hierarchical, amorphous TiO_2 nanofibers, not requiring UV activation, could possess comparable inherent wetting performance to crystalline anatase. These amorphous fiber coatings were synthesized by rapid (1 min) electrospinning leading to enhanced and prolonged (72 h in the darkness) superhydrophilicity. It was found that amorphous Ti-O bonds become predominant at 250 °C leading to a considerable reduction ($\Delta CA = 90°$) of the WCA. Calcination at 350 °C was required to remove most residual organics and obtain quasi-perfect superwetting (CA_d at 0.5 s < 10°). These low-temperature synthesized amorphous nanofibers have potential for the future development of superhydrophilic coatings with numerous applications, such as anti-fogging glass, microfluidic devices and water filtration membranes.

3.4. Experimental Section

Materials and Fabrication

Nanofibers were obtained by electrospinning of an ethanol-based sol-gel (0.06 g/mL PVP and 0.0936 g/mL $Ti(OiPr)_4$), with acetic acid as a hydrolysis promoter.[273] A PVP solution was first prepared by dissolving 0.6 g of PVP (Sigma Aldrich, M_w = 1,300,000) in 5 mL of ethanol (Sigma Aldrich, 200 proof). A sol-gel solution was then prepared using 2 mL of ethanol, 2 mL of acetic acid (glacial, Chem-Supply) and 1 mL of $Ti(OiPr)_4$ (Sigma Aldrich). Solutions were stirred for 10 min before introducing the sol-gel mixture into the PVP solution. A clear yellowish solution was obtained, which was electrospun after 1 hour of mixing. An applied voltage of 25 kV was used with a working distance and flow rate of 20 cm and 0.8 mL/hour, respectively, providing homogenous coverage of nanofibers on the glass substrates. Surface coverage was confirmed by optical microscopy. A deposition time of 1 minute was used to obtain clear, transparent coatings. Once collected on glass slides, the coatings were stored at room temperature for 5-6 h to allow for the completion of hydrolysis. Samples were then calcined for 1 hour (3 °C/min) between 100 °C and 500 °C (T_s).

Characterization

Calcined coatings were then kept in the dark at room temperature for 3 days before proceeding to the wetting studies. The dynamic WCA was measured by placing a drop of deionized water (5-6 µL) on the sample surface using a KSV CAM200 contact angle goniometer (Finland) with a heliopan ES43 camera (Japan). The CA was computed by a commercially available (CAM2008) program. Samples were analyzed using a Zeiss UltraPlus analytical scanning electron microscope (FESEM) at 3kV and a Hitachi H7100FA 125kV transmission electron microscope (TEM). Prior to examination, SEM specimens were platinum sputter-coated for 2 min at 20 mA. Average fiber diameters (d_{EM}) were determined by counting with ImageJ 20 fibers in each SEM micrograph. TEM specimens were suspended and dispersed in ethanol

(Sigma Aldrich, 200 proof) before they were deposited on 200-mesh nickel-copper grids (Formvar) and dried at room temperature. UV-vis analysis was conducted using a microplate reader (Tecan 200 PRO, Switzerland) from 300-800 nm with 10 scans per cycle. The visible wavelength ranges from 390 to 700 nm. Analysis of 2 point zones, such as 400 nm and 600 nm (without having to focus on the entire 390 to 700 nm range), provides a summary of the real-world optical transparency of the coatings. These datasets were then tabulated against the key investigation parameter (calcination temperature) to understand the optimization of optical properties. For reference, the optical transmittance typically increases from 400 to 700 nm, with an exponential rise to maximum behavior. The crystal phases, size (d_{XRD}) and surface compositions were analyzed by X-Ray diffraction (XRD, D2 Phaser, Bruker, U.S.A) and Fourier transform infrared spectroscopy (FTIR-ATR, Bruker-Alpha, U.S.A). Amorphous samples in XRD (< 400 °C) were normalized using the first crystalline anatase 101 peak achieved at 400 °C. The Brunauer-Emmett-Teller specific surface area (BET, SSA), pore volume and distribution of the as-prepared coatings were measured by N_2 adsorption using a porosity analyzer (Micromeritics, TriStar II, U.S.A). All samples were degassed at 300 °C for 5 h prior to analysis. Evaluation of the antifogging performance was conducted on selected coatings, on calcined coatings (300 °C, 350 °C and 500 °C) by exposure to a vapor stream 40 cm above boiling water for 5 - 10 s, as previously reported.[30] Thermogravimetric (TGA) and differential thermogravimetry (DTG) analysis were conducted from 100 - 800 °C (3 °C/min ramp) and isothermally at 350 °C for 1hr under atmospheric conditions (Perkin Elmer, STA 8000, U.S.A).

3.5. Supplementary Information

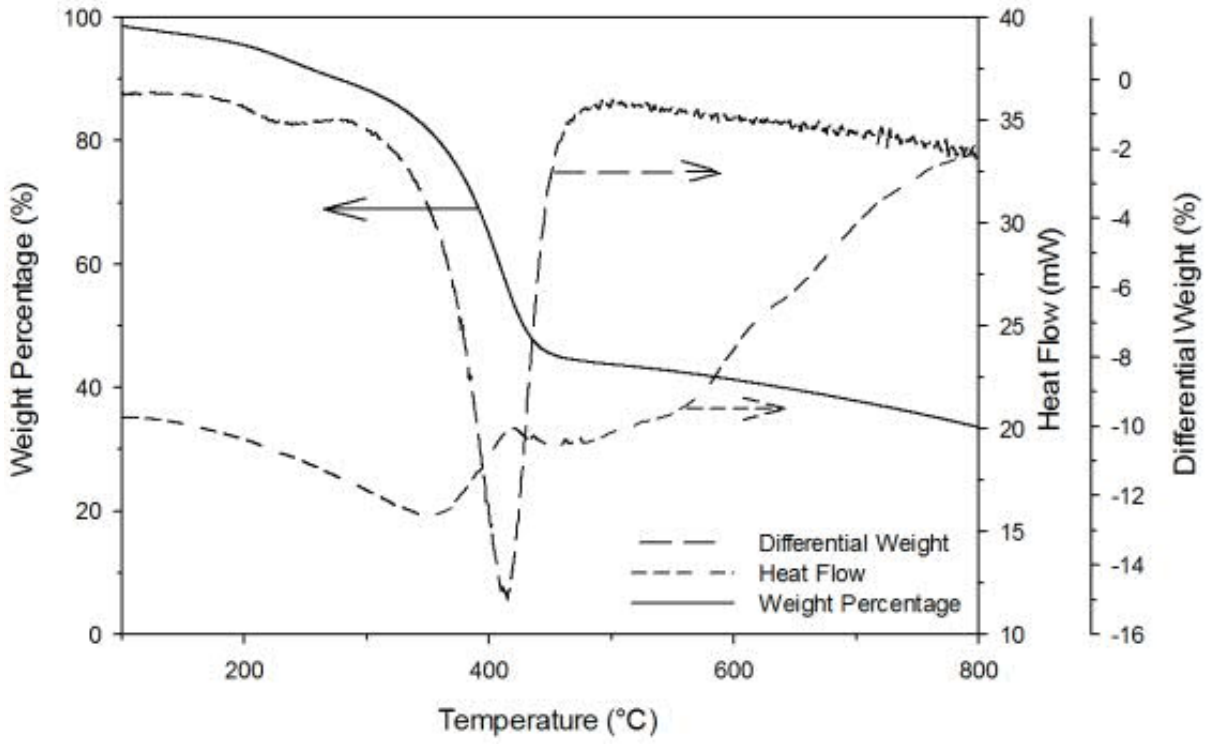

Figure S3.1. Thermogravimetric analysis (TGA) of as-prepared fiber mats from 100 - 800 °C.

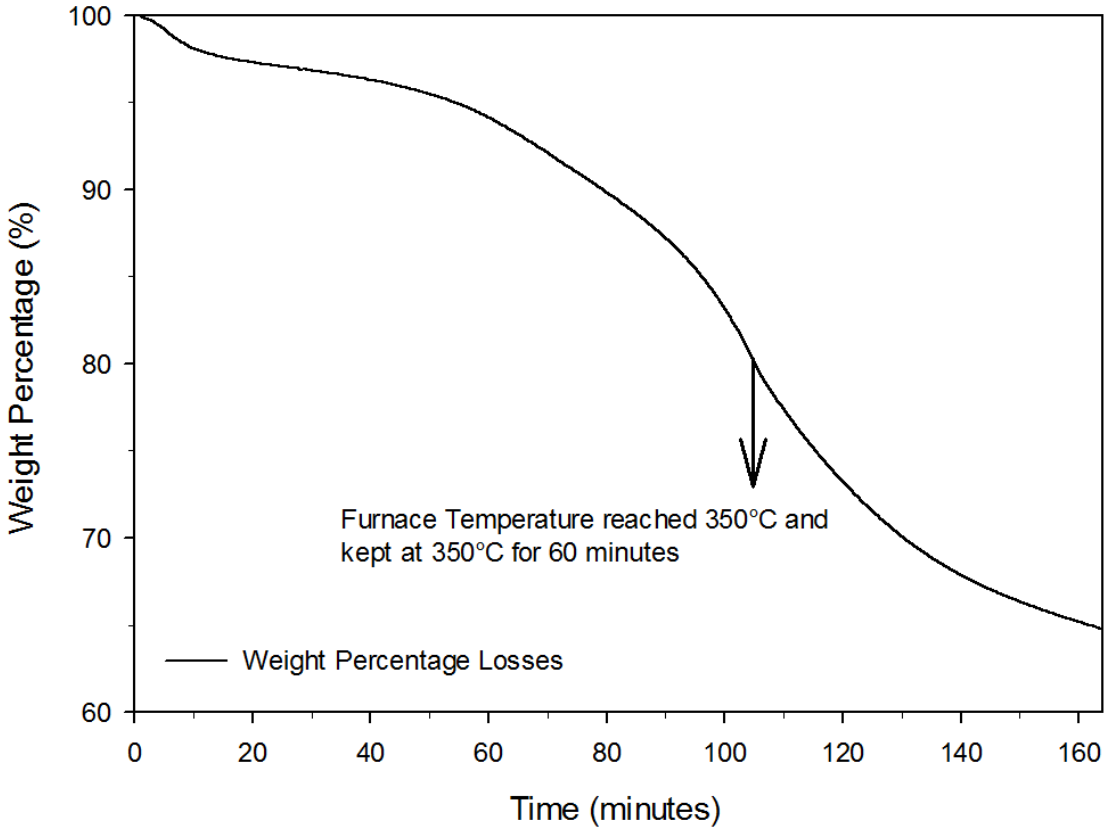

Figure S3.2. Thermogravimetric analysis (TGA) of as-prepared fiber mats from RTP to 350 °C.

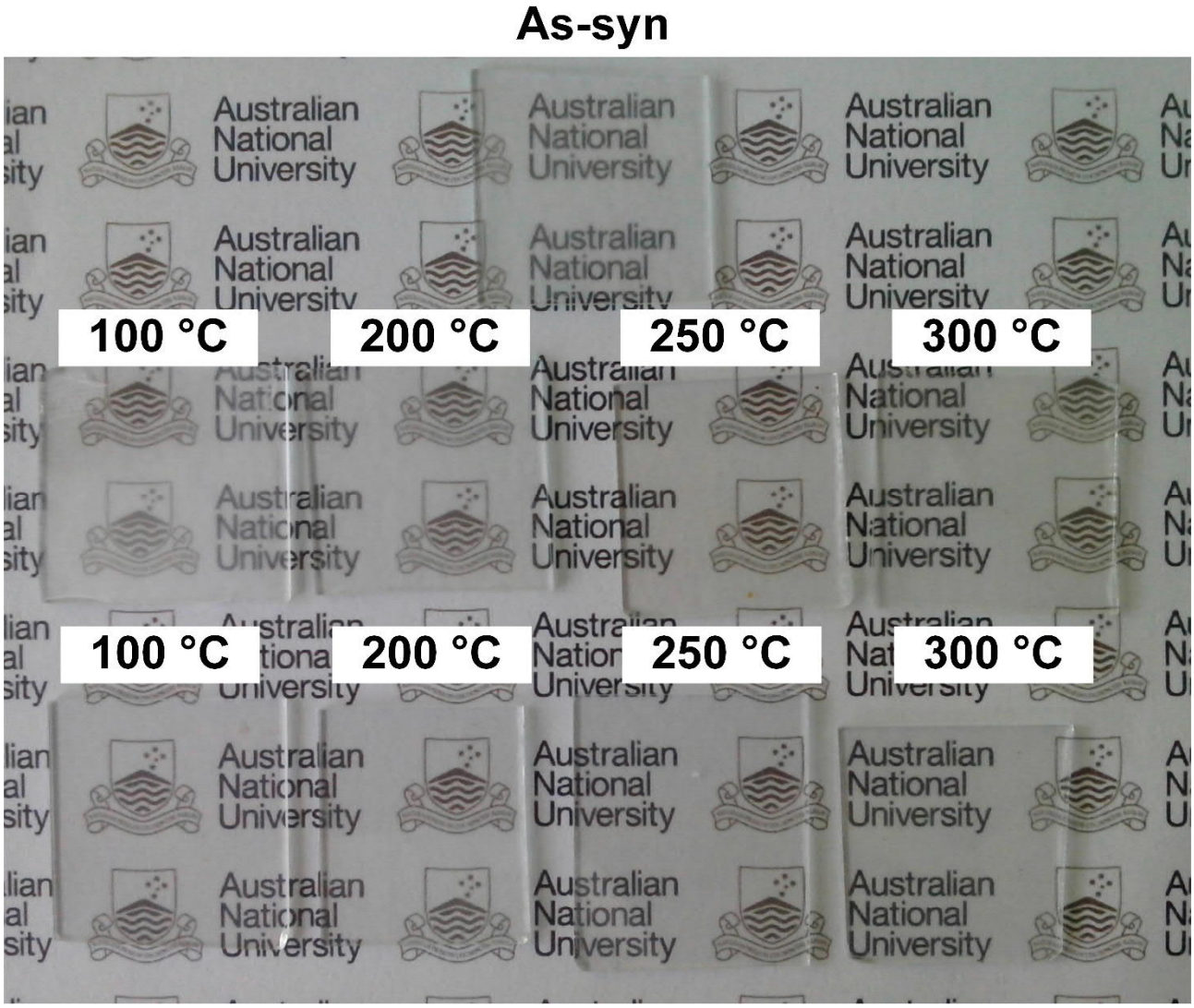

Figure S3.3. Higher resolution images of insets from Figure 3.5 with as-prepared (as-syn) nanofibrous samples up to 500 °C calcination treatment.

4. Adhesive Superhydrophobicity and the Ideal Petal-Effect

Abstract

Precise manipulation of water is a key step in numerous natural and synthetic processes. Here, a new flexible and transparent hierarchical structure is determined, which allows ultra-dexterous manipulation and lossless transfer of water droplets. A three-dimensional (3D) nano-mesh is fabricated in one-step by scalable electrospinning of low-cost PS solutions. Optimal structures are composed of a mesh of dense nanofiber layers vertically separated by isolated mesoporous micro-beads. This results in a highly adhesive superhydrophobic wetting state that perfectly mimics the rose petal effect. Structural-functional correlations are obtained over all key process parameters, enabling robust tailoring of the wetting properties from hydrophilicity to lotus-like Cassie-Baxter and rose-like Cassie-impregnating states. A mechanistic model of the droplet adhesion and release dynamics is obtained alongside the first demonstration of a mechanically induced transfer of micro-droplets between two adhesive superhydrophobic coatings. This low-temperature reaction-free material structure demonstrates a facile means for the fabrication of impenetrable residue-less rose petal-like surfaces with superhydrophobic contact angles (CAs) of 152 ± 2° and effective adhesion strength of up to 113 ± 20 μN. This is a significant step towards the development of parallel; multi-step droplet manipulation protocols, with applications ranging from flexible on-paper devices to micro-fluidics and portable/wearable biosensors.

4.1. Introduction

Water is a significant component of our biosphere; a universal solvent used in numerous synthetic and natural processes; and an essential molecule for life. Its precise manipulation holds significant industrial and scientific potential. In the last decades, fabrication of micro- and nano-scale features that enable tailored wetting states has revolutionized our ability to interact[179] with and process liquid H_2O[40]. This has led, for example, to the rapid development and commercialization of a new generation[574] of microfluidics devices with applications ranging from DNA sequencing[575] to micro-bioreactors for drug discovery[41]. Current droplet manipulation systems are limited by their inability in transferring and handling single droplets outside a carrier liquid. Engineering hierarchical surfaces capable of mechanically controllable droplet pinning and release is a key step toward development of smarter and more efficient[69,574] bio-sensing and processing technologies.

Droplet manipulation in microfluidic devices currently relies on the complementary usage of low adhesion lotus leaf-like surfaces with hydrophilic patterns. These coatings are, however, impractical for multi-step transport and transfer of micro-droplets. Hydrophilic and hydrophobic surfaces result in partial fluid dispersion and potential contamination of the initial droplet volume. Alternatively, impenetrable lotus-like coatings do not allow sufficient adhesion for droplet manipulation.[7,83,133] A very recently characterized wetting state, naturally observed on rose petals,[137,140] has been proposed as a potential bioinspired property that could impede surface wetting while achieving highly adhesive droplet pinning[38,143].

In contrast to the well-investigated lotus effect,[18] the fundamental mechanisms underlying rose petal surfaces are still heavily debated. Adhesive superhydrophobic coatings have only been sporadically reported, mostly, with no systematic investigation of the adhesion strength or droplet transferability. From a technical perspective, the rose petal effect was observed within transitional regions between Cassie-Baxter (non-wetting)[4] and Wenzel (full-wetting)[3] states and has been recently classified as Cassie-impregnating[10]. Contrary to both the Cassie and Wenzel states, the latter mechanism does

not require formation of large air pockets between surface asperities (Cassie),[4] or full penetration in micro-structural features (Wenzel).[3] Instead, it is proposed as an intermediate state achieved by partial penetration of one or more levels of surface features[10], maintaining smaller air pockets while enabling high droplet adhesion.[137]

Adhesive superhydrophobic coatings have been fabricated by several methods, such as the deposition of particulate raspberry-like films,[295] liquid flame spray,[135] templating,[138,143] and multi-step electrospinning of fluorinated PI films[142]. Very recently, PDMS pillars[39] and wrinkled gold films[17] have shown great potential for droplet manipulation. However, the achievement of ideal rose petal surfaces remains challenging and controlled release of micro-droplets between two non-wetting superhydrophobic surfaces has not yet been demonstrated. Its achievement represents key steps in enabling multi-step manipulation and processing. Thus, the identification of primary structural properties underlying a perfect Cassie-impregnating state is of considerable commercial and scientific impact.

Amongst scalable synthetic routes that enable fine-tuning of nano and micro-scale features, electrospinning is a very versatile, low-cost method offering a wide range of structural optimizations.[84] It has been previously applied to the fabrication of both superhydrophobic[83,373] and superhydrophilic coatings with hierarchically ordered micro- and nano-scale porosities[95]. Lotus leaf-like films with high CAs (> 150°) and low sliding/rolling angles (< 10°)[83,191] have been obtained by electrospinning beaded morphologies[133,371]. At the other structural extreme, fibrous morphologies result in WCAs below 150°, possibly due to water penetration within their comparatively larger surface porosity[133,373].

Here, we present a low temperature, reaction-free, facile and scalable method for the one-step synthesis of transparent rose petal biomimetic coatings for micro-droplet manipulation and lossless transfer. A high performing 3D nano-mesh morphology featuring highly adhesive superhydrophobic wetting was achieved by optimal electrospinning of hybrid fiber-bead hierarchical textures. Key

structural properties were determined to tune the wetting properties from lotus leaf-like to rose petal-like. These flexible nano-mesh morphologies result in robust superhydrophobic CAs of 152 ± 2° and effective adhesion strength of up to 113 ± 20 μN. Ultra-dexterous droplet manipulation was demonstrated by mechanically inducing the lossless transfer of micro-droplets between two superhydrophobic coatings, as defined by previous studies[138,143]. A mechanistic description of the wetting-transfer mechanism is proposed alongside the observed droplet release dynamics. The empirical model developed vastly improved understanding of the required key structural properties for the fabrication and analysis of the ideal petal-effect.

4.2. Results and Discussion

Nano-Mesh Self-Assembly

Optimal electrospinning of PS micro- and nano-structures was initially achieved by systematic investigation of a broad set of process parameters. These included spinning distance, electric potential, precursor concentration, composition and feed-rate. The incorporation of dodecyl trimethyl ammonium bromide (DTAB) was found to considerably increase control of structural features and coating homogeneity. This is in line with the current understanding of the interaction between cationic surfactants[576] with polymer solutions during electrospinning. The coating morphology was then tuned to three distinctive reproducible layered structures (Figure 4.1a-c), hereafter referred to as heavily beaded, partially beaded and fibrous. Fibrous films (Figure 4.1c) consisted of a vertically stacked network of mesoporous fiber layers. They featured the smallest (< 100 nm) surface pore size distribution (Figure 4.1f) and the largest variation in fiber diameters (Figure 4.1c) with an average fiber diameter of 5.0 ± 0.7 µm. The heavily beaded films (Figure 4.1a) were made of a dense assembly (ca. 650 beads / mm^2) of relatively small micro-beads, 7.1 ± 0.2 µm in diameter, occasionally separated by very thin nanofibers at 176 ± 3 nm in diameter. While these small fibers displayed mostly pore-free surfaces, the micro-beads revealed a mesoporous structure with most pores below 200 nm in diameter (Figure 4.1d).

A third distinctive morphology having a unique cross-sectional structure was achieved by controlled beading during electrospinning of fibrous films (Figure 4.1b). These were mostly composed of non-porous sub-micrometer fibers of 418 ± 38 nm (Figure 4.1b) in diameter and a few large beads (ca. 160 beads / mm^2) having an average diameter of 13.5 ± 0.6 µm (Figure 4.1e). The latter had a similar surface pore structure as that observed on the heavily beaded coatings with slightly larger pore diameters distributed between 200 and 400 nm. A key feature of these partially beaded films was the self-assembly of a stacked structure of hierarchical fibrous layers vertically spaced by the large micro-

beads. This 3D fiber layer distribution resulted in a nano-mesh structure with inter-fiber pores ranging from a few to tens of micrometers.

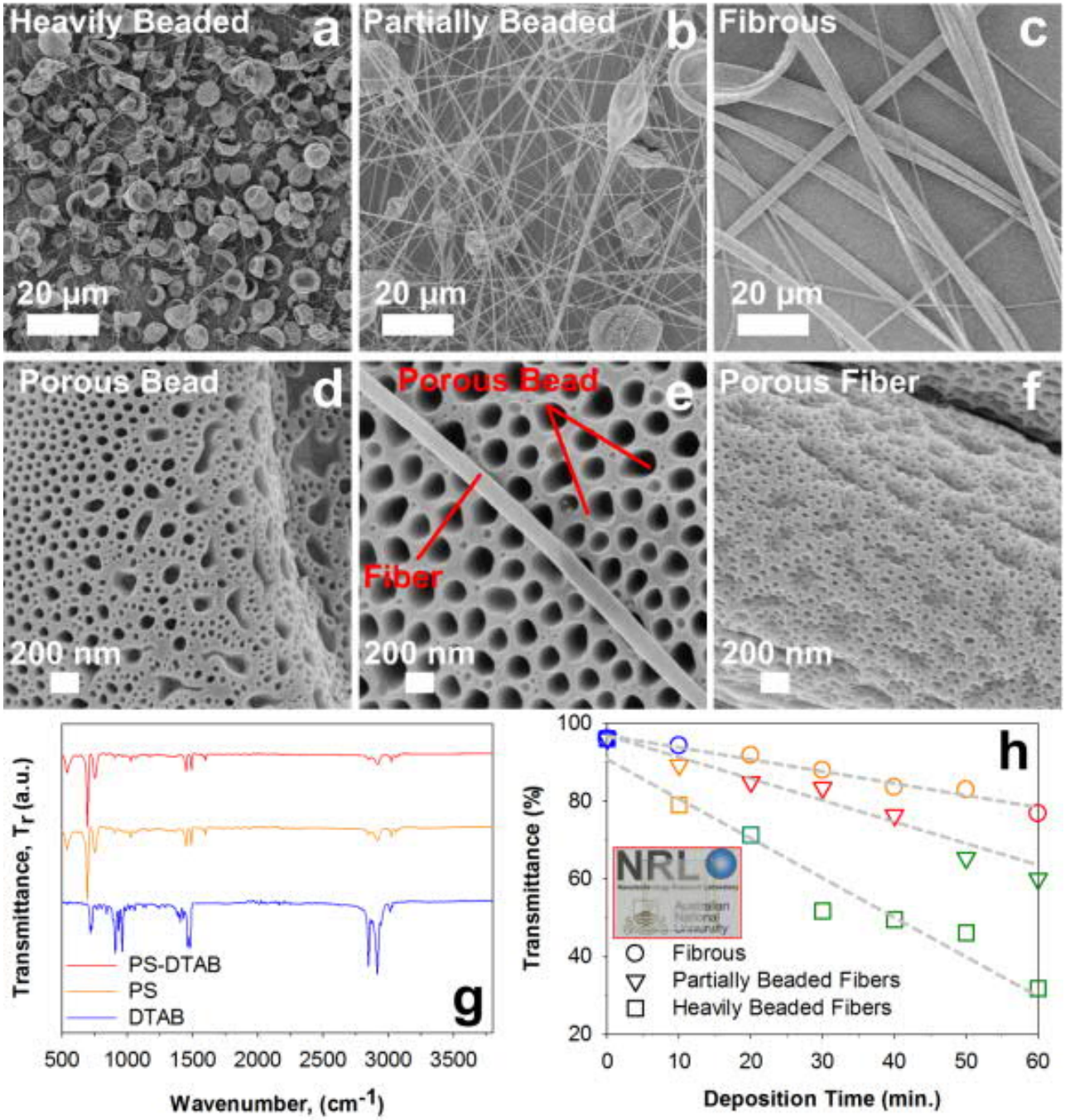

Figure 4.1. SEM structural analysis at low (a-c) and high (d-f) magnifications, and g) chemical and h) optical characterization of the three key PS hierarchical morphologies having distinctive functional wetting regimes. a) Heavily beaded films lead predominantly to lotus leaf-effect (h, green symbols), b) partially beaded to rose petal-effect (h, red symbols), and c) fibrous to hydrophobic/hydrophilic (h, blue and orange symbols). g) Fourier Transform Infrared Spectroscopy of all morphologies (red line) indicated a consistent pure PS (orange line) surface composition. Optical image (h, inset) of an ideal rose petal surface (30 min deposition) shows its transparency.

For all morphologies, Fourier Transform Infrared Spectroscopy (FTIR) analysis of the electrospun films (Figure 4.1g) reveals only the presence of PS. This indicates that DTAB is mainly contributing to the optimization of film morphology, with no significant alteration of its surface chemistry. This facilitated a direct structural comparison of the wetting performance between fibrous, partially and beaded films. Furthermore, notwithstanding the large variation in micro-structural morphology, all films possessed the hierarchical mesoporous conformation (Figure 4.1d-f) typically required for superhydrophobicity.[577] The nano-scaled structures (Figure 4.1d-f) on beads and fibers prevented complete droplet penetration, while the micro-voids (Figure 4.1a-c) present between fibers provided zones for partial penetration. The combination of such differentiating mophologies enabled the unique Cassie-impregnating regime. Macro-uniformity of our coating in this instance, corresponds to an average pitch distance of << 100 µm, and thus does not have any significant impact on effective wettability.

Optical UV-vis analysis of these three characteristic morphologies was performed as a function of the electrospinning time. This enabled the assessment of the impact behind hierarchical structural features on resulting film properties. This evolution was, more importantly, correlated with increasing cross-sectional thicknesses. The fibrous films were the most transparent (Figure 4.1h, circles), with transmittance in the visible range (λ = 600 nm) decreasing from 94% to 77% with deposition time increasing from 10 to 60 min. This was in line with the low scattering properties of micro-scale fibers and the inherently low absorption of PS at such low photon energy levels. Most importantly, the transmittance decreased linearly with increasing deposition time indicating uniform fiber formation and consistent structural properties within the range investigated. Up to 40 min, the optical properties of the partially beaded films (Figure 4.1h, triangles) closely followed that of the fibrous morphology with ca. 7% less transmittance. This is mainly attributed to light scattering from the few micro-sized beads distributed in the nano-mesh structure (Figure 4.1b). Further increasing the deposition time considerably increased the optical losses through these films, resulting in more than 15% less transmittance when compared to fibrous films at 50 and 60 min (Figure 4.1h, triangles and circles).

This suggests that, above 40 min of deposition time, the beads reach sufficient surface density to scatter a significant fraction of the incoming light. In line with the SEM analysis (Figure 4.1a), the heavily beaded films were the least transparent (Figure 4.1h, squares) with up to 15-50% lower transmittance than purely fibrous films. This is attributed to the high density of light-scattering beaded micro-structures, effectively coating the entire substrate surface. Within minor variations, the distinctive morphologies preserved their corresponding profiles with increasing deposition time.

Wetting Regimes and Performance

These three morphologies revealed a very distinctive wetting profile, with robust rose petal-like wetting achieved primarily with the partially beaded 3D nano-mesh structures (Table 4.1). For all films, the static CA (Figure 4.2a) increased continuously with increasing deposition time up to 30 min. Superhydrophobic wetting (CA > 150°) was attained for both heavily and partially beaded morphologies upon a deposition time of 20 min. In contrast, fibrous morphologies consistently required thicker films, resulting initially in hydrophilic coatings (Figure 4.2a, blue circles) and achieving mostly hydrophobic wetting (orange circles). Superhydrophobic adhesive wetting was obtained only after 60 min of deposition time. This was attributed to the large pore size of the purely fibrous morphology (Figure 4.1c) facilitating direct contact with the underlying hydrophilic glass substrate, and thus requiring thicker coatings. Upon 20 min of deposition, the heavily beaded films resulted in consistent lotus leaf-like droplet rolling seen in typical superhydrophobic dewetting (Figure 4.2a, green squares). This is attributed to the high density of hydrophobic PS beads that cover the substrate surface (Figure 4.1a), effectively impeding water penetration into the lower film layers.

In contrast, the partially beaded layered fiber morphology resulted initially in hydrophobic coatings and achieved rose petal-like Cassie-impregnating wetting between 20 to 40 min deposition time (Figure 4.2a, red triangles). Further increasing the deposition time to 50 and 60 min resulted in lotus leaf-like non-adhesive superhydrophobicity (green triangles). This behavior is consistent with the observed SEM structure and UV-vis time evolution, showing significantly high bead densities above

40 min deposition. Here, it is proposed that sufficient nano-mesh thickness is required to completely avoid water contact with the underlying substrate. However, exceedingly high film thicknesses result in high bead density (*e.g.* low pitch distances), effectively leading to wetting that is similar to that observed for the heavily beaded morphologies (Figure 4.2a, squares).

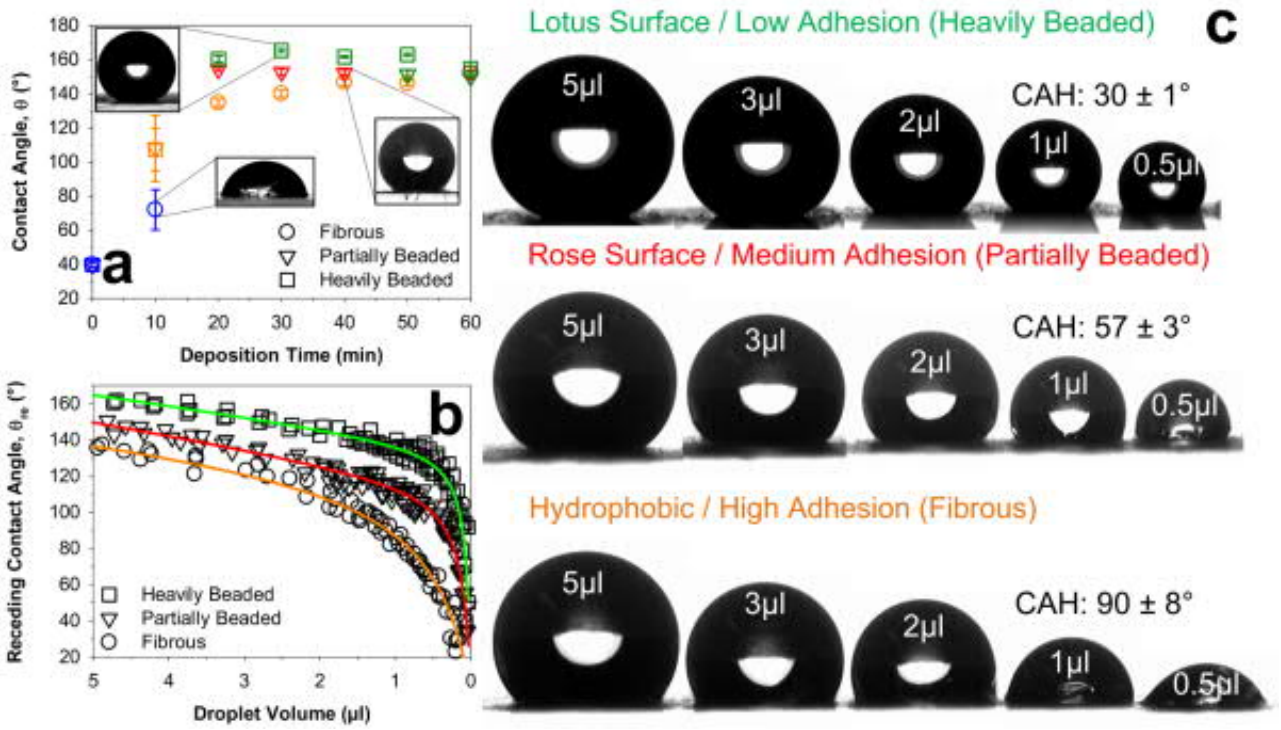

Figure 4.2. Functional-structural characterization of the three distinctive hierarchical morphologies. Measurement of the a) static CA as a function of the electrospinning time shows that both heavily (square) and partially (triangles) beaded films obtain superhydrophobic wetting upon 20 min, with the former leading to lotus leaf (green symbols) and the latter to rose petal effect (red symbols). In contrast, fibrous films wetting (circles) changes from hydrophilic (blue symbols) to hydrophobic (orange) and superhydrophobic with increasing deposition time. These regimes were confirmed (b-c) by RCA measurement[135] of fibrous, heavily and partially beaded films with a 40 min deposition time. ACAs were measured by the standard drop-out technique (Supporting Information, Table S4.1).

These findings were further confirmed by (evaporative) CAH characterization of representative film morphologies (Figure 4.2b,c). Overall, the results were in very good agreement with the observed structural-functional correlations (Figure 4.2a). They reveal a characteristic and well-defined wetting hysteresis profile for each morphology (Figure 4.2b, c). For a Cassie-impregnated regime the CA (θ) is expressed as:[132]

$$cos\theta = 1 + f_{SL}(cos\theta_0 - 1) \quad (4.1)$$

where f_{SL} is the fraction of solid-liquid interface, θ_0 is the characteristic static CA.

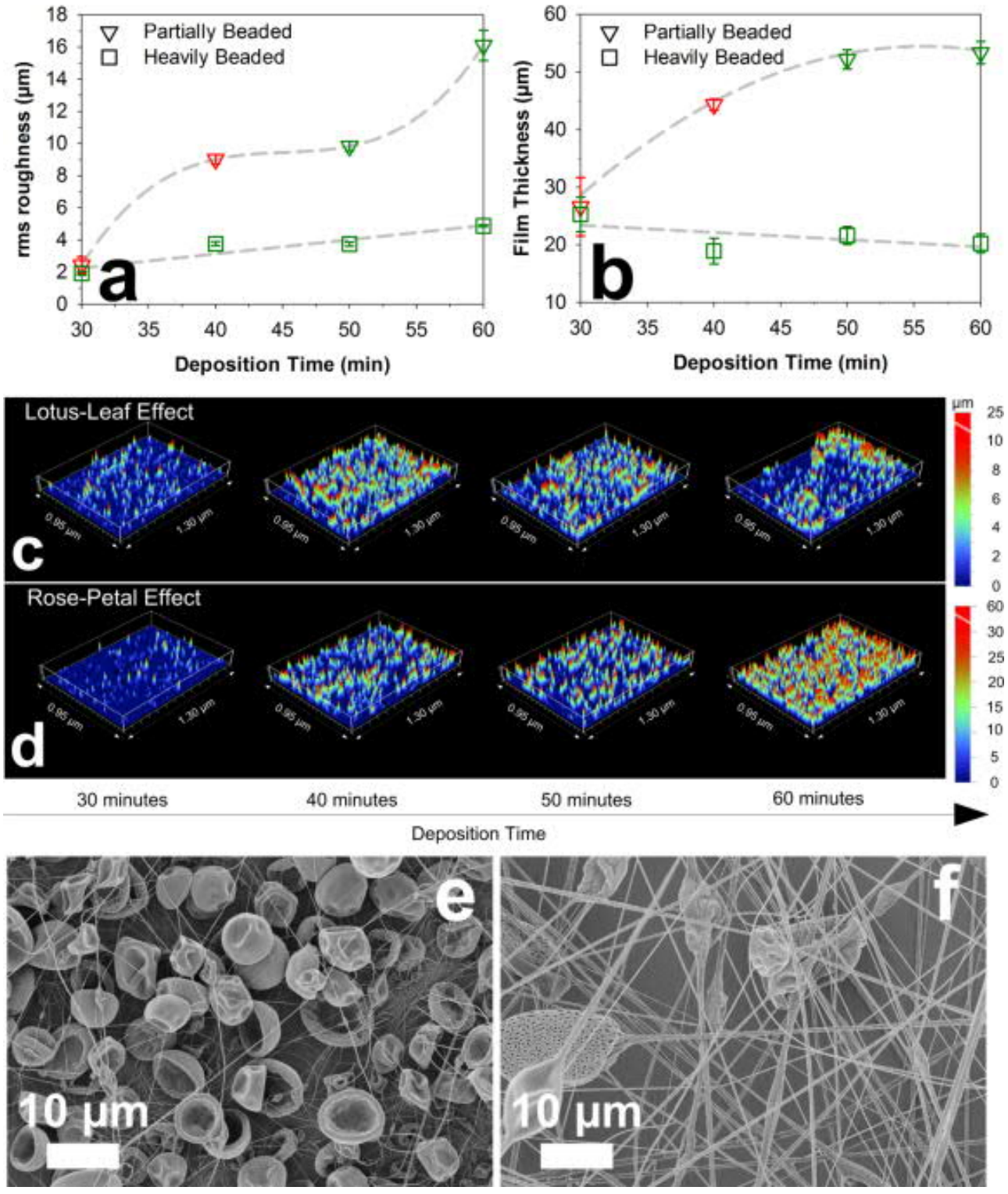

Figure 4.3. Structural evolution characterization of lotus leaf (green symbols) and rose petal-like (red symbols) wetting states. The a) root-mean-square roughness, rms, and b) thickness of heavily and partially beaded films was measured as a function of deposition time by white light interferometry (WLI) and critically compared to the resulting wetting properties. Their (c,d) macro-scale topologies and (e,f) SEM analysis confirm an increase in bead surface density with increasing deposition time that results in lotus leaf-like superhydrophobicity.

On an ideally smooth and homogenous surface, the static CA corresponds to a unique equilibrium position of the solid-liquid-air contact line (triple line). On a rough surface, there exists a range of equilibrium CAs. The use of CAH[135,137] is thus of key importance in assessing variable surface adhesion. In this work, CAHs computed from drop-out ACAs and evaporative RCAs[134,135] were used to analyze key differences between surfaces synthesized.

Heavily beaded films had a CAH of 30° ± 1° in line with previous reports on low adhesive lotus leaf-like surfaces.[135] Fibrous morphologies exhibited a CAH of 90° ± 8° that is common for overly adhesive hydrophobic coatings.[135] The nano-mesh structures (partially beaded layers) had a consistent CAH of 57° ± 3° exhibiting an intermediate adhesion state between lotus and hydrophobic films (Figure 4.2c). This unique domain preliminarily confirms the achievement of a rose petal-like Cassie-impregnating state.

The structural-wetting correlations observed for these three key morphologies (Figure 4.2) were further investigated (Figure 4.3) by white light interferometry (WLI). At up to 30 min deposition time, both heavily and partially beaded morphologies (Figure 4.3a,b) exhibited similar root mean square (rms) roughness (2 µm) and thicknesses (25 µm), with the former displaying a higher density of micro-sized structures (Figure 4.3c,d). This is in line with the SEM analysis (Figure 4.1a), and is attributed to the higher bead density in those morphologies. Increasing the deposition time increased the rms roughness of the heavily beaded films from 2 to ca. 4 µm while the detected WLI thickness was nearly constant. This is attributed to the limitations of the WLI technique in the analysis of film thicknesses for very rough films. These steady structural properties are in good agreement with the observed wetting behaviors of the heavily beaded films, which presented lotus-like superhydrophobicity for all deposition times.

In contrast, investigation of the partially beaded films revealed fundamentally different self-assembly dynamics. Their rms roughness increased rapidly from ca. 2 to 16 µm with deposition time increasing from 30 to 60 min (Figure 4.3a, triangles). In parallel, the film thicknesses increased from ca. 25 to

55 µm (Figure 4.3a, triangles). Cross-comparison with CA measurement (Figure 4.2a, triangles) indicated that film thickness and rms roughness below 50 and 9 µm, respectively, are required for achievement of a Cassie-impregnating wetting state. This is attributed to the droplet adhesion mechanism of the nano-mesh morphology. In fact, while the beads resulted in the formation of a distorted three-phase line promoting superhydrophobicity, the nano-fibrous mesh was found to serve as a penetrable layer for micro-droplet adhesion. Increasing the deposition time to 50 min, the nano-mesh films experienced a transition to lotus-like behavior with SAs of 40 - 50° (Table 4.1). This is attributed to the increase in surface roughness and bead density (Figure 4.3d). Presumably, the depositing bead-to-fiber ratio is higher than the ideal equilibrium ratio needed for the petal-effect. With increasing deposition time, increased bead density results in a hardly penetrable small-pore layer that causes a transitional drift from the petal- to the lotus- effect. These results demonstrate the first effective synthesis of highly adhesive superhydrophobic rose petal coatings by low-cost scalable electrospinning of optimal 3D hierarchical structures.

Table 4.1. Summary of the wetting and structural properties of representative morphologies.[a]

Sample Type	10 minutes	20 minutes	30 minutes	40 minutes	50 minutes	60 minutes
Heavily beaded fibers	Non-SH	Lotus SA: 28° ± 3°	Lotus SA: 37° ± 5°	Lotus SA: 57° ± 1°	Lotus SA: 72° ± 3°	Unstable Rose-Lotus
Partially beaded fibers	Non-SH	Defective Rose Effect	Rose Sticky SH	Rose Sticky SH	Lotus SA: 50° ± 5°	Lotus SA: 46° ± 4°
Pure fibers	Non-SH	Non-SH	Non-SH	Non-SH	Non-SH	Rose Sticky SH

[a]Non-SH - surfaces with static CAs of < 150°. Lotus - surfaces with static CAs of > 150° with a SA of < 90°. Rose - surfaces with static CAs of > 150° while being able to retain droplets at 180° inversion with perfect droplet transferability. Defective rose - rose-like behavior without perfect droplet transferability. Unstable Rose-Lotus - surfaces with static CAs of > 150° while being unstable in rose/lotus performance. SA of 5 µL micro-droplets.

Droplet Manipulation/Transfer and Mechanism

The feasibility of droplet manipulation and transfer by these different morphologies was assessed in terms of maximum adhesion strength and percentage of volume transferred (Figure 4.4). Despite the increasing research effort[21,38,135,138,142,143] on rose petal coatings, very few studies[138,143] have

demonstrated the transfer process (Table 4.2) or assessed post-transfer residue[578]. Here, the optimal nano-mesh structure resulted in an ideal rose petal-like Cassie-impregnating state demonstrating superhydrophobic wetting. It is capable of pinning 12 mg micro-droplets and 100% volume transfer with no detectable macro- and micro-residues on the original coating (Figure 4.4i).

Notably, variations of this ideal rose petal-like behavior were observed. One variant comes in the form of metastable rose-lotus transitional regions. Coatings from these domains possess very weak and unreliable adhesion strength (Figure S4.1). Alternatively, defective rose-like films possess exceedingly high adhesive strength, but suffers from poor transferability (Figure S4.2b). These were found to occur near the fringes of transitional hydrophobic-rose regimes (Figure 4.4d-g and Figures S4.3-4.4).

The adhesion strength of all morphologies decreased sharply for deposition times above 10 min. The heavily beaded films led to non-adhesive superhydrophobicity (Figure 4.4b, squares), the fibrous to highly adhesive hydrophilic/hydrophobic wetting (circles), and the partially beaded (triangles) to moderately adhesive rose petal-like pinning. This initial high adhesion state is attributed to interactions with the glass substrate and is in good agreement with the static CA analysis (Figure 4.2a). These thin films are, however, impractical for droplet manipulation as only small percentages of volumes were successfully transferred (Figure 4.4c) and they experienced large droplet to droplet variations.

Although the highest adhesion strength (Figure 4.4b, circles) was achieved with the fibrous films, these surfaces suffered from unreliability with persistent residual volume post-transfer (Figure 4.4c, circles). Furthermore, the excessive pinning could potentially lead to contamination. These defective regimes are attributed to the high instability of excessive surface porosity stemming from a predominantly fibrous interface, giving rise to disproportionate capillary/adhesion forces, thus preventing depinning. On the other extreme, the lotus leaf-like heavily beaded coatings had poor

droplet adhesion (Figure 4.4b, square), and were not capable of physical manipulation and controlled transfer.

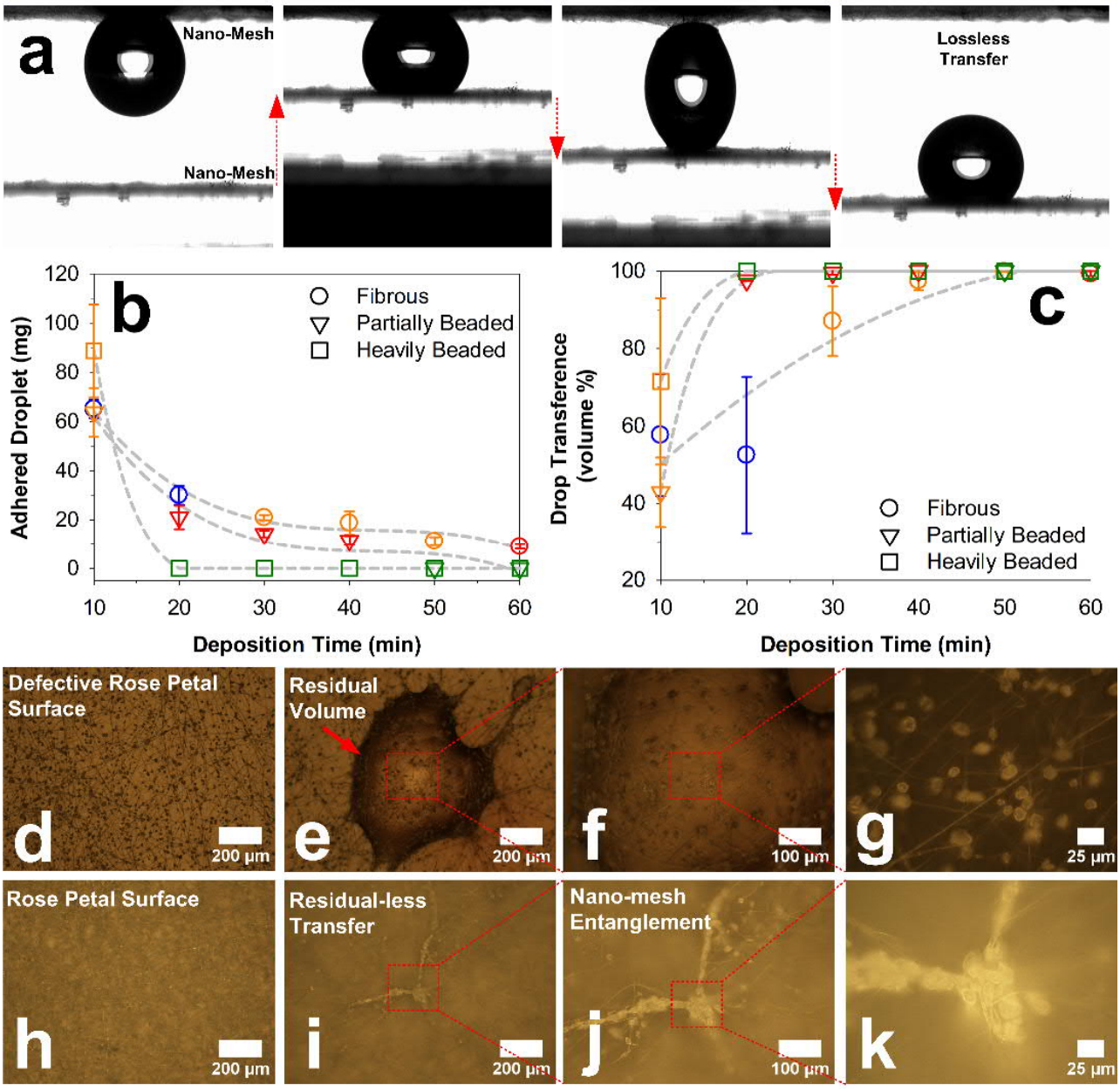

Figure 4.4. a) Demonstration of micro-droplet (5 µL) manipulation and lossless transfer between two optimal nano-mesh (40 min) superhydrophobic coatings. Characterization of droplet b) adhesion strength and c) transferability as a function of key structural properties (morphology and deposition time). Microscopic analysis of (d,e,f,g) residual volumes on defective rose petal surfaces and (h,i,j,k) residual-less transfer on rose petal surfaces.

The optimal nano-mesh coatings possessed a maximum adhesion strength of ca. 113 ± 20 µN corresponding to a droplet mass of 12 mg (Figure 4.4c, triangles). This also represents the maximum droplet size that can be transferred without cohesive failure. Here, we demonstrate the lossless[138,143]

micro-droplet transfer from a rose petal film to a hydrophilic glass slide (Figure S4.2a). A further exemplification of their superior capability was also demonstrated *via* the unprecedented cross-transfer of a 5 µL droplet between two superhydrophobic rose petal-like interfaces. This unique material wetting performance is of great potential for the development of advanced water and droplet manipulation devices.

The droplet transfer mechanism of the best performing nano-mesh structures (40 min deposition) were further investigated in detail. A main difference was observed between the transfer executed between rose petal to an equivalent rose petal or uncoated glass substrates. Upon contact, the latter showed an immediate (< 33 ms) desorption (Figure S4.2a) of the micro-droplet, while the former first required a mechanically induced pressure between the two substrates (Figure 4.4a). This is then followed by gradual separation along the vertical axes. The droplet transfer dynamics can be attributed to the different water desorption mechanism (Figure 4.5). Contact with the hydrophilic glass substrate resulted in the immediate horizontal spreading of the water on the lower hydrophilic interface. As a result, the droplet three-phase line on the top nano-mesh coating experienced a swift horizontal pull. This rapidly enlarged the contact area with the nano-mesh decreasing the amount of water trapped in each pore. This results in dominating surface tension forces that desorbs the droplet from the superhydrophobic petal-like surface. These forces are sufficient in overcoming both the Laplace pressure instituted by the original droplet profile and gravitational pull (Figure 4.5a).

In contrast, contact with another superhydrophobic nano-mesh coating preserved the initial droplet shape (Figure 4.5a). Thus, application of an external orthogonal force in releasing the droplet from its initial substrate is required. This slower mechanically-induced release enabled optical analysis[9] and quantification of the Laplace pressure and surface tension forces acting on the nano-mesh (Figure 4.5b).

Adhesion of the droplet to another rose petal-like coating was achieved by its compression between two substrates (Figure 4.5b, inset). This resulted in the highest Laplace pressure (Figure 4.5b, circles)

and minimal surface tension forces (triangles). The applied pressure was sufficiently high to overcome the Laplace pressure acting on the contact area (145 ± 0.1 μN/mm^2) and pushed the water-air interface through the pores of the bottom substrate nano-mesh.

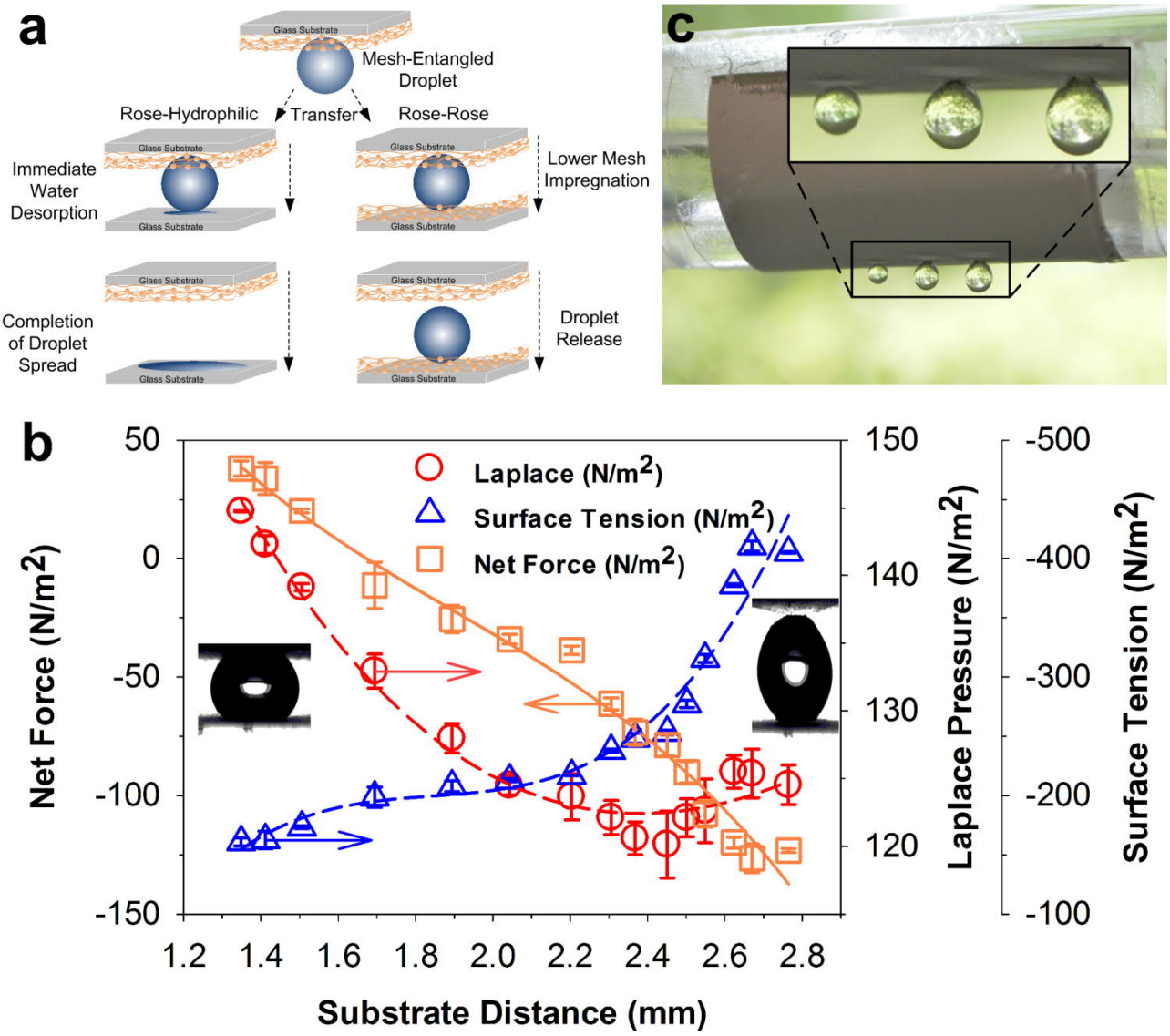

Figure 4.5. Schematic description a) of the droplet transfer mechanism from a nano-mesh coating to a hydrophilic surface and another rose petal coating. The nano-mesh release mechanics from b) rose to rose is explained through computation of the resultant force (square) acting on the mesh surface due to Laplace (circles), tension (blue) and gravitational forces as a function of the substrate distance. A positive force represents a repulsion and a negative one represents an attraction (pulling together) between the two surfaces exerted by the droplet. c) Application of the flexible nano-mesh coating (40 min) on a curved cylindrical surface exhibiting the rose petal effect (variable droplet size).

This enabled the partial infiltration of inter-layer spacing of the mesh (Figure 4.3f), resulting in the rapid relaxation of the curved water-air interface. In this state, the system experiences a local energy minimum. This results in an identical bottom and top adhesion strength, giving rise to a slight

repulsion force between the two substrates (Figure 4.5b, squares). Removal of the droplet from the surface requires overcoming the surface tension forces acting at the three-phase line which drives droplet adhesion.

Table 4.2. Comparison of Nano-Mesh performance with previous rose petal coatings.[b]

Synthesis Method	Process Steps	Static Contact Angle (°)	Static Droplet Size (µl)	Maximum Adhesion Strength (mg / µN / µNmm^{-2})	180° Inversion	Transferability of droplet (% vol.)	Ref.
Electrospun Nano-Mesh	1	152	5	12±2 mg / 113±20 µN / 144±23 µNmm^{-2}	Yes	100%	This Work
Electrospun Fibers	1	140	5	22±1 mg / 205±10 µN / 63±3 µNmm^{-2}	Yes	87%	This Work
SLSI-Lithography	5	151 / 154	5	-	Yes	-	[432]
Liquid Flame Spray NPs	1	159	10	-	No	-	[135]
Core Shell NPs	4	154	20	-	Yes	-	[433]
Electrospun F-PI	3	153	5	120 µN	Yes	-	[142]
Templating	5	151	3	12 mg	Yes	ca. 100%	[138]
Templating	2	162	3	59.8 µN	Yes	ca. 100%	[434]
Dropcasted RB NPs	4	146	5	37.5 µNmm^{-2}	Yes	-	[38]

[b]SLSI-Lithography - Soft-Lithography with NPs spray and immersion, NPs - Nanoparticles, F-PI - Fluoro-polyimides, RB - Raspberry-like hierarchical.

Increasing the substrate distance (Figure 4.5b) increases the surface tension forces while decreasing the repulsive Laplace pressure components, resulting in a pulling force between the substrates. This ultimately led to a higher force applied to the top nano-mesh, in part, due to the weight of the droplet (Figure 4.5b, squares). As a result, partial elastic deformation of the top nano-mesh (Figure 4.5b, inset) occurs, followed by pore enlargement and eventual droplet release. A maximum pulling force of 133 ± 0.4 µN/mm^2 was computed on the top surface just before droplet release. This force was found to be ca. 92% of the adhesion strength measured by gravimetric analysis (Figure 4.4c). Absolute force balances have also been included in the Supporting Information (Figure S4.5).

The droplet transfer mechanism from one petal surface to another was found to rely on an asymmetrical force balance (Figure 4.5b) caused by the gravitational force acting on the droplet mass (Figure 4.5b, insets). For a 5 mg droplet, this is 49 μN and is nearly half of the total net adhesion force exerted on the top mesh (Figure 4.5b and S4.5, orange lines). This results in a significant, ca. 50% higher force acting on the top nano-mesh that is sufficient to deform its pores enabling droplet detachment. This deformation strain is in line with the maximum droplet holding mass of 12 mg (113 ± 20 μN) upon which self-detachment occurs by the same pore stretching mechanism.

The adhesive strength of the optimal nano-mesh morphologies, achieved here, is among the highest reported for ideal Cassie-impregnating wetting (Table 4.2). The flexible hierarchical structure of the nano-mesh enables its application to both flat (Figure 4.4a) and curved substrates (Figure 4.5c). This is a key property that broadens its applicability to many applications such as micro-pipetting and -sampling.

4.3. Conclusions

A novel hierarchical material structure enabling reversible highly adhesive superhydrophobic pinning of micro-droplets has been demonstrated. This permits the robust one-step synthesis of biomimetic rose petal coatings by a scalable low-cost method. An optimal nano-mesh film morphology was obtained by 3D inter-stacking of biocompatible inert PS nanofiber layers separated by micro-beads, leading to an ideal Cassie-impregnating wetting state. This enabled the first complete micro-droplet transfer between two adhesive superhydrophobic surfaces, showcasing unique potential for water manipulation. This was a key step required for multi-step and multi-droplet parallel processing and thus represents a considerable leap-forward in numerous technologies such microfluidics systems, functional dry adhesives,[42] actuated droplet control systems,[39,42,579] and micro-reactor arrays[580]. A detailed mechanistic analysis of the droplet transfer dynamics was presented, providing an improved understanding of the Cassie-impregnating state. These findings demonstrate a low-cost scalable process for the engineering and fabrication of bioinspired petal-like surfaces. These proficient hierarchical textures provide highly precise volumetric manipulation, introducing an unexplored morphological profile for potential applications ranging from bio-sensing to water purification.

4.4. Experimental Section

Self-assembled hierarchical films of PS-based nano-structures were synthesized by electrospinning / spraying onto glass substrates as sticky superhydrophobic coatings. The use of dodecyl trimethyl ammonium bromide (DTAB) was used to improve electrospinning consistency; morphology and surface chemistry (enhancing surface charges). The one-step process of electrospinning and surface charge enhancement promotes the scalability of the method, in contrast to using a combination of hydrophilic-hydrophobic materials.[21,135,295,433]

Polymer Solution Preparation

PS (Sigma Aldrich, Mw = 280,000) (PS) solutions were made by dissolving respective masses (5-20 relative weight% of the solvent mass) in 10mL of tetrahydrofuran (Sigma Aldrich, anhydrous, ≥ 99.9%) (THF). Dodecyl trimethyl ammonium bromide (Sigma Aldrich, ≥ 98%) was also added to the polymer solutions at concentrations of 3.0 mg/mL. The polymer solutions appeared slightly clouded. Solutions were stirred for > 48 h prior to use. Care was also taken to ensure a homogenous suspension prior to and during electrospinning.

Electrospinning

An applied voltage of 5-25 kV was used with a working distance and flow rate of 10 cm and 1.0 mL h^{-1} respectively, providing homogenous coverage of fibers/beads on glass substrates mounted on a spinning drum for 10 min. Film morphologies belonging to films were determined by optical microscopy and analyzed as sets of matrices (data not presented). The reproducibility of these morphologies was established over three repeats, showing good reproducibility of structural and functional properties.

Various selected morphologies (heavily beaded/partially beaded fibers/fibrous) were further spun for 1 hour (on a spinning drum (diameter of 10 cm) rotating at between 300-400 RPM). The time-based spinning is hypothesized to allow effective control of pitch distances to achieve the desired wetting properties. Electrospinning was conducted using a 18G needle at 10-20 °C at a relative humidity of

between 40-60%. Samples chosen for assessment (through virtue of morphology) included the fibrous (20wt% PS at 2.5kV/cm), partially beaded (10wt% PS at 2.5kV/cm) and heavily beaded (8wt% PS at 1.5kV/cm).

Wetting Analysis

Films collected on glass slides were stored overnight to facilitate the completion of solvent evaporation prior to further testing. The static WCA was measured by placing and averaging 5 drops of deionized water (5-6 µL) on the sample surface. The SA was determined by placing a 5 µL drop of deionized water directly on sample surfaces prior to tilting *via* a goniometer. Results were averaged across 3 readings.

The CAH was measured from the drop-out ACAs (θ_{adv}, 0 to 5 µL) and evaporative receding angles (θ_{re}),[134,135] 3 readings each. The latter utilizes natural evaporation of a 5 µL droplet of deionized water. This evaporative procedure was chosen due to its greater sensitivity over the drop-in technique[135] as no interference from the deposition needle is present during withdrawal. The total evaporation time was mostly dependent from the coating and between 50 - 80 min at 20 - 25 °C and a relative humidity of 40 - 50% (Figure S4.6). Readings were taken at 5-minute intervals for the first 50 min and thereafter at 1-minute intervals until the droplet could no longer be determined *via* the computational fit (The fitting was deemed inaccurate below 0.5 µL).[135]

CAH was computed from the ACA at 5 µL ± 0.1 µL using the standard drop-in drop-out (DIDO) technique (0.5 µL/s) and the evaporative RCA at 0.5 µL ± 0.1 µL. Residual droplet analysis from the cross-transfer of water droplets was also assessed *via* optical fitting (before and after transfer to a hydrophilic glass slide). Dynamic and static images were recorded using a KSV CAM200 contact angle goniometer (Finland) with a heliopan ES43 camera (Japan).

The CA, SA and CAH were computed by a commercially available (CAM2008) program. Surface contamination analysis was further investigated by deionized water and a 1 wt% solution of silver nitrate (Univar, Ajax Chemicals), where 5 µL micro-droplets were deposited on various surfaces

using a micropipette followed by removal using a hydrophilic glass slide. Silver nitrate treated surfaces were then exposed to sunlight and allowed to dry while water-treated surfaces were analyzed within 60 s. Optical photographs (D3200, Nikon) and microscopic images (Nikon Eclipse E200, TV lens 0.55x DS) were later taken of the treated zones.

Adhesion Analysis

Adhesion forces of sticky superhydrophobic samples were analyzed *via* both optical and mechanical methods. The optical method involved the analysis of Laplace induced, surface tension and gravitational forces on the system.

$$F = \left(\pi R_3^2 \left(\frac{1}{R_1} + \frac{1}{R_2}\right) - 2\pi f R_3 \sin\theta\right)\sigma + m_o g \qquad (4.2)$$

Where σ is surface tension (0.072 N/m), θ represents the CA (measured on the right and left of droplet accounting to instances of asymmetry), f denotes the surface roughness, $m_o g$ is the gravitational force on the droplet and F is the net force centered on the top plate. Characteristic radii ($R_{1\text{-}2,}$ D_3) are elaborated in the Supporting Information (Figure S4.7).

Surface roughness (f) of 1 was used as per the standardized formulae. The actual f was computed based on 2 inverted droplets at equilibrium at 1.05 ± 0.01. An average contact area ($\pi D_3^2/4$) of 0.90 ± 0.03 mm^2 was used up to the beginning of significant droplet detachment. Thereafter, the contact area was measured for each frame varying from an initial 1.30 mm^2 to 0.22 mm^2. All frames were assessed using MSVisio at 400% magnification of native images.

The mechanical set-up which provided measurements of the maximum drop size (mass) held by inverted droplets (with a pinned feet of ca. 1.0 mm in diameter) was conducted using a mass balance with an accuracy of ±1 mg. Detailed experimental steps are included in the Supporting Information (Figure S4.8). Specific adhesion strength was calculated based on the pinned base area (ca. 1mm diameter) of the droplets on the best performing surfaces. Analysis was conducted between 12-15 °C at a relative humidity of 40-60%.

Surface Analysis

Morphological optimizations were first conducted using a light microscope (Nikon Eclipse E200, TV lens 0.55x DS) on coated glass substrates (Figure S4.9). These optimization experiments were conducted twice to ensure repeatability. The 3 distinct morphologies were segregated (data not presented) based on assessing the prevalence of beads over an area of ca. 0.31 mm^2 (480µm x 640µm). Selected samples were then analyzed *via* scanning electron microscopy (Zeiss UltraPlus analytical scanning electron microscope (FESEM) at 3kV) and white light interferometry (WLI). Prior to examination, SEM specimens were platinum sputter-coated for 2 min at 20 mA.

Average fiber and bead dimensions were analyzed *via* ImageJ using 50 counts of each nano / micro-structure. Selected sets of samples analyzed *via* a white light interferometer (Veeco, Wyko NT9100, U.S.A), was conducted at 50x magnification with a field of view of 1x *via* the vertical scanning interferometry (VSI) mode. An area of approximately 1.24 mm^2 was analyzed (typical wetting zone of superhydrophobic surfaces). A backscan of 60µm and length of 50µm was used with a modulation of 2% in order to cover the maximum height of films. Film thicknesses were then obtained by using the in-built "High Pass Filter" (Vision, Veeco) to remove anomalous data sets (data was computed from the origin). UV-vis analysis was conducted using a microplate reader (Tecan 200 PRO, Switzerland) from 300-800 nm with 10 scans per cycle. The visible wavelength ranges from 390 to 700 nm. Analysis of a point zone of 600 nm (without having to focus on the entire 390 to 700 nm range), provides a summary of the real-world optical transparency of the coatings. In addition, the use of 600 nm is almost in the middle of the visible wavelength, and is actually often used by biologists in determining optical density of cell cultures. Organic matter has the highest optical density at a wavelength of 600 nm, thus increasing sensitivity. These microdroplet reactors could eventually be used in droplet cell cultures, and representation of background spectroscopic data at 600 nm might be of future importance. Fourier Transform Infrared-Attenuated Total Reflectance (FTIR-ATR, Bruker-Alpha, U.S.A) was performed (24 scans from 400 to 4000cm^{-1}) on samples to

verify possible chemical modifications. All deviations are computed as standard errors unless otherwise indicated.

4.5. Supplementary Information

Figure S4.1. Unstable rose-lotus interface displaying weak surface penetration.

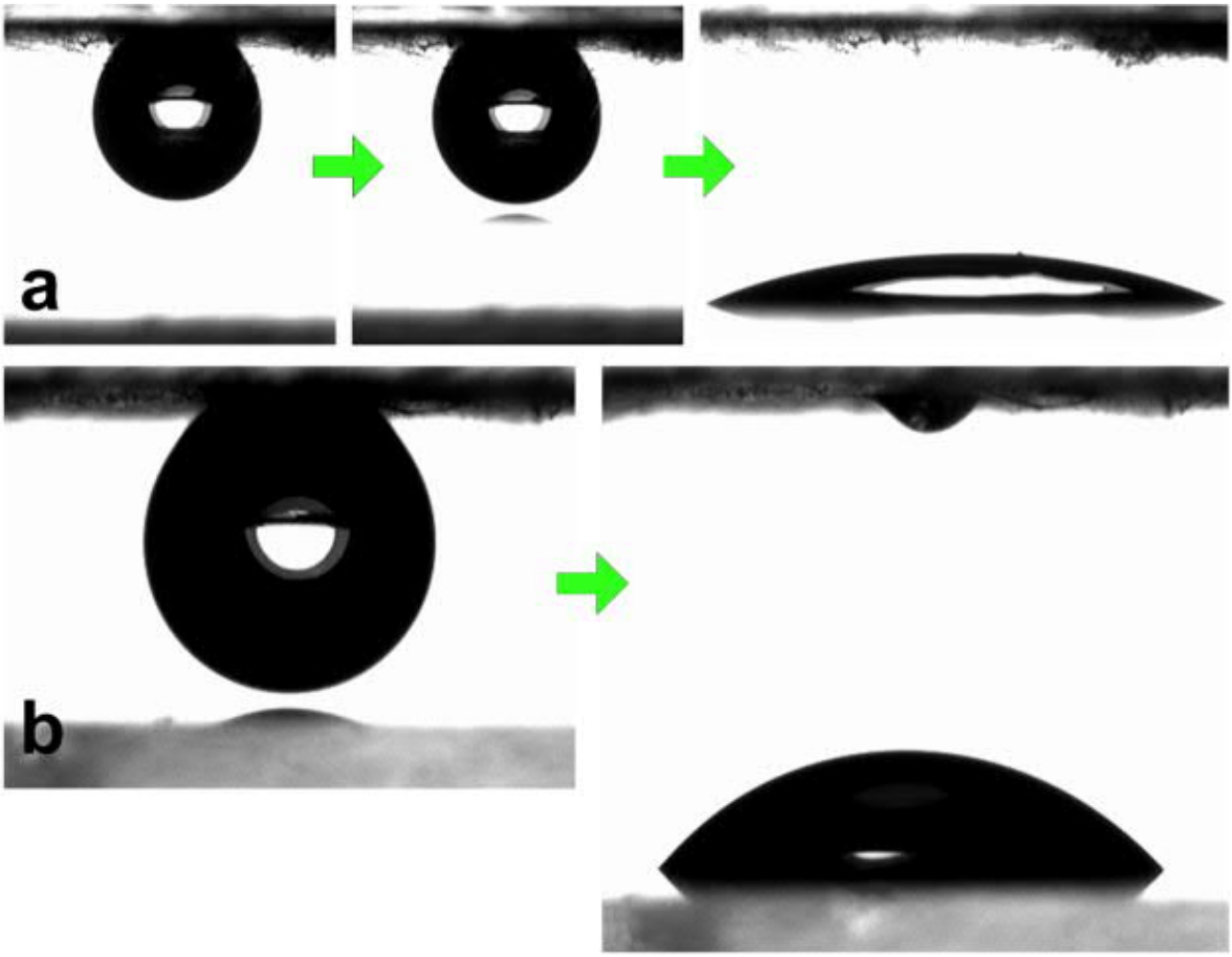

Figure S4.2. a) Droplet transfer between nano-mesh based rose petal and a hydrophilic surface. b) Overly adhesive (defective) rose petal surface with post-transfer residue.

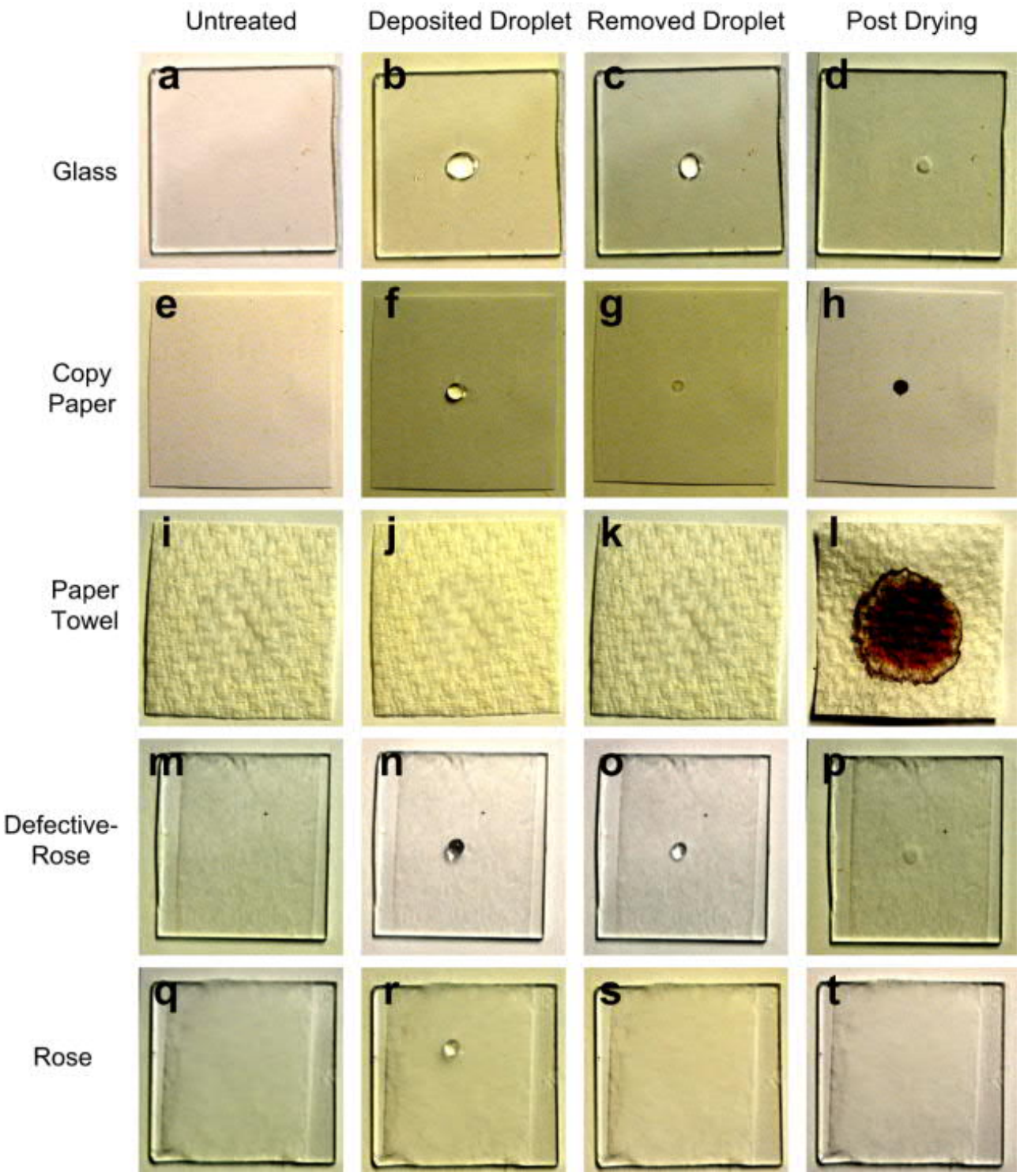

Figure S4.3. Staining of a (a,b,c,d) glass, (e,f,g,h) copy-paper, (i,j,k,l) paper towel, (m,n,o,p) defective rose petal and (q,r,s,t) ideal rose petal surface with a silver nitrate (1 wt%) water droplet.

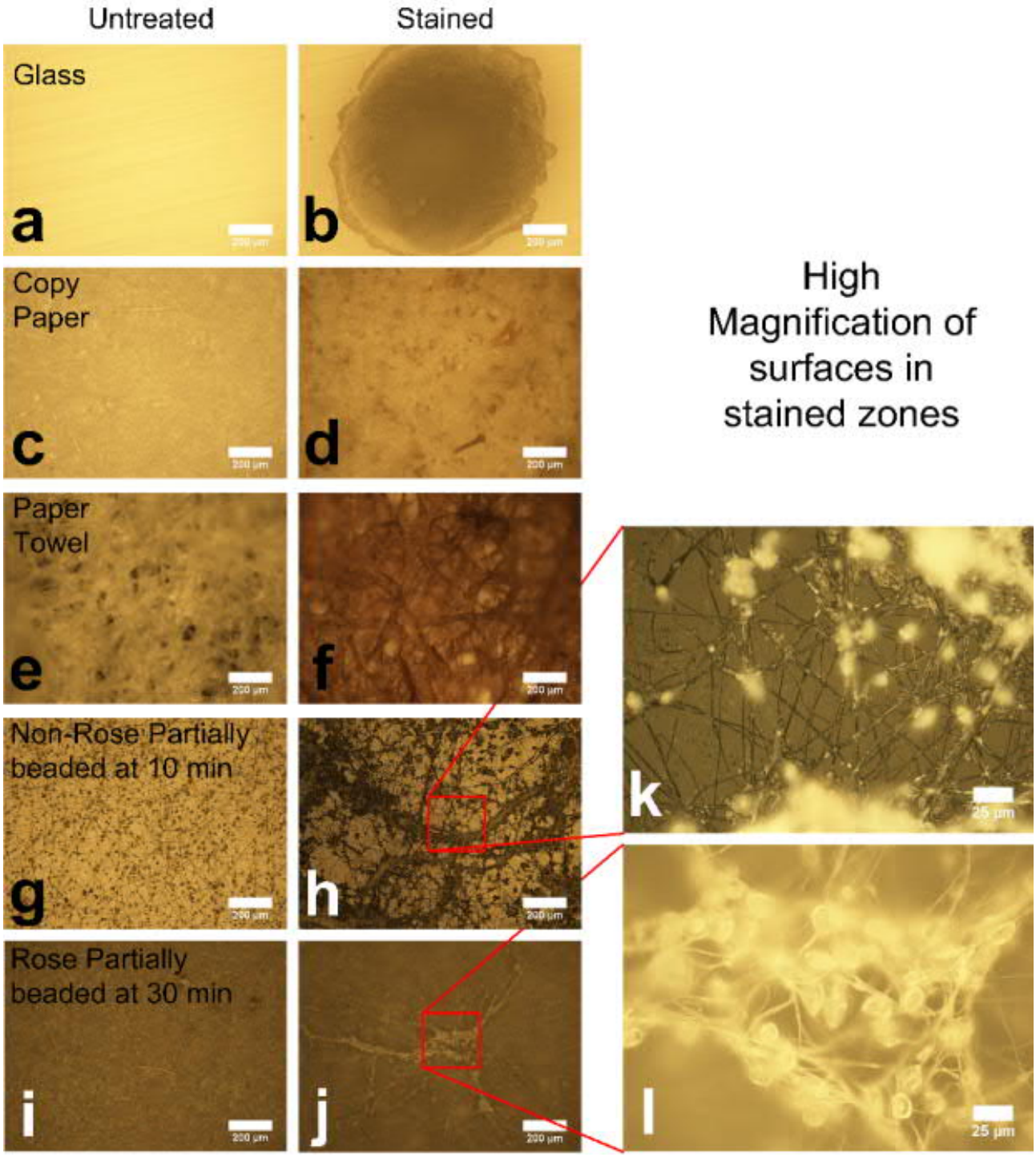

Figure S4.4. Staining dynamics of surfaces analyzed *via* optical microscopy for residue fluids for a (a,b) glass, (c,d) copy-paper, (e,f) paper towel, (g,h,k) defective rose petal and (i,j,l) ideal rose petal surface with a silver nitrate (1 wt%) water droplet.

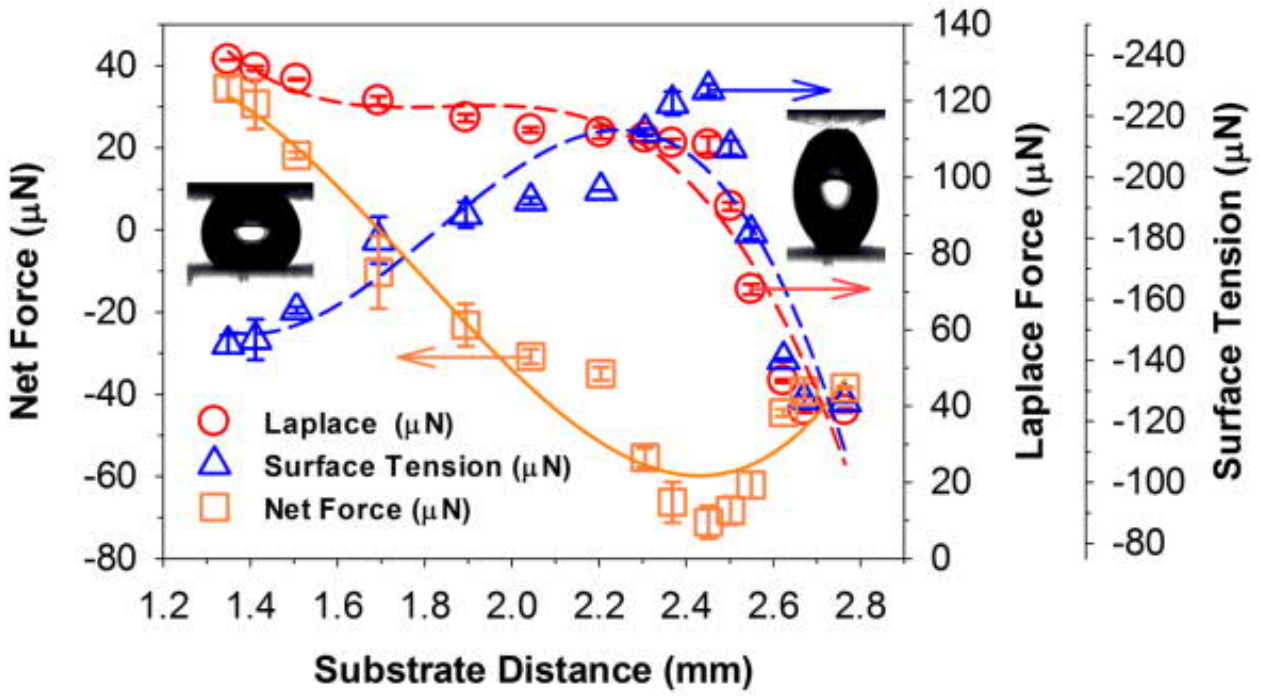

Figure S4.5. The nano-mesh release mechanics from rose to rose is explained through computation of the resultant force (square) acting on the mesh surface due to Laplace (circles), tension (blue) and gravitational forces as a function of the substrate distance. A positive force represents a repulsion and a negative one represents an attraction (pulling together) between the two surfaces exerted by the droplet.

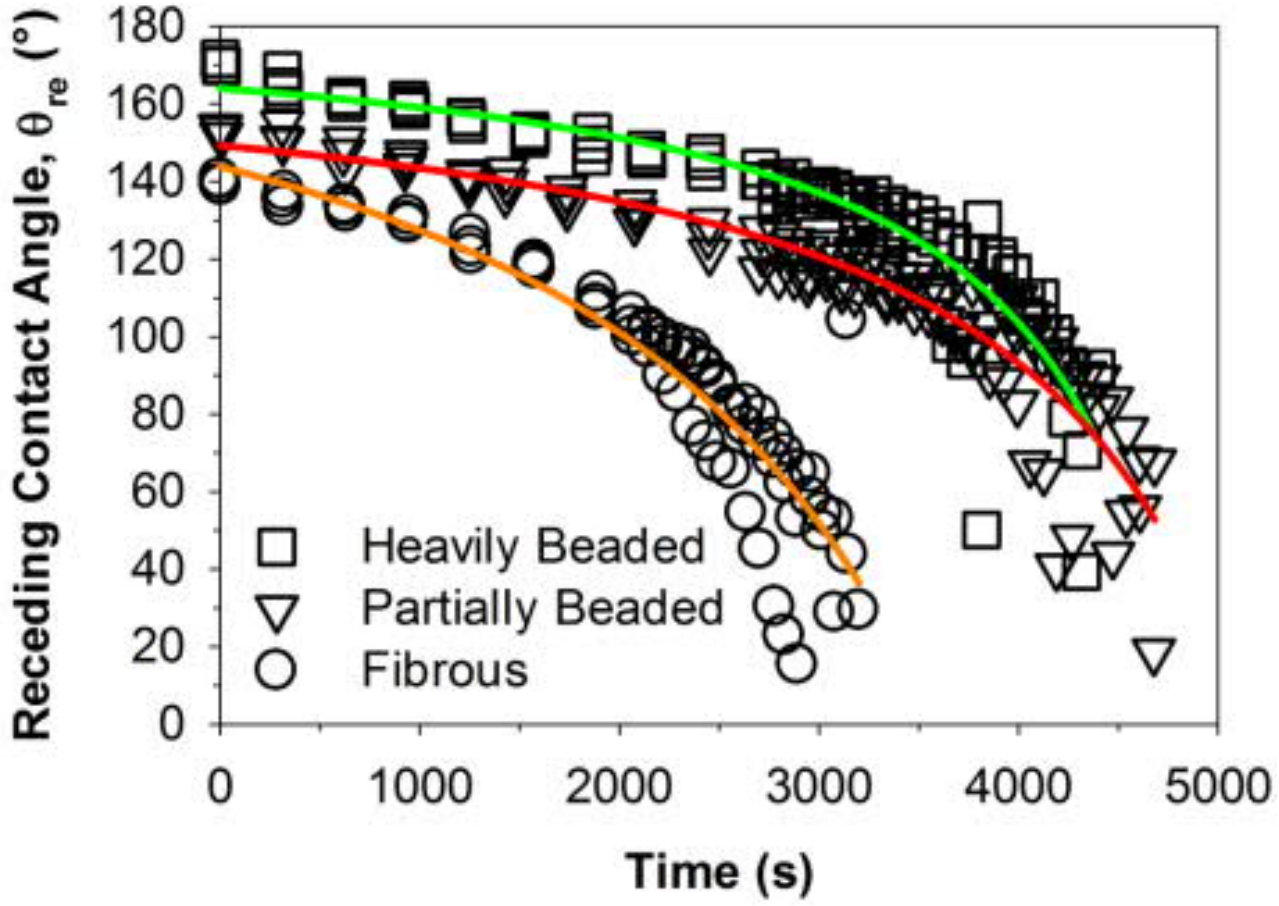

Figure S4.6. RCAs (°) as a function of evaporation time. Measurements were performed in a climate-controlled room with a temperature of 20-25 °C and a relative humidity of 40-50%.

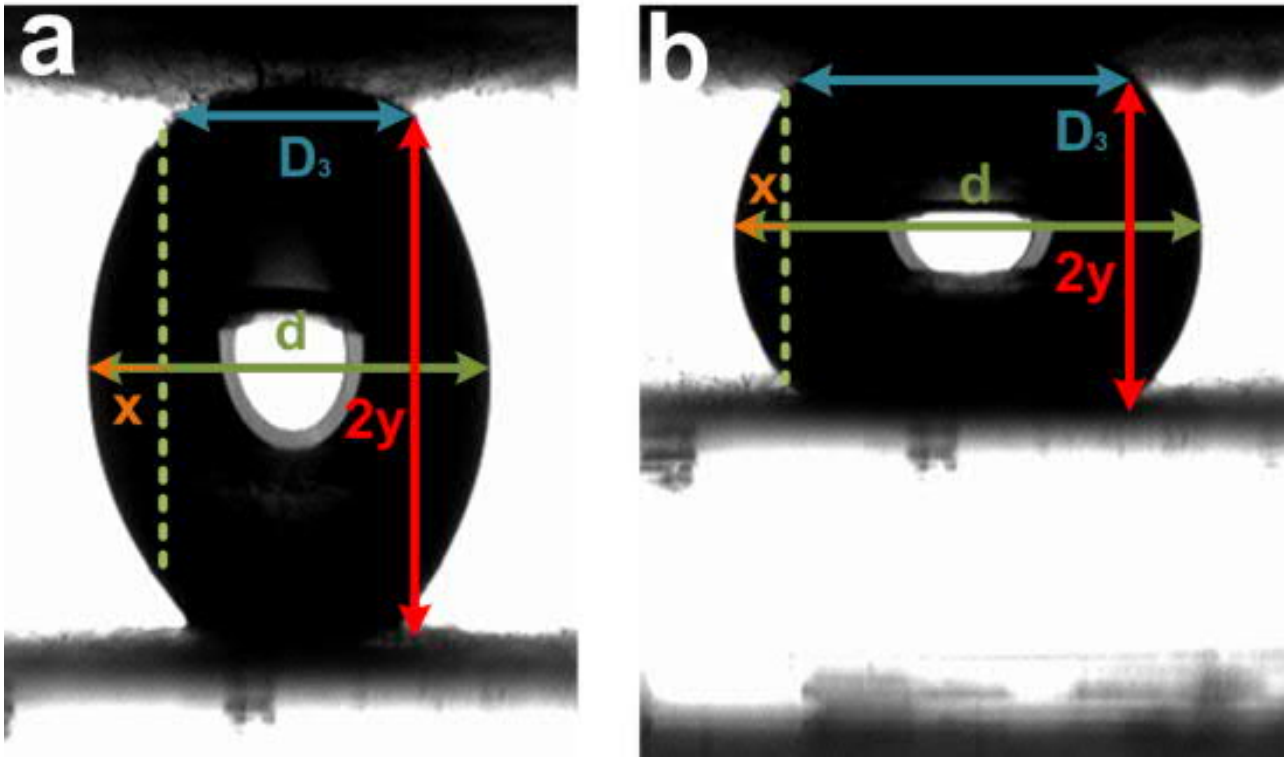

$$R_1 = d/2 \quad \text{(S4.1)}$$

$$R_2 = \frac{y^2+x^2}{2x} \quad \text{(S4.2)}$$

Figure S4.7. Diagram of droplet a) expanded and b) compressed between 2 rose petal surfaces with characteristic dimensions as indicated. Characteristic radii (S4.1) R1 and (S4.2) R2. Minor variations to measurements were also applied, depending on the symmetry of the distended droplet. Dimensions on both sides of the droplet (compressed / expanded) were measured to account for possible errors.

Measurement of maximum water droplet adhesion

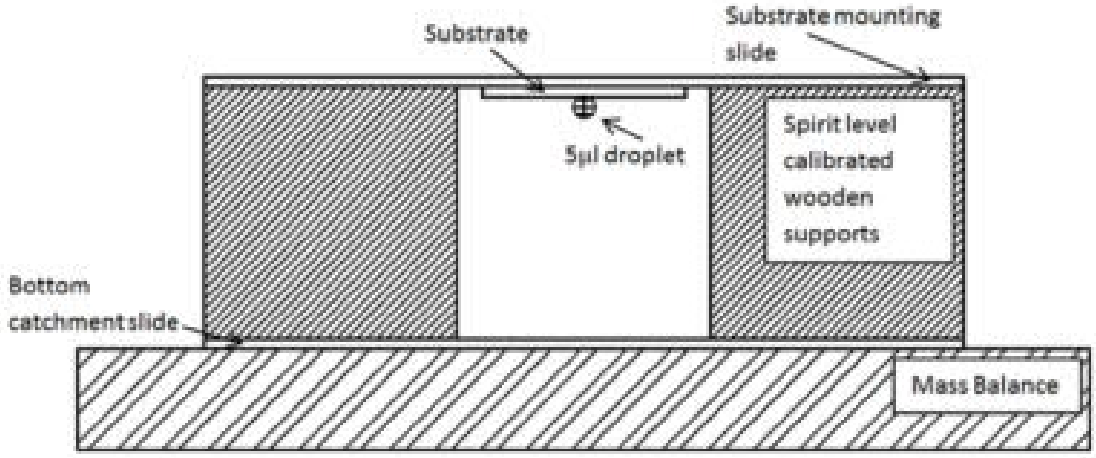

Figure S4.8. Measurement of adhesion strength (by mass) *via* set-up

1. Align stands using a spirit level to ensure horizontal alignment.
2. Set-up is placed onto a mass balance and zeroed.
3. A 5-6µl drop is placed onto the surface using a 25G needle. This ensures a pinning diameter of the droplet of about 1mm. Excessive droplet size may encourage a larger pinning diameter / vertical penetration, leading to false adhesion values.
4. Substrate is then carefully inverted and placed onto the stands (Figure S8).
5. Water is manually added to this drop (sub-dropwise [1-2mg]) using a 25G needle. Direct water contact between the pendant drop and needle should be avoided.
6. Finally, as the mass overwhelms the surface and drops, it detaches and lands on the bottom catchment slide.
7. Captured footage of the mass balance combined with the final mass measured allows computation of the net force exerted by the surface on the droplets by virtue of mass.
8. Steps 2-8 are repeated for 3 times and an average is taken as the maximum adhesion force.

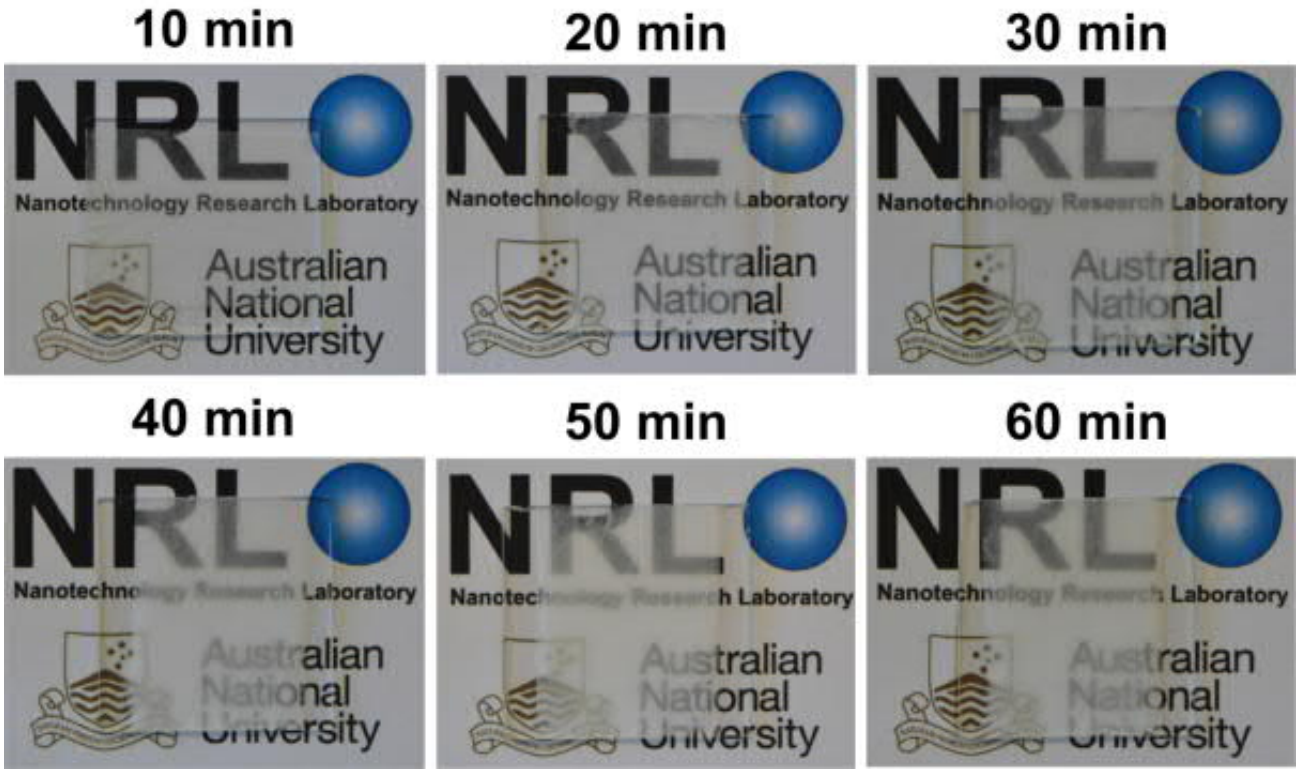

Figure S4.9. Optical photographs of partially beaded films developed from 10 to 60 min. The petal effects are achieved between 30-40 min while the lotus effect was achieved from 50-60 min.

Table S4.1. Summary of the ACA, RCA (Evaporative) and final CAH

Sample Type	Advancing Contact Angle	Receding Contact Angle	Contact Angle Hysteresis
Heavily beaded fibers	158° ± 2°	127° ± 5°	30° ± 1°
Partially beaded fibers	158° ± 7°	101° ± 2°	57° ± 3°
Pure fibers	151° ± 2°	62° ± 6°	90° ± 8°

5. Switchable Superhydrophobicity (Adhesive-to-Slippery)

Abstract

Surfaces with dynamically tunable wetting states are useful towards many applications, such as integrated micro-fluidics systems, flexible electronics and smart fabrics. Despite extensive progress, most switchable surfaces reported are based on ordered structures that suffer from poor scalability and high fabrication costs. Here, we demonstrate a robust and facile bottom-up approach that enables the fabrication of strain tunable wave-like nanofibers. Mechanical strain of the flexible nano-structures realizes the dynamical and reversible switching between lotus leaf (repulsive) and rose petal (adhesive) states. Interestingly, we find that controlled switching between these two distinctive states is correlated to the wave profile of the nanofibers. Moreover, the structural integrity of the nanofibers is fully preserved during multi-cycle dynamic switching. We showcase the application of these unique nanotextures as micro-mechanical hands. To this end, they demonstrated capacity for the directed capture of water micro-droplets and their subsequent release in a well-controlled manner. We envision that these low-cost and highly scalable nanotextures present a powerful platform for the design of microfluidics, droplet array and protein/DNA sequencing technologies.

5.1. Introduction

Development of novel multi-scale materials with dynamically tunable[512] wetting states bears significant research and commercial potential. Integration of such concepts into a fabric-like material[581] represents key steps towards the design of smart[582,583] adaptive materials. This could culminate in applications ranging from tissue engineering,[17] microfluidics[551,584] to drug delivery[26]. In particular, dynamically switchable[512,585] super-hydrophobic and -hydrophilic surfaces[586,587] present important insights towards the design of next generation micro-fluidics devices[551,588]. However, standard hydrophilicity encourages the Wenzel state of wetting, which is ultimately contamination-prone. Very recently, adhesion-tunable[587] superhydrophobic surfaces based on arrays of aligned nanopillars were achieved by controlled surface texturing.[26,540] However, wide-spread utilization of such lithography-based ordered structures[589] is limited due to poor scalability and high fabrication costs. Thus, the achievement of dynamically tunable adhesive-slippery superhydrophobicity based on disordered scalable morphologies remains of critical industrial importance.

Strain-induced modifications to the morphological features of a thin film, such as wrinkling and buckling is a phenomenon commonly found in a multitude of scales in nature. These range from bio-cellular epidermal layers of skin[414] to geological wrinkles[415]. Within the synthetic domain, spontaneous wrinkling of thin films[416] has traditionally been treated as defects. In fact, significant efforts were once directed toward the fabrication of perfectly flat surfaces, by selectively avoiding such imperfections[417]. Recently, numerous instances of artificial skin-like wrinkling materials were proposed for a plethora of engineering applications. These included functional engineering designs in flexible electronics,[590,591] self-assembling 3D architectures,[592,593] bioactive materials,[17,594] particle sieves[414] and membrane technologies[583,595]. These multi-scale films are commonly fabricated by the initial deposition of flat or even hierarchical films such as SiO_2,[414,594] gold,[17,596] carbon nanotubes (CNTs)[597], graphene[598] and PS[599] onto pre-stretched elastomeric substrates.

Relaxation of the pre-stretched substrate wrinkles the top film into a multi-scale hierarchical structure, with some demonstrated potential for tunable wettability.[17]

Here, we demonstrate an alternate concept for achieving dynamically reversible wetting states that range from hydrophobicity up to superhydrophobicity. Unique wetting properties achieved within these transitional states culminated in the demonstration of switchable droplet. This method is based on facile and scalable deposition of PS nanofibrous layers on soft elastic substrates. The anisotropic stretching and self-relaxation of the elastic substrate gives rise to shapeshifting of original nano-structures. To this end, the originally one-dimensional nanofibers are reversibly transformed into wave-like two-dimensional (2D) structures. Between these nanostructural states, a range of superhydrophobic wetting properties exists. Continuous strain-relaxation cycles demonstrate fully-reversible dynamic tuning of adhesive and repulsive superdewettability. Most specifically, droplet adhesion properties alternated between the repulsive lotus leaf-like[7] and adhesive rose petal-like[10] states. Application of these cyclic tunable micro-mechanical hands is demonstrated by the controlled capture, manipulation and release of micro-droplets. The bottom-up designs showcased here present a flexible platform for the fabrication of strain-tunable materials, such as flexible microelectronics,[590] tissue engineering[17,600] and 3D self-assembly[592].

5.2. Results and Discussion

One-dimensional PS nanofibers were synthesized by scalable, low cost electrospinning of polymer solutions. The average fiber diameter measured by scanning electron microscopy (SEM) was 170 ± 55 nm. To fabricate 2D wave-like nanofibers, we electrospun the nanofibers directly on pre-stretched PDMS films (Figure S5.1). These elastomeric films were subjected to up to 100% mono- or bi-axial pre-stretch. For reference, the as-prepared PDMS films (Figure S5.8) had inherent CAs of 119 ± 1.3°. In our experiments, three orientations of nanofibers relative to the pre-stretch direction were investigated, namely parallel-, orthogonally- and randomly aligned. Figure 5.1a schematizes the deposition of nanofibers aligned in a parallel orientation with the pre-stretching direction of the PDMS films. For such parallel-aligned fiber layers, relaxation of the PDMS substrate gives rise to the controlled compression of nanofibers in the axial direction. This leads to the assembly of in-plane and out-of-plane wave-like nano-structures (Figures 5.1a-b, S5.2a). The two stochastically formed styles of wave-like fibers were classified according to the orientation of their longitudinal axes. In-plane fibers have longitudinal axes that are parallel to the substrate while out-of-plane fibers have longitudinal axes that are partially perpendicular to the substrate. The differentiating classification enables the sequential identification of these two types of fibers. This was achieved by both SEM focal depth analysis and white light interferometry (WLI) (Figures S5.2a, S5.4, 5.5, 5.7). The relatively large amount of in-plane fibers, obtained here over that observed for previous single layer[590] studies, is tentatively attributed to both the affinity of the PDMS substrate with the PS nanofibers and the partial interweaving of the electrospun layers. These forces contribute towards the confinement and vertical displacement of the bottom and lower nanofiber layers during compression, resulting in a wave-like morphology. This assembly of in-plane and out-of-plane nanofibers possesses a corrugated, twisted surface[191] texture (Figure S5.2a) that resembles the characteristic morphology of the superhydrophobic silver ragwort leaves.[83,191] Wavelengths of the in-plane fibers decreased from 4.7 ± 1.3 µm to 2.3 ± 0.74 µm when pre-stretch was increased from 40% to 100% (Figure 5.1b). The out-of-plane nanofibers had nearly twice as large of a wavelength reaching 9.4 µm at 40% pre-

stretch. The amount of these out-of-plane fibers was found to decrease with decreasing film thickness. Optimal films were obtained with an electro-deposition time of 1 min, where a lower number of vertically-stock nanofiber layers was present. Longer deposition time (3 min) led to static repulsive lotus-like superhydrophobic surfaces that were not adhesion tunable. This is attributed to the poor transmission of substrate strain to the very top nanofiber layers through the highly porous profile. Assessment of the optimally tunable films (1 min deposition) using WLI optical profiling reveal an average thickness of 4.8 µm with a SEM-determined effective surface coverage of 56 ± 9% (Figure S5.3).

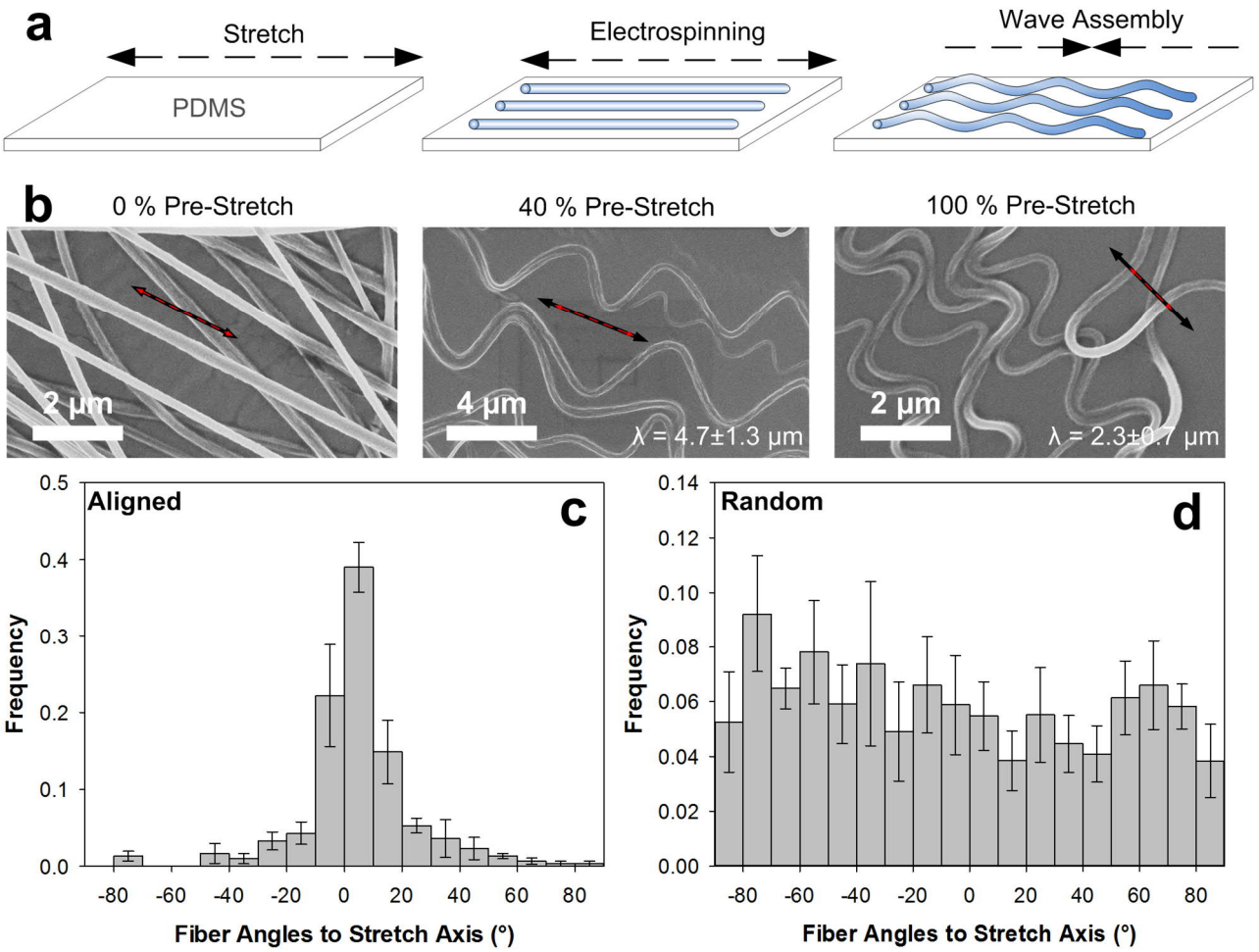

Figure 5.1. a) Schematic description of wave-like nanofiber synthesis by relaxation of electrospun layers of parallel-aligned nanofibers on pre-stretched substrates. b) Relaxation of the substrates gives rise to wave-like nanofibers with wavelengths of 4.7±1.3 µm and 2.3±0.7 µm at 40% and 100% pre-stretching, respectively. Black and red arrows indicate alignment direction and stretch-compression ratio, respectively. Histogram counts of fiber angle to pre-stretch axis for c) parallel- and d) randomly aligned electrospinning of nanofibers. The error bars represent the standard errors amongst 5 different batches.

Orthogonally and randomly orientated nanofiber films were obtained as control structures by placing counter electrodes on matching orthogonal extremities and on the perimeter of whole PDMS films (Figure S5.1c), respectively. The orthogonally-aligned fibers had an increased packing density but preserved their straight morphologies (Figure S5.4a-c). Randomly-aligned nanofibers had a few wave-like structures and some closely-packed domains showing an intermediary state between the former two alignment orientations (Figure S5.5f). Significantly less directional scattering was observed for the orthogonally aligned nanofibers than for the parallel-aligned ones (Figure S5.5a-b). Statistical investigation of the nanofiber alignment efficiency by SEM counting (Figure 5.1c) revealed successful orthogonal and parallel alignment to the stretch axis with 80% of the fibers contained within ± 15° (Figure 5.1c and Figure S5.5e). In contrast, for the randomly oriented layers, a uniform distribution of orientations was observed (Figure 5.1d and Figure S5.5f).

The feasibility of exploiting morphological variations between these nanofibrous layers to achieve a tailored wetting state, hereinafter referred to as static tuning (pre-stretch), was first assessed with respect to a range of pre-stretch and alignment parameters. Static tuning of the films' wetting properties was possible only with the parallel-aligned wave-like films (Figure 5.2a,b). At this juncture, owing to the impact of anisotropicity on the film wetting properties,[601,602] the CAs of nanofibrous films were imaged from two orthogonal viewpoints, parallel and perpendicular to the alignment of fibers (Figure S5.6). The largest variations in CAs were ca. 6.2° (Figure S5.6a), occurring for straight fibers (orthogonally-alignment) films with 100% pre-stretch. In contrast, the wave-like fibers, obtained by parallel-alignment, had negligible anisotropicity with CA variations smaller than < 1° for imaging angles of 0° and 90° to the fiber alignment (Figure S5.6b). This is tentatively attributed to their Cassie-Baxter wetting states, which limit interactions between solid substrate textures and the liquid droplet. These variations are well within the standard batch-to-batch CA variations (1-5°) of these films. With these findings as a priori, further CAs during dynamic tuning were reported for an imaging direction of 90° towards the direction of alignment.

For these films (parallel-aligned), increasing the pre-stretch from 0 to 100% increased the WCA from 138° to 167° (Figure 5.2a) and decreased the SA from 90° (pinning) to 5° (Figure 5.2b). Micro-droplets of 5 µL were used. Even with very mild pre-stretch ratios of 10% and 20%, these films transited from adhesive hydrophobic of the un-stretched films to lotus leaf-like repulsive superhydrophobicity. With a moderate pre-stretch of 40%, stable repulsive superhydrophobicity was achieved, resulting in static CAs in excess of 160° (Figure 5.2a), and SAs below 10° (Figure 5.2b). This demonstrates, for the first time that, low SA repulsive superhydrophobicity can be achieved by a wave-like nanofiber morphology. Notwithstanding further findings, this methodology offers a facile scalable approach for the rapid (1 min) fabrication of water-impenetrable superhydrophobic surfaces. Interestingly, one already evident advantage of this ultra-porous morphology lies in its easily achievable superhydrophobicity even using such low uni-axial strain. In contrast to the state-of-the-art, many 2D films morphologies commonly require relatively high biaxial strains for wettability variations[17]. The low-strain requirements can be attributed to the secondary degree of nano-scaled hierarchy naturally achieved by the in-plane curling of 1D nano-structures.

Alternatively, random and orthogonally-aligned nanofibers did not transit wetting states and preserved their initial adhesive hydrophobic properties (Figure 5.2a,b). Primarily, orthogonally-aligned fiber films did not form a wave-like morphology and thus could not undergo the wave-to-straight shapeshifting necessary for Cassie-Baxter to Wenzel transition. Similarly, the randomly-aligned fiber films had mostly straight fibers and only a few wave-like fibers, and thus were not able to induce a transition of wetting states at the macro-scale.

The statically tuned wetting properties of the optimal parallel-aligned wave-like nanofibers were further characterized by CAH. The CAH dropped steeply from 60° to 15°, with increasing pre-stretch from 0% to 40%. These results are in good agreement with their corresponding CA and SA analysis (Figure 5.2c). At 100% pre-stretch, a CAH of 7° was achieved. These results suggest that, as soon as a slight wave-like curvature is obtained (*e.g.* at 20% pre-stretch), the nanofiber layer becomes impenetrable to water. Based on these observations, the statically tunable wetting state of these

nanofiber layers is attributed to an active transition from dewetting Cassie-Baxter to the wetting Wenzel state through the Cassie-Impregnating regime. UV-vis analysis of the parallel-aligned nanofibers revealed a linear decrease in transmittance from 85% to 65% with increasing pre-stretch from 0 to 100% (Figure 5.2d). This is tentatively attributed to the formation of periodic micro-scale light-scattering structures and is in line with the fiber morphology observed by SEM.

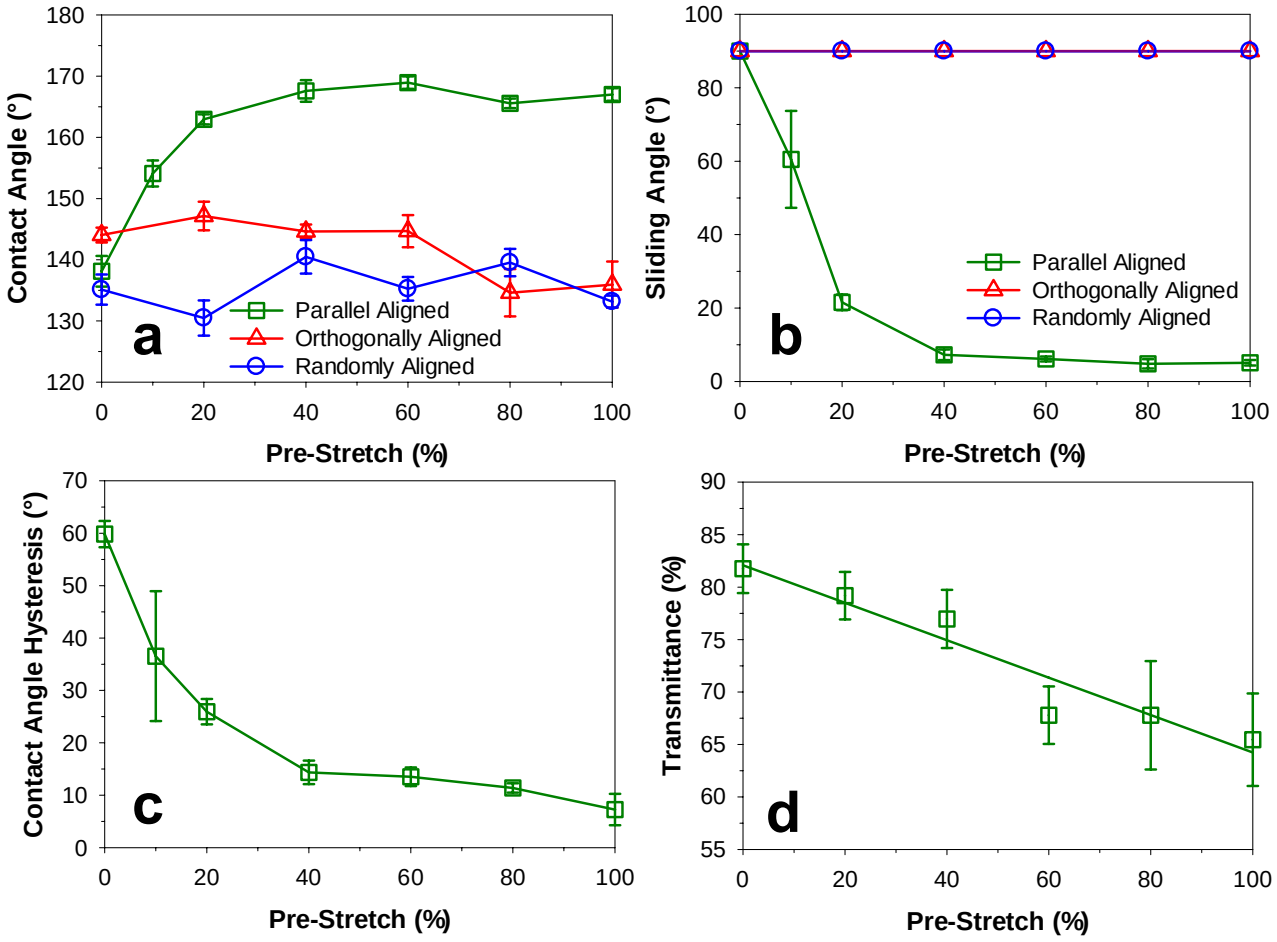

Figure 5.2. a) CAs and b) SAs as a function of the stretch ratio for parallel- (green), orthogonally- (red) and randomly aligned (blue) nanofiber layers on elastic PDMS substrates. c) CAH for parallel-aligned nanofiber layers as a function of the pre-stretch ratio. d) UV-vis transmittance at λ = 600 nm for the parallel-aligned nanofibers as a function of their pre-stretch.

To assess the feasibility of fabricating surfaces with continuously and reversibly tunable wettability, dynamic tuning (straining) was performed. Wave-like nanofiber films were dynamically strained while their wetting properties were simultaneously monitored. Owing to their intermediary behaviors, the 40% pre-stretched wave-like nanofibers were selected as the most promising morphology. In fact, while achieving the same repulsive superhydrophobicity behaviors of the 100% pre-stretched

samples, the larger wavelengths and smaller in-built stress of the former were beneficial in obtaining reversible deformation of the fiber shape.

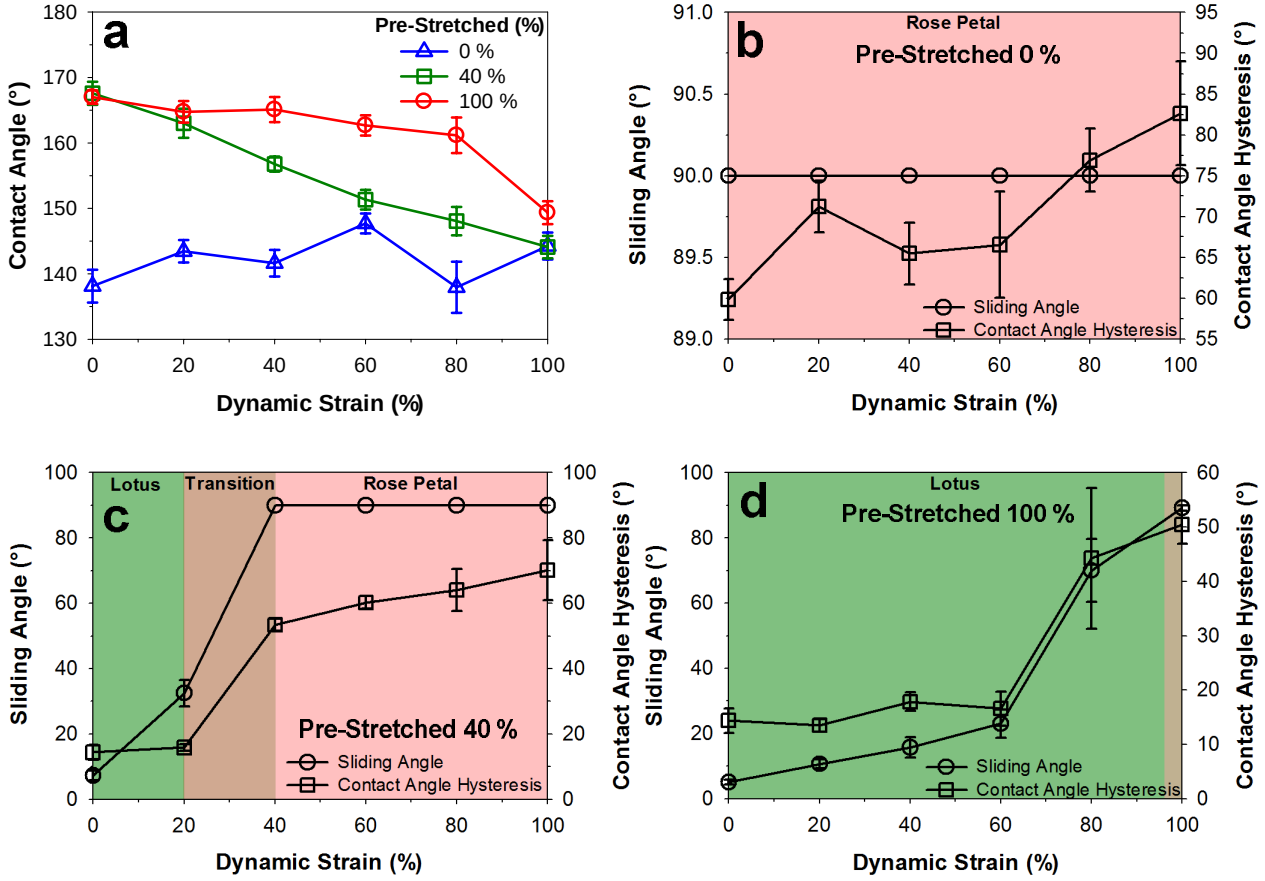

Figure 5.3. Variation of a) CAs, (b, c, d) SAs (left axis) and CAH (right axis) of the 0%, 40% and 100% pre-stretched films. Note that there is no wetting state transition for the films with 0% and 100% pre-stretch, while a distinctive wetting transition is achieved for the surface of the 40% pre-stretched films.

For the sake of comparison, the 100% pre-stretched and 0% unstretched parallel-aligned nanofibers were analyzed as control samples. For the latter, wetting analysis revealed negligible variations of the CA during dynamic straining of the PDMS substrates, resulting in static hydrophobic surfaces (Figure 5.3a, blue line). In contrast, the 40% and 100% pre-stretched films had gradually decreasing CAs with increasing dynamic strain (Figure 5.3a, green and red lines). Surprisingly, the transition to non-superhydrophobic CAs occurred for the 40% pre-stretched films only at a relatively high dynamic strain of 80% (Figure 5.3a, green line). This behavior translated even to the 100% pre-stretched films, where superhydrophobic CAs were maintained even up to 100% dynamic strain (Figure 5.3a, red

line). These results are indicative of a certain degree of morphological hysteresis during the stretching cycle.

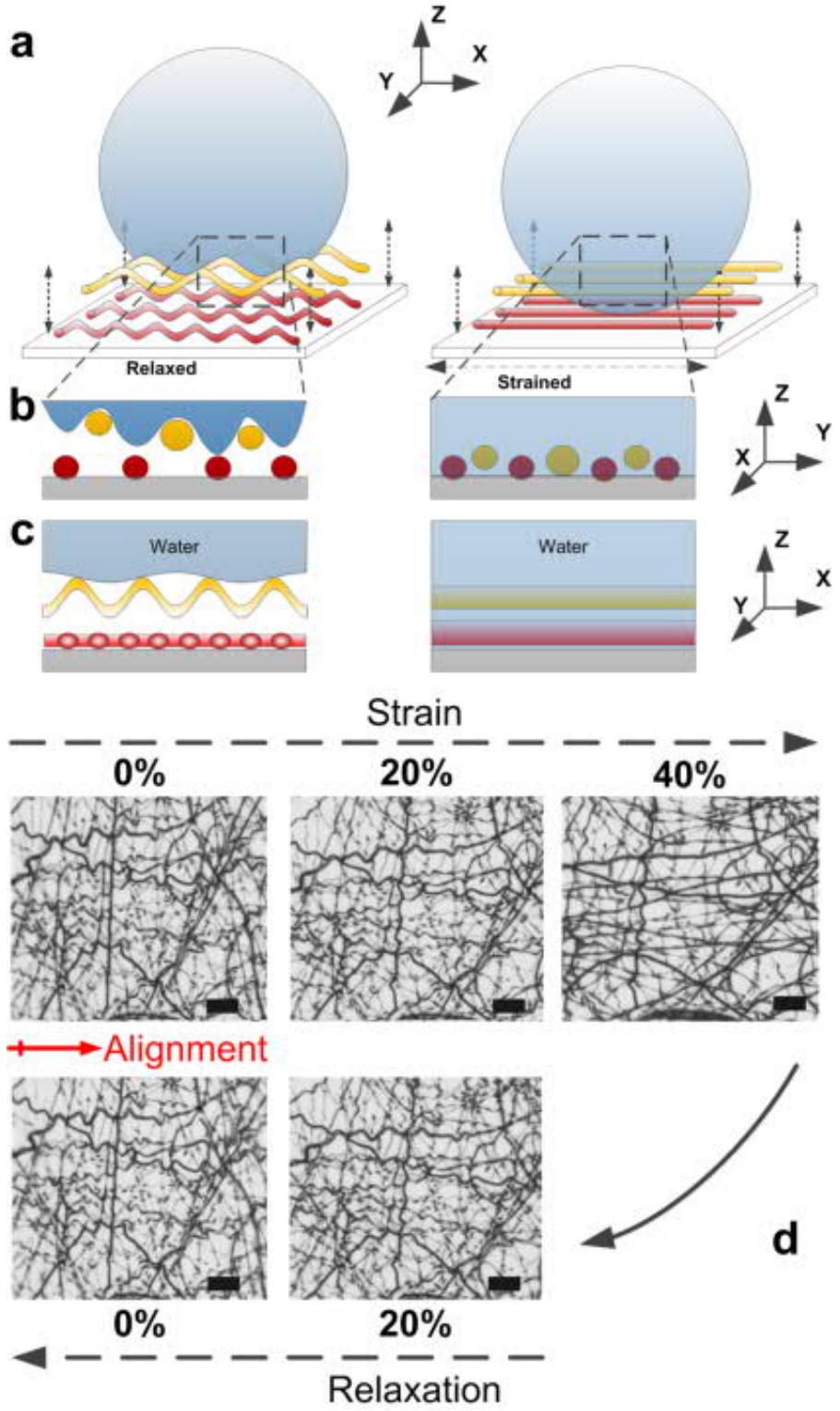

Figure 5.4. a) Schematic drawing describing the dynamic switching mechanism between Cassie-Baxter lotus-like to the Wenzel penetrated states through strain-induced straightening of in-plane and out-of-plane wave-like nanofibers (b,c). The strain of the wave-like nanofibers results in the release of the air gaps trapped within the bendings. d) *in situ* optical microscope images displaying a full strain-relaxation cycle. The scale bar is 10 µm.

The SA and CAH analysis during dynamic strain revealed further insights on the properties of these adhesion-tunable surfaces. No transitional behavior was detected for the 0% pre-stretched films, independent of the applied dynamic strain. More importantly, SAs and CAHs values were similar to those reported for typical adhesive hydrophobicity regimes[89] (Figure 5.3b).

A distinctive transitional behavior was, however, found for the 40% pre-stretched films. SA transition from repulsive superhydrophobicity to adhesive superhydrophobic droplet pinning (Figure 5.3c) occurred at a dynamic strain of 40%. A similar transitional behavior was achieved with the 100% pre-stretched developed films. However, SA switching from lotus to rose-like only occurred after approaching a dynamic strain of 100% (Figure 5.3d).

In good agreement with the SA analysis, the CAH of the 40% and 100% pre-stretched films approached the adhesive (rose petal) superhydrophobic region of 50°-60° at a dynamic strain of 40% and 100%, respectively.[89] For the 40% pre-stretched films, this was characterized by a sharp step increase of 38° in CAH with increasing dynamic strain from 20% to 40%. In contrast, the 0%, unstretched samples had the highest CAH of 83° resulting in robustly pinned micro-droplets independently of the applied dynamic strain.

These findings are indicative of the potential belonging to the 40% pre-stretched parallel-aligned nanofiber layers. They are, hereinafter, referred to as the optimal films, operating with a dynamic strain of between 20% to 40%. Coupling of the optimal films with ideal strain ratios possess the highest potential for fabricating dynamically switchable water adhesive-repulsive surfaces (Figure 5.3c).

This strain-tunable surface wetting was attributed to the 2D to 1D morphological transformation (Figure 5.4a-c) of the wave-like nanofibers during straightening. This is, notably different from the traditional wrinkling and buckling of flat dense films where a 3D to 2D transformation is imposed.[17,600] The 2D to 1D dynamic transformations and wetting mechanisms were investigated by an optical analysis of a complete strain-relaxation cycle (Figure 5.4d). In their relaxed morphology,

the optimal films form a series of air gaps trapped within the bendings of the wave-like nanofiber layers. This result in a uniquely achieved Cassie-Baxter state demonstrating a lotus-like water-impenetrable surface (Figure 5.4b,c). During dynamic strain, these bends within the wave-like nanofiber is lost (Figure 5.4c), thus enabling release of the trapped air.

The change in film morphology was also investigated by WLI (Figure S5.7), which revealed an average drop in film thickness of 500 nm with an increase of strain from 0% to 40%. This resulted in an active transition from the Cassie-Baxter to the impregnated Cassie state. This model matches well with the superhydrophobic water droplet pinning (Figure 5.3c) observed for the 40% strained optimal films. For a smaller original pre-stretch, the active transitions may even lead to the Wenzel wetting state.

The optimal films were tested for passive and active micro-droplet manipulation. As determined above, optimal superhydrophobic adhesion was coupled with a dynamic strain of 20-40%. More importantly, applying a dynamic strain below the original pre-stretch helps to maintain the film integrity. Passive droplet control was first demonstrated by dynamically switching of the surface's wettability from a repulsive (Figure 5.5a) to an adhesive hand (Figure 5.5b). Without strain, a 6 µL droplet is actively repelled by the film. However, with a strain ratio of 30%, it was now possible to stick and pick up the droplet.

We then pushed the limits of the operating system, where a dynamically responsive mechanical hand was achieved. This demonstrated feasibility of a system capable of continuous micro-droplet capture, manipulation and controlled release.

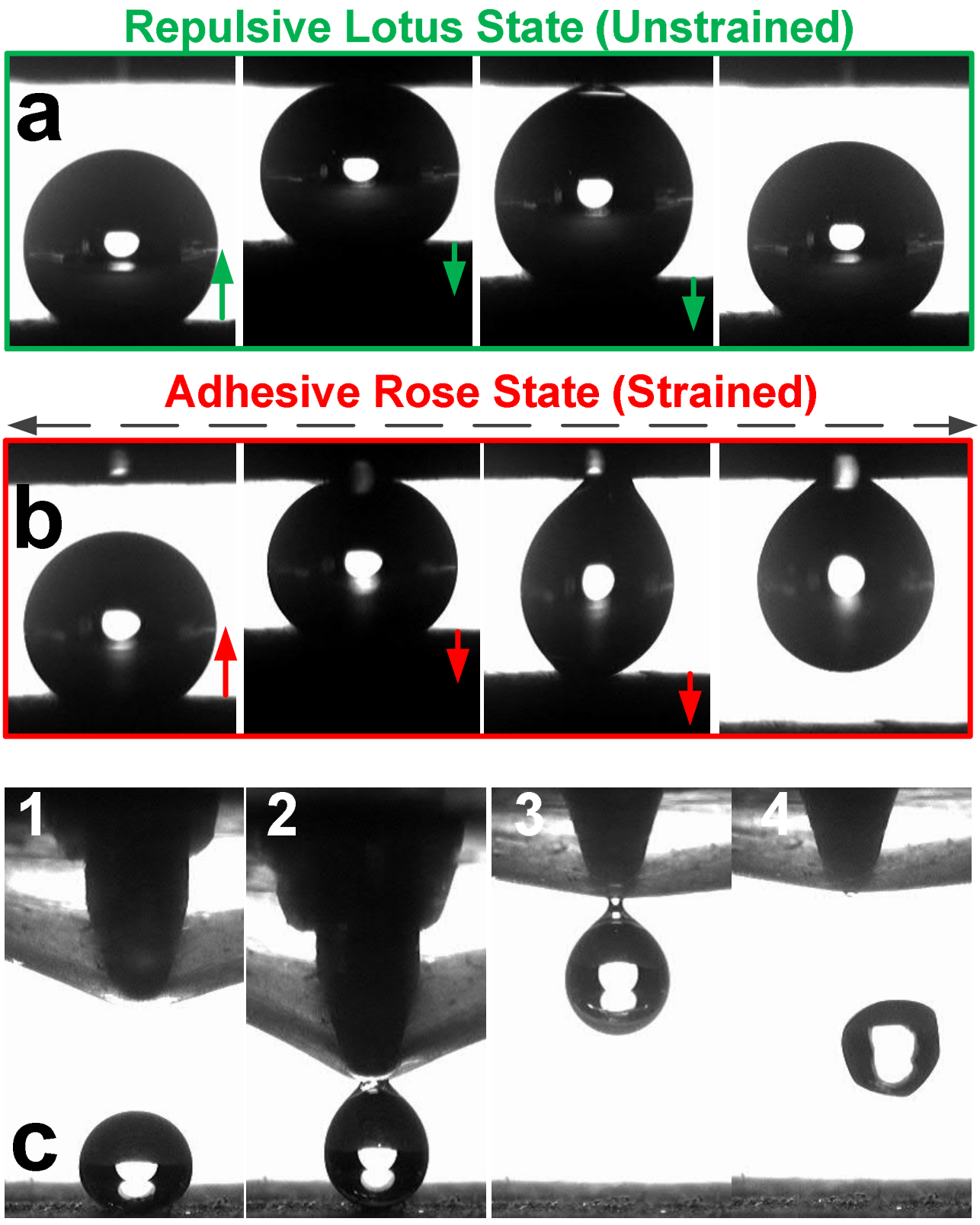

Figure 5.5. Dynamic tuning of surface wetting by dynamic straining of the parallel-aligned nanofiber layers (40% pre-stretched). Mild uni-axial straining from 0 to 30% enables switchable a) repulsive to b) adhesive superhydrophobic states. Demonstration of mechanical hand-like droplet manipulation by c) lift-off (2-3) of a 6 µl droplet and its controlled release (4).

This was readily achieved by dynamically straining the backside of the PDMS substrate with a tipped probe of 1 mm in diameter. The probe stretched the elastomeric PDMS film radially during the

downward motion. This was set to encounter a 6 µL micro-droplet placed at 10 mm distance from the PDMS substrate. The micro-droplet was then lifted from the lotus-like superhydrophobic surface on which it was previously placed. Thereafter, re-contraction of the adhesive rose petal-like surface occurs during the upward motion. This first vertically displaced the droplet and thereafter continuously increased the CA, eventually resulting in a repulsive lotus-like surface. Droplet release was achieved by natural breakage of the residual capillary bridge (Figure 5.5c). In this work, the largest droplet size held in the adhesive rose petal state was 10 µL, which is in line with previous studies.[89] The smallest droplet size captured and released was 3 µL. The small pore sizes of these films (5-6 µm) suggest that it should be possible to manipulate droplet sizes significantly smaller than 3 µL. The maximum droplet volume captured and released, here, was 6 µL.

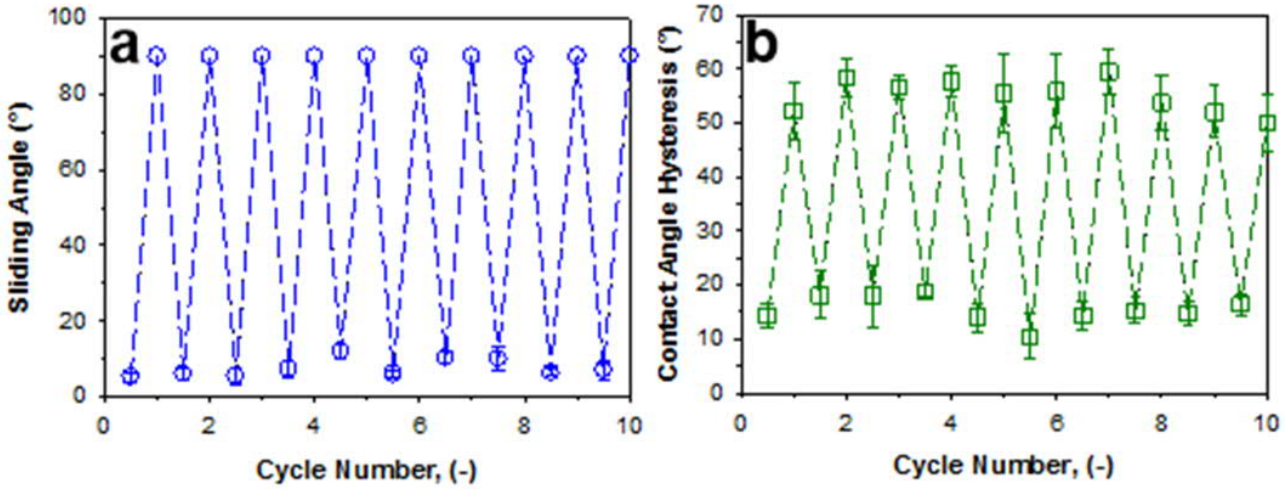

Figure 5.6. Cyclic switching of repulsive to adhesive superhydrophobic wetting state by application of uni-axial dynamic strain of 30% and relaxation showing fully reversible a) SAs and b) CAH.

Cyclic dynamic switching from an adhesive to a repulsive wetting state was demonstrated with the optimal films by periodic application of 30% dynamic strain and relaxation (Figure 5.6a-b). Analysis of the reversibility was performed with a series of 10 wetting cycles. The SAs were consistently tuned from pinned 90° to less than 10° between each cycle (Figure 5.6a). ACAs, RCAs (Figure S5.2c) and CAH (Figure 5.6b) further confirmed the switchable adhesive-repulsive states of the optimized films. Upon 30% dynamic strain, consistently high CAHs of 50-60° were maintained that are characteristic of adhesive rose petal-like surfaces[89] (Figure 5.6b). Upon relaxation, consistently low CAHs of

between 10-20° were recovered, indicative of a repulsive lotus leaf-like wetting state (Figure 5.6b). SEM characterization of the post-cycled films (Figure S5.2b) revealed that the nanofibers and the layers preserved their morphological integrity with no observable material cracks, fracture and discernable morphological variations from the as-prepared samples (Figure S5.2a). These results demonstrate the complete reversibility of wetting and structural properties switching despite the crystalline nature of PS. In the same vein, the robustness of these tunable surface textures was thus substantiated.

5.3. Conclusions

A novel nano-structured coating capable of static and dynamic reversible wettability switching was developed by a facile and scalable bottom-up approach. More specifically, the surface was capable of actively transiting from adhesive to highly repulsive states of superhydrophobicity. To this end, we demonstrated the unprecedented strain-induced transformation of 2D wave-like nanofibers into 1D straightened morphologies. These dynamically shapeshifting nano-structures enabled facile transitioning of wettabilities from the superdewetting Cassie-Baxter to the pinning Cassie-Impregnating and even the wettable Wenzel states. This was achieved by the mechanical strain tuning of a bi-layer profile comprised of an ultra-porous coating made up of aligned nanofibers supported by an elastomeric substrate. For our most optimally developed coatings, the multi-cycle tuning of SAs and CAHs from 8° to 90° (pinned) and 15° to 55° respectively, was achieved by low uni-axial dynamic strain of 30%. These coatings were capable of active mechanical hand-like manipulation of water droplets. This was demonstrated through the sequential lift-off, manipulation and controlled-release of 6 µL micro-droplets by simple pin-actuated radial stretching of optimal coatings. The highly performing bi-layer design showcases direct application in droplet control systems[26,579] and micro-reactor arrays[580]. Furthermore, it represents a low-cost and scalable concept that offers a flexible platform for the fabrication of smart, characteristically-tunable interfaces. These properties may be further exemplified in dynamically tunable membrane technologies[595], water harvesting[511], flexible electronics[590] and biosensors[603].

5.4. Experimental Section

Polymer Solution Preparation

PS (Sigma Aldrich, Mw = 280,000) (PS) solutions were made by dissolving 0.944 g of PS in 10 mL of N,N-dimethyl formamide (Sigma Aldrich, anhydrous, ≥ 99.8%) (DMF). Dodecyl trimethyl ammonium bromide (Sigma Aldrich, ≥ 98%) (DTAB) was added at to the PS solution at concentrations of 1.9 mg/mL.

Substrate Preparation

PDMS substrates were prepared using Sylgard 184 (Dow Corning), which comprises of a 10:1 ratio of base elastomer to curing agent. These were mixed vigorously together, casted on petri dishes and degassed for 30 min before a thermal curing procedure at 70 °C for 50 min. Surface energies of the bare PDMS surface was computed through a 5 point CA analysis (Figure S5.8) at 119 ± 1.3°. Casted PDMS slides possessed a thickness of 0.5 mm and dimensions were crafted so as to suit substrates for electrospinning (Figure S5.1b).

Electrospinning

Electrospinning of the PS nanofibrous layer on PDMS was developed using a vertical electrospinning setup (Electrospunra ES210, Singapore), at a working distance and flow rate of 10 cm and 1.0 mL h^{-1} with an applied voltage of 30 kV for 1 minute between 35-45% relative humidity. A travel distance of 7 cm with a speed of 2 cm s^{-1} was used to improve homogeneity. Copper masks were crafted to provide a charge collection zone with dimensions of 2.5 cm x 2.5 cm. Alignment was promoted by modification of the mask through selective insulation using PP sheets. Substrates were uniaxially pre-stretched and calibrated between 0% and 100% strain prior to deposition. The stretch of the substrate during fiber deposition is referred as “pre-stretch”. After electrospinning, the copper mask was gently removed while pressing the nanofiber film against the PDMS substrate with a square stamp of 2.5 cm x 2.5 cm. The PDMS substrate was thereafter relaxed, completing the synthesis of the nanofiber

coatings (Figure S5.1e). Samples were not moisture sensitive and could be stored indefinitely without losses in functionality. The two types of fibers were classified by the orientation of their longitudinal axes with in-plane fibers having longitudinal axes parallel to the substrate and out-of-plane fibers having longitudinal axes that are partially vertical to the substrate.

Wetting Analysis

Films collected were stored overnight to facilitate the completion of solvent evaporation prior to further testing. Wetting analysis was conducted within 48 h of synthesis. Owing to the impact of anisotropicity on the film wetting properties,[601,602] the CAs of the orthogonally- and parallel-aligned nanofibrous films were imaged (Figure S5.6) from different orientations (0° and 90°) to the fiber alignment and assessed for variations. The CA variations (Figure S5.6) were well within the standard batch-to-batch CA variations (1-9°) of both orthogonally- and parallel-aligned nanofibrous films, and further CAs during dynamic tuning were thus reported for an imaging direction of 90° to the fiber alignment only. The static WCA was measured by placing and averaging 6 drops of deionized water (5 µL) on sample surfaces produced across batches. The SA was determined by placing a 5 µL drop of deionized water directly on sample surfaces prior to tilting *via* an optical or mechanical goniometer. Results were averaged across 6 readings. The CAH was measured *via* the drop-in drop-out (DIDO) technique (1 - 9 µL, 3 readings), which involves subtraction of the RCA from the ACA. The former was measured at 1 µL while the latter was measured at 9 µL. Data was presented as mean ± standard errors (CA, SA and CAH). Parameters were collected for both statically and dynamically tuned films. The dynamic tuning of the wetting properties of the nanofiber films by applying a strain is referred as “strain”. A fresh droplet is placed each time on the dynamically strained films between further straining or relaxing the interface during CA, SA and CAH measurements. Dynamic and static images were recorded using a KSV CAM200 contact angle goniometer (Finland) with a heliopan ES43 camera (Japan). Whenever possible, the CA, SA and CAH were computed by a commercially available (CAM2008) program. All substrate extension and relaxation were conducted at approximately 0.625 mm/s using a custom-built electrically operated stretch apparatus.

Surface Analysis

Morphological optimizations were first conducted using a light microscope (Nikon Eclipse E200, TV lens 0.55x DS) on coated PDMS substrates. These optimization experiments were conducted four times to ensure repeatability. Samples were then analyzed *via* scanning electron microscopy (Zeiss UltraPlus analytical scanning electron microscope (FESEM) at 3kV). Prior to examination, SEM specimens were platinum sputter-coated for 2 min at 20 mA. Average fiber dimension was analyzed *via* ImageJ using 50 counts of each nano-structure. Data was presented as mean ± standard deviations. Fiber alignment was determined *via* observing SEM micrographs (4.4k and 8.8k magnifications) of straight aligned fibers (5 separate cross-batch samples), with between 60 - 100 counts / sample made on aligned and misaligned fibers. Statistical histogram analysis was thus computed through 300 fiber counts with standard errors analyzed through 5 batches for each type of nanofiber films (aligned or random). Wavelengths of in-plane waveformed fibers were determined based on 1-4 consecutive waves with at least 10 counts. Surface coverage was determined through ImageJ using SEMs based on optimizing contrast, enabling the estimation of fibrous domains through 6 cross-batch samples. Data was presented as mean ± standard deviations. UV-vis analysis was conducted using a microplate reader (Tecan 200 PRO, Switzerland) from 300-800 nm with 10 scans per cycle. Data was presented as mean ± standard errors. In situ optical analysis: The in situ optical analysis was performed with a Leica microscope (DM2700M) equipped with a long working distance 50× nosepiece and custom-made microscope -compatible stretching stage with 5 µm displacement accuracy. 3D optical profiler measurements were performed with the Bruker Contour GT-K with a 50 X lens and a 2 X multiplier. VXI acquisition mode was used in conjunction with a custom made stretching stage with 5 µm displacement accuracy.

5.5. Supplementary Information

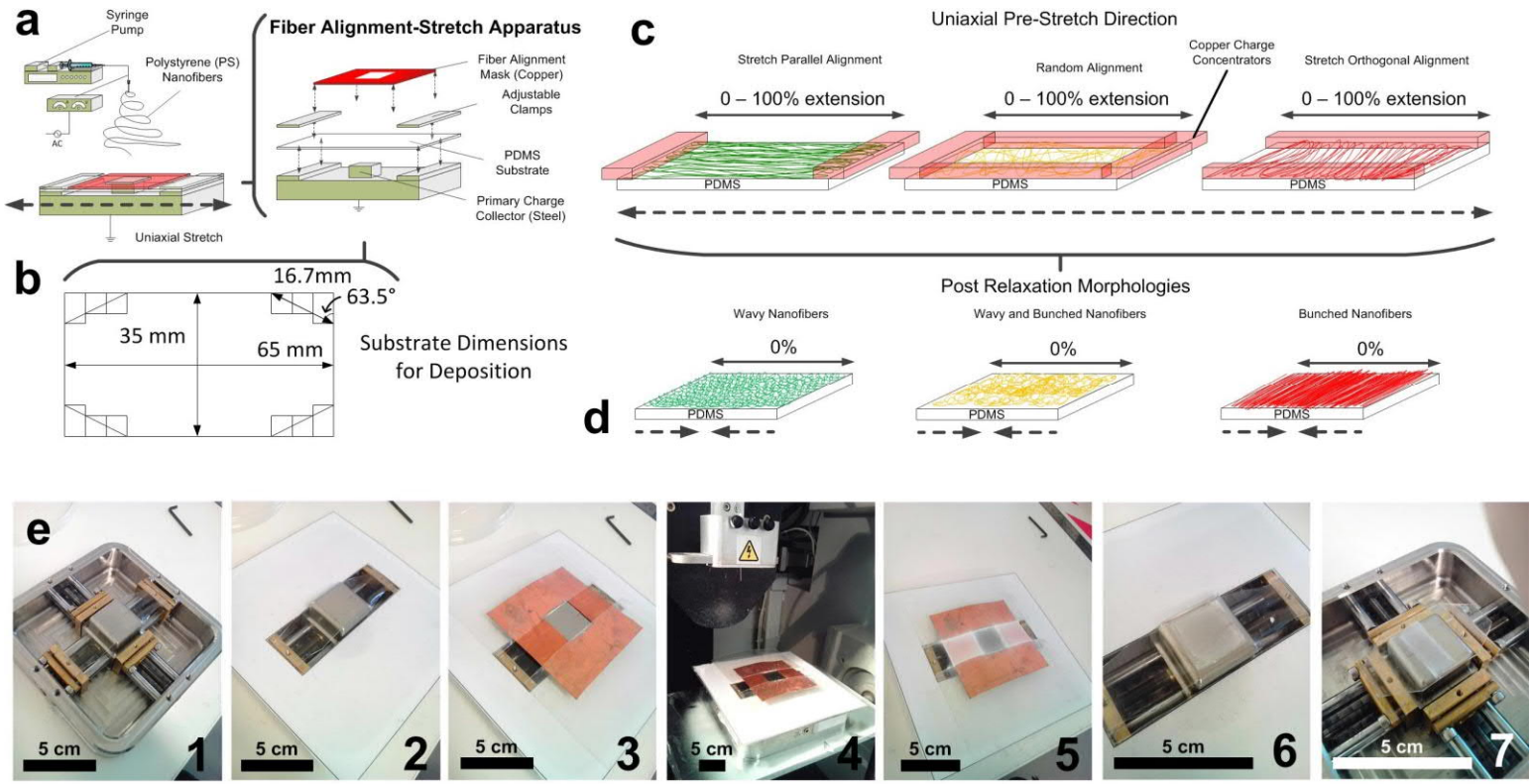

Figure S5.1. a) Fiber-alignment-stretch apparatus. b) PDMS substrate template with dimensions as indicated. c) Developmental schematic of ultra-thin PS nanofibers *via* a custom-made nanofiber alignment-stretch apparatus with pre-stretch (0-100%) PDMS substrates being deposited with aligned / random nanofibrous films - 1) randomly aligned, 2) stretch parallel or orthogonally aligned on uniaxially pre-stretched soft substrates. d) Post deposition relaxation of substrates formed various unique morphologies inclusive of 1) mixed waves and bunches, 2) packed bunched fibers and 3) wave-like nanofiber films, respectively. e) Optical photographs depicting the stretch-alignment deposition set-up. (1) pre-stretched PDMS substrate (100%, parallel-aligned), (2) Insulation coverage on stretcher, (3) Copper mask for charge concentration and alignment (with transparent insulation mask), (4) Electrospinning, (5) As-deposited nanofibers on pre-stretched substrate (showing masked alignment deposition), (6) Removal of copper mask, revealing the film coating, (7) Relaxation of the stretched film, giving rise to a laterally compressed nanofibrous film.

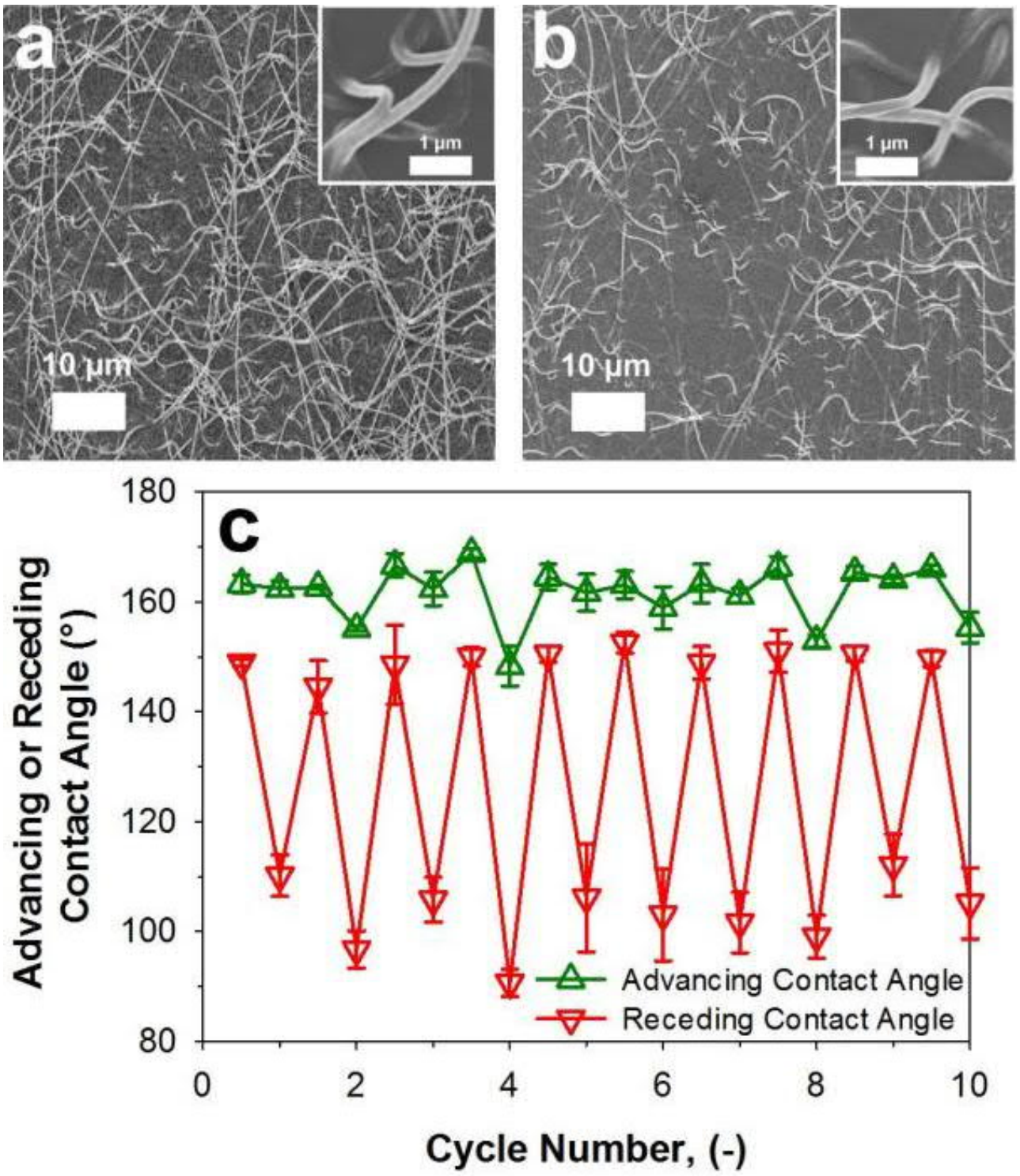

Figure S5.2. SEMs of stretch parallel aligned wavy nanofibers developed at 40% pre-stretch. Insets magnified at 70k. a) As-developed wavy nanofibers and b) post-deposition strained nanofibers (10 cycles). c) ACAs and RCAs with respect to dynamic strain-relaxation cycles.

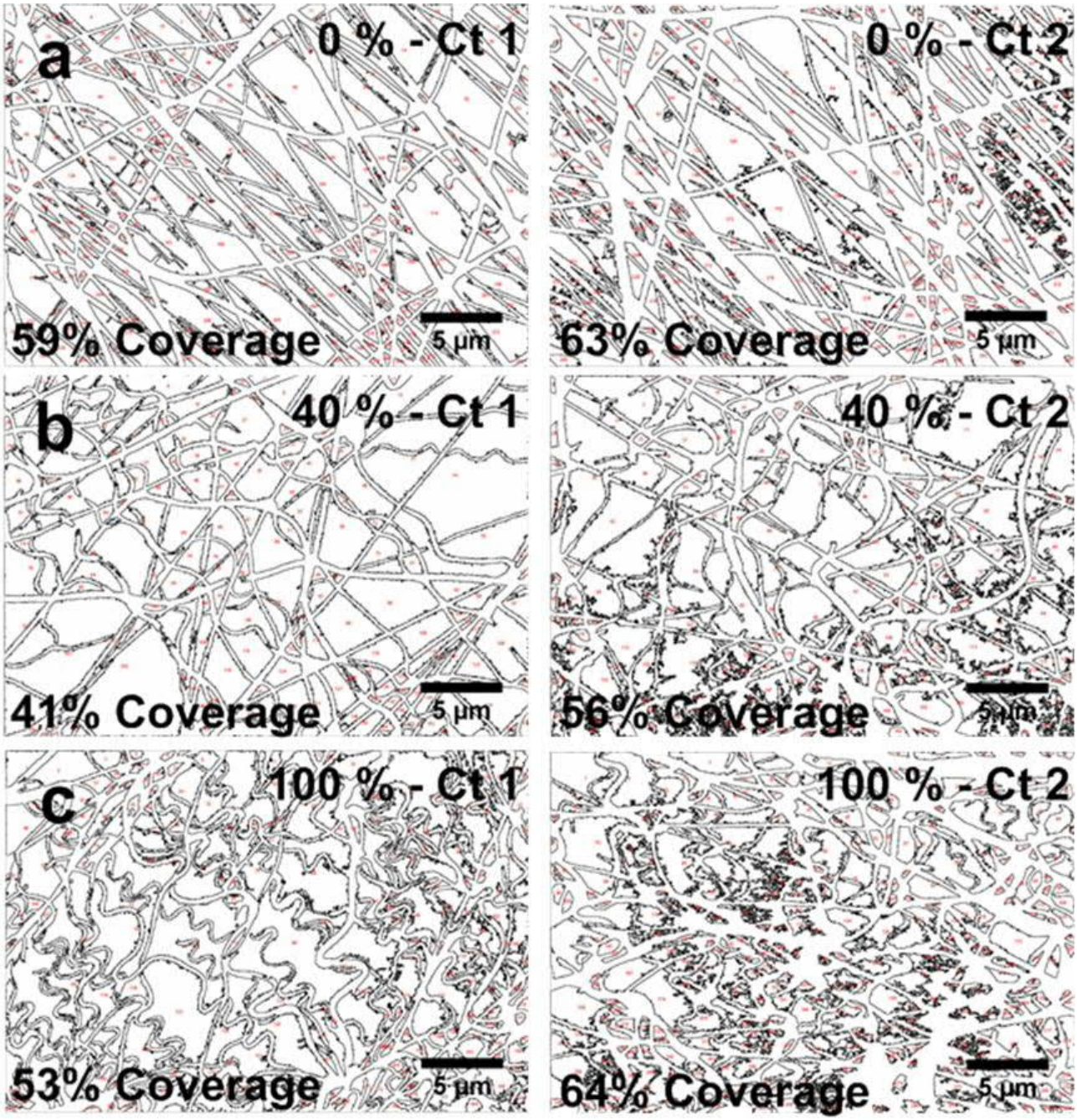

Figure S5.3. Surface coverage analysis of a) 0% pre-stretched, b) 40% pre-stretched, and c) 100% pre-stretched nanofibrous layers (2 repeats) over a macro-area (SEMs) through ImageJ and particle analyzer plugin.

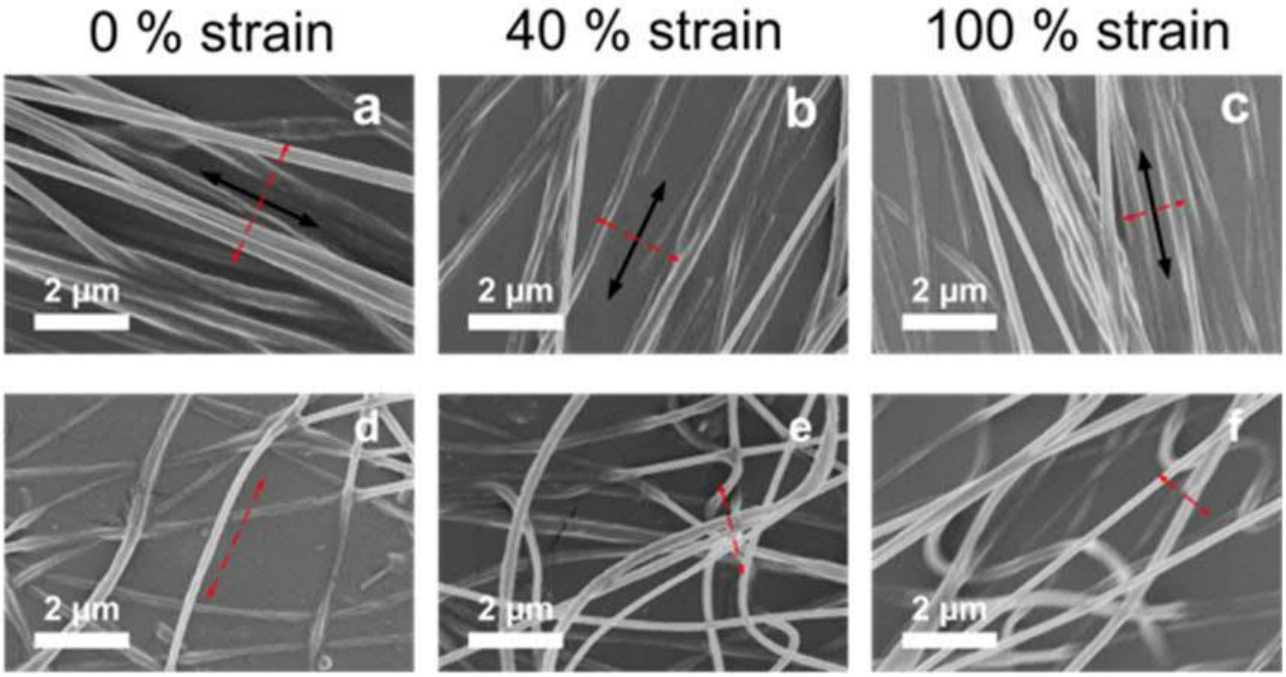

Figure S5.4. Variations to the alignment-stretch deposition of nanofibers at 0 - 100% strains. (a-c) Bunched fibers were formed for orthogonally aligned nanofibers while (d-f) random wave-bunched mixed fibers were formed for randomly aligned nanofibers. Black and red arrows indicate alignment direction and stretch-compression ratio, respectively.

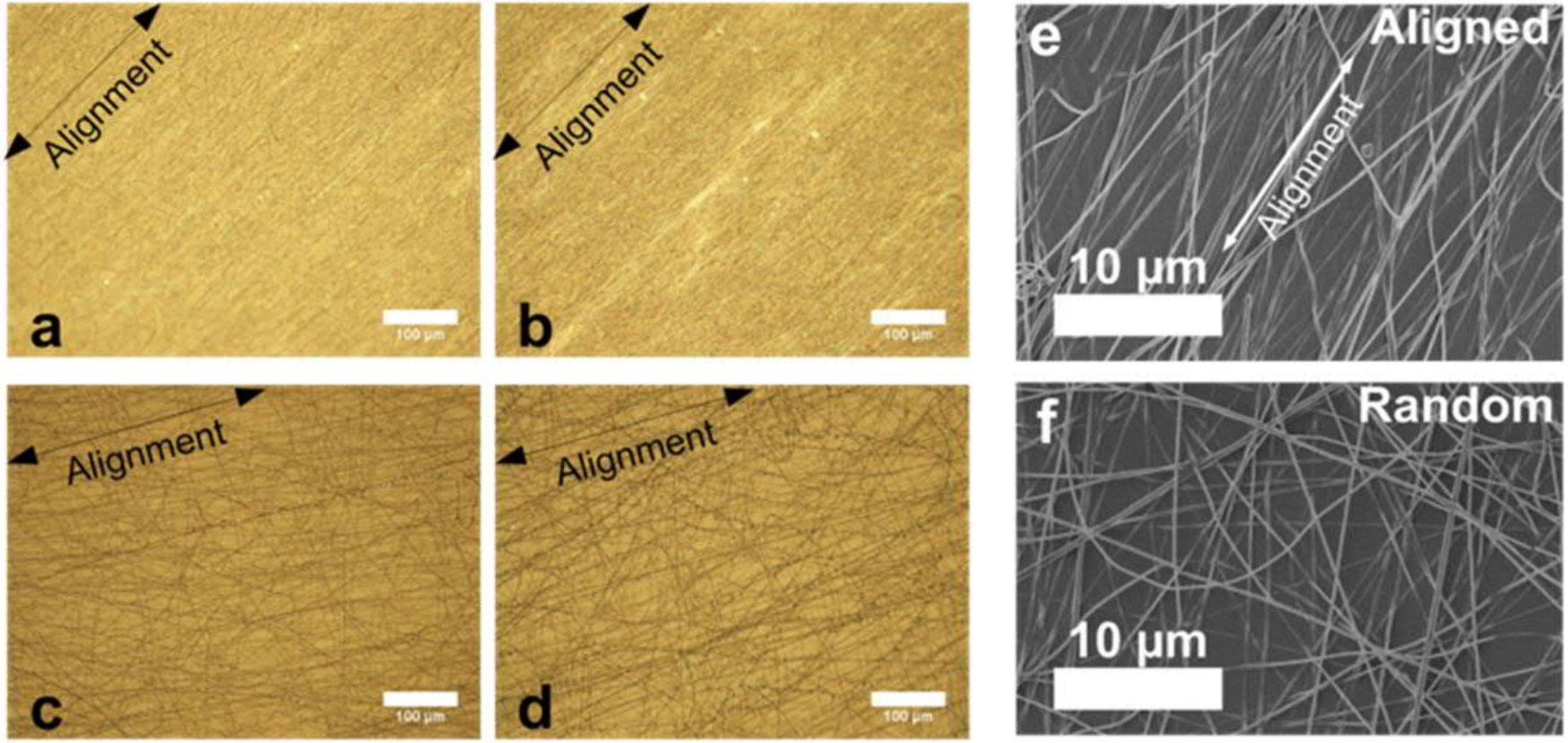

Figure S5.5. Optical microscopy of aligned nanofibers under different alignment direction and stretch ratios after relaxation. Orthogonally aligned at a) 40%, b) 100% and parallel aligned at c) 40%, d) 100%. High magnification (35.2k) of e) aligned and f) random nanofibrous surfaces.

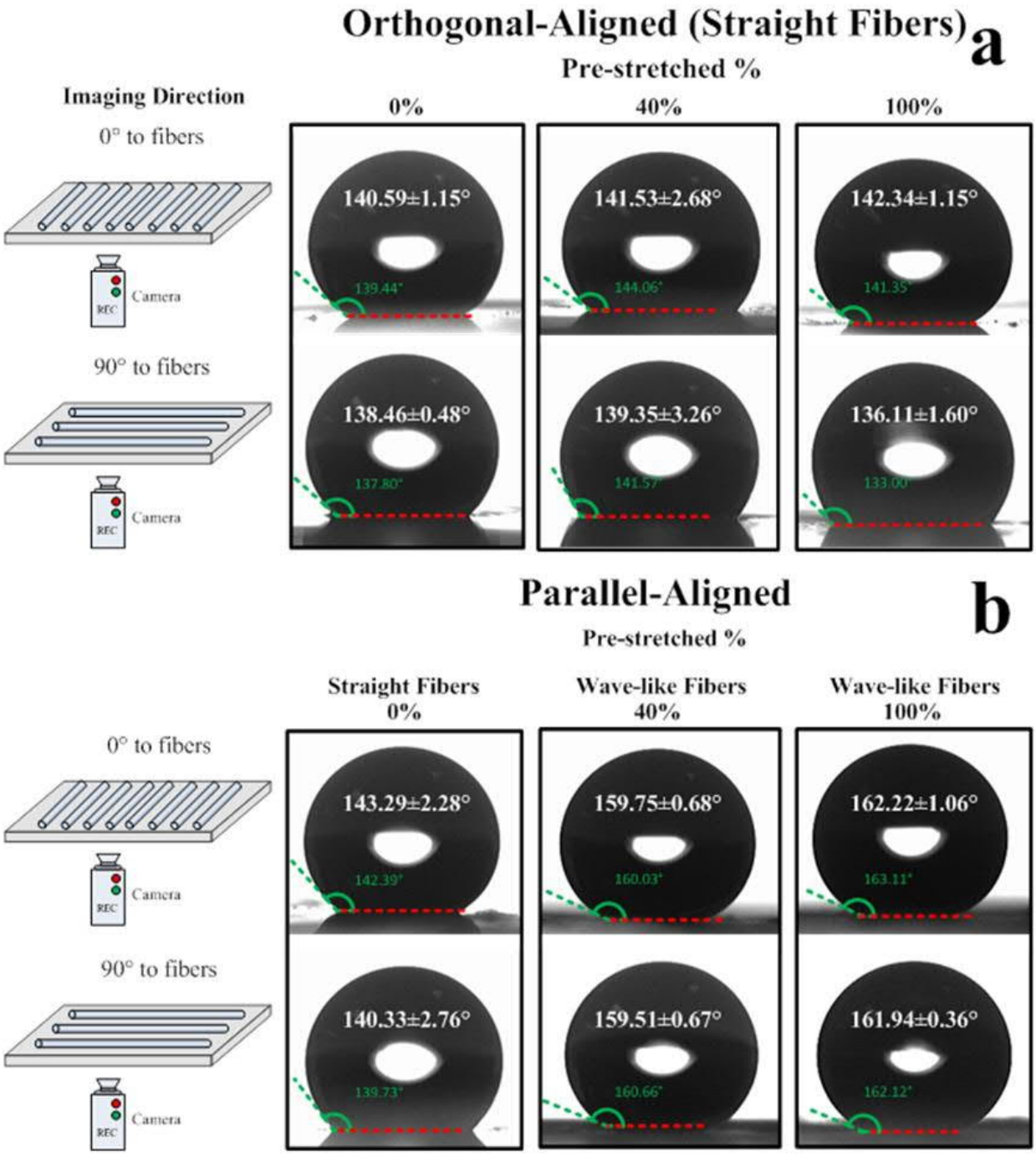

Figure S5.6. Impact of anisotropic interfaces on static WCA. a) Imaging of orthogonally aligned nanofibrous films from different orientations (0° and 90°), showing a maximum variation of 6.23°, which lies within the batch-to-batch WCA variations (2-9°) for orthogonally-aligned nanofibers. b) Imaging of parallel-aligned fibers from different orientations (0° and 90°), showing a maximum variation of 2.96°, which lies within the batch-to-batch WCA variations (1-5°) of the orthogonally-aligned nanofibers.

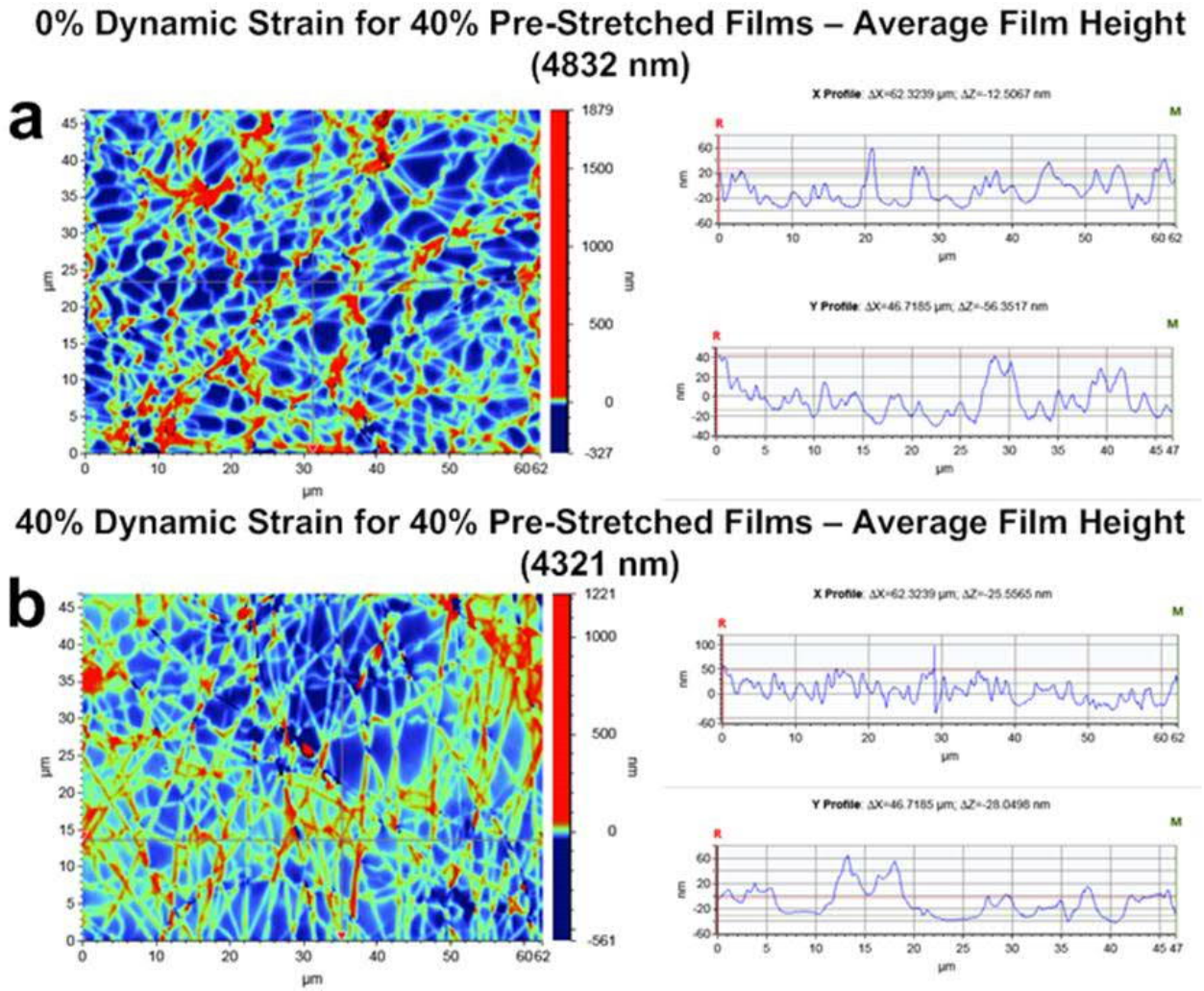

Figure S5.7. Dynamic strain of the wave-like nanofiber films synthesized at 40% pre-stretch. The WLI reveals an average drop in film thickness of ca. 500 nm from the a) relaxed state (0% strain) to b) 40% strain.

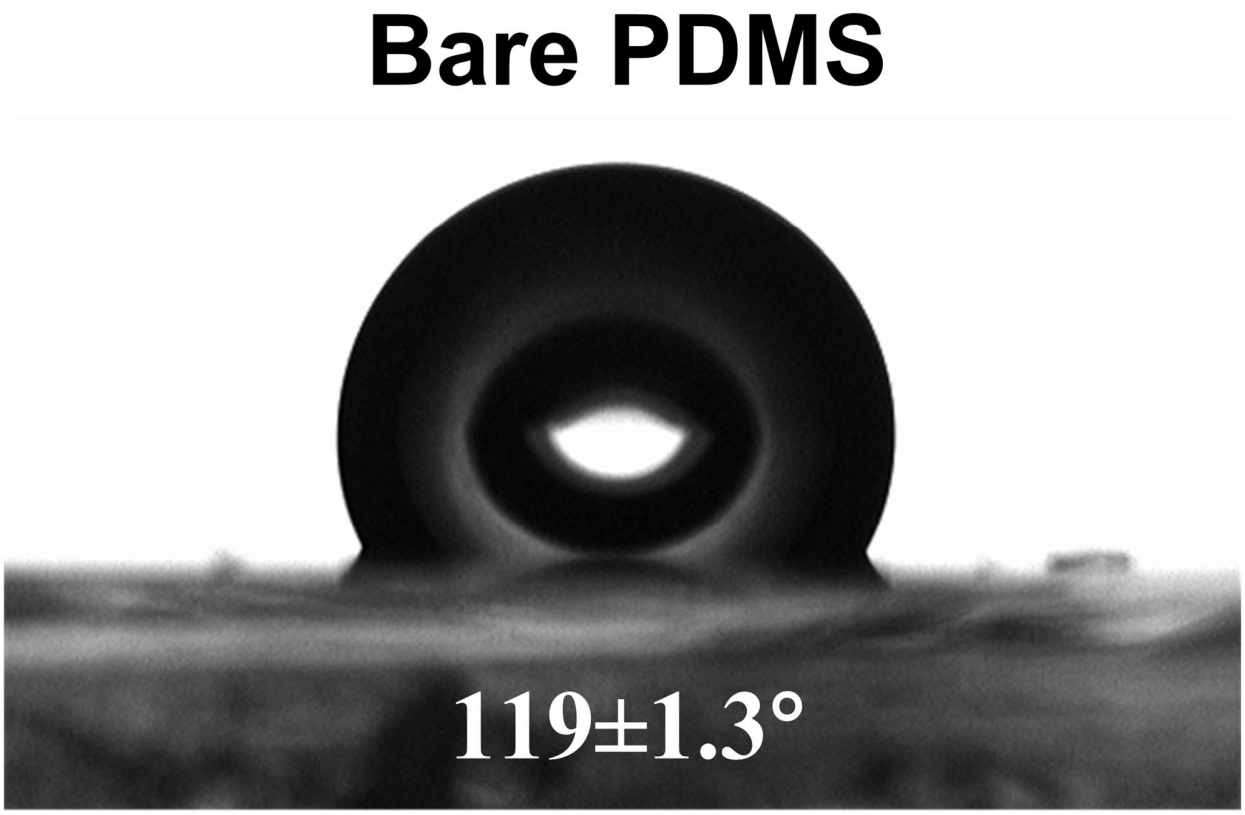

Figure S5.8. Surface wetting properties of an as-prepared bare PDMS substrate before electrospinning. The measured CA and variations were computed through a 5-point CA analysis of freshly cured PDMS strips (2.5 cm by 7.5 cm).

6. Slippery Superhydrophobicity with Ultra-Durable Properties

Abstract

In nature, durable self-cleaning surfaces such as the lotus leaf rely on both their multi-scale robust architectures and cohesive regenerative properties of organic tissue. Real-world impact of synthetic replicas has been limited by the poor physico-chemical stability required for attaining the lotus-like superhydrophobic state. Here, we present the low-cost synthesis of large-scale ultra-durable superhydrophobic coatings. The mechanical enhancement was achieved by the bottom-up hierarchical texturing of an interpenetrated polymer network (IPN) binder. We then integrate the soft yielding papillae textures with a layer of fluoro-functionalized nano-SiO_2. This combination assimilates inherent robustness to the functional nano-coating, thus coupling ultra-low surface energies with mechanical stability. The resulting coatings demonstrate outstanding anti-abrasion resistance, maintaining superhydrophobic water contact angles (WCAs) and a pristine lotus effect with sliding angles (SAs) of below 10° for up to 120 continuous abrasion cycles. They also possess excellent chemical- and photo-stability, preserving performance after more than 50 h exposure to intense UVC light (254 nm, 3.3 mW cm^{-2}), 24 h of oil (tetradecane) contamination and highly acidic conditions (1M HCl). The formulation is readily available in the form of a low-cost polyurethane-acrylic colloid and a fluorinated SiO_2 (F-SiO_2) suspension. The facile approach for substrate-independent fabrication of ultra-durable transparent self-cleaning surfaces with superior abrasion, chemical and UV-resistance holds immense industrial potential.

6.1. Introduction

Self-cleaning surfaces such as the lotus leaf rely on the formation of rolling water droplets that suspend and trap contaminants, resulting in their facile removal.[7] This extreme superdewetting effect is commonly attained by a combination of micro- and nano-texturing coupled to low solid phase surface energy that results in a Cassie-Baxter wetting state.[4] In nature, the durability of such self-cleaning surfaces is provided by the cohesiveness and self-healing properties of organic tissues. Today, large-scale synthetic superhydrophobic surfaces have largely surpassed natural self-cleaning in terms of dewetting performance.[29,604,605] However, their structural stability remains poor and often insufficient for many real-world applications.[445,606]

Fluoro-functionalized nano-structured silica (F-SiO_2), for example, is a highly performing superhydrophobic material that provides water SAs of ca. < 10°.[68,299,607] However, its commercial application remains largely impeded by poor mechanical durability, resulting in the rapid loss of superhydrophobicity upon abrasion damage.[68,297,300,353] Other more robust synthetic textures have achieved industrial-standard abrasion resilience, but require specific substrates,[36,205] suffer from poor optical transparency[29,207] and limited scalability.[608,609] Even amongst the most resilient surfaces, few have demonstrated stable SAs and CAH during abrasion,[29,231] both of which are fundamental for effective self-cleaning properties (SA < 10°).[89,134] Development of scalable approaches for the synthesis of durable superhydrophobic surfaces bears significant commercial impact.[29,605,610]

Synthesis of elastically-deformable hierarchical textures possesses potential for enhanced robustness and long-term stability. Promising concepts include mold-casted elastomers,[231] high functional content-based composites[29,207] and two-step fluoro-silane aided dipcoating[205]. Amongst these, interpenetrated polymer networks (IPNs) represent a class of extremely tough polymers.[611] They are

composed of two or more polymeric networks that are interlaced at the molecular scale without reciprocal covalent bonds.[612] However, IPN synthesis is highly sensitive to gelation and requires careful control of the net-to-net entanglement.[613] In particular, IPNs with polyurethane (PU) and PMMA components are extremely promising for structural stability. In fact, recent work has touted their potential for the fabrication of substitutes for bullet-proof glass.[611] Despite such advancements, the use of PU-PMMA IPNs for the fabrication of robust superhydrophobic self-cleaning surfaces has yet to be explored. This is largely attributed to the many challenges faced by micro- and nano-texturing IPN-typed materials.

Here, we report the synthesis of a self-stabilized PU-PMMA colloidal suspension that self-assembles and cures during spray-deposition. Coupling of the preformed colloid with spray-deposition enables the hierarchically structuring of an ultra-robust IPN coating. Integration of fluoro-functionalized SiO_2 nanoparticles on the curing IPN surface confers excellent superhydrophobicity and optical properties. Initial water contact and SAs of 159° and 0°, respectively were achieved alongside 85% visible light transmittance. Most notably, the IPN-F-SiO_2 coating features outstanding mechanical, chemical and photo-durability. A highly dewetting Cassie-Baxter state was preserved even after 250 rotary abrasion cycles; extended immersion in acidic conditions; oil contamination and even extended high intensity UVC photodegradation. These findings demonstrate a promising scalable and low-cost approach for the fabrication of highly transmissive self-cleaning coatings with superior durability, an enabling step for many real-world applications.

6.2. Results and Discussion

Synthesis of Robust Interpenetrated Networks

Synthesis of the sprayable IPN colloid is illustrated in Figure 6.1a. The colloidal suspension was prepared in two parts, a PMMA component in acetone and the polyurethane (PU) component in xylene. Upon mixing both solutions, each individual constituent crosslinks simultaneously, resulting in a colloidal suspension of PU-PMMA after 24 h of heated stirring. Spectroscopic analysis of the sprayed and dried (48 h) suspensions (Figure 6.1b-d) indicates complete polymerization of both the PU and PMMA components. Complete PU reaction is confirmed by the loss of the 2235 cm^{-1} N=C=O isocyanate stretch band (Figure 6.1c), and the 3227 cm^{-1} and 3492 cm^{-1} -OH stretch bands belonging to polytetramethylene ether glycol (PTHF) and tris(hydroxymethyl)propane (TRIOL), respectively. This was coupled with the formation of the 3300 cm^{-1} -NH stretch band (Figure 6.1b). Complete PMMA reaction is revealed by a loss of the 1637 cm^{-1} C=C stretch band, which represents the main chemical signature of methyl methacrylate (MMA) and its crosslinker (Figure 6.1d).

Homopolymeric PU and PMMA were also developed as cross-linking (Figure S6.1a-c) controls (Figures S6.2, S6.3). The mechanical properties of these materials were investigated by stress-strain analysis using a tensile tester (Instron 4505, U.S.A). The spray-deposited control PMMA samples were extremely hard to manipulate due to their brittle nature, and thus liquid-casted controls were further investigated (Figure 2a, blue line). The IPNs had a significantly higher Young's modulus (192 MPa) than the PU (87 MPa) and PMMA (50 MPa) controls. The IPNs also had nearly 11 times higher maximum tensile strength (16 MPa) than the PU (1.5 MPa) and 3 times that of the liquid-casted PMMA (5.4 MPa). Despite the significantly higher Young's modulus, the IPNs were also significantly tougher and were capable of absorbing significantly more energy before plastic fracture. The elongation at break (Figure 6.2a) of the IPNs was 179-210% and thus ca. 32 times higher than

that (5.5%) of the PU and up to 2 times higher than the liquid-casted PMMA (101%). These improved mechanical properties are attributed to the synergistic behaviour of both components, where the gradual cross-linking of PMMA is expected to form dispersed constituents within the much more rapidly developed PU networks.[611] These integrative constituents stabilize the continuous PU phase, enabling a toughened interface through molecular-level interlacing. Notably, the spray-developed IPN films easily matches and exceeds properties of commercially available state-of-the-art elastomers such as PDMS[614].

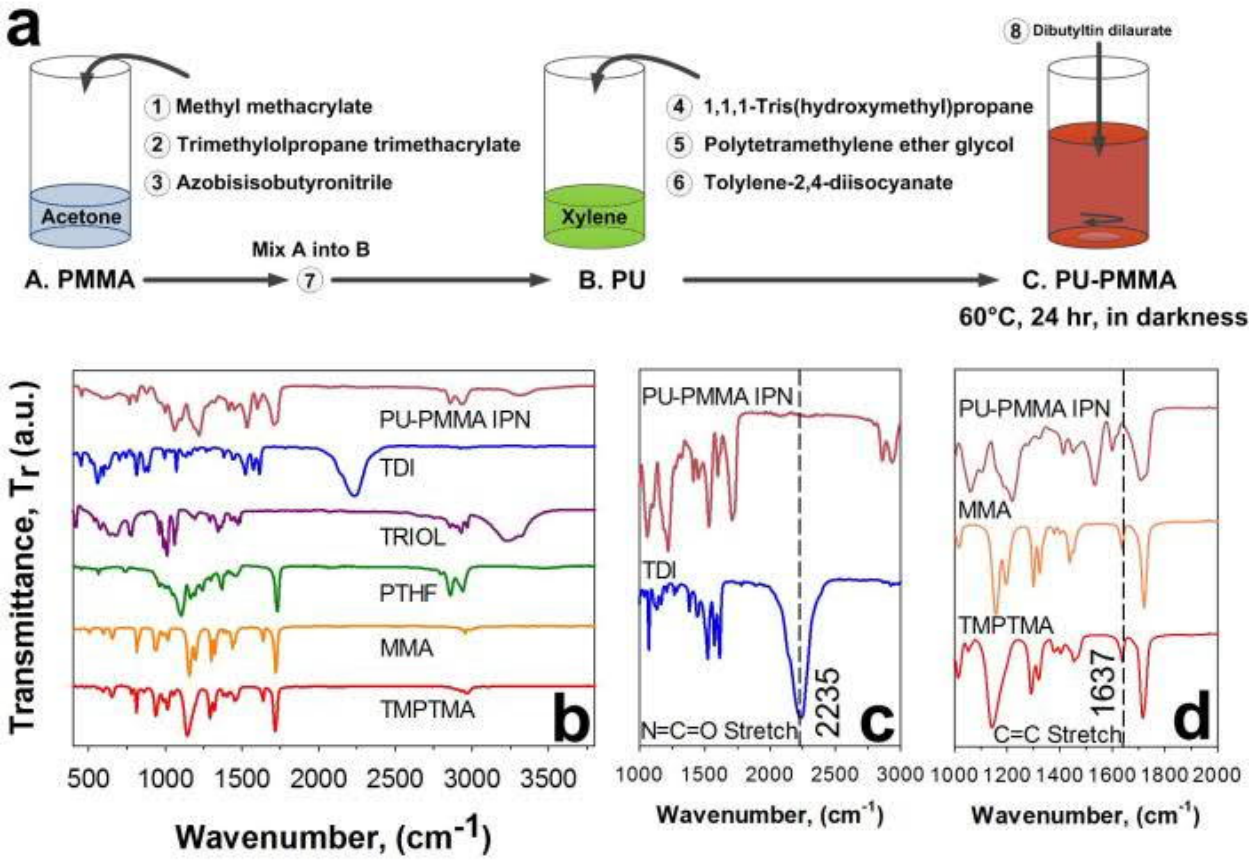

Figure 6.1. a) 2-pot synthesis of urethane and acrylic based sols that were mixed and reacted together to form a sprayable PU-PMMA colloidal suspension. b) Spectroscopic analysis of PU-PMMA IPN's precursor constituents. The c) PU reaction was notably achieved following the loss of 2235 cm^{-1} N=C=O isocyanate stretch and 3227 cm^{-1} and 3492 cm^{-1} -OH stretches belonging to PTHF and TRIOL respectively while forming the 3300 cm^{-1} -NH stretch. The d) PMMA reaction was also simultaneously observed through the loss of the 1637 cm^{-1} C=C stretch that constitutes the PMMA component in the IPN.

Thermal analysis of the IPN, PU and PMMA by differential scanning calorimetry (DSC) further supported the synthesis of a well-formed interpenetrated polymer network. Notably, in the IPN, the typical heat flow characteristics of the PU and PMMA constituents such as melting (T_m), glass transition (T_g) and thermal curing (T_{rxn}) temperatures were eliminated (Figure 6.2b). The mobility of the pendant soft segment, PTHF (Figure 6.2b, cyan line), indicated by the T_g of -75 °C and a T_m of 20 °C disappeared both in the crosslinked PU and the IPN.

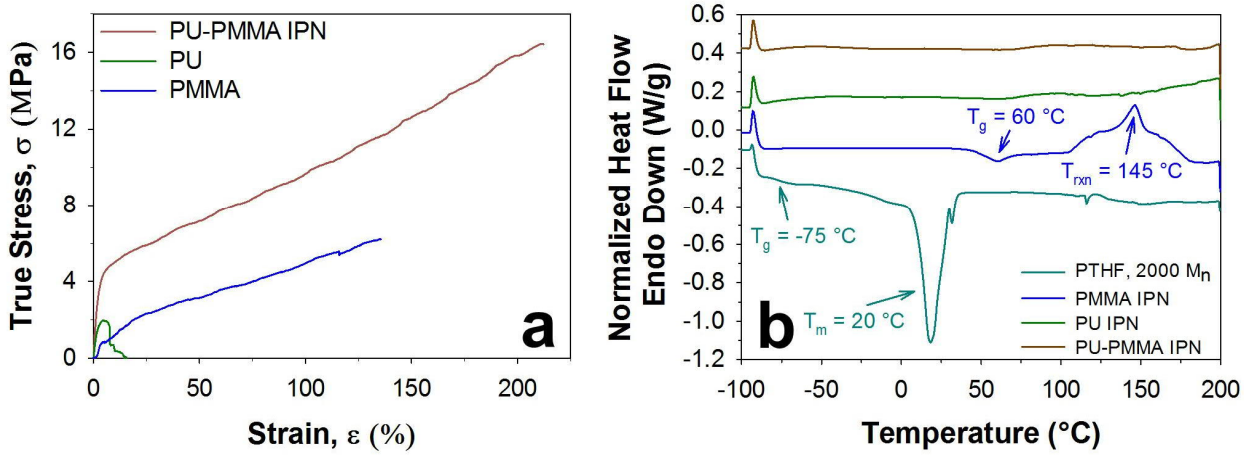

Figure 6.2. a) Tensile stress-strain tests on as-sprayed PU, PU-PMMA IPN and liquid casted PMMA coatings. b) Differential scanning calorimetric analysis of crosslinked PU, PMMA and PU-PMMA IPNs with PTHF, the PU's soft-segment.

The partially crosslinked PMMA showed a T_g of 60 °C and a final curing reaction T_{rxn} at 145 °C. However, for the IPN, these key thermal characteristics were suppressed and a nearly perfect constant heat flow was observed from -100 °C to 250 °C (Figure 6.2b and Figure S6.4b, brown lines). The lost of characteristic heat flow properties belonging to individual components is indicative of mobility-restriction and the formation of a well-integrated IPN with ideally entangled networks. These findings were further confirmed by high temperature thermogravimetric-DSC (TG-DSC) analysis of crosslinked controls and IPN samples from 50 °C to 900 °C (Figure S4a-b). Above 200 °C, 50% weight loss decomposition, T_{50}, was observed at 320 and 378 °C for the PU and PMMA respectively, while the PU-PMMA T_{50} was at 333 °C showing combined properties of the crosslinked components.

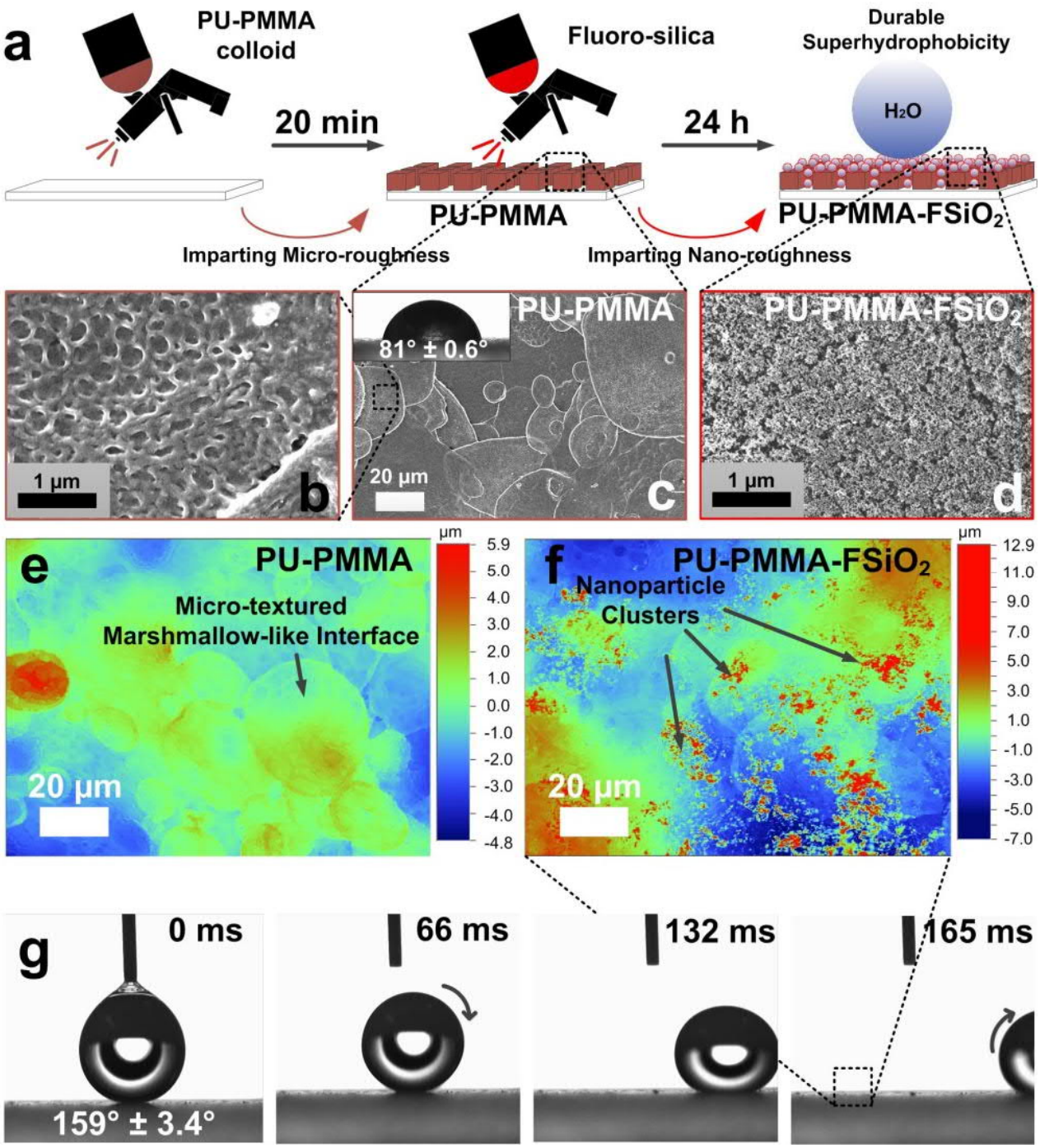

Figure 6.3. Sequential a) deposition of micro- and nano- roughness onto substrates, conferring a tough, rubbery and mechanically durable superhydrophobic interface through self-assembled micro-structures. PU-PMMA interpenetrated polymer network (IPN) with b) sub-micro and c) micro structures. As deposited d) F-SiO_2 nano-structures. (e-f) High magnification (500x) WLI color-map analysis on PU-PMMA IPNs before and after F-SiO_2 impregnation. g) Superhydrophobicity with a near 0° SA.

Further confirmation of successful IPN synthesis was conducted *via* immersion of thin (23 µm thick) strips of material in parent solvents (acetone, xylene) as well as harsher solvents (chloroform, tetrahydrofuran), all of which were insoluble over a period of 24 h (Figure S6.5).

Self-Assembly of Hierarchical Superhydrophobic Surfaces

The self-assembly of superhydrophobic hierarchically structured IPNs was achieved through a sequential spray-deposition step (Figure 6.3a-d). Surface microroughnesses (R_q) of the IPN and control coatings were first quantified by root-mean-square (rms) roughness with white light interferometry (WLI). The microroughness of the cross-linked PMMA and PU were 238 ± 47 nm and 2467 ± 102 nm, respectively. The PU-PMMA IPNs had a significantly higher microroughness of 3048 ± 398 nm. The crosslinked PU had a similar micro-scale morphology to the PU-PMMA IPNs (Figure S6.6), revealing its role as the continuous phase of the IPN.[612] One primary difference was the presence of sub-micro surface defects in the cross-linked PU (Figure S6.6). In addition, high magnification SEM micrographs (Figure 6.3b) also revealed sub-micro craters (diameter of 421 ± 99 nm) on the PU-PMMA IPNs' surfaces, which were not present on the PU. The WCAs (Figure 6.3c inset and S6.5 insets) of the IPN was 81 ± 0.6°, and thus between that of PMMA (76 ± 0.6°) and PU (101 ± 1.4°).

Superhydrophobicity was achieved (Figure 6.3a) by the integration of fluoro-functionalized SiO_2 (F-SiO_2) onto the IPNs and control textures (Figures S6.6, S6.7). An optimal wait-time of 20 min after deposition of the IPNs was found to improve anchoring of the F-SiO_2 nanoparticles into the IPN surface texture (Figure 6.3e-f). This is attributed to the staggered evaporation of volatile organic compounds (VOC) utilized in the IPN colloidal suspension (Figure 6.3a). This optimum F-SiO_2 deposition timeframe was determined by optical microscopy (Figure S6.8) and cyclic abrasion optimization (Figure S6.9-6.12). Initially, the IPN surface is soft and fully encapsulates the F-SiO_2

layer, resulting in the loss of superhydrophobicity. Over time, the IPN surface hardens and becomes less receptive to the incoming functional layer. For deposition wait-times longer than 20 min, anchoring of the F-SiO_2 became inferior, resulting in poorer mechanical stability (Figure S6.12). The optimal PU-PMMA-F-SiO_2 composite coatings (20 min) were highly superhydrophobic with SAs of ca. 0° (Figure 6.3g).

The transmittance spectra of the PU-PMMA-F-SiO_2 layers and PU-PMMA are shown in Figure 6.4a, compared against plain glass. At a wavelength of 600 nm, the net loss in transmittances was measured at 2.2, 5.0 and 14.8% for the F-SiO_2 (Figure S6.13), PU-PMMA and PU-PMMA-F-SiO_2 surfaces, respectively. This 14.8% transmittance loss did not affect the optical transmissivity of glass substrates, with printed text and images clearly visible when placed directly behind the PU-PMMA-F-SiO_2 coated glass slides (Figure 6.4a, inset).

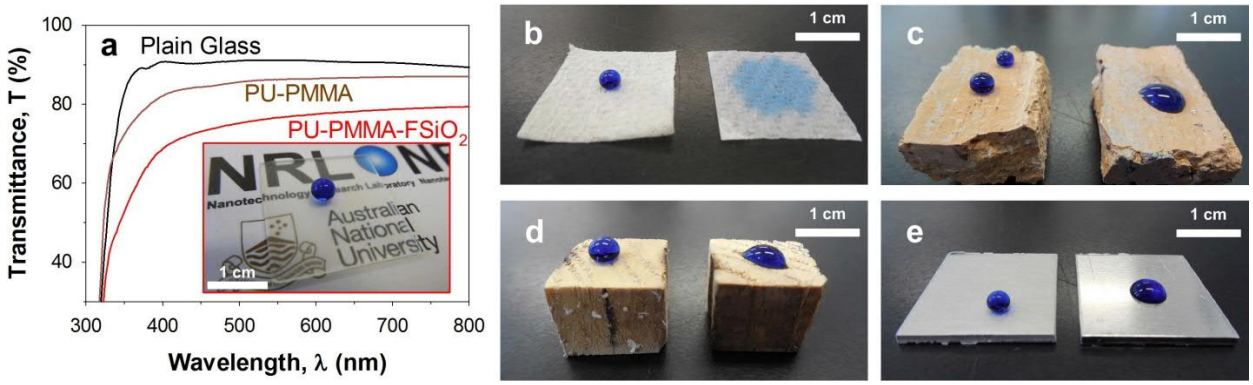

Figure 6.4. a) Transmittances of plain glass substrates vs. PU-PMMA IPN and optimized PU-PMMA-F-SiO_2 (inset of sample showcasing excellent transparency). PU-PMMA-F-SiO_2 coating on a variety of substrates, including b) absorbent paper towel, c) bricks (clay-stone), d) wood and e) aluminium.

The transmittance losses were attributed to higher refractive index (n) contrasts at the PU-PMMA (n ≈ 1.49-1.50) - fluorinated SiO_2 (n ≈ 1.46) interface. The substrate-independent self-assembly of the PU-PMMA-F-SiO_2 surfaces was demonstrated on a multitude of materials, namely paper towel, clay-stone based bricks, wood and aluminum (Figure 6.4b-e and S6.14).

The PU-PMMA formulation was also broadly applicable, and demonstrated compatibility even with flame-made superhydrophobic coatings,[135] achieving stabilization of these ultra-fragile fractal-like structures (Figure S6.15).[615]

Ultra-Robust Superhydrophobic Coatings

Tandem wetting-abrasion analysis (Figure 6.5a,b) of the PU-PMMA-F-SiO_2 surfaces highlighted the drastic enhancement in mechanical stability over the PU, PMMA and pure F-SiO_2 controls. The pure layers of F-SiO_2 deposited on the same glass substrates had an initial WCA of ca. 158° but lost their superhydrophobicity after just 5 abrasion cycles, resulting in WCAs of 101 ± 8°, indicative of wear-through (Figure 6.5c, red line). In stark contrast, the PU-PMMA-F-SiO_2 interfaces preserved superhydrophobicity with WCA > 150° for up to 250 cycles, with the WCA dropping to 143 ± 6° only after the 300th cycle (Figure 6.5c, brown line). This is in good agreement with the performance of the bare monolayers of PU-PMMA. The bare IPN layers preserved their inherent hydrophilic wetting properties with WCAs of ca. 80 - 88° during the entire 300 cycles of abrasion, with neither surface wear-through nor visible superficial damages (Figure 6.5c, green line). The surface textures provided by the cross-linked PMMA and PU controls had a significantly worse performance, which highlighted the importance of integrating the soft rubbery PU with the PMMA component (Figure S6.16). The PMMA supported F-SiO_2 layers experienced a rapid sharp drop in WCAs, losing superhydrophobicity after only 10 cycles with WCAs dropping to 131 ± 4°. After 40 cycles of abrasion, complete wear-through was observed with WCAs reaching 78 ± 7° (Figure S6.16, blue line). The PU integrated F-SiO_2 performed much better than the PMMA variants, with excellent preservation of superhydrophobicity until extensive wear-through occurred between the 100th to 140th cycles (Figure S6.16, green line). For these PU-F-SiO_2 surfaces, a sharp drop in WCAs from 165 ±

3° to 115 ± 24° occurred during the 100th to 120th cycle, which was mirrored by a steep increase in SA (Figure 6.5e) from 37 ± 5° to 81 ± 10°.

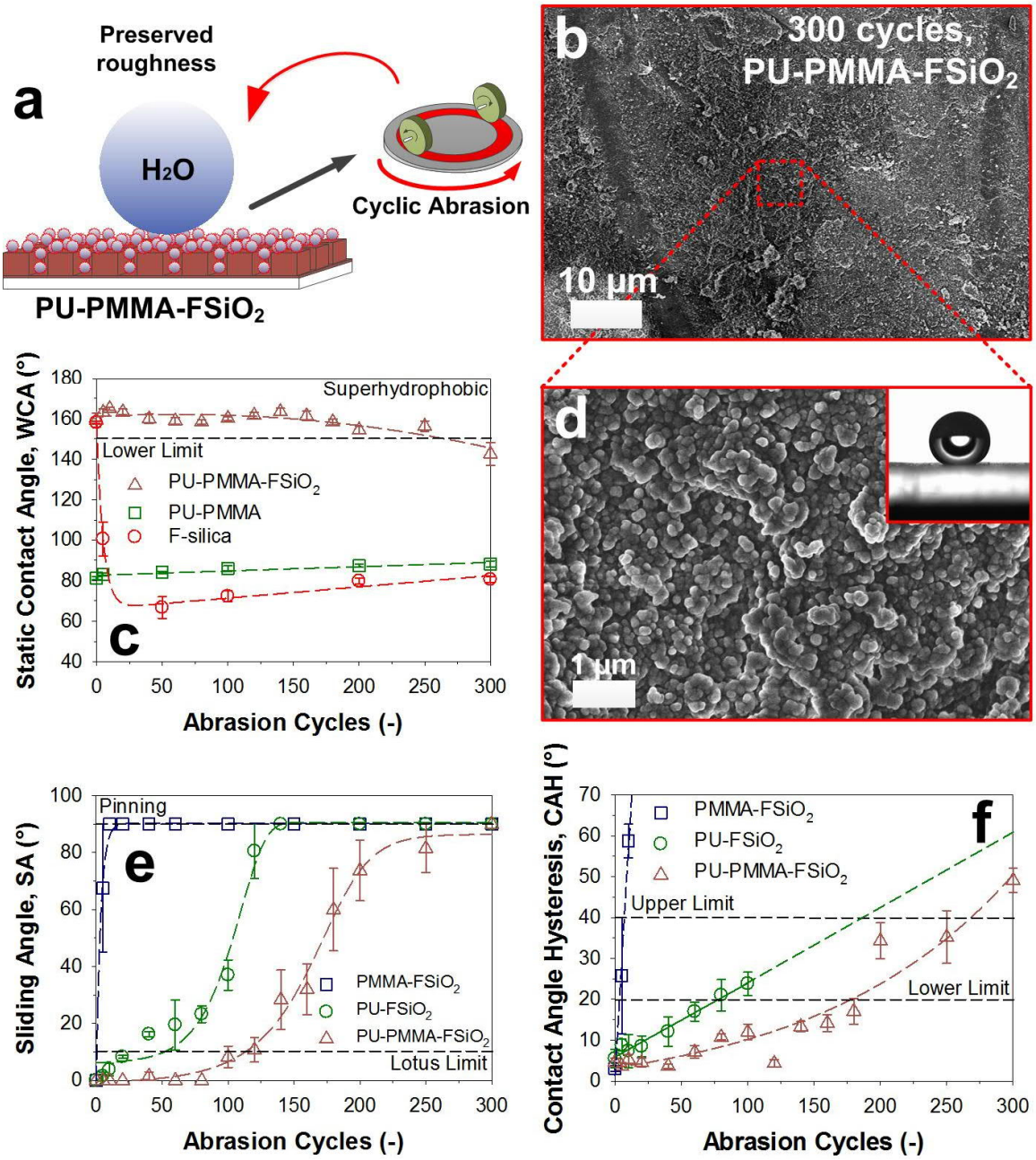

Figure 6.5. a) Tandem abrasion-wetting characterizations. Wetting characterization of b) cyclically abraded samples, with assessment of c) static WCAs of PU-PMMA-F-SiO_2 with PU-PMMA IPN and F-SiO_2 controls. d) High magnification SEM analysis at the loss of superhydrophobicity (WCA < 150°) of PU-PMMA-F-SiO_2 at 300 cycles showing the persistent presence of nanoparticles. e) SA and f) CAH of PU-F-SiO_2, PMMA-F-SiO_2 and PU-PMMA-F-SiO_2 revealed the enhanced damage resilience of the latter.

SA analysis (Figure 6.5e, brown line) of the abraded PU-PMMA-F-SiO_2 coatings was also sequentially performed. Here, the pristine lotus effect with a SA below 10° was preserved for up to 120 cycles while it gradually rose to pinning at the maximum 300th cycle measured. The enhanced functional robustness was attributed to excellent elastic properties of the hierarchical composite-IPN structure. As a result, the mechanical deformation did not affect nanoparticle retention, and the coatings were thus highly resilient to extended abrasive damage. The superdewetting data was coupled to further CAH analysis. Here, a significantly smaller drop in superdewetting properties per abrasion cycle was noted as compared to PU-F-SiO_2 and PMMA-F-SiO_2 variants (Figure 6.5f, brown line).

SEM analysis of the abraded PMMA-F-SiO_2 and PU-F-SiO_2 surfaces revealed extensive coating tearing and delamination at the 50th and 150th abrasion cycles, respectively (Figure S6.17d,e). The failure mode of spray-deposited PMMA coatings revealed unmistakable brittle fracturing, distinguished by sharp broken edges (Figure S6.17d,g).[616] The spray-deposited PU, alternatively, failed under ductile fracturing after abrasion damage (Figure S6.17h), in line with its rubbery nature.[616]

The excellent durability of the composited IPN is primarily attributed to the superior nanoparticle retention capabilities of PU, a soft elastic material, stabilized by the strong and unyielding characteristics of PMMA. The interlacing of PMMA's crystalline polymeric network preserved the mechanical integrity of the IPN, and vastly promoted wear resistance, enabling well-sustained damages without wear-through. This gave rise to a tough and elastic texture, which is capable of withstanding high mechanical stress while retaining key functional F-SiO_2 nanoparticles. Notably, high magnification SEM analysis of the PMMA-PU-F-SiO_2 after 300 abrasion cycles (Figure 6.5b,d) revealed only minimal variation of the surface morphology. However, randomly scattered

microscopic tears were present by the 300th cycle (Figures S6.17f and S6.18), which is attributed to the eventual loss of superhydrophobicity (WCAs of 143 ± 6°). Nonetheless, quantitative analysis of the surface roughness (Figure S6.19) indicates well-preserved micro-scale structures. Minimal variations were noted before and after abrasion, highlighting the excellent stability of the IPN's marshmallow-like construct (Figure 6.3c,e).

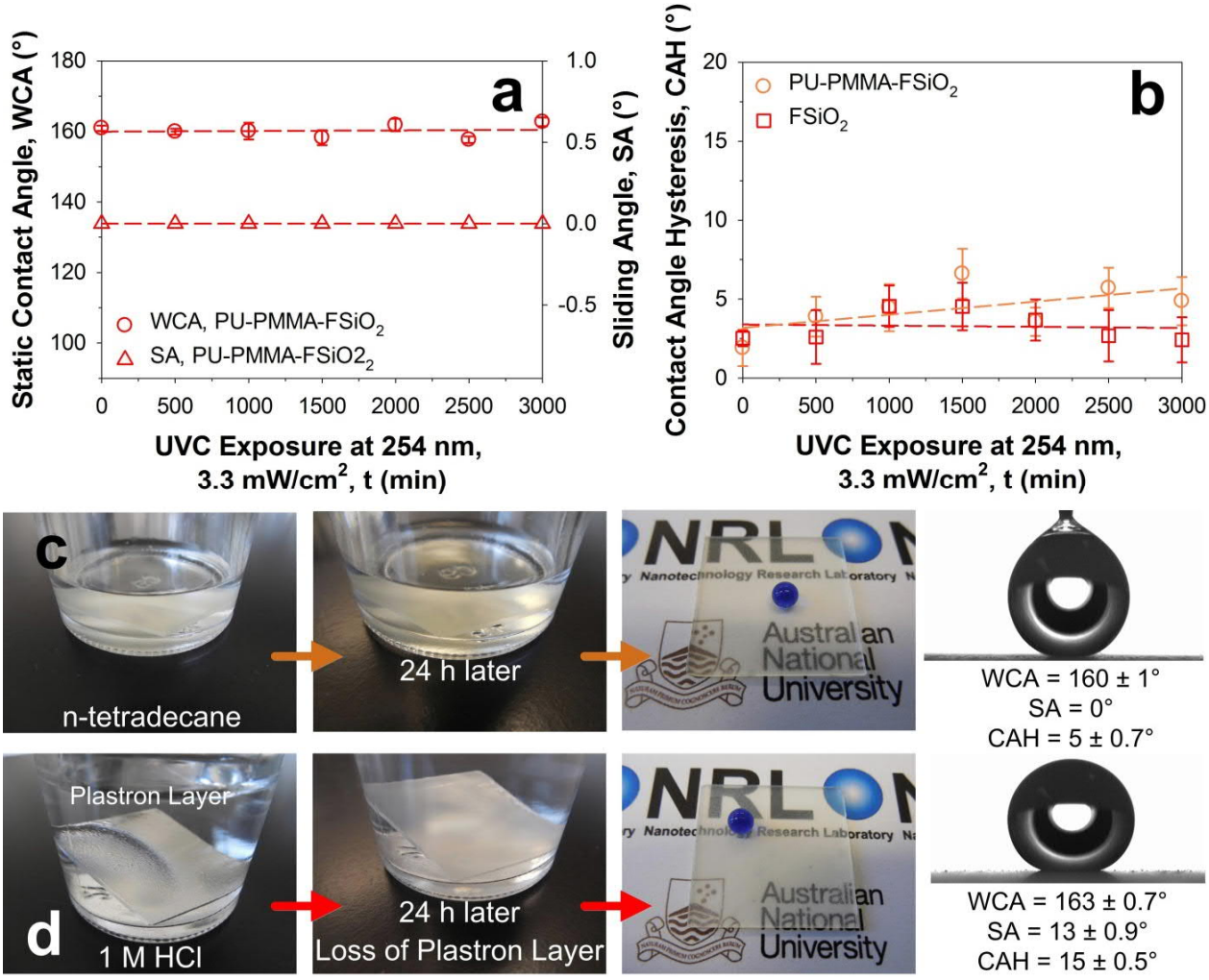

Figure 6.6. Real-world photodegradation and chemical damage resilience. (a-b) High intensity shortwave UVC (254 nm) resistance of PU-PMMA-F-SiO_2, with minimal observable impacts on SA, WCA and CAH during all 3000 min of testing. Immersion of F-SiO_2 integrated PU-PMMA IPNs into c) oil (tetradecane) and d) acid (1M HCl) for 24 h, with the subsequent loss of plastron layers in both, but demonstrated excellent damage resilience and readily recovered functionalities.

The superhydrophobic PU-PMMA-F-SiO_2 coatings were then tested for various real-world situational damage tests. These included a finger-wipe test,[29] UV-exposure, acid-exposure and hydrocarbon oil contamination. A finger-wipe test demonstrated the finger-touch resilience[29,617] of the PU-PMMA IPN integrated F-SiO_2 coating as compared to the bare F-SiO_2 coating, with full functional dewetting properties after a real-world damage situation.[29] The performance of these IPN-F-SiO_2 coatings challenges state-of-the-art mechanically[29] and chemically resistant coatings[67,618] while supplementing superior transmittance properties.

UV photodegradation tests (UV-C, 254 nm, 3.3 mW cm^{-2}) were also conducted up to 50 h, without any discernible changes in SAs and WCAs (Figures 6.6a and S6.20). The measured CAHs (Figure 6.6b) were very stable and within the standard batch-to-batch variations (± 5°). Lastly, 24 h extended immersion into an oil analog (n-tetradecane) and concentrated acid (1M HCl) resulted (Figure 6.6c,d) in minimal impact on the superhydrophobicity of the PU-PMMA-F-SiO_2 interfaces. The ease of oil-decontamination was also demonstrated using a jet of ethanol after retrieval (Figure S6.21), showing superior recoverability as compared to recent analogous materials and coatings[29,297,618]. This is of significant impact as the infiltration of oil into superhydrophobic materials is expected to cause micro-reorganization, resulting in smoother surfaces while impeding the recovery of superhydrophobicity[29,231]. Overall, the properties of these PU-PMMA coatings were compared with previous reports (Table S6.1), which revealed a unique combination of transparency, mechanical-, photo- and chemical- robustness.

6.3. Conclusions

The substrate-independent synthesis of ultra-robust and transparent superhydrophobic surfaces is achieved by a novel, low-cost and scalable approach. A sprayable IPN colloidal suspension was developed, which provides a mechanically and chemically resilient hierarchical texture for surface anchoring of highly hydrophobic F-SiO_2 nanoparticles. The resulting IPN-F-SiO_2 coatings possessed outstanding abrasion resistance, preserving SAs and WCAs of 10.8 ± 4.4° and 161.6 ± 1.5°, respectively, after 120 standard abrasion cycles. These excellent mechanical properties are attributed to the soft elastic deformation-recovery properties of the IPN texture. Real-world situational damage tests included abrasion, physical touch, high intensity UVC photodegradation (254 nm, 3.3 $mWcm^{-2}$, 50 h), extended immersion into concentrated acid (1M HCl, 24 h) and oil contamination (24 h). These tests were easily withstood with negligible impact to the coatings' superhydrophobic and transmissive properties. The sprayable polyurethane-acrylic IPN colloid represents a low-cost and highly scalable platform for the fabrication of transparent ultra-durable superhydrophobic textures. Its facile development and wide applicability can be easily exemplified as self-cleaning and protective coatings.

6.4. Experimental Section

Preparation of Polyurethane-Acrylic (PU-PMMA) Colloid

A cross-linking polymethyl methacrylate (PMMA) mixture (Pot A) was first prepared with the addition of 10 mL of acetone (Sigma Aldrich, ≥ 99.5%), followed by 1.01 mL of methyl methacrylate (MMA) (Sigma Aldrich, 99%), 47.2 µL of trimethylopropane trimethacrylate (Sigma Aldrich, 90%) and 30.4 µL of 2,2'-Azobis(2-methylpropionitrile) solution, AIBN (Sigma Aldrich, 0.2M in toluene). Almost simultaneously, a cross-linking polyurethane mixture (Pot B) was also prepared with the addition of 10 mL of m-xylene (Univar, 99%), followed by 0.220 g of 1,1,1-Tris(hydroxymethyl)propane (Sigma Aldrich, ≥ 98%), which was stirred rapidly (1500 RPM) for 5 min to disperse the solids. 1.01 mL of polytetramethylene ether glycol (Sigma Aldrich, M_n ~ 2000) was added and the (poly)-ols based mixture was further stirred for 5 min. 0.568 mL of tolylene-2,4-diisocyanate, TDI (Sigma Aldrich, 95%) was then added into the mixture of (poly)-ols. PTHF and TDI were first melted in a drying oven (60 °C) before addition. Pot A was then vortex mixed and poured directly into Pot B, forming the reaction pot, a clear solution. An initiator, dibutyltin dilaurate, DD (Sigma Aldrich, 95%) was then added before the reaction was sealed and incubated at 60 °C for 24 h in darkness with a constant stirring rate of 500 RPM to form a sprayable colloidal suspension (Figure S6.22). Excess isocyanate groups were added to compensate for its high reactivity, which is known to lead to some side networking reactions[619]. The post-reaction mixture is known as the sprayable PU-PMMA colloid (0.15 g mL^{-1}), which is made up of 66 w/w PU and 34 w/w PMMA. Homopolymeric cross-linked polyurethane (PU) and polymethyl methacrylate (PMMA) controls (Figures S6.1, S6.6) were prepared under identical reaction conditions, utilizing the same solvent, crosslinkers and initiators (AIBN and DD) ratios while excluding the constituents of the other polymer. Due to fundamentally different reaction environments (without its partner polymer), optimal

reaction conditions for sprayable controls varied slightly, with pure PU being synthesized at 0.075 g mL^{-1} while PMMA was synthesized at 0.4 g mL^{-1}. This was performed based on sequential concentration-spectroscopic analysis, aimed at the synthesis of a fluid pre-polymer solution while avoiding gelation. Spray-deposition was conducted within 48 h of reaction stoppage for all samples in efforts to preserve comparative consistency.

Functionalization of SiO_2 Nanoparticles for F-SiO_2

A round bottom flask was first charged with 80 mL of dry chloroform (Sigma Aldrich, ≥ 99%) and purged with dry nitrogen for 30 min. 2 g of fumed SiO_2 nanoparticles (Sigma Aldrich, 7 nm) with an effective surface area of 395 m^2 g^{-1} were then added into the flask under gentle stirring with a further nitrogen purge of 10 min. At a graft density of 4 µmol m^{-2}, 0.945 mL of 1H, 1H, 2H, 2H-Perfluorooctyldimethylchlorosilane (Novachem) was added into the flask. Reaction was then allowed to proceed at 25 °C at a stirring rate of 500 RPM for 48 h in an oil bath under dry nitrogen. Functionalized SiO_2 (F-SiO_2) were then washed in 3 cycles of dry chloroform (50 mL g^{-1}) and dried at 50 °C for 24 h. F-SiO_2 was re-suspended in acetone (Sigma Aldrich, ≥ 99.5%), at a concentration of 50 mg mL^{-1}. The dispersion was then immersed in a sonication bath for 60 min, interspersed with 15 min intervals of 10 s long vortex mixing. Spectroscopic analysis confirmed successful functionalization through the formation of peaks from 500 cm^{-1} to 1000 cm^{-1} indicative of CF_2 groups (Figure S6.7).[620] Thermogravimetric analysis indicates a functionalized w/w percentage of ca. 19.5% (Figure S6.7).

Spray-Coating of Polyurethane-Acrylic IPNs

Upon completion of synthesis, liquid-based solutions of the superhydrophobic SiO_2 (F-SiO_2) and PU-PMMA colloid are extremely stable, and can be stored for extended periods (6 months) without losses in functional properties. The PU-PMMA colloid was then loaded and spray-deposited at a pressure

of 2-3 bars with a flow rate of 0.2 mL s^{-1} from a 10 cm working distance (WD) using an artist's air brush (nozzle diameter, 0.2 mm). 5 mL of the colloid (0.15 g mL^{-1}) was typically sprayed onto glass substrates over an area of 2.5 cm by 10 cm. A traverse rate of ca. 10 cm s^{-1} was maintained using guide rails on a custom-built spray rig. Optimized sprayable conditions of controls were calibrated (PU, 10 mL, 10 cm WD and PMMA, 1.25 mL, 15 cm WD) to equalize the net deposition mass. Optimized coatings (23 µm thick, 5 mm width, 25 mm length) of PU-PMMA IPNs were immersed (5 mL) into its parent solvents (acetone and xylene) and two harsher solvents (THF, chloroform) for 2 h and imaged. These coatings were observed to be insoluble over a period of 24 h, with minimal swelling when contacting its parent solvents (Figure S6.5). Notably, they were also insoluble in THF and chloroform, although significant swelling of the coatings occurred, and they broke up mechanically upon swirling (Figure S6.5). The post-deposition insolubility in harsh solvents is characteristic of successfully interpenetrated polymeric networks.

Spray-coating of F-SiO_2

F-SiO_2 in acetone suspensions (50 mg mL^{-1}) were sprayed onto desired (coated or uncoated) substrates at 2-3 bars at a flow rate of 0.2 mL s^{-1} from a 10 cm working distance using an artist's air brush (nozzle diameter, 0.2 mm). 2 mL of the suspension was typically sprayed onto coated glass substrates with a dimensional area of 2.5 cm by 5 cm. A traverse rate of ca. 10 cm s^{-1} was maintained using guide rails on a custom-built spray rig. The VOC degassing time prior to the deposition of F-SiO_2 was varied and briefly studied between 10 to 40 min in optimally developed samples.

All coatings were stored for between 24-72 h in darkness prior to the commencement of testing. This enables complete curing, degassing and stabilization of intra-polymer stresses within the material prior to characterizations.

Wetting Analysis

WCAs were measured by placing and averaging 4 drops of deionized water (6.5 µL) on cross-batch (4) sample surfaces using the sessile drop method. Superhydrophobic interfaces demonstrating a SA with negligible tilt were classified under the SA of 0°. Abrasion damaged interfaces possessed higher SAs were analyzed *via* a custom-built tilting goniometer. The CAH was measured *via* the drop-in drop-out technique which provided the average ACA at 9 µL and the average RCA at 2 µL. 4 cross-batch readings were taken. Dynamic and static images were recorded using a KSV CAM200 contact angle goniometer (Finland) with a heliopan ES43 camera (Japan). The WCA, SA and CAH were computed by a commercially available (CAM2008) program. Data was presented as mean ± standard errors.

Abrasion Analysis

Quantitative abrasion damage analysis was conducted (Figure S6.23) using a rotary platform abrasion tester with two abrasive CS-10 (Calibrase, U.S.A) wheels (resurfaced with 150 grit discs) at 60 RPM based on the ASTM D4060 Taber standard. The load on each grinding wheel was 250 g. The CS-10 wheels' possessed widths of 12.7 mm and diameters of 51.7 mm. Assuming material properties[616] of wheels (Al_2O_3)[621] and substrates (soda-lime glass), with Poisson ratios of ν_{CS10} = 0.24 and $\nu_{substrate}$ = 0.23, and elastic moduli of E_{CS10} = 380 GPa and $E_{substrate}$ = 69 GPa respectively, a Hertzian cylinder-plane contact pressure of ca. 12.1 MPa was estimated.[622] This value aligned well with literature utilizing the rotary abrasion technique.[621] This test method was chosen largely due to its well-assessed and standardized approach.[297,353,608] Five sample types were chosen for representation, namely, PU-PMMA-F-SiO_2, PU-F-SiO_2, PMMA-F-SiO_2 as well as F-SiO_2 and PU-PMMA IPN controls. Samples were subjected to consecutive tandem abrasion-wetting characterization cycles

(between 0 to 300), enabling complete mapping of abrasion-affected WCAs, SAs and CAHs. Dust and debris were blown off the surfaces simultaneously with a pressurized air gun during cyclic testing.

UV Resistance Analysis

UV resistance was assessed in a short-wave (254 nm) UVC cross-linker (CL1000, Ultra-Violet Products, UK). Exposure times were cycled through 100 min cycles up to 3000 min (50 h). The UVC photodegradation experiments were halted after 50 h (Figure S6.24) based on the consideration of the state-of-the-art testing parameters employed for UV-resistant superhydrophobic materials at wavelengths (254-365 nm), intensity (2 mW cm^{-2}) and exposure timeline (250-300 min)[67,623]. Tests for superhydrophobicity were conducted after every 100 min cycle using a jet of water while CA measurements were taken every 500 min. The UV chamber was heated up by the mercury lamps to ca. 70-80 °C during use, but was cooled down prior to initializing the next cycle. Exposure intensity was measured at 3.3 mW cm^{-2} *via* the internal calibration of the instrument.

Contamination Analysis

As-synthesized optimal coatings were assessed for contamination resistance by soaking in oil, acid and a caustic base for 24 h at 25 °C. Analogs for oil, acid and base were represented by n-tetradecane, 1M HCl and 1M NaOH (Figure S6.25) respectively. After simulated contamination, interfaces were briefly cleaned by rinsing with ethanol (oil) and deionized water (corrosives) respectively. Wetting studies were conducted after blow drying these interfaces with a pressurized air gun.

Thermal and Mechanical Analysis

High and low temperature differential scanning calorimetry (DSC) analysis were conducted using the STA 8000 (Perkin Elmer, U.S.A) and DSC 1 STARe (Mettler Toledo, Switzerland) coupled to an

immersion cooler (Huber TC100, Germany), respectively using alumina and aluminum pans, from 50 to 900 °C and -100 to 200 °C at 10 °C min^{-1} ramp under nitrogen.

No annealing cycles were conducted to present accurate properties of as-synthesized materials. Thermogravimetric (TGA) and differential thermogravimetry (DTG) analysis were also simultaneously coupled to the high temperature DSC analysis. TGA analysis was also used to assess nanoparticle functionalization. Mechanical properties of polymeric IPNs (and controls) were mapped through a series of stress-strain tests using a tensile tester *via* an Instron 4505 (U.S.A), with a 10 N load cell and an extension rate of 1 mm min^{-1} until film breakage (20-25 °C, 20-30% relative humidity). The Young's modulus was automatically computed by the Bluehill® software. PU-PMMA and PU coatings were spray-coated at approximately 4-6 mm (width) with 20-30 µm (thickness) with a fixed test length of 10 mm.

As spray-coated PMMA coatings were too brittle for the required manipulation in tensile testing, they were instead liquid-casted at 30-70 µm (thickness) and dried-cured at room temperature for 72 h prior to use. As such, the liquid-casted PMMA coatings should not be deemed directly comparable to its sister coatings.

Coating thicknesses were analyzed *via* a coating thickness gauge (DT-156) while widths were measured *via* vernier calipers. Variations in material and coating uniformity were assessed across 5 measurements. Data was presented as mean ± standard errors. The most optimal runs amongst the repeat measurements were presented as a true stress vs. strain graph.

Surface Analysis

Selected samples were analyzed *via* scanning electron microscopy (Zeiss UltraPlus analytical scanning electron microscope (FESEM) at 3kV). Prior to examination, SEM specimens were

platinum sputter-coated for 2 min at 20 mA. Fourier Transform Infrared-Attenuated Total Reflectance (FTIR-ATR, Bruker-Alpha, U.S.A) was performed (24 scans from 400 to 4000cm^{-1}) on all as-synthesized samples and pre-synthesis constituents to verify all intended chemical reactions (functionalization, cross-linkages, polymerization). UV-vis analysis was conducted using a microplate reader (Tecan 200 PRO, Switzerland) from 300 to 800 nm with 10 scans per cycle under the Absorbance Scan mode. Time-controlled morphological variations were conducted using a light microscope (Nikon Eclipse E200, TV lens 0.55x DS) on coated glass substrates. This was performed immediately after spray-coating of the IPN, which was then optically micro-photographed in 2-min cycles up to 1 h, before being analyzed in hourly cycles up to 3 h and finally at 18 h (steady state). Surface analysis was also conducted *via* white light interferometer (Veeco, Wyko NT9100, USA), which provided 50x to 500x magnification with a field of view (FOV) of 1x *via* the vertical scanning interferometry (VSI) mode. The WLI technique enabled the mapping of the micro- nano-structural profiles before and after abrasion damage, improving understanding behind the naturally-agglomerated structures for abrasion-resilience. A magnification of 50x provided macro-view of the surfaces but did not provide micro- or nanoscale analytical accuracy. Magnifications of 200x and 500x provided higher analytical and color-mapping accuracy, and the former was used broadly to analyze potential microroughness variations induced by morphological damages. A backscan of 50 µm and length of 25 µm was used with a modulation of 3% in order to cover the maximum peak-to-trough heights of hierarchical coatings averaging 3 repeats on samples.

6.5. Supplementary Information

Table S6.1. Comparative performance with robust superhydrophobic coatings in the literature.

Material	Transmittance Losses (600 nm)	Abrasion Test	Abrasion Resistance[#]	UV-Resistance	Acid-Resistance	Ref.
PU-PMMA IPN-F-SiO_2	15%	ASTM D4060, Rotary Abrasion	300 cycles	≥ 50 h, 254 nm, 3.3 mW/cm^2	≥ 24 h, 1M HCl	This work
Fluoro-diatoms	N.A	ASTM D4060, Rotary Abrasion	200 cycles	N.A	N.A	[17]
Flame spray TiO_2/SiO_2	N.A	ASTM D4060, Rotary Abrasion	2-5 cycles	N.A	N.A	[13]
BOSTIK-FTiO_2	Not transparent	Sandpaper Abrasion Test (240 grit), 100 g mass	≥ 40 cycles	N.A	N.A	[5]
Acrylic-urethane-F-SiO_2	Not transparent	Sandpaper Abrasion Test (2000 mesh), 2 kPa	200 cycles	N.A	≥ 12 h, HCl, pH 1	[16]
Templated PU	N.A	Polished Aluminum Rubbing Test (3 kPa)	10,000 cycles	N.A	N.A	[19]
Silicone-F (oxides)	0-10%	Water test	Water jet, 45 kPa	N.A	N.A	[9]
F-SiO_2	< 5%	Water test	Water rinse	N.A	N.A	[11]
PU-F-SiO_2	0-10%	N.A	N.A	200-400 h, UV-A	N.A	[12]
F-SiO_2-ZnO nanorods	0-10%	N.A	N.A	≥ 300 min, 365 nm, 2 mW/cm^2	N.A	[32]
F-BiOCl	N.A	N.A	N.A	≥ 270 min, 254 - 365 nm	N.A	[37]

- Until loss of 150° CA.

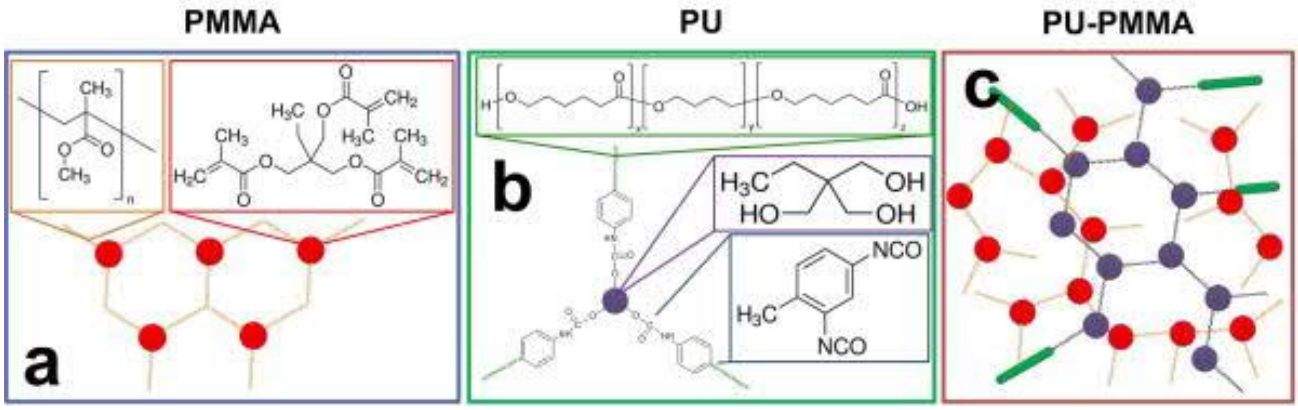

Figure S6.1. Molecular schematic of a) crosslinked PMMA, b) crosslinked PU and the optimally developed c) PU-PMMA Interpenetrated Polymer Networks (IPNs).

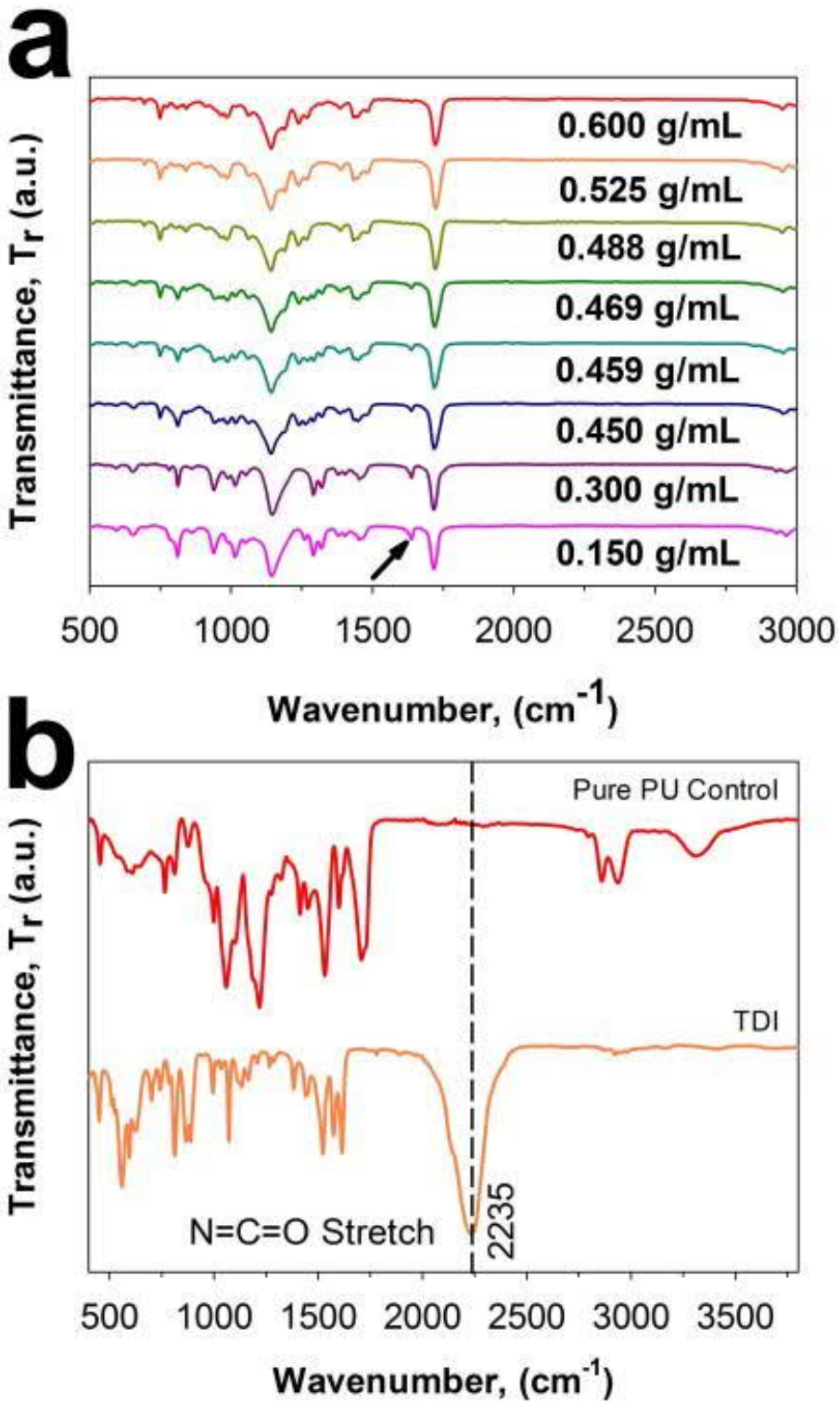

Figure S6.2. Development of optimal controls - cross-linked PU and PMMA. a) Spectroscopic analysis of optimal PU control developed at a polymer to solvent ratio of c) 0.075 g/mL, which revealed complete reaction of the isocyanate group at 2235 cm^{-1} and 3227 cm^{-1} and 3492 cm^{-1} -OH stretches belonging to PTHF and TRIOL respectively while forming the 3300 cm^{-1} -NH stretch, indicating complete formation of the cross-linked polymer. b) Spectroscopic analysis of optimal PMMA control developed at a polymer to solvent ratio of 0.450 g/mL, which revealed only partial reaction of C=C 1637 cm^{-1} stretch, while preserving sprayability (primary comparative property in this work).

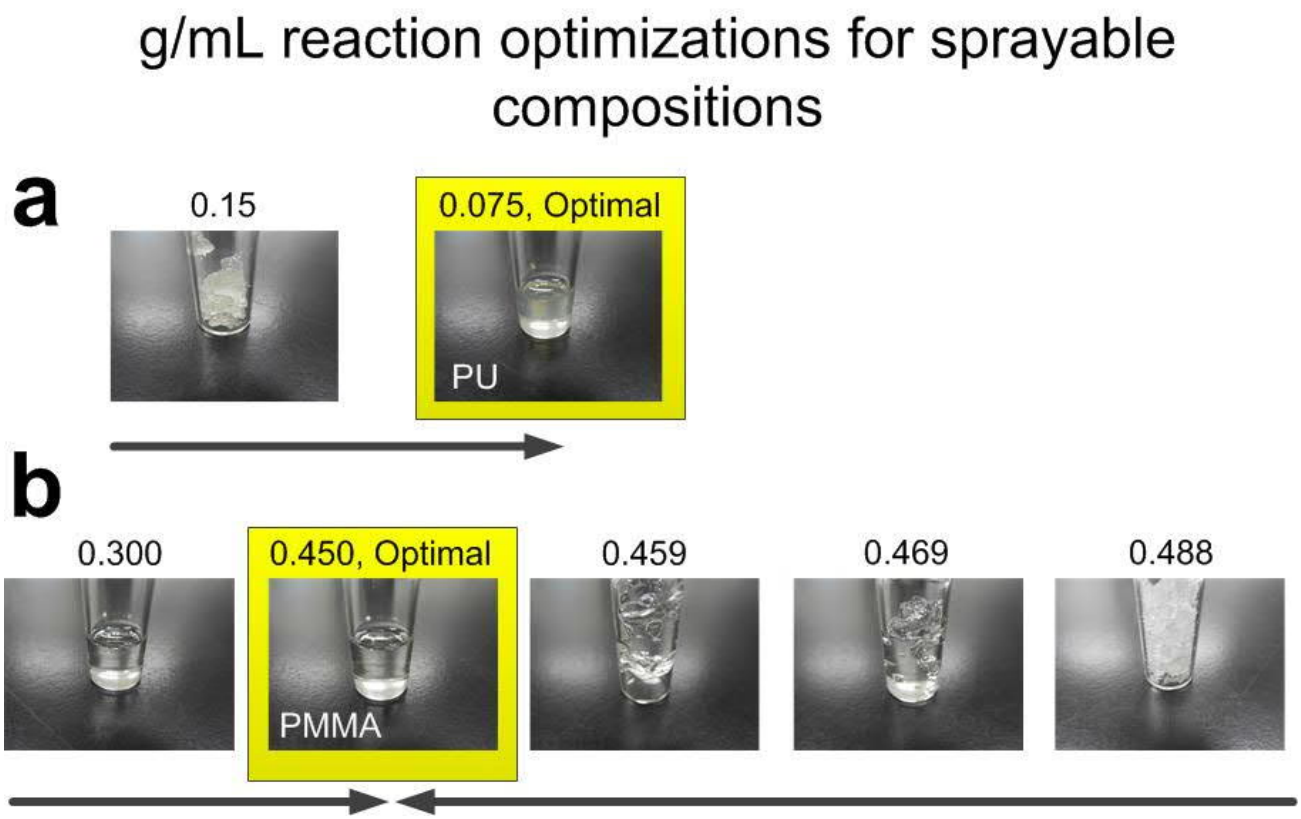

Figure S6.3. Optical photographs of optimized sprayable a) PU and b) PMMA crosslinked controls. It is notable that purely cross-linked PMMA developed in this solvent system (xylene:acetone), were not sprayable (See b, 0.488 - 0.600 polymer to solvent ratios).

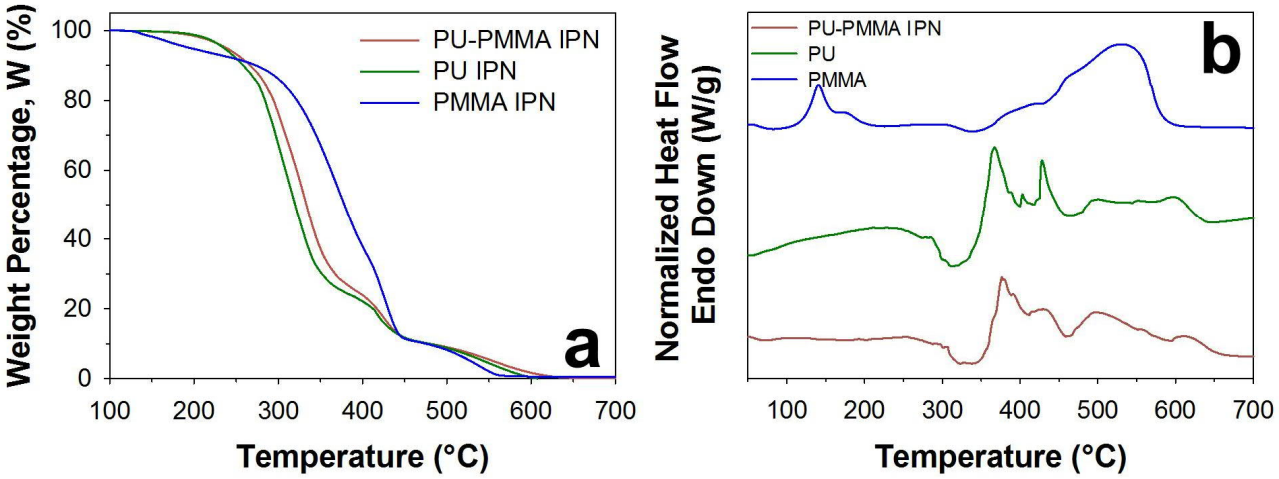

Figure S6.4. High temperature a) thermogravimetric- b) differential scanning calorimetric (TG-DSC) analysis of cross-linked PU, PMMA and PU-PMMA IPNs.

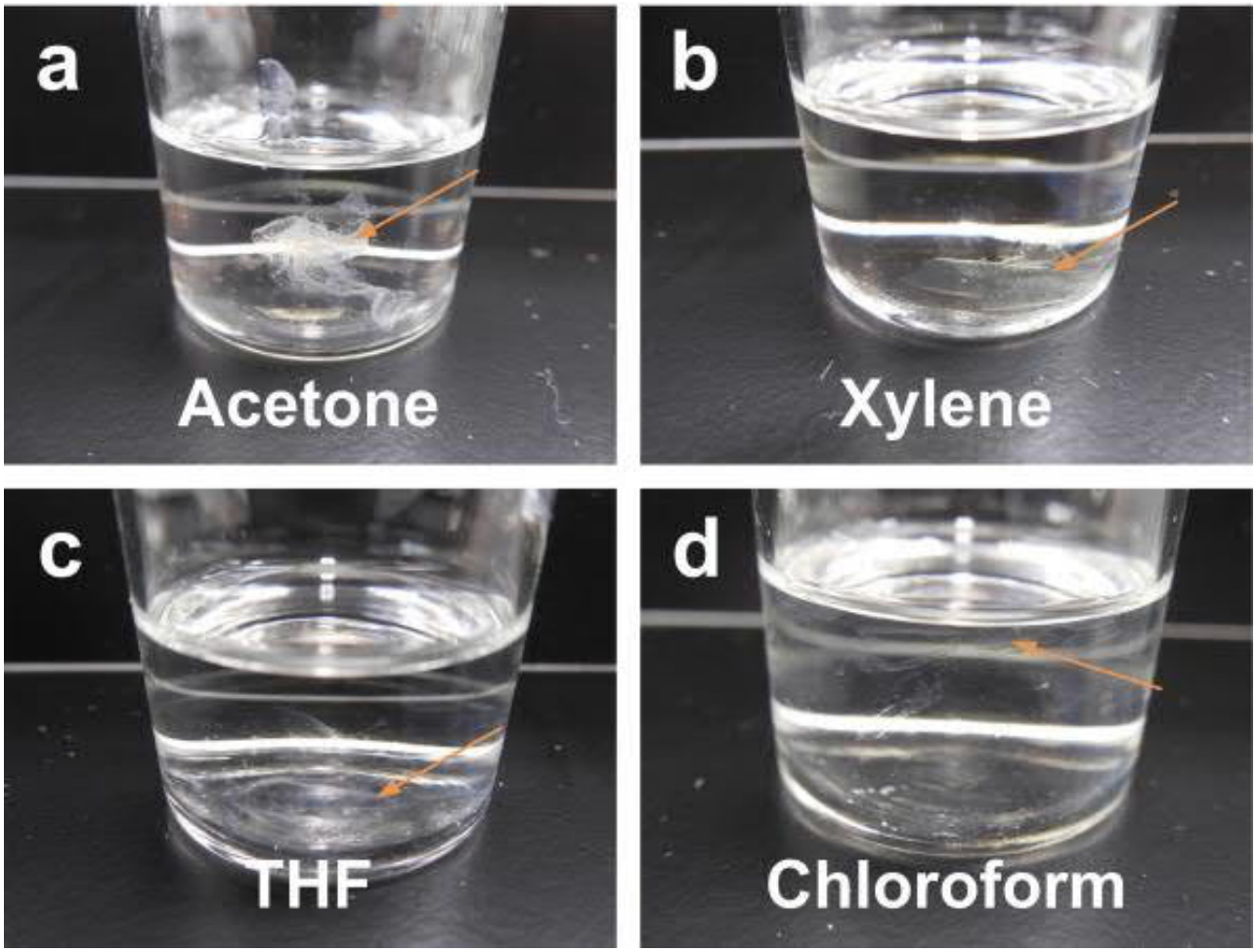

Figure S6.5. Determination of successfully synthesized interpenetrated networks (PU-PMMA IPN) through solvent-immersion tests over 2 h (and re-observed over 24 h with negligible differences). Thin films were notably not soluble in (a,b) parent solvents (acetone, xylene) while being swelled significantly in much (c,d) stronger solvents (THF and chloroform). Polymer coatings are indicated with orange arrows.

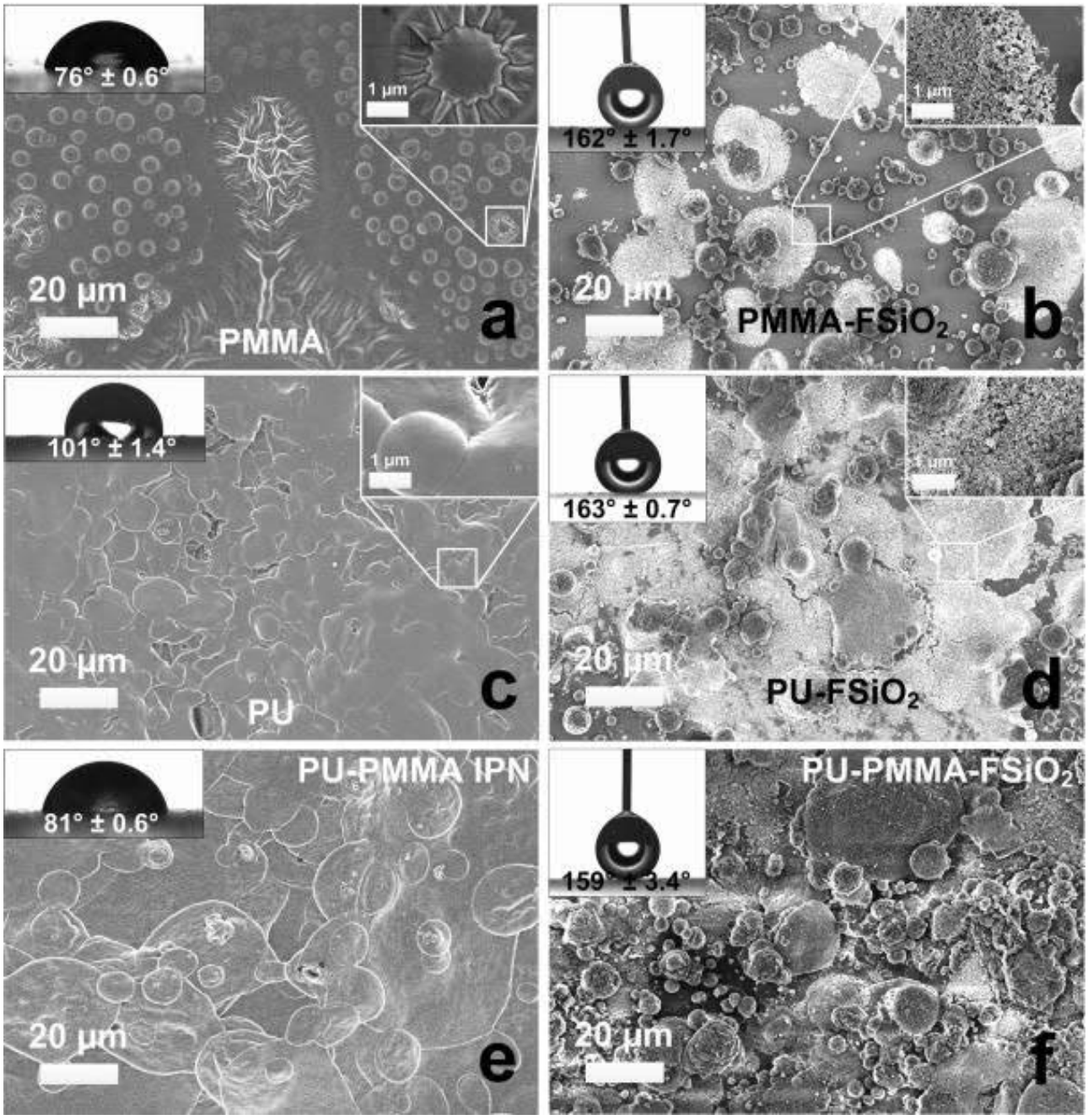

Figure S6.6. SEM analysis of crosslinked a) PMMA, c) PU and e) PU-PMMA IPNs before (a,c,e) and after integration with the (b,d,e) F-SiO_2 coating.

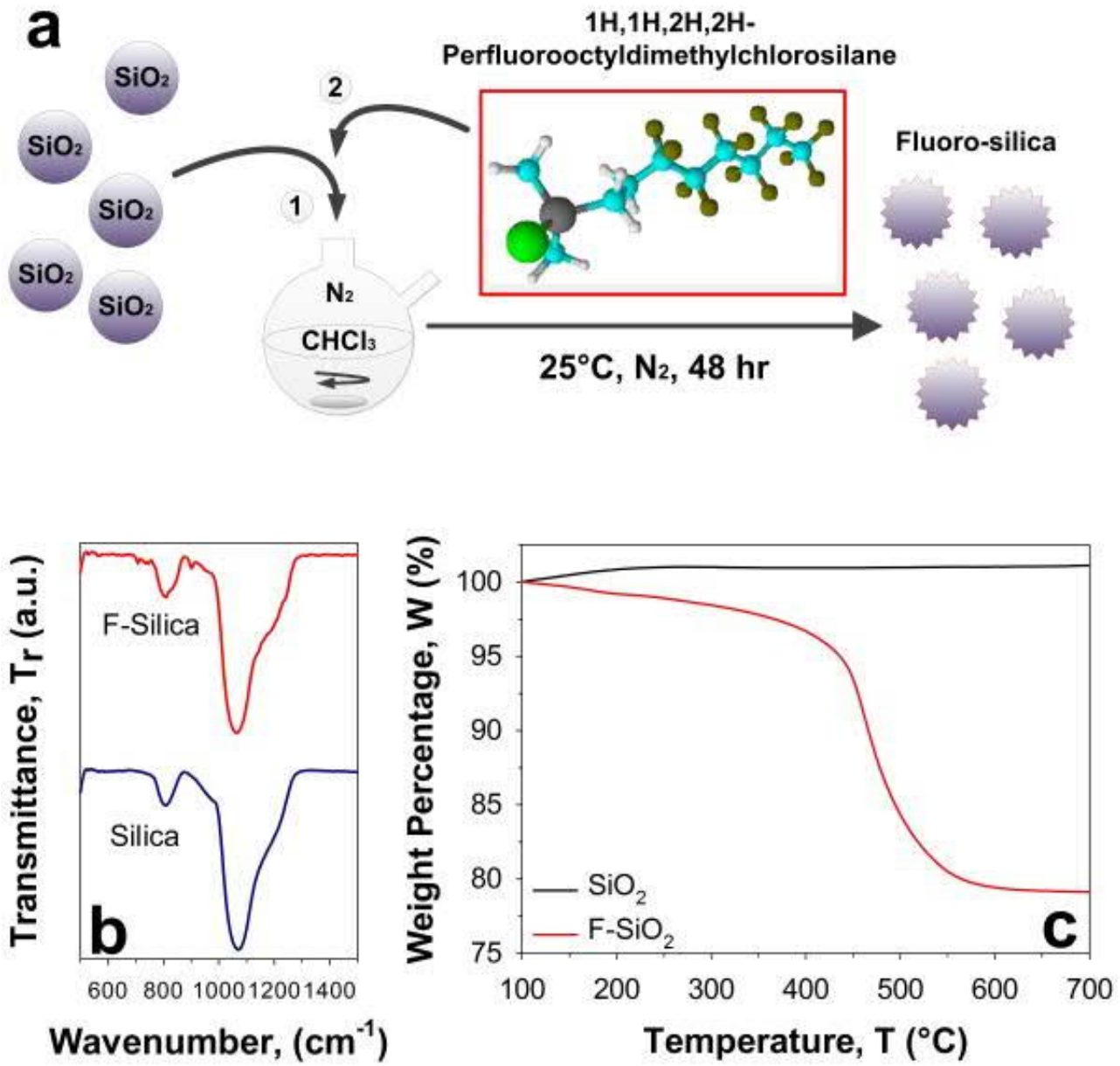

Figure S6.7. a) Functionalization of SiO_2 with 1H, 1H, 2H, 2H-Perfluorooctyldimethylchlorosilane, forming F-SiO_2, with b) additional organic signatures as highlighted in IR-spectroscopy. Functionalization was further confirmed by c) thermogravimetric analysis of the functionalized vs. control SiO_2.

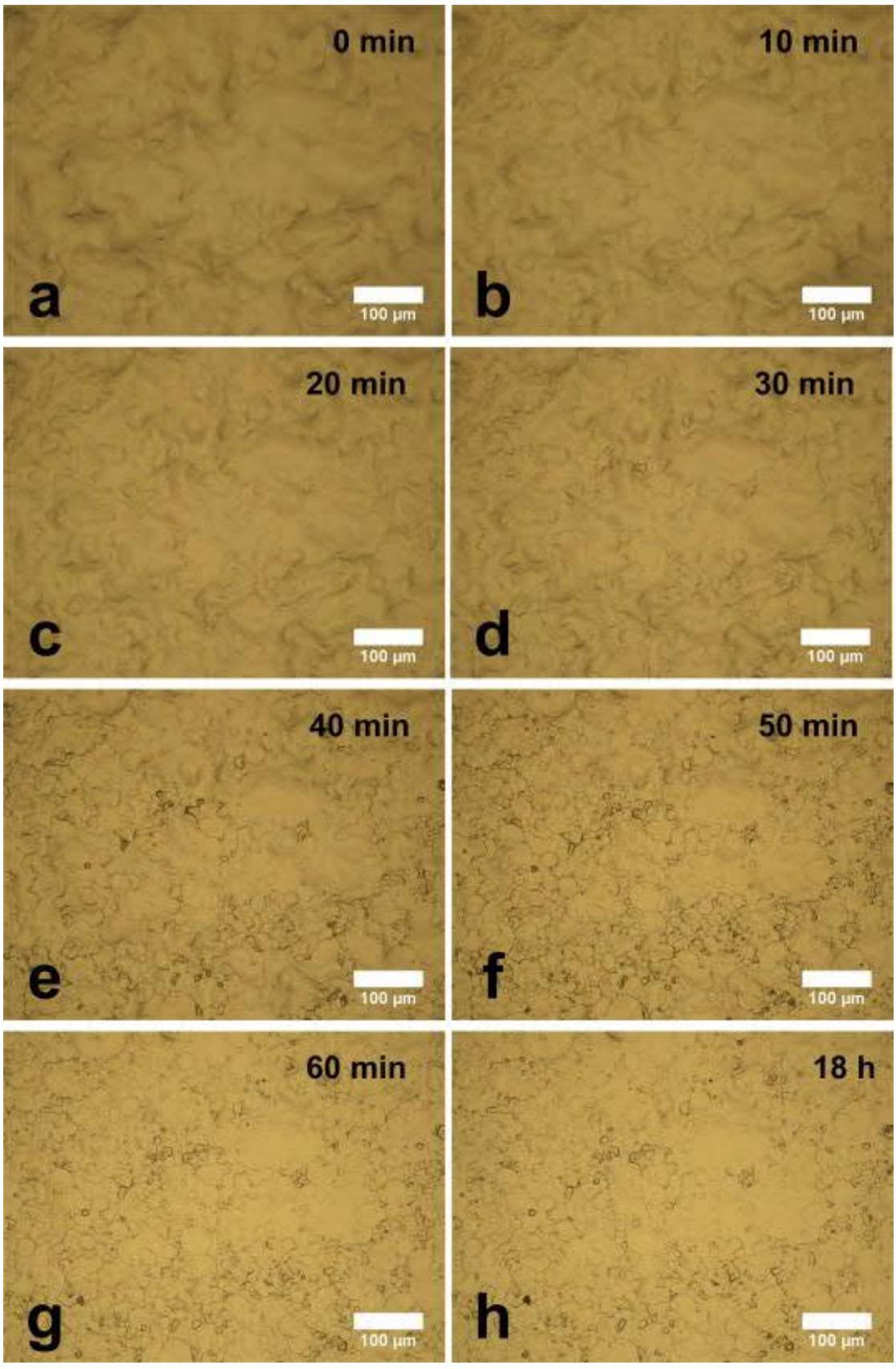

Figure S6.8. Optimization of VOC degassing (25 °C in a laboratory environment (50-60% humidity), kept out of direct sunlight) analyzed through optical microscopy from 0 min to 18 h. Biggest morphological changes from an agglomerated coating (0 mins) to a micro-textured coating (marshmallow-like) took place between 20 to 40 min, in close alignment with the optimal timeframe for degassing-abrasion studies.

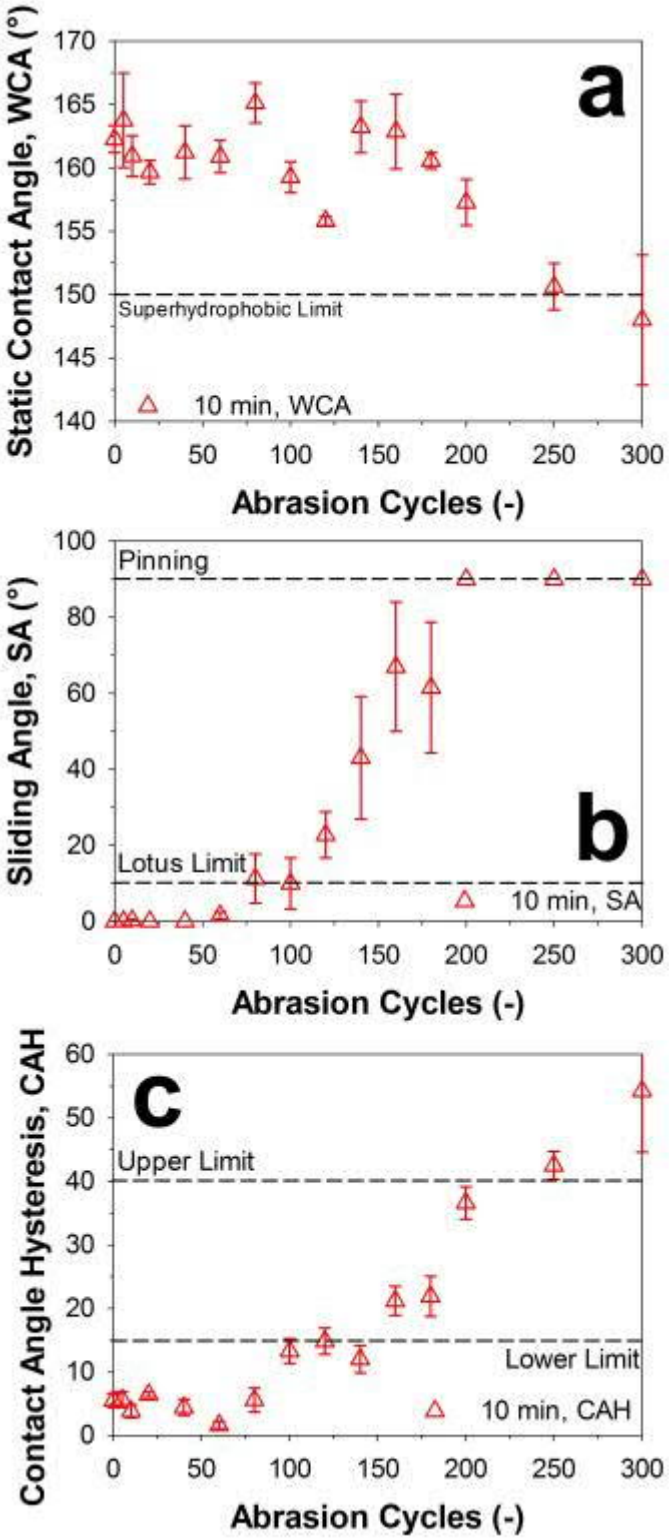

Figure S6.9. Isolated graphs demonstrating time-optimized abrasion-wetting characterizations. a) WCAs, b) SAs, c) CAHs. Lag time for VOC degassing prior to nanoparticle deposition at 10 min.

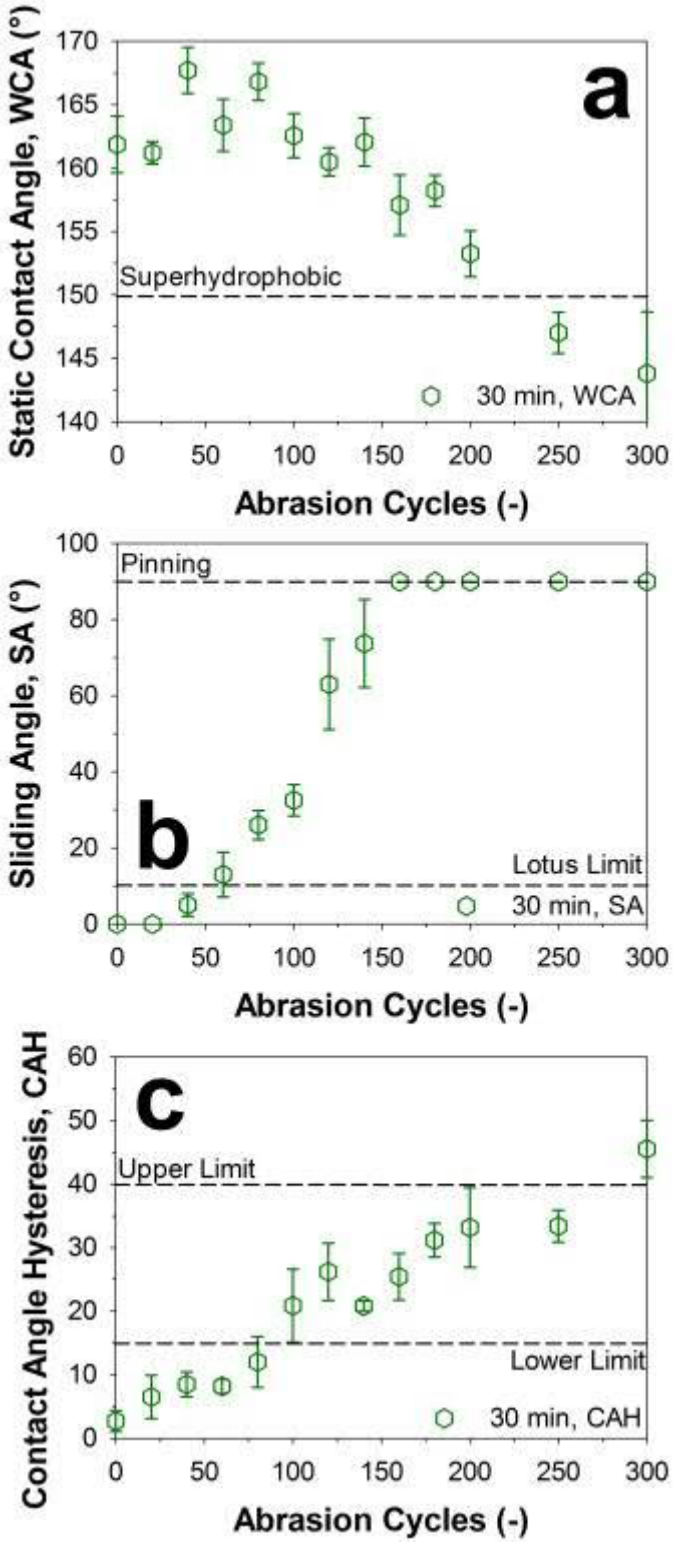

Figure S6.10. Isolated graphs demonstrating time-optimized abrasion-wetting characterizations. a) WCAs, b) SAs, c) CAHs. Lag time for VOC degassing prior to nanoparticle deposition at 30 min.

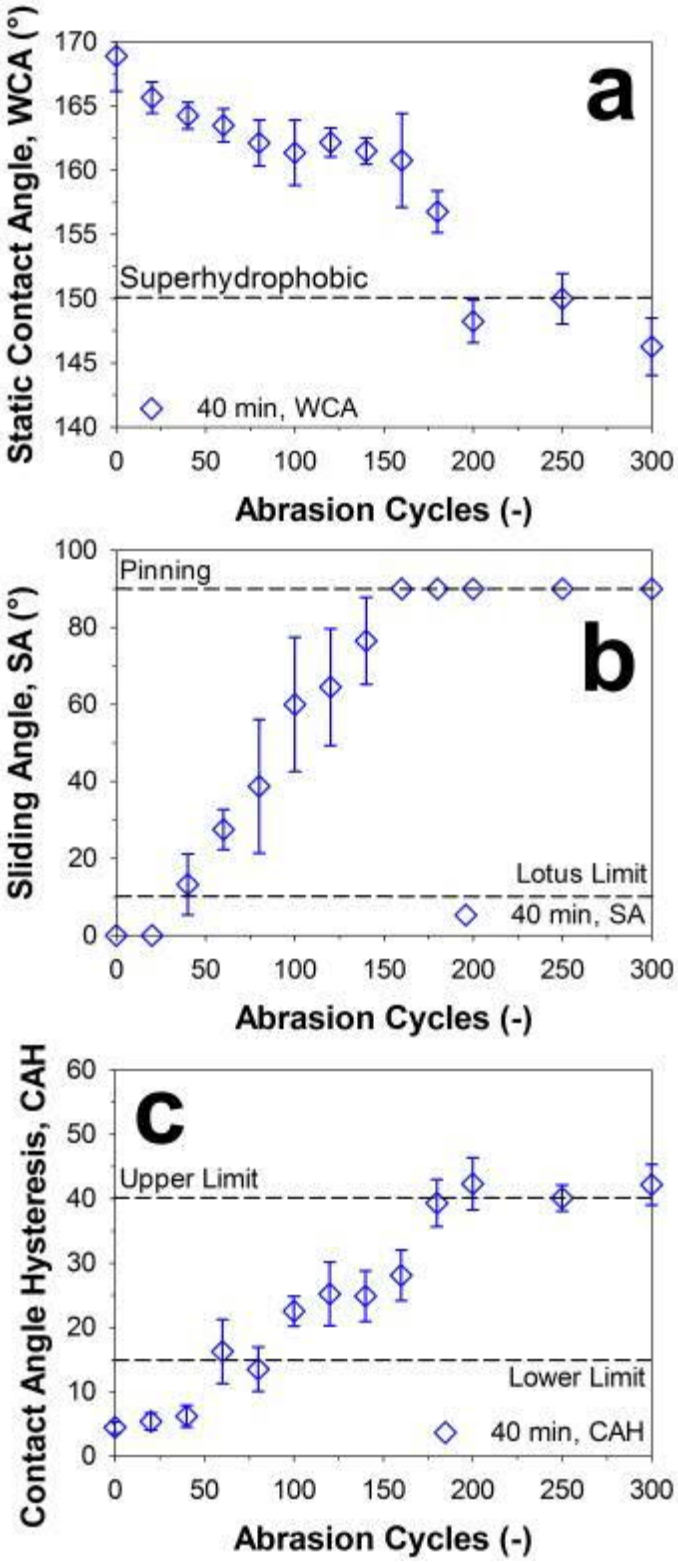

Figure S6.11. Isolated graphs demonstrating time-optimized abrasion-wetting characterizations. a) WCAs, b) SAs, c) CAHs. Lag time for VOC degassing prior to nanoparticle deposition at 40 min.

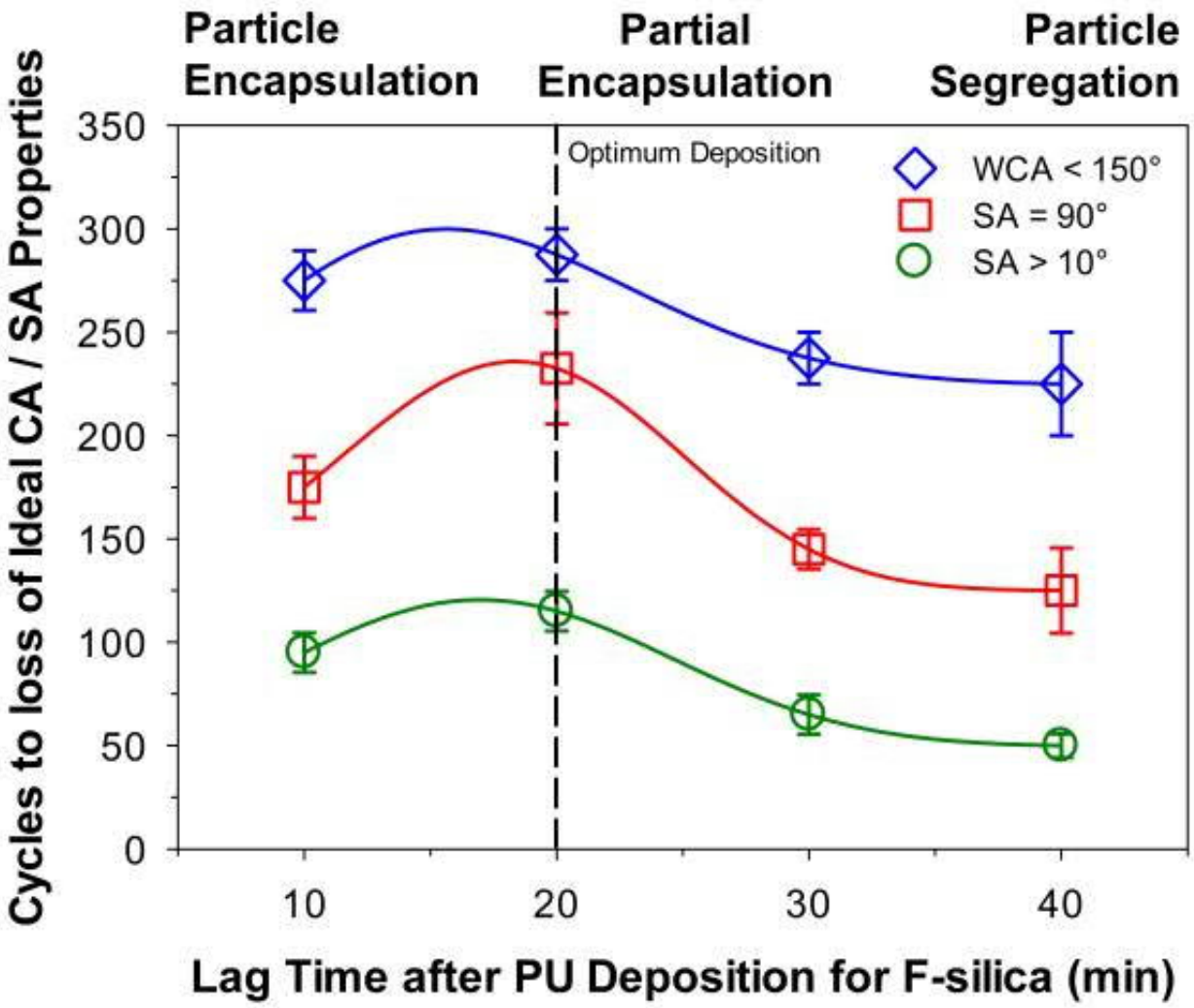

Figure S6.12. Optimization of VOC degassing analyzed through abrasion testing from 10 to 40 min, with a focus on WCA, SA and CAH properties. At < 10 min (*e.g.* 5 min), as-developed coatings were not superhydrophobic.

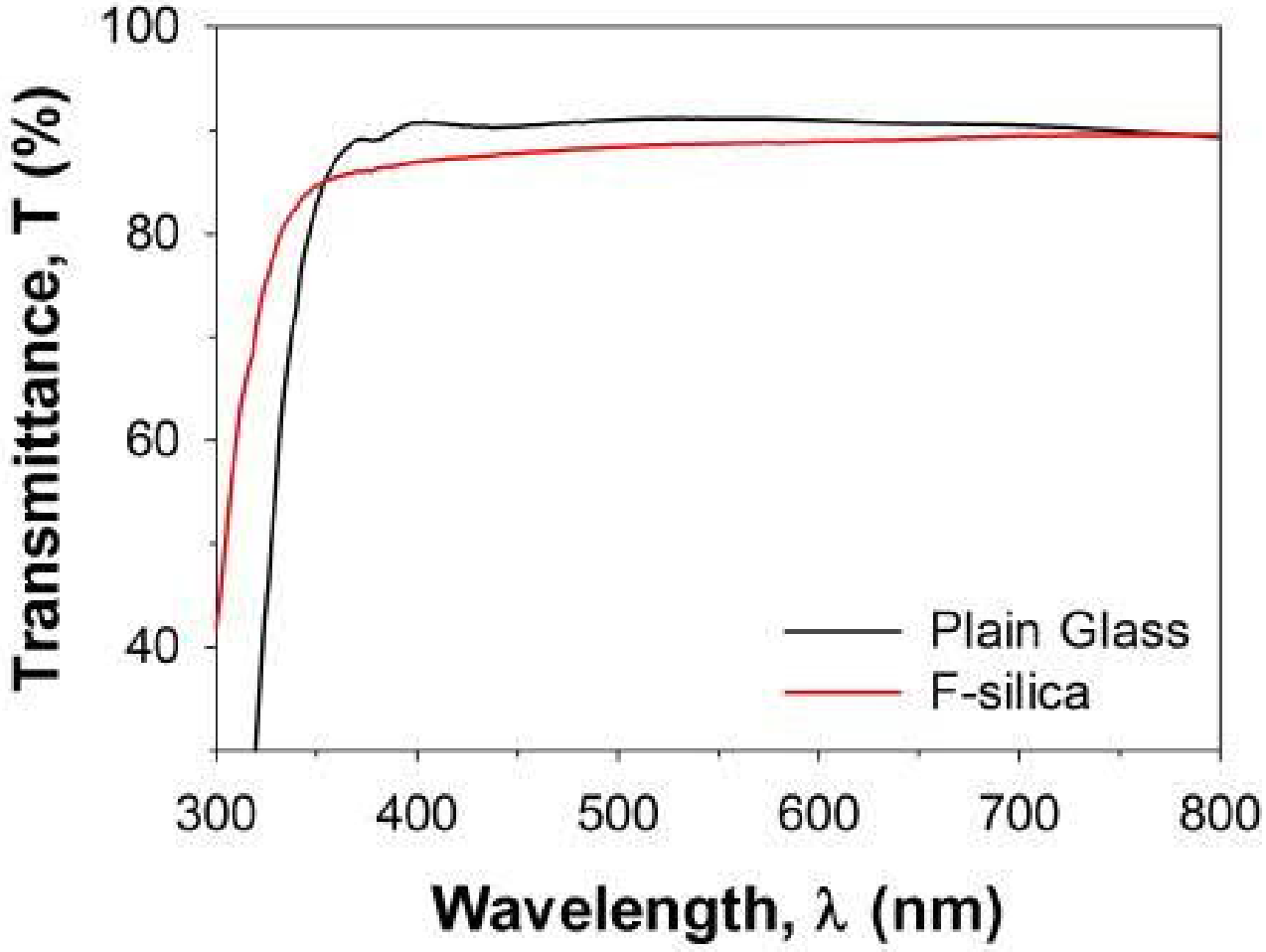

Figure S6.13. UV-vis analysis of F-SiO_2 coated glass and plain glass in the visible light spectrum.

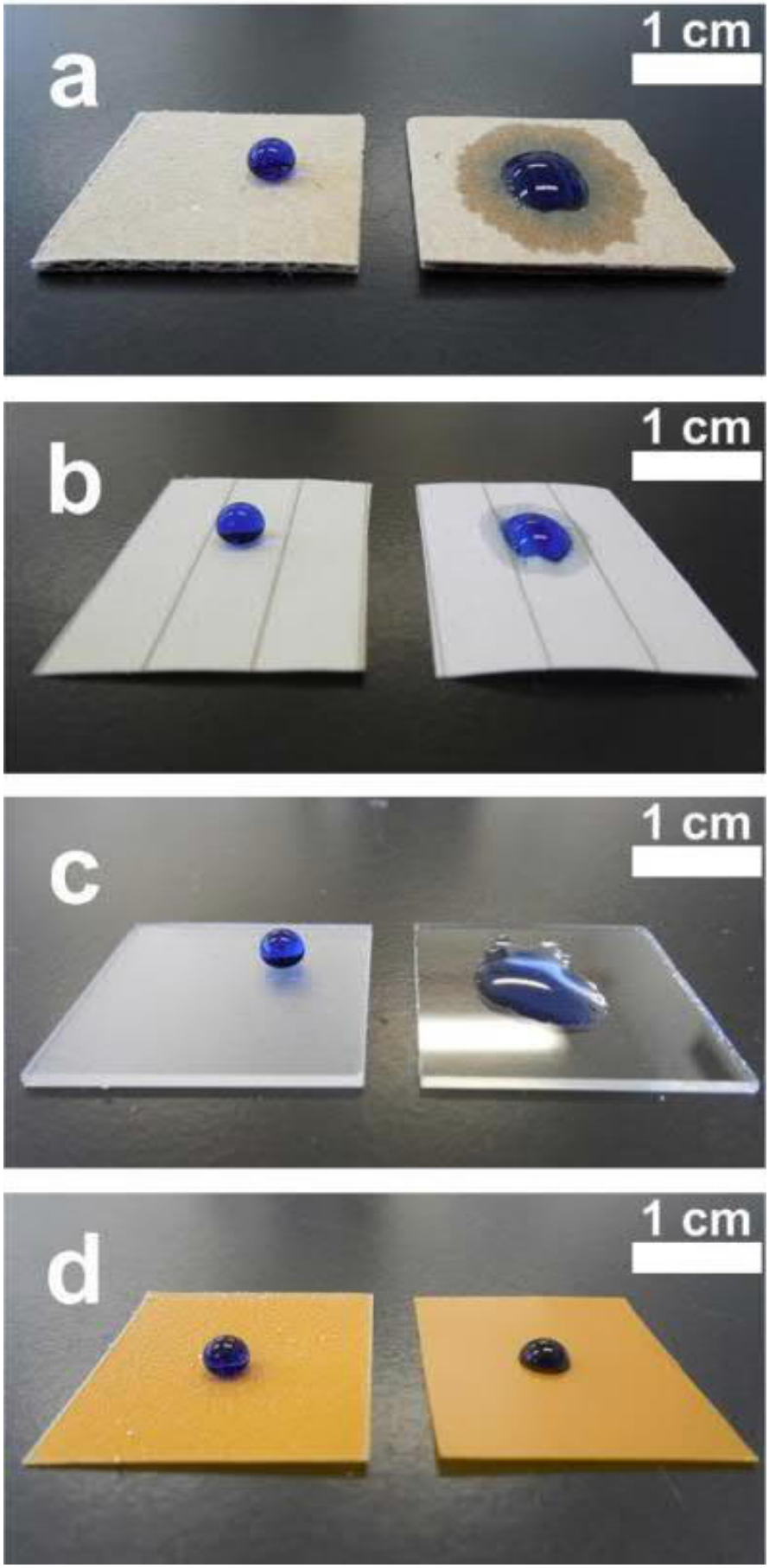

Figure S6.14. Multi-substrate compatibility, showing the PU-PMMA-F-SiO_2 coating on a) cardboard, b) writing paper, c) glass and d) kapton (PI).

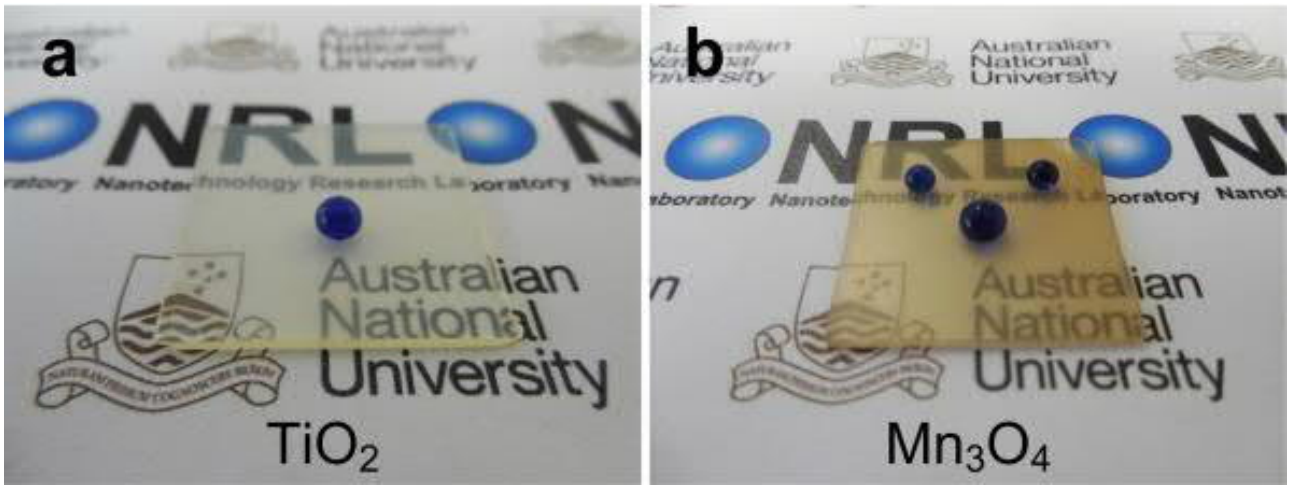

Figure S6.15. Suitability for alternative aerosol-based deposition methods (flame spray pyrolysis), including in-house developed superhydrophobic a) TiO_2 and b) M_3O_4 nanoparticles. This suggests immense potential for the micro-structural conferred robustness that could be extended beyond wet-spray designs for nanoparticle-based catalytic coatings.

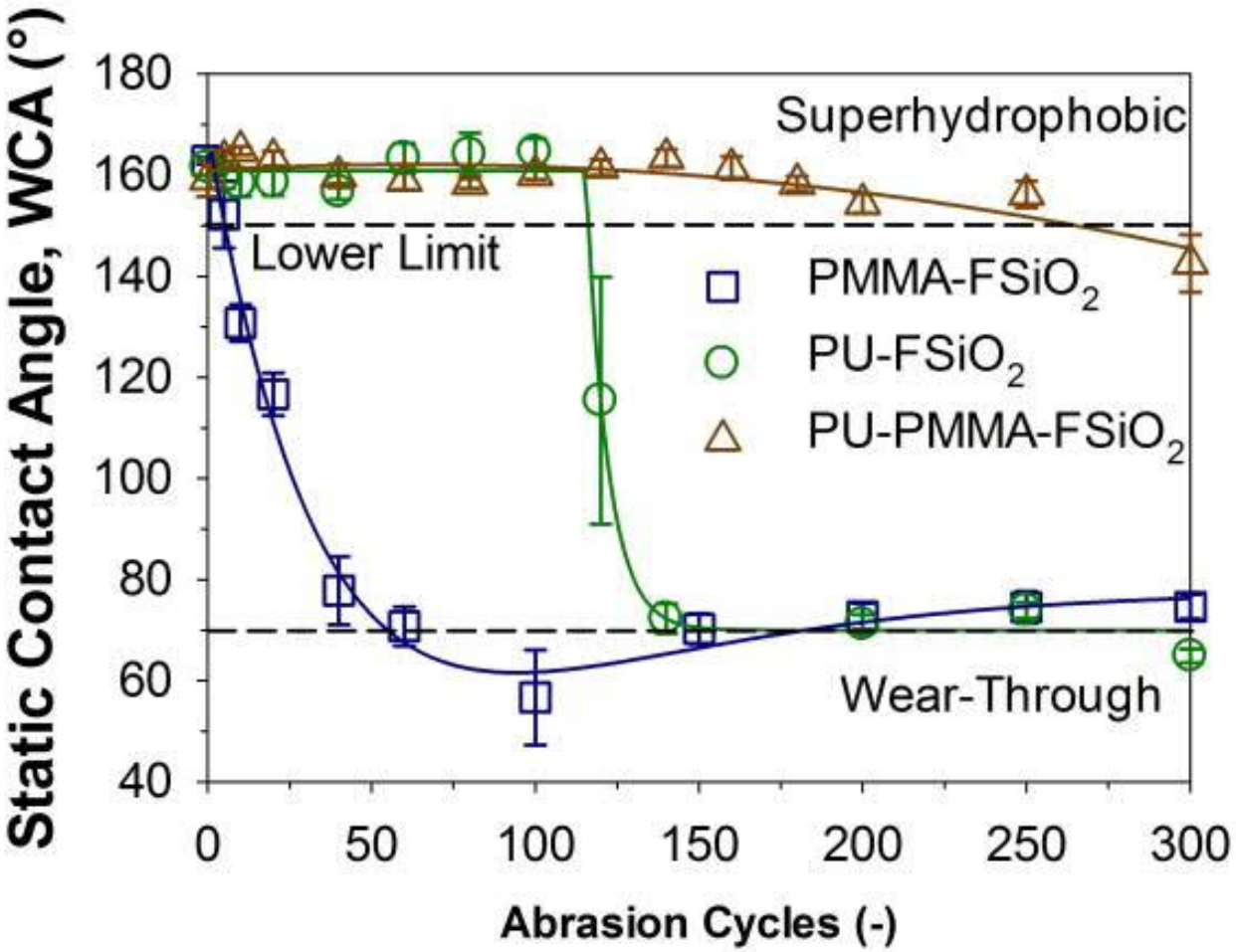

Figure S6.16. Tandem abrasion-wetting analysis for cross-linked polymeric controls with F-SiO_2 deposition versus optimized PU-PMMA-F-SiO_2 variants.

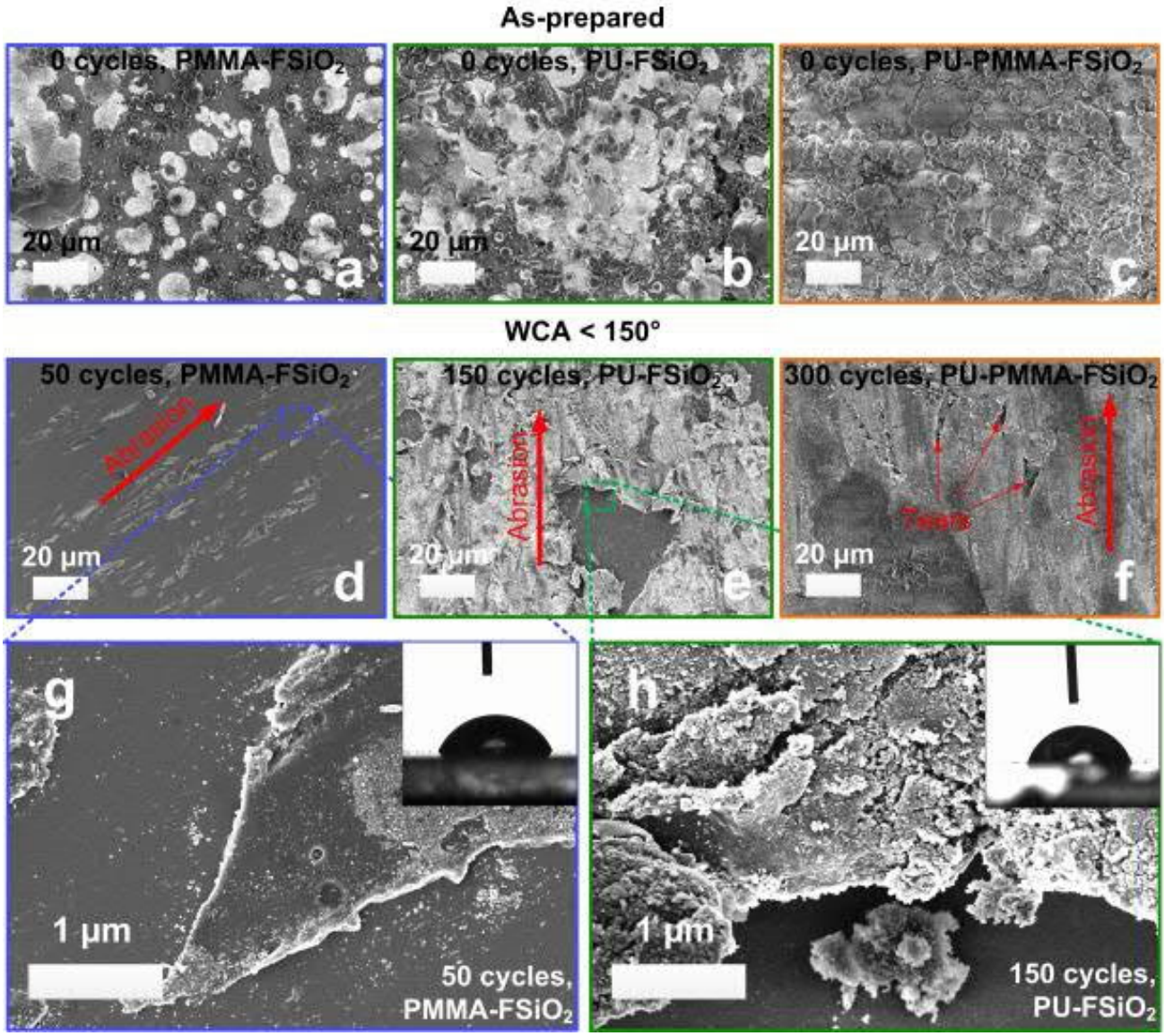

Figure S6.17. Low magnification SEM micrographs of (a-c) as-prepared and (d-f) cycled-to-failure (WCA < 150°) interfaces: (a,d) PMMA-F-SiO_2, (b,e) PU-F-SiO_2 and (c,f) PU-PMMA-F-SiO_2 IPNs. High magnification SEM micrographs showing the mode of failure (brittle and ductile) for both cross-linked PMMA and PU derived control coatings.

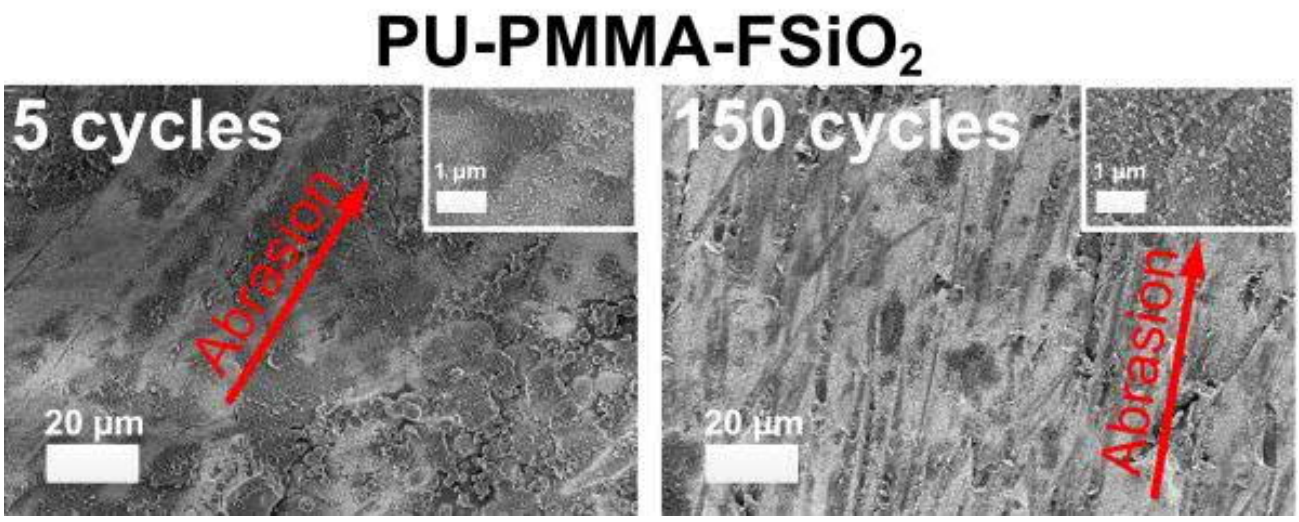

Figure S6.18. Intermediate cyclic damages of PU-PMMA-F-SiO_2 coatings from the 5th cycle up to the 150th cycle, with negligible damages to the IPN-F-SiO_2.

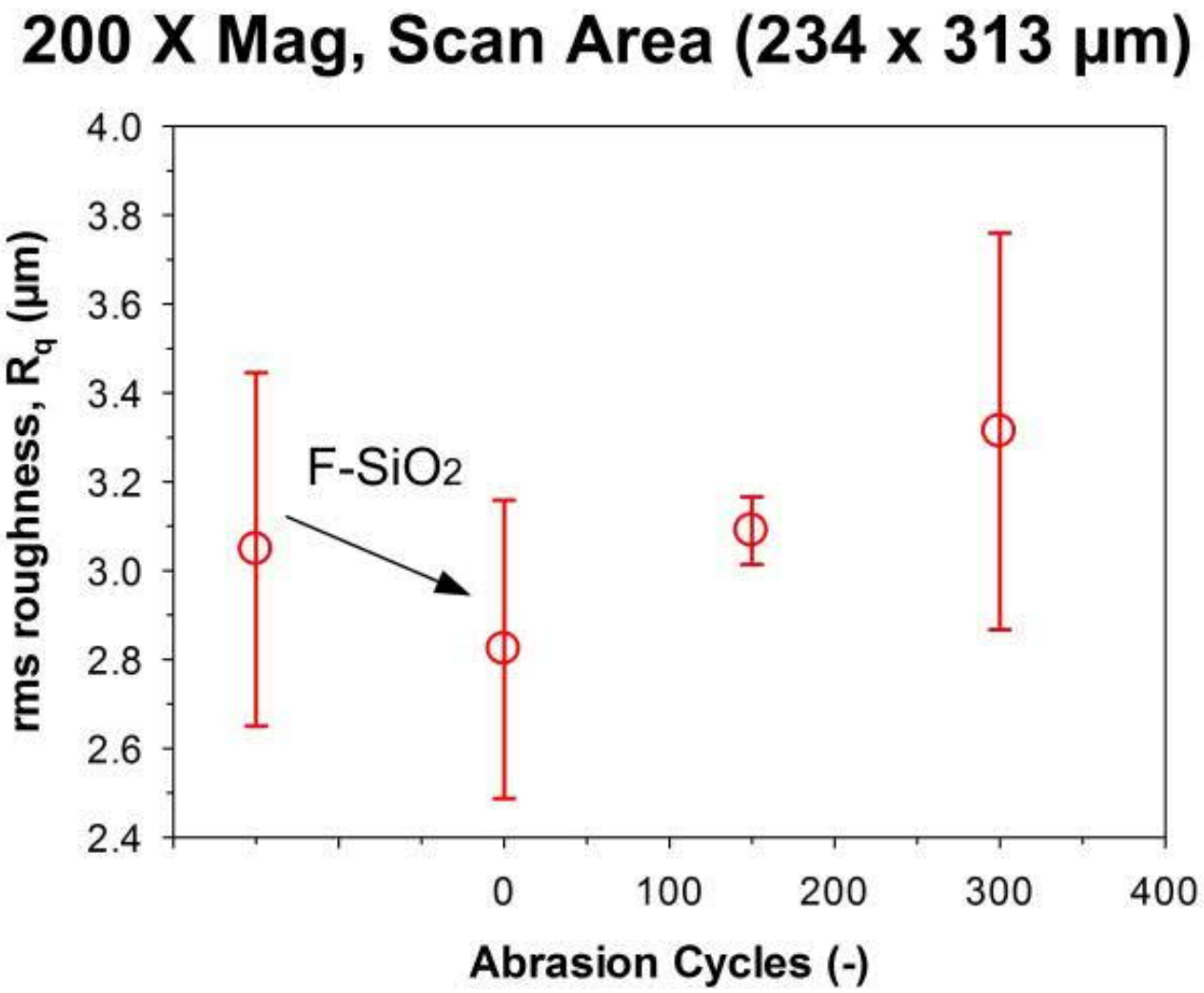

Figure S6.19. Impacts of F-SiO_2 coating and abrasion cycling on WLI-measured root-mean-square (rms) roughness at 200 X magnification. No trend was reasonably established at 200 X magnification, indicative of negligible micro-level abrasion-damages.

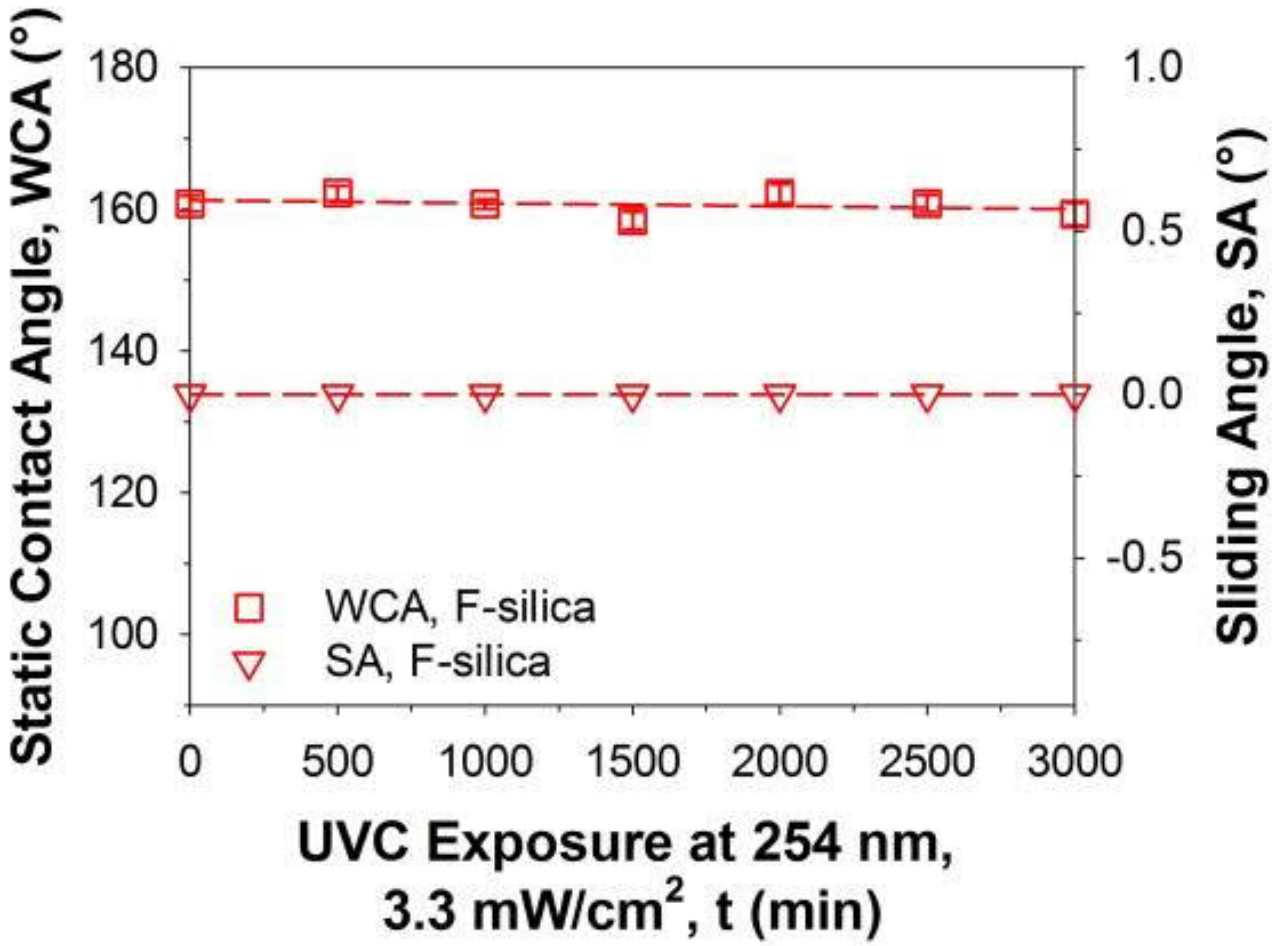

Figure S6.20. Stability of F-SiO_2 on glass under extended exposure to high intensity UVC.

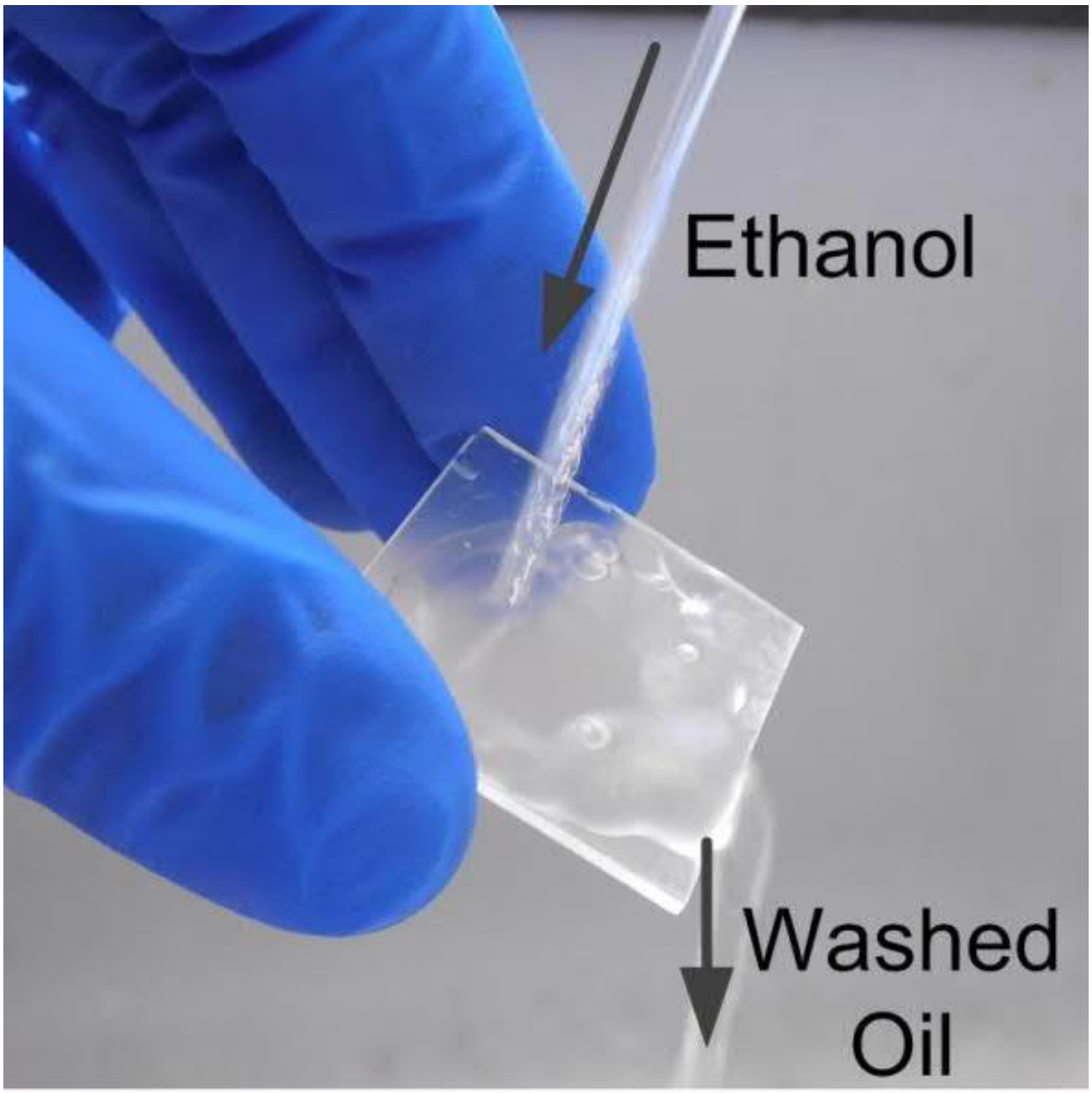

Figure S6.21. Ethanol decontamination of oil-immersed superhydrophobic glass slides

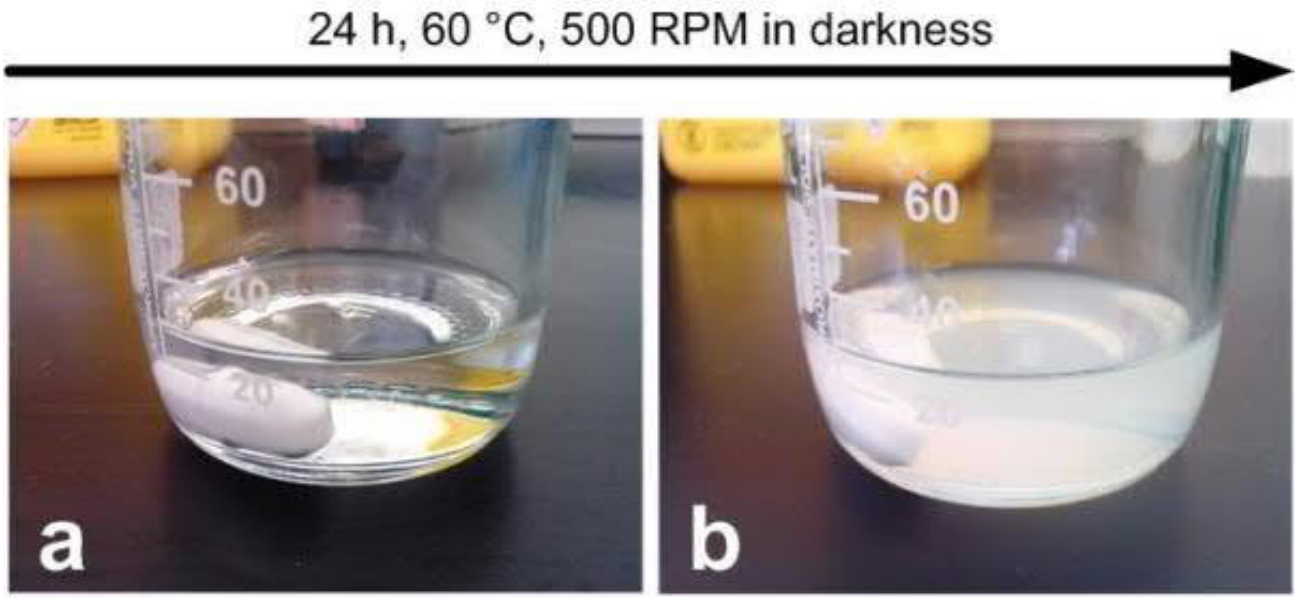

Figure S6.22. Reaction of a) PU-PMMA hybrid pot to give a b) sprayable colloidal suspension of PU-PMMA IPN solution. As-synthesized colloidal suspensions were stable for at least 6 months without any signs of settling.

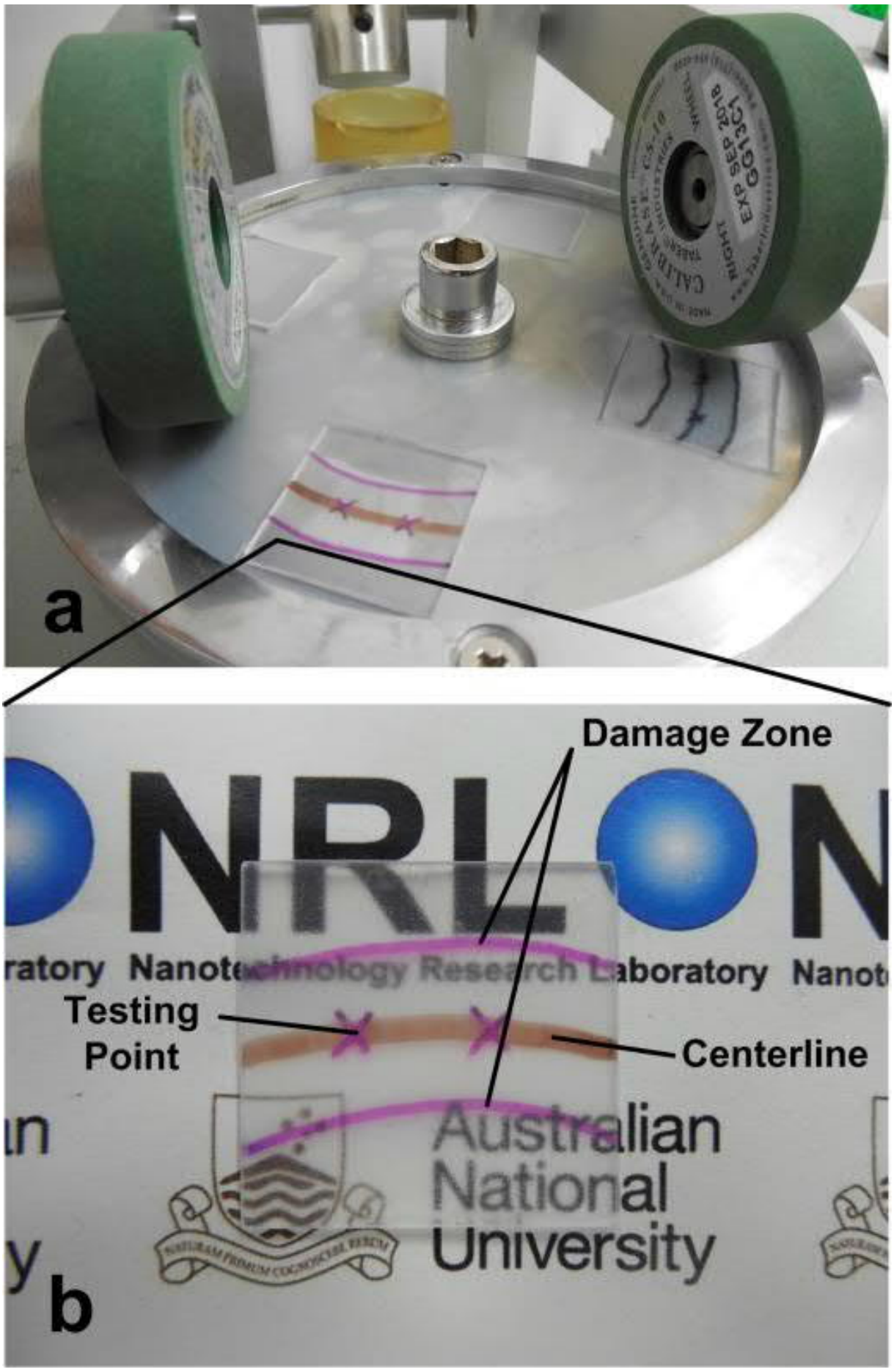

Figure S6.23. Cyclic a) abrasion-wetting characterization zone b) (along centerline).

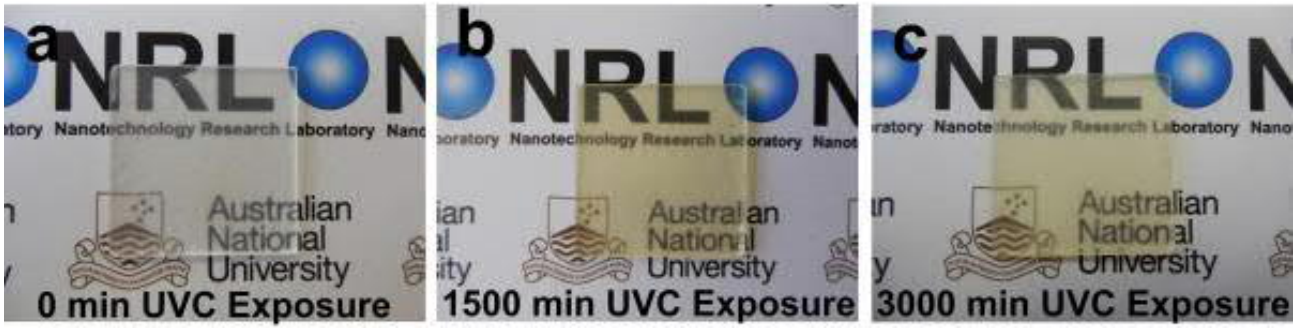

Figure S6.24. UVC damaged PU-PMMA-F-SiO_2 from a) 0 min to b) 1500 min and c) 3000 min exposure

Figure S6.25. Alkali-induced damage of the superhydrophobic layers in the PU-PMMA-F-SiO_2 system after extended immersion (etching) after losing the plastron layer.

7. Superhydrophilic-Superhydrophobic Janus Origami

Abstract

One of the innate fundamentals of living systems encompasses their ability to respond towards distinct stimuli by various self-organization behaviors. Despite extensive progress, spontaneous motion in synthetic materials still lacks the directionality, speed and scale observed in nature. Here, we report the directional self-organization of soft materials into 3D geometries by the rapid propagation of a folding stimulus along a predetermined path. A Janus bilayer architecture with superior chemical and mechanical properties was designed and engineered, enabling efficient transformation of surface energy into directional kinetic and elastic energies. The Janus bi-layer can respond to pinpoint water stimuli by a rapid, several centimeters long self-assembly that is reminiscent of the *Mimosa pudica*'s folding leaflets. During its dynamic assembly, the Janus bi-layers are capable of shuttling water at flow rates over two orders of magnitude as compared to traditional wicking-based devices. Experimentally determined data revealed that flow velocities reached up to 8 cm/s with net flow rates of 4.7 μL/s. With a remarkable aptitude for geometrical origami, this unique self-organization regime also showcased the assembly of curved, bent and split flexible channels. These were achieved with lengths more than 10 cm, demonstrating immediate applications for microfluidics, biosensors, water purification and collection.

7.1. Introduction

Biological systems in nature orchestrate rapid levels of responsivity to their environments using coupled stimuli-responsive reaction behaviors. These are distinguished under two overarching categories, namely static and dynamic self-assembly.[76,319] Static self-assembly is typically constrained by equilibrium thermodynamics.[624] For instance, the molecular-level crystallization-aided[625] assembly of nacre makes up the exoskeletal shells of numerous marine invertebrates.[626] More exciting, however, is the dynamically responsive nature of living organisms that often manifests in spontaneous motion. This is also sometimes referred to as self-organization.[627] For example, the *Mimosa pudica*, a thigmonastic plant, responds to the slightest contact pressure with a rapid dynamic folding of its leaflets. This centimeter long, negative tropism is transduced by a cascade of electrical potentials and osmotic pressure waves.[628] While specific mechanisms vary, fundamental structural and functional concepts found in natural organisms could provide important insights towards the rational design of new classes of self-organizing materials. Such inspiration could lead onto potential applications in biotechnology,[627] micromechanics,[629] microelectronics,[592] photonics[630] and fluidics[319].

To date, engineered systems capable of spontaneous motion rely largely on static self-organization mechanisms.[320,631] In these systems, material self-organization is localized around/in the proximity of the initial stimulus, which limits the scale of self-assembly. For example, in classical elasto-capillarity, a thin polymer sheet folds spontaneously around a water droplet. The droplet-interfacial energies provide input for initial folding and the subsequent residual propagation into the secondary segments of the sheet. However, owing to the low surface energy profile, and poor geometrical optimization, the scale of self-assembly remains largely static. The shape transformation becomes limited by droplet/stimuli sizes, and are typically restricted to ca. 10 mm, a very small fraction of scales observed in nature.[631]

Here, we report a means of achieving directional, dynamic self-organization of soft materials into large-scale geometries. This was realized by inducing a rapid cascade folding mechanism that is reminiscent of the Mimosa pudica's folding leaflets. To this end, we engineered a hybrid Janus bilayer film which possesses enhanced surface chemistry and physical properties. These soft materials are capable of imparting directional spontaneous motion in response to a pinpoint stimulus. The directional self-organization relies on the rapid propagation of a pinpoint stimulus alongside an orthogonal local material response, giving rise to continuous shape transformation. The longitudinal reconfiguration (stimulus propagation rate, max of 7.8 cm/s) is driven by capillary/Laplace pressure.[2] Synergizing with this reconfiguration, the elasto-capillarity driven orthogonal material response demonstrates much faster mechanical kinetics (folding at ca. 23.8 cm/s). The explosive reaction is in line with previous studies.[27,632,633] The coupled; synergized system induces the reversible self-assembly of 3D microfluidic channels *via* spontaneous liquid self-propulsion. Velocities of self-propulsion were found to be comparable to pneumatically actuated systems. This self-propelled, self-stimulated system is hereinafter named the Mimosa Origami regime. To the best of our knowledge, the Mimosa Origami regime represents the first large-scale self-assembly of a material powered by capillary-driven propagation of a pinpoint stimulus through a predetermined path.

7.2. Results and Discussion

A stack of multi-functional layers (Figure S1a-c) was designed to efficiently transform surface energy from wetting into directional kinetic and elastic energy. This was achieved through a soft, stimulus-responsive Janus film. The use of Janus materials has been well documented for nanoparticles where two distinct and sometimes opposite properties, such as hydrophilicity-hydrophobicity, are synergistically exploited.[546] Here, a cohesive Janus bilayer is obtained by a highly wettable functional polycaprolactone (PCL) nanofibrous layer adhered to a PVC microfibrous layer (Figure 7.1a). The PVC layer is designed to be highly superhydrophobic and flexible, serving as a water impenetrable backbone to the PCL layer. Adhesion between the PVC and PCL layers is excellent and cannot be easily separated without complete disintegration of the bilayer film. On the contrary, sequential deposition of PCL on PVP led to very weak bonding and layers were easily separated. Considering the similar nanostructural morphologies involved, adhesion properties are most likely attributed to preferential van der Waals (vdW) interactions instead of actual mechanical interlocking.

To attain sufficient mobility for vertical self-organization while suppressing in-plane wrinkling, the Janus bilayer is hosted on a superhydrophobic substrate (Figure S7.2a). This construct lowers the net film-to-film affinity between the PVC and the substrate layers (Figure 7.1b). The substrate is comprised of PS nanofibers, electrospun on a dense PDMS film (Figure S7.3a).

The multi-layer stack is easily assembled on a paper substrate using the sacrificial PVP layer for *in-situ* deposition of the Janus bilayer (Figure 7.1a, S7.1). In terms of wettability, the PCL layer has a Wenzel hemi-wicking (Figure S7.4) character, with WCAs approaching 0° (Figure 1d inset). This is achieved by a network of interwoven PCL nanofibers, possessing average diameters of 192 ± 49 nm (Figure 7.1d).

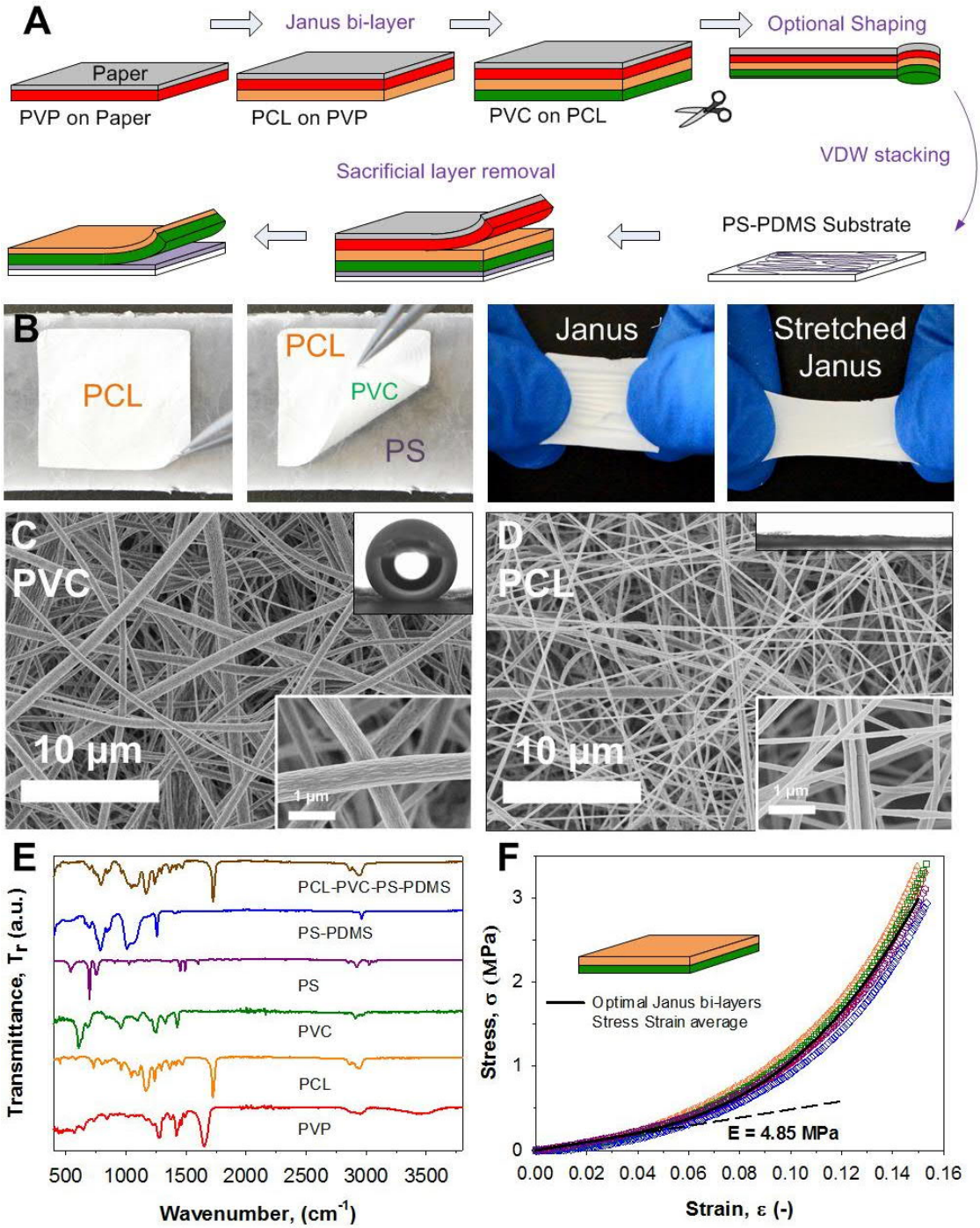

Figure 7.1. Preparation and characterization of the superhydrophilic/phobic Janus bilayer. a) Schematic illustration of the Janus bilayer assembly: a multi-functional stack is fabricated by sequential electrospinning of a protective PVP, a superhydrophilic PCL and a superhydrophobic PVC nanofiber layers on paper. This stack is shaped in a functional geometry and completed by mounting a peeled Janus bilayer on a PS coated PMDS substrate. The protective PVP layer and paper are easily peeled off by hand. b) Optical photographs show the isolated Janus bilayer, and its cohesive and stretching properties. (C-D) Scanning electron microscopic (SEM) analysis at low (8.8k) and high (70k) magnification images (insets, bottom right) of the Janus bilayer PVC and PCL surface, and their contrasting wetting (c,d insets). e) FTIR spectroscopic analysis of the multi-layer stack and isolated Janus bilayer confirming its PCL (orange line) and PVC (green line) composition. f) Dynamic mechanical stress-strain analysis (tension mode) of the Janus bilayer showing a soft rubbery nature with a Young's Modulus (E) of 4.85 MPa.

Similarly, the PVC backbone of the Janus bilayer is fabricated *in-situ*, on the PCL, by the deposition of sub-micro fibers with average diameters of 671 ± 305 nm (Figure 7.1d). The porous PVC structure is superhydrophobic with a WCA of 155° ± 7° and a CAH of 30° ± 10° (Figure 7.1c inset). Van der Waals stacking of the detached Janus bilayer on a PS-PDMS substrate completes the micro-device capable of functional self-assembly (Mimosa Origami). At this juncture, readers should note that the Janus bilayer is easily (re)-isolated from the protective PVP film (Figure S7.5) or even the PS-PDMS substrate (Figure 7.1b) by a physical peel-off.

The structural integrity and composition of the isolated bilayer is confirmed by its chemical signature (Figure 7.1e). The Fourier Transform Infrared Spectroscopic (FTIR) spectra of the multi-layer stack is characterized by five sharp peaks located at 1656 cm^{-1}, 1726 cm^{-1}, 612 cm^{-1}, 701 cm^{-1} and 789 cm^{-1}. These are attributed, respectively, to the C=O ring of PVP, carbonyl C=O stretch of PCL, C-Cl gauche of PVC, C-H aromatic ring of PS and the Si-C with CH3 rocking vibrations of PDMS, respectively.[620] The dominant presence of PCL and the lack of PVP in the final Mimosa Origami structure (PCL-PVC-PS-PDMS) confirm successful removal of originally attached sacrificial layers (Figure 7.1e). Similarly, chemical signatures of free-standing Janus bilayers (PCL-side) confirm the clean separation of Janus bilayers from the PS-PDMS substrate.

Key structural and chemical properties of the Janus bilayer, such as its elasto-capillary length, surface roughness (r) and energy (E_S) can be tuned far beyond that of conventional dense polymer films.[23] Optimization of the PCL and PVC layer thicknesses led to self-supported, free-standing, flexible and highly cohesive films (Figure S7.1b). SEM and gravimetric analysis reveal that the as-synthesized PCL possesses a surface roughness of 68 (Supplementary Text). This is significantly higher than that (r = 2-6) achieved by micro-texturing of dense films.[634] Moreover, this can be further tuned and enhanced by increasing PCL layer thickness or by decreasing the nanofiber diameter. Dynamic mechanical analysis (DMA) of the optimal Janus bilayer reveals a unique rubbery stress-strain nature (Figure 7.1f) with a Young's Modulus of 4.85 MPa. This is two to three orders of magnitude lower than that of bulk PVC (2700-3000 MPa)[635] and PCL (252-430 MPa)[636]. With the PVC-PCL layers'

combined thicknesses of 50 μm, a very low bending rigidity (K_b) of 68 nNm was computed. As such, a key film bending parameter, the elasto-capillary length (L_{EC}), of only 1 mm was derived.

$$L_{EC} = \frac{K_b}{\gamma_{LV}} \quad (7.1)$$

and γ_{LV} is the surface energy density of water (0.072 Nm^{-1}).

Figure S7.6 illustrates the transient elasto-capillarity response of the Janus bilayer to water. When a water droplet is gently placed on the superhydrophilic side of the circular-shaped bilayer, the latter partially detaches from the PS-PDMS substrate and encapsulates it by folding symmetrically. For a circular surface of 79 mm^2, this process takes less than 33 ms, ultimately resulting in the formation of a bulb containing the initial water volume. The presence of the PS-PDMS substrate and non-wetting superhydrophobic PVC backbone of the Janus bilayer are essential for the successful folding and subsequent leak-proof water encapsulation. Without the PVC layer, the non-Janus superhydrophilic PCL layer is susceptible to unwanted effects, such as uncontrolled in-plane wrinkling and eventual water leakage (Figure S7.7-7.8). Without the PS-PDMS substrate, the self-assembly is adversely affected by potential pinning to the host surface (Figure S7.7-7.8).

The rapid folding response of the Janus bilayer is attributed to its unique elasto-chemical properties. Notably, while the folding of thin dense films around a water droplet has been previously showcased as an exemplary application of elasto-capillarity, we unveil a primary challenge behind the use of highly porous hydrophilic layers. Despite the enhanced wettability (and thus folding affinity) induced by the ultra-porous surfaces, water leaks rapidly (Figure S7.7) through the film structure. The superhydrophilic-hydrophobic Janus layout significantly improves material response, avoiding wrinkling while preserving fluid encapsulation. As briefly mentioned before, the rough nano-structured morphology enables significantly higher surface energy density than that of 2D-textured dense films. Here, the Janus bilayer's surface energy density was estimated at 185 Jkg^{-1} (Supplementary Text), which is comparable to that of artificial muscles[629,637,638]. In fact, they are thus able to easily overcome the counteracting bending rigidity (68 nNm) of the Janus bilayer. The

unique Janus bilayer architecture/properties extend the working regime of classical capillary origami, enabling the folding of films with thicknesses an order larger than conventionally achieved[631]. The superior performance is attributed to the ultra-small elasto-capillary lengths, enabled through an exceptionally high surface roughness.

The Janus bilayer's properties can be exploited to induce an unprecedented directional self-organization of soft materials into functional 3D structures. Figure 7.2a shows the spontaneous construction of a straight micro-channel with a length of 6.5 cm. This was achieved by placing a water droplet with a diameter of 0.42 cm on the circular terminal of a rectangular strip of the Janus bilayer (Figures S7.5a and S7.9). This directional folding response is reminiscent of the mimosa's tropism in nature (Figure 7.2b), although the specific stimulus-propagation mechanisms of the Janus bilayer are different.

The reversibility of this self-organizing state is achieved by reinstating initial surface energy equilibrium. Figure 7.2c illustrates selected snapshots of the spontaneous unfolding process. Here, we used a low surface tension fluid, ethanol, to wet both the superhydrophobic and superhydrophilic sides of the Janus bilayer. This symmetric superwetting induced by ethanol facilitates the spontaneous disassembly. Spectroscopy maps the surface composition of the Janus bilayers during the folding-unfolding cycles. Results suggest clean desorption of both water and ethanol from the material during cyclic use, preserving initial polymeric compositions (Figure 7.2d). Desorption of water from the PCL side restores symmetry of the Janus bilayer surface energy (Figure 7.2e), thus unfolding the micro-channel back into its original flat shape. The unfolded Janus bilayer is easily reactivated (Experimental Section) and can be capable of multi-cycle self-assembly (Figure 7.2c,e).

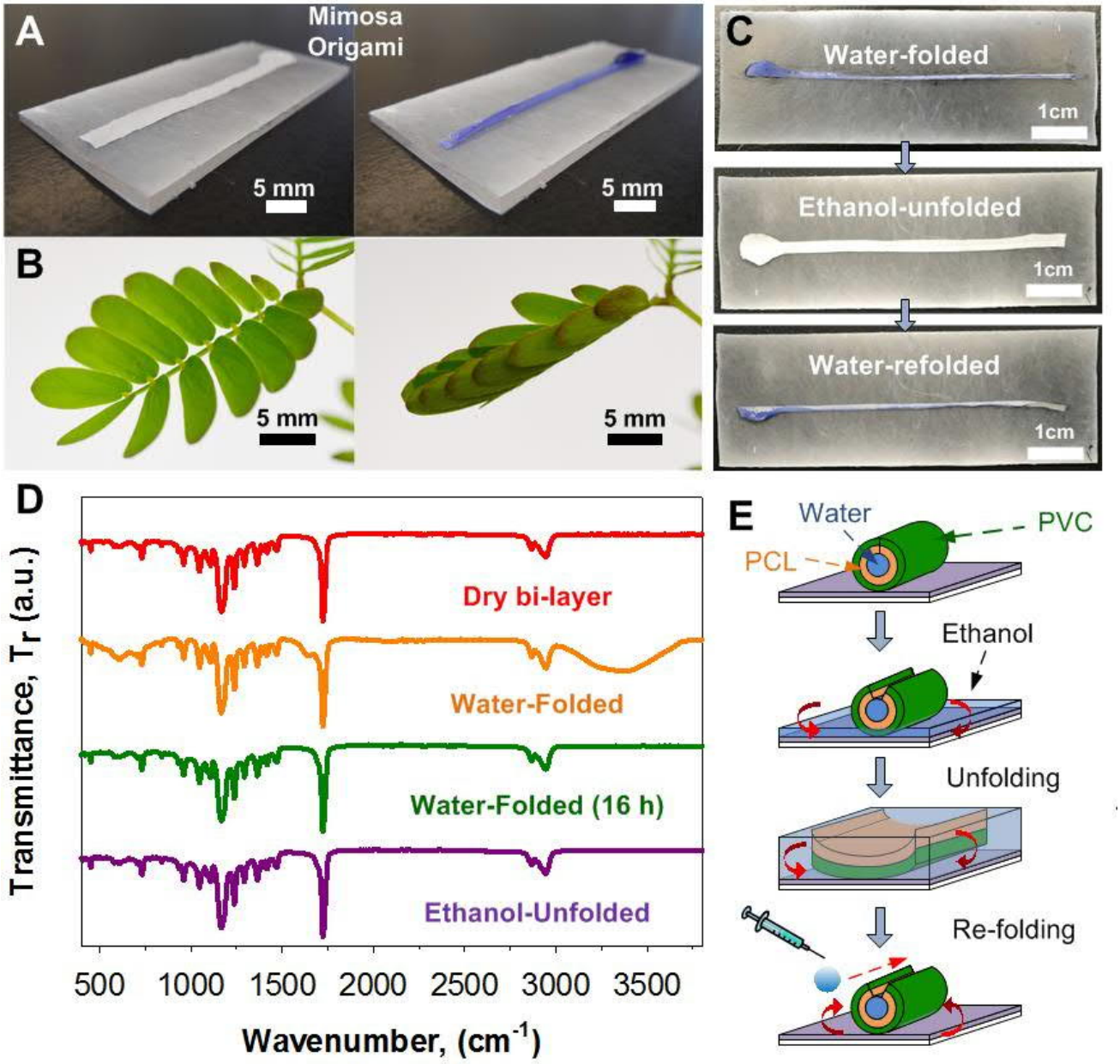

Figure 7.2. Demonstration of directional self-organization *via* Mimosa Origami self-assembly. a), Optical photographs of the spontaneous directional self-organization response of a rectangular-shaped Janus bilayer. A pinpoint water droplet stimulus results in the immediate self-assembly of a centimeter long micro-channel. b) This rapid motion is reminiscent of the stimulus-response propagation during the negative tropism of the *Mimosa pudica*‘s leaflets. c) The folded Janus bilayers are spontaneously unfolded by immersion in an ethanol bath. Restoration of the initial surface properties allows a novel folding cycle demonstrating the full reversibility of this self-organization state. d) FTIR spectroscopic analysis showing the variation in the surface composition of the Janus bilayer during the folding and unfolding cycle. e) Schematic illustrations of capillary-induced unfolding of the self-assembled micro-channel.

Figure 7.3a,b explains the mechanism of the Mimosa Origami’s self-assembly. A water-filled bulb first assembles (< 33 ms) in response to wetting of the Janus bilayer’s circular end. The liquid front advances into the rectangular strip at a relatively slow pace owing to the PCL layer’s hemi-wicking

properties. Once a critical amount of water is accumulated at the bulb-strip junction (< 110 ms), a quasi-cylindrical micro-channel is assembled from the rectangular strip. The formation of the 3D hollow architecture gives rise to strong capillary forces that rapidly propels water into the adjacent dry section (Figure S7.9).

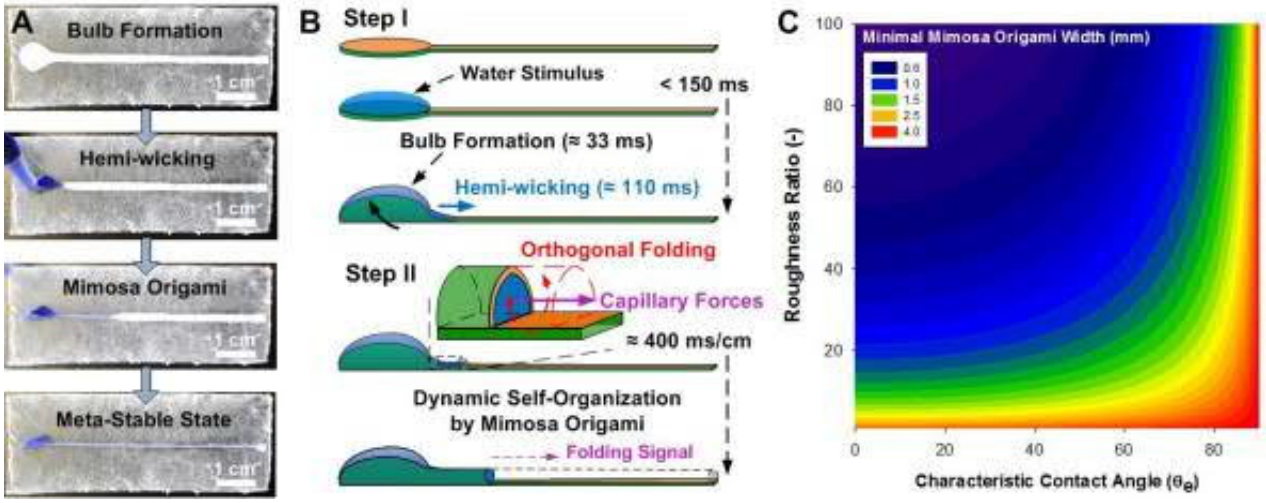

Figure 7.3. Mimosa Origami self-assembly mechanism and corresponding theoretical analysis. a) Optical photographs depicting the directional self-assembly of the Janus bilayers into a closed micro-channel. b) Schematic description of the self-assembly process: first a water-tight bulb is formed by rapid folding (33 ms) of the Janus bilayer terminal around a water droplet. Thereafter, the waterfront slowly advances from the bulb to the dry PCL surfaces. Once sufficient water has accumulated, the Janus bilayer strip transforms into a 3D cross-sectional cylinder. This leads to a Mimosa Origami propagation (400 ms cm^{-1}) of the folding stimulus by longitudinal propulsion of the waterfront and simultaneous orthogonal folding of the Janus bilayer strip. c) Theoretical model of the minimal strip width required for the spontaneous Mimosa Origami self-assembly regime, as a function of the surface roughness and characteristic CA (θ_e).

Most notably, the folding signal is transported at an average rate of 400 ms cm^{-1} or an average velocity of 2.5 cm s^{-1} over a strip length of 6.5 cm. For a droplet of 40 µL and a strip width of 2 mm, the instantaneous stimulus propagation rate decreases linearly from 7.8 cm^{-1} to a standstill over the length of 6.5 cm (Figure 7.4c). Distinct from typical self-assembling systems, the axial propagation is orthogonal to the local elasto-capillary potential that drives the strip folding. The rapid propagation of the pinpoint water stimulus and the orthogonal folding response (Figure 7.3b) results in a cascaded cycle of cross-sectional folding and directional mass transport. The effective capillary pressure decreases during self-assembly owing to a depleting fluid (energy) reservoir/bulb (Figure S7.4c). In

addition, the propagation is also countered by elastic folding and viscous capillary forces. The diminished capillary pressure, coupled with increasing elastic and viscous forces results in an exponential decrease in stimulus propagation rate (Figure 7.4c, S7.13). This ultimately halts the self-assembling process while some water is retained in the fluid reservoir/bulb. As a result, the initial scale of the self-assembly can be easily determined by initial droplet volume. Notably, the self-assembling process can be restarted by the supply of additional fluid to the reservoir/bulb.

We derived a mathematical model to determine the range of material and geometrical properties for enabling the spontaneous Mimosa Origami regime (Figure 7.3c). This is based on the extension of McHale's equations[632] to an infinitesimally small length of the rectangular strip belonging to the Janus bilayer. The primary assumption lies with keeping the top and bottom surfaces of the Janus bilayer in the Wenzel and Cassie-Baxter states, respectively.[632,633] Material properties (Figure 7.1f) and equations are described in the Supplementary Information. We found that the spontaneous formation of a 3D hollow cross-section necessitate a minimum critical width (w_c) of the Janus bilayer strip. This critical width is a function of the elasto-capillary length (L_{EC}), the characteristic CA (θ_e) and roughness factor (r) of the Janus bilayer top surface[3]. It can be estimated as:

$$W_c = 2\pi\sqrt{\frac{L_{EC}^2}{1+r\cos(\theta_e)}} \tag{7.2}$$

The roughness (r) of the nanofibrous PCL layer was computed from the ratio of its total surface area to its geometric surface area resulting in a surface roughness of 68,

$$r = \frac{4m\varnothing}{\pi\rho D^2} \tag{7.3}$$

where m is the mass (3.74×10^{-3} kg m^{-2}) of the monolayer PCL per cm^2, $\varnothing$ is the average circumference of a nanofiber (601×10^{-9} m), ρ is the density of PCL (1145 kg m^{-3}), D is the average diameter of a nanofiber (192×10^{-9} m).

Figure 7.3c shows contour plots of the minimum strip width for spontaneous folding as a function of the CA and roughness factor for hydrophilic films (θ_e < 90°), based on a constant elasto-capillary length (1 mm). On the basis of this theoretical model, the minimal width for Mimosa Origami decreases significantly with increasing surface roughness (Figure 7.3c). For dense flat films (r = 1), it is impossible to fully fold strips lesser than 4 mm in width. In stark contrast, for a film having comparable roughness (r = 68) to the top Janus bilayer surface, spontaneous complete folding is expected down to a strip width of 1.3 mm. This is extremely close to the elasto-capillary length of 1 mm, confirming the semi-empirical model. As a result, the small amounts of liquids transferred from the bulb to the dry strip interface by hemi-wicking are often sufficient in triggering the folding stimulus, cascading into the directional self-organization demonstrated. However, it should be noted that an upper limit for strip width exists for operational functionality. Beyond this dimension, the self-assembled hollow cross-sections could partially collapse under the inherent capillary tension.

A prompt and distal based motion that mimics the *Mimosa pudica's* mechanical response represents an essential improvement over state-of-the-art self-organization of soft materials.[631] With the new understanding of the critical strip width (w_c), we further optimized and assessed the self-assembly kinetics by varying the Janus bilayer's geometrical design. For a constant water droplet volume, the maximum self-assembly length is inversely proportional to the width of the strips (Figure 7.4a). This is in line with the theoretical and dynamic analysis of the self-organization process (Figure 7.3, 7.4b). It further confirms that, during Mimosa Origami, the flow is driven by the Laplace pressure of the self-assembled hollow cross-sections. For a rectangular strip having a width of 2 mm, the folding stimulus propagated through the complete strip length (6.5 cm) possesses an average flow velocity of 2.5 cm s^{-1} (Figure 7.4a,b). Notably, for this optimal geometry, the self-assembly length is only limited by the initial size of the strip. Significantly longer assembly lengths (ca. 200%) were easily achieved by increasing the path length. Increasing the strip width to more than 3 mm partially disrupts the shape of the hollow cross-section, and decreases the maximum lengths of self-assembled micro-channels (Figure 7.4a). This is attributed to the partial self-collapse of the Mimosa Origami effect for

strip sizes significantly above the elasto-capillary length. The average stimulus propagation velocity measured for a 2 mm width and 6.5 cm long strip was 2.5 cm s^{-1}, which is curiously comparable to the electrical signals (2-3 cm s^{-1}) found in the *Mimosa pudica*[628].

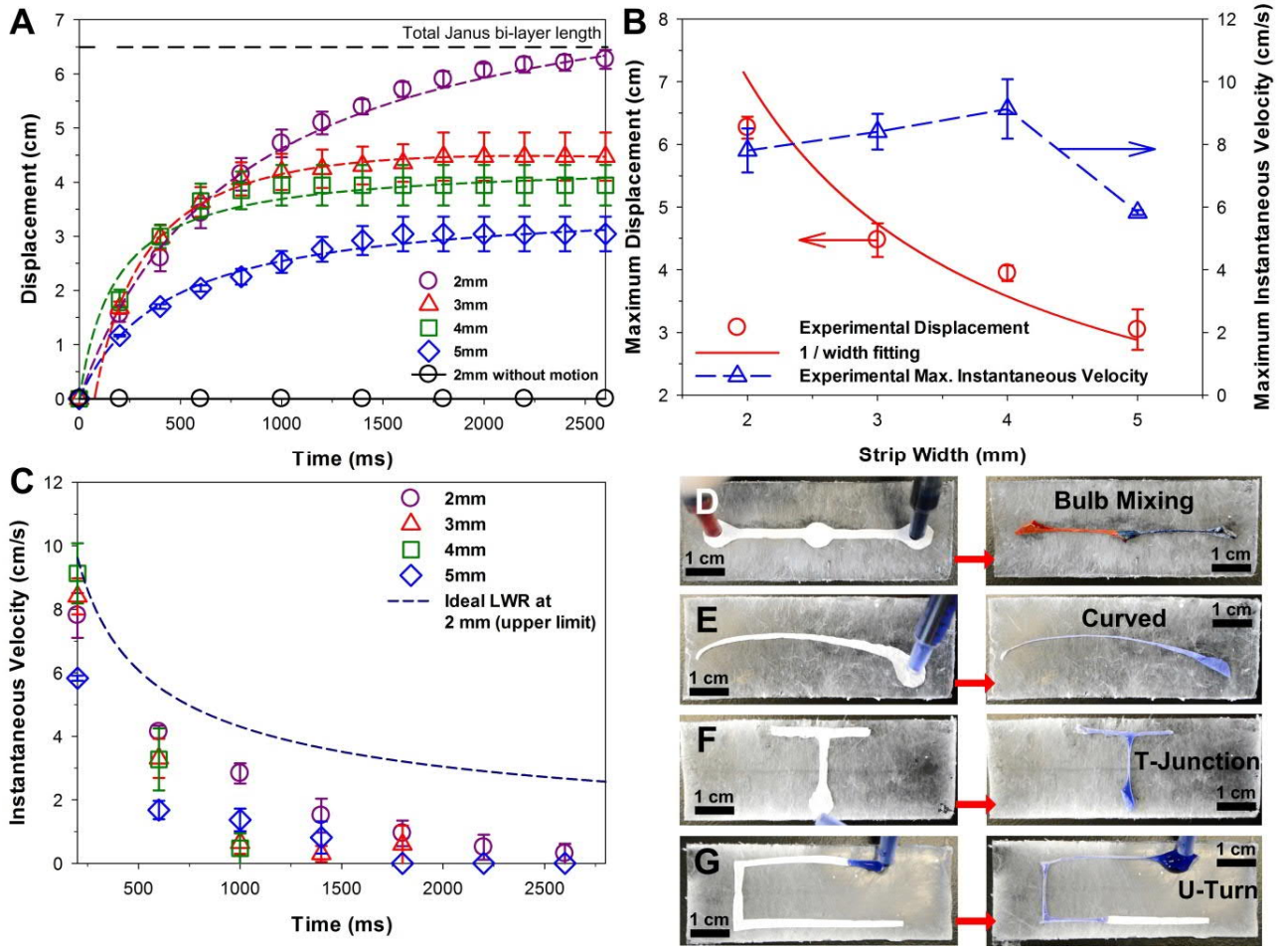

Figure 7.4. Application of the Mimosa Origami regime to microfluidics. a) Fluid displacement from the bulb during Mimosa Origami self-assembly as a function of the strip width and time. b) Maximum displacement and velocity as a function of strip width, and the 1/w capillary fit. c) Water instantaneous velocity as a function of the time since water droplet contacted the Janus bilayer surface. This is compared against the Lucas-Washburn-Rideal (LWR) equation for an ideal circular capillary. (D-G) Exemplary modular microfluidic designs obtained by the self-assembly of functionally-shaped Janus bilayer strips including d) mixing bulb channel, e) curved tapering channel, f) T-junctions and g) U-turns.

Remarkably, in an exemplification of bioinspired microfluidics, the optimized Janus bilayers conveyed fluids at an estimated initial volumetric flow rate of 14.7 µL s^{-1}. This is up to 10 times faster than state-of-the-art microfluidic propulsion systems based on wicking, evaporation, and degassing.[24] Notably, the optimal self-assembling Janus bilayers possess an initial flow velocity up

to 81% belonging to the ideal Lucas-Washburn-Rideal (LWR) capillary. The small delay is attributed to the time required for self-assembling the capillary structure before spontaneous fluid transport. The subsequent decrease in instantaneous velocity (stimulus propagation rate) scales with the ideal LWR capillary (Figure 7.4c) but eventually ceases. This is attributed to the decreasing effective capillary pressure (emptying fluid reservoir), coupled to counteracting elastic folding and viscous forces.

From an engineering perspective, the fluid propagation speeds rival some of the fastest pump-less microfluidic devices based on etched superhydrophilic V-shaped grooves.[203] The self-organization potential of these multi-layer structures extends beyond previous studies on utilizing water surface tension for the construction of complex but static 3D structures.[631,639,640] This was exemplified by modifying the directionalities and geometries of the Janus bilayers into several functional self-assembling shapes. Various key microfluidic modules with increasing degrees of difficulties were easily obtained. This included mixing bulbs, tapered curves, single and double right corners. The maximum demonstrated self-assembly length of 10 cm (Figure 7.4d-g) was achieved, which is at dimensions well-suited for the fabrication of flexible modular micro-flow devices (Figure 7.4d-g). Notably, such a scale represents an order of magnitude larger than that previously achieved by static elasto-capillarity based self-assembly.[631,641]

7.3. Conclusions

In summary, we have demonstrated a new self-organization mechanism, that over time enables the directional large-scale reconfiguration of soft materials. The observed self-assembly dynamics occurs through a cascade of thermodynamic states that are individually accessible by controlling water volume supplied to the Janus bilayer. As a result, this Mimosa Origami regime can overcome some of the limitations faced by traditional elasto-capillarity systems, with self-assembly scales that can theoretically cover unlimited lengths. Exemplification of this concept in micro-fluidics demonstrates record-high response times, as compared to conventional microfluidics[24], showcasing near-ideal capillary velocities. In addition, the self-assembly is reversible, capable of facile unfolding; recovery of initial surface properties. The orthogonal propagation of stimuli demonstrated by the Janus bilayers represents a unique mechanism that can be exploited by a myriad of research and commercial applications, such as stimuli-responsive materials,[537,642] fog-harvesting,[560] artificial muscles,[629,638] sensors,[643] switches[537] and power-independent devices[546].

7.4. Experimental Section

Polymer solution preparation

PVP solutions were made by dissolving 0.789 g of PVP (Sigma Aldrich, M_w = 1,300,000) in 10 mL of ethanol (Sigma Aldrich, anhydrous, ≥ 99.5%). PCL solutions were made by dissolving 0.948 g of PCL (Sigma Aldrich, M_n = 80,000) in 9 mL of chloroform (Sigma Aldrich, anhydrous, ≥ 99%) and 3 mL of methanol (Sigma Aldrich, anhydrous, ≥ 99.8%). PVC solutions were made by dissolving 1.335 g of PVC (Sigma Aldrich, M_w = 80,000) in 10 mL of tetrahydrofuran (Sigma Aldrich, anhydrous, ≥ 99.9%) (THF). PS solutions were made by dissolving 0.944 g of PS (Sigma Aldrich, M_w = 280,000) in 10 mL of N,N-dimethyl formamide (DMF, Sigma Aldrich, anhydrous, ≥ 99.8%). Dodecyltrimethylammonium bromide (DTAB, Sigma Aldrich, ≥ 98%) was added to the PVP, PCL, PVC and PS solutions at a concentration of 1.1, 3.0, 1.1 and 1.9 mg mL^{-1}, respectively.

Substrate preparation

PDMS substrates were prepared using Sylgard 184 (Dow Corning), which comprises of a 10:1 ratio of base elastomer to curing agent. These were mixed together, degassed and casted as rectangular PDMS slides with a dimension of 75 mm by 25 mm by 1 mm. Full curing of the substrates was conducted at 70 °C overnight (16 h) in a convection oven (MTI, U.S.A). Laboratory paper towel (Kimberly-Clark, Scott® Towel Roll) and cardboard (OfficeMax) substrates were used without further treatment.

Electrospinning of the Janus bilayers, protective PVP layer and dewetting PS-PDMS substrate

A horizontal electrospinning setup was utilized, with a spinning drum diameter of 10 cm and a rotation of 300-400 RPM. Optimal electrospinning of all layers (PVC, PCL and PVP) on paper towel (sacrificial substrate) was achieved by systematic optimization of key synthesis parameter matrix over an electrode working distance of 10 to 15 cm, an electric potentials from 5 to 30 kV, a solution concentrations from 2 to 30 w/w, a DTAB concentration from 0 mg mL^{-1} to 2 mg mL^{-1} and a polymer

solution feed rate from 0.5 mL h^{-1} to 2.0 mL h^{-1}. The optimization was aimed at producing pure beadless nanofibrous layers with desired wetting (PCL) and dewetting (PVC) properties.

As a result of this optimization, PVP nanofibers were electrospun at a working distance and flow rate of 10.5 cm and 1.2 mL h^{-1} with an applied voltage of 25 kV for 1 h. PCL nanofibers were electrospun at a working distance and flow rate of 15 cm and 1.5 mL h^{-1} with an applied voltage of 15 kV for 1 h as the primary functional layer. PVC nanofibers were electrospun at a working distance and flow rate of 10 cm and 1.0 mL h^{-1} with an applied voltage of 25 kV for 2 h as the encapsulation layer.

The addition of dodecyltrimethylammonium bromide (DTAB) aided the synthesis of pure nanofibrous layers through the enhancement of charge densities in the jet stream[576]. DTAB-aided electrospinning of PVP and PVC did not experience extreme wetting variations while PCL films electrospun under the influence of DTAB was observed to develop a highly hydrophilic interface, outlined by hemi-wicking properties. In contrast, PCL nanofibrous layers electrospun without DTAB (data not presented) exhibited hydrophobic properties that were in close alignment with the current literature[644]. The well-integrated PVC-PCL nanofibrous layers constitute the Janus bilayer. The tri-layer (with PVP) was developed between 50-60% relative humidity. As-developed tri-layers were then encased in aluminum foil and kept in a dry desiccated environment, enabling the preservation of its Janus functionality over extended periods (tested up to 6 months).

Electrospinning of the PS nanofibrous layer on PDMS was likewise optimized over a range of electrospinning parameters (see above), and was subsequently conducted using a vertical electrospinning setup (Electrospunra ES210, Singapore), at a working distance and flow rate of 10 cm and 1.0 mL h^{-1} with an applied voltage of 25 kV for 6 mins between 30-50% relative humidity. A lateral travel distance of 7 cm with a speed of 2 cm s^{-1} was used to improve homogeneity. PS nanofibers developed on PDMS were not moisture sensitive and could be stored indefinitely without loss in functionality.

Shaping of the Janus bilayers

The as-developed multi-layered nanofibrous films were shaped into the desired mimosa bilayer strips by cutting them across printed templates designed in graphics software. Template shapes included straight and curved channels, single and double right-angled turns, as well as a variety of mixing channels. The minimum Janus bilayer strip width tested here was 2 mm. The low adhesion between the PVP protective layer and the Janus bilayer enabled clean and easy removal of the paper substrate and PVP layer resulting in a free-standing functional strip (Figure S7.5a).

Alternatively, the surface properties of the Janus bilayer were enhanced by exposing peeled bilayers (PCL side) to water plasma for 3 mins at 50 watts resulting in superhydrophilic-superhydrophobic Janus bilayers. These Janus bilayer strips were thereafter placed onto several substrates, including polymers, papers and nanofibrous materials.

Mechanical and surface analysis of the Janus bilayer

The mechanical properties of the Janus bilayer were determined through a series of stress-strain tests using a Dynamical Mechanical Analyzer (DMA8000, PerkinElmer, U.S.A) with a tension-rectangle mode and a maximum load of 5 N at 0.2 $Nmin^{-1}$, a frequency of 1 Hz and a force multiplier of 1 at a controlled temperature of 25 °C. The Young's modulus was computed from 5 repeats of the linear region of the corrected stress-strain curve with a strain of 0 to 0.04 mm (Figure 7.1f).

The thicknesses of the Janus bilayers placed on PDMS were measured *via* a white light interferometer (Veeco, Wyko NT9100, USA). The vertical scanning interferometry (VSI) mode was used at 50X magnification with a field of view of 1X. A backscan of 50 µm with a scan-length of 100 µm was used with a modulation of 2%.

The film roughness (r) was computed as the ratio between actual surface area and geometrical surface area by gravimetric analysis (Perkin Elmer, STA 8000, U.S.A) and scanning electron microscopy (SEM) assisted fiber diameter counts over ca. 9 cm^2 in geometrical surface area for 3 cross-batch samples.

Morphological and chemical Analysis

All the nanofiber layers were analyzed with a Zeiss UltraPlus analytical scanning electron microscope (FESEM) at 3kV. Prior to SEM, the specimens were platinum sputter-coated for 2 mins at 20 mA. Fiber diameters were computed using ImageJ with 50 counts for each sample. Data was presented as mean ± standard deviations. Fourier Transform Infrared-Attenuated Total Reflectance (FTIR-ATR) was performed with a Bruker-Alpha FTIR (Bruker, U.S.A) at 24 scans from 400 to 4000 cm^{-1} on all samples.

Wetting analysis

The wetting properties of the Janus bilayer were assessed by CA measurements with a contact angle goniometer with a rotary stage. Dynamic and static images were recorded using a KSV CAM200 contact angle goniometer (Finland) with a heliopan ES43 camera (Japan). The PS-PDMS superhydrophobic substrates were tested as-prepared, while the Janus bilayers were first laminated onto sticky PDMS substrates prior to testing. Static CAs were measured using the sessile drop (5 µL) technique averaged over 5 repeats.

SAs were determined by placing a 10 µL drop of deionized water directly on sample surfaces prior to tilting *via* a goniometer. Results were averaged across 3 readings. CAH was measured *via* the drop-in drop-out (DIDO) technique which provided the average ACA between 8-9 µL and the average RCA between 1-2 µL. An average was determined over 5 repeats. Dynamic CAs were measured for the PCL side of the Janus bilayer. The CAs, SAs and CAHs were computed by a commercially available (CAM2008) program. Data is presented as mean ± standard deviations.

Analysis of the Mimosa Origami Self-Assembly

The directional self-organization of the Janus bilayers was assessed on the PS-PDMS substrate. Deionized water was dyed red and blue using Congo Red (Sigma Aldrich, 35% dye content), Methylene Blue (Sigma Aldrich, ≥ 82% dye content) and Trypan Blue (Sigma Aldrich, 60% dye

content) at concentrations of 1.5 mg mL^{-1}, 1.5 mg mL^{-1}, and 0.25 mg mL^{-1}, respectively to aid visualization. Mimosa Origami strips were approximately 6.5 cm in length. Strip widths of between 2 to 5 mm were used in conjunction with an actuation bulb of 7 mm in diameter. Mimosa Origami was initiated through a single 40 µL droplet deposited on the actuation bulb. A DSLR camera (Nikon D3200, Japan) was used to capture the dynamic origami at a resolution of 720p and 60 fps. Movies captured were then imported into Microsoft Movie Maker and analyzed at sequential frames of 30 ms. Repeatability was assessed through 5 different cross-batch repeats. Tests were conducted at approximately 20-25 °C and between 50-70% relative humidity. Spontaneous unfolding of Mimosa Origami assembled micro-channels was performed by immersing the as-folded channels into a dish of ethanol. Surface wetting of PVC side enabled a symmetrical restoration of the Janus bilayers' surface energies, enabling spontaneous disassembly. The unfolded channels were then lifted out of the ethanol and dried in a desiccated environment overnight before plasma reactivation (20 W, 1 min). Modular microfluidic-typed channels (tapered curves, right-angled turns and mixing channels) were also tested *via* the simultaneous deposition of colored micro-droplets on functional Janus bilayers geometries. Results demonstrated potential for the simple development of templated, single-step self-assembled microfluidic devices. Pump-aided inflation-deflation cycles were executed with a 10 mL syringe (Terumo, Japan) on a syringe pump (New Era Pump Systems, New York) operating at 10 mL h^{-1} to showcase suitability of pumped microfluidics.

7.5. Supplementary Information

Supplementary Text

Supplementary Calculations

Supplementary Material Data

Supplementary Equations

Figures. S7.1 to S7.13

7.5.1. Supplementary Text

Wetting properties of the PCL layer

Notably, the PCL-side of the Janus bilayers was not instantaneously superhydrophilic.[95] Its CA with water was initially 33° and gradually reached 0° in ca. 40 s (Figure S7.4). This was attributed to the gradual wicking of water through its porous fibrous interface. This unique droplet-interface regime has been previously coined as the sunny-side up state.[645] In such materials, the penetration front exceeds the contact radius and wicking-induced wetting is accounted to hydrodynamic effects.[124,645] While the hemi-wicking effect is well-studied through the Washburn equation[2] and was also recently modeled using experiments with regular micropillar forests,[124,645] its application for self-assembling soft materials remains unprecedented.[646]

Static self-assembly of the Janus bilayers

While the static self-assembly of thin flat solid films by elasto-capillarity has been demonstrated and described by Gao and McCarthy,[641] and McHale,[633] the cascade directional self-assembly presented here is unprecedented. A comparison with the previously reported elasto-capillarity folding of flat films was pursued by shaping the Janus bilayer into a circular shape with a diameter of 10 mm (Figure S7.6). Upon contacting the PCL side with a water droplet, the Janus bilayer folds violently. On the contrary, wetting of the superhydrophobic PVC side yields no response. This dichotomous effect is attributed to the very high surface roughness (r = 68) and total surface energy density of nanofiber-based PCL layer.

Such parameters significantly enhance the surface energy gradient which drives folding of the Janus bilayer during localized wetting far above that of dense polymer films. The swift clamping motion of the of the hydrophilic PCL rough interface around a droplet is extremely rapid[633,639,641] due to the much higher total surface energy of the porous nanofiber layer. In dense flat films, elasto-capillarity bending is driven by the reduction of overall surface energy whereby the vapor-liquid interface is replaced with the liquid-solid interface.[633] However, for a superhydrophobic porous surface such as

the PVC side of the Janus bilayer, water droplets contact only a fraction of the solid surface. As a result, the surface energy reduction driving the folding of the PVC side is dramatically reduced. As discussed in the theoretical model (Figure 7.3c and Supplementary Calculations below), a high surface energy density is critical for decreasing the minimal folding widths, thus enabling cascade propagation of the Mimosa Origami effect.

To further investigate the role of surface energy density on the Mimosa Origami effect, a Janus bilayer was subsequently produced by exposing a disc cutout of the bilayer to water vapor plasma (50 W, 3 mins). This superhydrophilic/superhydrophobic Janus bilayer also demonstrated a strong and rapid water-induced folding. However, after these initial trials, the plasma-induced superhydrophilic PCL interface was not further considered due to potential for complete infiltration (wet-through) and the general lack of inherent longevity (ease of contamination by airborne organics). Contrasting this, hemi-wicking/superhydrophobic Janus bilayers perfectly preserved desirable functional properties for extended periods (tested up to 6 months).

Role of substrate and bilayer composition on self-assembly dynamics during Mimosa Origami

Two key properties are required for the optimal dynamic self-assembly. Firstly, the nanofibrous hemiwicking PCL layer requires a superhydrophobic backbone. PCL monolayers suffer from rapid wet-through failure during utilization. This limits the capability of imparting a directionality to the self-assembly process, resulting in an inefficient conversion of chemical to kinetic energy. This was exemplified by the comparative analysis of the self-assembly of PCL monolayers and Janus bilayers on both paper and superhydrophobic dewetting substrates. On the paper substrates, PCL monolayers with a strip widths of 2 and 3 mm experienced catastrophic failures (Figure S7.8c,d), primarily by wet-through driven pinning to the substrate and some uncontrollable in-plane wrinkling. Contrastingly, the Janus bilayers retained complete functionality even on these paper (hydrophilic) substrates (Figure S7.8a,b) and dynamically self-assembled into micro-channels. However, the use of a PDMS-PS superhydrophobic substrate enabled much better performance in both situations. With

the use of a superhydrophobic substrate, even the PCL monolayer variant was capable of some partially directional self-organization (Figure S7.12). Nevertheless, the performance of the PCL monolayer was suboptimal and suffered from inevitable wet-through failure after a short self-assembly distance.

Secondly, the free-motion of the Janus bilayers is required for dynamic self-assembly to occur. Binding the Janus bilayers onto a sticky substrate physically hinders the self-assembly, which then prevents folding signal propagation. As a result, the cascade-dependent Mimosa Orgami effect becomes impossible.

7.5.2. Supplementary Calculations

Energy density of hemi-wicking PCL films

The energy density (u, Jkg^{-1}) of the hemi-wicking PCL nanofiber layer was computed from its material and surface properties as,

$$u = \frac{1}{m} [\pi D h \gamma_{LV} cos(\theta_e)] \quad \text{(S7.1)}$$

where, m is the PCL layer mass in kg, D is the average nanofiber diameter (m), h is the specific nanofiber length (mkg^{-1}), γ_{LV} is the surface energy density of water (0.072 Nm^{-1}) and θ_e is the characteristic CA.

The D is 192 ± 49 nm as measured by SEM. The θ_e is 81.9 ± 1.9° as averaged by static CAs measurements determined through 5 repeats on a quasi-flat interface of PCL fabricated by spincoating. The measured CAs were 83.24°, 82.25°, 81.93°, 83.37°, 78.64° and in line with the literature[647].

Based on the density of PCL, at 1145 kgm^{-3}, the specific length (h, mkg^{-1}) of the PCL layer was computed as,

$$h = \frac{4}{\pi \rho (D^2)} \quad \text{(S7.2)}$$

Through Equation S7.2, the specific length (h) was computed at 3.02 x 10^{10} mkg^{-1}. Inserting known values into Equation S7.1 gave the final energy density of the material, which was notably enhanced through the ultra-high surface area conferred by the nanofibrous nature of the material.

$$u = 185\, Jkg^{-1}$$

Roughness ratio analysis of PCL nanofibers (Gravimetric and SEM)

The roughness (r) of the nanofibrous PCL layer was computed from the ratio of the total surface area of the PCL layer to the geometric surface area,

$$r = \frac{4m\varnothing}{\pi\rho D^2} \quad \text{(S7.3)}$$

where m is the mass (3.74×10^{-3} kgm^{-2}) of the monolayer PCL per cm^2, $\varnothing$ is the average circumference of a nanofiber (601×10^{-9} m), ρ is the density of PCL (1145 kgm^{-3}), D is the average diameter of a nanofiber (192×10^{-9} m). Inserting these values into S3 results in a r of 67.8.

7.5.3. Supplementary Material Data

Self-assembled micro-channels and dimensions

The diameters of the self-assembled micro-channels were measured from photographic images and reported in Table S7.1.

Table. S7.1. Width to diameter ratios of Mimosa Origami assembled micro-channels

Janus Bilayer Strip Width (µm)	Assembled 3D Channel Diameter (µm)	Strip Width to Diameter Ratio
2000	490	4.08
3000	1050	2.86
4000	1720	2.33
5000	2700	1.85

Ideal self-assembly of cylindrical geometries from flat rectangles comprises of a width: diameter ratio of π. Values higher than π would have achieved idealized cylindrical folding (with some overlap) while values lower than π would have had folded into a suboptimal flattened cylinder.

Material analysis of PCL-PVC Janus bilayers by DMA and WLI

The thickness of the Janus bilayer (on PDMS) was measured by white light interferometry (WLI). The Janus bilayer's Young's Modulus was measured through stress-strain curves with a dynamical mechanical analyzer (DMA8000, PerkinElmer, U.S.A). The Poisson's ratio was assumed at 0.47, in accordance with previous studies.[367,648]

Table. S7.2. Material properties of Janus bilayers

Young's Modulus (E) - DMA	4.85 MPa
Poisson's ratio (v)[367,648]	0.47[367]
Film thickness (h) - WLI	51 µm

7.5.4. Supplementary Equations

McHale critical droplet size

$$L_{EC} = \frac{K_b}{\gamma_{LV}} \tag{S7.4}$$

$$K_b = \frac{Eh^3}{12(1-v)} \tag{S7.5}$$

where K_b is the bending rigidity, γ_{LV} is the surface energy density of water (0.072 Nm^{-1}), and E and v are the Young's Modulus and Poisson's ratio for the material.

Lucas-Washburn Rideal equation

$$x = \sqrt{\left(\frac{r\gamma}{\eta}\frac{\cos(\theta)}{2}\right)t} \tag{S7.6}$$

where x is the displacement (m), r is the radius of the capillary (m), γ is the surface tension of water (0.072 Nm^{-1}), θ is the apparent CA (°), t is the time (s) and η is the dynamic viscosity (1 mPa s^{-1}).

Laplace pressure in a capillary

$$\Delta P = \frac{2\gamma}{r} \quad \text{(S7.7)}$$

where ΔP is the Laplace pressure (Pa), γ is the surface tension of water (0.072 Nm^{-1}) and r is the radius of the capillary (m).

Solid surface energy estimation from contact angle

$$\gamma_{SV} \approx \gamma_{LV} \left(\frac{(1+\cos\theta_e)^2}{4\Phi^2}\right) \quad \text{(S7.8)}$$

where γ_{SV} is the surface energy density of the solid, γ_{LV} is the surface energy density of water (0.072 Nm^{-1}), θ_e is the characteristic CA, Φ is the ratio involving the free energies of adhesion and cohesion for two phases.[649]

$$\Phi = \frac{4(V_s V_l)^{1/3}}{(V_s^{1/3} V_l^{1/3})^2} \quad \text{(S7.9)}$$

where $V_{s/l}$ represents the molar volume, computed as $V_{s/l} = M/\rho$ where M is the molar mass ($kgmol^{-1}$), and ρ is density of the material (kgm^{-3}).

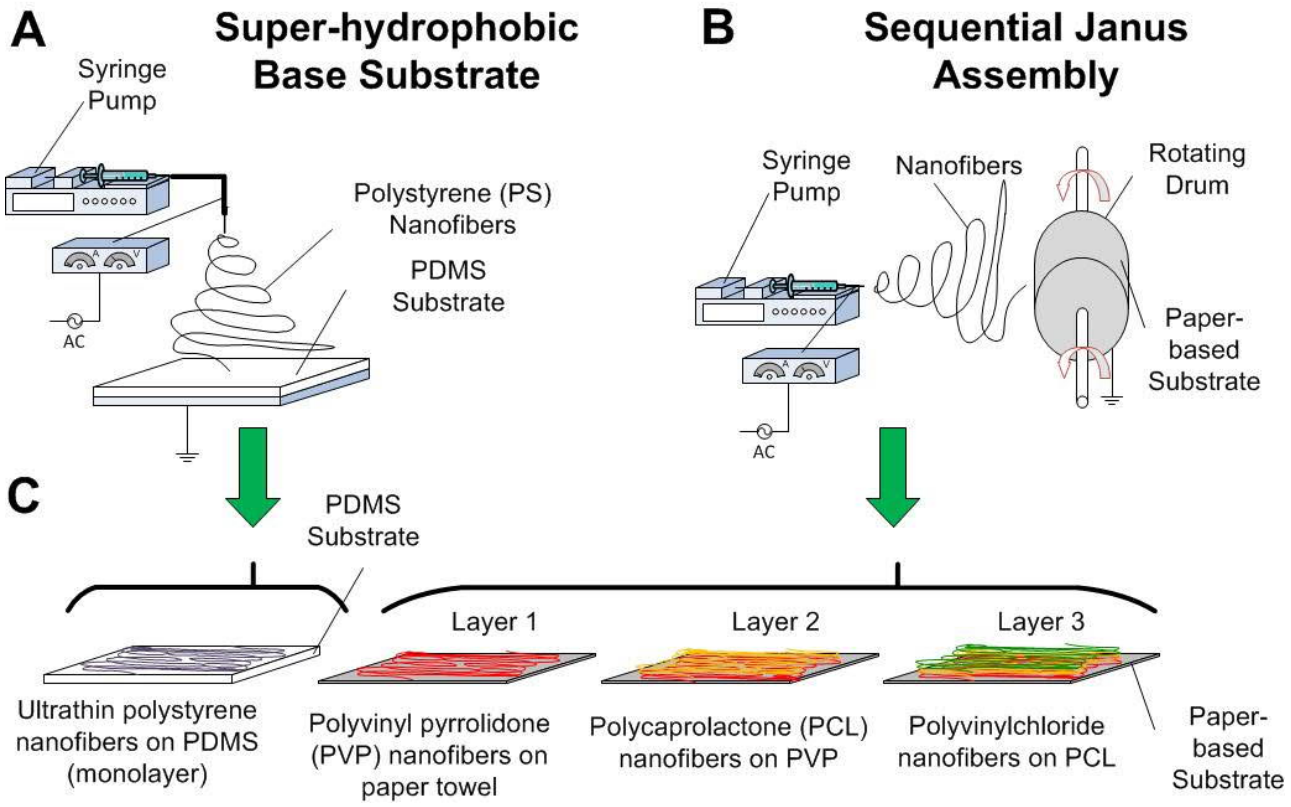

Figure S7.1. Synthesis of a nano-structured Janus bilayer by sequential electrospinning. The systems is made of nanofiber layers of a) superhydrophobic PS on a PDMS substrate and (b-c) Janus bilayer stack comprising a sacrificial PVP, a hemi-wicking PCL and a superhydrophobic PVC layer on a paper substrate.

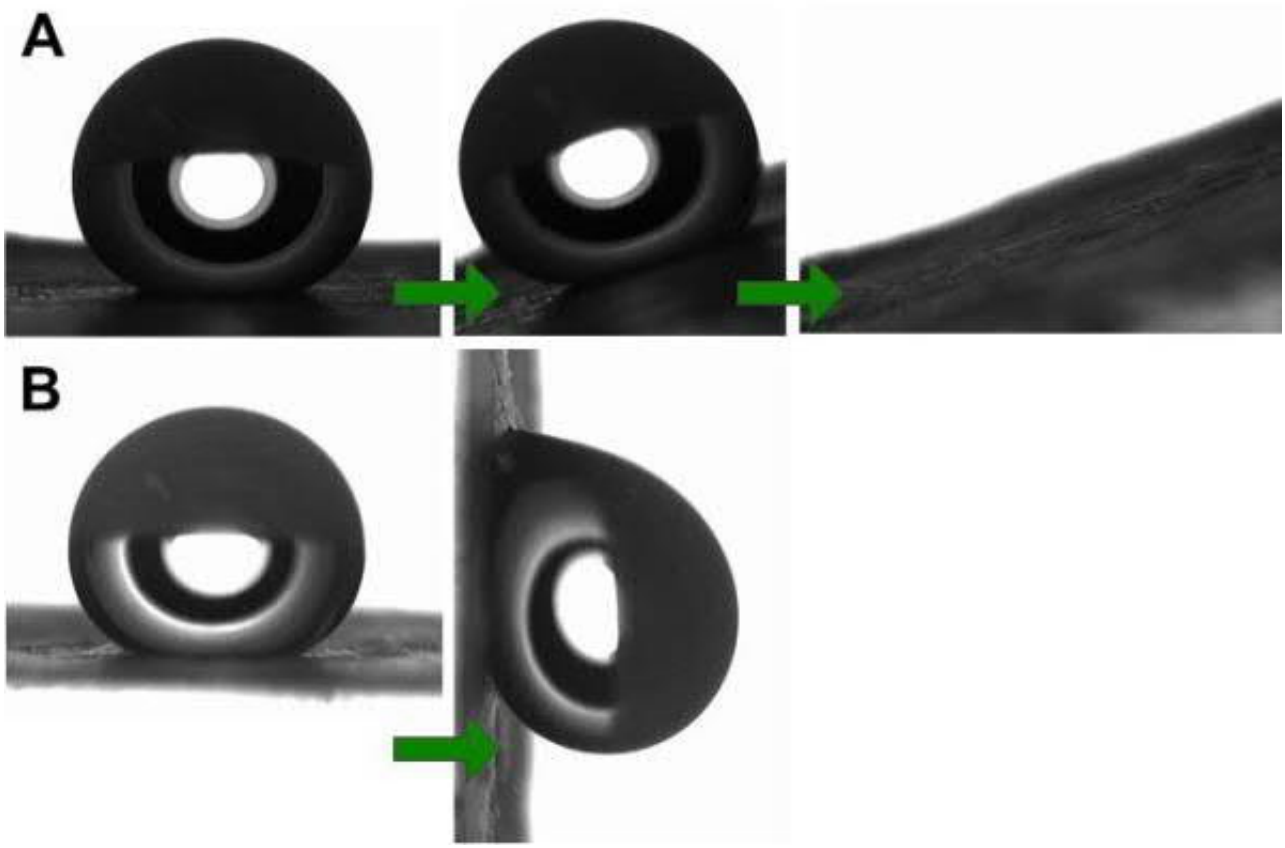

Figure S7.2. SA analysis of the superhydrophobic layers. a) Lotus superhydrophobic PS nanofiber layer and b) pinning superhydrophobic PVC layer.

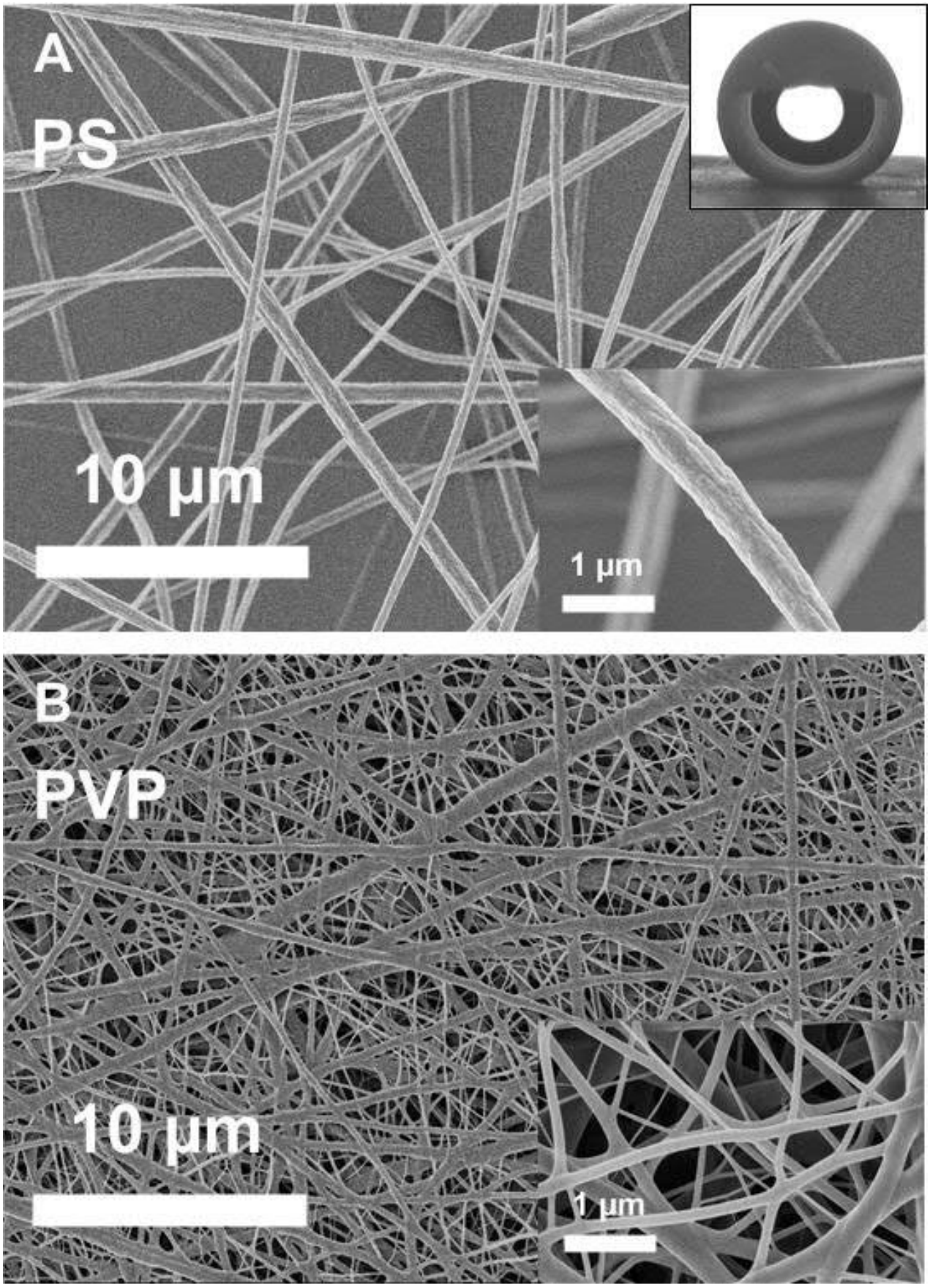

Figure S7.3. Morphological characterization (SEM) of the supporting and sacrificial layers. Nanofibrous a) PS as the dewetting platform and b) PVP as the hygroscopic protective sacrificial layer.

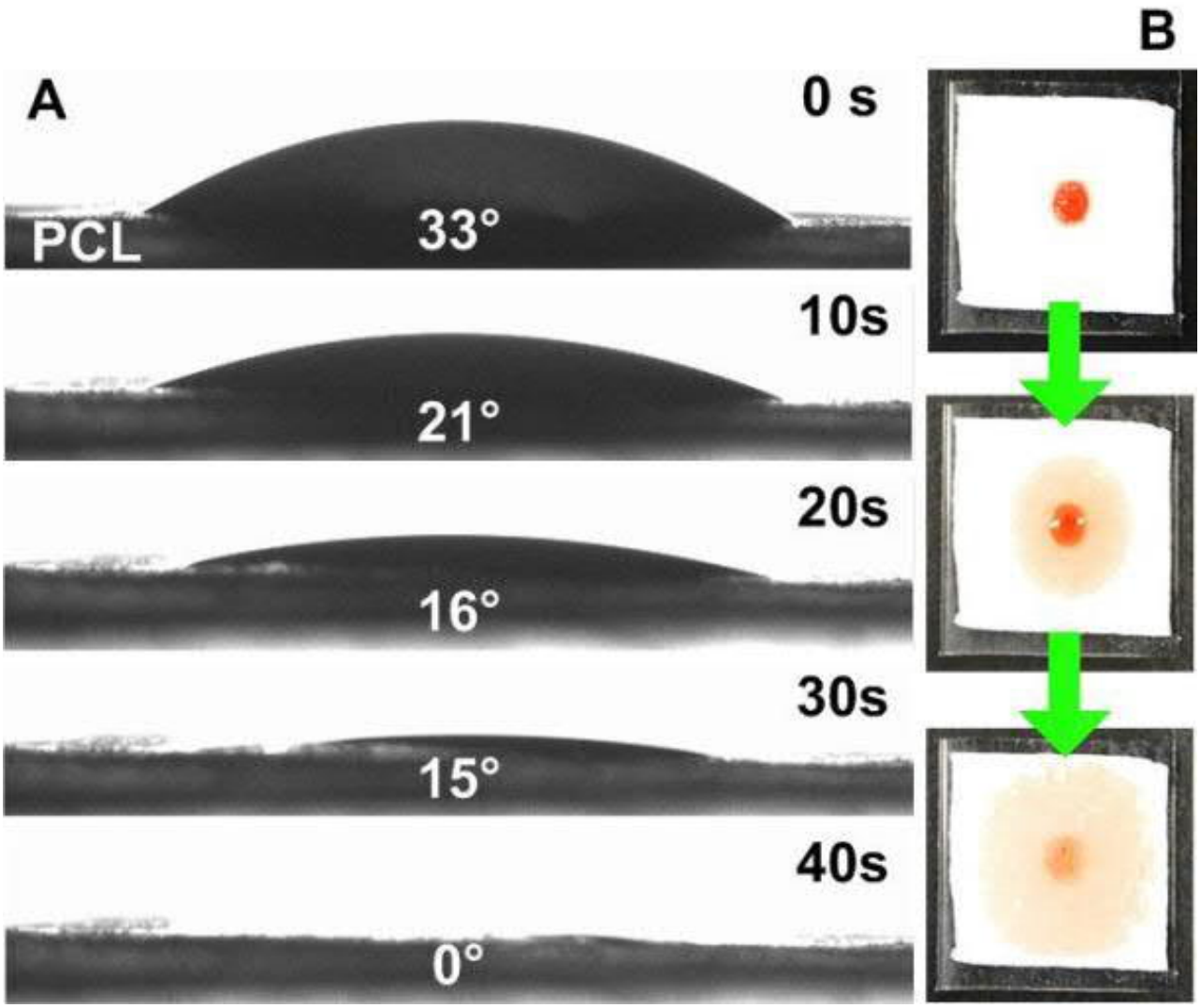

Figure S7.4. Hemi-wicking superhydrophilic nature of PCL layer. a) Side-profile and b) top-profile of the droplet wicking dynamics into a PCL monolayer.

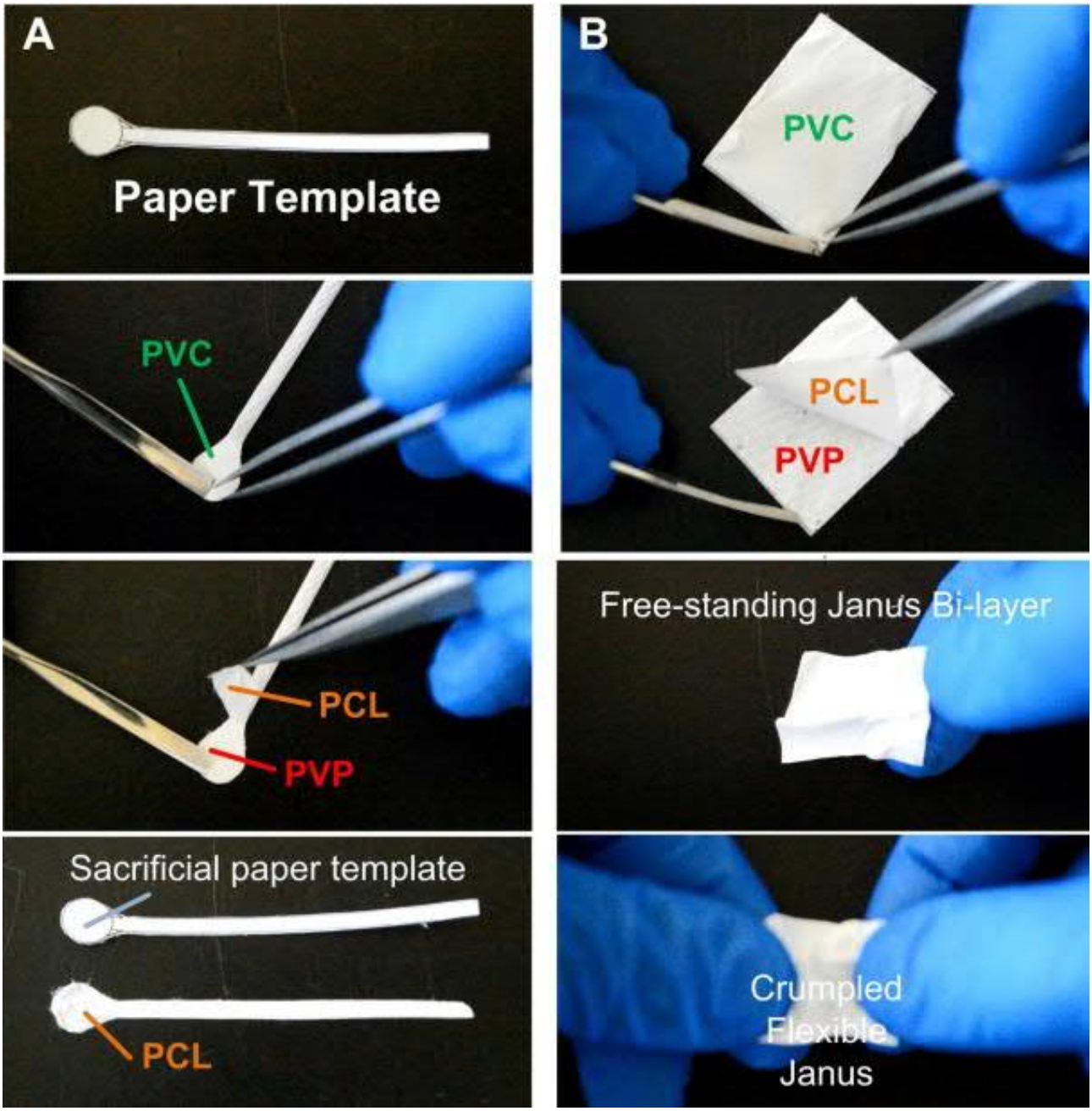

Figure S7.5. Separation of the Janus bilayer from the PVP protective layer. a) Separation of the functional Janus bilayer template geometry. b) Separation and manipulation of a rectangular-shaped free-standing Janus bilayer.

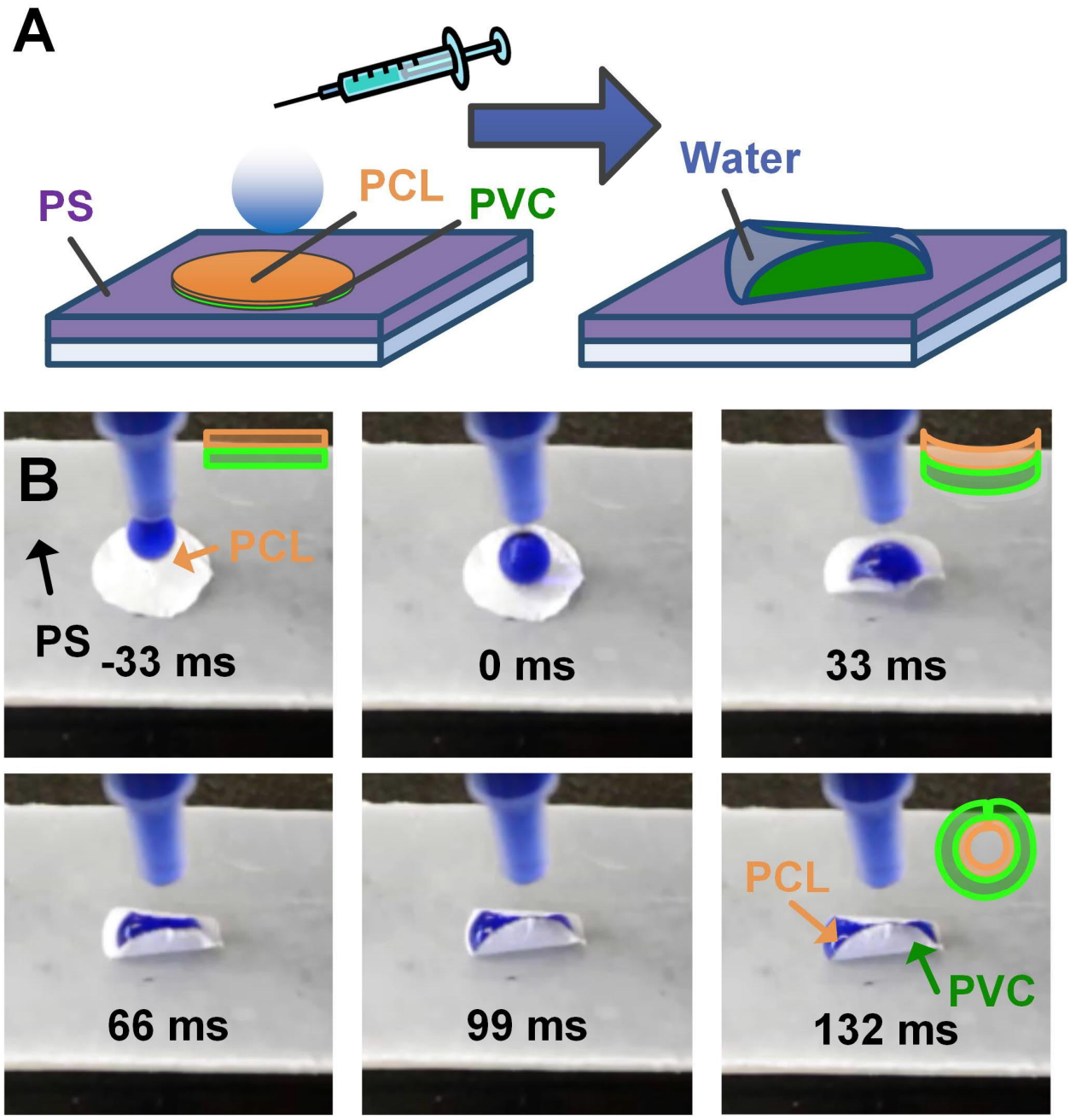

Figure S7.6. Static self-assembly of Janus bilayers. a) Schematic illustration of the static self-assembly of the Janus bilayer in response to a water droplet. b) Static self-assembly dynamics shown as a frame-by-frame analysis. The initial Janus bilayer response time was ≤ 33ms from droplet contact with the PCL surface.

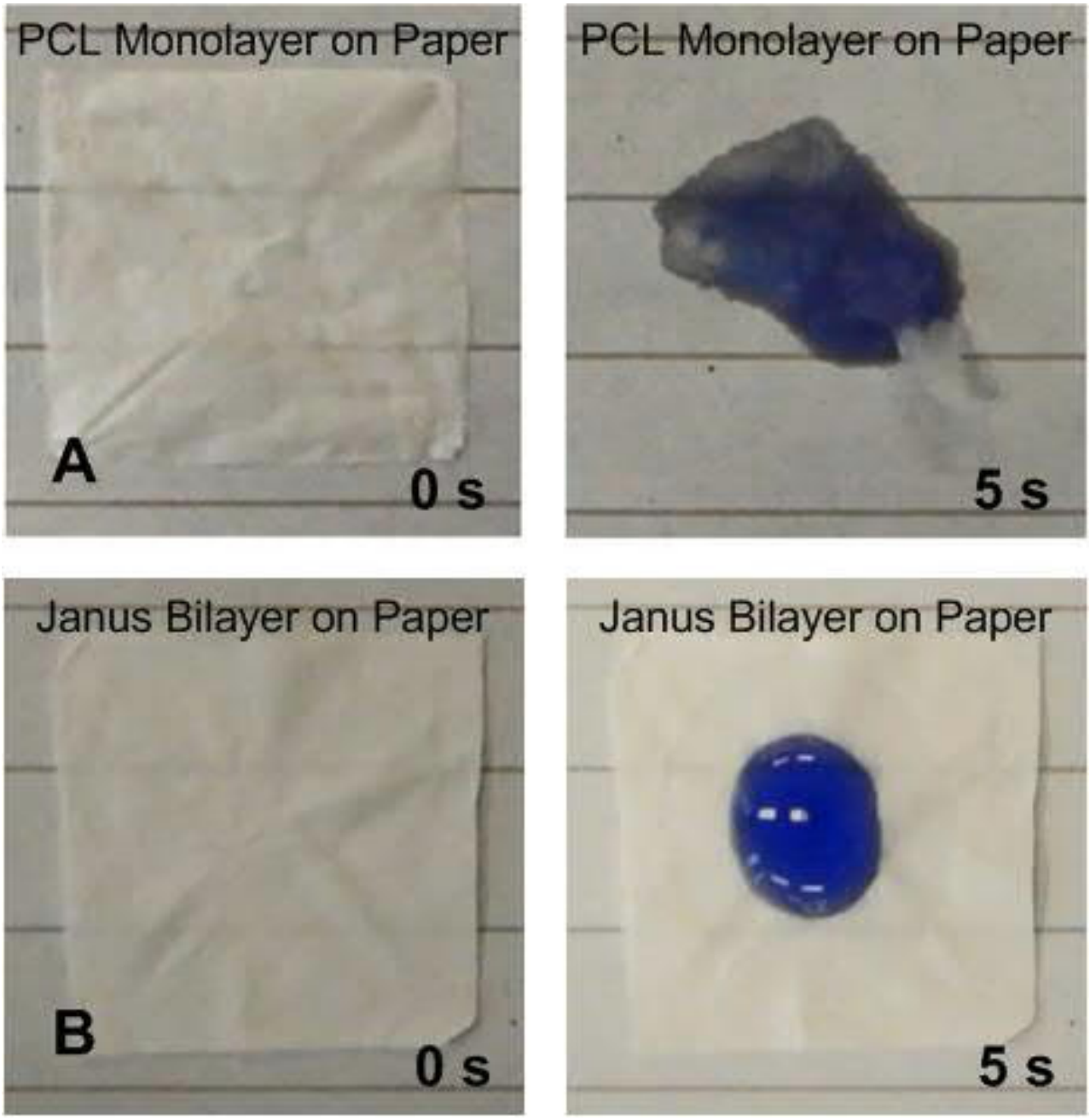

Figure S7.7. Janus bilayer and PCL monolayer response on hydrophilic (paper) substrates. a) Monolayer with wet-through failure albeit rapid folding-wrinkling and b) Janus bilayer with droplet holding capabilities showcasing a characteristic hemi-wicking droplet spreading.

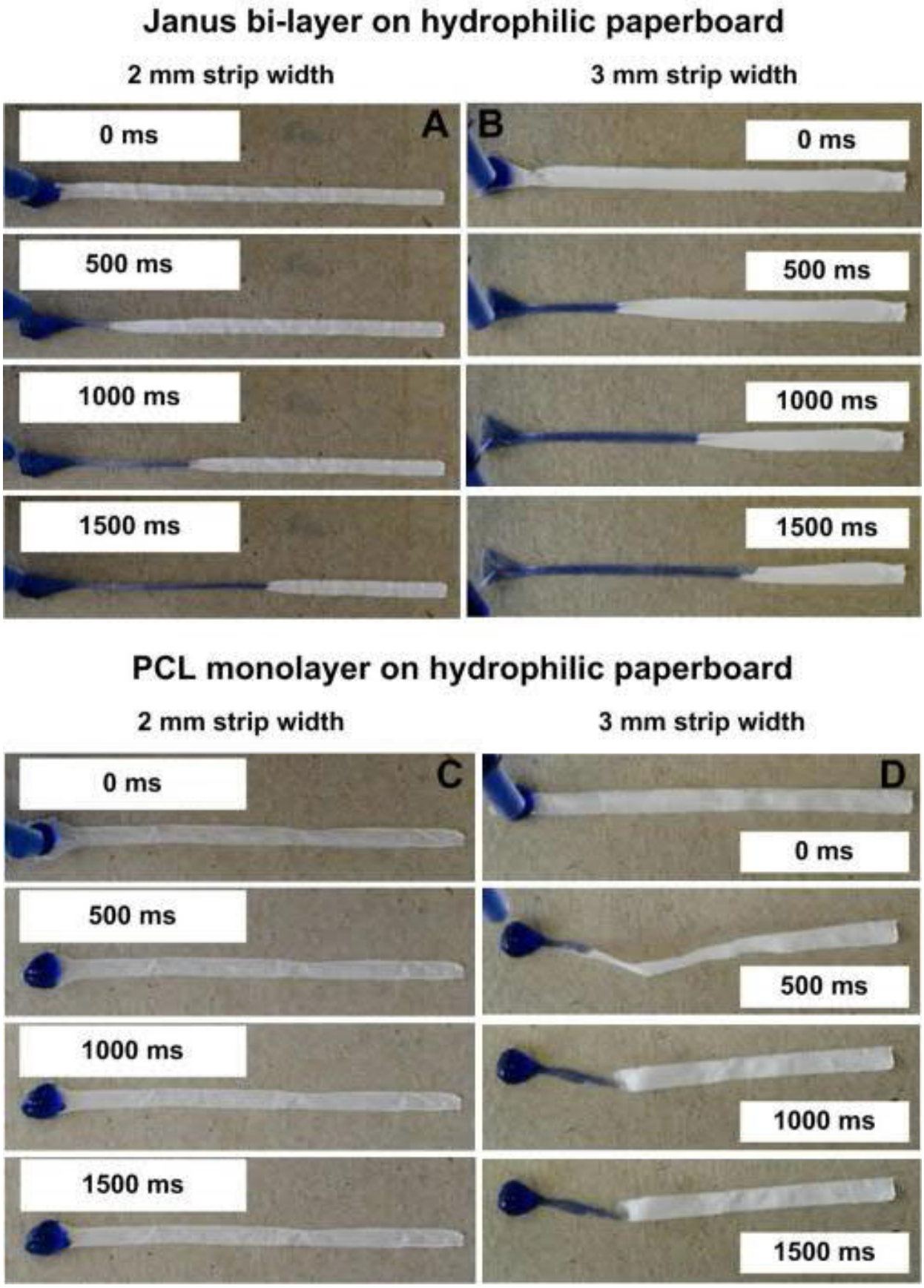

Figure S7.8. Qualitative wetting characterization of 2 and 3 mm strips of Janus bilayer and PCL monolayer on hydrophilic paperboard. (a-b) Janus bilayer with functionality at 2 and 3 mm widths respectively (albeit slower than on superhydrophobic PDMS-PS substrates) and (c-d) PCL monolayer with wetting failure at 2 and 3 mm widths, respectively.

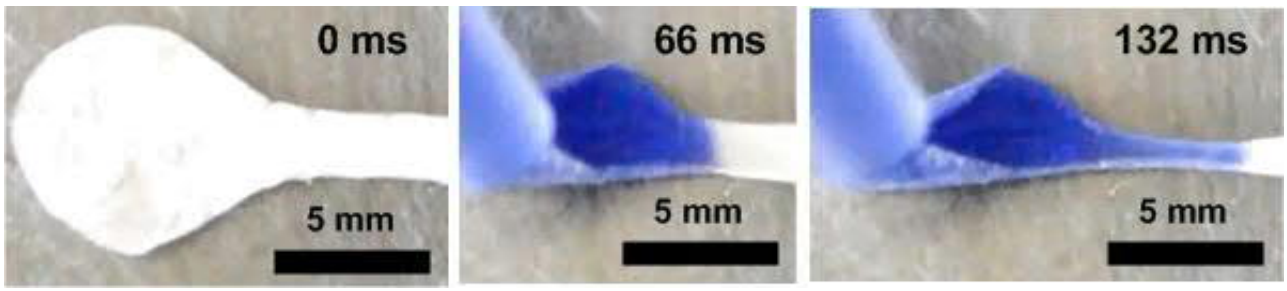

Figure S7.9. Enlarged images of initial Janus bilayer folding. The fluid transfer from bulb to the rectangular strip, revealing the formation of a quasi-cylindrical channel within 132 ms**.**

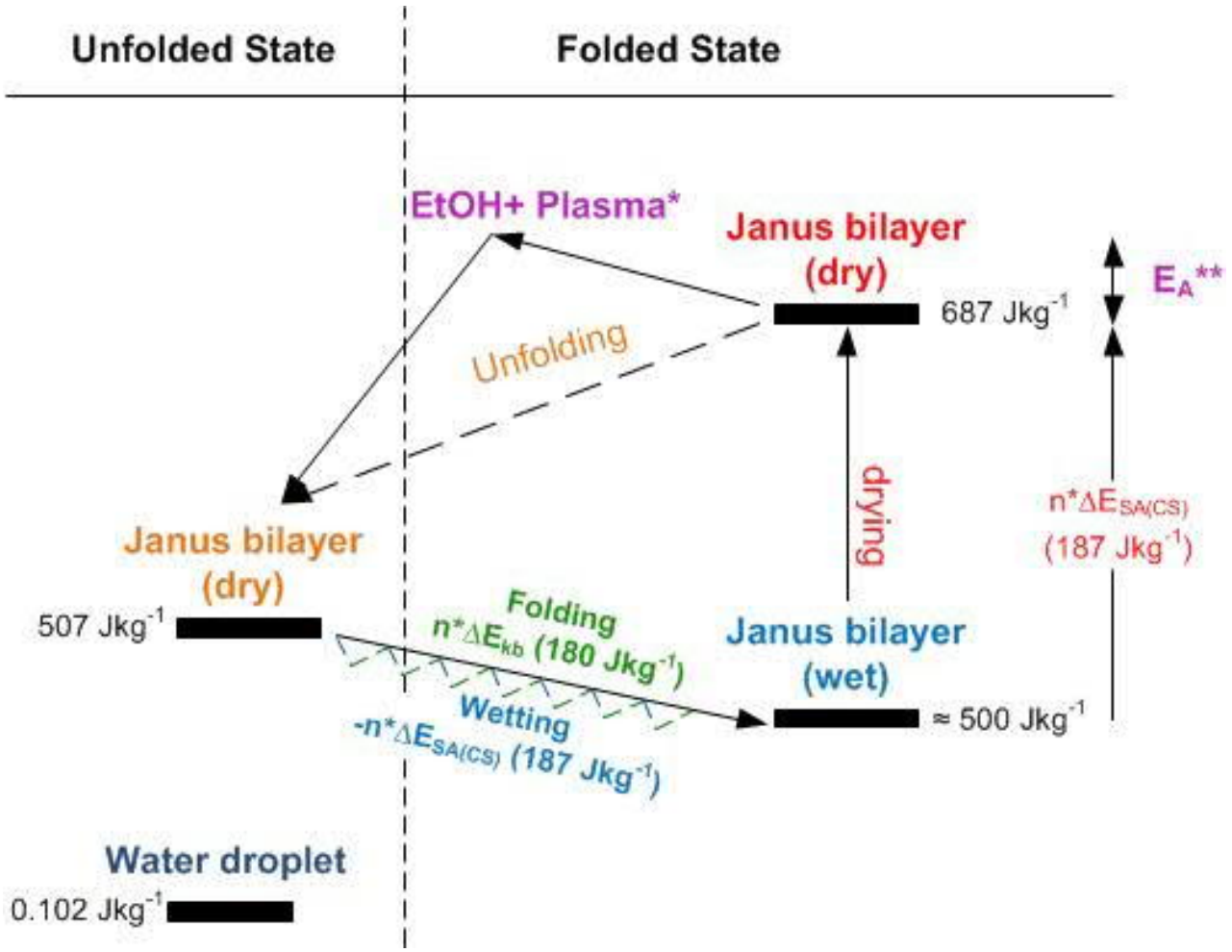

Figure S7.10. Representative thermodynamic states of the Janus bilayer during self-assembly. Wetting of the highly energetic dry-surface of the Janus bilayer (507 Jkg^{-1}) leads to a cascade (Mimosa Origami) of folding states (n) ultimately resulting in the folding of the whole Janus bi-layer length. The drop in surface energy ($\Delta E_{SA(CS)}$) is efficiently converted in elastic energy by the folding of each cross-sections ($\Delta E_{SA(CS)}$). The total energy density gain during wetting is estimated to 187 Jkg^{-1} and the elastic energy gain is estimated to 180 Jkg^{-1}. Drying of the folded Janus bi-layer results in the highest energy state (687 Jkg^{-1}) due to the contribution of the elastic energy ($n^*\Delta E_{kb}$). Immersion in the ethanol* bath supplies the activation energy (E_A**) to start the unfolding while plasma* treatment restores the initial surface energy enabling a new self-assembly cycle. Equations S7.8-7.9 were used for the computation of the surface energy (γ_{SV} and γ_{SL}) of the dry and wetted Janus bilayer.

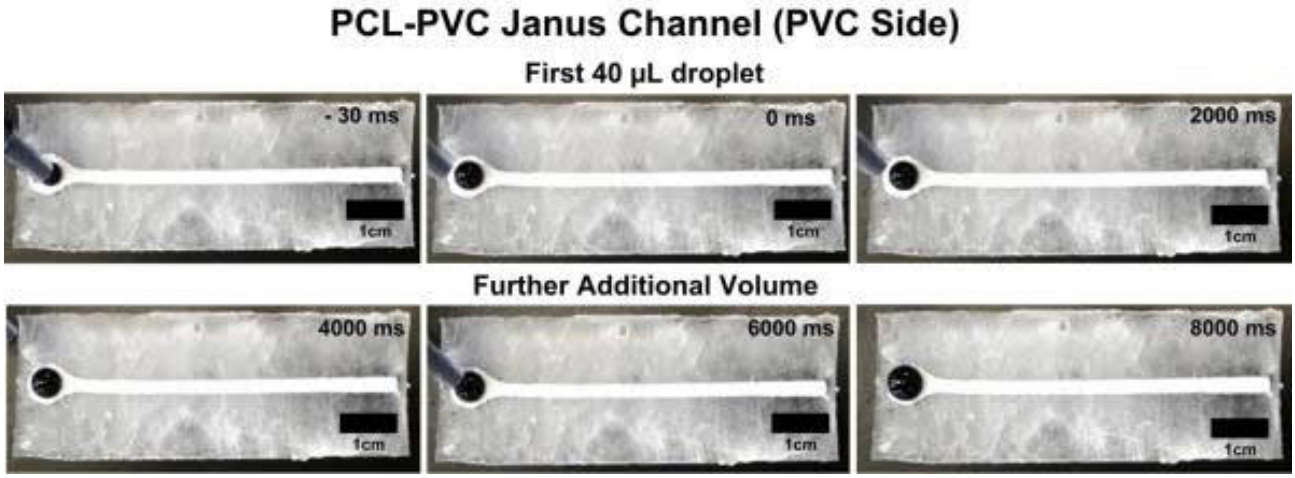

Figure S7.11. Response of the PVC side of the Janus bilayer to water. The wetting characterization of the opposing superhydrophobic PVC side of a 2 mm-wide strip of Janus bilayer on superhydrophobic nanofibrous substrates reveals no Mimosa Origami self-assembly.

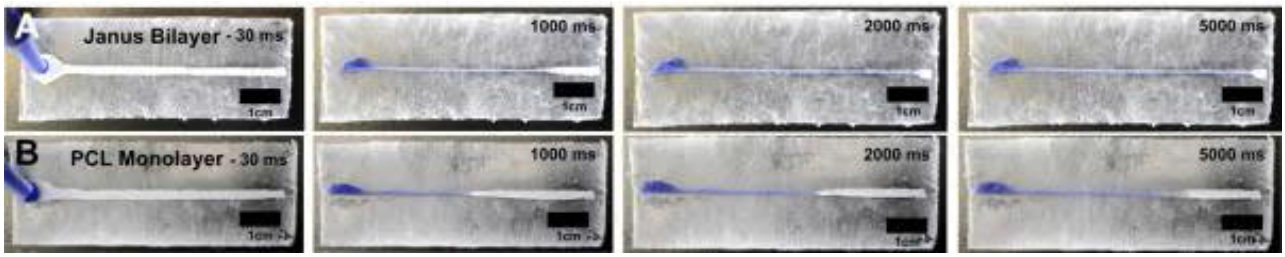

Figure S7.12. Mimosa Origami of a 2 mm strip of Janus bilayer and PCL monolayer on the PDMS-PS substrates. a) Janus bilayer with full functionality and b) PCL monolayer with suboptimal functionality due to wet-through failure.

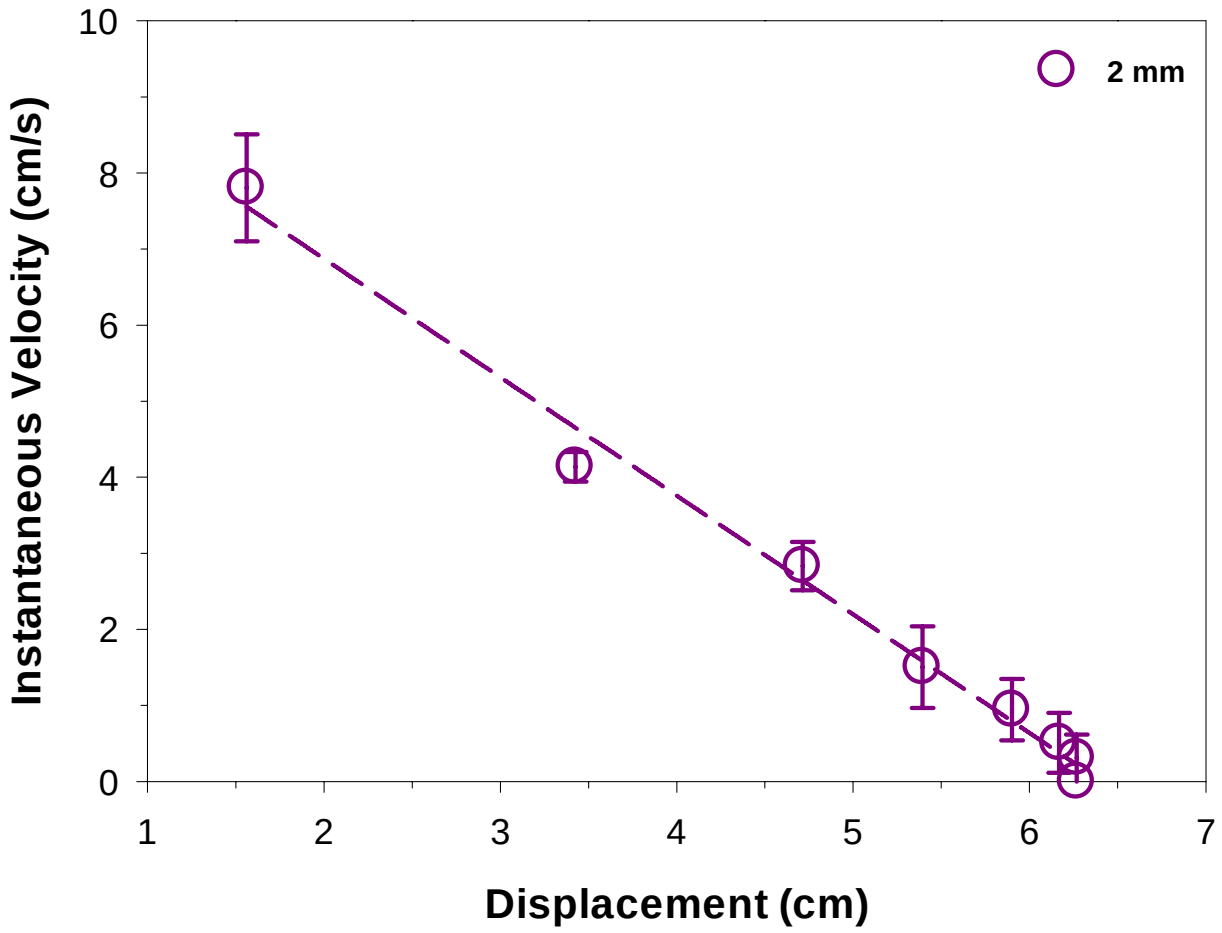

Figure S7.13. Decreasing stimulus propagation rate for a 2 mm wide strip and a stimulus droplet size of 40 µL.

8. Scalable, Transparent Reentrant-based Superamphiphobicity

Abstract

Development of ultra-transparent surface textures capable of repelling water, oil and other low surface tension fluids can revolutionize how we interact with wet environmental conditions. Despite extensive progress, current top-down methods are unanimously based on directional line-of-sight fabrication mechanisms. As such, they are largely limited by scale and cannot be applied to highly uneven, curved and enclosed surfaces. Alternatively, bottom-up techniques often suffer from poor controllability and optical transparency. Here, we present an approach that enables the rapid, omnidirectional synthesis of flexible and ultra-transparent (99.97%) super-hydrophobic and -oleophobic (super-amphiphobic) textures on many different surface types. These scalable textures were achieved by the spontaneous formation of multi re-entrant morphologies during the controlled self-assembly of nanoparticle aerosols. We also developed a mathematical model to explain the self-assembly dynamics, providing important insights for the rational engineering of such elusive but highly functional material constructs. Our findings represent a significant advance in imparting superoleo(amphi)phobicity to a so-far inapplicable family of materials and geometries for multifunctional applications.

8.1. Introduction

The design and synthesis of transparent surfaces that actively repel water,[650] oil[11] and other low surface-tension[12] organic liquids possesses immediate applications in the broad fields of fluidics,[63,651] chemical shielding,[65] stain-proof coatings,[57,161] membrane technologies[52] and anti-fouling.[446] While the development of superhydrophobic textures has been mastered to a quasi-commercial level,[91] advances in superoleophobic, superamphiphobic and superomniphobic surfaces are still impeded by significant challenges.[101] The low surface tensions of oils and organic fluids enable their ease of spread over a wide variety of materials and geometries that are functionally superhydrophobic.[360] Very recently, re-entrant or doubly re-entrant structures have unveiled the potential of countering wetting by low surface tension fluids. The unique surface architecture has led to the energetically unfavorable contact line advancements by the wetting fluids, thus enabling superdewetting.[11,12,155]

Despite much progress, the fabrication of re-entrant textures on non-flat surfaces has proven to be extremely challenging. A major limitation of both existing top-down and bottom-up approaches is revealed by their reliance on direct line-of-sight fabrication and synthesis mechanisms. As a result, it remains a far prospect in fabricating superamphiphobic textures by top-down lithography on substrates with highly uneven, curved or enclosed geometries. Alternatively, while providing better scalability, bottom-up synthesis techniques such as electrospinning,[482] candle soot[14] and wet-spray-deposition[161] typically require straight source-to-target trajectories. Thus, functional textures cannot be facilely self-assembled on surfaces with complex curvatures, such as the inner walls of tubes, coils and other curved surfaces.

Another real-world limitation of these oil repellent surfaces comes in the form of complicated, unscalable fabrication routes. While top-down processes offer superior control over the structural morphology,[12] they involve laborious fabrication processes which are problematic for scale-up. For instance, lithographical methods are applied to domain sizes of just a few square centimetres per hour

while requiring 3-6 sequential etching and templating steps.[12] Moreover, this approach is limited to the use of inherently flat substrates, such as silicon, glass[12] and templated silicone.[74] On the other hand, current bottom-up self-assembly approaches have not been able to match the fluid shedding performance of lithography-based textures. This is largely attributed to the lack of control by self-assembly methods on the resulting angle of re-entrancy, thus performance.[14,77,91,153]

In general, both current state-of-the-art lithographical and self-assembly developed nanotextures are further limited by transparency. The scattering sizes of micro- and nano- fibers,[90] or lithographic mushrooms[12] typically matches the visible spectrum, thus resulting in poor optical properties.

Here, we propose a rapid gas-phase concept for the bottom-up synthesis of highly transparent and flexible super -hydrophobic / -oleophobic (super-amphiphobic) textures on virtually any solid material and geometry. We exploited the omnidirectional self-assembly of nanoparticle aerosols for the synthesis of inverted trapezoidal nanotextures with potentially controllable angles of re-entrancy. The superamphiphobic coatings were optically superior, possessing up to 99.97% transparency on curved, enclosed and uneven surfaces. Gas-phase fluoro-silanization of these nanoscale structures gave rise to superamphiphobic surfaces capable of repelling liquids up to a minimum surface tension of 25 mN/m. We explained the results by developing a mathematical model that outlines the self-assembly dynamics, providing a flexible tool for the efficient, large-scale engineering of superamphiphobic nanotextures.

8.2. Results and Discussion

Figure 8.1a, b shows a schematic description of the nanotexturing approach. The omnidirectional nanoparticle flux is not limited[14] by line-of-sight trajectories, enabling the conformal coating of curved and highly uneven surfaces (root-mean-squared roughness upwards of 1-10 µm). These propitious conditions are utilized to synthesize inverted-cone structures that grow outward from the target surface. Figure 8.1e shows the exemplary nano-structures, formed by aerosol deposition of SiO_2 nanoparticles in the diffusion regime, for 15 s. Notably, these nano-structures reveal, for the first time, visible cross-sectional re-entrant profiles developed by bottom-up self-assembly. This morphology is reminiscent of the broccoli plant, where an array of stems (Figure 8.1e) is topped by the crown layer (Figures 8.1d, S8.7, S8.10). Increasing the aerosol deposition time to 120 s increased the nanotextures' thicknesses and crown diameters while decreasing the average pitch distances from tens to just several nanometers. The decrease in pitch distances is expected to decrease the smallest droplet size that can be repelled down to picoliters. This is superior to that of state-of-the-art optical lithography techniques which are limited to minimum pitch distances at the order of 1-2 µm.[652]

Upon complete self-assembly of these superamphiphilic SiO_2 nanotextures, a superoleophobic surface is easily obtained by vapor silanization with trichloro(1H,1H,2H,2H-perfluorooctyl)silane (Figure 8.1c). This is an atmospheric pressure chemical vapor deposition (APCVD) process that has been commercially implemented[652] with large-scale roll-to-roll[653] processes having substrate widths of up to 150 cm / 59 inches. The termination of SiO_2 surfaces with perfluorooctyl groups significantly decreases the nano-structures' surface energy. Energy-dispersive X-ray spectroscopy analysis of the thickest 7 µm nanotextures (T_d = 120 s) show that the perfluorooctyl groups are homogeneously distributed within their cross-sections (Figure 8.1f-i). This is attributed to the very high film porosity (ca. 98%) that allows rapid infiltration of the silane vapor throughout the whole structure. Transmission electron microscopic (TEM) analysis of the SiO_2 nanoparticles collected from the substrate surface show negligible differences in nanoparticle morphologies before and after

silanization (Figure S8.6a,b). This is in line with the formation of a terminal monolayer of perfluorooctyl groups.

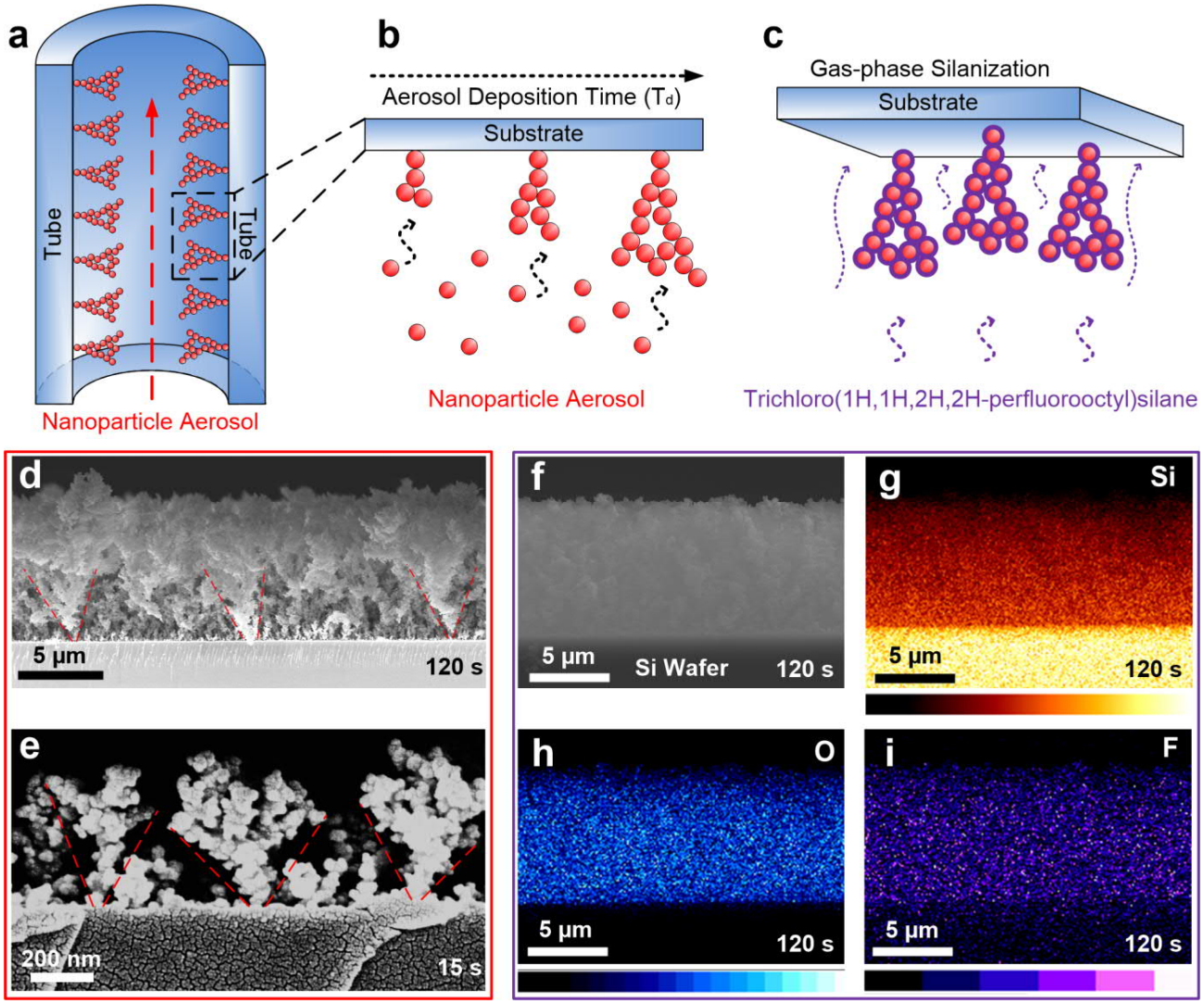

Figure 8.1. Self-assembly of omnidirectional re-entrant nanotextures. (a,b) Schematic description of the superoleophobic nanotexture fabrication by omnidirectional deposition of nanoparticle aerosols and c) fluorosilanization by APCVD. Cross-sectional SEM analyses of the nanotextures with an aerosol deposition time of d) 120 s and e) 15 s. Side-profile SEM micrograph depicting the characteristic broccoli-like growth of deposited nanoparticles. (f-i) Energy-dispersive X-ray spectroscopic mapping (EDX) of the side-profile after fluorosilanization showing successful functionalization with i) fluorine that is highlighted in purple.

Optical clarity and transparency of these functional nanotextures are unmatched (Figure S8.5). An aerosol deposition time of 15 s preserved 100% transmittance at a visible wavelength of 600 nm after subtracting losses induced by the soda-lime glass substrates (Figure 8.2a, circles). The total transmittance through the glass and coating is included in the Supporting Information (Figure S8.15) for reference. Increasing the aerosol deposition time to 120 s increases the texture thickness from 600

nm to 7 μm, resulting in ca. 13% optical losses. Fluorosilanization was found to increase the optical losses by 0.03% and 6% for an aerosol deposition time of 15 s and 120 s, respectively (Figure 8.2a, squares). At 15 s of deposition, nanotextures developed are scarcely detectable by highly sensitive optical instruments, while achieving superoleophobic/superamphiphobic properties against numerous low surface tension fluids such as hexadecane and tetradecane (Figure 8.2a). Alternatively, the thickest and most functional 7 μm textures were also barely observable with the naked eye (Figure 8.2b).

The wetting properties of these surfaces were further investigated as a function of the aerosol deposition time and liquid surface tension. Firstly, the impact of droplet size on the measured CA was sequentially assessed by using hexadecane as a standard oil on the 120 s aerosol-deposited nanotextures. Figure S8.13 shows the average measured CAs of hexadecane over 3 repeats on the 120 s aerosol-deposited nanotextures as a function of droplet sizes from 1 to 10 μL. These results reveal that average CAs increase only slightly from 162.6° to 165.5° with an order of magnitude increase in droplet volume from 1 to 10 μL. Such a relatively slight increase is comparable to the standard deviation across multiple measurements from different sample batches. These results are also in line with the conclusions of previous studies,[180] where it was found that testing conditions dominate measurement variations much more as compared to probe droplet sizes. These considerations were incorporated into subsequent wettability analysis.

To assess the hydro- and oleo- phobicity of these nanotextures, CAHs of water and hexadecane were measured according to Choi et al.[549], Zhao et al.[13] and Law et al.[654] Figure 8.2c,d shows the ACAs and RCAs obtained by the drop expansion/contraction (drop-in drop-out, DIDO) method.[549,654] The CAH of hexadecane decreases from 37° of the bare substrate to 17.7° of the thickest nanotextures (120 s). Superamphiphobic performance is in line with recent studies[13] based on lithographically-textured superamphiphobic surfaces with hexadecane SAs smaller than 6° and CAHs below 30°. Notably, even the thinnest nanotextures obtained here with an aerosol deposition time of 15 s has a CAH of 29.9° with hexadecane, indicative of a superoleophobic state.

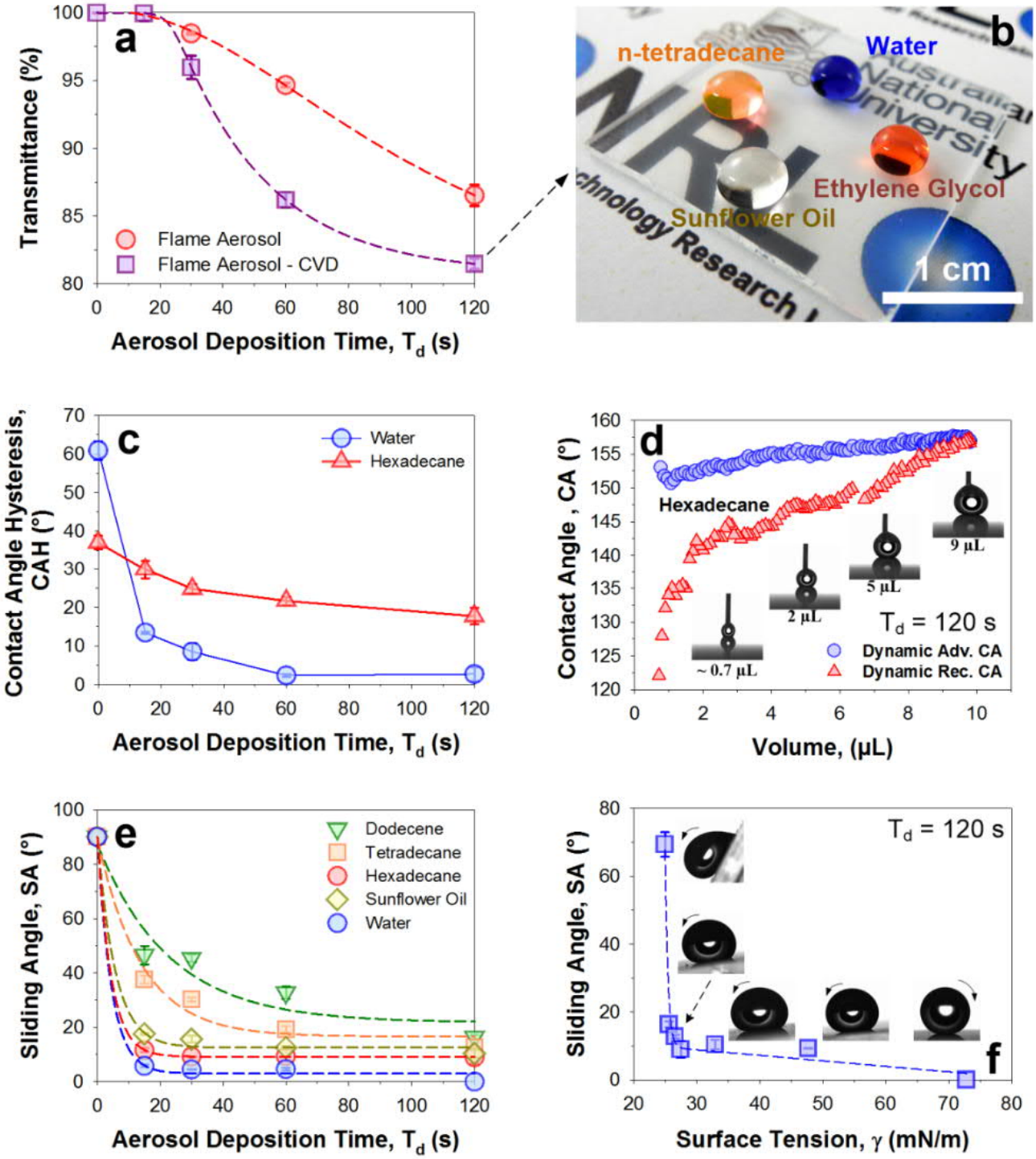

Figure 8.2. Transparency and wetting properties of self-assembled nanotextures. a) UV-vis transmittance profile of superoleophobic textures at 600 nm, reaching up to 99.97% at a deposition time of 15 s. The optical transmittance through the glass substrate has been subtracted. b) Optical image of the most superoleophobic textures on soda lime glass with several probe oils. c) CAH for water (72 mN/m) and hexadecane (27.47 mN/m) as a function of the aerosol deposition time. d) ACAs and RCAs for hexadecane on a nanotextured surface with an aerosol deposition time of 120s. e) SAs of water (72.8mN/m), sunflower oil (32.9 mN/m), hexadecane (27.47 mN/m), tetradecane (26.56 mN/m) and dodecene (25.6 mN/m) as a function of the aerosol deposition time. f) SAs on the 120 s aerosol deposited nanotextures as a function of probe liquid's surface tension.

Notably, the 99.97% transparent SiO_2 nanotextures, self-assembled within 15 s, gave rise to a super-hydrophobic and -oleophobic surface with CAs above 160° for oils down to a surface tension (γ) of 26.56 mN/m (Figure 8.3). As of the time of writing, the combined superdewetting-optical transmittance performance was unprecedented. While providing only minimal improvements in static CAs, increasing the aerosol deposition time significantly decreased the SAs for liquids having surface tensions below 40 mN/m. This is significant as low SAs facilitate improved self-cleaning and removal of small oil droplets. For example, the SAs for hexadecane (27.47 mN/m) and tetradecane (26.56 mN/m) decreased from 11.6° and 37.5° to 8.9° and 12.7°, respectively, with increasing aerosol deposition time from 15 s to 120 s. The 7 µm-thick nanotextures preserved SAs of 10-20° with fluids down to surface tensions of 25.6 mN/m (Figure 8.2e, dodecene). However, below a critical surface tension (γ_{crit}) of 25 mN/m (Figure 8.2f), SAs rose sharply, reaching ca. 70° for cyclohexane (24.95 mN/m).

The stronger superoleophobicity of the thicker nanotextures is attributed to the aerosol self-assembly kinetics and the resulting re-entrant particle-to-particle angles. While such fractal nanotextures cannot be directly correlated to a lithographically developed inverse trapezoid, the equivalent angle of re-entrancy (α_{eq}) can be estimated[153,159,160] from the following equation:

$$cos\theta < \frac{2cos\varphi}{1+cos[\theta_{adv}-\varphi]} \tag{8.1}$$

where θ and θ_{adv} are the Young's CA and ACA, respectively, on a flat untextured surface with the same composition as the textured surfaces; φ is the angle of the inverse trapezoidal side with the horizontal plane, which is complementary to the re-entrant angle (α). Computation of φ, and thus α is obtained from the critical lower surface tension for droplet pinning.[159] Equation 8.1 is independent of the pitch-to-pitch distance and valid only for a Cassie-Baxter wetting state, where sagging heights are smaller than feature height.[159] Here, before the critical surface tension was reached, fluids interacting with super-oleophobic (-amphiphobic) surfaces exhibited freely rolling behaviors. This is indicative of a Cassie-Baxter state (Figure 8.3), satisfying conditions for utilizing Equation 8.1.

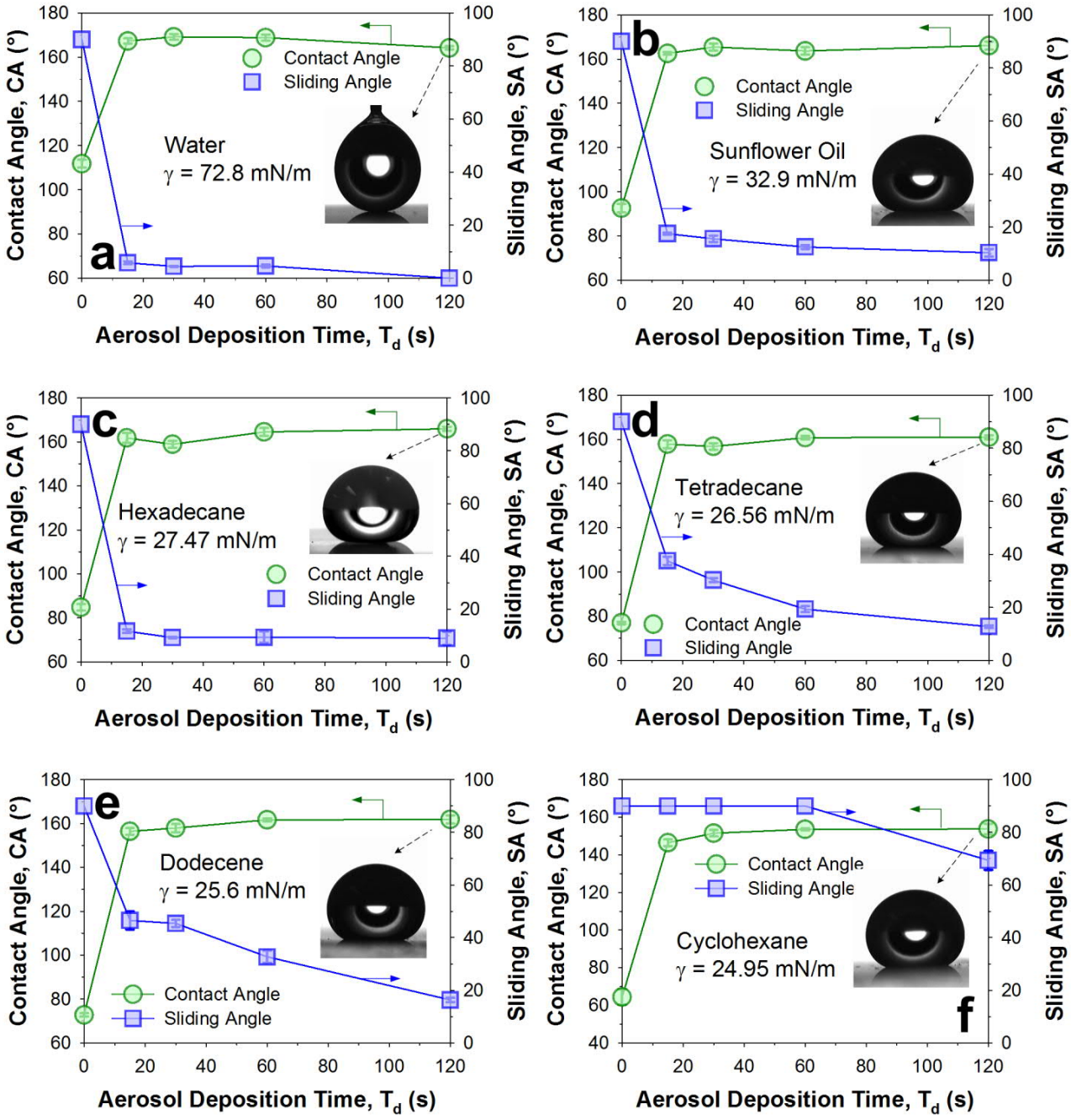

Figure 8.3. Wetting dynamics vs. surface tension. Static CAs and SAs of a) water (72.8 mN/m), b) sunflower oil (32.9 mN/m), c) hexadecane (27.47 mN/m), d) tetradecane (26.56 mN/m), e) dodecene (25.6 mN/m) and f) cyclohexane (24.95 mN/m) as a function of the nanotexture's deposition time.

More importantly, CAs for superoleophobic textures typically depend heavily on re-entrant angles of surface profiles,[13,159] and only slightly from pitch distances or surface area density. In contrast, the CAH is strongly influenced by the surface area density.[13,159] However, if the solid area fraction is decreased beyond a certain value, *e.g.* 0.04-0.07,[13] its influence on both CAs and CAH becomes very small (< 3º and < 9º respectively). Such deviations are comparable to batch to batch variations

across different measurements.[13] Here, for these aerosol self-assembled surface textures, the slice packing density (or solid fraction) of the top layers/surfaces rapidly approaches a value of 0.01, as previously discussed.[78] As a result, the pitch distance/surface area density becomes minor factors while the effect of re-entrancy is expected to dominate the wetting behaviors. Here, the critical surface tension is estimated at 25 mN/m for the 7 µm-thick textures (Figure 8.2f), and thus reasonably close to that belonging to cyclohexane (Figure 8.3a-f). From Equation 8.1, this results in an equivalent trapezoidal re-entrant angle (α_{eq}) of 25.3°. The wetting dynamics of oil droplets on the 7 µm thick nanotextures were assessed with a range of test fluids having surface tensions from 72 mN/m down to 17 mN/m (Figure 8.4a-c,e).

The rebounding dynamics were excellent, demonstrating a lower limit of 28 mN/m with toluene (Figure 8.4c), where clean rebounding and departure of impacting droplets striking the surface at 0.6 m/s was still observed. No satellite droplets were noted within these limits, indicating excellent interfacial stability. Given sufficiently small millimeter-sized droplets[655] and capillary numbers, $\eta V/\gamma$ (V as impact velocity, η as liquid viscosity),[178,655] impacting droplets are known to behave like harmonic springs. The balance of inertia and capillarity was computed,[178] providing a prediction for the measured contact time (t), known as the inertial capillary timescale (τ).

$$\tau = \sqrt{\frac{\rho R^3}{\gamma}} \tag{8.2}$$

where R is the drop radius, ρ is the density and γ is the surface tension of the probe liquid.

Here, tabulated values of t and τ were well-correlated (Figure 8.4d), approaching the physical limits of bouncing superoleophobicity.[18,178,655] The predicted physical limits are highlighted by Richard & Quere[178], suggesting that tau (τ) is the minimum possible contact time, t, for a drop of radius (R), density (ρ), and surface tension (γ).[178] In this limiting case, t and τ are the same and represented by a line through the origin with a gradient of 1.

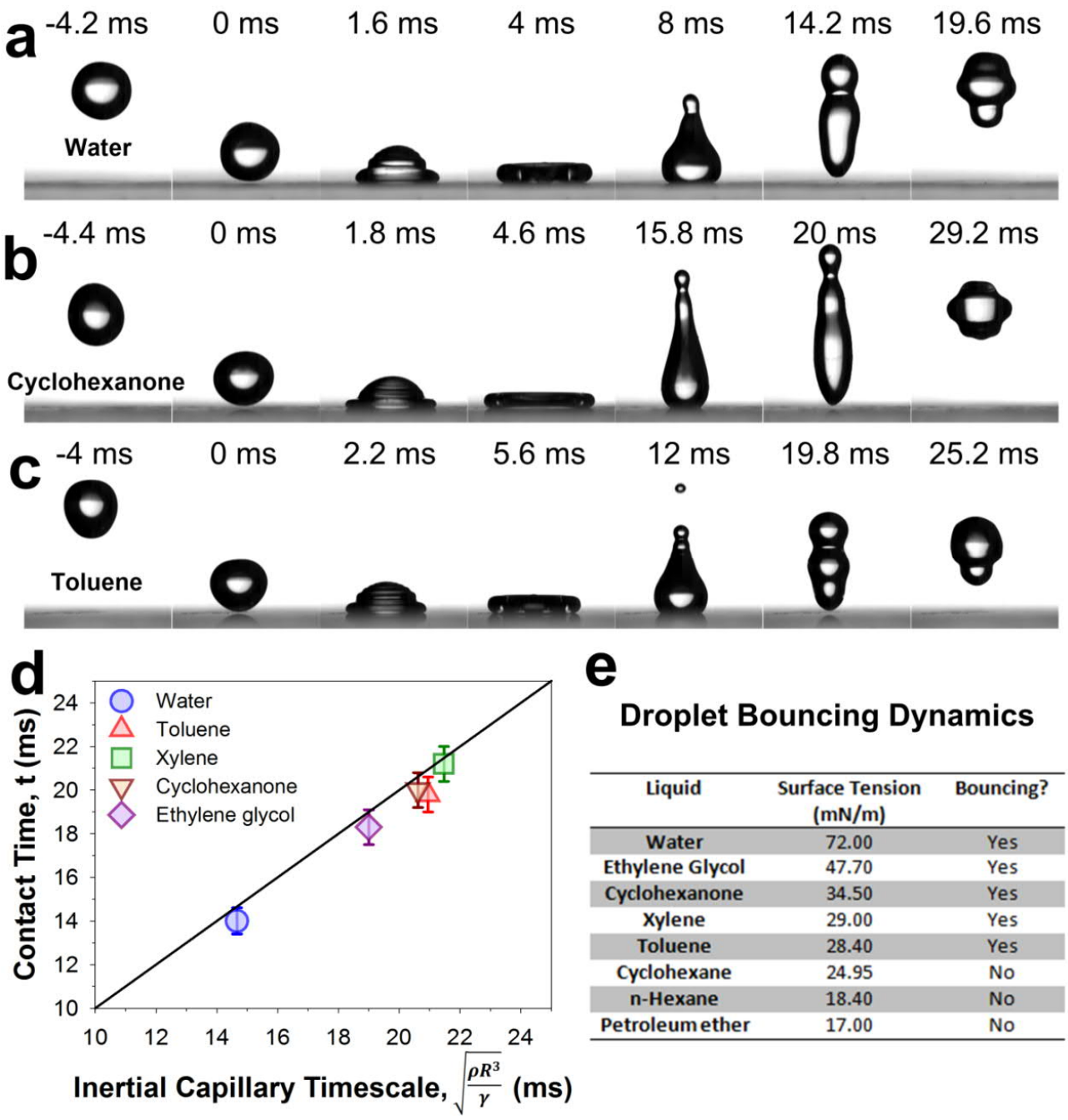

Liquid	Surface Tension (mN/m)	Bouncing?
Water	72.00	Yes
Ethylene Glycol	47.70	Yes
Cyclohexanone	34.50	Yes
Xylene	29.00	Yes
Toluene	28.40	Yes
Cyclohexane	24.95	No
n-Hexane	18.40	No
Petroleum ether	17.00	No

Figure 8.4. Low surface tension droplet bouncing dynamics. (a-c) Droplet impact dynamics with selected snapshots captured by a high-speed camera showing a drop (R ≈ 2.4 mm) of a) water, b) cyclohexanone and c) toluene, impacting on the superoleophobic surface at ca. 0.6 m/s d) Measured contact time t shows good agreement with the inertial capillary timescale (τ), against the theoretical limit[225] of t = τ (solid line). e) Droplet impact testing of different liquids.

A mathematical framework was developed to understand the formation of angles of re-entrancy in these fractal nanotextures. The self-assembly mechanisms of such ultra-fine nanoparticle aerosols have been recently modelled in our previous work[78]. These models indicate the formation of individual surface-bond agglomerates constituted by the depositing nanoparticles. The morphologies

of these agglomerates are highly reproducible and can be easily predicted by the scaled ratio between orthogonal/advective velocity and diffusivity, namely the Péclet number (Pe).[656] Figure 8.5a shows 3D visualizations of representative nanotextures formed in the diffusion and ballistic regimes, with a Pe of 10 and 10^{-3}, respectively. The full-scale simulations are reported in Figure S8.12, providing equivalent cross-sectional profiles to those shown in Figure 8.5a. Quantitative description of these fractal nanotextures is challenging as the surface agglomerates are not rotationally symmetric while the effective angle of re-entrancy encountered by the advancing contact line depends largely on specific localities.

To provide a qualitative description of the key re-entrant properties belonging to such nanotextures, we have computed the maximal slice-averaged particle-to-particle re-entrant angle ($\alpha_{p\text{-}p\_s\text{-}max}$) for all circumferential particle pairs located on the perimeter of the simulated agglomerates. We first computed the average re-entrant angle of each slice ($\alpha_{q,ave}$) by averaging the particle-to-particle re-entrant angles (α_q) of all particles located in the perimeter of the agglomerate (Figure S8.11). We then determined the maximum $\alpha_{p\text{-}p\_s\text{-}max}$ across the agglomerates, and repeated this computation over triplicated simulations. Notably, self-assembly in the diffusion regime results in visibly larger $\alpha_{p\text{-}p\_s\text{-}max}$ than that achieved in ballistic deposition regimes (Figure 8.5a).

Figure 8.5b shows a contour plot of the $\alpha_{p\text{-}p\_s\text{-}max}$ as a function of the Péclet number and the dimensionless film thickness (z/d_p). In the diffusion regime (*e.g.* Pe = 10^{-1}), the $\alpha_{p\text{-}p\_s\text{-}max}$ increased from 10° to 29° (Figure 8.5b) with increasing relative film thicknesses, from 30 to 120 d_p. The effect of film thickness is attributed to the confinement effects by side agglomerates. As previously shown,[78] at low film thicknesses, the agglomerate number (and film) density is the highest and this value rapidly drops with increasing film thickness. A high density of surrounding agglomerates shields other agglomerates from side particles coming at lower impact angles. As a result, the average re-entrant angle is decreased. Once a main agglomerate is formed, the other agglomerates do not grow anymore. The main agglomerate starts behaving like an antenna, collecting almost all incoming

particles. From a stochastic perspective, this results in lower impact angles at the agglomerates' edges and thus higher angles of re-entrancy.

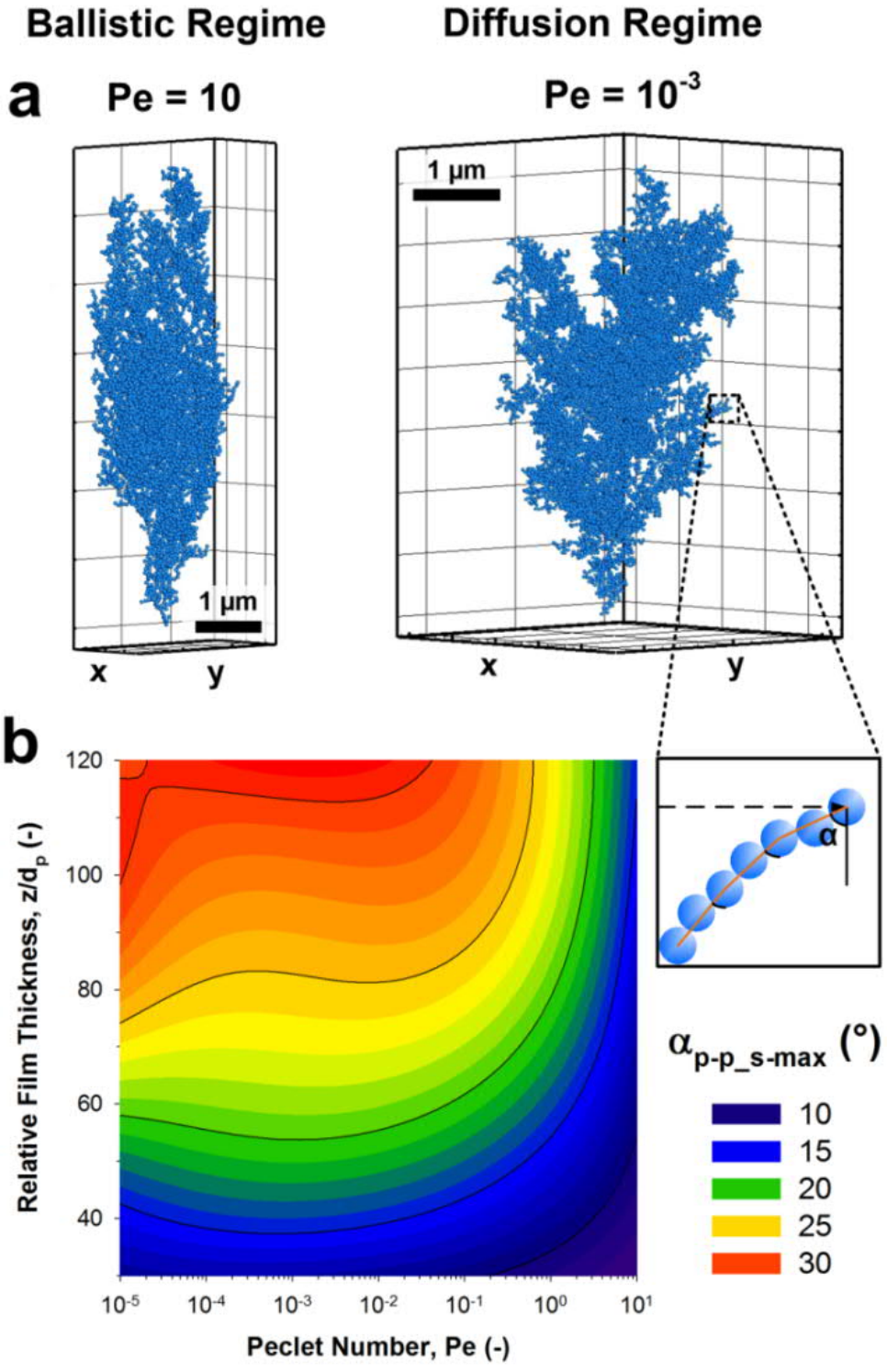

Figure 8.5. Mathematical model of the nanotexturing self-assembly process and computation of the maximal slice-averaged particle-to-particle re-entrant angle ($\alpha_{p\text{-}p\_s\text{-}max}$). a) 3D reconstruction of nanotextures assembled by aerosol deposition in the ballistic regime (Pe = 10) and diffusion regime (Pe =10^{-3}) with a thickness of 120 particle diameters. Single agglomerates were extracted from the simulated domains for the ease of visualization. b) Contour plot of the re-entrant angles ($\alpha_{p\text{-}p\_s\text{-}max}$) over the key process conditions, namely the Péclet number (Pe) and relative film thicknesses (z/d_p).

In the ballistic regime (*e.g.* Pe = 10), the $\alpha_{p\text{-}p\_s\text{-}max}$ reaches a maximum of 15° at 120 d_p, which is 50% smaller than that in the diffusion regime. This is attributed to the average angle of impact by the incoming particles. In previous models developed[78] on flame aerosol derived nanoparticle self-assembly, the average angle of impact decreases from 90° (orthogonal) for the ballistic regime to 45° (diagonal) for the diffusion regime. As a result, in the ballistic regimes, particle-to-particle re-entrancy tends to be smaller than those found in the diffusion regime, where depositing particles follow a diagonal trajectory. This effect is also qualitatively discernible in the 3D reconstructions of the self-assembled nanotextures in the ballistic and diffusion regimes (Figure 8.5a). Increasing the angle of re-entrancy above the 30° diffusion-limit may be achieved in the future by inversing thermophoretic flux outwards from the target substrate surface, thus further decreasing the angle of impact of the depositing particles.

Major challenges faced by state-of-the-art super-oleophobic, -amphiphobic and even -omniphobic nanotexturing approaches include substrate compatibility,[65,446] surface coloration,[57] poor optical clarity,[501] scalability,[66,74] and excessive processing temperatures[14]. Here, we demonstrate the potential of our technique in overcoming many of these issues. The omnidirectional self-assembly demonstrated here can be facilely applied to non-line-of-sight geometries and on many different material substrates. Figure 8.6a demonstrates the rapid synthesis of superamphiphoic coatings even on flexible plastic films. Notably, the super-oleophobicity (-amphiphobicity) is retained even after torsion and flex, to a radius of curvature of 1.25 cm (Figure 8.6a). This is attributed to the flexible nanotextures' morphologies, which do not suffer from vastly changing pitch distances under mild flex or strain, unlike conventional nano-structures.[90,657]

The stability was also assessed by sequential droplet impact tests on the flexed coatings, with the release of over 600 drops of sunflower oil (8.3 µL each) at a height of 1 cm. The continuous droplet impact had negligible impact on their wetting properties and functionality (Figure 8.6b). Immersion up to a tested hydrostatic height of ca. 1 cm of oil also resulted in negligible functionality variations. These nanotextures are, however, not stable against direct mechanical abrasion. While they may be

immediately implemented to produce stable super-oleophobic (-amphiphobic) tubes and needles, more work is required to synthesize abrasion resistant surfaces. On this note, we have recently demonstrated the pre-treatment of surfaces with sprayable interpenetrated polymer networks as binders for superdewetting interfaces. To this end, we showcased the drastically increased mechanical stability of fragile nanoparticle-based superhydrophobic textures.[91] The binder-based technique represents a potential avenue for the future development of mechanically robust super-oleophobic (-amphiphobic) coatings.

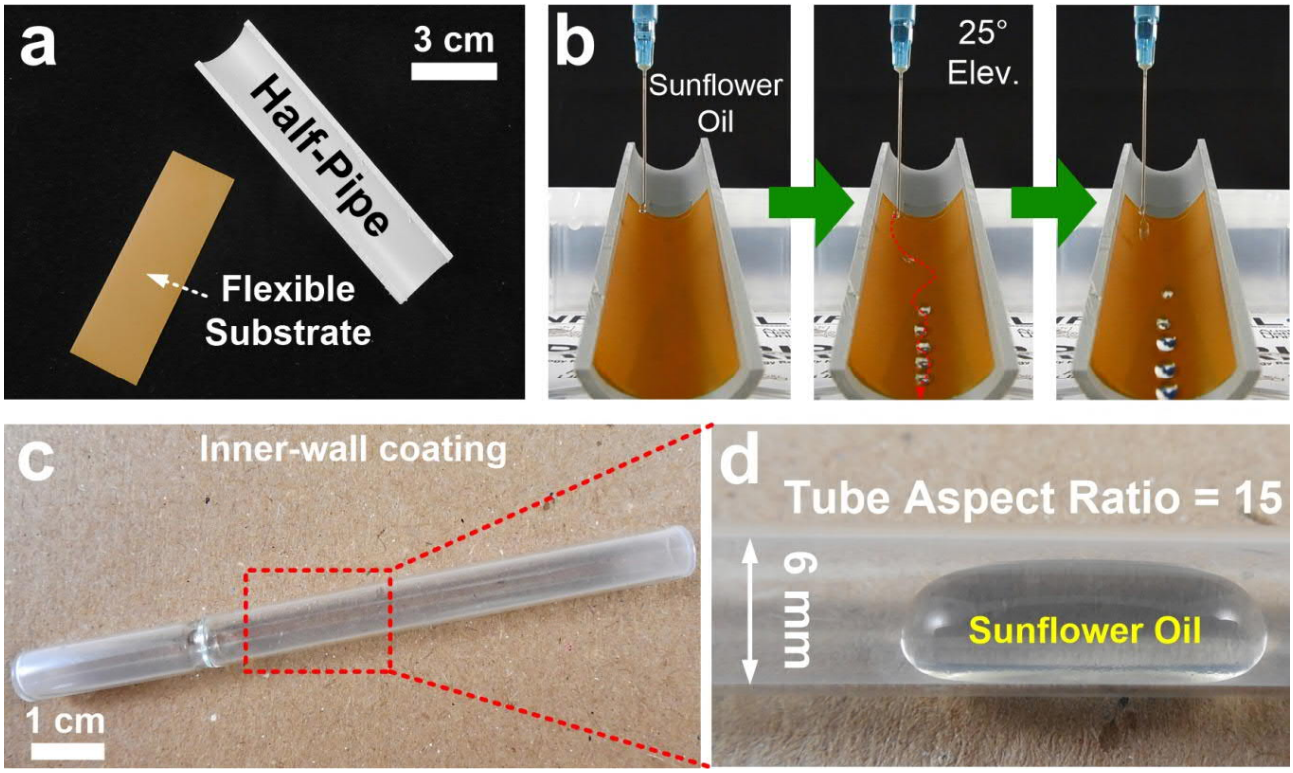

Figure 8.6. Applications from omnidirectional nanotexturing. (a-d) Nanotexturing of exemplary materials and geometries including flexible (a-b) plastic films (Kapton®) preserving functionality upon torsion and bending and (c-d) inner walls of high aspect ratio glass tubes with a diameter of 6 mm and a length of 90 mm. Sunflower oil droplets introduced into tubes d) show a balled-up Cassie-Baxter state.

These super-oleophobic (-amphiphobic) textures were applied to a variety of uneven profiles. This included the inner-side of a bowl-shaped crucible (Figure S8.8), as well as the inner walls of a closed-end cylinder (Figure S8.9) and a much thinner glass tube (Figure 8.6c) with a length to diameter aspect ratio of 15. Successful nanotexturing of the latter is indicated by the balling up of introduced oil in a Cassie-Baxter state (Figure 8.6d). Notably, inner walls of closed-end tubes / crucibles were

also successfully textured (Figure S8.9a-b), showcasing the viability of this self-assembly approach for a limitless variety of surface geometries. Most importantly, they hold immense potential for coating high aspect ratio enclosures, contrasting conventional wet-spray-coating systems and lithography. The homogeneity of coatings within high aspect ratio tube geometries was assessed along the longitudinal axis of 9 cm long tubes with an inner diameter of 6 mm. Figure S8.14 shows optical images of 3 oil droplets at distances of 1.5, 6 and 8 cm from the tube inlet. Optically, the coated tube can hardly be differentiated from the bare one (Figure S8.14a). With respect to superoleophobicity, the dodecene oil droplet remained in a beaded state and slides continuously from the start to the end of the tube and back. The nanotextured crucible preserved its functionality even after filling it with 5-10 mLs of oil (Figure S8.8a), enabling perfectly clean decantation (Figure S8.8b-c). With respect to the optimal aerosol deposition conditions, we have previously shown that; as long as the surface temperature is sufficiently cold to avoid strong coalescence of the depositing particles, an identical morphology can be facilely achieved by aerosol deposition in the diffusion regime.[77] However, considering an identical precursor formulation, deposition rates increase significantly with decreasing deposition distance (*e.g.* 20 cm to 10 cm) as the aerosol becomes much more concentrated. As a result, a significantly smaller deposition time should be utilized to obtain superior optical and dewetting performance as that achieved at higher deposition distances (*e.g.* 20 cm). Alternatively, deposition distance can simply be increased (*e.g.* 20 cm to 40 cm), so as to achieve a much more dilute but homogenous nanoparticle aerosol, thus enhancing scalability and conformity within complex geometries.[77] Overall, this gas-phase bottom-up approach demonstrates excellent versatility, tunability and scalability.

8.3. Conclusions

We have demonstrated the synthesis of transparent and flexible superamphiphobic surfaces by large-scale omnidirectional self-assembly of nanoparticle aerosols. This approach enables the rapid and low-cost synthesis of highly dewetting nanotextures on an extensive set of materials and geometries, which were not compatible with existing approaches. These superamphiphobic coatings also achieved unprecedentedly high transparency, at up to 99.97% transmittance. Our model and experiments indicate that the enhancement of superoleophobicity is achieved simply by increasing texture thicknesses. To this end, optimal coatings developed were superdewettable for many oils and low surface tension organic liquids, ranging down to 25 mN/m. Our model suggests that this is attributed to an increasing particle-to-particle angle that, in the diffusion regime, converges toward a maximum re-entrant angle of ca. 30°. The equivalent angle of re-entrancy was also experimentally determined based on an ideal inverse trapezdoidal profile,[159] achieving a value of 25.3°. We showcase the potential of this approach by the rapid synthesis of re-entrant nanotextures on flexible substrates, close-ended tubes, and several uneven geometries. These findings provide an improved understanding for the aerosol engineering of ultra-transparent superamphiphobic nanotextures, on a vast family of previously inapplicable material geometries.

8.4. Experimental Section

Nanotexture Self-Assembly

SiO_2 nano-layers were produced by flame spray pyrolysis of solutions containing hexamethyldisiloxane. Combustible liquid solutions were prepared by dissolving hexamethyldisiloxane (Sigma-Aldrich, purity ≥ 98.5%) in toluene (Sigma-Aldrich, 99.8%), to reach a total Si-atom concentration of 0.2 mol L^{-1}. This solution was fed at 5 ml min^{-1} rate through a custom build nozzle, and atomized with an oxygen flow ($O_{2\text{-}\Delta P}$ = 5 L min^{-1}, COREGAS grade 2.5) at a set pressure drop (ΔP = 2 bar). The resulting spray was ignited with a surrounding annular set of premixed methane/oxygen flame ($CH_{4\text{-flamlet}}$ = 0.5 L min^{-1}, $O_{2\text{-flamlet}}$ = 0.8 L min^{-1}, COREGAS grade 4.5). The glass slides were cleaned by sonication for 30 min in ethanol before deposition. The clean substrates were then mounted at a height above burner (HAB) of 19 cm on a copper substrate holder with water cooling for SiO_2 deposition (Figure S8.2a). The tailored aerosol of highly transparent nanoparticles (*e.g.* SiO_2)[30] was then synthesized by a highly scalable flame aerosol technique.

This aerosol was then directed to the target object without need of further refining. Within the boundary layer surrounding the object surface, aerosol convectional velocities decrease rapidly, eventually coming to a standstill. In non-turbulent conditions the thickness of the boundary layer is ca. 10-100 μm.[77] In the diffusion regime, this is a significant length that nanoparticles overcome by thermophoresis and diffusion. Notably, both thermophoretic and diffusive forces results in a net orthogonal displacement toward the surface.

Coating temperature was noted to be between 80-130 °C *via* a calibrated infrared thermometer. Further variation to the deposition protocol (HAB) could enable even lower coating temperatures. The deposition time was 15 s, 30 s, 60 s and 120 s. Samples were stored in ambient laboratory environments (20-25 °C, 40-70% relative humidity) and CVD was conducted within 24 h of synthesis.

Surface Silanization

A home-built (Figure S8.2b) CVD reactor (150 mL) was used to chemically functionalize the superamphiphilic FSP assembled SiO_2, so as to confer superoleophobicity. FSP-coated substrates were first placed in on an elevated stage before the deposition of 100 µL of trichloro(1H,1H,2H,2H-perfluorooctyl)silane (Sigma-Aldrich, 97%) below it in troughs. Flaps were constructed to facilitate even deposition. Dry nitrogen was then used to purge the CVD reactor for a period of 5 min before and after silane deposition and the entire set-up was doubly-sealed with silicone plugs and parafilm. The reactor was then placed in an air-tight, desiccated chamber. To increase the vapor pressure of the silane, the entire assembly was heated at 40 °C for 3 h. Thereafter, the substrates were retrieved and placed in a desiccator with applied vacuum for 1 h to remove unreacted silane residue. The entire CVD reactor was then flushed with water and ethanol to remove unreacted silane, followed by the disposal of one-use components (stage and troughs). The reactor walls were then flushed with acetone and scrubbed before being dried and re-used. Seals on the reactor were checked before each new process.

Wetting Analysis

Super-hydrophobicity and -oleophobicity was assessed through the measurement of static CAs, by placing and averaging 4 drops of water and respective low surface tension fluids (7 µL) on 2 cross-batch sample surfaces using the sessile drop method. SAs were assessed by the deposition of droplets (7 µL) on these surfaces followed by tilting the stage (custom-built tilting goniometer) until the droplet starts sliding off. The range of surface tensions used in the tests is as follows, water (72.8 mN/m), ethylene glycol (47.7 mN/m), sunflower oil (32.9 mN/m), n-tetradecane (26.56 mN/m), dodecene (25.6 mN/m) and cyclohexane (24.95 mN/m). CAs and SAs for sunflower oil were tested with droplets of 8-10 µL. The CAH for water and hexadecane were measured *via* the drop expansion-contraction technique[13,549,654] using a super-oleophobic (-amphiphobic) needle produced by the presented nanoparticle aerosol deposition - CVD approach. These measurements revealed average CAH between 2 to 9 µL. 3 cross-batch readings were taken. Dynamic and static images were recorded using a KSV CAM200 contact angle goniometer (Finland) with a heliopan ES43 camera (Japan). The

CA, SA and CAH were computed by a commercially available (CAM2008) program. Data was presented as mean ± standard errors.

Droplet Impact Dynamics

The droplet impact dynamics was evaluated in ambient environment, at room temperature with 60% relative humidity. Fluid drops of ~ 8 µL (corresponding to diameter ~ 2.4 mm) were released from pre-determined heights. The dynamics of drop impingement was recorded by a high-speed camera (Fastcam SA4, Photron) at the frame rate of 5,000 fps with a shutter speed 1/8,000 s.

Surface Analysis

Samples were analyzed *via* Zeiss UltraPlus field emission scanning electron microscopy (FESEM) at 3 kV and a Hitachi H7100FA transmission electron microscope (TEM) at 100 kV. Particle sizes were approximated over 100 counts in ImageJ across 4 images. Prior to examination, SEM specimens were platinum sputter-coated (3 nm) for 2 min at 20 mA. Optimized sample (FA-CVD-120s) was prepared for energy-dispersive X-ray spectroscopy (EDX) was carbon sputter-coated with a layer of 15 nm and analyzed *via* elemental mapping for 200 s (INCA Energy 450 EDXA, Oxford Instruments). Side-profile analyzed samples were platinum-coated and imaged at 3 kV. The UV-vis analysis was conducted using a microplate reader (Tecan 200 PRO, Switzerland) from 300 to 800 nm with 10 scans per cycle under the Absorbance Scan mode. Single-side coated samples on soda-lime glass were used for analysis. Optical losses induced by the soda-lime glass were subtracted, presenting the absolute transmittance through coatings. Optical profiling was also conducted *via* white light interferometer (Veeco, Wyko NT9100, USA), which provided 50x to 500x magnification with a field of view (FOV) of 1x *via* the vertical scanning interferometry (VSI) mode. A magnification of 50x-200x provided macro-view of the surfaces but did not provide nanoscale analytical accuracy. Magnifications 500x provided micro- and nanoscale analysis accuracy, and were broadly used to analyze morphological variations (Figure S8.3). A backscan of 50 µm and length of 25 µm was used

with a modulation of 3% to cover the maximum peak-to-trough heights of hierarchical coatings averaging 3 repeats at 500x respectively.

Computational Simulation

Particle dynamics were modelled for isothermal conditions at 298 K, considering the deposition of one particle at a time. To obtain true random motion before deposition, a particle is initially released into a cell where particle deposition and film growth are not allowed. The particles are released into this drop cell above a domain with a thickness of 140 d_p. Particle deposition occurs in the domain, but not in the drop cell. This means that once the film thickness (the highest deposited particle) reaches the lower boundary of the drop cell, the simulation is interrupted. The number of time steps that this corresponds to varies as a function of the Péclet number and diffusivity (particle size, temperature *etc.*). This approach was previously validated[77,78,171] and has shown that this leads to particle deposition and film growth in the diffusion and ballistic regimes. This simulates and maps the vertical growth of a nanoparticle-agglomerate film from the substrate, up to at least 3.6 µm. Here, particle dynamics simulations of the self-assembly process were performed by numerical solution of the Langevin's equation of motion over 6 orders of magnitude in Péclet number from the ballistic to the diffusion regimes. More details about the model outline are reported elsewhere.[78]

Particle analysis was performed over a range of Péclet numbers (from the ballistic to the diffusion regime), across a range of simulated film thicknesses, with a designated particle size of 30 nm. The total thickness was evaluated up to 3.6 µm and analyzed piece-wise (30-60 nm). This was performed with respect to maximal slice-averaged particle-to-particle re-entrant angle ($\alpha_{p\text{-}p\_s\text{-}max}$) for 2-particle (60 nm thick) segmental slices. Maximum particle-connected edge profiles were determined by these infinitesimal slices (Figure S8.11). All agglomerates (heights of at least 3.6 µm) within a domain size of 4.2 µm by 4.2 µm were isolated, computed and averaged over each re-entrant angle (dependent variable) across infinitesimal slices (Figure S8.11). Computational analysis was checked and re-validated across independently written scripts. Dependent variables were then determined based by

varying 2 independent variables, the relative film thickness, z/d_p and Péclet number, Pe (deposition regime). Contour plots were determined based on a spline-fit on the filtered batch of simulation data.

8.5. Supplementary Information

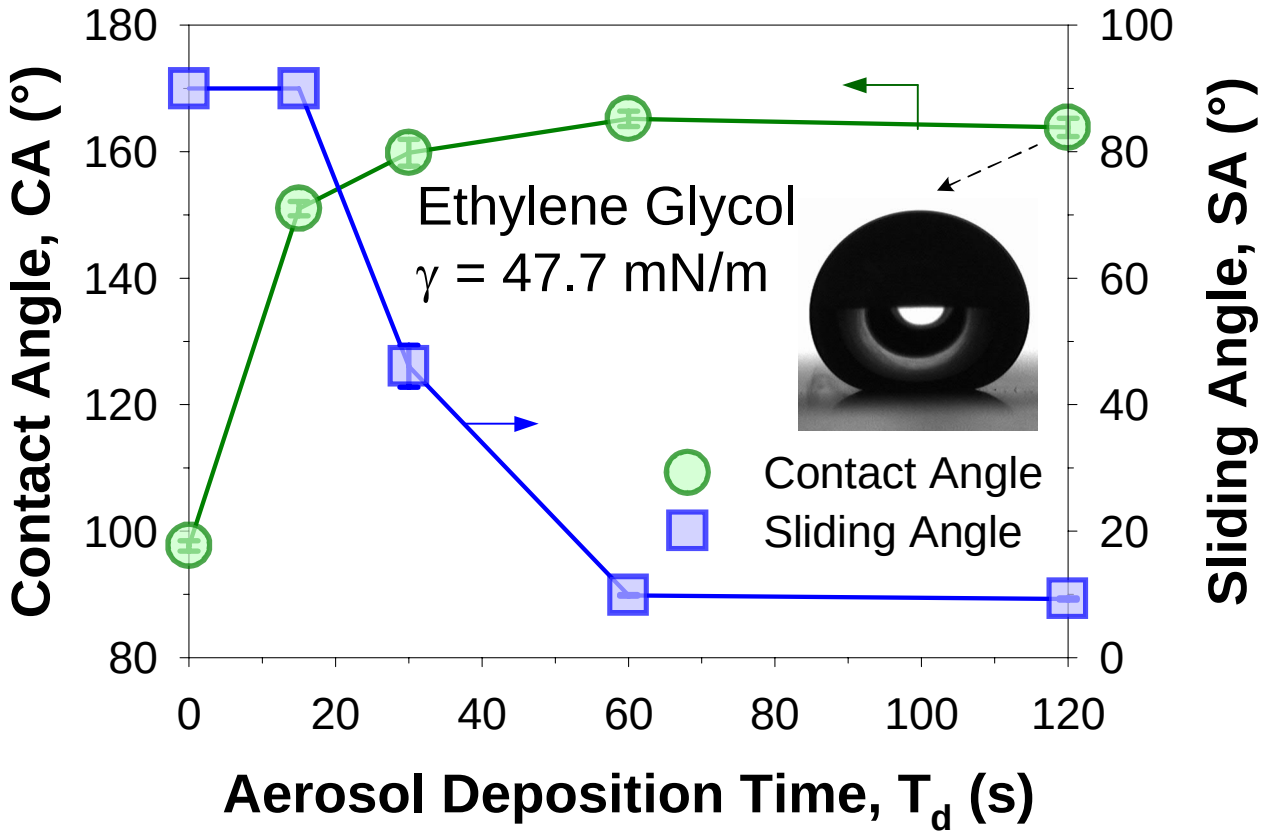

Figure S8.1. CA and SA for a polar fluid (ethylene glycol) with a surface tension of 47.7 mN/m, showing a non-parallel diminished performance.

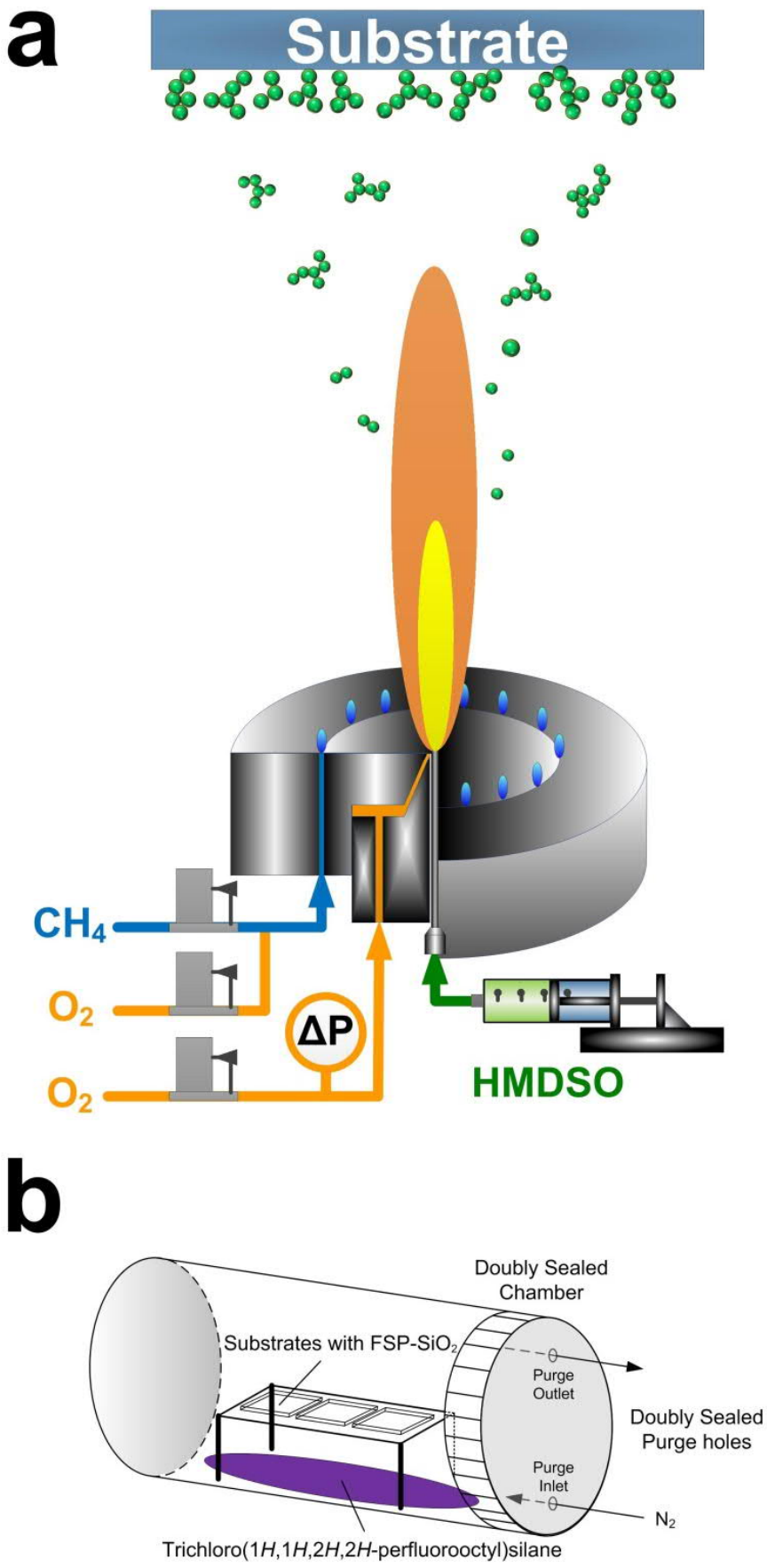

Figure S8.2. Experimental schematics of the facile two-step synthesis process for superoleophobic coatings. a) flame aerosol and b) CVD in an in-house built reactor.

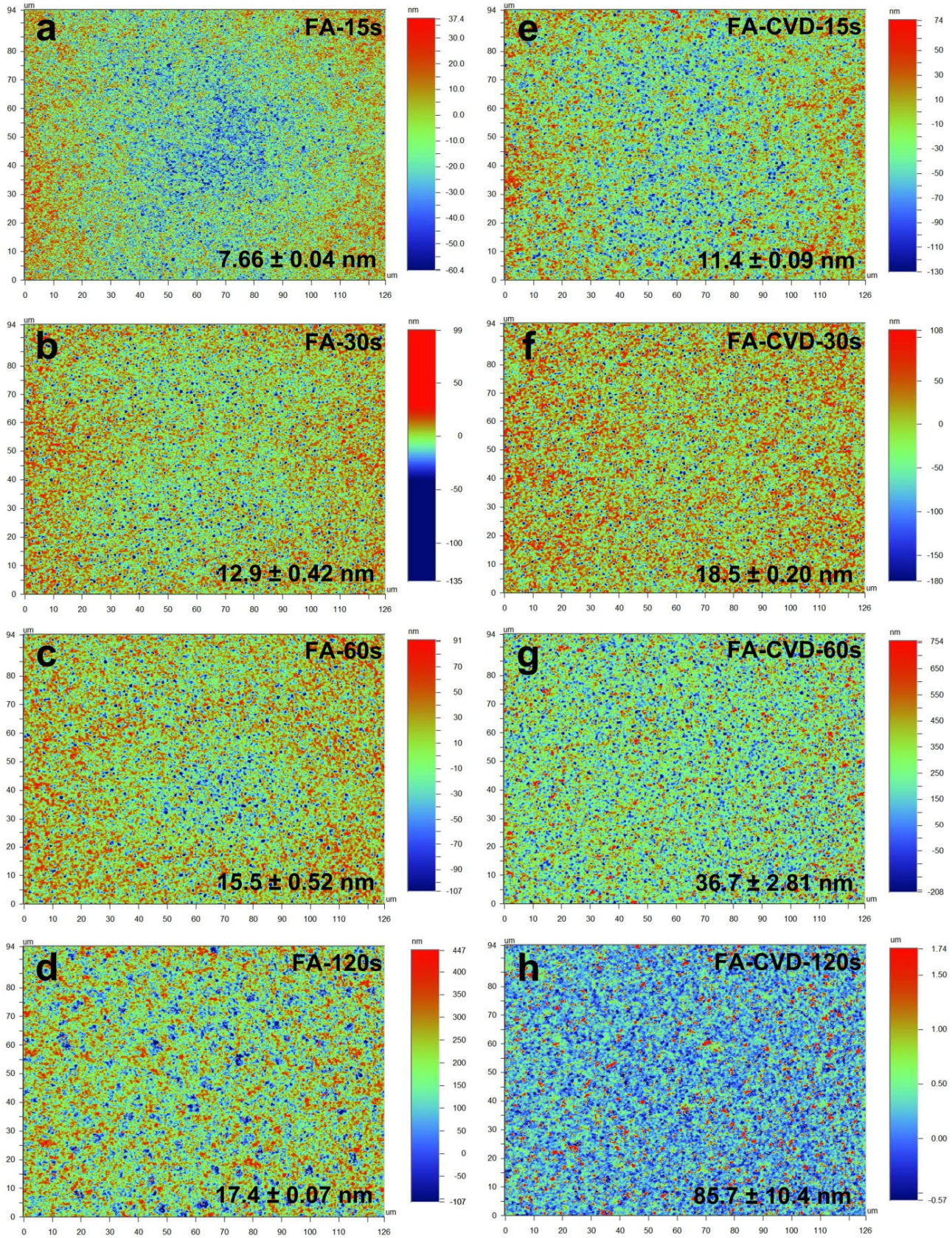

Figure S8.3. Surface roughness analysis (WLI). (a-d) White light interferometry (WLI) before and (e-h) after CVD with (a,e) 15s, (b,f) 30s, (c,g) 60s, (d,h) 120s of flame aerosol controlled deposition durations.

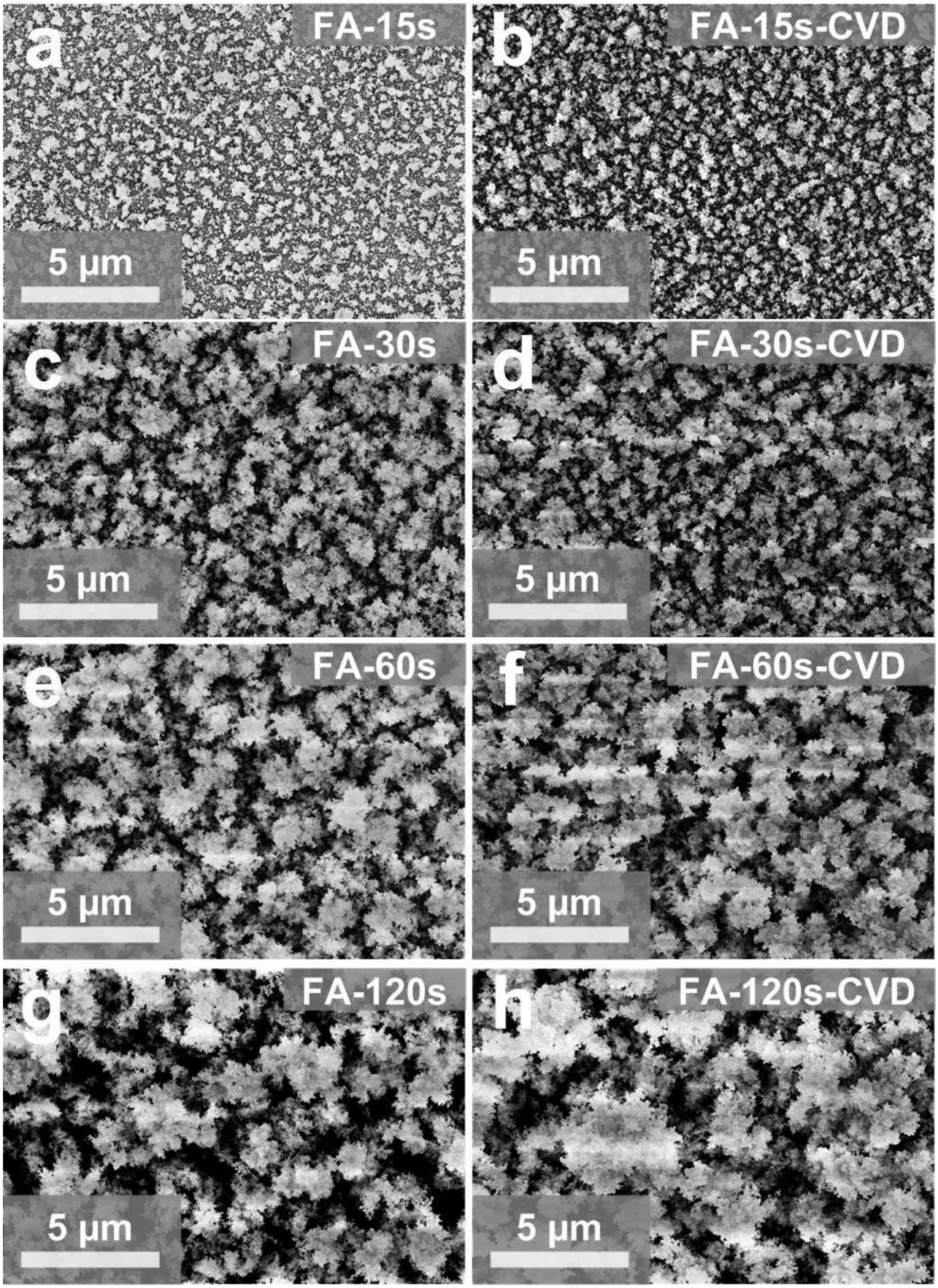

Figure S8.4. Supplementary scanning electron micrographs (SEMs). Top-down profiles of (a,c,e,g) flame-aerosol (FA) and (b,d,f,h) FA-CVD developed samples with increasing time.

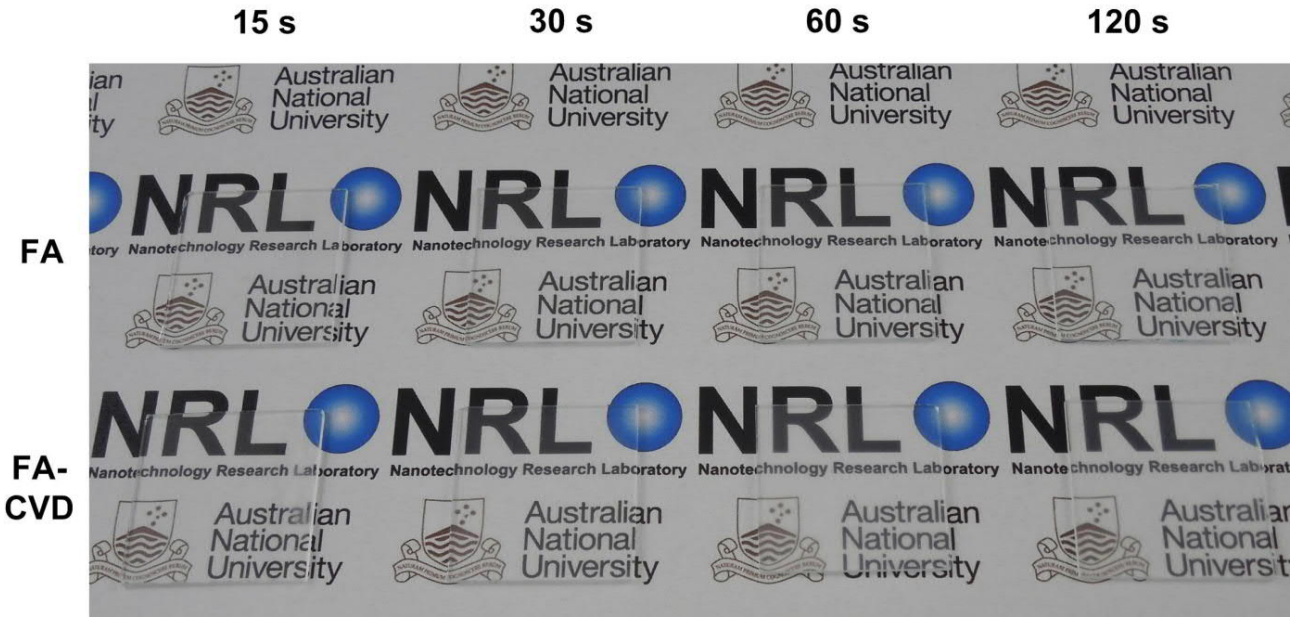

Figure S8.5. Optical images of coatings. Photographic images of (1st row) FA and (2nd row) FA-CVD developed nanoparticulate coatings. Deposition was optimized across (1st column) 15s to (4th column) 120s while preserving > 80% transmittance. NRL logo, copyright A. Tricoli. ANU logo, copyright the Australian National University.

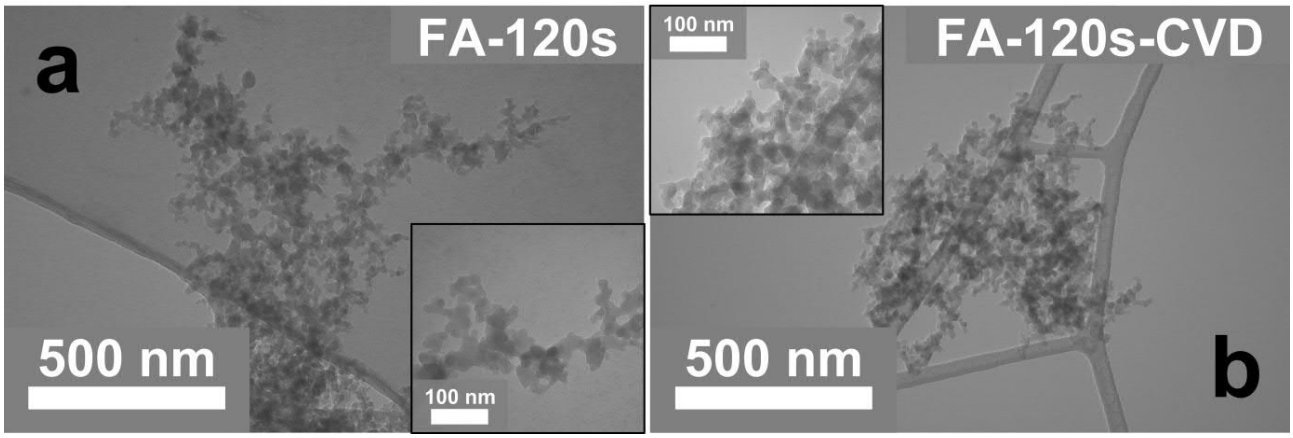

Figure S8.6. Transmission electron micrographs (TEMs) analysis. a) Pre- and b) post-CVD treated re-entrant typed nanoparticles, indicative of minimal size variations. Average particle diameter (d_p), estimated from 100 counts over 3 separate TEM micrographs of FA-120s gave a d_p of 22.1 ± 6.8 nm.

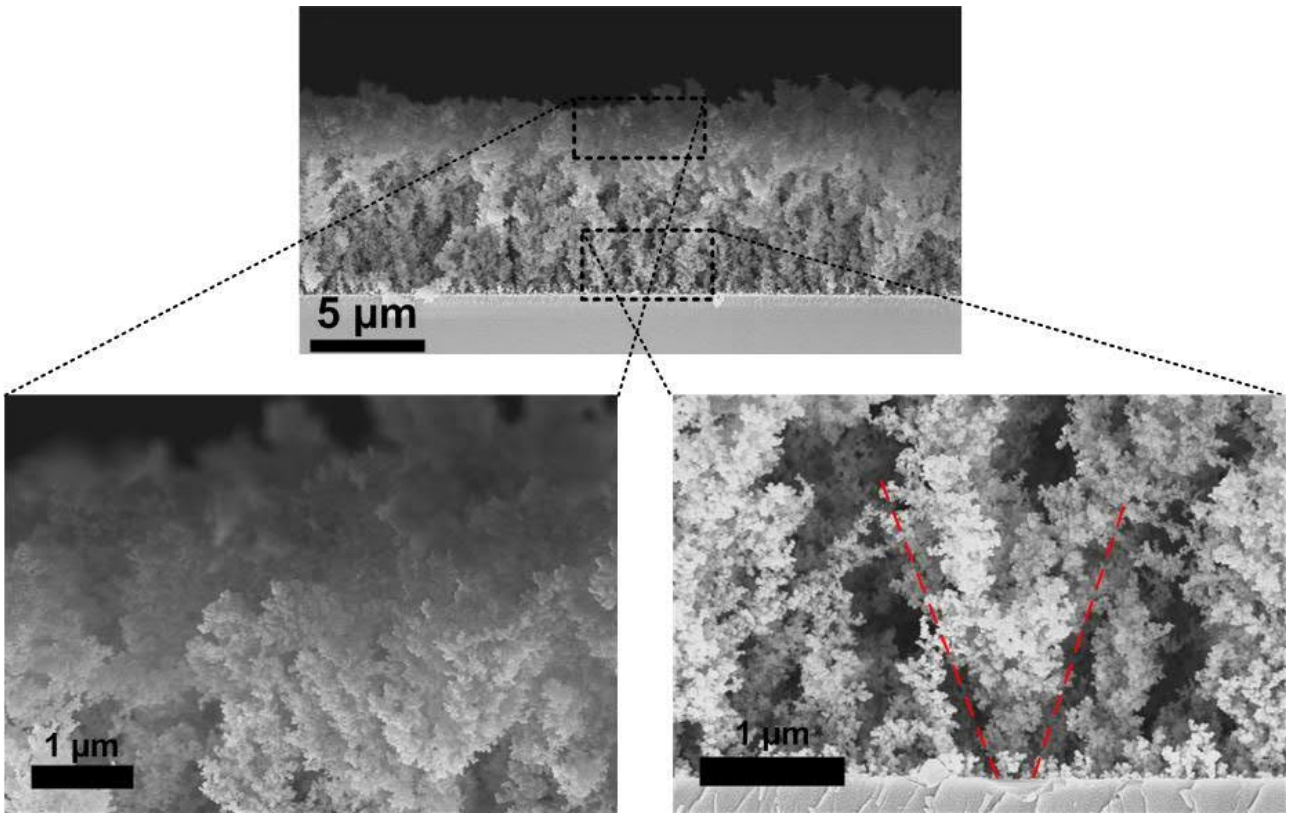

Figure S8.7. Side-profile SEMs of broccoli-like profiles. Reentrant profiles with insets showing the "roots" of the broccoli-like profiles (right) as well as the top-merged "foliage" of the reentrant structure (left).

Figure S8.8. Coated oil-containing-decanting crucible. a) Immersion stability, (b-c) completely clean oil decanting with no remnant droplets.

Figure S8.9. Exemplified coatings. a) Inner walls of a closed cylindrical tube, with a b) moderate aspect ratio (L/D) of 3, showcasing the omni-directional suitability of these super-oleophobic (-amphiphobic) coatings.

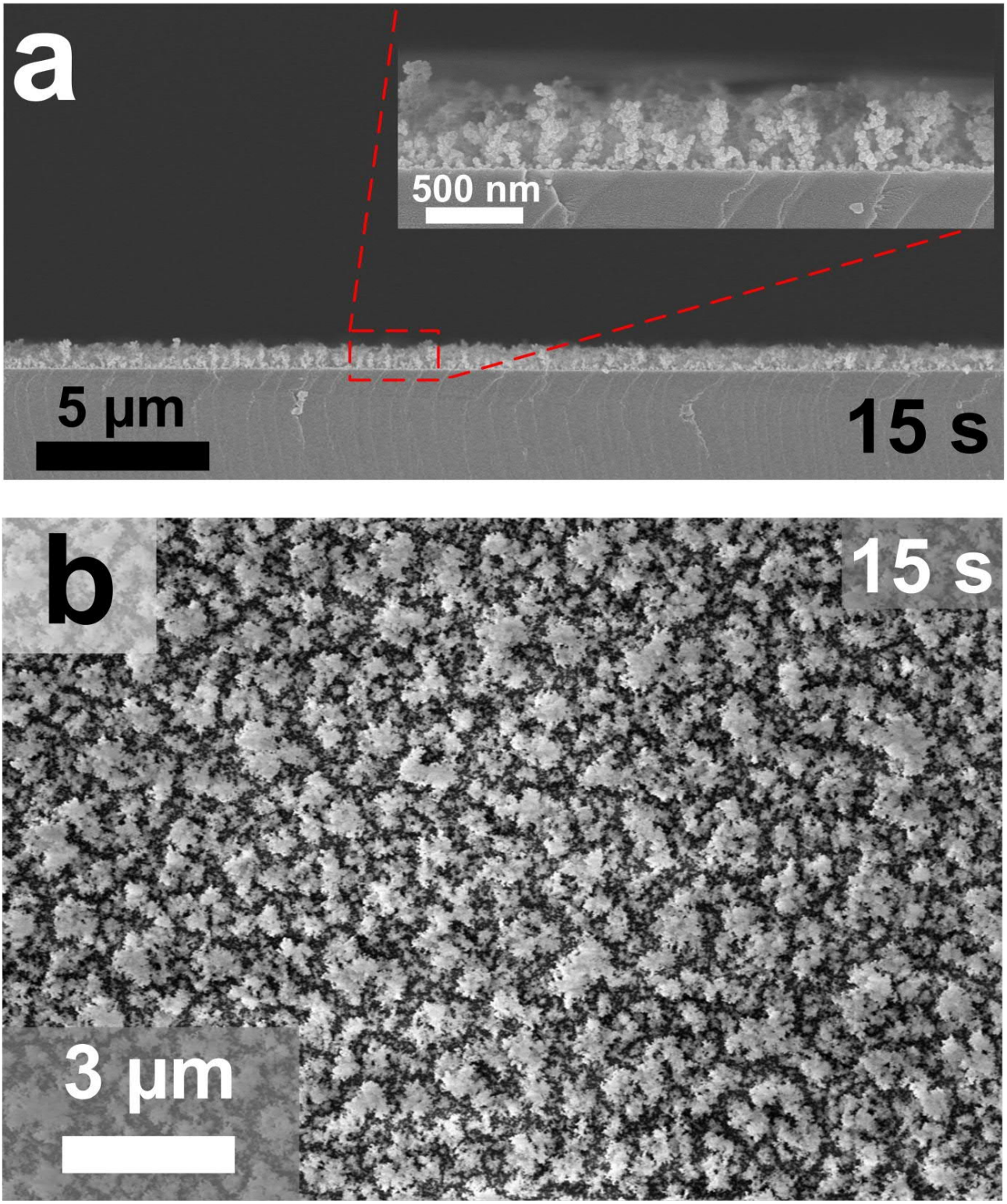

Figure S8.10. Supplementary SEMs (15s). a) Side- and b) Top-down profiles of the FA deposition at 15s, showing highly fractal-like self-similarity of the diffusive deposition process.

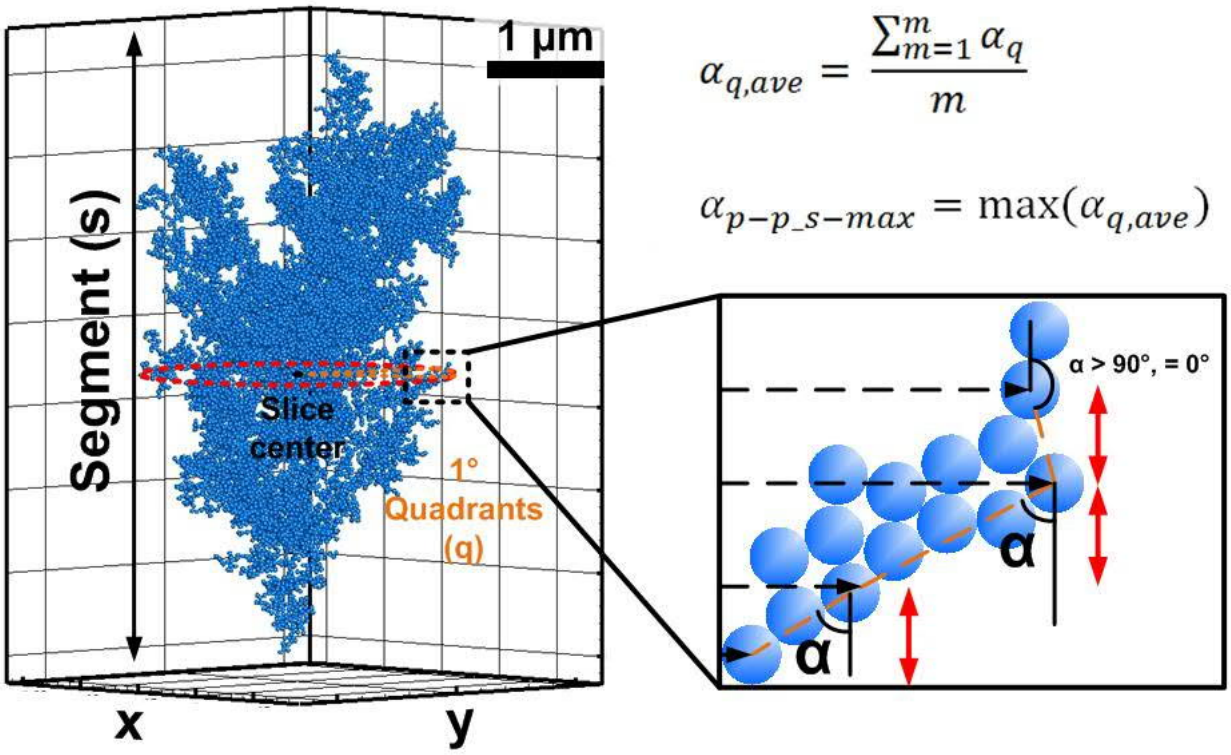

$$\alpha_{q,ave} = \frac{\sum_{m=1}^{m} \alpha_q}{m}$$

$$\alpha_{p-p\_s-max} = \max(\alpha_{q,ave})$$

Figure S8.11. Computation of the maximal slice-averaged particle-to-particle re-entrant angle (α_{p-p_s-max}) from the simulated nanotextures.

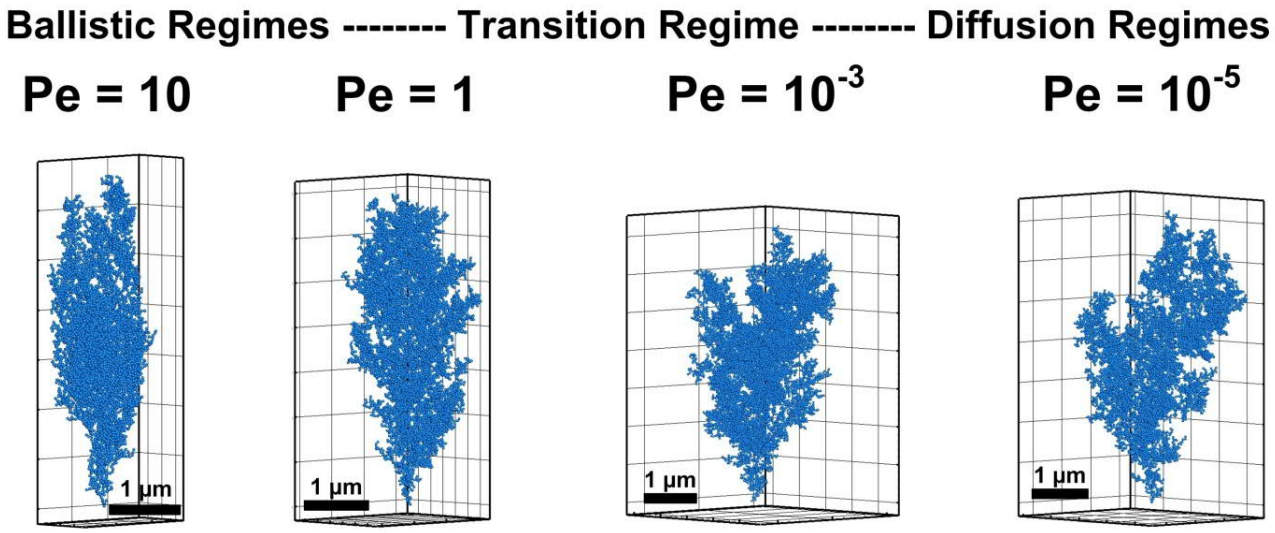

Figure S8.12. Simulated fractal nano-structures. Computationally simulated fractal nano-structures with inverse-cone profiles through Péclet numbers of 10 (Ballistic) to 10^{-5} (Diffusion).

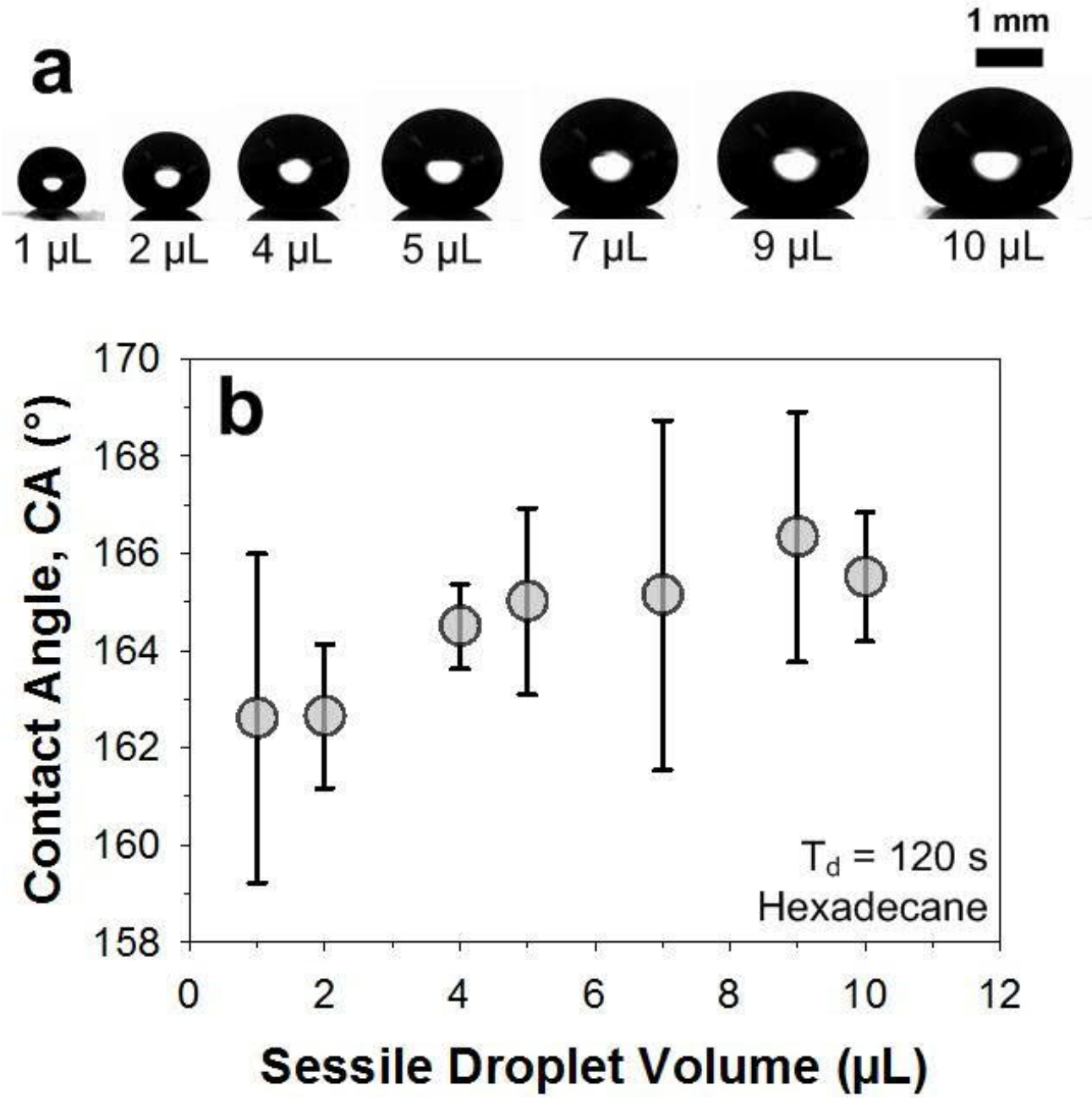

Figure S8.13. a) Probe droplets of hexadecane from 1 µL to 10 µL. b) Measured average CA from three measurements as a function of the droplet volume. The error bar represents the standard deviation.

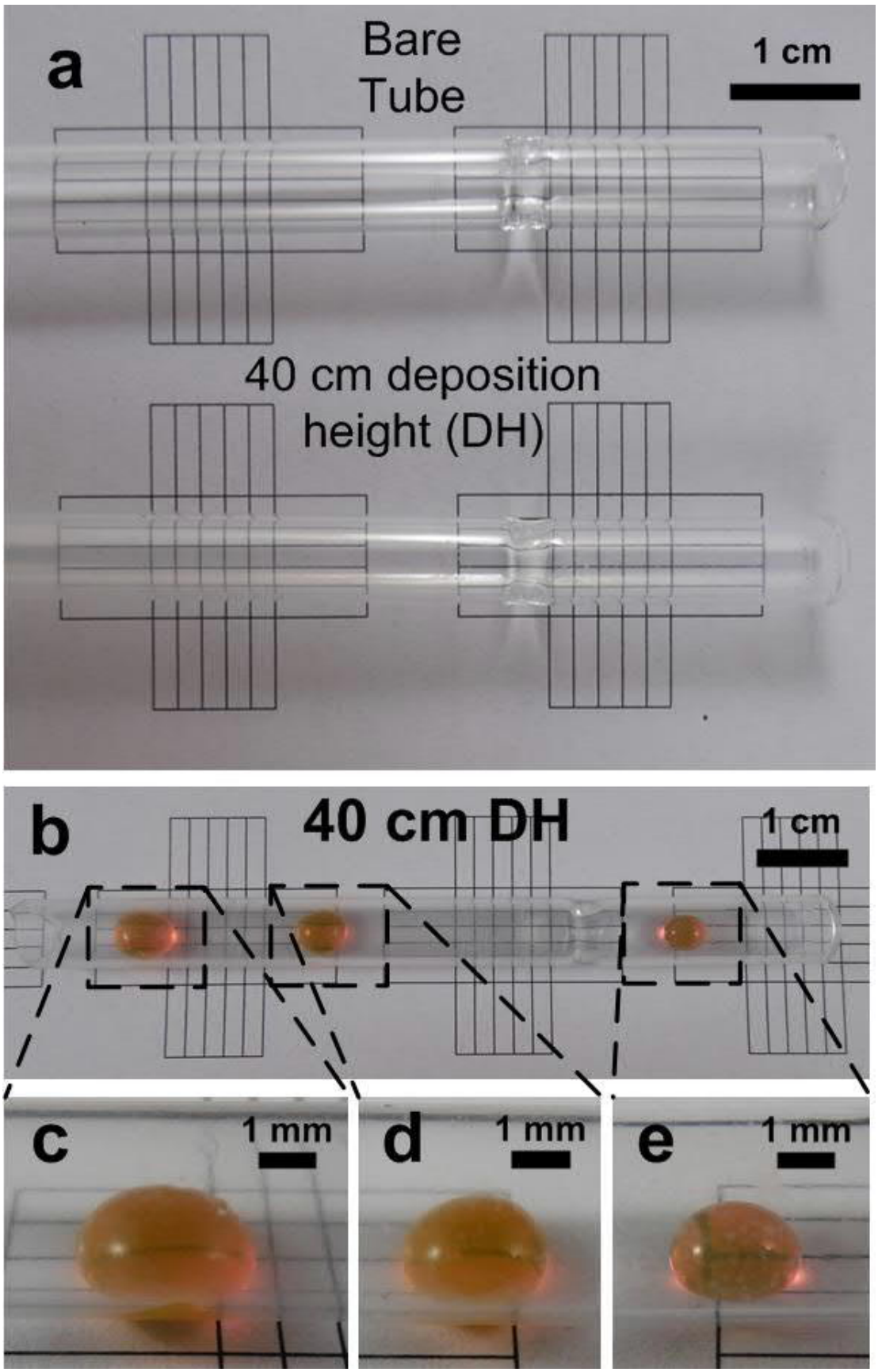

Figure S8.14. a) Characterization of the optical appearance of in-tube coatings and a bare tube. b) Superoleophobic functionality (dyed dodecene) is preserved throughout the 10 cm close-ended tube. Enlarged images of beaded oil droplets along distances of c) 8 cm, d) 6 cm and e) 1.5 cm from the tube inlet. The coating was deposited at 40 cm height (DH) from the flame nozzle.

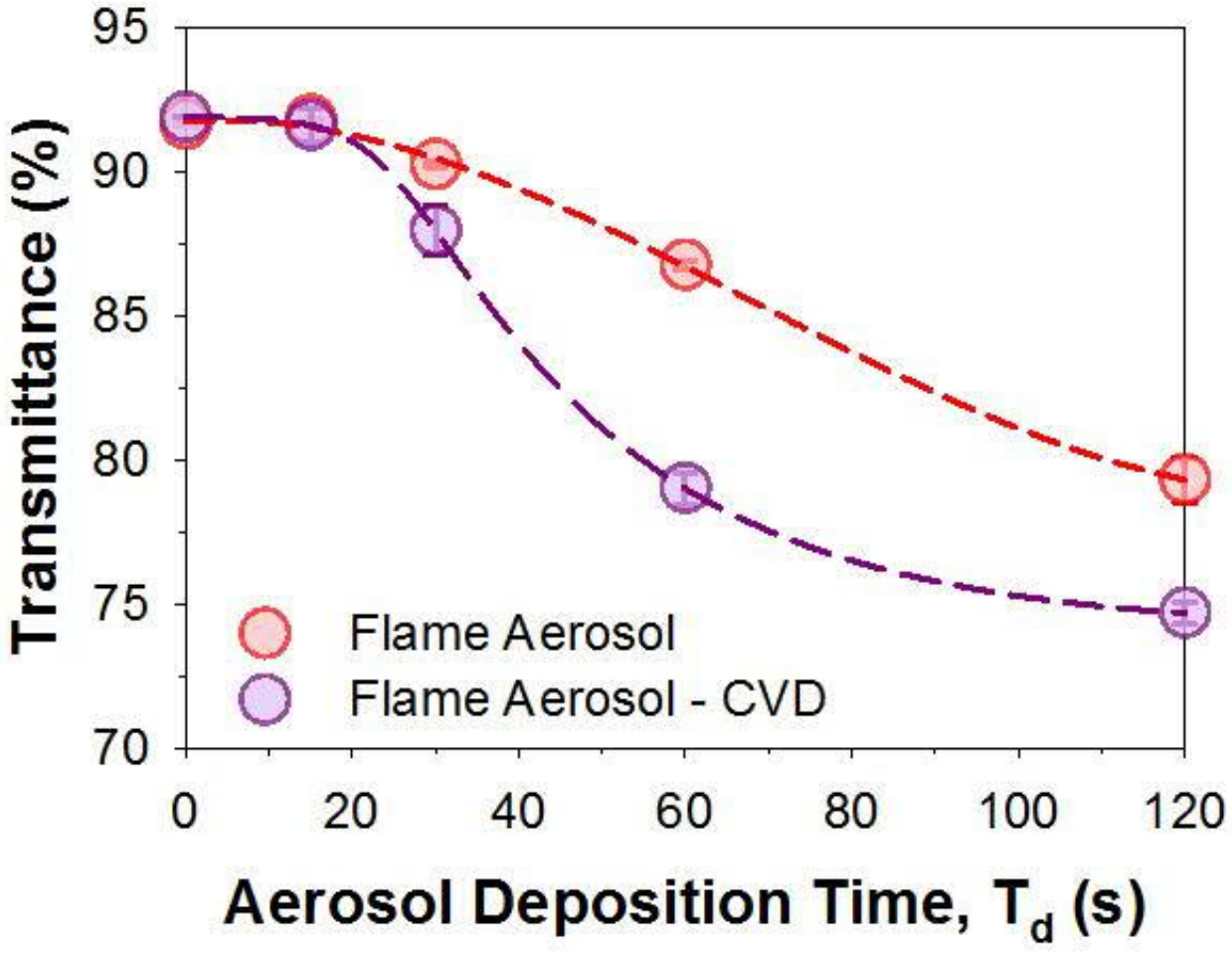

Figure S8.15. UV-vis transmittance profile of super-oleophobic (-amphiphobic) textures at 600 nm, without subtracting losses of the soda-lime glass substrates.

9. Superamphiphobic Bionic Proboscises

Abstract

Facile manipulation of nano-liter droplets is fundamentally vital towards many emerging technologies, such as microfluidics, droplet array systems, 3D printing or the inkjet-assisted fabrication of electronics. Despite much progress, contamination-proof generation and release of nano-liter droplets by compact low-cost devices remain elusive. Here, inspired by the butterfly's ability for minute fluid manipulation, we engineered a superamphiphobic bionic proboscis (SAP) for the control of fine droplets. The SAPs' droplet manipulation and contamination-proof properties outperformed several synthetic and natural designs. We demonstrate the scalable fabrication of SAPs, with tunable inner diameters down to 50 μm. This was achieved by rapid gas-phase nanotexturing of outer and inner surfaces of readily available hypodermic needles. Optimized SAPs achieved contamination-free manipulation of water and oil droplets down to a liquid surface tension of 26.56 mN/m with a minimum volume of 10 nL. The unique potential of our design is showcased by the rapid and carefully controlled in-air synthesis of core-shell droplets with well-controlled compositions. These findings provide a new low-cost tool for high-precision manipulation of nano-liter droplets, offering a powerful alternative to established thermal- and electrodynamic-based devices.

9.1. Introduction

The ability to generate and manipulate micro- or nano-liter fluids is of immense interest in many fields, including microfluidics,[69,93] inkjet printing,[658] micro-reactor engineering[41,89] and bio-sensing[541,575]. For example, *in vitro* evolution experiments for high speed DNA sequencing are currently achieved *via in vitro* compartmentalization of water-in-oil emulsion systems.[659] These water-in-oil droplet systems[536,660] drastically increase throughput rates as each nano-liter droplet functions as a separate reaction vessel. Despite much progress, the development of compact low-cost tools capable of contamination-free nano-liter droplet generation/manipulation remains elusive. Current approaches continue to rely on bulky mechanical-,[147] thermal-,[661] electrical-[662-664] and pyroelectrodynamics-driven[542] systems. These latter designs may experience contamination stemming from liquid residue adhering to the surfaces of tips or nozzles.[665] Despite numerous advantages, these techniques have strict requirements which comes in the form of high voltages,[542,662] heat injection,[542] or laser drilling.[147] Such draconian prerequisites result in increased manufacturing complexity while limiting end-user compatibility and, in some instances, scalability.

Biomimetics has inspired many sophisticated material designs that provide novel functionalities and real-world commercial applications.[666,667] Today, famous examples include self-cleaning superhydrophobic surfaces resembling the superdewetting lotus leaf,[7,29,36,91,299] and superhydrophilic anti-fogging glass inspired by superwetting moss.[20,95] Drawing parallels for the field of microfluidics, the butterfly's proboscis[216] enables direct and precise extraction of minuscule amounts of fluids[217]. This is attributed to the micrometer orifices (50-100 µm) belonging to the proboscis' dorsal ligulae, coupled with the hydrophobicity of the proboscis' terminal upper surfaces.[216] Despite its aptitude for microfluidics, the natural design remains "limited" by lower hydrophilic segments of the proboscis. Here, the surfaces are fairly wettable, showcasing WCAs of 45° which are thus easily contaminated by various fluids that they interact with.[216] Current advances in nanofabrication have since been used to reproduce the hydrophilic nature of the butterfly's proboscis. These proboscis

designs are realized by the fabricating oleophilic-wicking fibrous tubes, warranted by the decrease in energy required for fluid extraction and transport.[217] These oleophilic tubes are, however, also very prone to fluid contamination, due to the adhesion of liquid residue upon fluid interaction.[217] Other needle-based designs have been so far limited to the use of superhydrophobic surfaces that protect from water-based contaminants. However, they are insufficient for preventing fluid residue contamination by low surface tension liquids such as organic solvents or synthetic oils.[25] In fact, the adhesion and ascent of liquids on hydro- or oleo-philic surfaces remain a standing issue[665] for many bio-medical and -chemical applications. Risks ranges from simple volumetric inaccuracies to potentially catastrophic cross-contamination.[25]

Here, a super hydro- and oleo-phobic bionic proboscis (SAP) is developed, enabling contamination-free manipulation of simple and sophisticated core-shell nano-liter droplets. Superamphiphobic proboscises are fabricated by rapid gas-phase nanotexturing of inner and outer surfaces of hypodermic needles. This is an unprecedented achievement which enabled the well-controlled scalable fabrication of a broad set of SAP designs. These artificial proboscises demonstrate superior droplet manipulation performance as compared to both natural and synthetic variants. Optimal SAP designs precisely generate and dispense nano-liter water; oil and in-air core-shell droplets, down to 10 nL, showcasing the rapid fabrication of self-contained micro-reactors with immediate applications in chemistry and biology.

9.2. Results and Discussion

Design and Synthesis of Superamphiphobic Bionic Proboscises

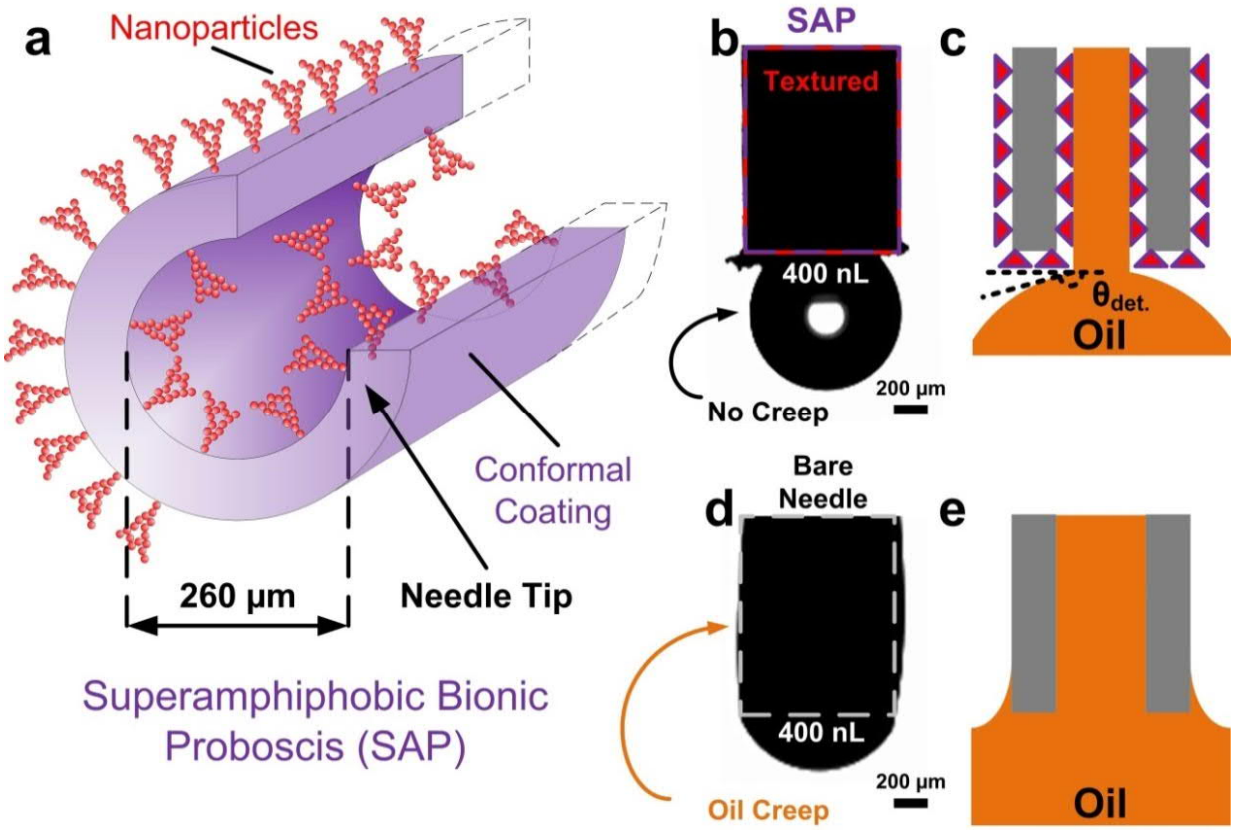

Figure 9.1. Synthesis of superamphiphobic bionic proboscises (SAPs) *via* a two-step aerosol nanotexturing - CVD silanization process. a) Micron-resolution surface texturing of ultra-fine tools, such as a thin hypodermic needle. Surface texturing enabled superior b) surface-oil interactions such as c) complete creep elimination as compared to severe d) oil creep in e) bare needles. Probe liquid, n-tetradecane (26.56 mN/m), 400 nL.

Figure 9.1a shows a schematic of the SAPs' nanostructural design. Coatings of re-entrant nanotextures were rapidly fabricated on the inner and outer walls of hypodermic needles by the aerosolized deposition of SiO_2 nanoparticles (Figures S9.1, S9.2).[92] This resulted in a self-assembled ultra-porous (98%) nanoparticle network that is, thereafter, functionalized by atmospheric chemical vapour deposition of low surface energy fluoro-groups. The inner wall functionalization prevented in-needle adhesion, enabling superior control over droplet release and thus sizes while resisting contamination by capillary rise (Figure 9.1b,c). The need to break capillary-bridges[90,147,662] for droplet detachment was also eliminated, further reducing the risk of contaminating inner walls with liquid residues.

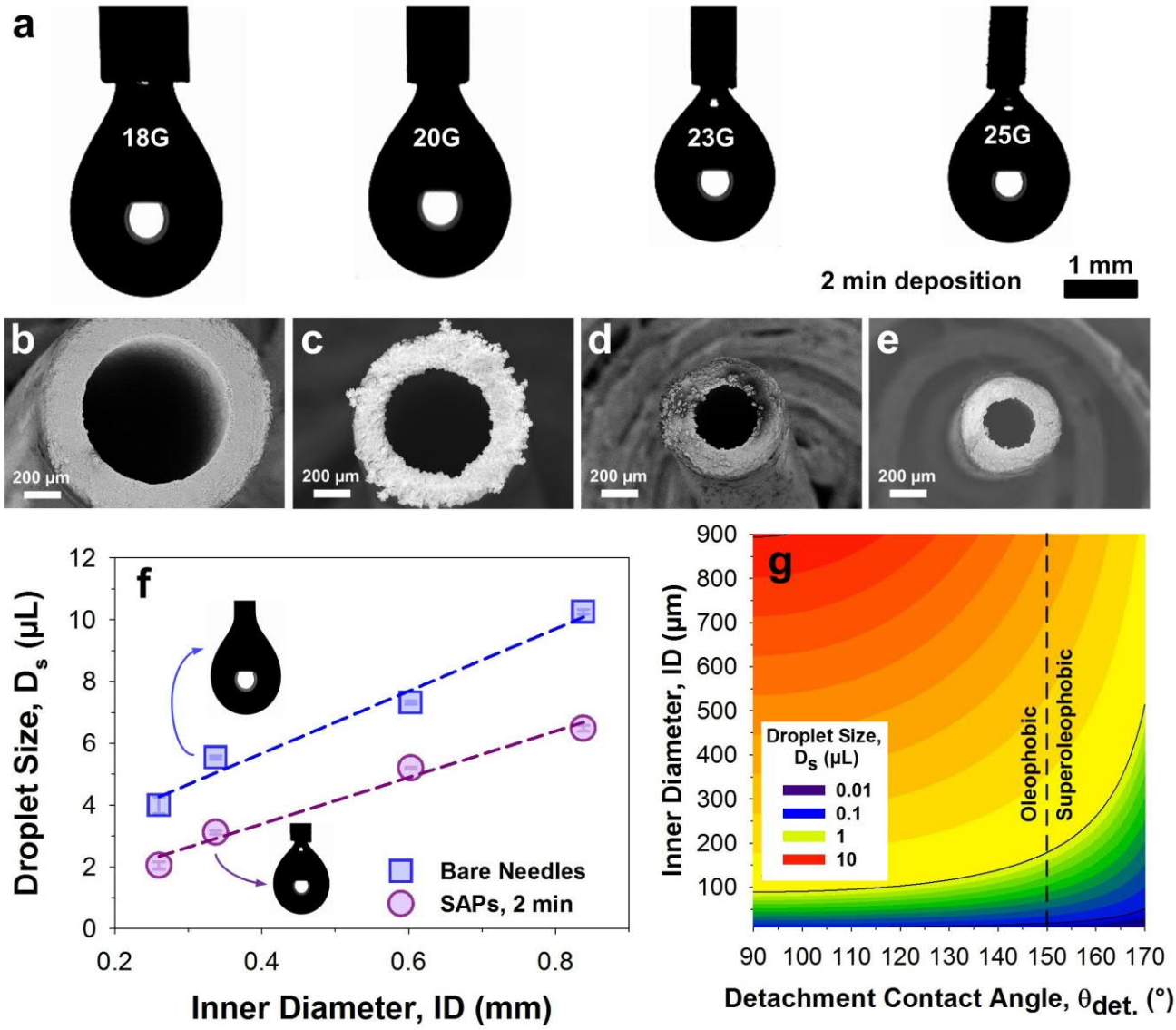

Figure 9.2. Demonstration and theoretical estimation of inner diameters vs. droplet sizes. a) SAPs at various gauge sizes showcasing elimination of tetradecane oil creep and b-e) SEM characterization of the ultra-thin conformal coatings. f) Tetradecane oil droplet sizes released by bare needles (squares) and SAPs as a function of their inner diameters. g) Theoretical estimation of the minimum detachable droplet size from a needle as a function of its inner diameter and tetradecane's interfacial CA. Superoleophobic needles such as the SAPs are expected to achieve nano-liter droplet production even with up to 10 times larger diameters than oleophobic needles.

The outer surface functionalization prevented contamination by creep during droplet generation and direct immersion of the SAPs in liquids (Figure 9.1d,e). The performance of this design was initially demonstrated by the generation of a 400 nL oil droplet (tetradecane as probe fluid) with a SAP and a bare needle, which served as the control behaviour. While the bare needle suffered from visible oil creep on its exteriors (Figure 9.1d, S9.3), the SAP preserved a pristine contamination-free surface during droplet generation and release (Figure 9.1b).

Figure 9.2a presents an experimental demonstration of this approach by the rapid fabrication of SAPs, starting from hypodermic needles with inner diameters that ranged from 838 to 260 µm. Aerosol deposition of SiO_2 nanoparticles for 2 min resulted in highly homogenous nanotextures on both inner and outer needle surfaces (Figure 9.2b-e). The textures' thicknesses were less than 10 µm and did not significantly affect inner and outer diameters of the needles. Analysis of the 2 min deposited textures (8 µm) on flat substrates using white light interferometry (WLI) revealed a root-mean-square (rms) nanoroughness of 85.7 ± 10.4 nm. The film porosity is estimated to be ca. 98-99%, measured by cross sectional SEM and mass or optical density. This is in line with previous experimental and theoretical studies[59,78,92] on aerosol deposited films. Notably, this rapid gas-phase nano-texturing approach (Figure S9.1) was successfully implemented down to 26-gauge (26G) needle tips having an inner diameter of just 260 µm. Even for such high aspect ratio geometries, the conformity of the textures was excellent. While the deposition is conformal along the circular cross-section of the inner needle surface, its thickness is expected to decrease with increased depth into the needle tip. This decrease would follow the reported scaling law for particle deposition in cylindrical tubes[668] and particle dynamic simulations of aerosol deposition into capillaries[1]. However, aerosol penetration can be increased by applying a pressure drop at the needles' outlet during aerosol assembly. However, even without this pressure drop, sufficient deposition depth was observed down to a needle inner diameter of 50 µm.

Upon fluorosilanization, all needles became superamphiphobic, with very high CAs (> 150°) with water and tetradecane (Figure S9.2). Notwithstanding their superior contamination resistance, these SAPs were not capable of nano-liter droplet generation, with the smallest droplets achieved at volumes of ca. 2 µL (Figure 9.2f).

Optimal SAP Design and Nanodroplet Manipulation

To achieve successful synthesis and manipulation of nano-liter fluids, droplet generation mechanism was mathematically modelled (Figure 9.2g) as a function of a couple of fundamental independent

variables (Experimental Section), namely inner diameter (ID) and liquid CA. Here, inner diameter (ID) was defined as the inner diameter of the needle tip, which was measured by SEM analysis. This dimension is known to be one of the two key parameters in controlling fluid-nozzle interactions. The minimum droplet volumes, which can be generated by a SAP, are directly proportional to the nozzles' inner diameters. However, minimum droplet volumes are also inversely proportional to the surfaces' CA, the second key parameter, and are thus strongly correlated to the needle's surface wetting properties. With decreasing inner diameters, the influence of CAs on the achievable minimum droplet size increases (Figure S9.4). For instance, a superoleophobic ($CA_{oil} \geq 150°$) needle with an inner diameter of 100 µm can produce nano-liter droplets of 560 nL, while an oleophobic ($CA_{oil} = 90°$) needle of the same diameter will not be able to produce droplets smaller than 1120 nL.

To decrease the needle's inner diameter to a suitable range for nanodroplet manipulation (ID < 100 µm), design of SAPs was further optimized on the 26G needles (Figure 9.3a). The 20G needles are presented alongside for comparison (Figure S9.5). The 20Gs and 26Gs have external and internal diameters of 908 µm and 464 µm; 603 µm and 260 µm, respectively. Their inner diameters were hereinafter further decreased by increasing the aerosol deposition time from 2 to 20 min (Figures 9.3b-g, S9.5). Freely detaching nano-liter oil droplets were achieved from the 26G SAPs with an aerosol deposition time above 5 min.

Scanning electron microscopy (SEM) analysis revealed that inner diameters were now achieved at dimensions smaller than 100 µm. At a deposition time of 10 min, the inner diameter was further reduced to ca. 50 µm (Figure 9.3b-g), one fifth of the original (260 µm). The correlations between deposition time; experimentally determined inner diameters (ID) and coating thicknesses (δ) are presented in the Supporting Information for reference (Figure S9.8). The droplet generation performance of these optimized SAPs matches well with the analytical model developed (Figure 9.4b).

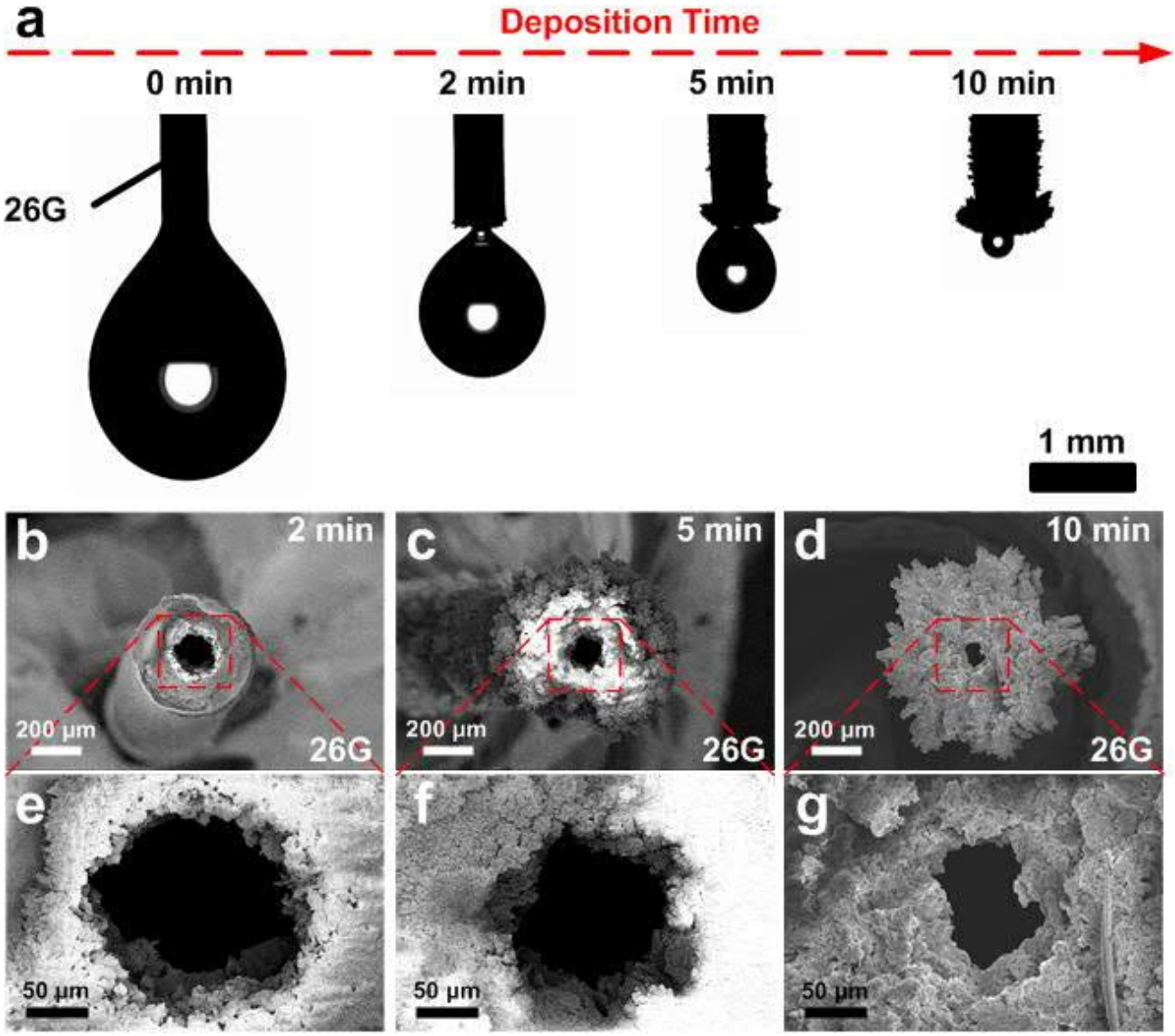

Figure 9.3. Optimization of SAPs' inner diameters for nanodroplet production. a) 26G needle tips were optimized for nano-liter droplet production, showcasing the droplet-interface 330 ms before detachment. b-g) Scanning electron micrographs (SEMs) on 26G SAPs as a function of the aerosol deposition time. The initial diameter of the bare needles was 260 µm.

Experimental data, analysed through the pendant droplet model, confirms that both nanotexturing and fluoro-silanization are needed for achieving superamphiphobicity. Negligible influence on droplet sizes was observed after fluoro-silanization of bare needles, while a significant impact on droplet sizes was noted upon combined nanotexturing and fluoro-silanization (Table S9.1). The SAPs with inner diameters of 50 µm achieved an average droplet size of 80 nL (Figure 9.4a). They were also capable of sequential nano-droplet production, showcasing excellent stability and size reproducibility over sequential generation of over 15 nano-liter droplets (Figure S9.6) at high (0.1 µL/s) and low (0.01 µL/s) production rates. These superamphiphobic SAPs can be repeatedly used under contact-

interaction, such as droplet production; fluid immersion and even droplet-injection (Figure 9.5). No noticeable losses in performance were noted during and after repeated usage.

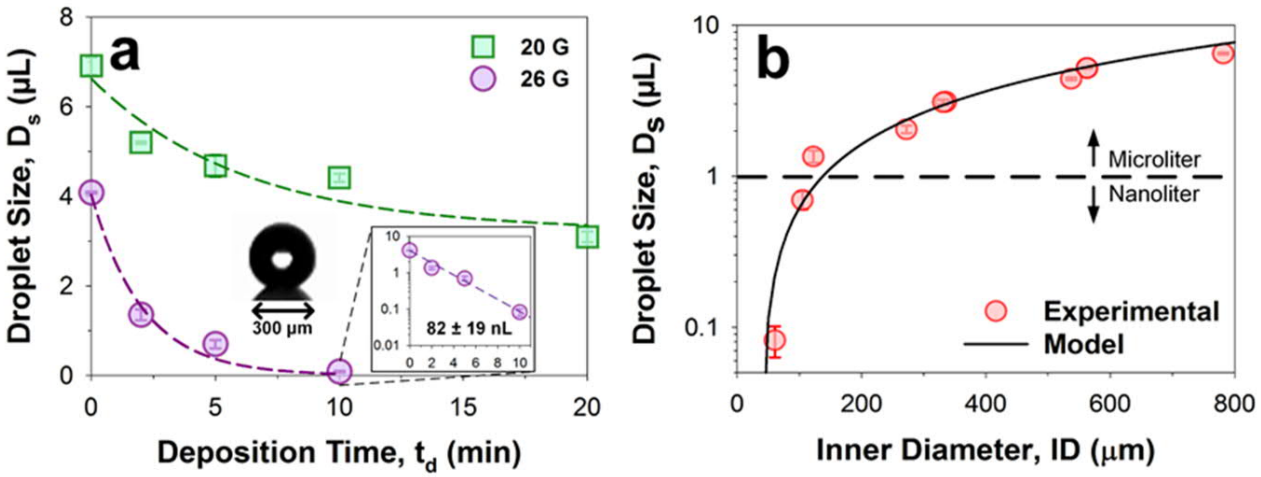

Figure 9.4. Characterization of the SAPs' nano-liter oil droplet (tetradecane) production as a function of aerosol deposition time. a) Tetradecane oil droplet sizes as a function of the deposition time for 20G and 26G SAPs, reaching down to 82 nL (inset). b) Experimental and modelled tetradecane oil droplet sizes as a function of the SAPs' inner diameters.

Contamination-Free Single and Core-Shell Droplet Manipulation

The contamination resistance of the SAPs was assessed using the capillary rise effect in oil baths. The SAPs and bare needles (Figure 9.5a,b) were dipped into a vial of n-tetradecane (γ, 26.56 mN/m), and the capillary rise was measured by virtue of the fluid mass in the capillary.

Capillary action was modelled as follows:

$$h = \frac{2\gamma\cos\theta}{\rho g r} \quad (9.1)$$

where h is the height of capillary rise, γ is the surface tension of probe fluid (26.56 mNm^{-1}), θ is the CA of the probe oil with the needle surface (equal to 0º), ρ is the density of the probe fluid (764 kgm^{-3}) and r is the radius of the capillary.

Notably, the SAP tips deformed and dimpled the fluid meniscus while revealing a shiny plastron air layer on their exteriors (Figure 9.5a). This effect is reminiscent of the water striders' superhydrophobic legs, and is vital towards their ability to walk on water.[669] Furthermore, upon

retrieval from the oil baths, SAPs remained perfectly dry. In contrast, the bare needles' exterior and interior surfaces were fully wetted (Figure 9.5b,c). Quantitative analysis of fluid penetration was performed using a mass-directed characterization. Bare needles and SAPs were weighed using a high-sensitivity mass balance (resolution of 0.1 mg) before and after deliberate immersion, with fluid penetration being assessed by the increase in mass (Figure 9.5c). A strong capillary rise of up to 7 mg n-tetradecane was observed for the bare needles. This was consistently larger than the theoretical estimates (Figure 9.5c), but can be attributed to the creep of oil on the needles' exteriors, which was not considered in the analytical solutions to the capillary rise equations (Further details in Experimental Section).

The facile and unique surface properties of SAPs enable their use as ultra-precision microtools for the delivery of nano-liter amounts of water and oils under challenging conditions. Here, we showcase their use as contamination-proof micromechanical hands for the ultra-dextrous manipulation of nano-droplets.

SAPs with inner diameters of 100 μm were used for the rapid sequential production of core-shell nano-liter droplets of oil and water in air. Firstly, a tetradecane oil droplet of a well-controlled size was generated and deposited on a superamphiphobic substrate (Figures 9.5d, S9.7). The droplet can also then be repositioned, if required, by applying suction through the same SAP. Thereafter, the SAP was reloaded with water, and pushed through the air-oil interface. A nano-liter water droplet was then generated and released within the oil droplet. The injected water droplet remains trapped within the oil shell due to its higher surface tension, resulting in the formation of a stable core-shell droplet with precisely controllable sizes (Figure 9.5d-g).

In stark contrast, bare needles were not capable of releasing water droplets within the oil shells due to the excessive adhesion between water and the bare needles' surfaces (Figure 9.5h-k). Moreover, fluid contamination in the bare needles was visually confirmed with evident oil (Figure 9.5i) and water (Figure 9.5k) adhesion upon retracting the needle from the oil droplet.

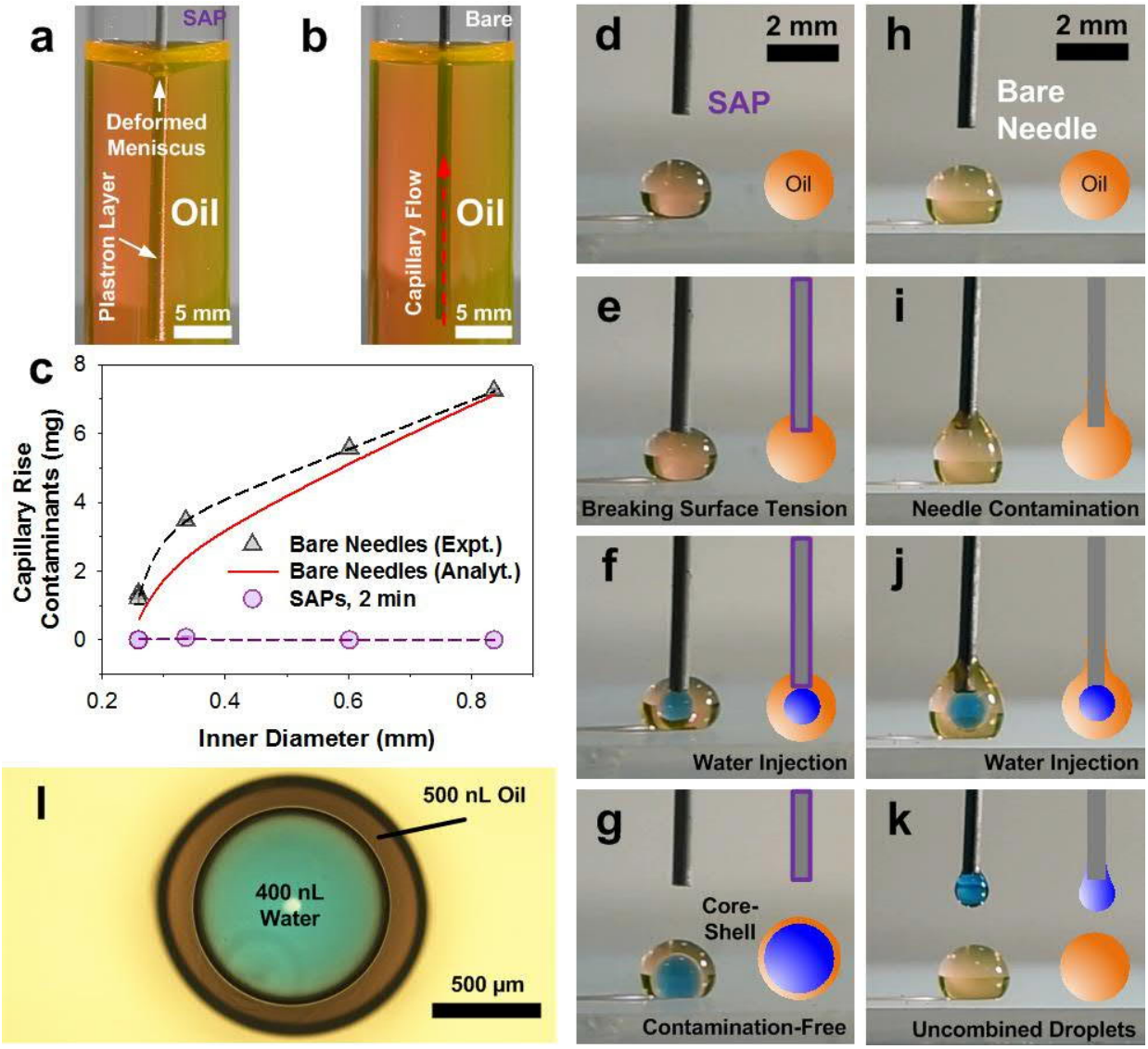

Figure 9.5. Contamination-free manipulation of core-shell droplets. Immersion of a) a SAP and b) a bare needle in tetradecane oil showcasing the contamination-free properties of the SAPs. c) Analysis of contamination of SAPs (circles) and bare needles (triangles) and their theoretical estimate (line) by capillary rise as a function of the gauge size from 18G to 26G. d-g) Demonstration of the facile in-air synthesis of core-shell oil-water nano-liter droplets with the SAPs. Droplet injection using a SAP, showcasing the superamphiphobic needle's superior contamination-free insertion of a nano-liter water droplet within an oil drop shell. In contrast, h-k) bare needles are not able to synthesize core-shell droplets due to excessive adhesion of the water droplets to the bare needles' surfaces. l) Microscope image of an in-air core-shell 400 nL water droplet in a 500 nL oil droplet, demonstrating unique control of complex droplet structures.

Alternatively, the SAPs remained completely dry after penetrating both oil and water layers. These unique results demonstrate the potential of such superamphiphobic micro-tools in revolutionizing the way we manipulate nano-liter fluids in both simple and sophisticated environments (Figure 9.5l). The immediate applications stemming from the precise use of such contamination-free microtools extend from micro-reaction engineering to emulsion microfluidics and DNA sequencing.

9.3. Conclusions

In summary, we have presented a novel approach for the facile and rapid fabrication of superamphiphobic bionic proboscises (SAPs), demonstrating immediate applications for minute fluid manipulation. These SAPs can produce ultra-small nano-liter liquid droplets, with an effective working surface tension range that extends down to ca. 26.56 mN/m. The outstanding performance was achieved by a novel design that enabled the controlled nanotexturing and surface energy modifications of commercially available hypodermic needles. These superamphiphobic bionic proboscises could produce nano-liter droplets down to just 10 nL while demonstrating contamination-free handling of oil and water droplets in both air and liquid environments. Their use as micromechanical bionic hands was presented by the unprecedented demonstration of facile and rapid in-air production of core-shell water-in-oil droplets. The SAPs' facile, cheap and superior superdewetting properties demonstrate much potential for numerous fields, including microfluidics,[536] drug delivery,[289] chemical- and bio- engineering[25,665].

9.4. Experimental Section

Materials

Flame Spray Pyrolysis (FSP) Assembled Nano-structures on Needles

SiO_2 nano-layers were produced by flame spray pyrolysis of solutions containing hexamethyldisiloxane. Combustible liquid solutions were prepared by dissolving hexamethyldisiloxane (Sigma-Aldrich, purity ≥ 98.5%) in toluene (Sigma-Aldrich, 99.8%), to reach a total Si-atom concentration of 0.2 mol L^{-1}. This solution was fed at 5 ml min^{-1} rate through a custom build nozzle, and atomized with an oxygen flow ($O_{2\text{-}\Delta P}$ = 5 L min^{-1}, COREGAS grade 2.5) at a set pressure drop (ΔP = 2.5 bar). The resulting spray was ignited with a surrounding annular set of premixed methane/oxygen flame ($CH_{4\text{-flamelet}}$ = 1.2 L min^{-1}, $O_{2\text{-flamelet}}$ = 2.0 L min^{-1}, COREGAS grade 4.5). Standard stainless steel dispensing needles (Terumo, Victor-G), were first cleaned with ethanol and then acetone. They were then mounted at a height above burner (HAB) of 15 cm without water cooling for SiO_2 deposition. Plastic tips of Terumo needles can be protected by using a water jacket. The deposition time was ranged from 2 to 20 min. Samples were stored in ambient laboratory environments (20-25 °C, 40-70% relative humidity) and CVD was conducted within 24 h of synthesis. Superamphiphobic glass substrates with nanodroplet carrying capacity were also made per the above procedures.

Chemical Vapor Deposition (CVD) of Trichloro(1H,1H,2H,2H-perfluorooctyl)silane

A home-built CVD reactor (150 mL) was used to chemically functionalize FSP-coated needles to confer superamphiphobicity. FSP-coated needles were placed in an inverted position above a trough containing a fluorosilane (Trichloro(1H,1H,2H,2H-perfluorooctyl)silane). Dry nitrogen was then used to purge the CVD reactor for a period of 5 min before and after silane deposition and the entire set-up was thereafter doubly-sealed with silicone plugs and parafilm. The reactor was then placed in an air-tight, desiccated chamber. To increase the vapor pressure of the silane (100 µL), the entire

assembly was heated at 40 °C for 30 min. Thereafter, the needles were retrieved and placed in a desiccator with applied vacuum for 1 h to remove unreacted silane residue.

The entire CVD reactor was then flushed with water and ethanol to remove unreacted silane, followed by the disposal of one-use components. The reactor was then flushed with acetone and scrubbed before being dried and re-used. Seals on the reactor were checked before each new process.

Characterization

Droplet Deposition and Needle Contamination Analysis

Core-shell droplets were made with an assortment of needles, primarily the 25G and 26G needles with a 2 minute or 5 minute flame aerosol coating, respectively. These enabled the facile production of micro- and nano- droplets. The injection was completed entirely using a syringe aided by a conventional syringe pump, although the careful manual operation of the syringe was also possible.

Contamination analysis was performed by the immersion of coated and uncoated needles (2 minute flame aerosol coating) into a vial of n-tetradecane. Capillary rise based contamination was then quantitatively assessed by a series of mass-measurements before and after immersion for the entire series of needles (18G, 20G, 23G, 25G, 26G). The capillary rise effect was not affected by depth of immersion, and thus all needle tips were immersed (10 s) at a depth of just 1 cm below the meniscus to reduce excessive oil sticking onto the outsides of uncoated needles.

A variation of 1 cm to 3 cm immersion gave rise to a 20-60% increase in contamination mass. This notably had no effect on the coated needles as the outsides were superamphiphobic as well. 3 repeats were performed for each sample. As thinner needles (26G, 25G and 23G) had predicted capillary rises larger than the entire needle length, these were also corrected to the maximum real physical length of the needles. Analytical and experimental solutions were presented in mean ± standard errors.

Droplet Size Analysis

SAPs were assessed through a contact angle goniometer as per the procedure for standard pendant- and sessile- droplet analysis. In this project, the chosen probe liquid was n-tetradecane (26.56 mN/m), owing to its organic similarities to real oils and its sufficiently low surface tension. Needles were first flushed at 1 µL/s with the probe liquid before droplet size analysis. N-tetradecane droplets were then dispensed at a rate of 0.1 µL/s for microdroplets (µL) and 0.01µL/s for nanodroplets (nL). These values were predetermined after estimations and thereafter, re-confirmations on the Weber number, $We = \frac{\rho v^2 D}{\sigma}$, corresponding to fluid surface tension σ, density ρ, linear injection speed v, and inner diameter D. We was determined to be $< 10^{-5}$ during nanodroplet production, ensuring that droplet volumes are not affected by injection speed. In micro- and nano- droplet production, the detaching volume is also determined by the competing gravitational forces on the pendant droplet and the drag provided by the needle tip. Fluid viscosity is known to affect droplet sizes by viscous, inertial and surface tension forces. This effect is represented by a dimensionless number, the Ohnsorge number,

$$Oh = \frac{\mu}{\sqrt{\rho \sigma D}} \tag{9.2}$$

Here, Oh was calculated at below 0.1 under all variations, confirming the negligible influence that viscosity has on droplet volumes.

Detached droplets were made to land on a flat version of the superamphiphobic interface, imaged, and later, sizes computed. 330 ms prior to detachment, CAs of detaching droplets ($\theta_{det.}$) were manually measured in MSVisio *via* blown-up images. Dynamic and static images were recorded using a KSV CAM200 contact angle goniometer (Finland) with a heliopan ES43 camera (Japan). Droplet sizes were computed by a commercially available (CAM2008) program. SAPs were cross-batch triplicated and 6 readings were recorded *via* sequential drops, assessing repeatability and stability simultaneously. Data was presented as mean ± standard errors. Owing to limitations of the instrument's syringe pump (minimum pulsating flow rate of between 0.01-0.05 µL/s), further optimization of the system below the lowest as-achieved droplet resolution sizes of 10 nL was impossible and not further pursued.

Needle Tip Analysis

Samples were analyzed *via* Zeiss UltraPlus field emission scanning electron microscopy (FESEM) at 2-3 kV. Prior to examination, SEM specimens were platinum sputter-coated for 2 min at 20 mA. Due to the corrugated nature of the coatings, needle diameter was determined over 10 averaged counts.

Surface Roughness Analysis

Optical profiling was also conducted *via* white light interferometry (Veeco, Wyko NT9100, USA), which provided 500x magnification with a field of view (FOV) of 1x *via* the vertical scanning interferometry (VSI) mode. This was broadly used to analyse the surfaces' nanoroughness. A backscan of 50 µm and length of 25 µm was used with a modulation of 3% to cover the maximum peak-to-trough heights of hierarchical coatings averaging 3 repeats.

Analytical Model

The droplet size that can be produced from a SAP is correlated directly to the drag force between the vertical component of the capillary between the pendant drop and the inner edges of the SAP. This gives,

$$\pi D_i \sigma \sin(\theta_{det}) \tag{9.3}$$

Balancing this capillary force with the gravitational pull on the pendant droplet, with an inner diameter of D_i, surface tension of σ and a detaching droplet CA of θ_{det}, results in a force balance that gives pendant drop volume (V) as,

$$V = \frac{\pi \sigma D_i \sin(\theta_{det})}{\rho g} \tag{9.4}$$

where g is the gravitational acceleration.

In both analytical and experimental results, the D_i and θ_{det} were measured directly from optical images captured by the contact angle goniometer ca. 330 ms before detachment. When this cannot be easily

determined due to overly tiny droplets, a value of 162.2° was used, per the average of triplicated samples (3 μL) on flat glass substrates. Computed data points were then regressed, modelled, and presented alongside experimental data.

9.5. Supplementary Information

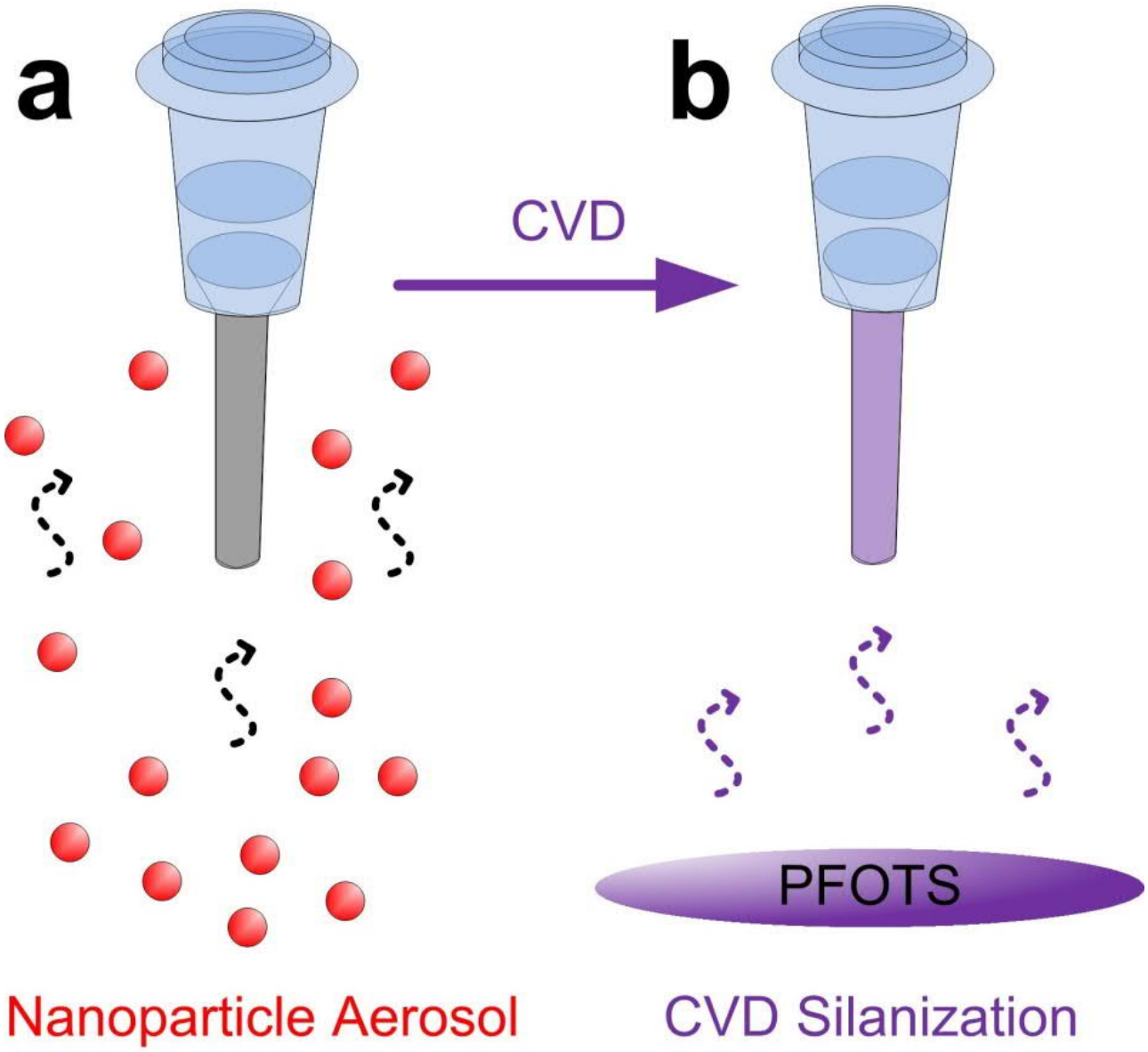

Figure S9.1. Synthesis of superamphiphobic SAPs from a sequential two-step nanoparticle aerosol-silanization process.

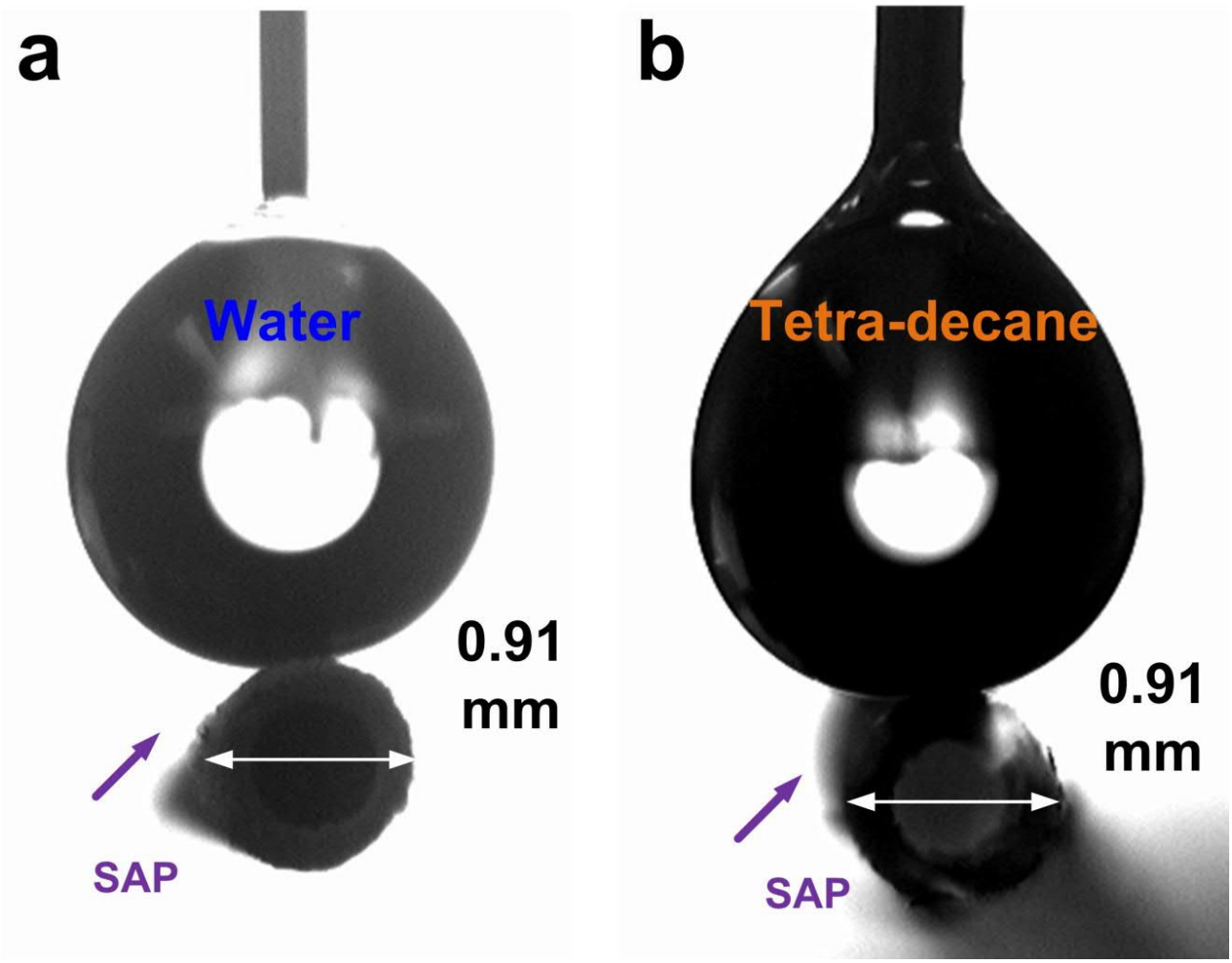

Figure S9.2. Superamphiphobic SAP exterior with a) a water droplet and b) a n-tetradecane droplet.

Figure S9.3. a) Reduced tetradecane oil creep with a CVD-treated needle (20G), b) interfacial interactions between a tetradecane droplet and bare needle controls.

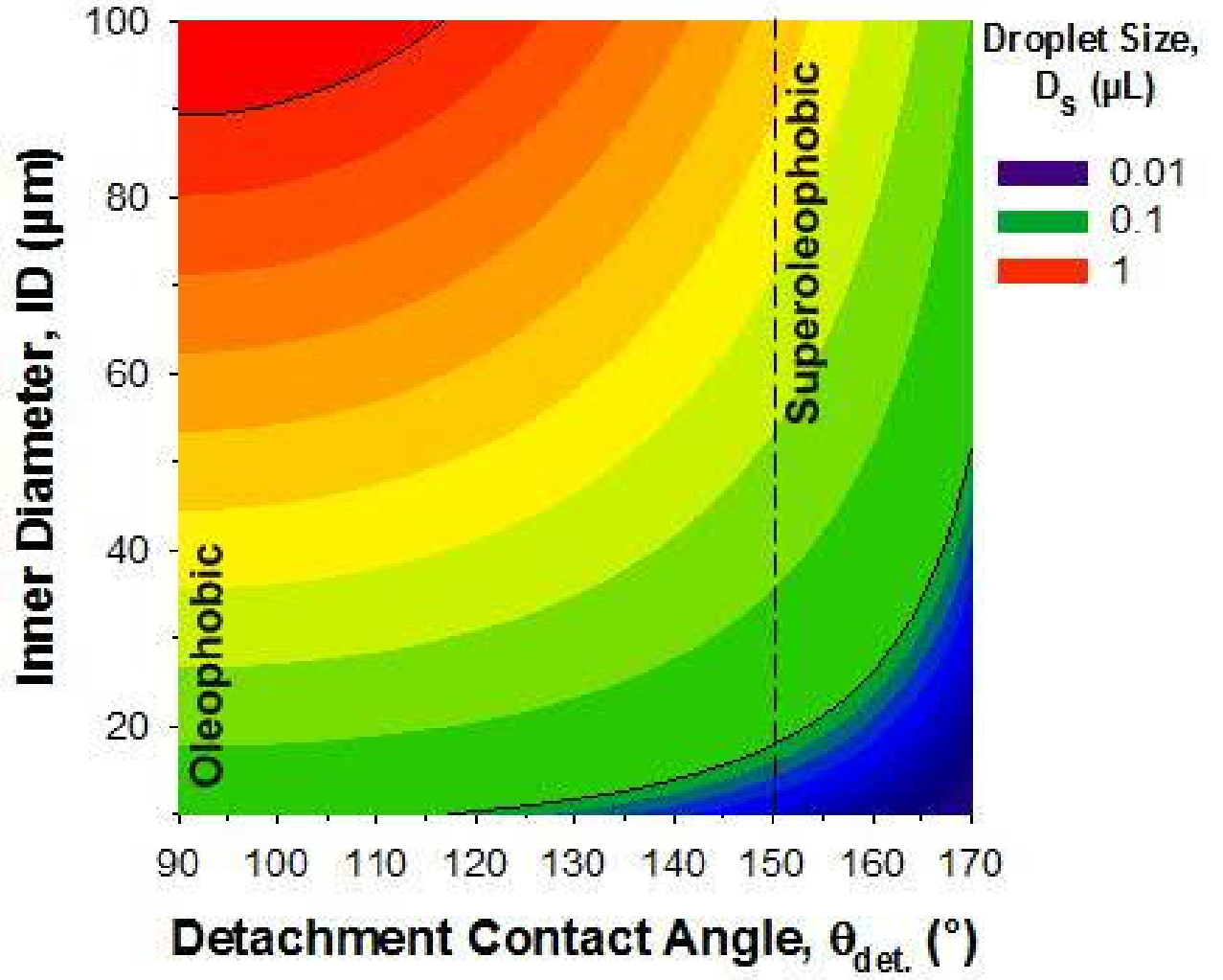

Figure S9.4. Simulations for nano-liter droplet production requirements based on tuning inner diameter and detachment CA, magnified down to 10 nL.

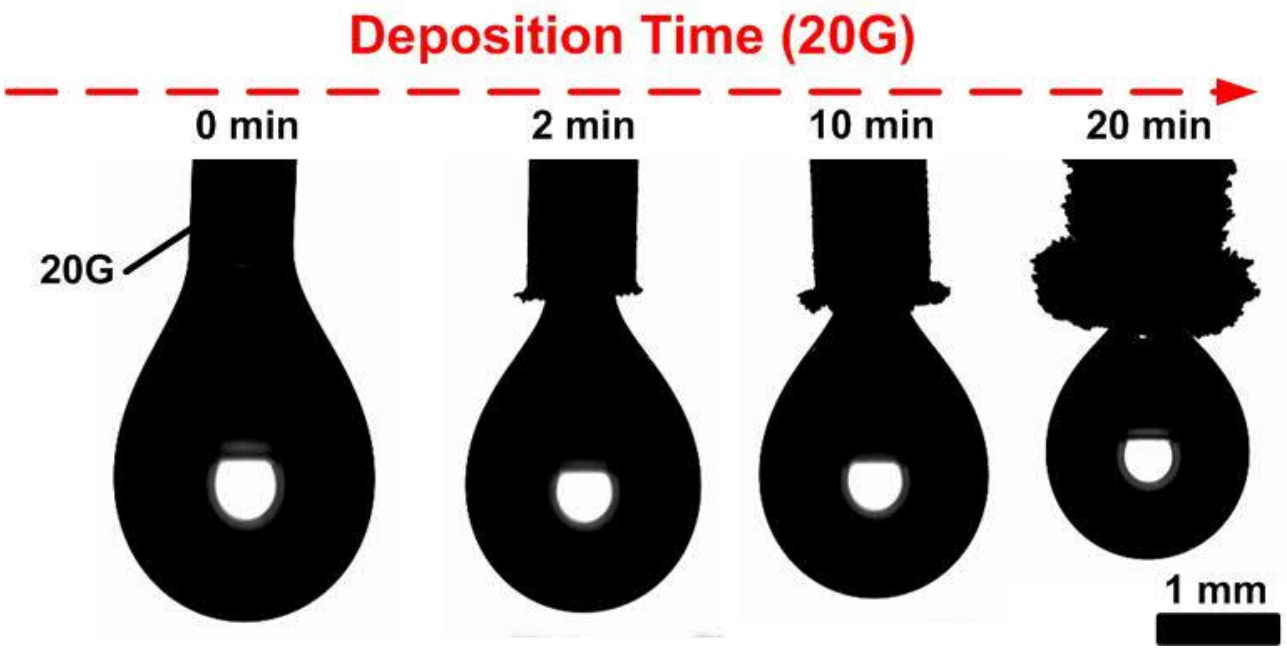

Figure S9.5. Interfacial interactions between a n-tetradecane droplet and SAPs from 20G needles with varying aerosol deposition times.

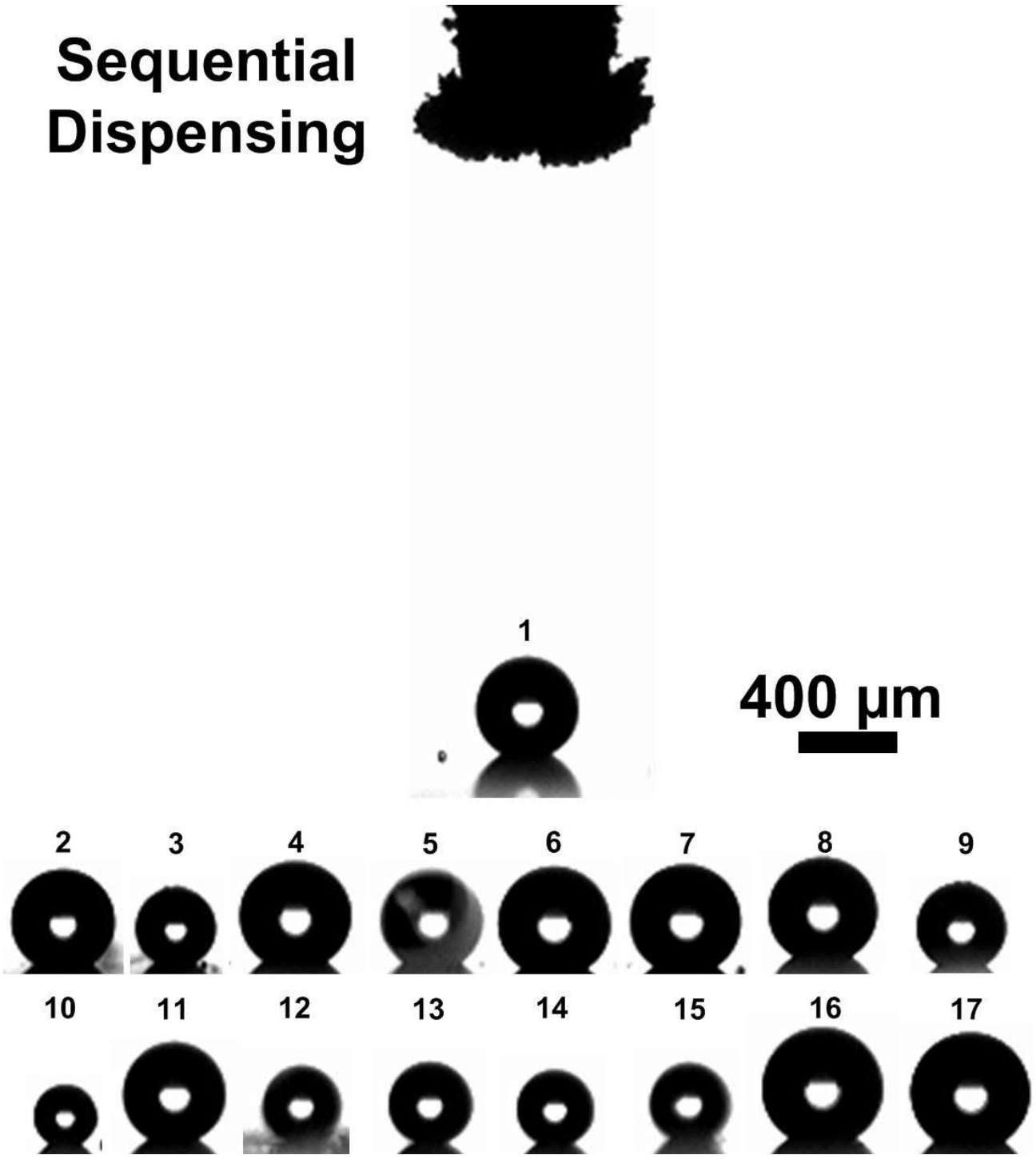

Figure S9.6. Multiple nano-droplets formed by the most optimally performing SAP, with a 26G needle after 10 min of aerosol deposition and 30 min of CVD. Droplets were produced by a series of rapid (0.1 µL/s) and slow (0.01 µL/s) injection rates. Smallest droplets are noted to be ca. 10 nL.

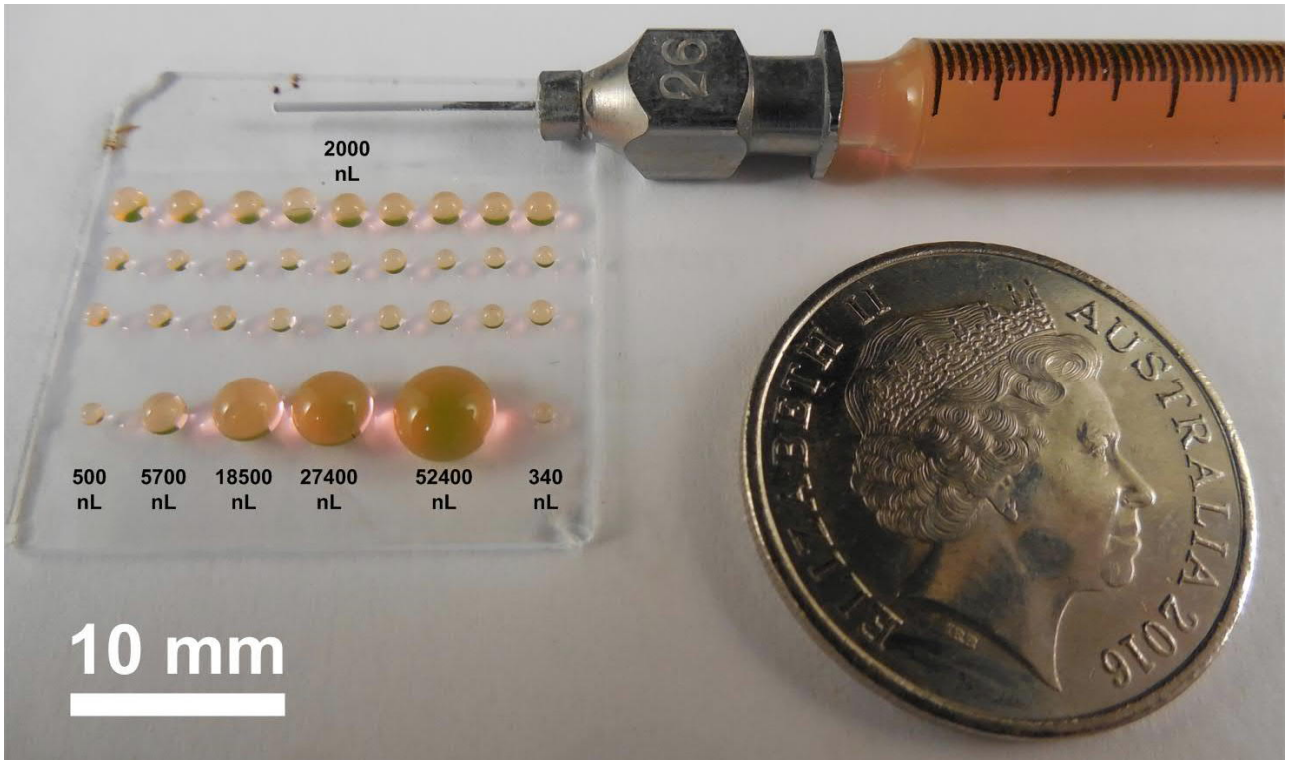

Figure S9.7. Manual droplet patterning using a SAP (26G) on a superamphiphobic substrate with superior user-controlled tunability.

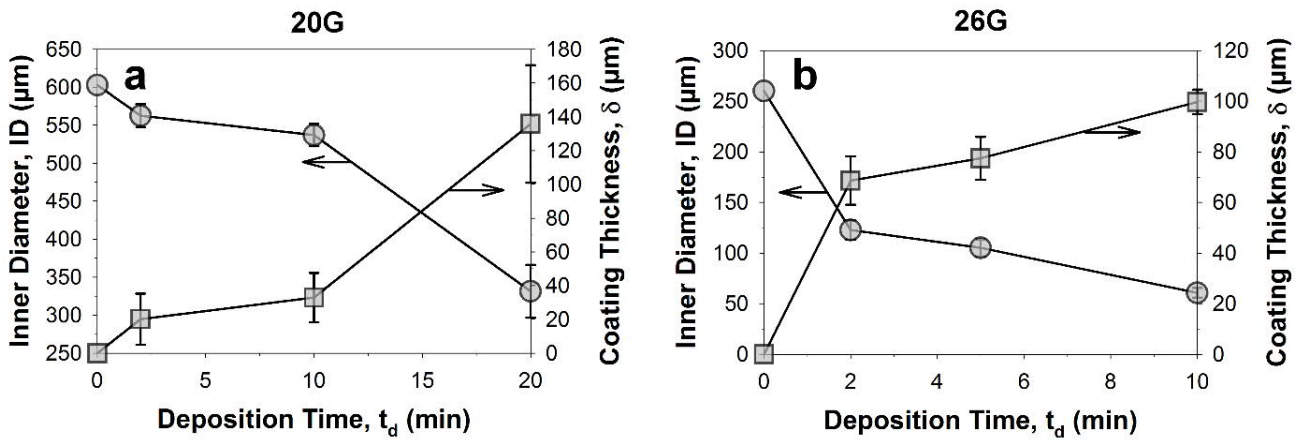

Figure S9.8. Textured hypodermic needles' inner diameters, ID and coating thicknesses, δ with respect to deposition time, t_d for the a) 20 gauge and b) 26 gauge needles.

Table S9.1. Comparison of droplet sizes produced with the bare fluoro-functionalized, and textured fluoro-functionalized needles.

20 G (original ID - 603 µm)

Droplet size (µL)	Fluorosilanized	Textured	Deposition time (min)
7.3 ± 0.13	No	No	0
6.9 ± 0.48	Yes	No	0
5.2 ± 0.07	Yes	Yes	2
4.7 ± 0.58	Yes	Yes	5
4.4 ± 0.22	Yes	Yes	10
3.1 ± 0.30	Yes	Yes	20

26 G (original ID - 260 µm)

Droplet size (µL)	Fluorosilanized	Textured	Deposition time (min)
4.0 ± 0.66	No	No	0
4.1 ± 0.05	Yes	No	0
1.4 ± 0.30	Yes	Yes	2
0.70 ± 0.23	Yes	Yes	5
0.08 ± 0.06	Yes	Yes	10

10. Amphiphilic Functionalization: Switchable Super(de)wetting

Abstract

In nature, cellular membranes perform critical functions such as endo- and exo-cytosis through smart fluid gating processes mediated by non-specific amphiphilic interactions. Despite considerable progress, artificial fluid gating membranes still rely on laborious stimuli-responsive mechanisms and triggering systems. Here, we present a room temperature gas-phase approach for dynamically switching a porous material from a superhydrophobic to a superhydrophilic wetting state and back. This was realized by the reversible attachment of bipolar amphiphiles, which promote surface wetting. Application of this reversible amphiphilic functionalization to an impermeable nanofibrous membrane induces a temporary state of superhydrophilicity resulting in its pressure-less permeation. This mechanism allows for rapid smart fluid gating processes that can be triggered at room temperature by variations in the environment of the membrane. Owing to the universal adsorption of volatile amphiphiles on surfaces, this approach is applicable to a broad range of materials and geometries enabling facile fabrication of valve-less flow systems, fluid-erasable microfluidic arrays and sophisticated microfluidic designs.

10.1. Introduction

Water is the universal solvent and one of the most ubiquitous forms of matter on Earth. Investigation of its interfacial interactions bears immense scientific and industrial potential.[19] In the last two decades, a series of sophisticated materials with unprecedented anti-fogging,[30,95,123] self-cleaning,[14,29,51,66,91,92,227,368,426] and self-assembly properties[93,319,632] have been fabricated by the careful engineering of hierarchical micro- and nano-structured surfaces. This has set the foundation for the next generation of functional surfaces with applications including droplet manipulation systems,[25,26,89,90] intelligent microfluidics,[40,48,217,588] textiles[54,202,511,581,657] and atmospheric water capture[225,670,671]. Despite much progress in achieving extreme static wetting states,[47,49,70,519] dynamic and reversibly switching between superhydrophilic to superhydrophobic states remain very challenging. Development of facile concepts for switchable super(de)wetting is of disruptive potential for a plethora of future applications including smart fluid-gating, wetting-switchable membranes and advanced micro-fluidics systems.[521,529]

In the early 1990s, Whitesides et al. pioneered the use of self-assembled monolayers (SAMs) for tuning the wettability of surfaces.[275-277] A combination of organothiols[275] and carboxylic acids[276,277] were used in conjunction with gold for self-assembling variable wetting surfaces *via* permanent sulphur-gold bonding[278]. Superhydrophobic states were thereafter achieved by imparting micro- and nano-scale roughness to the gold substrates.[236] The development of thiol-yne click chemistry enabled functionalization with polymer-based alkyne functional groups, thus decreasing substrate specificity.[15,45,289] Despite the gradual advancements, these surface functionalization approaches lead to largely permanent wetting properties.[15,45,277,289] Switchable super(de)wettability, namely, the reversible transitions between superhydrophobic and superhydrophilic states, is only possible through the use of energy intensive and laborious triggers such as thermal-,[514,515] electro-,[519] photo-[5,517] and mechanical-[518,520] stimuli.

Recent pH-responsive[518] designs solve some of these issues by using the fluid medium as the switching trigger. However, they are restricted to fairly specific fluid compositions.[518] Gas-phase based triggers are being proposed as a powerful alternative for switching the wettability of surfaces.[521,529] Amongst other benefits, they allow remote and non-invasive operation, providing significant potential for valve-less fluid gating systems. A major limitation of current gas-phase approaches lies with the strong intermolecular covalent bonds formed by the suitable functional groups (e.g. ammonium carboxylate). The latter requires the use of undesirable gases such as ammonia and high temperature thermal cleavage (> 120 °C) for achieving reversible switching between super-hydrophilic and -hydrophobic states.[521,529]

Herein, we report the first use of weakly bonded amphiphiles, supplied in the gas- or liquid-phases, for the facile and reversible switching between super(de)wetting states. We observe that this amphiphilic functionalization is easily reversible and can be triggered at room temperature by supplying common polar solvents like water. Inspired by the gating roles of cellular membranes, we showcase the application of this reversible amphiphilic functionalization (RAF) for dynamic fluid gating through hierarchical nanofibrous membranes. We demonstrate their remotely triggered switching between highly permeable and impermeable wetting states over 10 on/off cycles. We further explore the use of RAF for erasable fluid templating of porous thin films with applications in advanced droplet array systems and bio-analysis. The broad applicability of these findings provide a new flexible and easily applicable tool for the facile engineering of switchable super(de)wetting materials.

10.2. Results and Discussion

Reversible Amphiphilic Functionalization: A Temporal Wetting Concept

Today, surface functionalization[5,514-520] approaches typically revolve around states of permanent functionalization and are commonly directed towards achieving greater hydrophobicity by lowering the material surface energy.[29,300] Facile, non-invasive methods that allow reversible switching from a super-hydrophilic to -hydrophobic state at room temperature are lacking. Here, we demonstrate a concept for achieving a temporal and easily reversible superhydrophilic state starting from an initially nearly-superhydrophobic surface (Figure 10.1a-b).

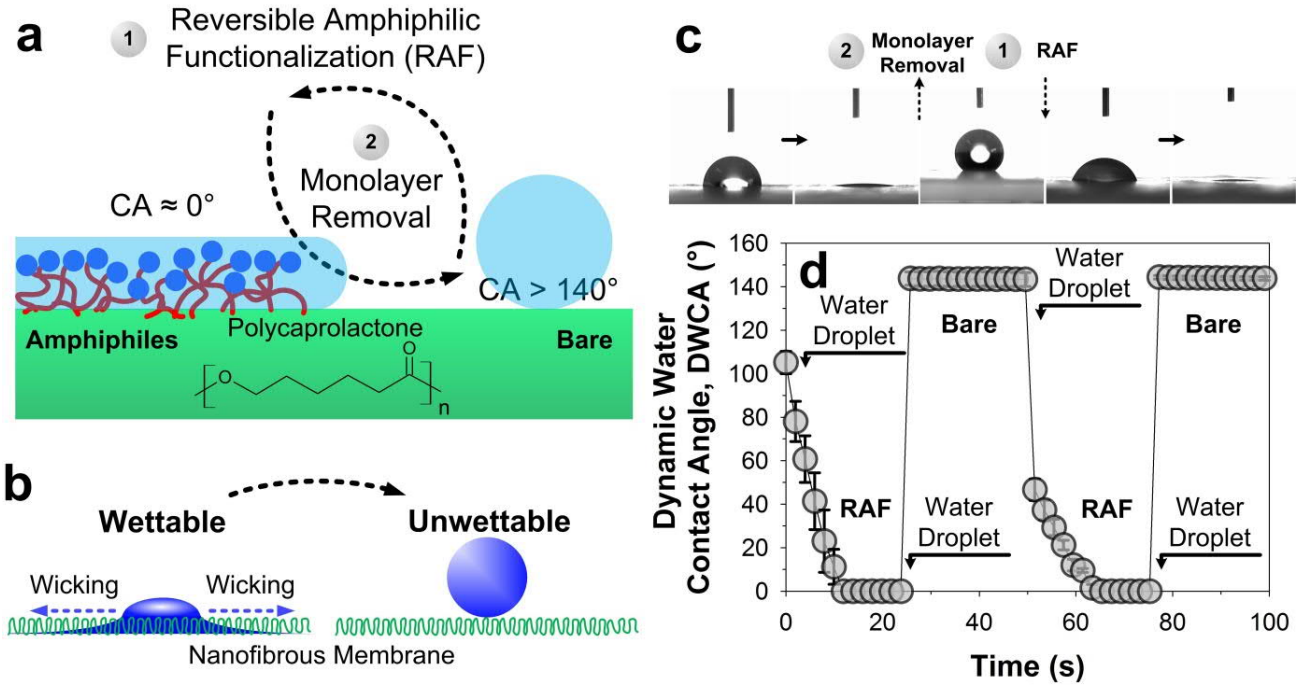

Figure 10.1. Schematic of a) reversible amphiphilic functionalization (RAF) of mono- (or multi-) layers on porous hierarchical materials, enabling tunable wicking superhydrophilicity and near-superhydrophobicity. b) Model amphiphilic hydrocarbons, such as dodecyl trimethyl ammonium bromide (DTAB) and 1-octanol can be used to induce a superhydrophilic state, while their removal results in a near-superhydrophobic state. c,d) Side-on c) optical and d) dynamic water droplet wetting profiles of RAF-treated (DTAB), monolayer-removed, and RAF-treated (Octanol) membranes.

The idea is to achieve a metastable superhydrophilic state by physisorption of amphiphilic molecules, which can be easily removed by the subsequent flow of a polar fluid. Amphiphilic molecules are known for their spontaneous self-assembly on surfaces, resulting in mono- and multi-layers that can tune the effective surface energy.[99] Self-assembly of amphiphilic molecules on a low energy,

possibly superhydrophobic, surface is expected to significantly increase its surface energy.[99] When associated with a suitable hierarchical morphology, this increase in surface energy can lead to a superhydrophilic wetting state. Desorption of the physisorbed amphiphiles during interactions with a fluid can restore the original surface energy (Figure 10.1c-d). As a result, upon termination of the fluid flow, the wetted areas demonstrate a superhydrophilic to superhydrophobic switch. This macro behavior is highly unintuitive as traditionally superhydrophilic surfaces, achieved with high surface energy materials, remain superhydrophilic upon wetting.[198]

We demonstrate a proof of this concept by switching the wettability of PCL nanofibrous membranes with two common non- and volatile amphiphiles (Figure 10.1c-d) such as dodecyl trimethyl ammonium bromide (DTAB) and octanol, respectively. First, functionalization of superhydrophobic PCL membranes by the non-volatile amphiphile DTAB were investigated (Figure 10.2, S2). Modifying the PCL surface with DTAB resulted in a highly permeable superhydrophilic membrane (Figure 10.2). The feasibility of reversing the amphiphilic DTAB functionalization of the membrane by its permeation with a fluid (Figure 10.2a-d) was assessed as a function of the fluid's polarity. Notably, while PCL is usually soluble in toluene and xylene, the high molecular weight PCL (M_n = 80,000) used here has higher chemical stability against common solvents.[672] Here, it was found that for the time and concentration of the elution process, the PCL membrane remained insoluble in all tested eluents including toluene and xylene.

Non-polar eluents resulted in marginal changes in CAs and flow-through permeability (Figure 10.2c-d, cyclohexane), suggesting incomplete amphiphile removal. Gradually increasing the eluent polarity improved the amphiphiles' elution (Figure 10.2c-d, S1-2). For instance, upon the flow-through of water, a near-superhydrophobic surface with static water CAs of 143° ± 1.5°, comparable to that of bare PCL membranes without DTAB functionalization (Figure 10.S3), was observed. This switch is attributed to the strong polar-to-polar interactions between water and the polar chain-ends of the amphiphile, which results in their solvation. However, solvation does not easily occur with non-polar

eluents as the van der Waals (vdW) forces between the DTAB and PCL surface are sufficiently strong to ensure anchoring of the functional layer (Figure 10.2c-d).

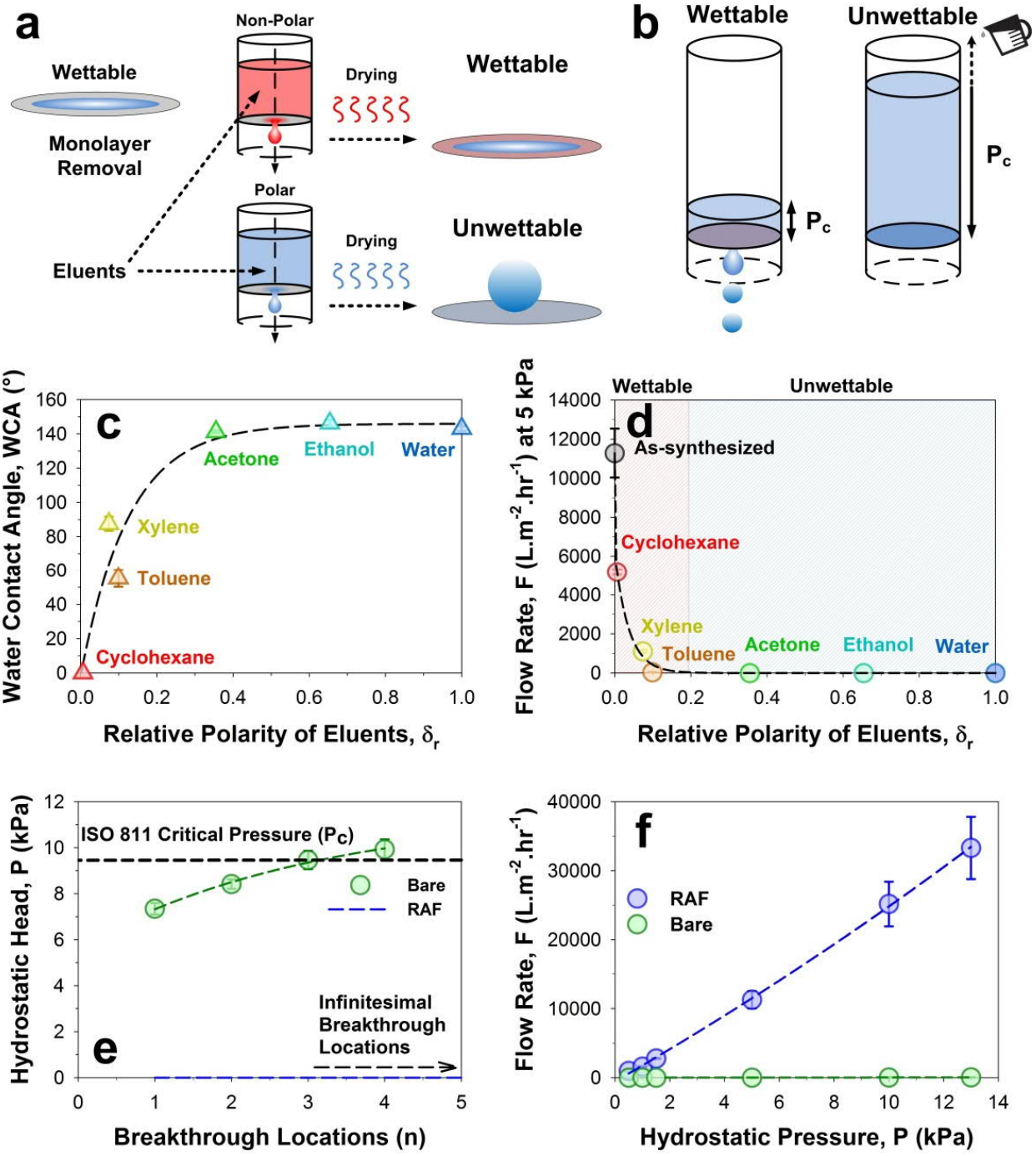

Figure 10.2. a) Schematic for fluid-tunable monolayer removal through polar (successful) and non-polar (unsuccessful) removal. Successful removal of the monolayer results in a near superhydrophobic state and vice versa. b) Polar fluid eluted membranes then possesses much higher critical breakthrough pressure as compared to those eluted by non-polar fluids. c, d) Stable c) WCAs on membranes and d) flow rate of water through membranes with respect to the relative polarity of eluents used on membranes. e) Critical breakthrough pressure (ISO 811) through bare membranes or with RAF modification. f) Flow rate of water through bare membranes with respect to hydrostatic head pressure.

This removal mechanism was supported by equilibrium WCA measurements (Figure 10.2c) and flow-through permeability (Figure 10.2d), which shows sharply enhanced membrane hydrophilicity and permeability upon the use of even marginally polar ($\delta_r > 0.2$) eluents. In addition to the membrane permeability tests, the critical breakthrough pressures for the DTAB-functionalized and bare PCL membranes were determined using the ISO 811 standard (Figure 10.2e-f). The critical breakthrough pressure of the bare membranes was between 9-10 kPa. In contrast, RAF-treated membranes were completely permeable without the need to apply any pressure, owing to their superhydrophilic properties. The fluid flow rates measured across the bare and RAF membranes with a fluid pressure of up to 13 kPa further confirm the stability of the impermeable and easily permeable states, respectively, (Figure 10.2f).

Remote Gas-Phase RAF with Volatile Molecules

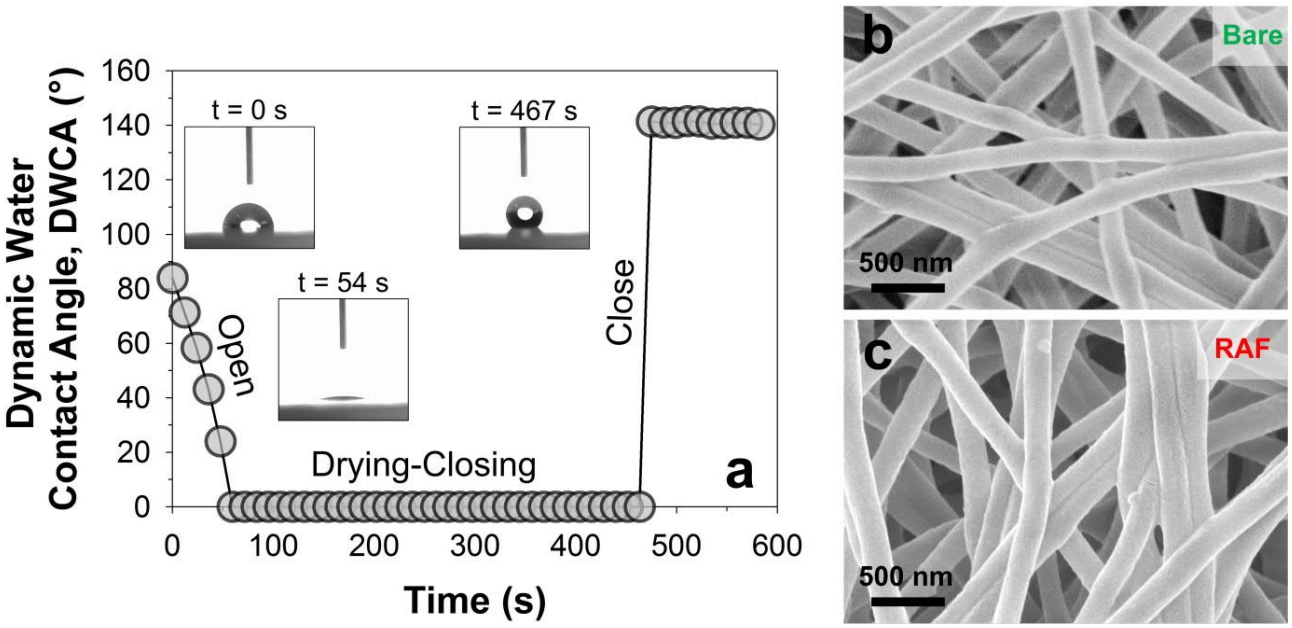

Figure 10.3. a) Single-continuous frame analysis of the reversible amphiphilic functionalization (RAF) regaining superhydrophobicity upon fluid-induced wetting transformation. b) Bare and RAF treated nanofibrous membranes show no morphological differences.

The use of DTAB for achieving fluidic gating is successful, but it suffers from inherent drawbacks such as poor cyclability, marine life toxicity and poor elution affinity with non-polar solvents, thus limiting the choice of solvents that can be used as a trigger. Octanol was further investigated as an exemplary volatile amphiphile of significantly easier application and removal. Octanol has a linear

chain comprising of just 8 CHx instead of the 12 CHx of DTAB. It should, however, be noted that they rely on the same functional principles underlying ultra-thin (sub-nanometer) layers of amphiphiles which induce a superwetting state. The thickness of the amphiphilic Octanol layer was estimated according to the van der Waals (vdW) interactions[673-676] (see Supporting Information).

It was found that octanol self-assembly would lead to a sub-monolayer at 0.219 nm thick. This is comparable to the 0.729 nm thick monolayers achieved using DTAB (Supplementary Calculations). Most importantly, both modes of functionalization enable a state of hemi-wicking superhydrophilicity, with minimal variations in practical performance and fluid-gating. Notably, due to its volatile nature, superhydrophilic functionalization with octanol is spontaneously removed if left in an octanol-free atmosphere for more than 1 h at room temperature. Alternatively, its superhydrophilicity can be preserved indefinitely when kept in an octanol-vapor saturated environment at room temperature. The octanol functionalization can also be easily reapplied, and its inherent temporal nature provides some unique advantages such as facile cyclability, universal applicability, environmentally friendliness and enhanced solvent elution affinity.

Figure 10.3a presents sequential frames showcasing the rapid and unintuitive wetting switchability achieved with this gas-phase approach. The extreme states of superhydrophilicity and superhydrophobicity occurred on the same surface location within 150 s after stopping the fluid flow. Scanning electron microscopy (SEM) revealed no morphological variations between RAF treated membranes and their associated bare membranes (Figure 10.3b-c). This indicates that switching of wetting states does not arise from the macro-scale arrangement of the nanofibers, but is instead attributed to the self-assembly of layers of amphiphiles on the nanofiber surface. Based on van der Waals (vdW) interactions, octanol physisorption is unlikely to achieve a full mono-layer coverage and are estimated to ca. 0.52-0.79 monolayer or 0.219 nm). However, the local surface energy is likely enhanced by this sub-monolayer,[99] leading to wetting of the nanofibrous matrix. The thickness of DTAB[677] has also been estimated to 1.46 monolayers or 0.729 nm as detailed in the

Supplementary Calculations. However, the local surface energy is likely enhanced by this sub-monolayer,[99] leading to wetting of the nanofibrous matrix.

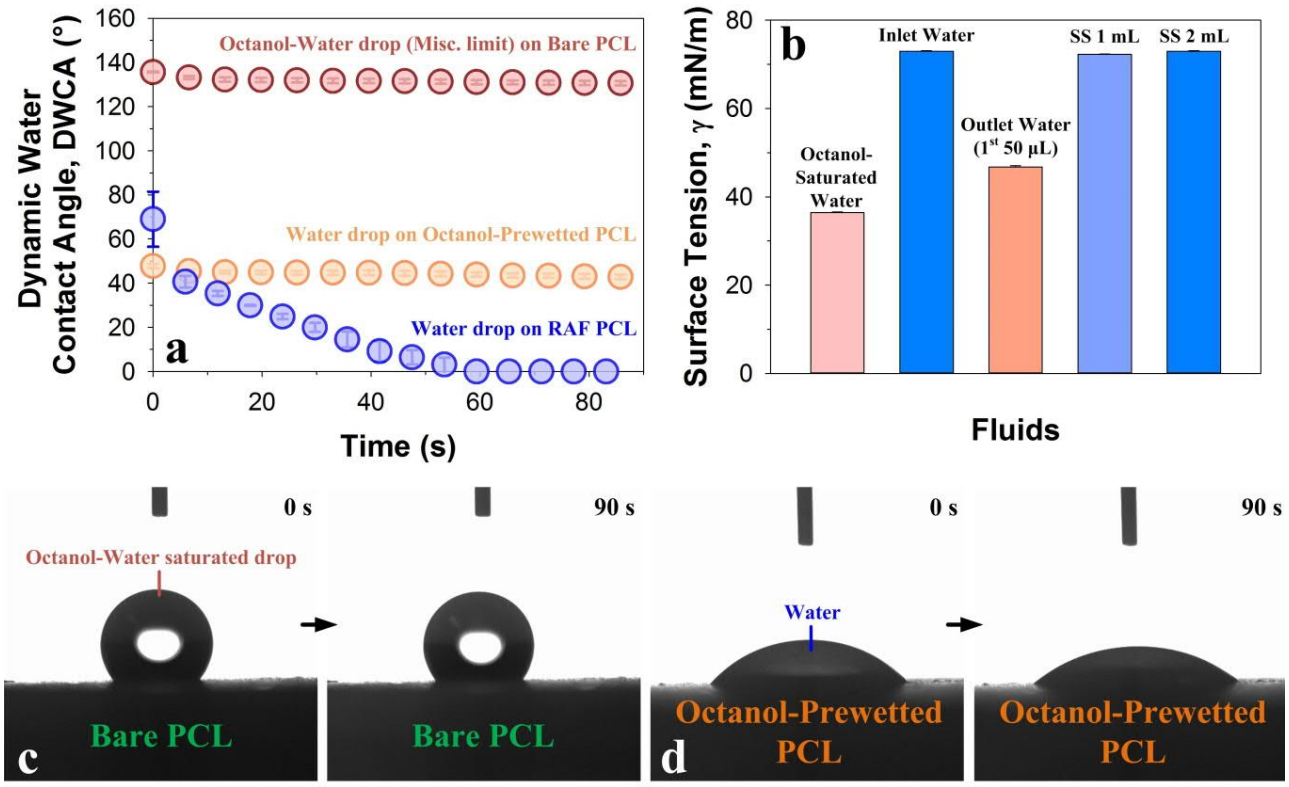

Figure 10.4. Surface configuration of vapor-deposited octanol on PCL membranes and corresponding variations. a) Dynamic WCA on membranes. Octanol-water droplet made at the miscibility limit, deposited on bare impermeable PCL (red circles). Deionized water droplet on an octanol-prewetted PCL membrane, physically wetted (orange circles). Deionized water droplet on a RAF treated PCL membrane (blue circles). b) Surface tension of (red) octanol-saturated water, (blue 1) water entering membrane, (orange) outlet water exiting membrane, 1st droplet, at ca. 50 µL, (blue 2,3) outlet water at steady-state (SS) after 1 mL and 2 mL of flow-through respectively. Optical images of c) Octanol-water saturated droplet on bare impermeable PCL membrane for 90 s and d) deionized water droplet on a physically pre-wetted PCL membrane for 90 s.

To substantiate the role of octanol in changing the surface energy and thus the wettability of the membrane, a couple of antithetical octanol configurations were tested. Firstly, a membrane soaked in octanol was tested to discard the possibility of pre-wetting effects. The latter was found to possess lower static and dynamic WCAs than the pure PCL. However, owing to the poor miscibility between water and octanol, the octanol-impregnated membranes remained completely impermeable (Figure 10.4a,d), and functioned akin to SLIPS[219] surfaces. Next, the possible impact of octanol in changing the surface energy of water,[678] and thus the thermodynamic potential driving wetting, was tested. A

water solution was completely saturated with octanol to its miscibility limit (ca. 0.46g/L) at room temperature. This solution was found to have a surface tension of just 36.4 mN/m, and thus significantly lower than water (72.8 mN/m). Despite the significantly lowered surface tension, water-octanol solution was unable to penetrate the bare PCL membranes and revealed large static and dynamic WCAs of ca. 131° (Figure 10.4a,c). These results support the proposed mechanism based on the localized increase in surface energy due to monolayer self-assembly. Notably, the permeation and flow of a small amount of water (45 $\mu L/cm^2$) through the membrane rapidly alters the local micro-environment desorbing the octanol monolayers and re-instating the superhydrophobic state (Figure 10.4b).

Functionalization Mechanism and Universal Nature of Amphiphilic Functionalization

The transient surface composition achieved by both the non-volatile (DTAB) and volatile (octanol) RAF was probed by X-ray photoelectron (XPS), Raman and Fourier Transform Infra-Red (FTIR) spectroscopies. The absence of measurable FTIR variations upon volatile and non-volatile RAF suggests that the functional groups have no bulk penetration suggesting that the strong variation in wettability is due to surface reconfiguration (Figure S10.4). The XPS spectra, tested at a penetration depth of 5-10 nm, confirm the presence of DTAB on the surfaces of PCL nanofibers via the appearance of the Br 3d peak at 68.3 eV (Figure 10.5a). However, the volatile octanol could not be assessed by XPS due to its rapid desorption during sample preparation. Notably, the Raman spectra of the membranes indicate the presence of a 1000 cm^{-1} peak immediately after octanol functionalization, as well as a noticeably modulated spectrum from 1200 to 1500 cm^{-2} (Figure 10.5b). This suggests the presence of octanol on the nanofibrous surfaces (Figure 10.5b). Notably, XPS and Raman confirmed that both amphiphiles are removed after elution with water showing indistinguishable spectra from those of the bare as-prepared membranes (Figure 10.5, S10.4). These results indicate that the RAF is limited to the surface of the nanofibrous membranes, explaining its ease of removal.

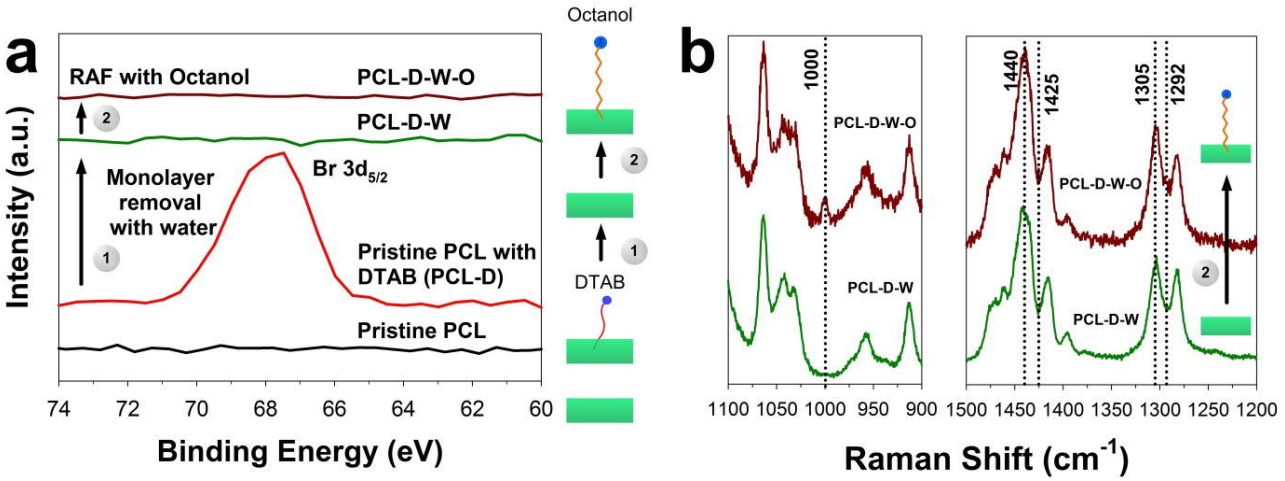

Figure 10.5. a) X-ray photoelectron spectroscopic (XPS) analysis for the detection of one-pot assembled monolayer of DTAB on nanofibers, showing the Br 3d at 68.3 eV in the case of DTAB-functionalised PCL. XPS, however, being a vacuum-based technique, is unable to detect the presence of octanol monolayers on the polymeric base. b) Raman spectroscopic analysis for detecting octanol monolayers on the surfaces of nanofibers, shows the presence of a 1000 cm^{-1} peak after functionalization, as well as a noticeably modulated spectrum between 1200 to 1500 cm^{-2}.

The application of this amphiphilic functionalization may be potentially universal, as it is based on the spontaneous physisorption and does requires neither specific materials nor reactions. Here, the RAF applicability was assessed with 3 other materials, namely flat glass and PDMS substrates, as well as a PS nanofiber membrane. Upon octanol-based RAF, the flat plasma-treated superhydrophilic glass substrates became slightly more hydrophobic with an increase in equilibrium CA from 0° to 13° (Figure 10.6a). In contrast, the flat PDMS films became slightly hydrophilic with a decrease in equilibrium CA from 116° to 78° (Figure 10.6b). While the relatively small variations in WCAs are attributed to the lack of a hierarchical surface structure, the inversion of the wetting trend suggests that the amphiphilic self-assembly is substrate dependent. In particular, for the hydrophobicized glass, it is proposed that potentially preferable hydrogen-bonding exists between hydroxyl groups (-OH) of the SiO_2 glass and amphiphilic octanol molecules.[679] This preferential association may induce surface-capture and preservation of octanol entities, thus conferring limited hydrophobicity. In fact, the near-superhydrophobic PS nanofibrous membrane became superhydrophilic upon RAF (Figure 10.6c), in line with observations on the PCL membrane. Interestingly, the PS membrane permeation was significantly more rapid,[30,95,123] and exceeded the rate of droplet spread observed with the PCL one despite having very similar micro- nano-structural configuration (Figure S10.5-10.6). This is

tentatively attributed to enhanced interactions between the octanol and the PS surface that may lead to higher surface coverage.

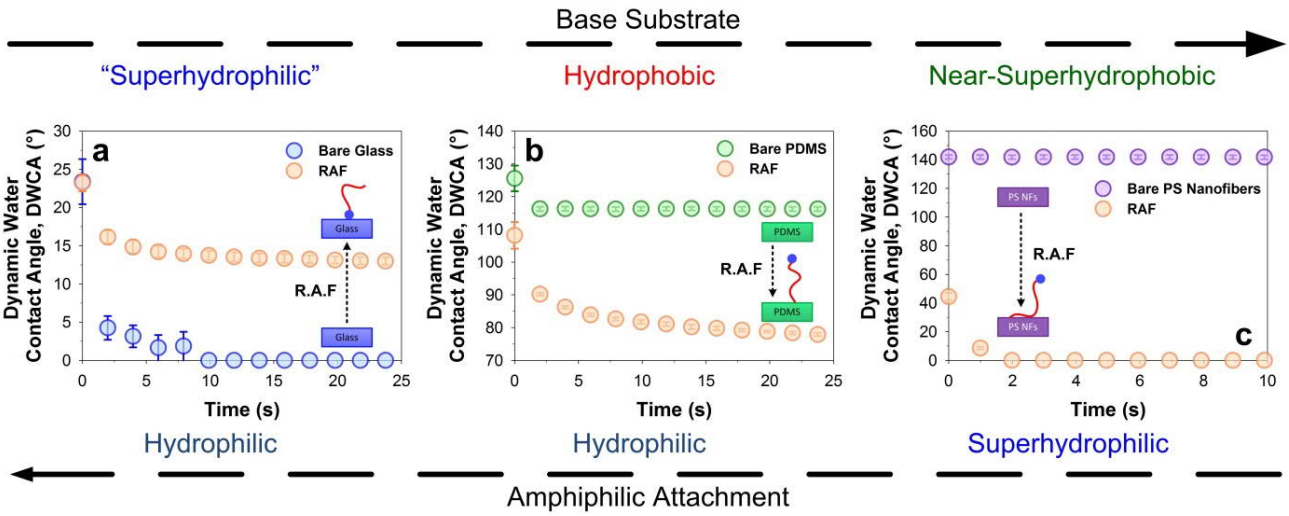

Figure 10.6. Universality of technique demonstrated in a) hydrophobicizing hydrophilic substrates, b) hydrophilicizing hydrophobic substrates and c) tuning superhydrophobic substrates superhydrophilic through molecular self-assembly using amphiphiles, exploiting specific molecular interactions.

Valve-less Cyclic Fluid-gating at Room Temperature

We further developed this RAF approach demonstrating vapor-triggered, valve-less cyclic fluid-gating at room temperature. Here, starting from a permeable DTAB-functionalized PCL membrane, 10 cycles of switchable fluid permeation were demonstrated with octanol-vapor re-functionalization (Figure 10.7a, S10.7). The membranes switched from superhydrophilic to near-superhydrophobic through each wetting cycle, while reinstating superhydrophilicity after RAF. The cyclic super(de)wetting performance was mirrored by the fluid-gating cycles, with no measurable degradation in performance (Figure 10.7b,e). No significant variations to the membrane morphology were observed through these cycles (Figure 10.7c), which under high magnification SEM, appear to be only slightly more compressed.

Expanding beyond these promising results, we designed and tested the potential of remotely opening a wetted membrane gate through the in-situ infusion of octanol vapor (Figure 10.8a). While initial tests revealed a functionalization and flow that is slower than that obtained by the functionalization

of the dry membranes, they demonstrate the first remote switching at room temperature. Specifically, further optimization may allow precise and remote chemical signaling of valve-less fluid gate systems.

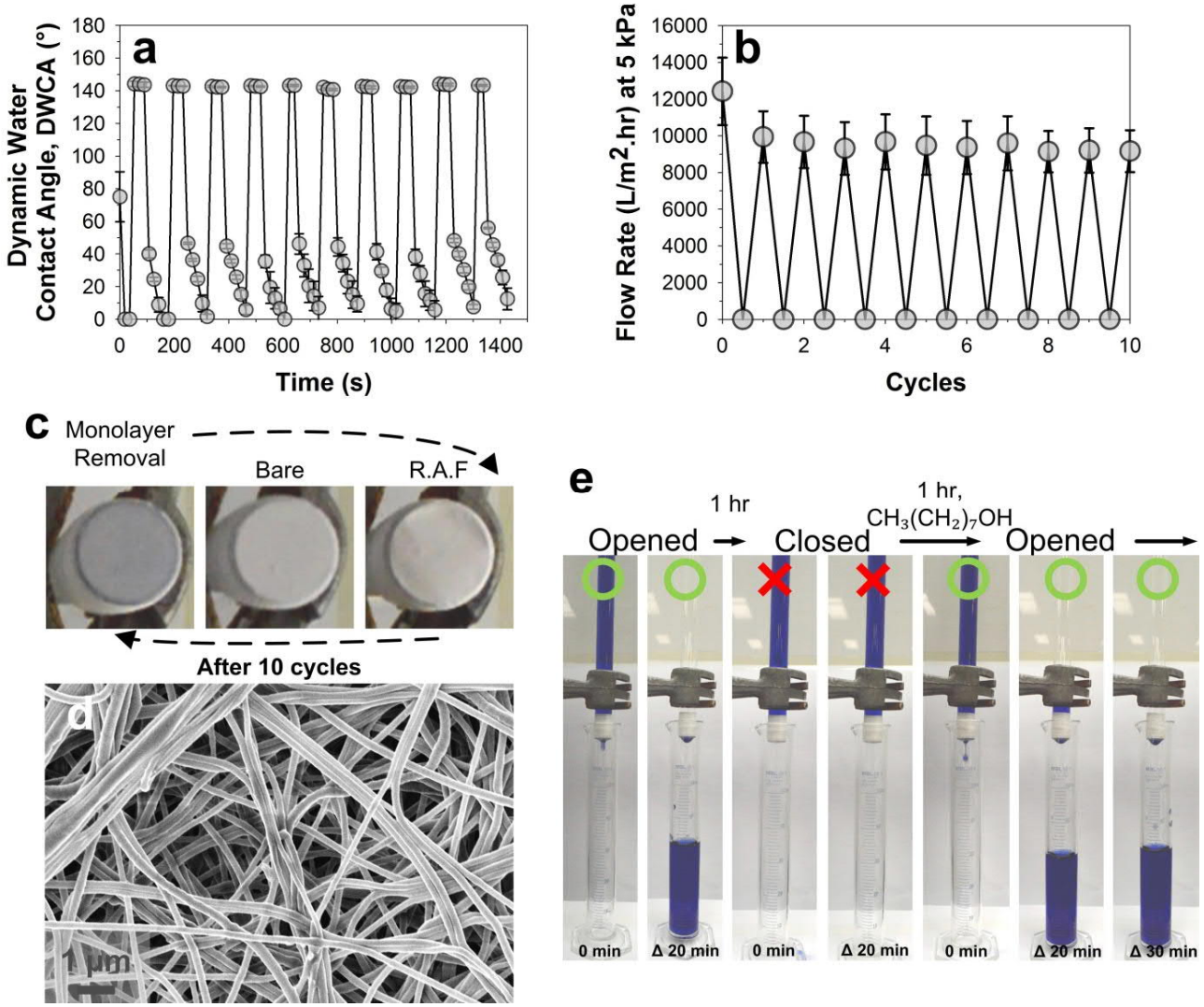

Figure 10.7. Cycling tests for wetting-dewetting cycles of reversible amphiphilic functionalization (RAF). Successful reversible tuning of a) dynamic WCAs and b) permeable-impermeable flow rates. c) Optical photographs, macro-images of membranes from bare and RAF treated membranes. d) Scanning electron micrograph of membrane morphology after 10 treatment cycles (wet-dry-wet), showing no significant degradation. e) Cyclically tested fluid gates (open-close-open) of RAF induced superhydrophilicity and water-wetting induced superhydrophobicity.

Owing to its versatile vapor-directed functionalization regime, RAF was also tested for fluid templating, a concept used in creating droplet arrays and microfluidic chips.[15,45] Here, a PCL membrane was sandwiched behind a simple shadow mask (Figure S10.8) and exposed to octanol vapors. After a brief exposure, imprinted superhydrophilic-superhydrophobic patterns were created (Figure 10.8b, S10.8). Such patterns were well-defined down to diameters of just 1 mm in resolution

(Figure 10.8c, S10.9) with potentially significantly smaller sizes achievable. Unlike conventional droplet arrays,[15,45] these RAF-templated microfluidic chips can be easily erased using water, enabling re-useability of the substrates.

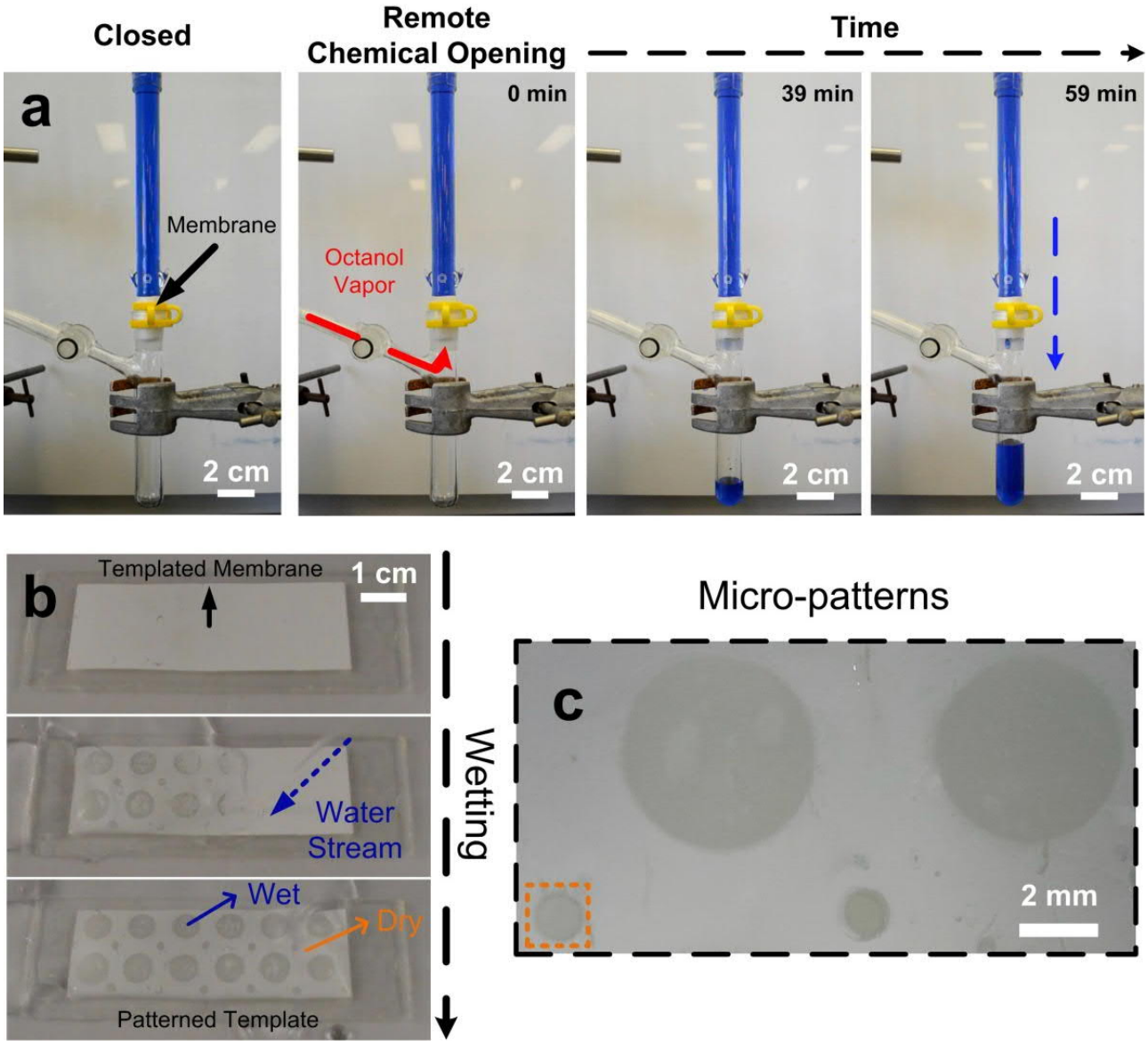

Figure 10.8. Exemplifications of technique in advanced fluid gating and patterning concepts. a) Remote chemical opening channels for fluid delivery. b) Templated membranes for superhydrophobic-superhydrophilic array patterns as cheap, readily erasable yet disposable microfluidics chips. c) Pattern resolution tested down to just 1 mm while being potentially further down-scalable to micron-size patterns due to the ease of gas movement into micro-gaps.

10.3. Conclusions

We presented a novel room-temperature approach for the facile and reversible switching of surfaces from a near-superhydrophobic to a superhydrophilic wetting state. This was achieved by the physisorption of weakly bonded bipolar amphiphiles, here termed as reversible amphiphilic functionalization, on micro- and nano-structured surfaces. This represents a significant advancement, improving upon established approaches based on covalently bonded molecules, thus allowing room-temperature reactant-free switching between extreme super(de)wetting states. We demonstrate this approach by the temporal self-assembly of amphiphilic monolayers on water impermeable nanofibrous membranes, rapidly achieving highly permeable superhydrophilic states. The initial impermeable near-superhydrophobic state was thereafter easily reinstated by desorption of the amphiphiles into the local fluid environment. We showcase the unique potential of this approach by demonstrating the first gas-phase triggered fluid-gating system operable at room-temperature. We further exemplify its broad use *via* the rapid fabrication of erasable microfluidic droplet arrays and valve-less fluid gating systems. We believe that this universal strategy for the dynamic and reversible switching of super(de)wetting bears numerous future applications including intelligent liquid management systems, valve-less gating in macro- and micro-fluidics, templated fluid arrays and smart textiles.

10.4. Experimental Section

Electrospinning of polycaprolactone (PCL) membranes (Hydrophobic)

PCL solutions were made by dissolving 0.948 g of PCL (Sigma Aldrich, M_n = 80,000) in 9 mL of chloroform (Sigma Aldrich, anhydrous, ≥ 99%) and 3 mL of methanol (Sigma Aldrich, anhydrous, ≥ 99.8%). The solution was stirred overnight and used for electrospinning. A horizontal electrospinning setup was utilized, with a spinning drum diameter of 10 cm and a rotation of 300-400 RPM. Electrospinning of PCL was performed at an electrode working distance of 10 cm, electrical potential of 15 kV, flowrate of 0.6 mL/h on 2 syringes for 3.5 hours. Nanofibrous PS membranes were made using the same technique. A PS solution was made using 1.888 g of PS (Sigma Aldrich, M_w = 280 000) in 20 mL of dimethylformamide (Sigma Aldrich, anhydrous, ≥ 99.8%). An electrode working distance of 10 cm, electrical potential of 30 kV, flowrate of 1.5 mL/h on 2 syringes for used 3.5 hours for developing membranes on a spinning drum diameter of 10 cm and a rotation of 300-400 RPM (Figure S10.5).

Gate-modification of polycaprolactone (PCL) membranes (Hydrophobic to Hydrophilic)

Superhydrophobic PCL membranes (Figure S10.3) are impermeable to hydrostatic water pressures of up to 10 kPa. Here, two modes of functionalization can be performed: a) non-volatile and b) volatile functionalization.

a) Non-volatile: 36 mg of dodecyltrimethylammonium bromide (DTAB, Sigma Aldrich, ≥ 98%) was added to the PCL solution prior to electrospinning.

b) Volatile: Dry membranes are kept in a vacuum chamber at room temperature with 1-octanol. An approximate concentration of 2.5 mL octanol in a 25 L chamber was used. The chamber was then kept at a mild vacuum of 10 kPa (ca. $P_{octanol}$ at room temperate) to induce re-assembly of hydrophilic moieties on nanofibrous interfaces. Membranes were left to sit in this environment for 1 hour at a height of 1 mm above the 1-octanol source prior to testing. Membranes produced from these methods are thereafter superhydrophilic.

Gate-modification of polycaprolactone (PCL) membranes (Hydrophilic to Hydrophobic)

Superhydrophobic modification of superhydrophilic PCL membranes was performed facilely by passing 10 mL of fluid through a membrane with a diameter of 11.88 mm (area of 110.85 mm^2). These membranes were then left to sit in an ambient environment (20-25 °C, 10-20% relative humidity) for drying, thus preventing capillary effects during later tests. The surface reorganization of amphiphiles occur during this wet-through stage, enabling the dry gating system.

Cyclic testing of reversibility in PCL-membranes

Tuning near-superhydrophobicity to hemi-wicking superhydrophilicity was performed via sequential exposure to either liquid water (which induces near-superhydrophobicity) or 1-octanol vapors (which induces (hemi-wicking) superhydrophilicity). Water-wetted membranes were dried before tests while 1-octanol-infused membranes were exposed at a height above source of 5 mm, to paper-soaked 1-octanol (2.5 mL in a 25 L chamber, 10kPa) for 1 hour before tests. One sequential exposure to water and 1-octanol vapors denotes 1 cycle. Tests of dynamic WCAs and water permeation rates (at 5kPa hydrostatic pressure) were both measured across 10 cycles. Fresh fluids were used for each cycle. Different climate chambers during adsorption-desorption were used to prevent cross-contamination. 4 cross-batch samples were assessed. Data was presented as mean ± standard errors.

Pressure testing of polycaprolactone (PCL) membranes

PCL membranes (pristine and modified) were then tested for breakthrough pressures based on using hydrostatic pressure of water *via* the ISO 811 standard. These were performed by calibrating a column of water on the membrane until fluid is permeated from the reverse side of the membrane. A membrane area of 110.85 mm^2 was used during the tests. Per the ISO 811 standard, the hydrostatic pressure at which the breakthrough occurred is recorded when water appears at the third location in the specimen. Fluid was dispensed onto the top-side of the membrane at a rate of 10 cmH_2O/min, with breakthrough pressures and water observed and recorded up to the fourth location.

Breakthroughs along the edge of the membrane were not ignored. 6 repeats on 3 cross-batch samples were performed. Data was presented as mean ± standard errors.

Flow testing of polycaprolactone (PCL) membranes

PCL membranes (pristine and modified) were then analyzed for flow rates under controlled hydrostatic pressure. These were performed by creating a column of water on the membrane until fluid starts to permeate from the reverse side of the membrane. A membrane area of 110.85 mm^2 was used during the tests. Flow rates were then measured up to 30 minutes or 35 mL of fluid, whichever first demonstrates steady state. Average flow rate based on these parameters were then computed. In the event that no flow occurs, all reverse sides of membranes were inspected, which all exhibited no signs of wetness. At least 4 cross-batch samples were assessed. Data was presented as mean ± standard errors.

Wettability tests

Wettability was assessed through the measurement of static and dynamic WCAs, by placing and averaging 4 drops of water (5 µL) on 4 cross-batch sample surfaces using the sessile drop method. The CAH for water was measured via the drop-in drop-out (DIDO) technique which provided the average ACA at 9 µL and the average RCA at 2 µL. 4 cross-batch readings were taken. Dynamic and static images were recorded using a KSV CAM200 contact angle goniometer (Finland) with a heliopan ES43 camera (Japan). The CA and CAH were computed by a commercially available (CAM2008) program. Data was presented as mean ± standard errors. To verify the effects of the octanol-assisted amphiphilic functionalization on wetting modifications, a solution of octanol-water was made at the miscibility limit (0.46 g/L). This solution was then centrifuged at 4000 RPM for 10 minutes, and the supernatant was decanted to remove any traces of octanol that remained insoluble. The remaining solution was then used for CA measurements as the probe fluid. The surface tension of the probe fluid was measured using the pendant drop technique. Static and dynamic WCAs were measured up to 100 seconds upon deposition of this fluid on an impermeable membrane in order to

analyze the effects of octanol-saturation on the membrane's impermeable-permeable nature. 4 cross-batch readings were taken. Data was presented as mean ± standard errors. Fluid entering and exiting an octanol-RAF treated membrane was also evaluated through the pendant droplet test. After surface functionalization, pristine deionized water (γ = 72.9 mN/m, 18.2 MΩ) was permeated through the membrane. The 1st 50 µL from a 110.85 mm^2 membrane was collected and evaluated. Steady state flows after 1 mL and 2 mL of eluent were also collected and evaluated. 4 cross-batch readings were taken. Data was presented as mean ± standard errors.

Surface and bulk analysis

Samples were analyzed via scanning electron microscopy (Zeiss UltraPlus analytical scanning electron microscope (FESEM) at 3kV). Prior to examination, SEM specimens were platinum sputter-coated for 2 min at 20 mA. Fourier Transform Infrared-Attenuated Total Reflectance (FTIR-ATR, Bruker-Alpha, U.S.A) was performed (24 scans from 400 to 4000 cm^{-1}) on samples through phases of transformation to analyse bulk properties (0.5 to 2.0 µm penetration). Raman spectroscopy (Horiba, LabRam HR Evolution) was performed, using a 532 nm laser at 22 mW and a 50 X objective at room temperature for 10s of acquisition, giving a quasi-surface resonance analysis (0.7 µm).

X-ray photoelectron spectroscopy (XPS) analysis was performed using an AXIS Nova spectrometer (Kratos Analytical Inc., Manchester, UK) with a monochromated Al Kα source at a power of 180 W (15 kV x 12 mA) and a hemispherical analyzer operating in the fixed analyser transmission mode. The total pressure in the main vacuum chamber during analysis was typically around 10^{-8} mbar. Two different locations were analyzed on each sample at a nominal photoelectron emission angle of 0º w.r.t. the surface normal. Since the actual emission angle is ill-defined in the case of fibers (ranging from 0º to 90º) the sampling depth may range from 0 nm to approx. 10 nm. All elements present were identified from survey spectra. The atomic concentrations of the detected elements were calculated using integral peak intensities and the sensitivity factors supplied by the manufacturer. The accuracy associated with quantitative XPS is ca. 10% - 15%. Precision (ie. reproducibility) depends on the

signal/noise ratio but is usually much better than 5%. The latter is relevant when comparing similar samples.

Membrane analysis was also conducted via white light interferometer (Veeco, Wyko NT9100, USA), which provided 50x to 500x magnification with a field of view (FOV) of 1x via the vertical scanning interferometry (VSI) mode. A backscan of 50 μm and length of 25 μm was used with a modulation of 3% in order to cover the maximum peak-to-trough heights of free-standing membranes.

Exemplifications

Liquid-induced patterning was performed by placing DTAB-fabricated membranes onto double-sided taped glass slides. Water-wetted membranes (DTAB removed) were dried in a vacuum environment before positive patterning. Membranes were then masked and placed at a height 5 mm above a source of paper-soaked 1-octanol (2.5 mL in a 25 L chamber, 10kPa) for 1 hour before use.

Fluid gating was performed using a membrane-gated channel. 2 separate designs were utilized. The first was a semi-continuous design, with the channel being opened to a water stream of 3kPa, then drying, demonstrating channel closure. This was followed by dry RAF functionalization for 1 hr, thereafter demonstrating channel opening. A series of videos were recorded, amounting to a total of 60 minutes. An alternate model of remote functionalization was also attempted, where hydrostatic water pressure of 3 kPa was exerted on the membrane before octanol (1.2 mL) was injected onto a heated source at t = 1 min, inducing vaporization. The octanol-source was 30 cm away from the membrane, and only a room temperature saturation of octanol was induced at the membrane's location. All valves were sealed during the *in situ* surface functionalization process, and the primary valve (Figure S10.8a) was only opened after t = 40 minutes of functionalization to equalize the pressure build-up in the system. A total of 60 minutes of continuous video was recorded throughout the process.

10.5. Supplementary Information

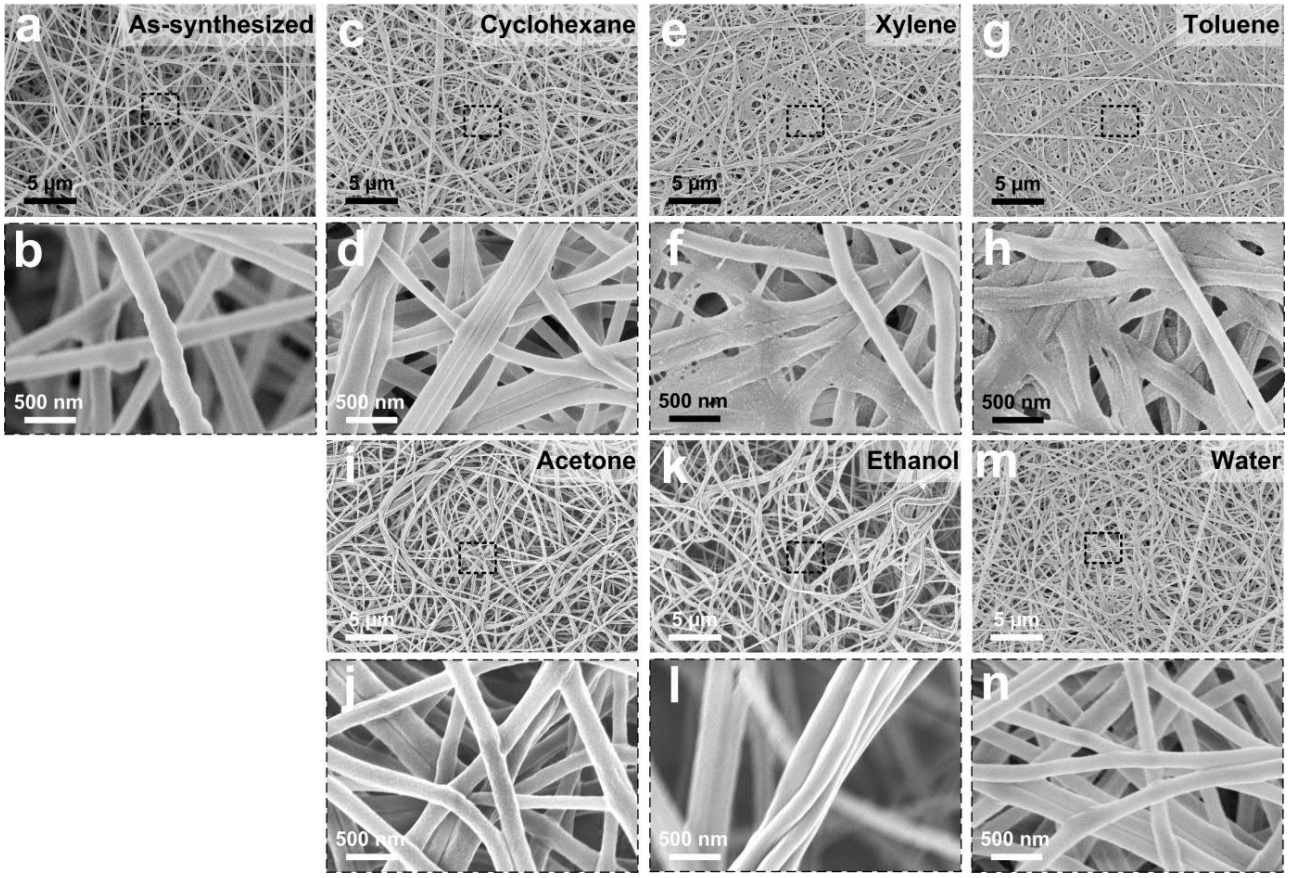

Figure S10.1. Scanning electron micrographs of a,b) as-synthesized, c,d) cyclohexane-, e,f) xylene-, g,h) toluene-, i,j) acetone-, k,l) ethanol and m,n) water eluted membranes.

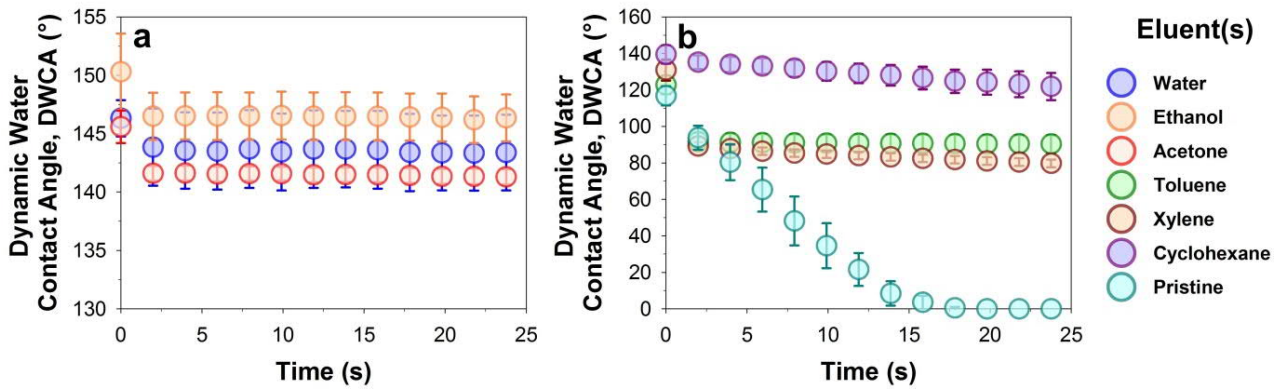

Figure S10.2. Dynamic WCAs of elution-treated membranes with respect to a) superhydrophobic impermeable membranes and b) superhydrophilic permeable membranes.

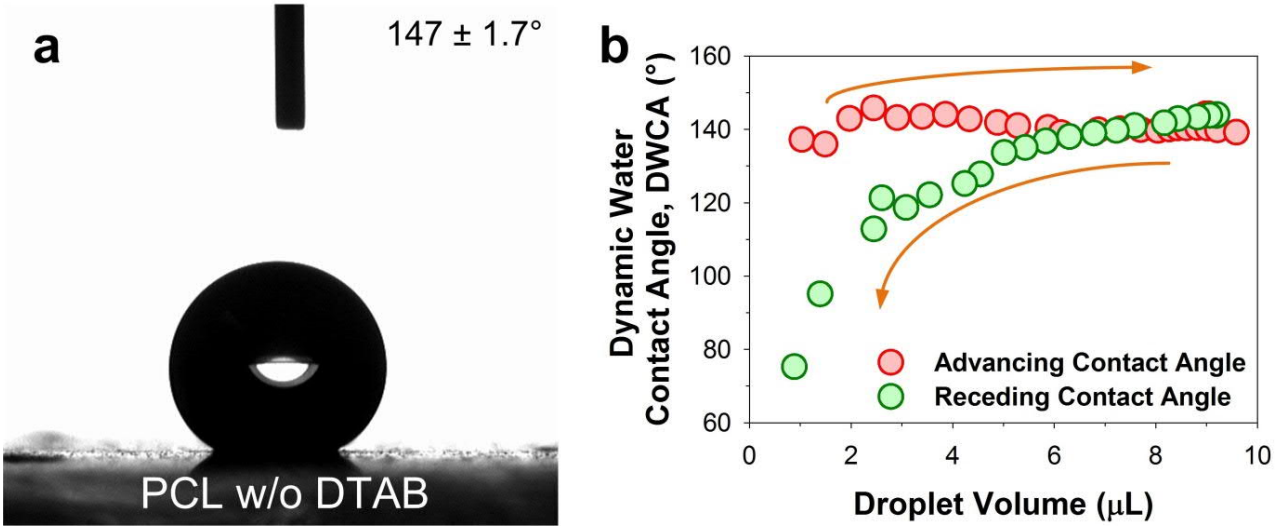

Figure S10.3. a) PCL electrospun without DTAB, highlighting a near-superhydrophobic state, indicative of the influence DTAB has as a one-pot amphiphile for the inducement of superhydrophilicity. b) Dynamic WCA showing ACA and RCA of the near-superhydrophobic state.

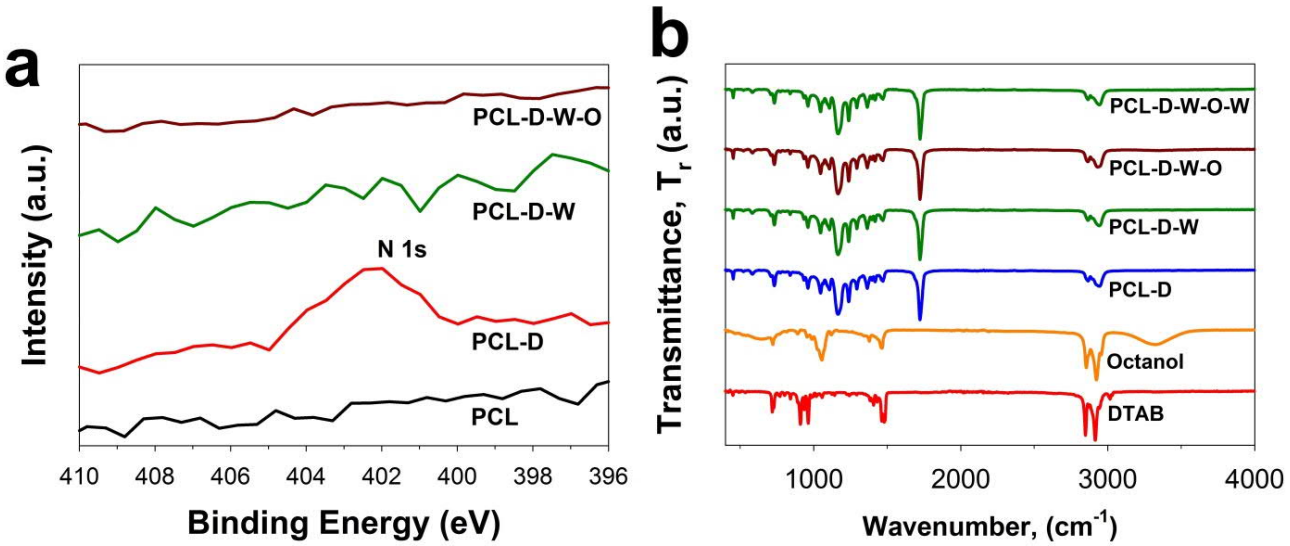

Figure S10.4. a) X-ray photoelectron spectroscopic (XPS) analysis for the detection of one-pot assembled monolayer of DTAB on nanofibers, showing the N 1s peak at 402 eV in the case of DTAB-functionalized PCL. b) Fourier-transform infra-red spectroscopic data showing the lack of detection of either DTAB or octanol in the bulk material of the RAF treated membranes.

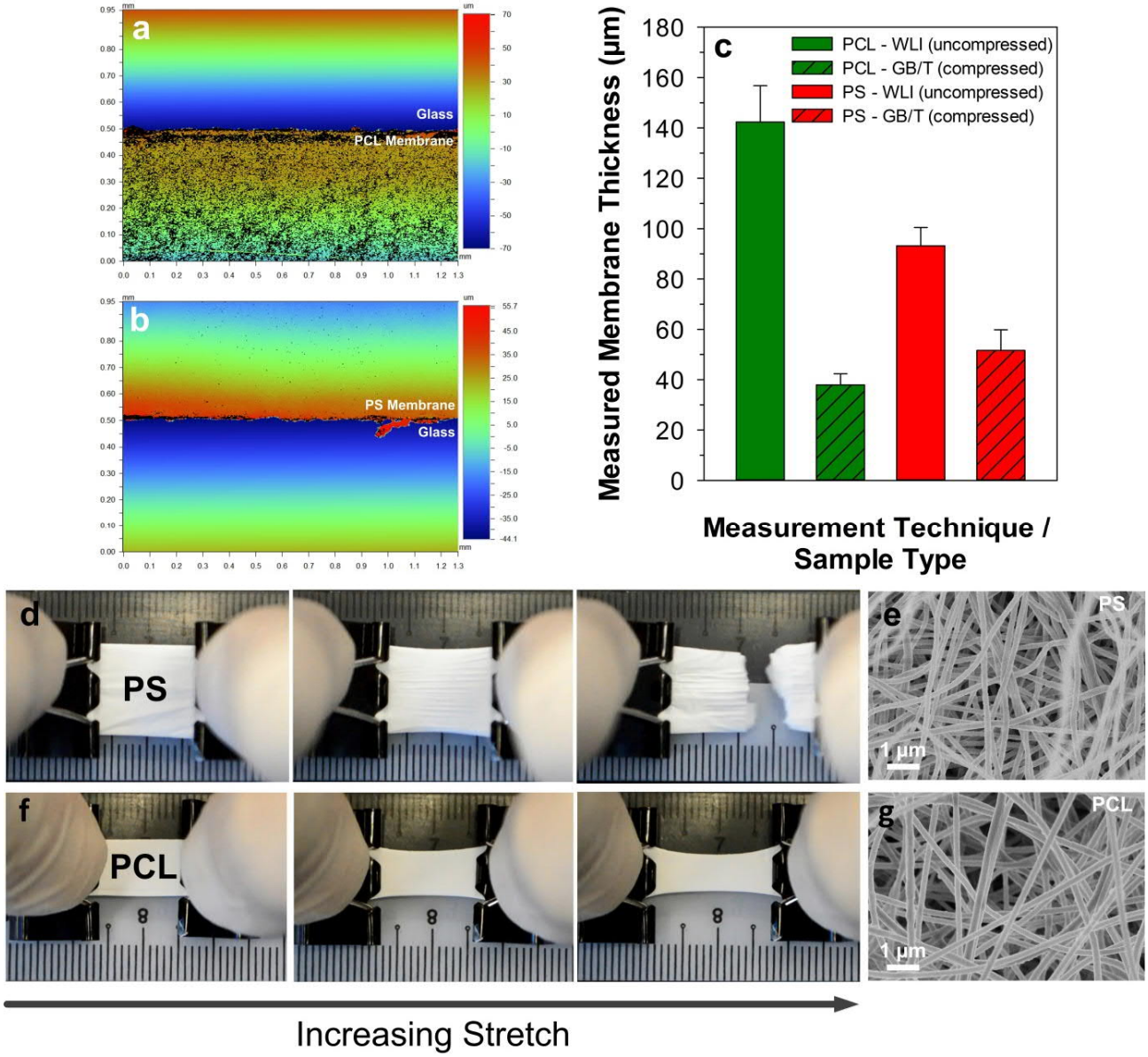

Figure S10.5. White light interferometry derived thicknesses of the developed a) PCL membrane and b) PS analog membrane. Thicknesses were also measured and compared via c) uncompressed (WLI) and compressed membranes (gauge-measured). d) PS membranes were noticeably less stretchable than PCL membranes.

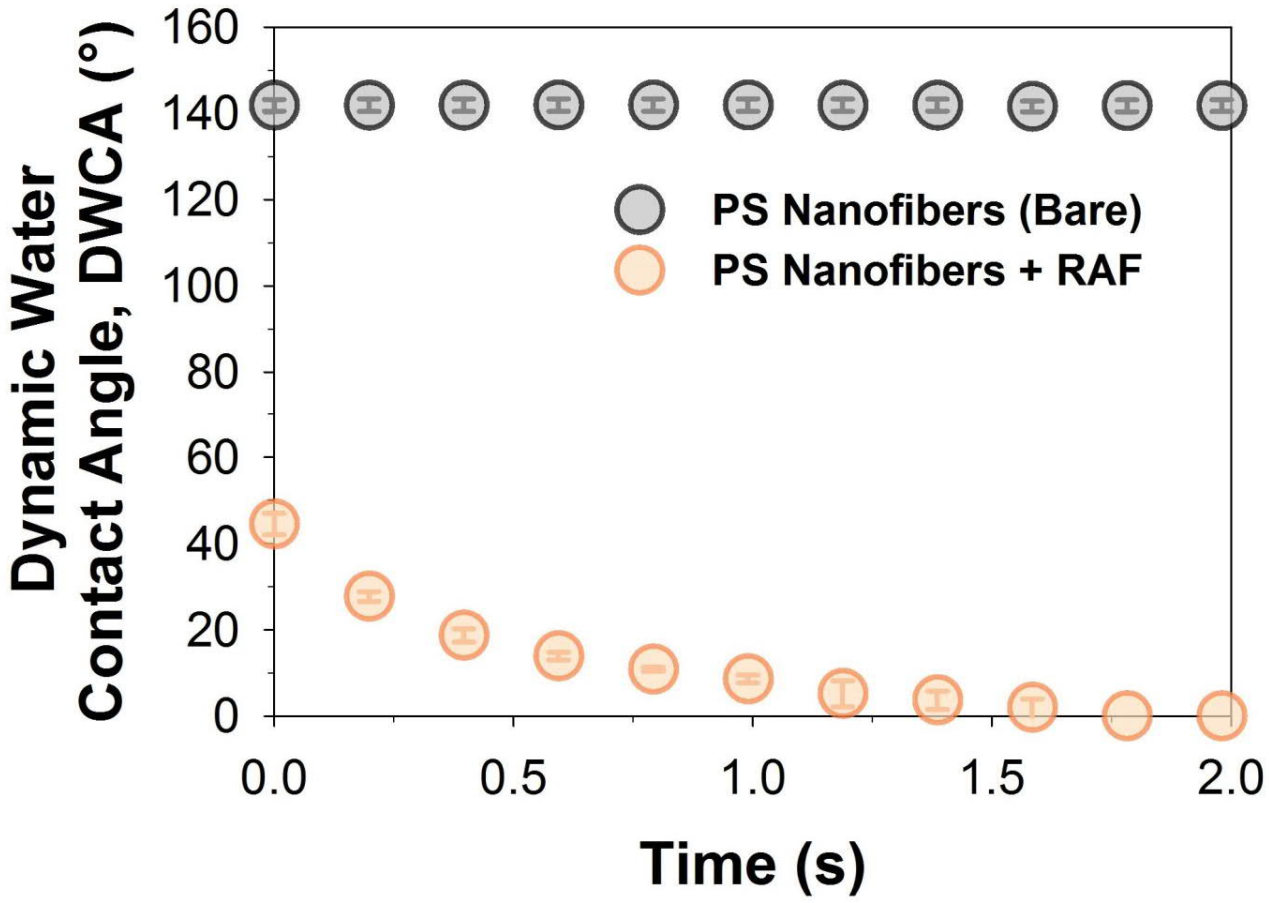

Figure S10.6. Analysis of the absolute superhydrophilicity exhibited by RAF treated PS membranes, with a DWCA drop to < 10 ° within 1 s.

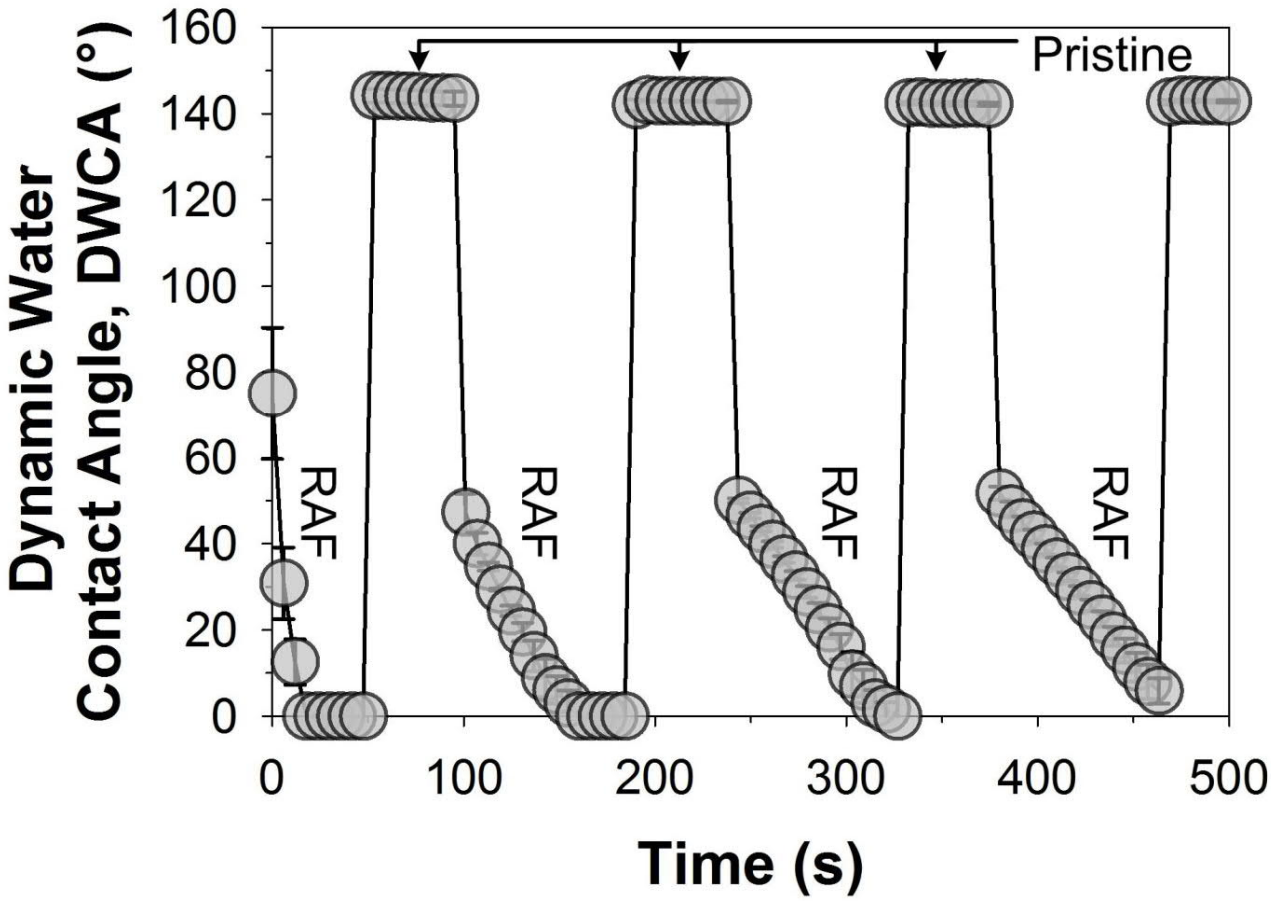

Figure S10.7. Magnified zoom image of 4 cycles of the RAF and elution treatment of membranes, leading to tunable superhydrophilic-superhydrophobic properties.

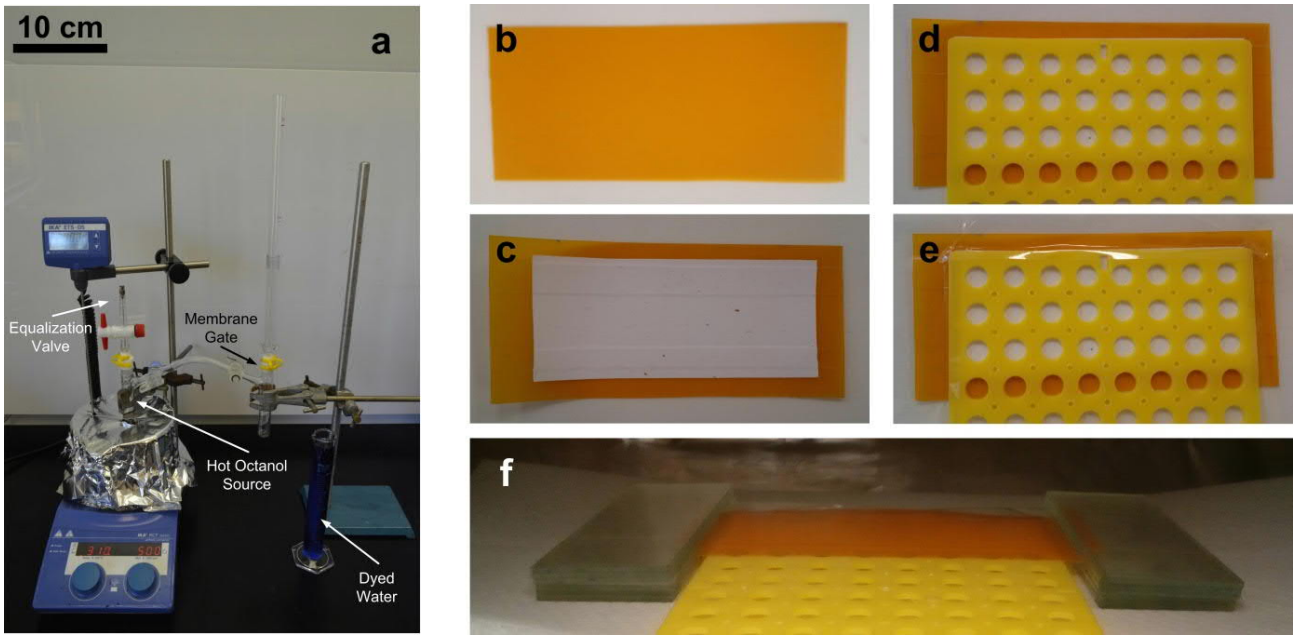

Figure S10.8. a) Set-up for the remote-opening of membrane gates for fluid delivery. Hot octanol source was heated at 200 °C, and valves were opened to influence membrane wettability. b-f) Templating membranes was performed using a simple shadow mask, and exposure of the clamped membrane to octanol vapors.

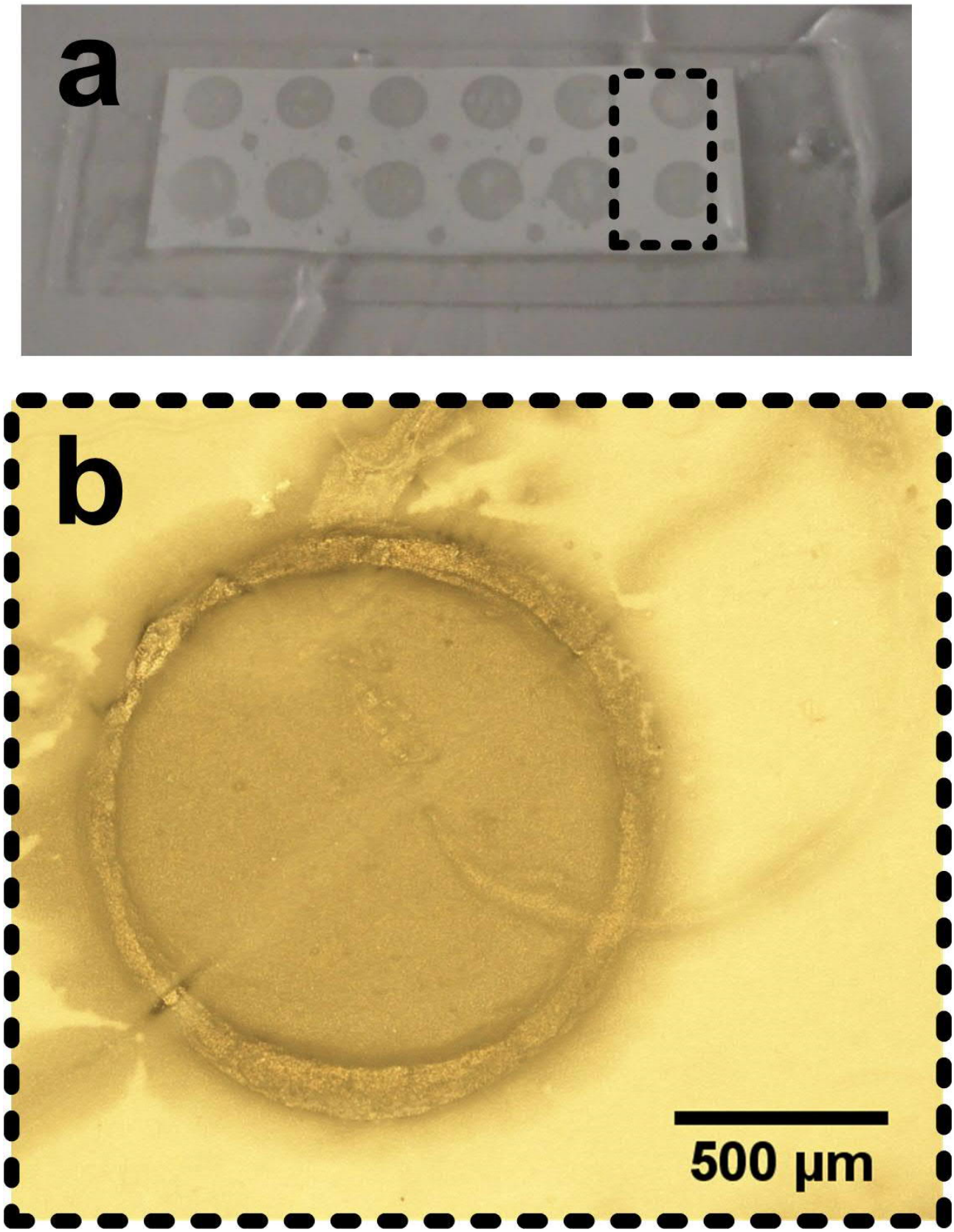

Figure S10.9. a) Templated membrane and an b) optically magnified image of the 1 mm wetted zone.

10.5.1. Supplementary Calculations

Film adsorption due to van der Waals (vdW) interactions

The adsorption of octanol to a hydrophobic surface is driven by dispersion forces therefore the equilibrium film thickness can be determined from the vapor pressure with the following expression,

$$\frac{p}{p_0} = \exp\left(\frac{A\nu}{6\pi D^3 kT}\right) \quad \text{(S10.1)}$$

where p/p_0 is the relative vapor pressure, A is the Hamaker constant (J), ν is the molecular volume (m^3), k is the Boltzmann constant (1.38 × 10-23 $m^2kgs^{-2}K^{-1}$), T is the temperature (K) and D is the equilibrium film thickness (m).

$$\nu = \frac{M}{\rho N_o} \quad \text{(S10.2)}$$

where M is the molecular weight ($kgmol^{-1}$), ρ is the density (kgm^{-3}), N_o is the avogadro's number ($6.02 \times 10^{23}\ mol^{-1}$). The Hamaker constant for this system is not known and cannot be readily calculated from Lifshitz theory due to the absence of the appropriate spectral data for the polymer substrate. The Hamaker constant is estimated to be confined between -0.2 to -0.7 x 10^{-20} J,[674] with the lower and upper limit representing water vapour adsorbing to octane in air or octane vapor adsorbing to quartz in air, respectively. At 298 K and a relative vapor pressure of 0.106,[673] the equilibrium film thickness (or coverage) is calculated to be 0.145-0.22 nm. Octanol's extended molecular length and width are approximately 1.17 nm[675] and 0.28 nm[676] respectively.

Per octanol's physical properties:

$$\nu = \frac{130.23\ x\ 10^{-3}}{(0.824\ x\ 10^3) * (6.02\ x\ 10^{23})}$$

$$\nu = 2.625\ x\ 10^{-28}\ m^3$$

Here, the Hamaker constant may range from -0.2 to -0.7 x 10^{-20} J,[674] with the upper limit modeled for octane vapour adsorbing to quartz in air.

At 298 K, at a relative vapor pressure of $p/p_0 = 0.106$, the equilibrium film thickness (at the upper limit) can be computed as follows:

$$\frac{p}{p_0} = \exp\left(\frac{A\nu}{6\pi D^3 kT}\right)$$

$$\ln\left(\frac{p}{p_0}\right) = \frac{Av}{6\pi D^3 kT}$$

$$D = \sqrt[3]{\frac{Av}{6\pi \ln\left(\frac{p}{p_0}\right) kT}}$$

$$D = \sqrt[3]{\frac{-0.7\ x\ 10^{-20} * 2.625\ x\ 10^{-28}}{6\pi * (-2.244) * 1.38\ x\ 10^{-23} * 298}}$$

$$D = \sqrt[3]{\frac{-1.84\ x\ 10^{-48}}{-1.74\ x\ 10^{-19}}}$$

$$D = 0.219\ nm$$

Table. S10.1. Monolayers of amphiphiles assembled (DTAB and Octanol)

PCL nanofibers, diameter = 156 nm, specific surface area = 22.4 m^2/g			
DTAB, M_w = 308.34		Octanol, M_w = 130.23	
Molecular Area (nm^2)	0.44[677] $Width_{max}$ = 5Å	Molecular Area (nm^2)	0.33[675,676] $Width_{max}$ = 2.8Å
Mass per unit area PCL (mg/m^2)	1.69	Mass per unit area PCL (mg/m^2)	0.52
Molar concentration per unit area (mol/m^2)	5.50 x 10^{-6}	Molar concentration per unit area (mol/m^2)	3.96 x 10^{-6}
Coverage (monolayers)	1.46	Coverage (monolayers)	0.78
Monolayer thickness (nm)	0.729	Monolayer thickness (nm)	0.219[673,674]

11. Conclusions

In this work, we first summarized the latest definitions in the field of wettability. Thereafter, we briefly covered the historical roots of super(de)wettability, which largely originated from bioinspiration. Following this, we described in detail, the most recent and significant advancements in the field of super(de)wetting materials. The techniques used, and their resulting morphological geometries are of particular focus. Surface features can stem from purely bioinspired designs, as well as artificially-augmented architectures. The findings with respect to the latter variant were surmised to be of immediate interest, owing to their potential for commercialization. We placed a particularly strong focus on scalable bottom-up techniques capable of achieving these different states of super(de)wettability. Findings from the state-of-the-art were used as a roadmap for material choices and hierarchical structural designs.

We then began our journey through the different domains of wettability, starting from highly surface energetic superhydrophilicity. It was here, where we discovered the use of low-temperature synthesized, ultra-high specific surface area, amorphous TiO_2 as scalable nanofibrous interfaces for transparent, anti-fogging superhydrophilic coatings. These coatings exhibited UV-independent superhydrophilic properties which resisted in-air storage contamination.[95]

We then moved into the regime of Cassie-Impregnating superhydrophobicity, where a state of adhesive superhydrophobicity exists as a balance between the Cassie-Baxter dewetting and Wenzel wetting states. We utilized a scalable electrospinning technique for the synthesis of unique bead-on-string stacking morphologies from PS, showcasing a rare case of the “ideal” petal-effect. In contrast to prior descriptions of the petal-effect, this idealized state demonstrated clean attachment, detachment and droplet removal. This work demonstrated immense potential for developing contamination-free mechanical hands for applications in fluid manipulation.[89]

After reconsidering the Cassie-Impregnating phenomenon, we designed a mechanically-actuated method for actively transiting between the Cassie-Impregnating and the Cassie-Baxter

superhydrophobic states. Through this, we designed a scalable system composed of wave-like nanofibers, where a fluid droplet is adhered and detached upon command (mechanical actuation). However, this dynamic system did not; unfortunately demonstrate clean fluid detachment as demonstrated in the “ideal” petal-effect before. This was attributed to the inherent difficulties in actively transiting between an “ideal” Cassie-Impregnating and standard Cassie-Baxter states. We were however, able to statically and dynamically switch between the two states without any significant functionality losses in the material.[90]

At this junction, we moved strictly into the domains of superdewetting materials, where the most standard mode of superhydrophobicity; the lotus-effect, was re-visited. Here, we performed an extensive literature review, and found several key weaknesses in the technology, namely 1) robustness, 2) transparency and 3) prolonged functionality. We successfully tackled these problems by creating a robust, highly functional and scalable design with highly transmissive properties. This was enabled through a uniquely formulated binder solution, which we used as a support layer for a standardized superhydrophobic nanomaterial (fluorinated SiO_2). The binder comprised of a sprayable interpenetrated polymeric network, representing a first in the field. This unique material was synthesized as a metastable colloid that gels and sets upon being spray-deposited. Its flexible, yet tough nature enabled elastic recovery of the nanoparticulate coating during wear, thus preventing losses in functionality through extensive abrasion cycles. The casted IPN is also a highly transparent and colorless polymer, with highly tunable transmittance and transparency properties.[91]

Superoleo(amphi)phobicity, or the ability to actively repel oils and other low surface tension fluids, naturally represented the next milestone for the scalable synthesis of superdewetting interfaces. Here, we exploited the well-known but under-utilized liquid flame spray pyrolysis technique for creating re-entrant nanotextures for superoleo(amphi)phobicity. The re-entrant texturing capabilities of the technique were verified by both computational simulations and experimental validation. This demonstration of explicit re-entrancy in superoleo(amphi)phobicity represents a first in the development of highly scalable superoleo(amphi)phobic nanotextured coatings. Moreover, it also

showcased very well-defined re-entrant nanotextures that were self-assembled from a nanoparticle aerosol. Its capability for coating convoluted and uneven substrate surfaces was also unprecedented.[92]

At this point, we have journeyed through all domains of super(de)wettability (with the exception of superomniphobicity) *via* highly scalable techniques. The potential of these scalable techniques were then exemplified through the design of fluidic-functional micro-devices. The first concept stems from exploiting the counter-intuitive combination of superhydrophilic and superhydrophobic materials in a unified Janus interface. This work showcased the unique ability of harvesting wetting surface energies into mechanical motion, through a stimuli-responsive concept for microfluidic applications.[93] The second concept culminates from the burgeoning interest behind developments in switchable wettability. This stimulated the development of a membrane gate that is activated by amphiphilic functionalization, showcasing capability for room-temperature reversible super(de)wettability. The third concept made use of super(oleo)amphiphobic coatings in and on ultra-fine hypodermic needle tips, thus culminating in the production of contamination-proof fluid manipulation microtools. These tools were able to manipulate/dispense micro- and nano-droplets of water, oil and low-surface tension organic solvents, demonstrating great promise for droplet analysis, microfluidics and micromechanical hands.[94]

11.1. Future Work and Unexplored Horizons

The work here has demonstrated our journey through scalable engineering techniques for exploring the entire spectrum of wettability. This has ranged from superwetting states of superhydrophilicity,[95] to adhesive[89] and slippery superhydrophobicity.[90,91] We then surpassed the superhydrophobic state, and moved into domains of superoleo(amphi)phobicity.[92] Applications[89-95,360] owing to all 4 states of wettability were hypothesized, designed and demonstrated. This ranged from simple surface coating technologies[91,92,95,360] to complex systems comprising of fluid gates and self-assembling micro-devices[89,90,93,94].

Regardless of the progress, much work remains to be achieved in the field. For instance, the proof-of-concepts demonstrated for superoleo(amphi)phobicity and (potentially?) superomniphobicity are currently still too fragile for direct industrial application. Moreover, research directions set out by the community have placed overwhelming focus on specific geometries which are physically metastable.

This emphasis and dogma could limit the further research and development, while affecting its commercial scalability and continued industrialization. The research community must strive to depart from this self-imposed limitation, while proposing and exploring venues which could lead to simpler methods for achieving industrially applicable superamphi(omni)phobic states.

11.2. Postscript

Despite rapid advancements in the field, surface wettability continues to be a complex scientific and engineering problem. Notwithstanding the visually simplistic outlook of the field, many parameters are attributed to each and every single phenomenon. Fully understanding the nature and inner workings of surface wettability is no humble endeavour. We are constantly reminded of this through the continuously changing definitions governing superhydrophilicity, superhydrophobicity, superoleo(amphi)phobicity, superomniphobicity and even SLIPS. The emergence of new surface wetting phenomenon and dynamic analysis constantly brings about fundamental changes in our understanding of the field. The revolutionized understanding of the area continuously threatens to overhaul traditional theories in the field. For instance, is the hydrophilic-hydrophobic limit now established at a Young's CA of 65°? What will now happen to the Cassie-Baxter and Wenzel equations, and the years of theoretical build-up that utilizes these as base assumptions? What about the influence of these so-called re-entrant geometries which are seemingly required for superoleo(amphi- and omni-)phobicity, when an increasing amount of research seems to suggest alternate pathways. We should also not consider the multiple parallel fields of wettability as separate domains of research. How will the field of super(de)wettability fit in with its younger counterparts such as the slippery fluid-infused porous surfaces (SLIPs)? Alternatively, how well will they continue to synergise with older concepts such as the Leidenfrost effect? Given the field's rapid approach towards superoleo(amphi)phobicity and superomniphobicity, will superhydrophobicity start to lose its importance and significance in the eyes of the research and industrial communities? In addition, how would these parallel wetting states measure up to new engineering problems such as anti-biofouling, drag reduction or supericephobicity (anti-icing)?

“Fahre fort, übe nicht allein die Kunst, sondern dringe auch in ihr Inneres; sie verdient es, denn nur die Kunst und die Wissenschaft erhöhen den Menschen bis zur Gottheit.”

“Don’t only practice your art, but force your way into its secrets, for it and knowledge can raise men to the divine.”

Ludwig van Beethoven (1770-1827)

References

1. T. Young, *Phil. Trans. R. Soc.* **1805**, *95*, 65.
2. E. W. Washburn, *Phys. Rev.* **1921**, *17*, 273.
3. R. N. Wenzel, *Ind. Eng. Chem. Res.* **1936**, *28*, 988.
4. A. Cassie; S. Baxter, *J. Chem. Soc. Faraday Trans.* **1944**, *40*, 546.
5. R. Wang; K. Hashimoto; A. Fujishima; M. Chikuni; E. Kojima; A. Kitamura; M. Shimohigoshi; T. Watanabe, *Nature* **1997**, *388*, 431.
6. C. Neinhuis; W. Barthlott, *Ann. Bot* **1997**, *79*, 667.
7. W. Barthlott; C. Neinhuis, *Planta* **1997**, *202*, 1.
8. J. Drelich; E. Chibowski; D. D. Meng; K. Terpilowski, *Soft Matter* **2011**, *7*, 9804.
9. A. Lafuma; D. Quere, *Nature Mater.* **2003**, *2*, 457.
10. L. Feng; Y. Zhang; J. Xi; Y. Zhu; N. Wang; F. Xia; L. Jiang, *Langmuir* **2008**, *24*, 4114.
11. A. Tuteja; W. Choi; M. Ma; J. M. Mabry; S. A. Mazzella; G. C. Rutledge; G. H. McKinley; R. E. Cohen, *Science* **2007**, *318*, 1618.
12. T. L. Liu; C.-J. C. Kim, *Science* **2014**, *346*, 1096.
13. H. Zhao; K. C. Park; K. Y. Law, *Langmuir* **2012**, *28*, 14925.
14. X. Deng; L. Mammen; H.-J. Butt; D. Vollmer, *Science* **2012**, *335*, 67.
15. E. Ueda; P. A. Levkin, *Adv. Mater.* **2013**, *25*, 1234.
16. J. Drelich; E. Chibowski, *Langmuir* **2010**, *26*, 18621.
17. C. Cao; H. F. Chan; J. Zang; K. W. Leong; X. Zhao, *Adv. Mater.* **2014**, *26*, 1763.
18. J. C. Bird; R. Dhiman; H. M. Kwon; K. K. Varanasi, *Nature* **2013**, *503*, 385.
19. S. Wang; K. Liu; X. Yao; L. Jiang, *Chem. Rev.* **2015**, *115*, 8230.
20. K. Koch; W. Barthlott, *Phil. Trans. R. Soc. Lond. A* **2009**, *367*, 1487.
21. D. Ebert; B. Bhushan, *J. Colloid Interface Sci.* **2012**, *384*, 182.
22. R. Hensel; A. Finn; R. Helbig; H.-G. Braun; C. Neinhuis; W.-J. Fischer; C. Werner, *Adv. Mater.* **2014**, *26*, 2029.
23. D. Quéré, *Annu. Rev. Mater. Res.* **2008**, *38*, 71.
24. X. Wang; J. A. Hagen; I. Papautsky, *Biomicrofluidics* **2013**, *7*, 14107.
25. Z. Dong; J. Ma; L. Jiang, *ACS Nano* **2013**, *7*, 10371.
26. D. Wu; S. Z. Wu; Q. D. Chen; Y. L. Zhang; J. Yao; X. Yao; L. G. Niu; J. N. Wang; L. Jiang; H. B. Sun, *Adv. Mater.* **2011**, *23*, 545.
27. C. Py; P. Reverdy; L. Doppler; J. Bico; B. Roman; C. N. Baroud, *Phys. Rev. Lett.* **2007**, *98*, 156103.
28. J. Gu; P. Xiao; J. Chen; J. Zhang; Y. Huang; T. Chen, *ACS Appl. Mater. Interfaces* **2014**, *6*, 16204.
29. Y. Lu; S. Sathasivam; J. Song; C. R. Crick; C. J. Carmalt; I. P. Parkin, *Science* **2015**, *347*, 1132.
30. A. Tricoli; M. Righettoni; S. E. Pratsinis, *Langmuir* **2009**, *25*, 12578.
31. H. Thissen; T. Gengenbach; R. du Toit; D. F. Sweeney; P. Kingshott; H. J. Griesser; L. Meagher, *Biomaterials* **2010**, *31*, 5510.
32. M. L. Carman; T. G. Estes; A. W. Feinberg; J. F. Schumacher; W. Wilkerson; L. H. Wilson; M. E. Callow; J. A. Callow; A. B. Brennan, *Biofouling* **2006**, *22*, 11.
33. C. Li; Z. Wang; P. I. Wang; Y. Peles; N. Koratkar; G. P. Peterson, *Small* **2008**, *4*, 1084.
34. T. M. Schutzius; S. Jung; T. Maitra; P. Eberle; C. Antonini; C. Stamatopoulos; D. Poulikakos, *Langmuir* **2015**, *31*, 4807.
35. S. Zhang; X. Ouyang; J. Li; S. Gao; S. Han; L. Liu; H. Wei, *Langmuir* **2015**, *31*, 587.
36. C. H. Xue; Y. R. Li; P. Zhang; J. Z. Ma; S. T. Jia, *ACS Appl. Mater. Interfaces* **2014**, *6*, 10153.
37. G. Azimi; R. Dhiman; H.-M. Kwon; A. T. Paxson; K. K. Varanasi, *Nature Mater.* **2013**, *12*, 315.
38. A. M. Telford; B. S. Hawkett; C. Such; C. Neto, *Chem. Mater.* **2013**, *25*, 3472.

39. D. Wu; S. Z. Wu; Q. D. Chen; Y. L. Zhang; J. Yao; X. Yao; L. G. Niu; J. N. Wang; L. Jiang; H. B. Sun, *Adv. Mater.* **2011**, *23*, 545.
40. D. Zahner; J. Abagat; F. Svec; J. M. Frechet; P. A. Levkin, *Adv. Mater.* **2011**, *23*, 3030.
41. L. Mazutis; J. Gilbert; W. L. Ung; D. A. Weitz; A. D. Griffiths; J. A. Heyman, *Nature Protoc.* **2013**, *8*, 870.
42. Z. Rong; Y. Zhou; B. Chen; J. Robertson; W. Federle; S. Hofmann; U. Steiner; P. Goldberg-Oppenheimer, *Adv. Mater.* **2014**, *26*, 1456.
43. X. Hong; X. Gao; L. Jiang, *J. Am. Chem. Soc.* **2007**, *129*, 1478.
44. K.-C. Park; S. S. Chhatre; S. Srinivasan; R. E. Cohen; G. H. McKinley, *Langmuir* **2013**, *29*, 13269.
45. W. Feng; L. Li; E. Ueda; J. Li; S. Heißler; A. Welle; O. Trapp; P. A. Levkin, *Adv. Mater. Interfaces* **2014**, *1*, doi: 10.1002/admi.201400269.
46. A. N. Efremov; M. Grunze; P. A. Levkin, *Adv. Mater. Interfaces* **2014**, *1: 1300075*.
47. K. Sasaki; M. Tenjimbayashi; K. Manabe; S. Shiratori, *ACS Appl. Mater. Interfaces* **2016**, *8*, 651.
48. X. Hou; Y. Hu; A. Grinthal; M. Khan; J. Aizenberg, *Nature* **2015**, *519*, 70.
49. X. Tian; H. Jin; J. Sainio; R. H. A. Ras; O. Ikkala, *Adv. Funct. Mater.* **2014**, *24*, 6023.
50. Z. Xu; Y. Zhao; H. Wang; X. Wang; T. Lin, *Angew. Chem. Int. Ed.* **2015**, *54*, 4527.
51. J. Zhang; S. Seeger, *Angew. Chem. Int. Ed.* **2011**, *50*, 6652.
52. J. Zhang; S. Seeger, *Adv. Funct. Mater.* **2011**, *21*, 4699.
53. P. S. Brown; B. Bhushan, *Sci. Rep.* **2015**, *5*, 8701.
54. J. Zimmermann; F. A. Reifler; G. Fortunato; L.-C. Gerhardt; S. Seeger, *Adv. Funct. Mater.* **2008**, *18*, 3662.
55. K. Tsujii; T. Yamamoto; T. Onda; S. Shibuichi, *Angew. Chem. Int. Ed.* **1997**, *36*, 1011.
56. A. K. Kota; Y. Li; J. M. Mabry; A. Tuteja, *Adv. Mater.* **2012**, *24*, 5838.
57. T. C. Rangel; A. F. Michels; F. Horowitz; D. E. Weibel, *Langmuir* **2015**, *31*, 3465.
58. A. K. Epstein; B. Pokroy; A. Seminara; J. Aizenberg, *Proc. Natl. Acad. Sci. U.S.A.* **2011**, *108*, 995.
59. H. Vahabi; W. Wang; S. Movafaghi; A. K. Kota, *ACS Appl. Mater. Interfaces* **2016**, *8*, 21962.
60. W. Feng; L. Li; X. Du; A. Welle; P. A. Levkin, *Adv. Mater.* **2016**, *28*, 3202.
61. S. Pan; R. Guo; W. Xu, *AlChE J.* **2014**, *60*, 2752.
62. J. Yang; Z. Zhang; X. Xu; X. Zhu; X. Men; X. Zhou, *J. Mater. Chem.* **2012**, *22*, 2834.
63. X. Yao; J. Gao; Y. Song; L. Jiang, *Adv. Funct. Mater.* **2011**, *21*, 4270.
64. J. Li; Q. H. Qin; A. Shah; R. H. A. Ras; X. Tian; V. Jokinen, *Sci. Adv.* **2016**, *2*.
65. S. Pan; A. K. Kota; J. M. Mabry; A. Tuteja, *J. Am. Chem. Soc.* **2013**, *135*, 578.
66. K. Golovin; D. H. Lee; J. M. Mabry; A. Tuteja, *Angew. Chem. Int. Ed.* **2013**, *52*, 13007.
67. Y. Gao; I. Gereige; A. El Labban; D. Cha; T. T. Isimjan; P. M. Beaujuge, *ACS Appl. Mater. Interfaces* **2014**, *6*, 2219.
68. D. Ebert; B. Bhushan, *Langmuir* **2012**, *28*, 11391.
69. G. M. Whitesides, *Nature* **2006**, *442*, 368.
70. A. K. Kota; G. Kwon; W. Choi; J. M. Mabry; A. Tuteja, *Nat. Commun.* **2012**, *3*, 1025.
71. J. Yeo; M. J. Choi; D. S. Kim, *J. Micromech. Microeng.* **2010**, *20*, 025028.
72. H. Zhao; K.-Y. Law; V. Sambhy, *Langmuir* **2011**, *27*, 5927.
73. K. Li; J. Ju; Z. Xue; J. Ma; L. Feng; S. Gao; L. Jiang, *Nat. Commun.* **2013**, *4*.
74. M. Im; H. Im; J.-H. Lee; J.-B. Yoon; Y.-K. Choi, *Soft Matter* **2010**, *6*, 1401.
75. R. Hensel; R. Helbig; S. Aland; H.-G. Braun; A. Voigt; C. Neinhuis; C. Werner, *Langmuir* **2013**, *29*, 1100.
76. G. M. Whitesides; B. Grzybowski, *Science* **2002**, *295*, 2418.
77. A. Tricoli; T. D. Elmøe, *AlChE J.* **2012**, *58*, 3578.
78. N. Nasiri; T. D. Elmoe; Y. Liu; Q. H. Qin; A. Tricoli, *Nanoscale* **2015**, *7*, 9859.
79. T. D. Elmøe; A. Tricoli; J.-D. Grunwaldt, *Powder Technol.* **2011**, *207*, 279.

80. A. Tricoli; M. Graf; F. Mayer; S. Kuühne; A. Hierlemann; S. E. Pratsinis, *Adv. Mater.* **2008**, *20*, 3005.
81. G. Liu; J. Hall; N. Nasiri; T. Gengenbach; L. Spiccia; M. H. Cheah; A. Tricoli, *ChemSusChem* **2015**, *8*, 4162.
82. J. Zhang; K. Qiu; B. Sun; J. Fang; K. Zhang; H. Ei-Hamshary; S. S. Al-Deyab; X. Mo, *J. Mater. Chem. B* **2014**, *2*, 7945.
83. Y. Miyauchi; B. Ding; S. Shiratori, *Nanotechnology* **2006**, *17*, 5151.
84. C.-L. Pai; M. C. Boyce; G. C. Rutledge, *Macromolecules* **2009**, *42*, 2102.
85. A. Das; T. M. Schutzius; I. S. Bayer; C. M. Megaridis, *Carbon* **2012**, *50*, 1346.
86. Y. Li; S. Chen; M. Wu; J. Sun, *Adv. Mater.* **2014**, *26*, 3344.
87. A. Steele; I. Bayer; E. Loth, *Nano Lett.* **2009**, *9*, 501.
88. W. Wu; X. Wang; X. Liu; F. Zhou, *ACS Appl. Mater. Interfaces* **2009**, *1*, 1656.
89. W. S. Y. Wong; N. Nasiri; G. Liu; N. Rumsey-Hill; V. S. J. Craig; D. R. Nisbet; A. Tricoli, *Adv. Mater. Interfaces* **2015**, *2*, doi: 10.1002/admi.201500071.
90. W. S. Y. Wong; P. Gutruf; S. Sriram; M. Bhaskaran; Z. Wang; A. Tricoli, *Adv. Funct. Mater.* **2016**, *26*, 399.
91. W. S. Y. Wong; Z. H. Stachurski; D. R. Nisbet; A. Tricoli, *ACS Appl. Mater. Interfaces* **2016**, *8*, 13615.
92. W. S. Y. Wong; G. Liu; N. Nasiri; C. Hao; Z. Wang; A. Tricoli, *ACS Nano* **2016**, *11*, 587.
93. W. S. Y. Wong; M. Li; D. R. Nisbet; V. S. J. Craig; Z. Wang; A. Tricoli, *Sci. Adv.* **2016**, *2*, e1600417.
94. W. S. Y. Wong; G. Liu; A. Tricoli, *Small* **2017**, *13*, 1603688.
95. W. S. Y. Wong; N. Nasiri; A. L. Rodriguez; D. R. Nisbet; A. Tricoli, *J. Mater. Chem. A* **2014**, *2*, 15575.
96. R. E. Johnson; R. H. Dettre, *J. Phys. Chem.* **1964**, *68*, 1744.
97. R. H. Dettre; R. E. Johnson, *J. Phys. Chem.* **1965**, *69*, 1507.
98. F. E. Bartell; J. W. Shepard, *J. Phys. Chem.* **1953**, *57*, 455.
99. J. M. Berg; L. G. T. Eriksson; P. M. Claesson; K. G. N. Borve, *Langmuir* **1994**, *10*, 1225.
100. S. Li; J. Huang; Z. Chen; G. Chen; Y. Lai, *J. Mater. Chem. A* **2017**, *5*, 31.
101. B. Su; Y. Tian; L. Jiang, *J. Am. Chem. Soc.* **2016**, *138*, 1727.
102. E. A. Vogler, *Adv. Colloid Interface Sci.* **1998**, *74*, 69.
103. T. Nishino; M. Meguro; K. Nakamae; M. Matsushita; Y. Ueda, *Langmuir* **1999**, *15*, 4321.
104. C. O. Timmons; W. A. Zisman, *J. Colloid Interface Sci.* **1966**, *22*, 165.
105. P. Brunet; F. Lapierre; V. Thomy; Y. Coffinier; R. Boukherroub, *Langmuir* **2009**, *25*, 3321.
106. M. V. Panchagnula; S. Vedantam, *Langmuir* **2007**, *23*, 13242.
107. L. Gao; T. J. McCarthy, *Langmuir* **2007**, *23*, 13243.
108. M. Nosonovsky, *Langmuir* **2007**, *23*, 9919.
109. L. Gao; T. J. McCarthy, *Langmuir* **2007**, *23*, 3762.
110. C. W. Extrand, *Langmuir* **2003**, *19*, 3793.
111. P. G. de Gennes, *Rev. Mod. Phys.* **1985**, *57*, 827.
112. D. Orejon; K. Sefiane; M. E. R. Shanahan, *Langmuir* **2011**, *27*, 12834.
113. G. McHale, *Langmuir* **2007**, *23*, 8200.
114. A. Marmur; E. Bittoun, *Langmuir* **2009**, *25*, 1277.
115. H. Y. Erbil; C. E. Cansoy, *Langmuir* **2009**, *25*, 14135.
116. Y. Pomeau; J. Vannimenus, *J. Colloid Interface Sci.* **1985**, *104*, 477.
117. J. F. Joanny; P. G. de Gennes, *J. Chem. Phys.* **1984**, *81*, 552.
118. D. Öner; T. J. McCarthy, *Langmuir* **2000**, *16*, 7777.
119. E. Chibowski, *Adv. Colloid Interface Sci.* **2003**, *103*, 149.
120. E. J. Chibowski, *Adv. Colloid Interface Sci.* **2005**, *113*, 121.
121. E. Chibowski, *Adv. Colloid Interface Sci.* **2007**, *133*, 51.
122. C. W. Extrand; Y. Kumagai, *J. Colloid Interface Sci.* **1995**, *170*, 515.
123. F. Ç. Cebeci; Z. Wu; L. Zhai; R. E. Cohen; M. F. Rubner, *Langmuir* **2006**, *22*, 2856.

124. C. Ishino; M. Reyssat; E. Reyssat; K. Okumura; D. Quéré, *EPL* **2007**, *79*, 56005.
125. E. Martines; K. Seunarine; H. Morgan; N. Gadegaard; C. D. W. Wilkinson; M. O. Riehle, *Nano Lett.* **2005**, *5*, 2097.
126. A. Y. Vorobyev; C. Guo, *Opt. Express* **2010**, *18*, 6455.
127. J. Bico; U. Thiele; D. Quéré, *Colloids Surf. A* **2002**, *206*, 41.
128. B. S. Kim; S. Shin; S. J. Shin; K. M. Kim; H. H. Cho, *Langmuir* **2011**, *27*, 10148.
129. S. Shahi, *Nature Photon.* **2010**, *4*, 350.
130. L. Courbin; J. C. Bird; M. Reyssat; H. A. Stone, *J. Phys. Condens. Matter* **2009**, *21*, 464127.
131. E. Bormashenko, *Phil. Trans. R. Soc. A* **2010**, *368*, 4695.
132. M. Nosonovsky; B. Bhushan. *Lotus Versus Rose: Biomimetic Surface Effects*. Springer: Berlin, Germany, 2012; doi: 10.1007/978-3-642-23681-5_2p 25.
133. L. Jiang; Y. Zhao; J. Zhai, *Angew. Chem. Int. Ed.* **2004**, *43*, 4338.
134. E. Bormashenko; Y. Bormashenko; G. Whyman; R. Pogreb; A. Musin; R. Jager; Z. Barkay, *Langmuir* **2008**, *24*, 4020.
135. H. Teisala; M. Tuominen; M. Aromaa; M. Stepien; J. M. Makela; J. J. Saarinen; M. Toivakka; J. Kuusipalo, *Langmuir* **2012**, *28*, 3138.
136. B. Bhushan; Y. C. Jung; K. Koch, *Philosophical transactions. Series A, Mathematical, physical, and engineering sciences* **2009**, *367*, 1631.
137. B. Bhushan; M. Nosonovsky, *Phil. Trans. R. Soc. A* **2010**, *368*, 4713.
138. W. K. Cho; I. S. Choi, *Adv. Funct. Mater.* **2008**, *18*, 1089.
139. M. Nosonovsky; B. Bhushan. *Gecko-Effect and Smart Adhesion*. Springer Berlin Heidelberg: Berlin, Heidelberg, 2008; 10.1007/978-3-540-78425-8_12p 231.
140. J. Wang; Q. Yang; M. Wang; C. Wang; L. Jiang, *Soft Matter* **2012**, *8*, 2261.
141. S. Y. Chou; C. C. Yu; Y. T. Yen; K. T. Lin; H. L. Chen; W. F. Su, *Anal. Chem.* **2015**, *87*, 6017.
142. G. Guangming; W. Juntao; Z. Yong; L. Jingang; J. Xu; J. Lei, *Soft Matter* **2014**, *10*, 549.
143. M. Jin; X. Feng; L. Feng; T. Sun; J. Zhai; T. Li; L. Jiang, *Adv. Mater.* **2005**, *17*, 1977.
144. G. Ding; W. Jiao; R. Wang; Y. Niu; L. Hao; F. Yang; W. Liu, *J. Mater. Chem. A* **2017**, *5*, 17325.
145. X. Tang; P. Zhu; Y. Tian; X. Zhou; T. Kong; L. Wang, *Nat. Commun.* **2017**, *8*, 14831.
146. W. Liang; L. Zhu; W. Li; C. Xu; H. Liu, *Langmuir* **2016**, *32*, 5519.
147. L. Wu; Z. Dong; N. Li; F. Li; L. Jiang; Y. Song, *Small* **2015**, *11*, 4837.
148. W. Chen; A. Y. Fadeev; M. C. Hsieh; D. Öner; J. Youngblood; T. J. McCarthy, *Langmuir* **1999**, *15*, 3395.
149. H. Y. Erbil; A. L. Demirel; Y. Avcı; O. Mert, *Science* **2003**, *299*, 1377.
150. W. Ming; D. Wu; R. van Benthem; G. de With, *Nano Lett.* **2005**, *5*, 2298.
151. A. Tuteja; W. Choi; G. H. McKinley; R. E. Cohen; M. F. Rubner, *MRS Bull.* **2008**, *33*, 752.
152. A. Ahuja; J. A. Taylor; V. Lifton; A. A. Sidorenko; T. R. Salamon; E. J. Lobaton; P. Kolodner; T. N. Krupenkin, *Langmuir* **2008**, *24*, 9.
153. J. Song; S. Huang; K. Hu; Y. Lu; X. Liu; W. Xu, *J. Mater. Chem. A* **2013**, *1*, 14783.
154. L. Junyan; W. Li; B. Jingxian; H. Ling, *J. Mater. Chem. A* **2015**, *3*, 20134.
155. P. S. Brown; B. Bhushan, *Sci. Rep.* **2016**, *6*, 21048.
156. A. Tuteja; W. Choi; J. M. Mabry; G. H. McKinley; R. E. Cohen, *Proc. Natl. Acad. Sci. U.S.A.* **2008**, *105*, 18200.
157. A. R. Bielinski; M. Boban; Y. He; E. Kazyak; D. H. Lee; C. Wang; A. Tuteja; N. P. Dasgupta, *ACS Nano* **2017**, *11*, 478.
158. P. S. Brown; B. Bhushan, *APL Mater.* **2016**, *4*, 015703.
159. J. Zhang; H. Zhao, *Surf. Innov.* **2014**, *2*, 103.
160. P. S. Brown; B. Bhushan, *APL Mat.* **2016**, *4*, 015703.
161. J. Yang; Z. Zhang; X. Men; X. Xu; X. Zhu, *New J. Chem.* **2011**, *35*, 576.
162. T. T. Tan; M. R. Reithofer; E. Y. Chen; A. G. Menon; T. S. Hor; J. Xu; J. M. Chin, *J. Am. Chem. Soc.* **2013**, *135*, 16272.

163. N. Vogel; R. A. Belisle; B. Hatton; T. S. Wong; J. Aizenberg, *Nat. Commun.* **2013**, *4*, 2167.
164. W. Kwak; W. Hwang, *Nanotechnology* **2016**, *27*, 055301.
165. J. Yong; F. Chen; Q. Yang; J. Huo; X. Hou, *Chem. Soc. Rev.* **2017**, *46*, 4168.
166. S. P. R. Kobaku; A. K. Kota; D. H. Lee; J. M. Mabry; A. Tuteja, *Angew. Chem. Int. Ed.* **2012**, *51*, 10109.
167. A. Grigoryev; I. Tokarev; K. G. Kornev; I. Luzinov; S. Minko, *J. Am. Chem. Soc.* **2012**, *134*, 12916.
168. Z. Chu; Y. Feng; S. Seeger, *Angew. Chem. Int. Ed.* **2015**, *54*, 2328.
169. Y. K. Lai; Y. X. Tang; J. Y. Huang; F. Pan; Z. Chen; K. Q. Zhang; H. Fuchs; L. F. Chi, *Sci. Rep.* **2013**, *3*, 3009.
170. S. Yang; Y. Si; Q. Fu; F. Hong; J. Yu; S. S. Al-Deyab; M. El-Newehy; B. Ding, *Nanoscale* **2014**, *6*, 12445.
171. M. Liu; S. Wang; Z. Wei; Y. Song; L. Jiang, *Advanced Materials* **2009**, *21*, 665.
172. M. Jin; S. Li; J. Wang; Z. Xue; M. Liao; S. Wang, *Chem. Commun.* **2012**, *48*, 11745.
173. D. Zang; C. Wu; R. Zhu; W. Zhang; X. Yu; Y. Zhang, *Chem. Commun.* **2013**, *49*, 8410.
174. H. Cho; J. Lee; S. Lee; W. Hwang, *Phys. Chem. Chem. Phys.* **2015**, *17*, 6786.
175. C.-F. Wang; H.-C. Huang; L.-T. Chen, *Sci. Rep.* **2015**, *5*, 14294.
176. S. B. G. M. O'Brien; B. H. A. A. van den Brule, *J. Chem. Soc. Faraday Trans.* **1991**, *87*, 1579.
177. M. N. Kavalenka; F. Vüllers; S. Lischker; C. Zeiger; A. Hopf; M. Röhrig; B. E. Rapp; M. Worgull; H. Hölscher, *ACS Appl. Mater. Interfaces* **2015**, *7*, 10651.
178. D. Richard; C. Clanet; D. Quere, *Nature* **2002**, *417*, 811.
179. Y. Liu; L. Moevius; X. Xu; T. Qian; J. M. Yeomans; Z. Wang, *Nature Phys.* **2014**, *10*, 515.
180. S. Srinivasan; G. H. McKinley; R. E. Cohen, *Langmuir* **2011**, *27*, 13582.
181. H. B. Eral; D. J. C. M. 't Mannetje; J. M. Oh, *Colloid Polym. Sci.* **2013**, *291*, 247.
182. J. T. Korhonen; T. Huhtamaki; O. Ikkala; R. H. Ras, *Langmuir* **2013**, *29*, 3858.
183. G. Lamour; A. Hamraoui; A. Buvailo; Y. Xing; S. Keuleyan; V. Prakash; A. Eftekhari-Bafrooei; E. Borguet, *J. Chem. Educ.* **2010**, *87*, 1403.
184. E. Dussan V., *J. Fluid Mech.* **1985**, *151*, 1.
185. J. J. Bikerman, *J. Colloid Sci.* **1950**, *5*, 349.
186. T. L. Liu; C. C. Kim, *Sci. Rep.* **2017**, *7*, 740.
187. H. Zhao; K. Y. Law; V. Sambhy, *Langmuir* **2011**, *27*, 5927.
188. L. Feng; S. Li; Y. Li; H. Li; L. Zhang; J. Zhai; Y. Song; B. Liu; L. Jiang; D. Zhu, *Adv. Mater.* **2002**, *14*, 1857.
189. L. Gao; T. J. McCarthy, *J. Am. Chem. Soc.* **2006**, *128*, 9052.
190. C. Hao; J. Li; Y. Liu; X. Zhou; Y. Liu; R. Liu; L. Che; W. Zhou; D. Sun; L. Li; L. Xu; Z. Wang, *Nat. Commun.* **2015**, *6*, 7986.
191. J. Lin; Y. Cai; X. Wang; B. Ding; J. Yu; M. Wang, *Nanoscale* **2011**, *3*, 1258.
192. W. J. P. Barnes, *Science* **2007**, *318*, 203.
193. K. G. Kornev; D. Monaenkova; P. H. Adler; C. E. Beard; W.-K. Lee. In *The butterfly proboscis as a fiber-based, self-cleaning, micro-fluidic system*, SPIE Newsroom. DOI: 10.1117/2.1201604.006419, 2016; pp 979705.
194. A. J. Werth; J. Potvin, *PLoS ONE* **2016**, *11*, e0150106.
195. F. Migliardini; V. De Luca; V. Carginale; M. Rossi; P. Corbo; C. T. Supuran; C. Capasso, *J. Enzyme Inhib. Med. Chem.* **2014**, *29*, 146.
196. M. Wehner; R. L. Truby; D. J. Fitzgerald; B. Mosadegh; G. M. Whitesides; J. A. Lewis; R. J. Wood, *Nature* **2016**, *536*, 451.
197. L. Wen; J. C. Weaver; G. V. Lauder, *J. Exp. Biol.* **2014**, *217*, 1656.
198. K. Koch; W. Barthlott, *Phil. Trans. R. Soc. A* **2009**, *367*, 1487.
199. K. Koch; I. C. Blecher; G. König; S. Kehraus; W. Barthlott, *Funct. Plant Biol.* **2009**, *36*, 339.

200. T.-S. Wong; S. H. Kang; S. K. Y. Tang; E. J. Smythe; B. D. Hatton; A. Grinthal; J. Aizenberg, *Nature* **2011**, *477*, 443.
201. M. Machida; K. Norimoto; T. Watanabe; K. Hashimoto; A. Fujishima, *J. Mater. Sci.* **1999**, *34*, 2569.
202. M. Ashraf; C. Campagne; A. Perwuelz; P. Champagne; A. Leriche; C. Courtois, *J. Colloid Interface Sci.* **2013**, *394*, 545.
203. J. Tian; D. Kannangara; X. Li; W. Shen, *Lab Chip* **2010**, *10*, 2258.
204. X. Deng; L. Mammen; Y. Zhao; P. Lellig; K. Mullen; C. Li; H. J. Butt; D. Vollmer, *Adv. Mater.* **2011**, *23*, 2962.
205. H. Zhou; H. Wang; H. Niu; A. Gestos; X. Wang; T. Lin, *Adv. Mater.* **2012**, *24*, 2409.
206. Y. Liao; R. Wang; A. G. Fane, *Environ. Sci. Technol.* **2014**, *48*, 6335.
207. F. Xue; D. Jia; Y. Li; X. Jing, *J. Mater. Chem. A* **2015**, *3*, 13856.
208. E. Huovinen; L. Takkunen; T. Korpela; M. Suvanto; T. T. Pakkanen; T. A. Pakkanen, *Langmuir* **2014**, *30*, 1435.
209. Y. Zheng; X. Gao; L. Jiang, *Soft Matter* **2007**, *3*, 178.
210. W. J. Hamilton; M. K. Seely, *Nature* **1976**, *262*, 284.
211. A. R. Parker; C. R. Lawrence, *Nature* **2001**, *414*, 33.
212. X. Gao; X. Yan; X. Yao; L. Xu; K. Zhang; J. Zhang; B. Yang; L. Jiang, *Adv. Mater.* **2007**, *19*, 2213.
213. X. Gao; L. Jiang, *Nature* **2004**, *432*, 36.
214. J.-S. Koh; E. Yang; G.-P. Jung; S.-P. Jung; J. H. Son; S.-I. Lee; P. G. Jablonski; R. J. Wood; H.-Y. Kim; K.-J. Cho, *Science* **2015**, *349*, 517.
215. W. Barthlott; T. Schimmel; S. Wiersch; K. Koch; M. Brede; M. Barczewski; S. Walheim; A. Weis; A. Kaltenmaier; A. Leder; H. F. Bohn, *Adv. Mater.* **2010**, *22*, 2325.
216. M. S. Lehnert; D. Monaenkova; T. Andrukh; C. E. Beard; P. H. Adler; K. G. Kornev, *J. Royal Soc. Interface* **2013**, *10*, 20130336.
217. C. C. Tsai; P. Mikes; T. Andrukh; E. White; D. Monaenkova; O. Burtovyy; R. Burtovyy; B. Rubin; D. Lukas; I. Luzinov; J. R. Owens; K. G. Kornev, *Nanoscale* **2011**, *3*, 4685.
218. H. F. Bohn; W. Federle, *Proc. Natl. Acad. Sci. U.S.A.* **2004**, *101*, 14138.
219. T. S. Wong; S. H. Kang; S. K. Tang; E. J. Smythe; B. D. Hatton; A. Grinthal; J. Aizenberg, *Nature* **2011**, *477*, 443.
220. A. B. Tesler; P. Kim; S. Kolle; C. Howell; O. Ahanotu; J. Aizenberg, *Nat. Commun.* **2015**, *6*, 8649.
221. Q. Liu; Y. Yang; M. Huang; Y. Zhou; Y. Liu; X. Liang, *Appl. Surf. Sci.* **2015**, *346*, 68.
222. H. Y. Erbil, *Surf. Innov.* **2016**, *4*, 214.
223. J. Abe; M. Tenjimbayashi; S. Shiratori, *RSC Adv.* **2016**, *6*, 38018.
224. Y. Liu; M. Andrew; J. Li; J. M. Yeomans; Z. Wang, *Nat. Commun.* **2015**, *6*.
225. C. Hao; Y. Liu; X. Chen; J. Li; M. Zhang; Y. Zhao; Z. Wang, *Small* **2016**, *12*, 1825.
226. F. Schellenberger; J. Xie; N. Encinas; A. Hardy; M. Klapper; P. Papadopoulos; H.-J. Butt; D. Vollmer, *Soft Matter* **2015**, *11*, 7617.
227. L. Feng; Y. Song; J. Zhai; B. Liu; J. Xu; L. Jiang; D. Zhu, *Angew. Chem. Int. Ed.* **2003**, *42*, 800.
228. C. Guo; L. Feng; J. Zhai; G. Wang; Y. Song; L. Jiang; D. Zhu, *ChemPhysChem* **2004**, *5*, 750.
229. S.-H. Jeong; H.-Y. Hwang; S.-K. Hwang; K.-H. Lee, *Carbon* **2004**, *42*, 2073.
230. L. Feng; S. Li; H. Li; J. Zhai; Y. Song; L. Jiang; D. Zhu, *Angew. Chem. Int. Ed.* **2002**, *41*, 1221.
231. C. Su; Y. Xu; F. Gong; F. Wang; C. Li, *Soft Matter* **2010**, *6*, 6068.
232. W. Ye; Q. Shi; J. Hou; J. Jin; Q. Fan; S.-C. Wong; X. Xu; J. Yin, *J. Mater. Chem. B* **2014**, *2*, 7186.
233. P. Peng; Q. Ke; G. Zhou; T. Tang, *J. Colloid Interface Sci.* **2013**, *395*, 326.
234. S.-S. Zhou; Z.-S. Guan; Y. Pang, *Polym. Plast. Technol. Eng.* **2012**, *51*, 845.

235. E. Mele; S. Girardo; D. Pisignano, *Langmuir* **2012**, *28*, 5312.
236. H. Notsu; W. Kubo; I. Shitanda; T. Tatsuma, *J. Mater. Chem.* **2005**, *15*, 1523.
237. A. Tuteja; W. Choi; J. M. Mabry; G. H. McKinley; R. E. Cohen, *Proc. Natl. Acad. Sci. U.S.A.* **2008**, *105*, 18200.
238. M. E. Schrader, *J. Colloid Interface Sci.* **1984**, *100*, 372.
239. P. Sherman. *Emulsion science*. Academic Press: London; New York, 1968.
240. C. J. van Oss. *Interfacial Forces in Aqueous Media, Second Edition*. CRC Press: 2006.
241. S. Wu. *Polymer Interface and Adhesion*. Taylor & Francis: 1982.
242. J. P. Fernández-Blázquez; D. Fell; E. Bonaccurso; A. d. Campo, *J. Colloid Interface Sci.* **2011**, *357*, 234.
243. K.-T. Huang; S.-B. Yeh; C.-J. Huang, *ACS Appl. Mater. Interfaces* **2015**, *7*, 21021.
244. L.-A. O'Hare; S. Leadley; B. Parbhoo, *Surf. Interface Anal.* **2002**, *33*, 335.
245. M. Strobel; V. Jones; C. S. Lyons; M. Ulsh; M. J. Kushner; R. Dorai; M. C. Branch, *Plasma Process. Polym.* **2003**, *8*, 61.
246. K. Li; Q. Shen; Y. Xie; M. You; L. Huang; X. Zheng, *J. Biomater. Appl.* **2016**, *31*, 1062.
247. Sunarso; R. Toita; K. Tsuru; K. Ishikawa, *J. Mater. Sci. Mater. Med.* **2016**, *27*, 127.
248. S. Farris; S. Pozzoli; P. Biagioni; L. Duó; S. Mancinelli; L. Piergiovanni, *Polymer* **2010**, *51*, 3591.
249. Y. Okabe; S. Kurihara; T. Yajima; Y. Seki; I. Nakamura; I. Takano, *Surf. Coat. Technol.* **2005**, *196*, 303.
250. Y. Zhu; J. Zhang; Y. Zheng; Z. Huang; L. Feng; L. Jiang, *Adv. Funct. Mater.* **2006**, *16*, 568.
251. K. S. Siow; L. Britcher; S. Kumar; H. J. Griesser, *Plasma Process. Polym.* **2006**, *3*, 392.
252. S. Tugulu; K. Löwe; D. Scharnweber; F. Schlottig, *J. Mater. Sci. Mater. Med.* **2010**, *21*, 2751.
253. T. Fujima; E. Futakuchi; T. Tomita; Y. Orai; T. Sunaoshi, *Langmuir* **2014**, *30*, 14494.
254. Z. Wang; C. W. Macosko; F. S. Bates, *ACS Appl. Mater. Interfaces* **2014**, *6*, 11640.
255. J. Drelich; T. Payne; J. H. Kim; J. D. Miller; R. Kobler; S. Christiansen, *Polym. Eng. Sci.* **1998**, *38*, 1378.
256. K. Tsougeni; N. Vourdas; A. Tserepi; E. Gogolides; C. Cardinaud, *Langmuir* **2009**, *25*, 11748.
257. P. Patel; C. K. Choi; D. D. Meng, *J. Lab. Autom.* **2010**, *15*, 114.
258. S. Karuppuchamy; J. M. Jeong, *Mater. Chem. Phys.* **2005**, *93*, 251.
259. A. Eshaghi; A. Eshaghi, *Bull. Mater. Sci.* **2012**, *35*, 137.
260. A. Kanta; R. Sedev; J. Ralston, *Langmuir* **2005**, *21*, 2400.
261. V. A. Ganesh; A. S. Nair; H. K. Raut; T. M. Walsh; S. Ramakrishna, *RSC Adv.* **2012**, *2*, 2067.
262. F. Li; Q. Li; H. Kim, *Appl. Surf. Sci.* **2013**, *276*, 390.
263. Q. Li; D. Sun; H. Kim, *Mater. Res. Bull.* **2011**, *46*, 2094.
264. K. Liu; M. Cao; A. Fujishima; L. Jiang, *Chem. Rev.* **2014**, *114*, 10044.
265. X. Zhou; X. Guo; W. Ding; Y. Chen, *Appl. Surf. Sci.* **2008**, *255*, 3371.
266. K. Guan, *Surf. Coat. Technol.* **2005**, *191*, 155.
267. Y. Gao; Y. Masuda; K. Koumoto, *Langmuir* **2004**, *20*, 3188.
268. J. Yu; X. Zhao; Q. Zhao; G. Wang, *Mater. Chem. Phys.* **2001**, *68*, 253.
269. S. Permpoon; M. Houmard; D. Riassetto; L. Rapenne; G. Berthomé; B. Baroux; J. C. Joud; M. Langlet, *Thin Solid Films* **2008**, *516*, 957.
270. H. Y. Lee; Y. H. Park; K. H. Ko, *Langmuir* **2000**, *16*, 7289.
271. J.-M. Wu; H. C. Shih; W.-T. Wu, *Chem. Phys. Lett.* **2005**, *413*, 490.
272. H. Dong; P. Ye; M. Zhong; J. Pietrasik; R. Drumright; K. Matyjaszewski, *Langmuir* **2010**, *26*, 15567.
273. D. Li; Y. Xia, *Nano Lett.* **2003**, *3*, 555.
274. S. H. Hwang; C. Kim; H. Song; S. Son; J. Jang, *ACS Appl. Mater. Interfaces* **2012**, *4*, 5287.

275. C. D. Bain; E. B. Troughton; Y. T. Tao; J. Evall; G. M. Whitesides; R. G. Nuzzo, *J. Am. Chem. Soc.* **1989**, *111*, 321.
276. C. D. Bain; G. M. Whitesides, *Langmuir* **1989**, *5*, 1370.
277. T. R. Lee; R. I. Carey; H. A. Biebuyck; G. M. Whitesides, *Langmuir* **1994**, *10*, 741.
278. H. Hakkinen, *Nature Chem.* **2012**, *4*, 443.
279. J. W. Goodwin; R. S. Harbron; P. A. Reynolds, *Colloid Polym. Sci.* **1990**, *268*, 766.
280. A. Y. Fadeev; T. J. McCarthy, *Langmuir* **1999**, *15*, 3759.
281. M. Lessel; O. Bäumchen; M. Klos; H. Hähl; R. Fetzer; M. Paulus; R. Seemann; K. Jacobs, *Surf. Interface Anal.* **2015**, *47*, 557.
282. J. Sagiv, *J. Am. Chem. Soc.* **1980**, *102*, 92.
283. K. M. R. Kallury; M. Cheung; V. Ghaemmaghami; U. J. Krull; M. Thompson, *Colloids Surf.* **1992**, *63*, 1.
284. D. G. Kurth; T. Bein, *J. Phys. Chem.* **1992**, *96*, 6707.
285. A. Y. Fadeev; R. Helmy; S. Marcinko, *Langmuir* **2002**, *18*, 7521.
286. H. Bader; L. C. Cross; I. Heilbron; E. R. H. Jones, *J. Chem. Soc.* **1949**, 10.1039/JR9490000619, 619.
287. H. Bader, *J. Chem. Soc.* **1956**, 10.1039/JR9560000116, 116.
288. B. D. Fairbanks; T. F. Scott; C. J. Kloxin; K. S. Anseth; C. N. Bowman, *Macromolecules* **2009**, *42*, 211.
289. W. Feng; L. Li; X. Du; A. Welle; P. A. Levkin, *Adv. Mater.* **2016**, *28*, 3202.
290. A. Ulman. *An Introduction to Ultrathin Organic Films: From Langmuir--Blodgett to Self--Assembly*. Elsevier Science: 2013.
291. C. D. Bain; E. B. Troughton; Y. T. Tao; J. Evall; G. M. Whitesides; R. G. Nuzzo, *Journal of the American Chemical Society* **1989**, *111*, 321.
292. S. Pechook; B. Pokroy, *Soft Matter* **2013**, *9*, 5710.
293. W. Zhang; P. Lu; L. Qian; H. Xiao, *Chem. Eng. J.* **2014**, *250*, 431.
294. X. Li; G. Chen; Y. Ma; L. Feng; H. Zhao; L. Jiang; F. Wang, *Polymer* **2006**, *47*, 506.
295. D. Xu; M. Wang; X. Ge; M. Hon-Wah Lam; X. Ge, *J. Mater. Chem.* **2012**, *22*, 5784.
296. Y. Lai; C. Lin; J. Huang; H. Zhuang; L. Sun; T. Nguyen, *Langmuir* **2008**, *24*, 3867.
297. M. Stepien; G. Chinga-Carrasco; J. J. Saarinen; H. Teisala; M. Tuominen; M. Aromaa; J. Haapanen; J. Kuusipalo; J. M. Mäkelä; M. Toivakka, *Wear* **2013**, *307*, 112.
298. Y. Matsumoto; M. Ishida, *Sens. Actuator A-Phys.* **2000**, *83*, 179.
299. J. Bravo; L. Zhai; Z. Wu; R. E. Cohen; M. F. Rubner, *Langmuir* **2007**, *23*, 7293.
300. L. Xu; R. G. Karunakaran; J. Guo; S. Yang, *ACS Appl. Mater. Interfaces* **2012**, *4*, 1118.
301. M. Morra; E. Occhiello; F. Garbassi, *Langmuir* **1989**, *5*, 872.
302. I. Woodward; W. C. E. Schofield; V. Roucoules; J. P. S. Badyal, *Langmuir* **2003**, *19*, 3432.
303. J. Fresnais; J. P. Chapel; F. Poncin-Epaillard, *Surf. Coat. Technol.* **2006**, *200*, 5296.
304. S. R. Coulson; I. Woodward; J. P. S. Badyal; S. A. Brewer; C. Willis, *J. Phys. Chem. B* **2000**, *104*, 8836.
305. Y. Zhang; E. T. Kang; K. G. Neoh; W. Huang; A. C. H. Huan; H. Zhang; R. N. Lamb, *Polymer* **2002**, *43*, 7279.
306. P. Favia; G. Cicala; A. Milella; F. Palumbo; P. Rossini; R. d'Agostino, *Surf. Coat. Technol.* **2003**, *169*, 609.
307. X. Lu; C. Zhang; Y. Han, *Macromol. Rapid Commun.* **2004**, *25*, 1606.
308. Y. Zhang; H. Wang; B. Yan; Y. Zhang; P. Yin; G. Shen; R. Yu, *J. Mater. Chem.* **2008**, *18*, 4442.
309. K. Tadanaga; N. Katata; T. Minami, *J. Am. Ceram. Soc.* **1997**, *80*, 1040.
310. K. Tadanaga; K. Kitamuro; J. Morinaga; Y. Kotani; A. Matsuda; T. Minami, *Chem. Lett.* **2000**, *29*, 864.
311. H. M. Shang; Y. Wang; S. J. Limmer; T. P. Chou; K. Takahashi; G. Z. Cao, *Thin Solid Films* **2005**, *472*, 37.
312. N. J. Shirtcliffe; G. McHale; M. I. Newton; C. C. Perry, *Langmuir* **2003**, *19*, 5626.

313. X. Feng; J. Zhai; L. Jiang, *Angew. Chem. Int. Ed.* **2005**, *44*, 5115.
314. T. Rezayi; M. H. Entezari, *J. Colloid Interface Sci.* **2016**, *463*, 37.
315. W. Zhu; X. Feng; L. Feng; L. Jiang, *Chem. Commun.* **2006**, 10.1039/B603634A, 2753.
316. M. Xing; D. Qi; J. Zhang; F. Chen; B. Tian; S. Bagwas; M. Anpo, *J. Catal.* **2012**, *294*, 37.
317. K. Tadanaga; J. Morinaga; A. Matsuda; T. Minami, *Chem. Mater.* **2000**, *12*, 590.
318. X. Feng; L. Feng; M. Jin; J. Zhai; L. Jiang; D. Zhu, *J. Am. Chem. Soc.* **2004**, *126*, 62.
319. J. V. I. Timonen; M. Latikka; L. Leibler; R. H. A. Ras; O. Ikkala, *Science* **2013**, *341*, 253.
320. J. Boekhoven; W. E. Hendriksen; G. J. M. Koper; R. Eelkema; J. H. van Esch, *Science* **2015**, *349*, 1075.
321. D. A. B. a. G. M. W. Mila Boncheva, *Pure Appl. Chem.* **2003**, *75*, 621.
322. D. H. Gracias; V. Kavthekar; J. C. Love; K. E. Paul; G. M. Whitesides, *Adv. Mater.* **2002**, *14*, 235.
323. U. C. Fischer; H. P. Zingsheim, *J. Vac. Sci. Technol.* **1981**, *19*, 881.
324. J. C. Love; B. D. Gates; D. B. Wolfe; K. E. Paul; G. M. Whitesides, *Nano Lett.* **2002**, *2*, 891.
325. G. Zhang; D. Wang; Z.-Z. Gu; H. Möhwald, *Langmuir* **2005**, *21*, 9143.
326. Z.-Z. Gu; H. Uetsuka; K. Takahashi; R. Nakajima; H. Onishi; A. Fujishima; O. Sato, *Angew. Chem. Int. Ed.* **2003**, *42*, 894.
327. T. N. Van; Y. K. Lee; J. Lee; J. Y. Park, *Langmuir* **2013**, *29*, 3054.
328. Z.-Z. Gu; A. Fujishima; O. Sato, *Appl. Phys. Lett.* **2004**, *85*, 5067.
329. J. Wang; Y. Wen; J. Hu; Y. Song; L. Jiang, *Adv. Funct. Mater.* **2007**, *17*, 219.
330. J. Wang; X. Chen; Y. Kang; G. Yang; L. Yu; P. Zhang, *Appl. Surf. Sci.* **2010**, *257*, 1473.
331. S.-D. Wang; Y.-Y. Shu, *J. Coat. Technol. Res.* **2013**, *10*, 527.
332. X. Yonghao; Z. Lingbo; D. Hess; C. P. Wong. In *Superhydrophobic silicone/PTFE films for biocompatible application in encapsulation of implantable microelectronics devices*, 56th Electronic Components and Technology Conference 2006, 2006; p 7.
333. H. Zhang; X. Zeng; Y. Gao; F. Shi; P. Zhang; J.-F. Chen, *Ind. Eng. Chem. Res.* **2011**, *50*, 3089.
334. J. Lin; C. Zheng; W. Ye; H. Wang; D. Feng; Q. Li; B. Huan, *J. Appl. Polym. Sci.* **2015**, *132*, n/a.
335. T. Wang; G. Liu; J. Kong, *Sci. Rep.* **2015**, *5*, 18328.
336. R. G. Karunakaran; C.-H. Lu; Z. Zhang; S. Yang, *Langmuir* **2011**, *27*, 4594.
337. W. Zhao; X. Wang; M. Li; W. Xi; M. Liu, *Chem. Res. Chin. Univ.* **2014**, *30*, 1071.
338. C. L. Haynes; R. P. Van Duyne, *J. Phys. Chem. B* **2001**, *105*, 5599.
339. J. H. Moon; S. G. Jang; J. M. Lim; S. M. Yang, *Adv. Mater.* **2005**, *17*, 2559.
340. A. Kosiorek; W. Kandulski; H. Glaczynska; M. Giersig, *Small* **2005**, *1*, 439.
341. G. Zhang; D. Wang; H. Möhwald, *Nano Lett.* **2007**, *7*, 127.
342. G. Zhang; D. Wang; H. Möhwald, *Nano Lett.* **2007**, *7*, 3410.
343. L. Zhai; F. Ç. Cebeci; R. E. Cohen; M. F. Rubner, *Nano Lett.* **2004**, *4*, 1349.
344. X. Du; J. He, *ACS Appl. Mater. Interfaces* **2011**, *3*, 1269.
345. J. J. Richardson; M. Björnmalm; F. Caruso, *Science* **2015**, *348*.
346. T. Soeno; K. Inokuchi; S. Shiratori, *Appl. Surf. Sci.* **2004**, *237*, 539.
347. J. Ji; J. Fu; J. Shen, *Adv. Mater.* **2006**, *18*, 1441.
348. X. Zhang; F. Shi; X. Yu; H. Liu; Y. Fu; Z. Wang; L. Jiang; X. Li, *J. Am. Chem. Soc.* **2004**, *126*, 3064.
349. Y. Li; X. Li; W. Guo; M. Wu; J. Sun, *Sci. China Chem.* **2016**, *59*, 1568.
350. H. S. Hwang; N. H. Kim; S. G. Lee; D. Y. Lee; K. Cho; I. Park, *ACS Appl. Mater. Interfaces* **2011**, *3*, 2179.
351. X. H. Xu; Z. Z. Zhang; J. Yang; X. Zhu, *Colloids Surf. A* **2011**, *377*, 70.
352. H. Ogihara; J. Xie; J. Okagaki; T. Saji, *Langmuir* **2012**, *28*, 4605.
353. D. A. Schaeffer; G. Polizos; D. B. Smith; D. F. Lee; S. R. Hunter; P. G. Datskos, *Nanotechnology* **2015**, *26*, 055602.

354. N. Yokoi; K. Manabe; M. Tenjimbayashi; S. Shiratori, *ACS Appl. Mater. Interfaces* **2015**, *7*, 4809.
355. X. Xu; Z. Zhang; W. Liu, *Colloids Surf. A* **2009**, *341*, 21.
356. S. G. Lee; D. S. Ham; D. Y. Lee; H. Bong; K. Cho, *Langmuir* **2013**, *29*, 15051.
357. K. Y. Kim; W. R. Marshall, *AlChE J.* **1971**, *17*, 575.
358. A. Camenzind; H. Schulz; A. Teleki; G. Beaucage; T. Narayanan; S. E. Pratsinis, *Eur. J. Inorg. Chem.* **2008**, *2008*, 911.
359. J. M. Mäkelä; M. Aromaa; H. Teisala; M. Tuominen; M. Stepien; J. J. Saarinen; M. Toivakka; J. Kuusipalo, *Aerosol Sci. Tech.* **2011**, *45*, 827.
360. G. Liu; W. S. Y. Wong; N. Nasiri; A. Tricoli, *Nanoscale* **2016**, *8*, 6085.
361. M. Stepien; J. J. Saarinen; H. Teisala; M. Tuominen; M. Aromaa; J. Haapanen; J. Kuusipalo; J. M. Mäkelä; M. Toivakka, *Langmuir* **2013**, *29*, 3780.
362. M. Stepien; J. J. Saarinen; H. Teisala; M. Tuominen; M. Aromaa; J. Kuusipalo; J. M. Mäkelä; M. Toivakka, *Surf. Coat. Technol.* **2012**, *208*, 73.
363. M. Aromaa; A. Arffman; H. Suhonen; J. Haapanen; J. Keskinen; M. Honkanen; J.-P. Nikkanen; E. Levänen; M. E. Messing; K. Deppert; H. Teisala; M. Tuominen; J. Kuusipalo; M. Stepien; J. J. Saarinen; M. Toivakka; J. M. Mäkelä, *J. Aerosol Sci.* **2012**, *52*, 57.
364. H. Teisala; M. Tuominen; M. Aromaa; J. M. Mäkelä; M. Stepien; J. J. Saarinen; M. Toivakka; J. Kuusipalo, *Surf. Coat. Technol.* **2010**, *205*, 436.
365. H. Teisala; M. Tuominen; M. Stepien; J. Haapanen; J. M. Mákelá; J. J. Saarinen; M. Toivakka; J. Kuusipalo, *Cellulose* **2013**, *20*, 391.
366. J. Lin; B. Ding; J. Yu, *ACS Appl. Mater. Interfaces* **2010**, *2*, 521.
367. T. Brown; A. Slotosch; L. Thibaudeau; A. Taubenberger; D. Loessner; C. Vaquette; P. Dalton; D. Hutmacher, *Biointerphases* **2012**, *7*, 1.
368. N. Nuraje; W. S. Khan; Y. Lei; M. Ceylan; R. Asmatulu, *J. Mater. Chem. A* **2013**, *1*, 1929.
369. I. Sas; R. E. Gorga; J. A. Joines; K. A. Thoney, *J. Polym. Sci. Part B Polym. Phys.* **2012**, *50*, 824.
370. J. Wu; N. Wang; Y. Zhao; L. Jiang, *J. Mater. Chem. A* **2013**, *1*, 7290.
371. N. Zhan; Y. Li; C. Zhang; Y. Song; H. Wang; L. Sun; Q. Yang; X. Hong, *J. Colloid Interface Sci.* **2010**, *345*, 491.
372. L. Jiang; Y. Zhao; J. Zhai, *Angew. Chem. Int. Ed.* **2004**, *43*, 4338.
373. J. Zheng; A. He; J. Li; J. Xu; C. C. Han, *Polymer* **2006**, *47*, 7095.
374. R. Asmatulu; M. Ceylan; N. Nuraje, *Langmuir* **2011**, *27*, 504.
375. N. Zhao; F. Shi; Z. Wang; X. Zhang, *Langmuir* **2005**, *21*, 4713.
376. S. Khorsand; K. Raeissi; F. Ashrafizadeh; M. A. Arenas; A. Conde, *Appl. Surf. Sci.* **2016**, *364*, 349.
377. B. Zhang; Y. Li; B. Hou, *RSC Adv.* **2015**, *5*, 100000.
378. M. H. Kwon; H. S. Shin; C. N. Chu, *Appl. Surf. Sci.* **2014**, *288*, 222.
379. Y. Liu; K. Zhang; W. Yao; C. Zhang; Z. Han; L. Ren, *Ind. Eng. Chem. Res.* **2016**, *55*, 2704.
380. A. Haghdoost; R. Pitchumani, *Langmuir* **2014**, *30*, 4183.
381. S. Wang; L. Feng; H. Liu; T. Sun; X. Zhang; L. Jiang; D. Zhu, *ChemPhysChem* **2005**, *6*, 1475.
382. N. Xu; D. K. Sarkar; X. Grant Chen; H. Zhang; W. Tong, *RSC Adv.* **2016**, *6*, 35466.
383. T. Darmanin; M. Nicolas; F. Guittard, *Phys. Chem. Chem. Phys.* **2008**, *10*, 4322.
384. T. Darmanin; E. Taffin de Givenchy; S. Amigoni; F. Guittard, *Langmuir* **2010**, *26*, 17596.
385. T. Darmanin; F. Guittard, *Synth. Met.* **2015**, *205*, 58.
386. A. Hozumi; O. Takai, *Thin Solid Films* **1997**, *303*, 222.
387. S. Li; H. Li; X. Wang; Y. Song; Y. Liu; L. Jiang; D. Zhu, *J. Phys. Chem. B* **2002**, *106*, 9274.
388. K. K. S. Lau; J. Bico; K. B. K. Teo; M. Chhowalla; G. A. J. Amaratunga; W. I. Milne; G. H. McKinley; K. K. Gleason, *Nano Lett.* **2003**, *3*, 1701.
389. X. Song; J. Zhai; Y. Wang; L. Jiang, *J. Colloid Interface Sci.* **2006**, *298*, 267.

390. G. R. J. Artus; S. Jung; J. Zimmermann; H. P. Gautschi; K. Marquardt; S. Seeger, *Adv. Mater.* **2006**, *18*, 2758.
391. H. Tavana; A. Amirfazli; A. W. Neumann, *Langmuir* **2006**, *22*, 5556.
392. Y. Wu; H. Sugimura; Y. Inoue; O. Takai, *Chem. Vap. Deposition* **2002**, *8*, 47.
393. Y. Wu; Y. Inoue; H. Sugimura; O. Takai; H. Kato; S. Murai; H. Oda, *Thin Solid Films* **2002**, *407*, 45.
394. Y. Wu; M. Bekke; Y. Inoue; H. Sugimura; H. Kitaguchi; C. Liu; O. Takai, *Thin Solid Films* **2004**, *457*, 122.
395. J. D. Miller; S. Veeramasuneni; J. Drelich; M. R. Yalamanchili; G. Yamauchi, *Polym. Eng. Sci.* **1996**, *36*, 1849.
396. Z.-X. Yan; Y.-L. Zhang; W. Wang; X.-Y. Fu; H.-B. Jiang; Y.-Q. Liu; P. Verma; S. Kawata; H.-B. Sun, *ACS Appl. Mater. Interfaces* **2015**, *7*, 27059.
397. C. Becker; J. Petersen; G. Mertz; D. Ruch; A. Dinia, *J. Phys. Chem. C* **2011**, *115*, 10675.
398. R. Jafari; R. Menini; M. Farzaneh, *Appl. Surf. Sci.* **2010**, *257*, 1540.
399. H. Notsu; W. Kubo; I. Shitanda; T. Tatsuma, *J. Mater. Chem.* **2005**, *15*, 1523.
400. Z. Aoyun; R. Liao; C. Guo; Z. Zuo; Y. Yuan. In *Preparation of a superhydrophobic surface by RF magnetron sputtering and its anti-icing performance*, 2015 IEEE Conference on Electrical Insulation and Dielectric Phenomena (CEIDP), 18-21 Oct. 2015; 2015; pp 158.
401. M. Drábik; O. Polonskyi; O. Kylián; J. Čechvala; A. Artemenko; I. Gordeev; A. Choukourov; D. Slavínská; I. Matolínová; H. Biederman, *Plasma Process. Polym.* **2010**, *7*, 544.
402. L. Guoxing; W. Bo; L. Yi; T. Tian; S. Xuemei; L. Er; Y. Hui, *Sci. Technol. Adv. Mater.* **2008**, *9*, 025006.
403. J. Lv; Z. Gong; Z. He; J. Yang; Y. Chen; C. Tang; Y. Liu; M. Fan; W.-M. Lau, *J. Mater. Chem. A* **2017**, *5*, 12435.
404. L. R. J. Scarratt; B. S. Hoatson; E. S. Wood; B. S. Hawkett; C. Neto, *ACS Appl. Mater. Interfaces* **2016**, *8*, 6743.
405. M. Röhrig; M. Mail; M. Schneider; H. Louvin; A. Hopf; T. Schimmel; M. Worgull; H. Hölscher, *Adv. Mater. Interfaces* **2014**, *1*, 1300083.
406. L. Li; V. Breedveld; D. W. Hess, *ACS Appl. Mater. Interfaces* **2012**, *4*, 4549.
407. H. R. T. Bahrami; B. Ahmadi; H. Saffari, *Mater. Res. Express* **2017**, *4*, 055014.
408. M. P. Sousa; J. F. Mano, *Cellulose* **2013**, *20*, 2185.
409. J. S. Li; E. Ueda; A. Nallapaneni; L. X. Li; P. A. Levkin, *Langmuir* **2012**, *28*, 8286.
410. L. Zhang; J. Wu; M. N. Hedhili; X. Yang; P. Wang, *J. Mater. Chem. A* **2015**, *3*, 2844.
411. K. Nakata; S. Nishimoto; Y. Yuda; T. Ochiai; T. Murakami; A. Fujishima, *Langmuir* **2010**, *26*, 11628.
412. S. Nishimoto; A. Kubo; K. Nohara; X. Zhang; N. Taneichi; T. Okui; Z. Liu; K. Nakata; H. Sakai; T. Murakami; M. Abe; T. Komine; A. Fujishima, *Appl. Surf. Sci.* **2009**, *255*, 6221.
413. C.-V. Ngo; D.-M. Chun, *Sci. Rep.* **2016**, *6*, 36735.
414. K. Efimenko; M. Rackaitis; E. Manias; A. Vaziri; L. Mahadevan; J. Genzer, *Nature Mater.* **2005**, *4*, 293.
415. P. K. Byrne; C. Klimczak; A. M. Celal Sengor; S. C. Solomon; T. R. Watters; I. I. S. A. Hauck, *Nature Geosci.* **2014**, *7*, 301.
416. C. F. Guo; V. Nayyar; Z. Zhang; Y. Chen; J. Miao; R. Huang; Q. Liu, *Adv. Mater.* **2012**, *24*, 3010.
417. J. Y. Chung; T. Q. Chastek; M. J. Fasolka; H. W. Ro; C. M. Stafford, *ACS Nano* **2009**, *3*, 844.
418. A. Sabbah; A. Youssef; P. Damman, *Appl. Sci.* **2016**, *6*.
419. J. Xie; X. Han; H. Ji; J. Wang; J. Zhao; C. Lu, *Sci. Rep.* **2016**, *6*, 36686.
420. A. Drame; T. Darmanin; S. Y. Dieng; E. Taffin de Givenchy; F. Guittard, *RSC Adv.* **2014**, *4*, 10935.
421. Y. Li; S. Dai; J. John; K. R. Carter, *ACS Appl. Mater. Interfaces* **2013**, *5*, 11066.

422. S. Varagnolo; F. Raccanello; M. Pierno; G. Mistura; M. Moffa; L. Persano; D. Pisignano, *RSC Adv.* **2017**, *7*, 5836.
423. R. Michael; S. Marc; E. Guénola; O. Farid; P. Fabian; K. Alexander; W. Matthias; H. Hendrik, *J. Micromech. Microeng.* **2013**, *23*, 105014.
424. M. N. Kavalenka; F. Vüllers; J. Kumberg; C. Zeiger; V. Trouillet; S. Stein; T. T. Ava; C. Li; M. Worgull; H. Hölscher, *Sci. Rep.* **2017**, *7*, 39970.
425. C. Zeiger; J. Kumberg; F. Vullers; M. Worgull; H. Holscher; M. N. Kavalenka, *RSC Adv.* **2017**, *7*, 32806.
426. F. Vüllers; G. Gomard; J. B. Preinfalk; E. Klampaftis; M. Worgull; B. Richards; H. Hölscher; M. N. Kavalenka, *Small* **2016**, *12*, 6144.
427. P. Varshney; S. S. Mohapatra; A. Kumar, *International Journal of Smart and Nano Materials* **2016**, *7*, 248.
428. X. Yang; X. Liu; Y. Lu; S. Zhou; M. Gao; J. Song; W. Xu, *Sci. Rep.* **2016**, *6*, 23985.
429. Y. Huang; D. K. Sarkar; X. Grant Chen, *Appl. Surf. Sci.* **2015**, *356*, 1012.
430. S. Wang; L. Jiang, *Adv. Mater.* **2007**, *19*, 3423.
431. Y. Hu; G. Li; J. Cai; C. Zhang; J. Li; J. Chu; W. Huang, *AIP Adv.* **2014**, *4*, 127141.
432. D. Ebert; B. Bhushan, *J. Colloid Interface Sci.* **2012**, *384*, 182.
433. Z. M. Chen, *Express Polym. Lett.* **2010**, *5*, 38.
434. M. Jin; X. Feng; L. Feng; T. Sun; J. Zhai; T. Li; L. Jiang, *Adv. Mater.* **2005**, *17*, 1977.
435. R. Ramanathan; D. E. Weibel, *Appl. Surf. Sci.* **2012**, *258*, 7950.
436. A. Gao; Y. Zhao; Q. Yang; Y. Fu; L. Xue, *J. Mater. Chem. A* **2016**, *4*, 12058.
437. M. J. Nine; T. T. Tung; F. Alotaibi; D. N. H. Tran; D. Losic, *ACS Appl. Mater. Interfaces* **2017**, *9*, 8393.
438. Y. Lai; Y. Chen; Y. Tang; D. Gong; Z. Chen; C. Lin, *Electrochem. Commun.* **2009**, *11*, 2268.
439. K. Okada; Y. Tokudome; P. Falcaro; Y. Takamatsu; A. Nakahira; M. Takahashi, *Chem. Commun.* **2012**, *48*, 6130.
440. M. T. Y. Paul; B. D. Gates, *Colloids Surf. A* **2016**, *498*, 42.
441. H. Yoshida; D. Klee; M. Möller; M. Akashi, *Adv. Funct. Mater.* **2014**, *24*, 6359.
442. M. Cao; X. Jin; Y. Peng; C. Yu; K. Li; K. Liu; L. Jiang, *Adv. Mater.* **2017**, *29*, 1606869.
443. X. Tang; P. Zhu; Y. Tian; X. Zhou; T. Kong; L. Wang, *Nature communications* **2017**, *8*, 14831.
444. M. M. Stanton; R. E. Ducker; J. C. MacDonald; C. R. Lambert; W. G. McGimpsey, *J. Colloid Interface Sci.* **2012**, *367*, 502.
445. S. Yang; S. Chen; Y. Tian; C. Feng; L. Chen, *Chem. Mater.* **2008**, *20*, 1233.
446. J. Yang; Z. Zhang; X. Xu; X. Men; X. Zhu; X. Zhou, *New J. Chem.* **2011**, *35*, 2422.
447. R. Campos; A. J. Guenthner; A. J. Meuler; A. Tuteja; R. E. Cohen; G. H. McKinley; T. S. Haddad; J. M. Mabry, *Langmuir* **2012**, *28*, 9834.
448. T. Darmanin; F. Guittard, *J. Am. Chem. Soc.* **2009**, *131*, 7928.
449. J. M. Mabry; A. Vij; S. T. Iacono; B. D. Viers, *Angew. Chem. Int. Ed.* **2008**, *47*, 4137.
450. M. Tenjimbayashi; M. Higashi; T. Yamazaki; I. Takenaka; T. Matsubayashi; T. Moriya; M. Komine; R. Yoshikawa; K. Manabe; S. Shiratori, *ACS Appl. Mater. Interfaces* **2017**, *9*, 10371.
451. Z. Wang; T. Wu, *J. Phys. Chem. C* **2015**, *119*, 12916.
452. H. Wang; Y. Xue; T. Lin, *Soft Matter* **2011**, *7*, 8158.
453. J. Zimmermann; M. Rabe; G. R. J. Artus; S. Seeger, *Soft Matter* **2008**, *4*, 450.
454. L. Li; V. Breedveld; D. W. Hess, *ACS Appl. Mater. Interfaces* **2013**, *5*, 5381.
455. L. Jiang; Z. Tang; R. M. Clinton; V. Breedveld; D. W. Hess, *ACS Appl. Mater. Interfaces* **2017**, *9*, 9195.
456. H. Zhou; H. Wang; H. Niu; Y. Zhao; Z. Xu; T. Lin, *Adv. Funct. Mater.* **2017**, *27*, 1604261.
457. Z. Xu; Y. Zhao; H. Wang; X. Wang; T. Lin, *Angew. Chem. Int. Ed.* **2015**, *54*, 4527.

458. D. D. Lovingood; W. B. Salter; K. R. Griffith; K. M. Simpson; J. D. Hearn; J. R. Owens, *Langmuir* **2013**, *29*, 15043.
459. B. Leng; Z. Shao; G. de With; W. Ming, *Langmuir* **2009**, *25*, 2456.
460. H. Wang; Y. Xue; J. Ding; L. Feng; X. Wang; T. Lin, *Angew. Chem. Int. Ed.* **2011**, *50*, 11433.
461. H. Zhou; H. Wang; H. Niu; A. Gestos; T. Lin, *Adv. Funct. Mater.* **2013**, *23*, 1664.
462. X. Zhu; Z. Zhang; G. Ren; X. Men; B. Ge; X. Zhou, *J. Colloid Interface Sci.* **2014**, *421*, 141.
463. G. Hayase; K. Nonomura; G. Hasegawa; K. Kanamori; K. Nakanishi, *Chem. Mater.* **2014**, *27*, 3.
464. B. Li; J. Zhang; Z. Gao; Q. Wei, *J. Mater. Chem. A* **2016**, *4*, 953.
465. X. Wang; H. Hu; Q. Ye; T. Gao; F. Zhou; Q. Xue, *J. Mater. Chem.* **2012**, *22*, 9624.
466. B. Li; J. Zhang, *Chem. Commun.* **2016**, *52*, 2744.
467. H. Jin; M. Kettunen; A. Laiho; H. Pynnonen; J. Paltakari; A. Marmur; O. Ikkala; R. H. Ras, *Langmuir* **2011**, *27*, 1930.
468. Y. Wang; B. Bhushan, *ACS Appl. Mater. Interfaces* **2015**, *7*, 743.
469. M. Zhang; T. Zhang; T. Cui, *Langmuir* **2011**, *27*, 9295.
470. C.-T. Hsieh; F.-L. Wu; W.-Y. Chen, *J. Phys. Chem. C* **2009**, *113*, 13683.
471. Z. He; M. Ma; X. Lan; F. Chen; K. Wang; H. Deng; Q. Zhang; Q. Fu, *Soft Matter* **2011**, *7*, 6435.
472. P. S. Brown; B. Bhushan, *J. Colloid Interface Sci.* **2015**, *456*, 210.
473. P. S. Brown; B. Bhushan, *Sci Rep* **2015**, *5*, 8701.
474. P. S. Brown; B. Bhushan, *Sci. Rep.* **2015**, *5*, 14030.
475. Y.-C. Sheen; Y.-C. Huang; C.-S. Liao; H.-Y. Chou; F.-C. Chang, *J. Polym. Sci. Part B Polym. Phys.* **2008**, *46*, 1984.
476. H. Jin; X. Tian; O. Ikkala; R. H. Ras, *ACS Appl. Mater. Interfaces* **2013**, *5*, 485.
477. K. Ellinas; A. Tserepi; E. Gogolides, *Langmuir* **2011**, *27*, 3960.
478. S. Pechook; N. Kornblum; B. Pokroy, *Adv. Funct. Mater.* **2013**, *23*, 4572.
479. X. Zhu; Z. Zhang; X. Xu; X. Men; J. Yang; X. Zhou; Q. Xue, *Langmuir* **2011**, *27*, 14508.
480. J. Zhang; X. Deng; H.-J. Butt; D. Vollmer, *Langmuir* **2014**, *30*, 10637.
481. C.-T. Hsieh; J.-M. Chen; R.-R. Kuo; T.-S. Lin; C.-F. Wu, *Appl. Surf. Sci.* **2005**, *240*, 318.
482. S. Srinivasan; S. S. Chhatre; J. M. Mabry; R. E. Cohen; G. H. McKinley, *Polymer* **2011**, *52*, 3209.
483. P. Muthiah; B. Bhushan; K. Yun; H. Kondo, *J. Colloid Interface Sci.* **2013**, *409*, 227.
484. L. Xiong; L. L. Kendrick; H. Heusser; J. C. Webb; B. J. Sparks; J. T. Goetz; W. Guo; C. M. Stafford; M. D. Blanton; S. Nazarenko; D. L. Patton, *ACS Appl. Mater. Interfaces* **2014**, *6*, 10763.
485. M. Tuominen; H. Teisala; J. Haapanen; J. M. Mäkelä; M. Honkanen; M. Vippola; S. Bardage; M. E. P. Wålinder; A. Swerin, *Appl. Surf. Sci.* **2016**, *389*, 135.
486. G.-R. Choi; J. Park; J.-W. Ha; W.-D. Kim; H. Lim, *Macromol. Mater. Eng.* **2010**, *295*, 995.
487. L. Yi; X. Meng; X. Tian; W. Zhou; R. Chen, *J. Phys. Chem. C* **2014**, *118*, 26671.
488. V. A. Ganesh; S. S. Dinachali; A. S. Nair; S. Ramakrishna, *ACS Appl. Mater. Interfaces* **2013**, *5*, 1527.
489. D. Han; A. J. Steckl, *Langmuir* **2009**, *25*, 9454.
490. T. Fujii; Y. Aoki; H. Habazaki, *Langmuir* **2011**, *27*, 11752.
491. W. Wu; X. Wang; D. Wang; M. Chen; F. Zhou; W. Liu; Q. Xue, *Chem. Commun.* **2009**, 10.1039/B818633B, 1043.
492. D. Wang; X. Wang; X. Liu; F. Zhou, *J. Phys. Chem. C* **2010**, *114*, 9938.
493. L. Cao; T. P. Price; M. Weiss; D. Gao, *Langmuir* **2008**, *24*, 1640.
494. H. Bellanger; T. Darmanin; F. Guittard, *Langmuir* **2012**, *28*, 186.
495. F. Chen; J. Song; Y. Lu; S. Huang; X. Liu; J. Sun; C. J. Carmalt; I. P. Parkin; W. Xu, *J. Mater. Chem. A* **2015**, *3*, 20999.

496. H. Meng; S. Wang; J. Xi; Z. Tang; L. Jiang, *J. Phys. Chem. C* **2008**, *112*, 11454.
497. X. Wang; X. Liu; F. Zhou; W. Liu, *Chem. Commun.* **2011**, *47*, 2324.
498. K. Ellinas; S. P. Pujari; D. A. Dragatogiannis; C. A. Charitidis; A. Tserepi; H. Zuilhof; E. Gogolides, *ACS Appl. Mater. Interfaces* **2014**, *6*, 6510.
499. A. K. Gnanappa; D. P. Papageorgiou; E. Gogolides; A. Tserepi; A. G. Papathanasiou; A. G. Boudouvis, *Plasma Process. Polym.* **2012**, *9*, 304.
500. J. Yu; H. Wang; N. Yin; X. Xu, *RSC Adv.* **2014**, *4*, 24163.
501. J. Y. Lee; S. Pechook; B. Pokroy; J. S. Yeo, *Langmuir* **2014**, *30*, 15568.
502. J. Ou; W. Hu; S. Liu; M. Xue; F. Wang; W. Li, *ACS Appl. Mater. Interfaces* **2013**, *5*, 10035.
503. X. Yao; J. Gao; Y. Song; L. Jiang, *Adv. Funct. Mater.* **2011**, *21*, 4270.
504. Z. Yuan; J. Xiao; C. Wang; J. Zeng; S. Xing; J. Liu, *J. Coat. Technol. Res.* **2011**, *8*, 773.
505. J. Choi; W. Jo; S. Y. Lee; Y. S. Jung; S.-H. Kim; H.-T. Kim, *ACS Nano* **2017**, *11*, 7821.
506. E. F. Hare, *J. Phys. Chem.*, *58*, 236.
507. A. K. Kota; G. Kwon; A. Tuteja, *NPG Asia Mater.* **2014**, *6*, e109.
508. J. M. Mabry; A. Vij; S. T. Iacono; B. D. Viers, *Angew. Chem. Int. Ed.* **2008**, *47*, 4137.
509. K. Nakayama; E. Tsuji; Y. Aoki; S.-G. Park; H. Habazaki, *J. Phys. Chem. C* **2016**, *120*, 15684.
510. A. Grigoryev; I. Tokarev; K. G. Kornev; I. Luzinov; S. Minko, *J Am Chem Soc* **2012**, *134*, 12916.
511. H. Zhou; H. Wang; H. Niu; T. Lin, *Sci. Rep.* **2013**, *3*, 2964.
512. A. R. Wheeler, *Science* **2008**, *322*, 539.
513. J. J. Gilman, *Journal of Applied Physics* **1960**, *31*, 2208.
514. Q. Fu; G. V. Rama Rao; S. B. Basame; D. J. Keller; K. Artyushkova; J. E. Fulghum; G. P. López, *J. Am. Chem. Soc.* **2004**, *126*, 8904.
515. T. Sun; G. Wang; L. Feng; B. Liu; Y. Ma; L. Jiang; D. Zhu, *Angew. Chem. Int. Ed.* **2004**, *43*, 357.
516. R. Wang; K. Hashimoto; A. Fujishima; M. Chikuni; E. Kojima; A. Kitamura; M. Shimohigoshi; T. Watanabe, *Advanced Materials* **1998**, *10*, 135.
517. R. Wang; K. Hashimoto; A. Fujishima; M. Chikuni; E. Kojima; A. Kitamura; M. Shimohigoshi; T. Watanabe, *Adv. Mater.* **1998**, *10*, 135.
518. X. Huang; Y. Sun; S. Soh, *Adv. Mater.* **2015**, *27*, 4062.
519. G. Kwon; A. K. Kota; Y. Li; A. Sohani; J. M. Mabry; A. Tuteja, *Adv. Mater.* **2012**, *24*, 3666.
520. J. Zhang; X. Lu; W. Huang; Y. Han, *Macromol. Rapid Commun.* **2005**, *26*, 477.
521. Z. Xu; Y. Zhao; H. Wang; X. Wang; T. Lin, *Angew. Chem. Int. Ed.* **2015**, *54*, 4527.
522. T. N. Krupenkin; J. A. Taylor; T. M. Schneider; S. Yang, *Langmuir* **2004**, *20*, 3824.
523. X. Yu; Z. Wang; Y. Jiang; F. Shi; X. Zhang, *Adv. Mater.* **2005**, *17*, 1289.
524. A. Nakajima; S.-i. Koizumi; T. Watanabe; K. Hashimoto, *Langmuir* **2000**, *16*, 7048.
525. S. Pan; R. Guo; W. Xu, *Soft Matter* **2014**, *10*, 9187.
526. H. S. Lim; D. Kwak; D. Y. Lee; S. G. Lee; K. Cho, *J. Am. Chem. Soc.* **2007**, *129*, 4128.
527. J. Zhang; J. Li; Y. Han, *Macromol. Rapid Commun.* **2004**, *25*, 1105.
528. J. Lahann; S. Mitragotri; T.-N. Tran; H. Kaido; J. Sundaram; I. S. Choi; S. Hoffer; G. A. Somorjai; R. Langer, *Science* **2003**, *299*, 371.
529. W. Zhu; J. Zhai; Z. Sun; L. Jiang, *J. Phys. Chem. C* **2008**, *112*, 8338.
530. B. Xin; J. Hao, *Chem. Soc. Rev.* **2010**, *39*, 769.
531. G. K. Jennings; E. L. Brantley, *Adv. Mater.* **2004**, *16*, 1983.
532. S. G. Boyes; W. J. Brittain; X. Weng; S. Z. D. Cheng, *Macromolecules* **2002**, *35*, 4960.
533. F. Zhou; H. Hu; B. Yu; V. L. Osborne; W. T. S. Huck; W. Liu, *Anal. Chem.* **2007**, *79*, 176.
534. O. Azzaroni; A. A. Brown; W. T. S. Huck, *Adv. Mater.* **2007**, *19*, 151.
535. B. H. W. Hendriks; S. Kuiper; M. A. J. As; C. A. Renders; T. W. Tukker, *Opt. Rev.* **2005**, *12*, 255.
536. D. Brassard; L. Malic; F. Normandin; M. Tabrizian; T. Veres, *Lab Chip* **2008**, *8*, 1342.

537. S. W. Hwang; S. K. Kang; X. Huang; M. A. Brenckle; F. G. Omenetto; J. A. Rogers, *Adv. Mater.* **2015**, *27*, 47.
538. H. S. Lim; S. H. Park; S. H. Koo; Y. J. Kwark; E. L. Thomas; Y. Jeong; J. H. Cho, *Langmuir* **2010**, *26*, 19159.
539. C. R. Crick; J. A. Gibbins; I. P. Parkin, *J. Mater. Chem. A* **2013**, *1*, 5943.
540. Q. Cheng; M. Li; Y. Zheng; B. Su; S. Wang; L. Jiang, *Soft Matter* **2011**, *7*, 5948.
541. H. Li; Q. Yang; G. Li; M. Li; S. Wang; Y. Song, *ACS Appl. Mater. Interfaces* **2015**, *7*, 9060.
542. P. Ferraro; S. Coppola; S. Grilli; M. Paturzo; V. Vespini, *Nature Nano.* **2010**, *5*, 429.
543. A. Walther; A. H. Muller, *Chem. Rev.* **2013**, *113*, 5194.
544. N. Zhao; M. Gao, *Adv. Mater.* **2009**, *21*, 184.
545. M. M. Kulkarni; R. Bandyopadhyaya; A. Sharma, *J. Mater. Chem.* **2008**, *18*, 1021.
546. X. Pang; C. Wan; M. Wang; Z. Lin, *Angew. Chem. Int. Ed.* **2014**, *53*, 5524.
547. H.-C. Yang; J. Hou; L.-S. Wan; V. Chen; Z.-K. Xu, *Adv. Mater. Interfaces* **2016**, *3*.
548. K. L. Mittal. *Contact Angle, Wettability and Adhesion.* CRC Press: 2009.
549. W. Choi; A. Tuteja; J. M. Mabry; R. E. Cohen; G. H. McKinley, *J. Colloid Interface Sci.* **2009**, *339*, 208.
550. S. C. Lee; B. H. Kim; S. J. Lee, *J. Exp. Biol.* **2014**, *217*, 2013.
551. D. J. Babu; S. N. Varanakkottu; A. Eifert; D. de Koning; G. Cherkashinin; S. Hardt; J. J. Schneider, *Adv. Mater. Interfaces* **2014**, 10.1002/admi.201300049, doi: 10.1002/admi.201300049.
552. K. Golovin; S. P. R. Kobaku; D. H. Lee; E. T. DiLoreto; J. M. Mabry; A. Tuteja, *Sci. Adv.* **2016**, *2*.
553. D. C. Leslie; A. Waterhouse; J. B. Berthet; T. M. Valentin; A. L. Watters; A. Jain; P. Kim; B. D. Hatton; A. Nedder; K. Donovan; E. H. Super; C. Howell; C. P. Johnson; T. L. Vu; D. E. Bolgen; S. Rifai; A. R. Hansen; M. Aizenberg; M. Super; J. Aizenberg; D. E. Ingber, *Nature Biotech.* **2014**, *32*, 1134.
554. A. K. Epstein; B. Pokroy; A. Seminara; J. Aizenberg, *Proceedings of the National Academy of Sciences* **2011**, *108*, 995.
555. D. Glöß; P. Frach; O. Zywitzki; T. Modes; S. Klinkenberg; C. Gottfried, *Surf. Coat. Technol.* **2005**, *200*, 967.
556. D. Tahk; T.-i. Kim; H. Yoon; M. Choi; K. Shin; K. Y. Suh, *Langmuir* **2010**, *26*, 2240.
557. R. Blossey, *Nat. Mater.* **2003**, *2*, 301.
558. S. Shahi, *Nature Photonics* **2010**, *4*, 350.
559. E. Ueda; P. A. Levkin, *Adv. Mater.* **2013**, *25*, 1234.
560. R. P. Garrod; L. G. Harris; W. C. E. Schofield; J. McGettrick; L. J. Ward; D. O. H. Teare; J. P. S. Badyal, *Langmuir* **2006**, *23*, 689.
561. M. Harju; E. Levänen; T. Mäntylä, *Appl. Surf. Sci.* **2006**, *252*, 8514.
562. M. M. Gentleman; J. A. Ruud, *Langmuir* **2009**, *26*, 1408.
563. A. Mills; M. Crow, *Int. J. Photoenergy* **2008**, *2008*, 1.
564. A. Kumar; R. Jose; K. Fujihara; J. Wang; S. Ramakrishna, *Chem. Mater.* **2007**, *19*, 6536.
565. I.-D. Kim; A. Rothschild; B. H. Lee; D. Y. Kim; S. M. Jo; H. L. Tuller, *Nano Lett.* **2006**, *6*, 2009.
566. A. S. Zuruzi; Y. H. Yeo; A. J. Monkowski; C. S. Ding; N. C. MacDonald, *Nanotechnology* **2013**, *24*, 245304.
567. Y. Wang; W. Jia; T. Strout; Y. Ding; Y. Lei, *Sensors* **2009**, *9*.
568. W. Zhang; R. Zhu; L. Ke; X. Liu; B. Liu; S. Ramakrishna, *Small* **2010**, *6*, 2176.
569. P. S. Kumar; S. A. S. Nizar; J. Sundaramurthy; P. Ragupathy; V. Thavasi; S. G. Mhaisalkar; S. Ramakrishna, *J. Mater. Chem.* **2011**, *21*, 9784.
570. D. Dollimore; G. R. Heal, *Carbon* **1967**, *5*, 65.
571. M. I. Loría-Bastarrachea; W. Herrera-Kao; J. V. Cauich-Rodríguez; J. M. Cervantes-Uc; H. Vázquez-Torres; A. Ávila-Ortega, *J. Therm. Anal. Calorim.* **2010**, *104*, 737.

572. Y. Borodko; S. E. Habas; M. Koebel; P. Yang; H. Frei; G. A. Somorjai, *J. Phys. Chem. B* **2006**, *110*, 23052.
573. N. B. Colthup; L. H. Daly; S. E. Wiberley. *Introduction to infrared and Raman spectroscopy*. Academic Press: 1990.
574. H. A. Stone, *Nature Phys.* **2009**, *5*, 178.
575. P. A. Sims; W. J. Greenleaf; H. Duan; X. S. Xie, *Nature Methods* **2011**, *8*, 575.
576. P. T. Hammond. Surface-Directed Colloid Patterning: Selective Deposition via Electrostatic and Secondary Interactions. In *Colloids and Colloid Assemblies: Synthesis, Modification, Organization and Utilization of Colloid Particles*, Caruso, F., Ed. Wiley: Weinheim, Germany, 2003; 10.1002/3527602100.ch10pp 317.
577. Y. Tian; B. Su; L. Jiang, *Adv. Mater.* **2014**, *26*, 6872.
578. S. Tian; L. Li; W. Sun; X. Xia; D. Han; J. Li; C. Gu, *Sci. Rep.* **2012**, *2*, 511.
579. B. A. Kakade, *Nanoscale* **2013**, *5*, 7011.
580. W. H. Chong; L. K. Chin; R. L. Tan; H. Wang; A. Q. Liu; H. Chen, *Angew. Chem. Int. Ed.* **2013**, *52*, 8570.
581. T. Zhu; C. Cai; C. Duan; S. Zhai; S. Liang; Y. Jin; N. Zhao; J. Xu, *ACS Appl. Mater. Interfaces* **2015**, *7*, 13996.
582. X. Yao; Y. Hu; A. Grinthal; T.-S. Wong; L. Mahadevan; J. Aizenberg, *Nature Mater.* **2013**, *12*, 529.
583. Y. Si; Q. Fu; X. Wang; J. Zhu; J. Yu; G. Sun; B. Ding, *ACS Nano* **2015**, *9*, 3791.
584. Z. Wang; L. Ci; L. Chen; S. Nayak; P. M. Ajayan; N. Koratkar, *Nano Lett.* **2007**, *7*, 697.
585. Z. Han; B. Tay; C. Tan; M. Shakerzadeh; K. Ostrikov, *ACS Nano* **2009**, *3*, 3031.
586. B. Kakade; R. Mehta; A. Durge; S. Kulkarni; V. Pillai, *Nano Lett.* **2008**, *8*, 2693.
587. J. Rafiee; M. A. Rafiee; Z.-Z. Yu; N. Koratkar, *Adv. Mater.* **2010**, *22*, 2151.
588. F. Mumm; A. T. J. van Helvoort; P. Sikorski, *ACS Nano* **2009**, *3*, 2647.
589. N. Verplanck; E. Galopin; J.-C. Camart; V. Thomy; Y. Coffinier; R. Boukherroub, *Nano Lett.* **2007**, *7*, 813.
590. Y. Duan; Y. Huang; Z. Yin; N. Bu; W. Dong, *Nanoscale* **2014**, *6*, 3289.
591. R. J. Hamers, *Nature* **2001**, *412*, 489.
592. S. Xu; Z. Yan; K.-I. Jang; W. Huang; H. Fu; J. Kim; Z. Wei; M. Flavin; J. McCracken; R. Wang; A. Badea; Y. Liu; D. Xiao; G. Zhou; J. Lee; H. U. Chung; H. Cheng; W. Ren; A. Banks; X. Li; U. Paik; R. G. Nuzzo; Y. Huang; Y. Zhang; J. A. Rogers, *Science* **2015**, *347*, 154.
593. Y. H. Kim; Y. M. Lee; J. Y. Lee; M. J. Ko; P. J. Yoo, *ACS Nano* **2012**, *6*, 1082.
594. A. K. Epstein; D. Hong; P. Kim; J. Aizenberg, *New J. Phys.* **2013**, *15*, 095018.
595. S. J. Cho; H. Nam; H. Ryu; G. Lim, *Adv. Funct. Mater.* **2013**, *23*, 5577.
596. J. Y. Sun; S. Xia; M. W. Moon; K. H. Oh; K. S. Kim, *Proc. R. Soc. A* **2011**, *468*, 932.
597. D. Kim; D. Jung; J. H. Yoo; Y. Lee; W. Choi; G. S. Lee; K. Yoo; J.-B. Lee, *J. Micromech. Microeng.* **2014**, *24*, 055018.
598. J. Zang; S. Ryu; N. Pugno; Q. Wang; Q. Tu; M. J. Buehler; X. Zhao, *Nature Mater.* **2013**, *12*, 321.
599. Y. C. Chen; A. J. Crosby, *Adv. Mater.* **2014**, *26*, 5626.
600. J. S. Choi; Y. Piao; T. S. Seo, *Biotechnol. Bioprocess Eng.* **2014**, *19*, 269.
601. N. Kashaninejad; W. K. Chan; N.-T. Nguyen, *Langmuir* **2012**, *28*, 4793.
602. N. Kashaninejad; N.-T. Nguyen; W. K. Chan, *Soft Matter* **2013**, *9*, 527.
603. P. K. Chow; E. Singh; B. C. Viana; J. Gao; J. Luo; J. Li; Z. Lin; A. L. Elías; Y. Shi; Z. Wang; M. Terrones; N. Koratkar, *ACS Nano* **2015**, *9*, 3023.
604. Q. Wei; C. Schlaich; S. Prévost; A. Schulz; C. Böttcher; M. Gradzielski; Z. Qi; R. Haag; C. A. Schalley, *Adv. Mater.* **2014**, *26*, 7358.
605. H. Wang; Y. Xue; J. Ding; L. Feng; X. Wang; T. Lin, *Angew. Chem. Int. Ed.* **2011**, *50*, 11433.
606. M. E. Buck; S. C. Schwartz; D. M. Lynn, *Chem. Mater.* **2010**, *22*, 6319.

607. M. Hikita; K. Tanaka; T. Nakamura; T. Kajiyama; A. Takahara, *Langmuir* **2005**, *21*, 7299.
608. G. Polizos; K. Winter; M. J. Lance; H. M. Meyer; B. L. Armstrong; D. A. Schaeffer; J. T. Simpson; S. R. Hunter; P. G. Datskos, *Appl. Surf. Sci.* **2014**, *292*, 563.
609. I.-K. Oh; K. Kim; Z. Lee; K. Y. Ko; C.-W. Lee; S. J. Lee; J. M. Myung; C. Lansalot-Matras; W. Noh; C. Dussarrat; H. Kim; H.-B.-R. Lee, *Chem. Mater.* **2015**, *27*, 148.
610. Y. C. Jung; B. Bhushan, *ACS Nano* **2009**, *3*, 4155.
611. S. A. Bird; D. Clary; K. C. Jajam; H. V. Tippur; M. L. Auad, *Polym. Eng. Sci.* **2013**, *53*, 716.
612. S. C. Kim; D. Klempner; K. S. Frisch; W. Radigan; H. L. Frisch, *Macromolecules* **1976**, *9*, 258.
613. V. Mishra; F. E. Du Prez; E. Gosen; E. J. Goethals; L. H. Sperling, *J. Appl. Polym. Sci.* **1995**, *58*, 331.
614. J. Streque; A. Talbi; P. Pernod; V. Preobrazhensky, *J. Micromech. Microeng.* **2012**, *22*, 095020.
615. G. Liu; W. S. Y. Wong; N. Nasiri; A. Tricoli, *Nanoscale* **2016**, 10.1039/C5NR09000H.
616. W. D. Callister; W. D. C. William D. *Materials Science and Engineering: An Introduction, 7th Edition Wiley Plus Set*. John Wiley & Sons, Limited: 2007.
617. H. Chang; K. Tu; X. Wang; J. Liu, *RSC Adv.* **2015**, *5*, 30647.
618. L. Gao; Y. Lu; X. Zhan; J. Li; Q. Sun, *Surf. Coat. Technol.* **2015**, *262*, 33.
619. K. Dusek; M. Spirkova; I. Havlicek, *Macromolecules* **1990**, *23*, 1774.
620. N. B. Colthup; L. H. Daly; S. E. Wiberley. *Introduction to infrared and Raman spectroscopy*. 3 ed.; Academic Press: 1990; p 542.
621. T. J. Rupert; W. Cai; C. A. Schuh, *Wear* **2013**, *298-299*, 120.
622. R. G. Budynas; J. K. Nisbett; J. E. Shigley. *Shigley's mechanical engineering design*. McGraw-Hill: 2008.
623. Y. Li; J. Liu; J. Jiang; J. Yu, *Dalton Trans.* **2011**, *40*, 6632.
624. J. S. Moore; M. L. Kraft, *Science* **2008**, *320*, 620.
625. W. L. Noorduin; A. Grinthal; L. Mahadevan; J. Aizenberg, *Science* **2013**, *340*, 832.
626. M. Suzuki; K. Saruwatari; T. Kogure; Y. Yamamoto; T. Nishimura; T. Kato; H. Nagasawa, *Science* **2009**, *325*, 1388.
627. J. R. Capadona; K. Shanmuganathan; D. J. Tyler; S. J. Rowan; C. Weder, *Science* **2008**, *319*, 1370.
628. A. G. Volkov; J. C. Foster; V. S. Markin, *Plant Cell Environ.* **2010**, *33*, 816.
629. M. Ma; L. Guo; D. G. Anderson; R. Langer, *Science* **2013**, *339*, 186.
630. Y. A. Vlasov; X.-Z. Bo; J. C. Sturm; D. J. Norris, *Nature* **2001**, *414*, 289.
631. J. D. Paulsen; V. Demery; C. D. Santangelo; T. P. Russell; B. Davidovitch; N. Menon, *Nature Mater.* **2015**, 10.1038/nmat4397, doi: 10.1038/nmat4397.
632. G. McHale; M. I. Newton; N. J. Shirtcliffe; N. R. Geraldi, *Beilstein J. Nanotechnol.* **2011**, *2*, 145.
633. G. McHale, *Langmuir* **2009**, *25*, 7185.
634. B. Bhushan; Y. Chae Jung, *Ultramicroscopy* **2007**, *107*, 1033.
635. P. T. Anastas; W. Leitner; P. G. Jessop. *Handbook of Green Chemistry, Green Solvents, Supercritical Solvents*. Wiley: 2014; Vol. 4.
636. S. Eshraghi; S. Das, *Acta Biomater.* **2010**, *6*, 2467.
637. Q. M. Zhang; V. Bharti; X. Zhao, *Science* **1998**, *280*, 2101.
638. M. Shahinpoor, *J. Intell. Material Syst. Struct.* **1995**, *6*, 307.
639. C. Py; P. Reverdy; L. Doppler; J. Bico; B. Roman; C. N. Baroud, *Eur. Phys. J. ST* **2009**, *166*, 67.
640. X. Guo; H. Li; B. Yeop Ahn; E. B. Duoss; K. J. Hsia; J. A. Lewis; R. G. Nuzzo, *Proc. Natl. Acad. Sci. U.S.A.* **2009**, *106*, 20149.
641. L. Gao; T. J. McCarthy, *Langmuir* **2008**, *24*, 9183.

642. S. Xu; Z. Yan; K. I. Jang; W. Huang; H. Fu; J. Kim; Z. Wei; M. Flavin; J. McCracken; R. Wang; A. Badea; Y. Liu; D. Xiao; G. Zhou; J. Lee; H. U. Chung; H. Cheng; W. Ren; A. Banks; X. Li; U. Paik; R. G. Nuzzo; Y. Huang; Y. Zhang; J. A. Rogers, *Science* **2015**, *347*, 154.
643. A. W. Martinez; S. T. Phillips; G. M. Whitesides; E. Carrilho, *Anal. Chem.* **2009**, *82*, 3.
644. F. Chen; C. N. Lee; S. H. Teoh, *Mater. Sci. Eng. C.* **2007**, *27*, 325.
645. C. Ishino; K. Okumura, *The European physical journal. E, Soft matter* **2008**, *25*, 415.
646. M. H. Zhao; X. P. Chen; Q. Wang, *Sci. Rep.* **2014**, *4*, 5376.
647. L. Liu; S. Guo; J. Chang; C. Ning; C. Dong; D. Yan, *J. Biomed. Mater. Res. Part B Appl. Biomater* **2008**, *87*, 244.
648. C. Wan; B. Chen, *J. Mater. Chem.* **2012**, *22*, 3637.
649. L. A. Girifalco; R. J. Good, *J. Phys. Chem.* **1957**, *61*, 904.
650. T. M. Schutzius; S. Jung; T. Maitra; G. Graeber; M. Köhme; D. Poulikakos, *Nature* **2015**, *527*, 82.
651. M. Liu; S. Wang; Z. Wei; Y. Song; L. Jiang, *Adv. Mater.* **2009**, *21*, 665.
652. W. Kern; G. L. Schnable, *IEEE Trans. Electron Dev.* **1979**, *26*, 647.
653. E. S. Polsen; D. Q. McNerny; B. Viswanath; S. W. Pattinson; A. John Hart, *Sci. Rep.* **2015**, *5*, 10257.
654. K.-Y. Law, *Pure Appl. Chem.* **2015**, *87*.
655. M. Reyssat; D. Richard; C. Clanet; D. Quere, *Faraday Discuss.* **2010**, *146*, 19.
656. J. L. Castillo; S. Martin; D. Rodriguez-Perez; A. Perea; P. L. Garcia-Ybarra, *KONA Powder Part. J.* **2014**, *31*, 214.
657. W. Choi; A. Tuteja; S. Chhatre; J. M. Mabry; R. E. Cohen; G. H. McKinley, *Adv. Mater.* **2009**, *21*, 2190.
658. J. U. Park; M. Hardy; S. J. Kang; K. Barton; K. Adair; D. K. Mukhopadhyay; C. Y. Lee; M. S. Strano; A. G. Alleyne; J. G. Georgiadis; P. M. Ferreira; J. A. Rogers, *Nature Mater.* **2007**, *6*, 782.
659. D. S. Tawfik; A. D. Griffiths, *Nature Biotech.* **1998**, *16*, 652.
660. Y. Schaerli; F. Hollfelder, *Mol. Biosyst.* **2009**, *5*, 1392.
661. A. A. Darhuber; J. P. Valentino; S. M. Troian, *Lab Chip* **2010**, *10*, 1061.
662. J. S. Hong; B. S. Lee; D. Moon; J. G. Lee; I. S. Kang, *Electrophoresis* **2010**, *31*, 1357.
663. J. Y. Huang; Y.-C. Lo; J. J. Niu; A. Kushima; X. Qian; L. Zhong; S. X. Mao; J. Li, *Nature Nano.* **2013**, *8*, 277.
664. D. Byun; Y. Lee; S. B. Q. Tran; V. D. Nugyen; S. Kim; B. Park; S. Lee; N. Inamdar; H. H. Bau, *Appl. Phys. Lett.* **2008**, *92*, 093507.
665. L. Fan; B. Li; J. Zhang, *Adv. Mater. Interfaces* **2015**, *2*, 1500019.
666. G. L. Li; M. Schenderlein; Y. Men; H. Möhwald; D. G. Shchukin, *Adv. Mater. Interfaces* **2014**, 1, DOI: 10.1002/admi.201300019.
667. G. L. Li; Z. Zheng; H. Möhwald; D. G. Shchukin, *ACS Nano* **2013**, *7*, 2470.
668. W. C. Hinds. *Aerosol Technology: Properties, Behavior, and Measurement of Airborne Particles*. John Wiley & Sons: 1982.
669. X.-Q. Feng; X. Gao; Z. Wu; L. Jiang; Q.-S. Zheng, *Langmuir* **2007**, *23*, 4892.
670. Y. Hou; M. Yu; X. Chen; Z. Wang; S. Yao, *ACS Nano* **2015**, *9*, 71.
671. X. Chen; J. Wu; R. Ma; M. Hua; N. Koratkar; S. Yao; Z. Wang, *Adv. Funct. Mater.* **2011**, *21*, 4617.
672. C. Bordes; V. Fréville; E. Ruffin; P. Marote; J. Y. Gauvrit; S. Briançon; P. Lantéri, *Int. J. Pharm.* **2010**, *383*, 236.
673. G. Geiseler; J. Fruwert; R. Hüttig, *Chem. Ber.* **1966**, *99*, 1594.
674. J. N. Israelachvili. *Intermolecular and Surface Forces: With Applications to Colloidal and Biological Systems*. Academic Press: 1985.
675. W. H. Steel; R. A. Walker, *Nature* **2003**, *424*, 296.

676. J. L. C. Santos; P. de Beukelaar; I. F. J. Vankelecom; S. Velizarov; J. G. Crespo, *Sep. Purif. Technol.* **2006**, *50*, 122.
677. D. J. Lyttle; J. R. Lu; T. J. Su; R. K. Thomas; J. Penfold, *Langmuir* **1995**, *11*, 1001.
678. M. Krasowska; M. Ferrari; L. Liggieri; K. Malysa, *Phys. Chem. Chem. Phys.* **2011**, *13*, 9452.
679. J. L. MacCallum; D. P. Tieleman, *J. Am. Chem. Soc.* **2002**, *124*, 15085.